Yanpeng Zhang
Zhiqiang Nie
Min Xiao

Coherent Co
Four-Wave M

Yanpeng Zhang
Zhiqiang Nie
Min Xiao

Coherent Control of Four-Wave Mixing

Yanpeng Zhang
Zhiqiang Nie
Min Xiao

Coherent Control of Four-Wave Mixing

With 190 figures

高等教育出版社
HIGHER EDUCATION PRESS

Springer

Authors:

Prof. Yanpeng Zhang
Key Laboratory for Physical Electronics and Devices of the Ministry of Education
Xi'an Jiaotong University
Xi'an 710049, China
E-mail: ypzhang@mail.xjtu.edu.cn

Zhiqiang Nie
Department of Electronics Science and Technology
Xi'an Jiaotong University
Xi'an 710049, China
E-mail: 01051138@163.com

Prof. Min Xiao
Department of Physics
University of Arkansas
Fayetteville Arkansas 72701, U.S.A.
E-mail: mxiao@uark.edu

ISBN 978-7-04-031339-0
Higher Education Press, Beijing

ISBN 978-3-642-19114-5 ISBN 978-3-642-19115-2 (eBook)
Springer Heidelberg Dordrecht London New York

Printed on acid-free paper

Springer is part of Springer Science + Business Media (www.springer.com)

Preface

The field of nonlinear optics has developed rapidly since the invention of the first laser exactly 50 years ago. Many interesting scientific discoveries and technical applications have been made with nonlinear optical effects in all kinds of nonlinear materials. There are already several excellent general textbooks covering various aspects of nonlinear optics, including *Nonlinear Optics* by Robert W. Boyd, *Nonlinear Optics* by Yuen-Ron Shen, *Quantum Electronics* by Amnon Yariv, *Nonlinear Fiber Optics* by Govind P. Agrawal, etc. These textbooks have provided solid foundations for readers to understand various (secondand third-order) nonlinear optical processes in atomic gas and solid media. The earlier monograph by the authors, *Multi-wave Mixing Processes*, published last year, has presented experimental and theoretical studies of several topics related to multi-wave mixing processes (MWM) previously done in the authors' group. The topics covered in that monograph include ultrafast polarization beats of four-wave mixing (FWM) processes; heterodyne detections of FWM, six-wave mixing (SWM), and eight-wave mixing (EWM) processes; Raman and Rayleigh enhanced polarization beats; coexistence and interactions of MWM processes via electromagnetically induced transparency (EIT). The monograph shows the effects of high-order correlation functions of different noisy fields on the femto- and atto-second polarization beats, and heterodyne/homodyne detections of ultrafast third-order polarization beats. It has also shown the coexistence of FWM and SWM processes in several multi-level EIT systems, as well as interactions between these two different orders of nonlinearities.

This new monograph builds on and extends the previous works, and presents additional and new works done in recent years in the authors' group. Many newly obtained results, extended detail calculations, and more discussions are provided, which can help readers to better understand these interesting nonlinear optical phenomena. Other than showing more results on controls and interactions between MWM processes in hot atomic media, several novel types of spatial solitons in FWM signals are presented and discussed, which are new phenomena in multi-level atomic systems. Chapter 1 reviews some basic concepts to be used in later chapters, such as the nonlinear susceptibility, coherence functions and doubledressing schemes. Chapter 2 extends the previous results on polarization beats to include both difference-frequency femtosecond and sum-frequency attosecond beats in the multi-level

media depending on the specially arranged relative time delays in the multi-colored laser beams. Chapter 3 gives results on Raman, Raman-Rayleigh, Rayleigh-Brillouin, and coexisting Raman-Rayleigh-Brillouin-enhanced polarization beats. Chapter 4 presents multi-dressing FWM processes in confined and non-confined atomic systems with specially-designed spatial patterns and phase-matching conditions for laser beams. Chapter 5 shows enhancement and suppression in FWM processes in multi-level atomic media, generated FWM signals can be selectively enhanced and suppressed via an EIT window. The evolution of dressed effects can be from pure enhancement into pure suppression in degenerate-FWM processes. Chapter 6 demonstrates the modification and control of MWM processes by manipulating the dark-state or EIT windows with polarization states of laser beams via multiple Zeeman sublevels. Chapter 7 shows spatial dispersion properties of the probe and generated FWM beams which can lead to spatial shift and splitting of these weak laser beams. Chapter 8 presents the observations of several novel types of solitons, such as gap, dipole, and vortex solitons, for generated FWM beams in different experimental parametric regions.

Authors believe that this monograph treats some special topics of coherent controls of FWM and MWM and can be useful to researchers interested in related nonlinear MWM processes. Several features presented here are distinctly different and advantageous over previously reported works. For example, authors have shown evolutions of enhancement and suppression of FWM signals due to various dressing schemes by scanning the dressing field detuning. Also theoretical calculations are in good agreement with experimentally measured results in demonstrating enhancement and suppression of MWM processes. Efficient spatial-temporal interference between FWM and SWM signals generated in a four-level atomic system has been carefully investigated, which exhibits controllable interactions between two different (third- and fifth-) order nonlinear optical processes. Such controllable high-order nonlinear optical processes can be used for designing new schemes for all-optical communication and quantum information processing. Authors also experimentally demonstrate that by arranging the strong pump and coupling laser beams in specially-designed spatial configurations (to satisfy phase-matching conditions for efficient FWM processes), generated FWM signals can be spatially shifted and split easily by the cross-phase modulation (XPM) in the Kerr nonlinear medium. Moreover, when the spatial diffraction is balanced by XPM, spatial beam profiles of FWM signals can become stable to form spatial optical solitons. For different input orientations and experimental parameters (such as laser powers, frequency detunings, and temperature), novel gap, vortex, and dipole solitons have been shown to exist in the multi-level atomic systems in vapour cell. These studies have opened the door for achieving rapid responding all-optical controlled spatial switch, routing, and soliton communications.

This monograph serves as a reference book intended for scientists, researchers, advanced undergraduate and graduate students in nonlinear op-

tics.

We take this opportunity to thank many researchers and collaborators who have worked on the research projects as described in this book.

Yanpeng Zhang
Zhiqiang Nie
Min Xiao
October 2010

Contents

3.1.2 Homodyne Detection of Sum-frequency REPB · · · · · · · 89
3.1.3 Heterodyne Detection of Difference-frequency REPB · 104
3.2 Competition Between Raman and Rayleigh-enhanced Four-Wave Mixings in Attosecond Polarization Beats · · · · · · · · · · · 112
3.2.1 Basic Theory · 113
3.2.2 Stochastic Correlation Effects of Rayleigh and Raman-enhanced FWM · 116
3.2.3 The Raman and Rayleigh-enhanced Nonlinear Susceptibility in cw Limit · 124
3.2.4 Homodyne Detection of ASPB · · · · · · · · · · · · · · · · · · · 126
3.2.5 Heterodyne Detection of ASPB · · · · · · · · · · · · · · · · · · 132
3.2.6 Discussion and Conclusion · 140
3.3 Coexisting Brillouin, Rayleigh and Raman-enhanced Four-Wave Mixings · 144
3.3.1 Basic Theory · 145
3.3.2 Homodyne Detection of ASPB · · · · · · · · · · · · · · · · · · · 148
3.3.3 Heterodyne Detection of ASPB · · · · · · · · · · · · · · · · · · 152
3.3.4 Phase Angle · 162
3.3.5 Discussion and Conclusion · 164
References · 166

4 Multi-Dressing Four-Wave Mixing Processes in Confined and Non-confined Atomic System · 169
4.1 Temporal and Spatial Interference Between Four-Wave Mixing and Six-Wave Mixing Channels · · · · · · · · · · · · · · · · · · 169
4.2 Intermixing Between Four-Wave Mixing and Six-Wave Mixing in a Four-level Atomic System · · · · · · · · · · · · · · · · · · 176
4.2.1 Interplay Between FWM and SWM · · · · · · · · · · · · · · · 177
4.2.2 Discussion · 183
4.3 Coexistence of Four-Wave, Six-Wave and Eight-Wave Mixing Processes in Multi-dressed Atomic Systems · · · · · · · · 183
4.3.1 Parallel and Nested Dressing Schemes · · · · · · · · · · · · · 185
4.3.2 Interplay Among Coexisting FWM, SWM and EWM Processes · 193
4.4 Controlled Multi-Wave Mixing via Interacting Dark States in a Five-level System · 198
4.4.1 Basic Theory · 199
4.4.2 Numerical Results · 208

1 Introduction

The subjects of this book focus on mainly around two topics. The first topic (Chapters 2 and 3) covers the ultrafast four-wave mixing (FWM) polarization beats due to interactions between multi-colored laser beams and multi-level media. Both difference-frequency femtosecond and sum-frequency attosecond polarization beats can be observed in multi-level media depending on the specially arranged relative time delays in multi-colored laser beams. The polarization beat signal is shown to be particularly sensitive to the statistical properties of the Markovian stochastic light fields with arbitrary bandwidth. Also, the Raman, Raman-Rayleigh, Rayleigh-Brillouin, coexisting Raman-Rayleigh-Brillouin-enhanced polarization beats due to color-locking noisy field correlations have been studied. Polarization beats between various FWM processes are among the most important ways to study transient properties of media. The second topic (Chapters 4 – 8) relates to the frequency domain and spatial interplays of FWM processes induced by atomic coherence in multi-level atomic systems. FWM processes with different kinds of dual-dressed schemes in ultra-thin, micrometer and long atomic cells, selectively enhanced and suppressed FWM signals via an electromagnetically induced transparency (EIT) window are described, co-existing FWM and six-wave mixing (SWM) processes, especially temporal and spatial interference between them in multi-level EIT media are presented in Chapter 4. Furthermore, These effects of spatial displacements and splitting of the probe and generated FWM beams, as well as the observations of gap soliton trains, vortex solitons of FWM, stable multicomponent vector solitons consisting of two perpendicular FWM dipole components induced by nonlinear cross-phase modulation (XPM) in multi-level atomic media, are shown and investigated in Chapters 5 – 8. Experimental results will be presented and compared with the theoretical calculations throughout the book. Also, emphasis will be given only to the works done by the authors' groups in the past few years. Some of the works presented in this book are built upon our previous book (*Multi-wave Mixing Processes* published by High Education Press & Springer 2009), where we have mainly discussed the co-existence and interactions between efficient multi-wave mixing (MWM) processes enhanced by atomic coherence in multilevel atomic systems. Before starting the main topics of this book, some basic physical concepts and mathematical techniques, which are useful and needed in the later chapters, will be briefly introduced and discussed in

this chapter.

1.1 Nonlinear Susceptibility

For over a decade, one of useful nonlinear optical techniques is the so-called "noisy" light spectroscopy. The ultrashort time resolution of material dynamics has been accomplished by the interferometric probing of wave mixing with broadband, nontransform-limited noisy light beams. The time resolution is determined by the ultrafast correlation time of noisy light and not by its temporal envelope, which is typically a few nanoseconds [1–6]. Such the noisy light source is usually derived from a dye laser modified to permit oscillation over almost the entire bandwidth of the broadband source. The typical bandwidth of the noisy light is about 100/cm, and has a correlation time of 100 fs [7]. In fact, the multimode broadband light has an autocorrelation time similar to the autocorrelation time of the transform-limited femtosecond laser pulse of equivalent bandwidth, although the broadband light can, in principle, be a continuous wave (cw).

In order to describe more precisely what we mean by optical nonlinearity, let us consider how the dipole moment per unit volume, or polarization $\boldsymbol{P}$, of a material system depends on the strength $\boldsymbol{E}$ of the applied optical field. The induced polarization depends nonlinearly on the electric field strength of the applied field in a manner that can be described by the relation $\boldsymbol{P} = \boldsymbol{P}_L + \boldsymbol{P}_{NL}$ [8, 9]. Here, $\boldsymbol{P}_L = \boldsymbol{P}^{(1)} = \varepsilon_0 \boldsymbol{\chi}^{(1)} \cdot \boldsymbol{E}$ and $\boldsymbol{P}_{NL} = \boldsymbol{P}^{(2)} + \boldsymbol{P}^{(3)} + \cdots = \varepsilon_0(\boldsymbol{\chi}^{(2)} : \boldsymbol{EE} + \boldsymbol{\chi}^{(3)} \vdots \boldsymbol{EEE} + \cdots)$.

When we only consider the atomic system (which are isotropic and have inversion symmetry), we can write the total polarization as $P = \varepsilon_0 \chi E$ in general, where the total effective optical susceptibility can be described by a generalized expression of $\chi = \sum_{j=0}^{\infty} \chi^{(2j+1)} |E|^{2j}$. The terms with even-order powers in the applied field strength vanish [8]. The lowest order term $\chi^{(1)}(j = 0)$ is independent of the field strength and is known as the linear susceptibility. The next two terms in the summation, $\chi^{(3)}$ and $\chi^{(5)}$, are known as the third- and fifth-order nonlinear optical susceptibilities, respectively.

FWM refers to nonlinear optical processes with four interacting electromagnetic waves (i.e., with three applied fields to generate the fourth field). In the weak interaction limit, FWM is a pure third-order nonlinear optical process and is governed by the third-order nonlinear susceptibility [8]. Let us consider a special case of FWM processes. The third-order nonlinear polarization governing the process has, in general, three components with different wave vectors $\boldsymbol{k}_1, \boldsymbol{k}_2$, and $\boldsymbol{k}_2'$. $E_1(\omega_1), E_2(\omega_2)$, and $E_2'(\omega_2)$ denote the three input laser fields. Here, ω_i and $\boldsymbol{k}_i$ are the frequency and propagation wave vectors of the ith beam. We can choose to have a small angle θ between the

input pump laser beams $\boldsymbol{k}_2$ and $\boldsymbol{k}_2'$. The probe laser beam (beam $\boldsymbol{k}_1$) propagates along a direction that is almost opposite to that of the beam $\boldsymbol{k}_2$ (see Fig. 1.1). The corresponding nonlinear atomic polarization $P^{(3)}(\omega_1)$ along the $i(i = x, y)$ direction, from first-order perturbation theory, is given by [10]

$$P_i^{(3)}(\omega_1) = \varepsilon_0 \sum_{jkl} \chi_{ijkl}^{(3)} E_{1j}(\omega_1) E_{2k}'^{*}(\omega_2) E_{2l}(\omega_2), \tag{1.1}$$

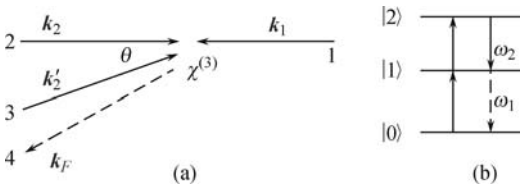

Fig. 1.1. (a) Schematic diagram for the phase-conjugate FWM process. (b) Energy-level diagram for FWM in a close-cycled three-level cascade system.

where the third-order susceptibility contains the microscopic information about the atomic system. The susceptibility of the nonlinear tensor $\chi_{ijkl}^{(3)}(\omega_F; \omega_1, -\omega_2, \omega_2)$ is also related to polarization components of incident and generated fields. For an isotropic medium, as in the atomic vapor, only four elements are not zero, and they are related to each other by $\chi_{xxxx} = \chi_{xxyy} + \chi_{yxxy} + \chi_{yxyx}$. For the generated SWM signal E_S (fields E_2 and E_3 propagate along the direction of beam 2 and E_2' and E_3' propagate along beam 3), the fifth-order nonlinear polarization $P^{(5)}(\omega_1)$ along the $i(i = x, y)$ direction is then given by

$$P_i^{(5)}(\omega_1) = \varepsilon_0 \sum_{jklmn} \chi_{ijklmn}^{(5)} E_{1j}(\omega_1) E_{2k}'^{*}(\omega_2) E_{2l}(\omega_2) E_{3m}'^{*}(\omega_3) E_{3n}(\omega_3), \tag{1.2}$$

where $\chi_{ijklmn}^{(5)}$ is the fifth-order nonlinear susceptibility. For an isotropic medium, there are sixteen nonzero components and only fifteen of them are independent because they are related to each other by

$$\begin{aligned} 3\chi_{xxxxxx} = {} & \chi_{yyxxxx} + \chi_{yxyxxx} + \chi_{yxxyxx} + \chi_{yxxxyx} + \chi_{yxxxxy} + \\ & \chi_{xyyxxx} + \chi_{xyxyxx} + \chi_{xyxxyx} + \chi_{xyxxxy} + \chi_{xxyyxx} + \\ & \chi_{xxyyxx} + \chi_{xxyxyx} + \chi_{xxyxxy} + \chi_{xxxyxy} + \chi_{xxxxyy}. \end{aligned} \tag{1.3}$$

1.2 Coherence Functions

Lasers are inherently noisy devices, in which both phase and amplitude of the field can fluctuate. There are many different stochastic models to describe laser fields. However, since many models of fluctuating laser fields

have identical second-order field correlations, differences among them will become important only if observable effects depend on higher-order field correlations. Noisy light can be used to probe atomic and molecular dynamics, and it offers an unique alternative to the more conventional frequency-domain spectroscopies and ultrashort time-domain spectroscopies [1, 11 – 14]. When the laser field is sufficiently intense that multi-photon interactions occur, the laser spectral bandwidth or spectral shape, obtained from the second-order correlation function, is inadequate to characterize the field. Rather than using higher-order correlation functions explicitly, three different Markovian fields are considered: i.e., (a) the chaotic field, (b) the phase-diffusion field, and (c) the Gaussian-amplitude field.

If laser sources have Lorentzian line shape, we have the second-order coherence function $\langle u_i(t_1)u_i^*(t_2)\rangle = \exp(-\alpha_i|t_1 - t_2|)$ (i.e., $\langle|u_i(t)|^2\rangle = 1$ when $t = t_1 = t_2$). Here, $\alpha_i = \delta\omega_i/2$, with $\delta\omega_i$ being the linewidth of the laser with frequency ω_i. On the other hand, if laser sources are assumed to have Gaussian line shape, then we have

$$\langle u_i(t_1)u_i^*(t_2)\rangle = \exp\Big\{ - \Big[\alpha_i(t_1 - t_2)/2\sqrt{\ln 2}\Big]^2\Big\}.$$

In the following, we only consider the former case. In fact, the form of the second-order coherence function shown above, which is determined by the laser line shape, is the general feature of stochastic models [15].

In this section, three Markovian noise stochastic models, the chaotic field model (CFM), the phase-diffusion model (PDM), and the Gaussian-amplitude model (GAM) are considered at a high enough intensity level to fully appreciate the subtle features of FWM spectroscopy [16, 17].

First, in CFM, we assume that the pump laser is a multimode thermal source and $u(t) = a(t)\mathrm{e}^{\mathrm{i}\phi(t)}$, where $a(t)$ is the fluctuating modulus and $\phi(t)$ is the fluctuating phase. In this case, $u(t)$ has Gaussian statistics with its fourth-order coherence function satisfying [18] $\langle u_i(t_1)u_i(t_2)u_i^*(t_3)u_i^*(t_4)\rangle_{CFM} = \langle u_i(t_1)u_i^*(t_3)\rangle\langle u_i(t_2)u_i^*(t_4)\rangle + \langle u_i(t_1)u_i^*(t_4)\rangle\langle u_i(t_2)u_i^*(t_3)\rangle = \exp[-\alpha_i(|t_1 - t_3| + |t_2 - t_4|)] + \exp[-\alpha_i(|t_1 - t_4| + |t_2 - t_3|)]$. In fact, all higher order coherence functions can be expressed in terms of products of second-order coherence functions. Thus any given $2n$th-order coherence function may be decomposed into the sum of $n!$ terms, each consisting of the product of n second-order coherence functions. The general expression can be obtained as, $\langle u_i(t_1)\cdots u_i(t_n)u_i^*(t_{n+1})\cdots u_i^*(t_{2n})\rangle_{CFM} = \sum_{\pi}\langle u_i(t_1)u_i^*(t_p)\rangle\langle u_i(t_2)u_i^*(t_q)\rangle \cdots \langle u_i(t_n)u_i^*(t_r)\rangle$, where $\sum_{\pi}$ denotes a summation over the $n!$ possible permutations of $(1, 2, \ldots, n)$.

Second, in PDM the dimensionless statistical factor can be written as $u(t) = \mathrm{e}^{\mathrm{i}\phi(t)}$ (i.e., $|u(t)| = 1$) with $\dot{\phi}(t) = \omega(t), \langle\omega_i(t)\omega_i(t')\rangle = 2\alpha_i\delta(t - t'), \langle\omega_j(t)\omega_j(t')\rangle = 2\alpha_j\delta(t - t')$ and $\langle\omega_i(t)\omega_j(t')\rangle = 0$. The second-order co-

herence function for a beam with Lorentzian line shape is given by [19]

$$\begin{aligned}\langle u(t_1)u^*(t_2)\rangle &= \langle \exp i\Delta\phi\rangle \\ &= \exp\left[-\int_0^{t_1-t_2}(t_1-t_2-t)\langle\omega(t_1)\omega(t_1-t)\rangle \mathrm{d}t\right] = \exp(-\alpha|t_1-t_2|).\end{aligned}$$

Here, $\Delta\phi = \phi(t_1) - \phi(t_2) = \int_{t_2}^{t_1}\omega(t)\mathrm{d}t$ has Gaussian statistics, so that $\langle \exp i\Delta\phi\rangle = \exp(-\sigma_{\Delta\phi}^2/2)$. By the classical relation of linear filtering, we have

$$\sigma_{\Delta\phi}^2 = L(t_1-t_2) = 2\int_0^{t_1-t_2}(t_1-t_2-t)\langle\omega(t_1)\omega(t_1-t)\rangle \mathrm{d}t.$$

Now, the fourth-order coherence function can be calculated, which can be written as

$$\begin{aligned}&\langle u_i(t_1)u_i(t_2)u_i^*(t_3)u_i^*(t_4)\rangle_{PDM} \\ &\quad= \exp\{-[L(t_1-t_3)+L(t_1-t_4)+L(t_2-t_3)+L(t_2-t_4)- \\ &\qquad L(t_1-t_2)-L(t_3-t_4)]\} \\ &\quad= \exp[-\alpha_i(|t_1-t_3|+|t_1-t_4|+|t_2-t_3|+|t_2-t_4|)]\times \\ &\qquad \exp[\alpha_i(|t_1-t_2|+|t_3-t_4|)] \\ &\quad= \frac{\langle u_i(t_1)u_i^*(t_3)\rangle\langle u_i(t_2)u_i^*(t_4)\rangle\langle u_i(t_1)u_i^*(t_4)\rangle\langle u_i(t_2)u_i^*(t_3)\rangle}{\langle u_i(t_1)u_i^*(t_2)\rangle\langle u_i(t_3)u_i^*(t_4)\rangle}.\end{aligned}$$

Furthermore, we have the general expression for the second-order coherence function as

$$\begin{aligned}&\langle u_i(t_1)\cdots u_i(t_n)u_i^*(t_{n+1})\cdots u_i^*(t_{2n})\rangle_{PDM} \\ &\qquad= \frac{\prod_{p=1}^{n}\prod_{q=1}^{n}\langle u_i(t_p)u_i^*(t_{n+q})\rangle}{\prod_{p=1}^{n}\prod_{q=p+1}^{n}\langle u_i(t_p)u_i^*(t_q)\rangle\langle u_i(t_{n+p})u_i^*(t_{n+q})\rangle}.\end{aligned}$$

Finally, in GAM, one has $u(t) = a(t)$, where $a(t)$ is real and Gaussian, and fluctuates about a mean value of zero. The fourth-order coherence function of $u(t)$ satisfies [20]

$$\begin{aligned}&\langle u_i(t_1)u_i(t_2)u_i(t_3)u_i(t_4)\rangle_{GAM} \\ &\quad= \langle u_i(t_1)u_i(t_3)\rangle\langle u_i(t_2)u_i(t_4)\rangle + \langle u_i(t_1)u_i(t_4)\rangle\langle u_i(t_2)u_i(t_3)\rangle + \\ &\qquad \langle u_i(t_1)u_i(t_2)\rangle\langle u_i(t_3)u_i(t_4)\rangle \\ &\quad= \langle u_i(t_1)u_i(t_2)u_i(t_3)u_i(t_4)\rangle_{CFM} + \langle u_i(t_1)u_i(t_2)\rangle\langle u_i(t_3)u_i(t_4)\rangle \\ &\quad= \exp[-\alpha_i(|t_1-t_3|+|t_2-t_4|)] + \exp[-\alpha_i(|t_1-t_4|+|t_2-t_3|)] + \\ &\qquad \exp[-\alpha_i(|t_1-t_2|+|t_3-t_4|)].\end{aligned}$$

In fact, according to the moment theorem for real Gaussian random variables, we have the general expression for the $2n$th-order coherence function, as

$$\langle u_i(t_1)\cdots u_i(t_n)u_i(t_{n+1})\cdots u_i(t_{2n})\rangle_{GAM} = \sum_P \prod_{j\neq k'}^{2n} \langle u_i(t_1)u_i(t_k)\rangle,$$

where $\sum_P$ indicates the summation over all possible distinct combinations of the $2n$ variables in pairs.

1.3 Suppression and Enhancement of FWM Processes

In presence of a strong dressing field G_2, the dressed states $|+\rangle$ and $|-\rangle$ can be generated with the separation $\Delta_\pm = 2|G_2|$, as shown in Fig. 1.2. When scanning the frequency of the dressing field, we can obtain the EIT for the probe field and a suppressed FWM signal [Fig. 1.2 (b)], or electromagnetically induced absorption (EIA) for the probe field and an enhanced FWM [Fig. 1.2 (c)]. For the probe field propagating through the medium, we define the baseline versus the dressing field detuning Δ_2 to be at the probe field intensity without the dressing field. Thus, this baseline is just the Doppler-broadened absorption signal of the material. With G_2 beam on, we can obtain one EIT peak at $\Delta_1 + \Delta_2 = 0$, where the transmitted intensity is largest comparing to the baseline. Since there is no energy level in the original position of $|1\rangle$ and the probe field is no longer absorbed by the material, the degree of transmission (or suppression of absorption) of the probe field is highest. An EIA dip is obtained at $\Delta_1 + \Delta_2 = |G_2|^2/\Delta_1$, where the transmitted intensity is smallest compared to the baseline. The reason is that the dressed state $|+\rangle$ or $|-\rangle$ is resonant with the probe field which is absorbed by the material and the degree of transmission (or enhancement of absorption) of the

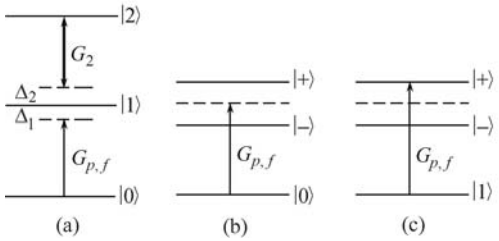

Fig. 1.2. (a) The diagram of the three-level ladder-type system with a dressing field G_2 (and detuning Δ_2). The dressed-state pictures of the (b) suppression (EIT) and (c) enhancement (EIA) of FWM G_f (or probe field G_p with detuning Δ_1) for the two-level system, respectively.

probe field is lowest. Moreover, at $\Delta_1 = 0$, since the transparent degree (or suppression of absorption) of the probe field G_1 is largest, the EIT peak for G_2 is highest. While at certain detuning $|\Delta_1|$, the induced transparent degree decreases and the EIT peak changes lower. When the detuning $|\Delta_1|$ becomes much larger, the degree of transparency decreases and the suppression of absorption changes to an enhancement of absorption.

Then, the enhancement and suppression of FWM signals can be understood as follows: The background versus the dressing field detuning Δ_2 represents the signal intensity of the FWM without dressing field. The dips lower than the background (or suppression peaks at $\Delta_1 + \Delta_2 = 0$) and the peaks higher than the background (enhancement peaks at $\Delta_1 + \Delta_2 = |G_2|^2/\Delta_1$) represent that FWM signals are suppressed and enhanced, respectively.

Figure 1.3 presents suppressed and enhanced FWM signals and the corresponding probe transmission signal versus the probe field detuining Δ_1 and versus the dressing field detuning Δ_3. In this system, two pump fields E_2 and E_2' induce the EIT satisfying the two-photon resonant condition $\Delta_1 + \Delta_2 = 0$ [see the general baseline in Fig. 1.3 (a) versus Δ_1] and generate the FWM signal [see the general background in Fig. 1.3 (b) versus Δ_1]. The dressing field E_3 induces each EIT peak versus Δ_3 (satisfying the condition $\Delta_1 + \Delta_3 = 0$) in Fig. 1.3 (a) and generates the enhancement and suppression of FWM signals versus Δ_3 as shown in Fig. 1.3 (b). Moreover, Fig. 1.3 (c) shows the normalized enhancement and suppression of FWM signals by dividing the background (i.e., the signal intensity of the FWM without dressing field) versu Δ_3.

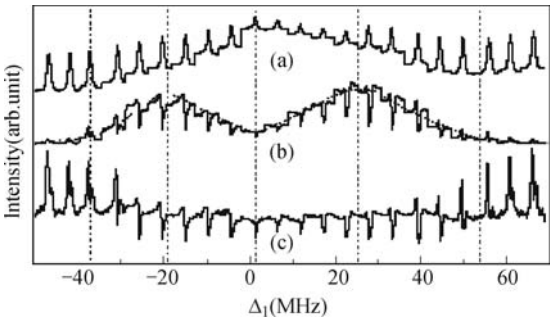

Fig. 1.3. (a) The probe transmission signal; (b) the enhancement and suppression of the FWM signal versus the dressing field detuning Δ_3 for the different value of the probe field detuining Δ_1; (c) the FWM signal normalized by the double-peak FWM signal [dashed curve in (b)].

In Fig. 1.3 (a) one can see that the EIT peaks at large detuning Δ_1 are higher than those near $\Delta_1 = 0$. This phenomenon can be explained as follows: although E_2 EIT window cannot be observed directly when scanning the detuning Δ_3, the E_2 dressing at $\Delta_1 = -\Delta_3 = -\Delta_2 \approx 0$ results in an up-lift of the probe transmission baseline, and the suppression of the probe transmission. At the large detuning of Δ_1 [Fig. 2 (b)], the E_2 field basically

cannot affect the E_3 EIT peaks. Moreover, at certain large detunings of Δ_1, the enhancement of absorption of probe beams will show up.

For the enhancement and suppression of FWM signals in Figs. 1.3 (b) and (c), the curves show enhancement and suppression evolution behaviors when increasing Δ_1. Specifically, FWM signals change from all-enhanced to half-suppressed and half-enhanced, then to all-suppressed around the resonant point, and then to half-suppressed and half-enhanced, and finally to all-enhanced. On the other hand, the suppression of FWM signals at the detunings Δ_1 corresponding to the FWM signal peaks is more obvious than those suppression or enhancement at large Δ_1 in Fig. 1.3 (b), while the normalized all-enhancement of FWM signals at large Δ_1 in Fig. 1.3 (c) is much larger than the cases with half-suppression, half-enhancement and all-suppression signals at small Δ_1.

1.4 Double Dressing Schemes of Probe and Four-Wave Mixing Fields

Recently, Investigations about dressed and doubly-dressed states in multi-level atomic systems interacting with multiple electromagnetic fields have attracted many interests [21 – 24]. The interaction of double-dark states (equivalent to nested scheme of doubly-dressing) and splitting of dark states (equivalent to the secondarily-dressed state) in four-level atomic systems were studied theoretically [25]. Then doubly-dressed states in cold atoms were experimentally observed, in which the triple-photon absorption spectrum exhibits a constructive interference between excitation paths of two closely-spaced, doubly-dressed states [26]. Similar results were obtained in the inverted-Y system [27] and double-Λ system [28].

Similar to the probe field, the generated FWM beam (between states $|0\rangle$ and $|1\rangle$) has the same doubly-dressing behavior. Figure 1.4 shows three kinds of schemes in three four-level systems, respectively, i.e., the nested-cascade scheme in the four-level ladder-type system [Fig. 1.4 (a)], parallel-cascade scheme in the four-level V-type system [Fig. 1.4 (b)], and sequential-cascade scheme in the four-level Y-type system [Fig. 1.4 (c)].

For the nested-cascade doubly-dressing scheme of the probe or FWM field, the two dressing fields (with frequencies ω_2 and ω_3, and Rabi frequencies G_2 and G_3, respectively) connect three neighboring levels ($|1\rangle, |2\rangle$ and $|3\rangle$) and the outer dressing field G_3 is based on the inner dressing field G_2, while this inner field dresses the state of FWM processes. In the perturbation the chain $\rho_{10} \xrightarrow{G_2} \rho_{20} \xrightarrow{G_3} \rho_{30} \xrightarrow{G_3^*} \rho_{20} \xrightarrow{G_2^*} \rho_{10}$ [16], the two dressing fields G_2 and G_3 are intertwined tightly with each other which gives the strongest interaction. In this case, only one term in the FWM expression

$$\rho_{10}^{(3)} \propto G_a\{\Gamma_{10}+\mathrm{i}\Delta_p+G_2^2/[\Gamma_{20}+\mathrm{i}(\Delta_p+\Delta_2)+G_3^2/(\Gamma_{30}+\mathrm{i}(\Delta_p+\Delta_2+\Delta_3))]\}^{-1}$$

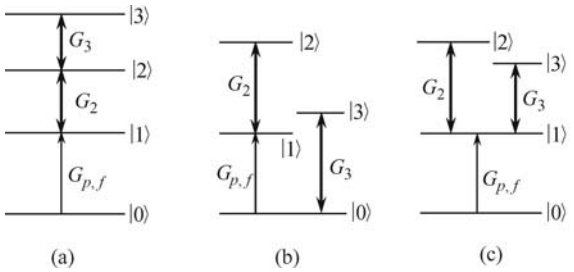

Fig. 1.4. Sketches of the (a) nested-cascade scheme in the four-level ladder-type system; (b) parallel-cascade scheme in the four-level V-type system; and (c) sequential-cascade scheme in the four-level Y-type system. $G_f(G_p, G_2$ and $G_3)$ are the Rabi frequencies of FWM (the probe and the coupling) fields, respectively.

is modified by the dressing fields and if the Rabi frequency of the inner dressing field G_2 is zero, the term for the outer dressing field disappears also, where $G_a = G_p$ for the doubly-dressed probe (DDP) field and $G_a = G_p G_1 G_1'^{*} \Gamma_{00}^{-1} (\Gamma_{10} + \mathrm{i}\Delta_p)^{-1}$ for the doubly-dressed FWM (DDFWM). Γ_{ij} is the transverse relaxation rate between $|i\rangle$ and $|j\rangle$, and Δ_p, Δ_2, and Δ_3 are the frequency detunings of the probe and the coupling fields, respectively. On the other hand, for parallel-cascade double dressing scheme, the dressing fields G_2 and G_3 dress the two different states ($|0\rangle$ and $|1\rangle$, respectively) directly and independently, as shown in Fig. 1.4 (b). In the perturbation the chain $\rho_{10} \xrightarrow{G_2} \rho_{20} \xrightarrow{G_2^*} \rho_{10}$ and $\rho_{10} \xrightarrow{G_3} \rho_{13} \xrightarrow{G_3^*} \rho_{10}$, these two dressing processes are separated and the corresponding terms of dressing fields are independent in the expression of

$$\rho_{10}^{(3)} \propto G_b[\Gamma_{10} + \mathrm{i}\Delta_p + G_2^2/(\Gamma_{20} + \mathrm{i}\Delta_p + \mathrm{i}\Delta_2)]^{-1}[\Gamma_{10} + G_3^2/(\Gamma_{13} + \mathrm{i}\Delta_p - \mathrm{i}\Delta_3)]^{-1},$$

where $G_b = G_p$ for DDP field and $G_b = G_p G_1 G_1'^{*} \Gamma_{00}^{-1}$ for DDFWM. Finally, for the sequential-cascade doubly-dressing scheme, the dressing fields also dress the states directly and independently [both on level $|1\rangle$ as shown in Fig. 1.4 (c)], however, two dressing processes are conjoined by the same density-matrix element in the perturbation the chain $\rho_{10} \xrightarrow{G_2} \rho_{20} \xrightarrow{G_2^*} \rho_{10} \xrightarrow{G_3} \rho_{30} \xrightarrow{G_3^*} \rho_{10}$, so only one term in FWM is modified by the dressing field in the expression:

$$\rho_{10}^{(3)} \propto G_c[\Gamma_{10} + \mathrm{i}\Delta_p + G_2^2/(\Gamma_{20} + \mathrm{i}\Delta_p + \mathrm{i}\Delta_2) + G_3^2/(\Gamma_{30} + \mathrm{i}\Delta_p + \mathrm{i}\Delta_3)]^{-1},$$

where $G_c = G_p$ for DDP field and $G_c = G_p G_1 G_1'^{*} \Gamma_{00}^{-1} (\Gamma_{10} + \mathrm{i}\Delta_p)^{-1}$ for DDFWM.

The interaction between two dressing fields in the nested-cascade scheme is the strongest, and it is the weakest in the parallel-cascade scheme. The sequential-cascade scheme is an intermediate case between the other two

cases. Also, from the dressed-state picture, the dressing fields of the nested-cascade scheme are intertwined tightly with each other. Only the inner dressing field can create primary dressed states, and the outer dressing field can only create secondary dressed states [29, 30]. While for the parallel-cascade scheme, the dressing fields have a weaker interaction, and they can directly create two independent dressed states [31, 32]. However, for the sequential-cascade scheme the dressing field can also directly create dressed states but they have a strong interaction to create primary and secondary dressed states [30]. On the other hand, forms of the nested- and parallel-cascade DDFWM expressions can be converted into forms of the sequential-cascade DDFWM case under the conditions that the outer dressing field is weak or its detuning is large for nested-cascade DDFWM and the two dressing fields are weak for parallel-cascade DDFWM, respectively [30]. Investigations of those different doubly-dressing schemes in multi-level atomic systems can help us to understand the underlying physical mechanisms and to effectively optimize the generated multi-channel nonlinear optical signals. Controlling these processes can have important applications in designing novel nonlinear optical devices in multi-state systems.

1.5 Spatial Optical Modulation via Kerr Nonlinearities

The Kerr effect is a special kind of nonlinear optical phenomenon occurring when intense light beams propagate in crystals, glasses, or gases. Its physical origin is a third-order nonlinear polarization generated in the medium. For self-Kerr nonlinearity, the intense light modifies its own propagation properties, while for the cross-Kerr nonlinearity the propagation properties of a light beam are modified by the interaction with another overlapping beam in a Kerr medium. Actually, the Kerr effect originates from an instantaneously occurring third-order nonlinear response, which can be described as a modification of the refractive index. The refractive index of many optical materials depends on the intensity of the light beam due to special third-order nonlinear responses, which can be written as $n = n_0 + n_2 I$. Here, n_2 is the Kerr nonlinear index proportional to $\chi^{(3)}$. If higher-order (such as fifth) nonlinearity is considered, the nonlinear index n_2 will be influenced by the intensity of the light beam [33]. With weak cw diode lasers in three-level systems sharp dispersion of n_0 can be induced due to the EIT [34], which can slow down the optical pulse propagation. Also, the third-order nonlinear optical Kerr coefficient n_2 of the three-level EIT system has been measured which is greatly enhanced comparing to its two-level subsystem [35]. Since the Kerr nonlinear dispersion in such EIT medium has been shown to have an opposite sign (anomalous dispersion) from the linear dispersion (Fig. 1.5), and they change dramatically near the EIT resonance, the cavity transmission linewidth with such and EIT medium can be greatly modified due to the modified group

index:

$$n_g = (n_0 + n_2 I_p) + \omega_P(\partial n_0/\partial\omega_P + I_p \partial n_2/\partial\omega_P),$$

where I_p is the probe beam intensity, and ω_P is the probe laser beam frequency [36]. The linear and nonlinear dispersion terms (the derivatives) dominate in n_g. Since the two derivatives have opposite signs [8], n_g can take either positive or negative values, depending on the frequency detuning and probe intensity.

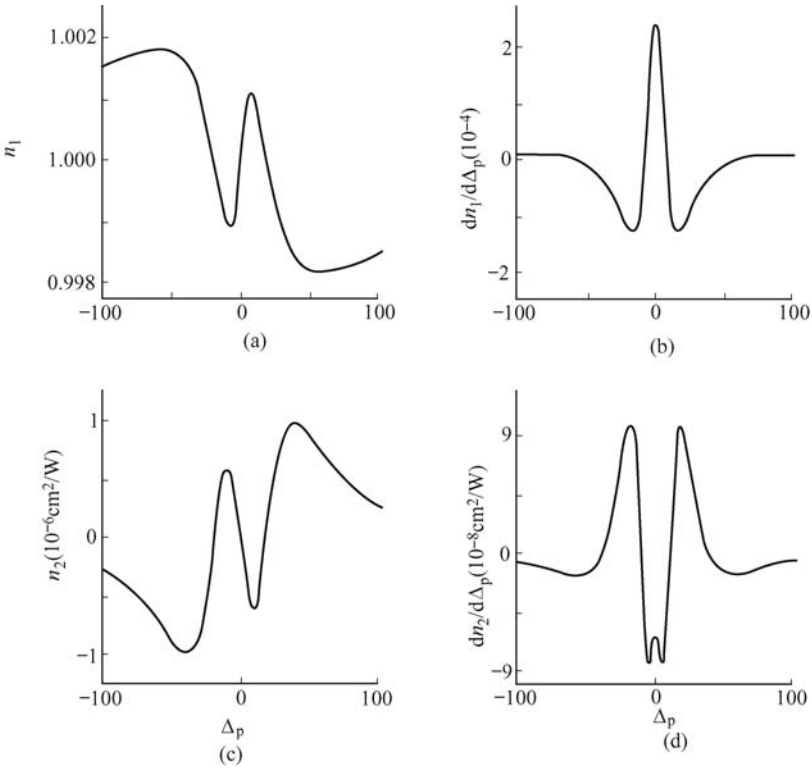

Fig. 1.5. (a) Linear and (c) nonlinear refractive indices and their derivatives (b) and (d), respectively, as a function of Δ_p. Adopted from Ref. [36].

Effects of self- and cross-Kerr nonlinearities also induce phenomena of the self-phase-modulation (SPM) and cross-phase-modulation (XPM) [37] which modulate spatial optical beams. Depending on the sign of the nonlinear refractive index, such an intensity-dependent refractive index can produce either a converging or a diverging wave front to change the transverse beam profile during beam propagation. With SPM a single beam modulates itself during its propagation through medium. When two copropagating or counterpropagating beams modulate each other via nonlinear interaction, it is due to XPM. When $n_2 > 0$, the converging wave front counteracts against diffraction-induced spatial spreading, which can focus the optical

beam to demonstrate the self-focused or the cross-focused beam when the beam power exceeds a critical value. Similarly, when $n_2 < 0$ the diverging wave front increases the natural diverging, which gives the self-defocused or cross-defocused beam. In 1990 Agrawal reported the phenomenon of induced focusing occurring in the self-defocusing nonlinear media as a result of XPM. When a weak optical beam copropagates with an intense pump beam, the XPM-induced interaction between two beams can focus the weak beam, even though the pump beam exhibits self-defocusing. [37] Also, the electromagnetically-induced focusing (EIF) phenomenon was reported in the three-level atomic system [38]. In the three-level EIT system the radial intensity profile of the strong pump laser can generate a modified spatial refractive index profile which is experienced by the weak probe laser as it tunes through the transparency window near resonance. It leads to spatial focusing and defocusing of the probe beam [38].

Equations (1.4 – 1.6) are the Maxwell-Bloch equations under rotating-wave and slowly-vary-envelope approximations, which give the mathematical description of the SPM- and XPM-induced spatial interactions among the probe and two FWM beams for the system as shown in Fig. 1.4.

$$\begin{aligned}
&\frac{\partial E_p}{\partial z}+\frac{\partial E_p}{c\partial t}-\frac{\mathrm{i}\partial^2 E_p}{2\partial t^2}-\frac{\mathrm{i}\nabla_\perp^2 E_p}{2k_p}\\
&\quad=\frac{\mathrm{i}k_p}{n_0}\left[n_1+n_2^{S1}\left|E_p\right|^2+2n_2^{X1}\left|E_1'\right|^2+2n_2^{X2}\left|E_2'\right|^2\right]E_p+\\
&\quad\quad\eta_1 E_1(E_1')^* E_{F1}+\eta_2 E_2(E_2')^* E_{F2}, \qquad (1.4)
\end{aligned}$$

$$\begin{aligned}
&\frac{\partial E_{F1}}{\partial z}+\frac{\partial E_{F1}}{c\partial t}-\frac{\mathrm{i}\partial^2 E_{F1}}{2\partial t^2}-\frac{\mathrm{i}\nabla_\perp^2 E_{F1}}{2k_{F1}}\\
&\quad=\frac{\mathrm{i}k_{F1}}{n_0}\left[n_1+n_2^{S2}\left|E_{F1}\right|^2+2n_2^{X3}\left|E_1'\right|^2\right]E_{F1}+\\
&\quad\quad\eta_3 E_1(E_1')^* E_p+\eta_4 E_2(E_2')^* E_{F2}, \qquad (1.5)
\end{aligned}$$

$$\begin{aligned}
&\frac{\partial E_{F2}}{\partial z}+\frac{\partial E_{F2}}{c\partial t}-\frac{\mathrm{i}\partial^2 E_{F2}}{2\partial t^2}-\frac{\mathrm{i}\nabla_\perp^2 E_{F2}}{2k_{F2}}\\
&\quad=\frac{\mathrm{i}k_{F2}}{n_0}\left[n_1+n_2^{S3}\left|E_{F2}\right|^2+2n_2^{X4}\left|E_2'\right|^2\right]E_{F2}+\\
&\quad\quad\eta_5 E_1(E_1')^* E_{F1}+\eta_6 E_2(E_2')^* E_p. \qquad (1.6)
\end{aligned}$$

Here, on the left side of these equations, the first terms describe the beam propagation, the second terms give the dispersion ones, the third terms are for the second-order dispersion, and the fourth terms describe the diffraction of the beams diverging propagation. On the right hand, the first terms are the linear response, the second terms are for the nonlinear self-Kerr effects, the third terms [the third and fourth terms for Eq. (1.4)] describe nonlinear cross-Kerr effects, the fourth and fifth terms [the fifth and sixth terms for Eq. (1.4)] represent the phase-matched coherent FWM process. z is the longitudinal

coordinate in the propagation direction and $k_p = k_{F1} = \omega_1 n_0/c$. n_0 and n_1 are the linear refractive index at ω_1 in vacuum and medium, respectively. n_2^{S1} is the self-Kerr nonlinear coefficient of the field $\boldsymbol{E}_3, n_2^{S2}$ is the self-Kerr nonlinear coefficient for the generated FWM field $\boldsymbol{E}_{F1}$, and n_2^{S3} is the self-Kerr nonlinear coefficient for the generated FWM field $\boldsymbol{E}_{F2}$. n_2^{X1} is the cross-Kerr nonlinear coefficient of the field $\boldsymbol{E}_3$ induced by the strong pump field $\boldsymbol{E}_1', n_2^{X2}$ is the cross-Kerr nonlinear coefficient of the field $\boldsymbol{E}_3$ induced by the strong pump field $\boldsymbol{E}_2', n_2^{X3}$ is the cross-Kerr nonlinear coefficient of the field $\boldsymbol{E}_{F1}$ induced by the strong pump field $\boldsymbol{E}_1', n_2^{X4}$ is the cross-Kerr nonlinear coefficient of the field $\boldsymbol{E}_{F2}$ induced by the strong pump field $\boldsymbol{E}_2'$. In general the Kerr nonlinear coefficients can be defined as $n_2 = Re\,\chi^{(3)}/(\varepsilon_0 c n_0)$, where the third-order nonlinear susceptibility is given by $\chi^{(3)} = D\rho_{10}^{(3)}$ with $D = N\mu_p^2\mu_{i0}^2/(\hbar^3\varepsilon_0 G_p G_i^2)$. $\mu_p(\mu_{i0})$ is the dipole matrix element between the states coupled by the probe beam $\boldsymbol{E}_p$ (between $|i\rangle$ and $|0\rangle$). η_i are the constants. $\rho_{10}^{(3)}$ can be determined from the density-matrix equations for the multi-level medium.

The strong pump beam distorts the phase profiles of the probe and FWM beams through XPM, which induces spatial modifications of the probe and FWM beams, including spatial displacement and splitting, and produces spatial solitons. Thus, we can neglect the dispersion, linear term, and coherent FWM processes in the equations, for the moment for simplicity. Actually, these simplified differential equations are still difficult to solve analytically. By assuming Gaussian profiles for input fields, we can use a numerical approach (i.e., the split-step Fourier method [37]) to solve Eqs. (1.4–1.6). However, the numerical solution of three-dimensional equations requires a considerable computing resource with both x and y directions. For simplicity, we only consider one dimension in the y-direction. For example, one can consider Eq. (1.5) and obtain

$$\frac{\partial E_{F1}(z,y)}{\partial z} = \left[\frac{\mathrm{i}}{2k_{F1}}\frac{\partial}{\partial y^2} + \frac{\mathrm{i}k_{F1}}{n_0}\left(n_2^{S2}\left|E_{F1}\right|^2 + 2n_2^{X3}\left|E_1'\right|^2\right)\right]E_{F1}(z,y). \tag{1.7}$$

The solution of this equation is approximately $E_{F1}(z+h,y) \approx Exp[\mathrm{i}h\hat{D}] \cdot Exp[\mathrm{i}h\hat{N}]E_{F1}(z,y)$ [37]. Here h is the step-length, $\hat{D} = (2k_{F1})^{-1}\partial/\partial y^2$ is the diffraction functor and $\hat{N} = k_{F1}(n_2^{S2}\left|E_{F1}\right|^2 + 2n_2^{X3}\left|E_1'\right|^2)/n_0$ is the SPM and XPM functor. Finally we can use the split-step Fourier method to obtain the numerical solution. Furthermore, If we also neglect the diffraction term and the small SPM contribution, Eqs. (1.4–1.6) can be readily solved to obtain the XPM-induced phase shift ϕ_{NL} imposed on the probe and FWM beams by the pump. In this case, Equation (1.7) reduces to

$$\frac{\partial E_{F1}(z,y)}{\partial z} = \left(\frac{\mathrm{i}2k_{F1}}{n_0}n_2^{X3}\left|E_1'\right|^2\right)E_{F1}(z,y), \tag{1.8}$$

which gives $E_{F1}(z,y) = E_{F1}(0,y)\exp(\mathrm{i}\phi_{NL})$ with $\phi_{NL}(z,y) = 2k_{F1}n_2^{X3} \cdot \left|E_1'\right|^2 z/n_0$. The additional transverse propagation wave-vector is $dk_y = \phi'_{NL}$

[37]. Here, the strong field E' has a Gaussian profile, like the solid line in Fig. 1.6 (a). In this case, when $n_2^{X3} > 0, \phi_{NL}$ has a positive Gaussian profile [see the thick solid line in Fig. 1.6 (a)] and dk_y is shown by the dash line in Fig. 1.6 (a). The arrows in Fig. 1.6 (a) represent the direction of dk_y. The direction of dk_y is always towards the beam center of the pump field, and therefore, the weak $\boldsymbol{E}_{p,F1,F2}$ fields [the thin solid lines in Fig. 1.6 (a)] are shifted to the pump field center. When $n_2^{X3} < 0, \phi_{NL}$ has a negative Gaussian profile [see the thick solid line in Fig. 1.6 (b)] and the direction of dk_y [the dash line in Fig. 1.6 (b)] is outward from the beam center of the pump field, thus $\boldsymbol{E}_{p,F1,F2}$ is shifted away from the pump field [see Fig. 1.6 (b)].

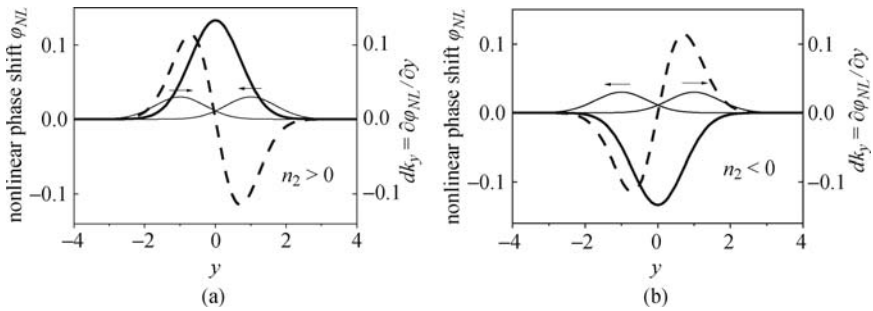

Fig. 1.6. Instantaneous nonlinear phase shift induced by a Gaussian beam in a (a) focusing and (b) defocusing nonlinear medium and the corresponding contribution to the one-dimensional component of the propagation vector.

Recently, spatial displacements of the probe and generated FWM beams have been observed in a three-level V-type, and two-level atomic systems near resonance [39]. The observed spatial shift curves as a function of frequency detuning reflect the typical enhanced cross-Kerr nonlinear dispersion properties in the EIT system. This dispersion-like spatial deflection is named as electromagnetically-induced spatial dispersion (EISD). The spatial beam displacements can be controlled by the strong control laser beam and the atomic density. Such EISD can be used as a single way to measure the Kerr-nonlinear refractive indices for the multi-level atomic media. Also, it can be used for controllable all-optical spatial switching and routing of optical signals [40]. The spot shifts of the FWM and probe laser beams can be used as the "on" and "off" states of the spatial all-optical switch. The extinction ratio for the on/off state, as well as the beam shift distances and directions, can be optimized by modulating frequency detunings, intensities, and temperature of the medium. At the same time, beam shifts in opposite directions have been realized simultaneously for different FWM beams, which could be employed to construct switching/routing arrays. Then, spatial shifts and splittings of FWM signal beams induced by additional dressing laser beams were investigated which are caused by the enhanced cross-Kerr nonlinearity due to atomic coherence in the atomic system. The spatial separation and number of the split FWM beam can both be controlled by the

intensity of the dressing beam, and by the modified Kerr nonlinearity and atomic density. Although the spatial beam shifting and splitting have been reported in previous works [41], current atomic systems have some advantages: (1) large beam shift and splitting can be achieved due to enhanced Kerr nonlinearity induced by atomic coherence; (2) the "dispersion" curve for the beam displacement has been measured for the probe beam and matched to the calculated cross-Kerr nonlinear index; (3) displacements and splitting of FWM signal beams are experimentally demonstrated, which have never been done before; (4) specially-designed spatial beam configuration was used to achieve the unique phase-matching conditions for FWM processes, and for the beam shiftings and splittings at the same time; (5) current multi-level systems have much better experimental controls with additional laser beams; (6) such studies can have important applications in the spatial image storage, spatial entanglement, and spatial quantum correlation of laser beams.

1.6 Formations and Dynamics of Novel Spatial Solitons

A spatial soliton can be formed when the diffraction of a laser beam is compensated by self-focusing or cross-Kerr effects in a Kerr nonlinear medium [42, 43]. In recent years, many new spatial soliton effects, such as discrete solitons [44, 45], gap solitons [46], surface gap solitons [47, 48], and vortex solitons [49], have been investigated (both theoretically and experimentally) in waveguide arrays [48], fiber Bragg gratings [50], Bose-Einstein condensates [51], and photorefractive crystals [44, 45]. In achieving such interesting spatial effects, large refractive index modulations are needed by either fixed periodic structures (such as waveguide arrays and fiber Bragg grating) or reconfigurable optical lattices by laser beams as in the photorefractive crystals [46]. Gap soliton exists in band gaps of the linear spectra in various structures, and the forward- and backward-propagating waves both experience Bragg scattering and form of the periodic structure, which are coupled nonlinearly [42]. A vortex soliton appears as the self-trapping of a phase singularity and from which a screw-type phase distribution is generated where the real and imaginary parts of the field amplitude are zero. Spatially modulated vortex solitons (azimuthons) have been theoretically considered in self-focusing nonlinear media [49]. Transverse energy flow occurs between the intensity peaks (solitons) associated with the phase structure, which is a staircase-like nonlinear function described by the factor $\exp(im\varphi)$, where φ is the azimuthal coordinate and the integer number m is defined as the topological charge. If a phase mask is used to introduce certain phase delay for half of the soliton beam, the soliton can split into two parts with opposite (π) phases between them, called dipole-mode vector soliton with a Hermite-Gaussian mode structure [52]. The dipole-mode vector soliton is a vector soliton originated from trapping of a dipole-mode beam. In an optically-induced two-dimensional

photonic lattice, dipole-mode solitons can be created with either opposite phases or same phase between the two parts [53]. Vector solitons with one nodeless fundamental component and another dipole-mode component can couple to each other and be trapped jointly in the photonic lattices [52, 54]. A radially symmetric vortex-mode soliton can decay into a radially asymmetric dipole-mode soliton that has a nonzero angular momentum, which can survive for a very long propagation distance [52]. Spatial multi-component soliton has vectorial interaction, mutually self-trapping in a nonlinear medium, and their total intensity profile exhibits multiple humps [55].

Spatial gap solitons, dipole mode spatial solitons, and modulated vortex solitons of FWM in multi-level atomic systems are presented in Chapter 8 with details. For example, Section 8.3 shows the experimental observation of vortex solitons of FWM in the multi-level atomic media created by interference patterns with three or more superposition waves. The modulation effect of vortex solitons is induced by the cross-Kerr nonlinear dispersion due to atomic coherence in the multi-level atomic system. These FWM vortex patterns are explained via the three-, four- and five-wave interference topologies. The complex amplitude vectors can be overlaid at the observation plane and give rise to the total complex amplitude vector (C_X, C_Y) of interfering planewaves [13, 14]. The local structures of optical vortices are given by the polarization ellipse relation

$$[C_X^2/(T_X^2+T_Y^2)]\sin^2(\beta+\alpha)+[C_Y^2/(T_X^2+T_Y^2)]\cos^2(\beta+\alpha)=1, \qquad (1.9)$$

where $\beta=\arctan(T_X/T_Y)$, and α is the ellipse orientation. The ellipse axes T_X, T_Y are related to the spatial configuration of laser beams (including the incident beam directions, phase differences between beams, etc.) and their intensities. Section 3.1 presents experimental results of generating gap soliton trains in FWM signals. Such novel spatial FWM gap soliton trains are induced in the periodically modulated self-defocusing atomic medium by the cross-phase modulation, which can be reshaped under different experimental conditions, such as different atomic densities, nonlinear dispersions, and dressing fields. Effects due to the frequency detuning and intensity dependences of the refractive index are considered in addition to its one-dimensional (axis ξ) periodic variation by using $n(\Delta, I, \xi)=n_1(\Delta)+n_2(\Delta)I+\delta n(\xi)$, where I is the dressing field intensity. $\delta n=n_2\cos(2\pi\xi/\Lambda)$ accounts for the periodic index variation inside the grating. The grating period is given by $\Lambda=\lambda/\theta$, where θ is the angle between the two pump beams. Section 3.2 describes the formation of a novel type of stable multicomponent vector solitons consisting of two perpendicular FWM dipole components induced by XPM. The formation and steering of the steady dipole solitons and their dynamical (energy transfer) effects have been analyzed. The dipole-mode solitons of two FWM processes have horizontal and vertical orientations, respectively, which can coexist in the same atomic system, and their characteristics can be compared directly. In detail, we consider the incoherent superposition of two dipole components, u_2 and u_3, as a generalization of a two-component dipole-model

soliton $\{u_1, V\}$. This two-component come from a three-component solution $\{u_1, u_2, u_3\}$. The transformation of the dipole components is $V \rightarrow \{u_2, u_3\}$, where $u_2 = V\cos\alpha$ and $u_3 = V\sin\alpha$ (α is a transformation parameter). Such a straightforward generalization is indeed possible for an N-component system [55].

The gap, dipole and vortex solitons have all been observed before in photorefractive crystals [56 – 61]. However, the works presented in Chapter 8 are done in multi-level atomic systems, which have quite different nonlinear properties compared to the photorefractive systems used before to observe such as gap, dipole and vortex solitons. As we have demonstrated, the multi-level atomic systems have well-controlled linear, as well as nonlinear, absorption and dispersion properties, which are essential in generating such interesting spatial gap, vortex and multi-component dipole solitons in atomic meida. Without the enhanced Kerr nonlinearities due to atomic choherence [23], it will be hard to reach the needed index contrast for observing these novel spatial soliton phenomena. With several well-controlled experimental parameters, one can drive the Kerr medium to different parameter regions to investigate richer spatial soliton phenomena (such as formation and dynamics), better explore parametric spaces, and compare with theoretical predictions. Observing such solitons and studying their dynamics in FWM is not a simple extension of previous results, but a significant breakthrough to explore different nonlinear regions and mechanism for forming such spatial dipole solitons and their evolutions. In solid-state materials, tenable parametric spaces are limited, so certain theoretically predicted phenomena are not reachable in the experiments. However, in multi-level atomic systems, the tenable region for parameters is broadened, which can be used to explore interesting phenomena, such as transition from one type of spatial soliton to another and energy transfer between different dipole modes. Also, previous spatial solitons in solid materials were all done in the probe beam, not for FWM beams as in the multi-level atomic media, where Kerr-nonlinear FWM processes are greatly enhanced and become more efficient. The tenable parameters, such as atomic density, coupling/pumping field intensities, and frequency detunings can be easily and independently controlled experimentally, which are important in reaching different regions of the system. Due to the nature of induced atomic coherence in the system, the enhanced Kerr indices change dramatically with experimental parameters and can reach high values. Combining with the use of pulsed laser beams with high beam intensities, the refractive index contrast $\Delta n = n_2 I$ in the multi-level atomic system reaches the high value, so those interesting novel solitons can be observed. Also, since the high Kerr index is induced by the strong dressing/pumping laser beams, it is the cross-Kerr nonlinearity that plays an essential role in controlling these novel solitons, not the self-Kerr coefficients as in the cases for photon-refractive materials. The basic behaviors and mechanics are different between the multi-level atomic systems and photorefractive crystals in observing these novel solitons. Such controllable spatial dispersion properties

and spatial solitons can find useful applications in designing new devices for spatial all-optical switching and logic gate for optical communications and all-optical signal processing.

References

[1] Morita N, Yajima T. Ultrahigh-time-resolution coherent transient spectroscopy with incoherent light. Phys Rev A, 1984, 30: 2525 – 2536.

[2] Golub J E, Mossberg T W. Studies of picosecond collisional dephasing in atomic sodium vapor using broad-bandwidth transient 4-wave-mixing. J Opt Soc Am B, 1986, 3: 554 – 559.

[3] Ulness D J, Stimson M J, Kirkwood J C, et al. Time-resolved coherent Raman spectroscopy controlled by spectrally tailored noisy light. J Raman Spectrosc 1997, 28: 917 – 925.

[4] Ulness D J, Albrecht A C. Four-wave mixing in a Bloch two-level system with incoherent laser light having a Lorentzian spectral density: analytic solution, a diagrammatic approach. Phys Rev A, 1996, 53: 1081 – 1095.

[5] DeMott D C, Ulness D J, Albrecht A C. Femtosecond temporal probes using spectrally tailored noisy quasi-cw laser light. Phys Rev A, 1997, 55: 761 – 771.

[6] Kirkwood J C, Albrecht A C. Down-conversion of electronic frequencies and their dephasing dynamics: Interferometric four-wave-mixing spectroscopy with broadband light. Phys Rev A, 2000, 61: 033802.

[7] Kirkwood J C, Albrecht A C, Ulness D J, et al. Fifth-order nonlinear Raman processes in molecular liquids using quasi-cw noisy light. II Experiment. J Chem Phys, 1999, 111: 272 – 280.

[8] Boyd R W. Nonlinear optics. New York: Academic Press, 1992.

[9] Shen Y R. The principles of nonlinear optics. New York: Wiley, 1984.

[10] Zhu C J, Senin A A, Lu Z H, et al. Polarization of signal wave radiation generated by parametric four-wave mixing in rubidium vapor: Ultrafast (∼150-fs) and nanosecond time scale excitation. Phys Rev A, 2005, 72: 023811.

[11] Ulness D J. On the role of classical field time correlations in noisy light spectroscopy: color locking and a spectral filter analogy. J Phys Chem A, 2003, 107: 8111 – 8123.

[12] Kirkwood J C, Ulness D J, Albrecht A C. On the classification of the electric field spectroscopies: application to Raman scattering. J Phys Chem A, 2000, 104: 4167 – 4173.

[13] Booth E C, Berger B G, Johnson Z C, et al. Analysis of Raman-enhanced nondegenerate four-wave mixing with factorized time correlator diagrams. J Opt Soc Am B, 2006, 23: 885 – 892.

[14] Ulness D J, Albrecht A C. Theory of time-resolved coherent Raman scattering with spectrally tailored noisy light. J Raman Spectrosc, 1997, 28: 571 – 578.

[15] Georges A T. Resonance fluorescence in Markovian stochastic fields. Phys Rev A 1980, 21: 1561 – 1572.

[16] Zhang Y P, Gan C L, Song J P, et al. Coherent laser control in attosecond sum-frequency polarization beats using twin noisy driving fields. Phys Rev A, 2005, 71: 023802.

[17] Zhang Y P, Araujo C B, Eyler E E. Higher-order correlation on polarization beats in Markovian stochastic fields. Phys Rev A, 2001, 63: 043802.

[18] Fu P M, Jiang Q, Mi X, et al. Rayleigh-type nondegenerate four-wave mixing: ultrafast measurement and field correlation. Phys Rev Lett, 2002, 88: 113902.

[19] Picinbono B, Boileau E. Higher-order coherence functions of optical fields and phase fluctuations. J Opt Soc Am, 1968, 58: 784 – 786.

[20] Goodman J W. Statistical optics. New York: Wiley, 1985, Chap 2.

[21] Harris S E. Electromagnetically induced transparency. Phys Today, 1997, 50: 36 – 42.

[22] Gea-Banacloche J, Li Y, Jin S, et al. Electromagnetically induced transparency in ladder-type inhomogeneously broadened media: Theory and experiment. Phys Rev A,1995, 51: 576 – 584.

[23] Wu Y, Saldana J, Zhu Y F. Large enhancement of four-wave mixing by suppression of photon absorption from electromagnetically induced transparency. Phys Rev A, 2003, 67: 013811.

[24] Wilson E A, Manson N B, Wei C. Perturbing an electromagnetically induced transparency in a Λ system using a low-frequency driving field. II. Four-level system. Phys Rev A, 2005, 72: 063814.

[25] Lukin M D, Yelin S F, Fleischhauer M, et al. Quantum interference effects induced by interacting dark resonances. Phys Rev A,1999, 60: 3225.

[26] Yan M, Rickey E G, Zhu Y F. Observation of doubly dressed states in cold atoms. Phys Rev A, 2001, 64: 013412.

[27] Drampyan R, Pustelny S, Gawlik W. Electromagnetically induced transparency versus nonlinear Faraday effect: Coherent control of light-beam polarization. Phys Rev A, 2009, 80: 033815; Joshi A and Xiao M Phase gate with a four-level inverted-Y system. Phys Rev A, 2005, 72: 062319; Joshi A and Xiao M Generalized dark-state polaritons for photon memory in multilevel atomic media Phys Rev A, 2005, 71: 041801.

[28] Han Y, Liu Y, Zhang C, et al. Interacting dark states with enhanced nonlinearity in an ideal four-level tripod atomic system. Phys Rev A, 2008, 77: 023824; Rebic S, Vitali D, Ottaviani C, et al. Polarization phase gate with a tripod atomic system. Phys Rev A, 2004, 70: 032317.

[29] Zhang Y P, Xiao M. Generalized dressed and doubly-dressed multiwave mixing. Opt Exp, 2007, 15: 7182 – 7189.

[30] Nie Z Q, Zheng H B, Li P Z, et al. Interacting multiwave mixing in a five-level atomic system. Phys Rev A, 2008, 77: 063829.

[31] Zhang Y P, Anderson B, Xiao M. Coexistence of four-wave, six-wave and eight-wave mixing processes in multi-dressed atomic systems. J Phys B: At Mol Opt Phys, 2008, 41: 045502 – 045513.

[32] Nie Z Q, Zhang Y P, Zhao Y, et al, Enhancing and suppressing four-wavemixing in electromagnetically induced transparency window. J Raman Spectrosc, 2010, 41: 409 – 419.

[33] Michinel H, Paz-Alonso M J, Perez-Garcia V M. Turning light into a liquid via atomic coherence. Phys Rev Lett, 2006, 96: 023903.

[34] Xiao M, Li Y Q, Jin S, et al. Measurement of dispersive properties of electromagnetically induced transparency in rubidium atoms. Phys Rev Lett, 1995, 74: 666 – 669.

[35] Wang H, Goorskey D, Xiao M. Enhanced Kerr nonlinearity via atomic coherence in a three-level atomic system. Phys Rev Lett, 2001, 87: 073601.

[36] Wu H B, Xiao M, Cavity linewidth narrowing and broadening due to competing linear and nonlinear dispersions. Opt Lett, 2007, 32: 3122 – 3124.

[37] Agrawal G P Induced focusing of optical beams in self-defocusing nonlinear media. Phys Rev Lett, 1990, 64: 2487.

[38] Moseley R R, Shepherd S, Fulton D J, et al. Spatial consequences of Electromagnetically Induced Transparency: observation of Electromagnetically Induced Focusing. Phys Rev Lett, 1995, 74: 670 – 672.

[39] Zhang Y P, Nie Z Q, Zheng H B, et al. Electromagnetically-induced spatial nonlinear dispersion in four-wave mixing. Phys Rev A, 2009, 80: 013835.

[40] Nie Z Q, Zheng H B, Zhang Y P, et al. Experimental demonstration of optical switching and routing via four-wave mixing spatial shift. Opt Exp, 2010, 18: 899 – 902.

[41] Hickmann J M, Gomes A S L, Araujo C B. Observation of spatial cross-phase modulation effects in a self-defocusing nonlinear medium. Phys Rev Lett, 1992, 68: 3547 – 3550.

[42] Kivshar Y S, Agrawal G P. Optical solitons: from fibers to photonic crystals. San Diego: Academic, 2003.

[43] Swartzlander A G, Law C T. Optical vortex solitons observed in Kerr nonlinear media. Phys Rev Lett, 1992, 69, 2503 – 2506.

[44] Chen Z G, Martin H, Eugenieva E D, et al. Formation of discrete solitons in light-induced photonic lattices. Opt Express, 2005, 13: 1816 – 1819.

[45] Zhang P, Liu S, Zhao J, et al. Optically induced transition between discrete and gap solitions in a nonconventionally biased photorefractive crystal. Opt Let, 2008, 33: 878 – 880.

[46] Neshev D, Sukhorukov A A, Hanna B, et al. Controlled Generation and Steering of Spatial Gap Solitions. Phys Rev Lett, 2004, 93: 083905.

[47] Kartashov Y V, Vysloukh V A, Torner L Surface Gap Solitons. Phys Rev Lett, 2006, 96: 073901.

[48] Rosberg C R, Neshev D N, Krolikowski W, et al. Observation of Surface Gap Solitons in Semi-Infinite Waveguide Arrays. Phys Rev Lett, 2006, 97, 083901.

[49] Desyatnikov A S, Sukhorukov A A, Kivshar Y S. Azimuthons: Spatially Modulated Vortex Solitons. Phys Rev Lett, 2005, 95: 203904.

[50] Eggleton B J, Slusher R E, Sterke C M, et al. Grating Solitons. Phys Rev Lett, 1996, 76: 1627 – 1630.

[51] Eiermann B, Anker Th, Albiez M, et al. Bright bose-einstein gap solitons of atoms with repulsive interaction. Phys Rev Lett, 2004, 92: 230401.

[52] Krolikowski W, Ostrovskaya E A, Weilnau C, et al. Observation of Dipole-Mode Vector Solitons. Phys Rev Lett, 2000, 85: 1424 – 1427.

[53] Yang J K, Makasyuk I, Bezryadina A, et al. Dipole solitons in optically induced two-dimensional photonic lattices. Opt Lett, 2004, 29: 1662 – 1664.

[54] Chen Z G, Bezryadina A, Makasyuk I, et al. Observation of two-dimensional lattice vector solitons. Opt Lett, 2004, 29: 1656 – 1658.

[55] Desyatnikov A S, Kivshar Y S, Motzek K, et al. Multicomponent dipole-mode spatial solitons, Opt Let 2002, 27, 634 – 636.

[56] Anderson B P, Haljan P C, Regal C A, et al. Watching dark solitons decay into vortex rings in a Bose-Einstein condensate. Phys Rev Lett, 2001, 86: 2926 – 2929.

[57] Williams J E, Holland M J. Preparing topological states of a Bose-Einstein condensate. Nature, 1999, 401: 568 – 572.

[58] Matthews M R, Anderson B P, Haljan P C, et al. Vortices in a Bose-Einstein Condensate. Phys Rev Lett, 1999, 83: 2498 – 2501.

[59] Gorbach A V, Skryabin D V, Harvey C N. Vortex solitons in an off-resonant Raman medium. Phys Rev A, 2008, 77: 063810.

[60] Gorbach A V, Skryabin D V. Cascaded generation of multiply charged optical vortices and spatiotemporal helical beams in a Raman medium. Phys Rev Lett, 2007, 98: 243601.

[61] Tang L G, Lou C B, Wang X S, et al. Observation of dipole-like gap solitons in self-defocusing waveguide lattices. Opt Lett, 2007, 32: 3011 – 3014; Petrov D V, Torner L, Martorell J, et al. Observation of azimuthal modulational instability and formation of patterns of optical solitons in a quadratic nonlinear crystal. Opt Lett, 1998, 23: 1444 – 1446.

2 Ultrafast Polarization Beats of Four-Wave Mixing Processes

Four-level difference-frequency polarization beat (FLPB) and attosecond sum-frequency polarization beat (ASPB) with broadband noisy light are investigated using chaotic field, phase-diffusion, and Gaussian-amplitude models. The difference-frequency polarization beat signal is shown to be particularly sensitive to statistical properties of Markovian stochastic light fields with arbitrary bandwidth. Different stochastic models of laser fields only affect fourth-order coherence functions. The constant background of beat signal originates from the amplitude fluctuation of Markovian stochastic fields. The Gaussian-amplitude field shows fluctuations larger than the chaotic field, which again exhibits fluctuations much larger than those for the phase-diffusion field with pure phase fluctuations caused by spontaneous emission. It has been also found that asymmetric behaviors of polarization beat signals due to the unbalanced dispersion effects between two arms of interferometer and Doppler-width do not affect the overall accuracy in case using FLPB to measure the energy-level difference between two states, which are dipolar forbidden from the ground state. On the other hand, a Doppler-free precision in the measurement of the energy-level sum can be achieved with an arbitrary bandwidth. The advantage of ASPB is that the ultrafast modulation period 900 as can still be improved, because the energy-level interval between ground state and excited state can be widely separated.

2.1 Four-level Polarization Beats with Broadband Noisy Light

Statistical properties of the broadband noisy (nontransform limited) light field are of particular importance for nonlinear optical processes since these are often sensitive to higher-order correlations in the field. The effects of such correlations have been studied in several nonlinear processes characterized by either Markovian or non-Markovian fluctuations [1 – 5]. The Markovian field is now described statistically in terms of marginal and conditional probability densities [6, 7]. The atomic response to non-Markovian fields is much less well understood [4]. This is primarily because the complete hierarchy of con-

ditional probabilities must be known in order to describe a non-Markovian process. Some non-Markovian processes can be made Markovian by extension to higher dimensions.

The atomic response to Markovian stochastic optical fields is now largely well understood [1 – 3, 5]. When the laser field is sufficiently intense that many photon interactions occur, the laser spectral bandwidth or spectral shape, obtained from the second-order correlation function, is inadequate to characterize the field. Rather than using higher-order correlation functions explicitly, three different Markovian fields are considered: (a) the chaotic field, (b) the phase-diffusion field, and (c) the Gaussian-amplitude field. The chaotic field undergoes both amplitude and phase fluctuations and corresponds to a multimode laser field with a large number of uncorrelated modes, or a single-mode laser emitting light below threshold. Since a chaotic field does not possess any intensity stabilization mechanism, the field can take on any value in a two-dimensional region of the complex plane centered about the origin. The phase-diffusion field undergoes only phase fluctuations and corresponds to an intensity-stabilized single-mode laser field. The phase of the laser field, however, has no natural stabilizing mechanism [5]. The Gaussian-amplitude field undergoes only amplitude fluctuations. Although pure amplitude fluctuations cannot be produced by a nonadiabatic process, we do consider the Gaussian-amplitude field for two reasons. First, it allows us to isolate those effects due solely to amplitude fluctuations; and second, it is an example of a field which undergoes stronger amplitude (intensity) fluctuations than a chaotic field. By comparing the results for the chaotic field and the Gaussian-amplitude field, we can determine the effect of increasing amplitude fluctuations [6, 7].

The chaotic field, the Brownian-motion phase-diffusion field, and the Gaussian-amplitude field are considered in parallel with a discussion on four-level atom transitions. We develop a unified theory which involves fourth-order coherence-function to study the influence of partial-coherence properties and unbalance dispersion effects of pump beams on polarization beats. Polarization beats, which originate from the interference between the macroscopic polarizations, have attracted a lot of attention recently [8 – 16]. It is closely related to quantum beat spectroscopy. DeBeer et al. performed the first ultrafast modulation spectroscopy (UMS) experiment in sodium vapor [17]. Fu et al. [18] then analyzed the UMS with phase-conjugate geometry in a Doppler-broadened system by a second-order coherence-function theory. They found that a Doppler-free precision in the measurement of the energy-level splitting could be achieved.

In this section, we investigated the effects of Markovian field fluctuations in four-level polarization beats. Based on three types of models described above, we studied the influence of various quantities, such as light statistics, laser linewidth, Doppler width, and unbalance dispersion. One of relevant problems is the stationary four-wave mixing (FWM) with broadband noisy light, which was proposed by Morita et al. [19], to achieve an ultrafast temporal resolution of relaxation processes. Since they assumed that laser linewidth

is much longer than transverse relaxation rate, their theory cannot be used to study the effect of the light bandwidth on the Bragg reflection signal. Asaka et al. [20] considered the finite linewidth effect. However, the constant background contribution has been ignored in their analysis. Our higher-order correlation on polarization beats includes the finite light bandwidth effect, constant background contribution, and controllable dispersion effects [21]. Different roles of the phase fluctuation and amplitude fluctuation have been pointed out in the time domain. If the FLPB is employed for the energy-level difference measurement, there are advantages that the energy-level difference between two states which are dipolar forbidden from the ground state can be widely separated and a Doppler-free precision in the measurement can be achieved. the FLPB is closely related to the Doppler-free two-photon absorption spectroscopy with a resonant intermediate state and the sum-frequency tri-level photon-echo when the pump beams are narrow band and broadband linewidth, respectively [16]. However, it possesses the main advantages of these techniques in the frequency domain and in the time domain.

2.1.1 Basic Theory

The FLPB is a polarization beat phenomenon originating from the interference between two two-photon processes. Let us consider a four-level system (Fig. 2.1) with a ground state $|0\rangle$, an intermediate state $|1\rangle$ and two excited

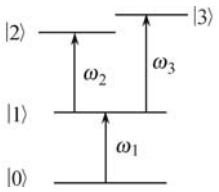

Fig. 2.1. Four-level configuration to be treated by FLPB.

states $|2\rangle$ and $|3\rangle$. States between $|0\rangle$ and $|1\rangle$ and between $|1\rangle$ and $|2\rangle(|3\rangle)$ are coupled by dipolar transition with resonant frequencies Ω_1 and $\Omega_2(\Omega_3)$, respectively, while states between $|2\rangle$ and $|3\rangle$ and between $|0\rangle$ and $|2\rangle(|3\rangle)$ are dipolar forbidden. We consider in this four-level system a double-frequency time-delay FWM experiment in which the beams 2 and 3 consist of two frequency components ω_2 and ω_3, while beam 1 has frequency ω_1 (Fig. 2.2). We assume that $\omega_1 \approx \Omega_1$ and $\omega_2 \approx \Omega_2(\omega_3 \approx \Omega_3)$, therefore ω_1 and $\omega_2(\omega_3)$ will drive the transitions from $|0\rangle$ to $|1\rangle$ and from $|1\rangle$ to $|2\rangle(|3\rangle)$, respectively. In this double-frequency time-delay FWM, the beam 1 with frequency ω_1 and the $\omega_2(\omega_3)$ frequency component of the beam 2 induce coherence between $|0\rangle$ and $|2\rangle$ $(|3\rangle)$ by two-photon transition, the which is then probed by the $\omega_2(\omega_3)$ frequency component of the beam 3. These are two-photon FWM with a resonant intermediate state and the frequency of the signal (beam 4)

equals ω_1.

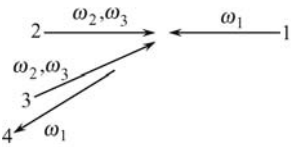

Fig. 2.2. Schematic diagram of the geometry of FLPB.

The complex electric fields of the beam 2, $E_{p2}(\boldsymbol{r},t)$, and the beam 3, $E_{p3}(\boldsymbol{r},t)$, can be written as

$$\begin{aligned} E_{p2}(\boldsymbol{r},t) &= A_2(\boldsymbol{r},t)\exp(-\mathrm{i}\omega_2 t) + A_3(\boldsymbol{r},t)\exp(-\mathrm{i}\omega_3 t) \\ &= \varepsilon_2 u_2(t)\exp[\mathrm{i}(\boldsymbol{k}_2\cdot\boldsymbol{r}-\omega_2 t)] + \varepsilon_3 u_3(t)\exp[\mathrm{i}(\boldsymbol{k}_3\cdot\boldsymbol{r}-\omega_3 t)], \quad (2.1) \end{aligned}$$

$$\begin{aligned} E_{P3}(\boldsymbol{r},t) &= A_2'(\boldsymbol{r},t)\exp(-\mathrm{i}\omega_2 t) + A_3'(\boldsymbol{r},t)\exp(-\mathrm{i}\omega_3 t) \\ &= \varepsilon_2' u_2(t-\tau)\exp[\mathrm{i}(\boldsymbol{k}_2'\cdot\boldsymbol{r}-\omega_2 t+\omega_2\tau)] + \\ &\quad \varepsilon_3' u_3(t-\tau+\delta\tau)\exp[\mathrm{i}(\boldsymbol{k}_3'\cdot\boldsymbol{r}-\omega_3 t+\omega_3\tau-\omega_3\delta\tau)]. \quad (2.2) \end{aligned}$$

Here, $\varepsilon_i, \boldsymbol{k}_i(\varepsilon_i', \boldsymbol{k}_i')$ are the constant field amplitude and the wave vector of ω_i component in the beam 2 (beam 3), respectively. $u_i(t)$ is a dimensionless statistical factor that contains phase and amplitude fluctuations. $\delta\tau$ denotes the difference in the zero time delay ($\delta\tau > 0$). We assume that the $\omega_2(\omega_3)$ component of $E_{p2}(r,t)$ and $E_{p3}(r,t)$ comes from a single laser source, and τ is the time delay of the beam 3 with respect to the beam 2. On the other hand, the beam 1 is assumed to be a quasimonochromatic light, the complex electric fields of beam 1 can be written as

$$E_{P_1}(\boldsymbol{r},t) = A_1(r,t)\exp(-\mathrm{i}\omega_1 t) = \varepsilon_1 u_1(t)\exp[\mathrm{i}(k_1\cdot\boldsymbol{r}-\omega_1 t)]. \quad (2.3)$$

Here, $u_1(t) \approx 1, \varepsilon_1$ and $\boldsymbol{k}_1$ are the field amplitude and the wave vector of the field, respectively.

We employ perturbation theory to calculate the density matrix elements. In the following perturbation chains:

$$\begin{aligned} &(\mathrm{I})\ \rho_{00}^{(0)} \xrightarrow{\omega_1} \rho_{10}^{(1)} \xrightarrow{\omega_2} \rho_{20}^{(2)} \xrightarrow{-\omega_2} \rho_{10}^{(3)} \\ &(\mathrm{II})\ \rho_{00}^{(0)} \xrightarrow{\omega_1} \rho_{10}^{(1)} \xrightarrow{\omega_3} \rho_{30}^{(2)} \xrightarrow{-\omega_3} \rho_{10}^{(3)} \end{aligned} \quad (2.4)$$

Chains (I) and (II) (2.4) correspond to the processes with two-photon transitions from $|0\rangle$ to $|2\rangle$ and from $|0\rangle$ to $|3\rangle$, respectively. We obtain the third-order off-diagonal density matrix element $\rho_{10}^{(3)}$ which has wave vector $\boldsymbol{k}_2 - \boldsymbol{k}_2' + \boldsymbol{k}_1$ or $\boldsymbol{k}_3 - \boldsymbol{k}_3' + \boldsymbol{k}_1, \rho^{(3)} = \rho^{(\mathrm{I})} + \rho^{(\mathrm{II})}$. Here g_R and $\rho^{(\mathrm{II})}$ corresponding

to $\rho_{10}^{(3)}$ of the perturbation chains (I) and (II), respectively, are

$$\rho^{(\mathrm{I})} = -\frac{\mathrm{i}\mu_1\mu_2^2}{\hbar^3}\exp(-\mathrm{i}\omega_1 t)\int_{-\infty}^{+\infty}\mathrm{d}\boldsymbol{v}w(v)\int_0^{\infty}\mathrm{d}t_3\int_0^{\infty}\mathrm{d}t_2\times \int_0^{\infty}\mathrm{d}t_1 H_1(t_1)H_2(t_2)H_1(t_3)\times A_1(t-t_1-t_2-t_3)A_2(t-t_2-t_3)[A_2'(t-t_3-\tau)]^*, \tag{2.5}$$

$$\rho^{(\mathrm{II})} = -\frac{\mathrm{i}\mu_1\mu_3^2}{\hbar^3}\exp(-\mathrm{i}\omega_1 t)\int_{-\infty}^{+\infty}\mathrm{d}\boldsymbol{v}w(v)\int_0^{\infty}\mathrm{d}t_3\int_0^{\infty}\mathrm{d}t_2\times \int_0^{\infty}\mathrm{d}t_1 H_1(t_1)H_3(t_2)H_1(t_3)\times A_1(t-t_1-t_2-t_3)A_3(t-t_2-t_3)[A_3'(t-t_3-\tau)]^*. \tag{2.6}$$

Here, $H_1(t) = \exp[-(\Gamma_{10}+\mathrm{i}\Delta_1)t], H_2(t) = \exp[-(\Gamma_{20}+\mathrm{i}\Delta_1+\mathrm{i}\Delta_2)t]$, $H_3(t) = \exp[-(\Gamma_{30}+\mathrm{i}\Delta_1+\mathrm{i}\Delta_3)t]; \mu_1$ and $\mu_2(\mu_3)$ are dipole moment matrix elements between $|0\rangle$ and $|1\rangle$ and between $|1\rangle$ and $|2\rangle(|3\rangle)$, respectively; $\Delta_1 = \Omega_1 - \omega_1, \Delta_2 = \Omega_2 - \omega_2, \Delta_3 = \Omega_3 - \omega_3; \Gamma_{10}$ and $\Gamma_{20}(\Gamma_{30})$ are transverse relaxation rates of the coherence between states $|0\rangle$ and $|1\rangle$ and between $|0\rangle$ and $|2\rangle(|3\rangle)$, respectively.

The nonlinear polarization $P^{(3)}$ responsible for the phase-conjugate FWM signal is given by averaging over the velocity distribution function $w(\boldsymbol{v})$, i.e.,

$$P^{(3)} = N\mu_1\int_{-\infty}^{+\infty}\mathrm{d}\boldsymbol{v}w(\boldsymbol{v})\rho_{10}^{(3)}(\boldsymbol{v}).$$

Here, $\boldsymbol{v}$ is the atomic velocity, N is the density of atoms. For a Doppler-broadened atomic system, we have

$$w(\boldsymbol{v}) = \frac{1}{\sqrt{\pi}u}\exp[-(\boldsymbol{v}/u)^2].$$

Thus the total polarization is $P^{(3)} = P^{(\mathrm{I})} + P^{(\mathrm{II})}$. Here $P^{(\mathrm{I})}$ and $P^{(\mathrm{II})}$ corresponding to polarizations of the perturbation chains (I) and (II), respectively, are

$$P^{(\mathrm{I})} = S_1(\boldsymbol{r})\exp[-\mathrm{i}(\omega_1 t+\omega_2\tau)]\int_{-\infty}^{+\infty}\mathrm{d}\boldsymbol{v}w(\boldsymbol{v})\int_0^{\infty}\mathrm{d}t_3\int_0^{\infty}\mathrm{d}t_2\times \int_0^{\infty}\mathrm{d}t_1\exp[-\mathrm{i}\theta_{\mathrm{I}}(\boldsymbol{v})]\times H_1(t_1)H_2(t_2)H_1(t_3)\times u_1(t-t_1-t_2-t_3)u_2(t-t_2-t_3)u_2^*(t-t_3-\tau), \tag{2.7}$$

$$P^{(\mathrm{II})} = S_2(\boldsymbol{r}) \exp[-\mathrm{i}(\omega_1 t + \omega_3 \tau - \omega_3 \delta\tau)] \int_{-\infty}^{+\infty} \mathrm{d}\boldsymbol{v} w(\boldsymbol{v}) \int_0^{\infty} \mathrm{d}t_3 \int_0^{\infty} \mathrm{d}t_2 \times \int_0^{\infty} \mathrm{d}t_1 \exp[-\mathrm{i}\theta_{\mathrm{II}}(\boldsymbol{v})] \times H_1(t_1) H_3(t_2) H_1(t_3) u_1(t - t_1 - t_2 - t_3) \times u_3(t - t_2 - t_3) u_3^*(t - t_3 - \tau + \delta\tau). \tag{2.8}$$

Here,

$$S_1(r) = -\frac{\mathrm{i}N\mu_1^2\mu_2^2}{\hbar^3} \varepsilon_1 \varepsilon_2 (\varepsilon_2')^* \exp[\mathrm{i}(k_1 + k_2 - k_2') \cdot r],$$
$$S_2(r) = -\frac{\mathrm{i}N\mu_1^2\mu_3^2}{\hbar^3} \varepsilon_1 \varepsilon_3 (\varepsilon_3')^* \exp[\mathrm{i}(k_1 + k_3 - k_3') \cdot r];$$
$$\theta_{\mathrm{I}}(v) = v \cdot [k_1(t_1 + t_2 + t_3) + k_2(t_2 + t_3) - k_2' t_3],$$
$$\theta_{\mathrm{II}}(v) = v \cdot [k_1(t_1 + t_2 + t_3) + k_3(t_2 + t_3) - k_3' t_3].$$

The FWM signal is proportional to average of the absolute square of $P^{(3)}$ over the random variable of the stochastic process $\langle |P^{(3)}|^2 \rangle$, which involves fourth- and second-order coherence functions of $u_i(t)$ in phase–conjugation geometry. While the FWM signal intensity in Debeer's self-diffraction geometry is related to the sixth-order coherence functions of incident fields. We first assume that the beam 2 (beam 3) is a multimode thermal source. $u_i(t)$ has Gaussian statistics with its fourth-order coherence function satisfying [6, 7]

$$\langle u_i(t_1) u_i(t_2) u_i^*(t_3) u_i^*(t_4) \rangle = \langle u_i(t_1) u_i^*(t_3) \rangle \langle u_i(t_2) u_i^*(t_4) \rangle + \langle u_i(t_1) u_i^*(t_4) \rangle \langle u_i(t_2) u_i^*(t_3) \rangle. \tag{2.9}$$

Furthermore, assuming that beam 2 (beam 3) has Lorentzian line shape, then we have

$$\langle u_i(t_1) u_i^*(t_2) \rangle = \exp(-\alpha_i |t_1 - t_2|) \tag{2.10}$$

here $\alpha_i = \dfrac{1}{2}\delta\omega_i$ with $\delta\omega_i$ the linewidth of the laser with frequency ω_i. The form of the second-order coherence function, which is determined by the laser line shape, as expressed in Eq. (2.10), is general feature of the three different stochastic models [6, 7].

We first consider the case that the beams 2 and 3 are a narrow band so that $\alpha_2, \alpha_3 << \Gamma_{10}, \Gamma_{20}, \Gamma_{30}$ and $\Gamma_{20}|\tau|, \Gamma_{30}|\tau| >> 1$. Performing the tedious integration, the beat signal intensity then becomes

$$\begin{aligned} I(\tau, \boldsymbol{r}) &\propto \langle |P^{(3)}|^2 \rangle \\ &= B_1 + |\eta|^2 B_2 + |B_3|^2 \exp(-2\alpha_2|\tau|) + |\eta B_4|^2 \exp(-2\alpha_3|\tau - \delta\tau|) + \\ &\quad \exp(-\alpha_2|\tau| - \alpha_3|\tau - \delta\tau|) \times \\ &\quad \{\eta B_3^* B_4 \exp[-\mathrm{i}\Delta k \cdot r - \mathrm{i}(\omega_3 - \omega_2)\tau + \mathrm{i}\omega_3 \delta\tau]\} + \\ &\quad \exp(-\alpha_2|\tau| - \alpha_3|\tau - \delta\tau|) \times \\ &\quad \{\eta^* B_3 B_4^* \exp[\mathrm{i}\Delta k \cdot r + i(\omega_3 - \omega_2)\tau - \mathrm{i}\omega_3 \delta\tau]\}. \end{aligned} \tag{2.11}$$

where

$$\Delta k = (k_2 - k'_2) - (k_3 - k'_3),$$

$$B_1 = B_3 \left\{ \frac{\Gamma_{10} + 2\alpha_2}{\Gamma_{10}[\Gamma_{20} - \mathrm{i}(\Delta_1 + \Delta_2)]} - \frac{\Gamma_{10}^2 + \Delta_1^2}{2\Gamma_{10}\Gamma_{20}(\Gamma_{10} + \Gamma_{20} - \mathrm{i}\Delta_2)} \right\},$$

$$B_2 = B_4 \left\{ \frac{\Gamma_{10} + 2\alpha_3}{\Gamma_{10}[\Gamma_{30} - \mathrm{i}(\Delta_1 + \Delta_3)]} - \frac{\Gamma_{10}^2 + \Delta_1^2}{2\Gamma_{10}\Gamma_{30}(\Gamma_{10} + \Gamma_{30} - \mathrm{i}\Delta_3)} \right\},$$

$$B_3 = \frac{1}{\Gamma_{20} + \mathrm{i}\Delta_1 + \mathrm{i}\Delta_2},$$

$$B_4 = \frac{1}{\Gamma_{30} + \mathrm{i}\Delta_1 + \mathrm{i}\Delta_3},$$

$$\eta = \frac{u_3^2}{u_2^2} \frac{\varepsilon_3(\varepsilon'_3)^*}{\varepsilon_2(\varepsilon'_2)^*}.$$

Relation (2.10) consists of five terms. The first and third terms, which is the auto-correlation intensity for two-photon transition from $|0\rangle$ to $|2\rangle$, are dependent on the $u_2(t)$ fourth-order coherence function, while the second and fourth terms, which is the auto-correlation intensity for two-photon transition from $|0\rangle$ to $|3\rangle$, are dependent on the $u_3(t)$ fourth-coherence function. The first and second terms originating from the amplitude fluctuation of the chaotic field are independent of the relative time-delay between the beams 2 and 3. The third and fourth terms indicate an exponential decay of the beat signal as $|\tau|$ increases. The fifth term depending on $u_2(t)$ and $u_3(t)$ second-order coherence functions, which is determined by the laser line shape, gives rise to the modulation of the beat signal.

Equation (2.11) indicates that beat signal oscillates not only temporally but also spatially with a period $2\pi/\Delta k$ along the direction Δk, which is almost perpendicular to the propagation direction of the beat signal. Here $\Delta k \approx 2\pi|\lambda_2 - \lambda_3|\theta/\lambda_3\lambda_2, \theta$ is the angle between the beam 2 and beam 3. Physically, the polarization-beat model assumes that both the pump beams are plane waves. Therefore two two-photon FWM signals, which propagate along $k_{s_1} = k_2 - k'_2 + k_1$ and $k_{s_2} = k_3 - k_3 + k_1$, respectively, are plane waves also. Since two two-photon FWM propagate along slightly different direction, the interference between them leads to the spatial oscillation. Equation (2.11) also indicates that beat signal modulates temporally with a frequency $\omega_3 - \omega_2$ as τ is varied. In this case that ω_2 and ω_3 are tuned to the resonant frequencies of the transitions from $|1\rangle$ to $|2\rangle$ and from $|1\rangle$ and $|3\rangle$, respectively, then the modulation frequency equals $\Omega_3 - \Omega_2$. In other words, we can obtain beating between the resonant frequencies of a four-level system. A Doppler-free precision can be achieved in the measurement of $\Omega_3 - \Omega_2$.

We then consider the case that the beams 2 and 3 are broadband, i.e., α_2, $\alpha_3 >> \Gamma_{10}, \Gamma_{20}, \Gamma_{30}$.

(i) $\tau > \delta\tau$, the beat signal rises to its maximum quickly and then decays with time constant mainly determined by the transverse relaxation times of

the system. Although the beat signal modulation is complicated in general, at the tail of the signal (i.e., $\alpha_2|\tau| >> 1, \alpha_3|\tau| >> 1$) we have

$$\begin{aligned} I(\tau, \boldsymbol{r}) &\propto \langle |P^{(3)}|^2 \rangle \\ &= B_5 + |\eta|^2 B_6 + |B_7|^2 \exp(-2\Gamma_{20}|\tau|) + \\ &\quad |\eta B_8|^2 \exp(-2\Gamma_{30}|\tau - \delta\tau|) + B_7 B_8 \exp(-\Gamma_{20}|\tau| - \\ &\quad \Gamma_{30}|\tau - \delta\tau|)\{\eta \exp[-\mathrm{i}\Delta k \cdot \boldsymbol{r} - \mathrm{i}(\Omega_3 - \Omega_2)\tau + \mathrm{i}\Omega_3\delta\tau] + \\ &\quad \eta^* \exp[\mathrm{i}\Delta k \cdot \boldsymbol{r} + \mathrm{i}(\Omega_3 - \Omega_2)\tau - \mathrm{i}\Omega_3\delta\tau]\}, \end{aligned} \tag{2.12}$$

where

$$B_5 = \frac{\Gamma_{10}^2 + \Delta_1^2}{2\Gamma_{10}} \left\{ \frac{2\alpha_2^2 + \mathrm{i}\alpha_2\Delta_1 - \mathrm{i}\Gamma_{20}\Delta_2}{\alpha_2\Gamma_{20}(2\alpha_2 + \mathrm{i}\Delta_1)[\alpha_2^2 + (\Delta_1 + \Delta_2)^2]} - \frac{1}{\alpha_2 - \mathrm{i}(\Delta_1 + \Delta_2)} \times \left[\frac{1}{(2\alpha_2 - \mathrm{i}\Delta_1)[\alpha_2 - \mathrm{i}(\Delta_1 + \Delta_2)]} - \frac{\Gamma_{10} + \Gamma_{20} + \mathrm{i}\Delta_2}{\Gamma_{20}[(\Gamma_{10} + \mathrm{i}\Delta_2)^2 - \alpha_2^2]} \right] \right\},$$

$$B_6 = \frac{\Gamma_{10}^2 + \Delta_1^2}{2\Gamma_{10}} \left\{ \frac{2\alpha_3^2 + \mathrm{i}\alpha_3\Delta_1}{\alpha_3\Gamma_{30}(2\alpha_3 + \mathrm{i}\Delta_1)[\alpha_3^2 + (\Delta_1 + \Delta_3)^2]} - \frac{1}{\alpha_3 - \mathrm{i}(\Delta_1 + \Delta_3)} \times \left[\frac{1}{(2\alpha_3 - \mathrm{i}\Delta_1)[\alpha_3 - \mathrm{i}(\Delta_1 + \Delta_3)]} - \frac{\Gamma_{10} + \Gamma_{30} + \mathrm{i}\Delta_3}{\Gamma_{30}[(\Gamma_{10} + \mathrm{i}\Delta_3)^2 - \alpha_3^2]} \right] \right\},$$

$$B_7 = \frac{2\alpha_2}{\alpha_2^2 + (\Delta_1 + \Delta_2)^2}, \quad B_8 = \frac{2\alpha_3}{\alpha_3^2 + (\Delta_1 + \Delta_3)^2}.$$

Relation (2.12) also consists of five terms. The first and third terms for two-photon transition from $|0\rangle$ to $|2\rangle$ are dependent on the $u_2(t)$ fourth-order coherence function, while the second and fourth terms for two-photon transition from $|0\rangle$ to $|3\rangle$ are dependent on the $u_3(t)$ fourth-coherence function. The third and fourth terms indicate an exponential decay of the beat signal as $|\tau|$ increases. The fifth term depending on the $u_2(t)$ and $u_3(t)$ second-order coherence functions, which is determined by the laser line shape, gives rise to the modulation of the beat signal. Equation (2.12) indicates that the temporal modulation frequency of the beat signal equals $\Omega_3 - \Omega_2$ when $\delta\tau = 0$. The overall accuracy of using FLPB with broadband lights to measure the energy-level difference between two excited states is limited by the homogeneous linewidths [13].

(ii) $0 < \tau < \delta\tau, \alpha_2|\tau| >> 1$

$$\begin{aligned} I(\tau, \boldsymbol{r}) &\propto \langle |P^{(3)}|^2 \rangle \\ &= B_5 + |\eta|^2 B_6 + |B_7|^2 \exp(-2\Gamma_{20}|\tau|) + |\eta B_9|^2 \exp(-2\alpha_3|\tau - \delta\tau|) + \\ &\quad B_7 \exp(-\Gamma_{20}|\tau| - \alpha_3|\tau - \delta\tau|)\{\eta B_9 \exp[-\mathrm{i}\Delta k \cdot \boldsymbol{r} - \mathrm{i}(\omega_3 - \omega_2)\tau + \\ &\quad \mathrm{i}\omega_3\delta\tau - \mathrm{i}(\Delta_1 + \Delta_2)\tau] + \eta^* B_9^* \exp[\mathrm{i}\Delta\boldsymbol{k} \cdot \boldsymbol{r} + \mathrm{i}(\omega_3 - \omega_2)\tau - \\ &\quad \mathrm{i}\omega_3\delta\tau + \mathrm{i}(\Delta_1 + \Delta_2)\tau]\}, \end{aligned} \tag{2.13}$$

where $B_9 = \dfrac{1}{\alpha_3 - \mathrm{i}(\Delta_1 + \Delta_2)}$.

(iii) $\tau < 0$

$$
\begin{aligned}
I(\tau, \boldsymbol{r}) &\propto \langle |P^{(3)}|^2 \rangle \\
&= B_5 + |\eta|^2 B_6 + |B_{10}|^2 \exp(-2\alpha_2|\tau|) + |\eta B_{11}|^2 \exp(-2\alpha_3|\tau - \delta\tau|) + \\
&\quad \exp(-\alpha_2|\tau| - \alpha_3|\tau - \delta\tau|)\{\eta B_{10} B_{11}^* \exp[-\mathrm{i}\Delta\boldsymbol{k} \cdot \boldsymbol{r} - \mathrm{i}(\omega_3 - \omega_2)\tau + \\
&\quad \mathrm{i}\omega_3\delta\tau] + \eta^* B_{10} B_{11}^* \exp[\mathrm{i}\Delta\boldsymbol{k} \cdot \boldsymbol{r} + \mathrm{i}(\omega_3 - \omega_2)\tau - \mathrm{i}\omega_3\delta\tau]\}, \qquad (2.14)
\end{aligned}
$$

where $B_{10} = \dfrac{1}{\alpha_2 + \mathrm{i}(\Delta_1 + \Delta_2)}, B_{11} = \dfrac{1}{\alpha_3 + \mathrm{i}(\Delta_1 + \Delta_3)}$. For simplicity, here we neglect the Doppler effect only in final expressions B_1 to B_{11}.

This equation is consistent with Eq. (2.11). Therefore, the requirement for the existence of a τ-dependent beat signal for $\tau < 0$ is that the phase-correlated subpulses in the beams 2 and 3 are overlapped temporally. Since the beams 2 and 3 are mutually coherent, the temporal behavior of the beat signal should coincide with the case when the beams 2 and 3 are nearly monochromatic [13, 18].

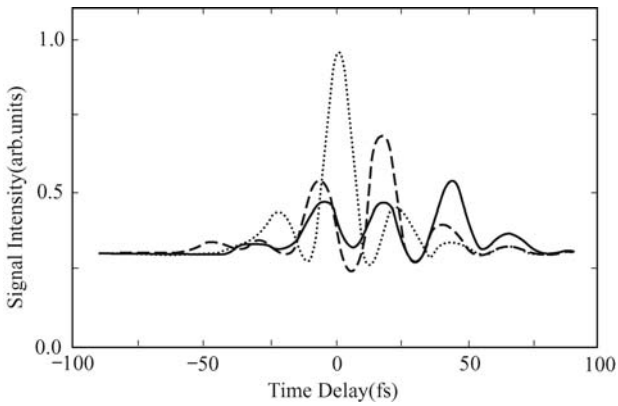

Fig. 2.3. The beat signal intensity versus relative time delay. The parameters are $\Omega_3 - \Omega_2 = 254\ \mathrm{ps}^{-1}, \Omega_3 = 3317\ \mathrm{ps}^{-1}, \Delta k = 0, \eta = 1, B_i = 0.6, \Gamma_{20} = 12.5\ \mathrm{ps}^{-1}, \Gamma_{30} = 14.5\ \mathrm{ps}^{-1}$; while $\delta\tau = 0$ fs for dotted line, $\delta\tau = 43$ fs for dashed line and $\delta\tau = 100$ fs for solid line. Adopted from Ref. [22].

Figure 2.3 shows the interferograms of the beat signal intensity versus relative time delay for three different values of the reduced offset imbalance $\delta\tau$, and the parameters are $\Omega_3 - \Omega_2 = 254\ \mathrm{ps}^{-1}, \Omega_3 = 3317\ \mathrm{ps}^{-1}, \Delta k = 0, \eta = 1, B_i = 0.6, \Gamma_{20} = 12.5\ \mathrm{ps}^{-1}, \Gamma_{30} = 14.5\ \mathrm{ps}^{-1}$; while $\delta\tau = 0$ fs for dotted line, $\delta\tau = 43$ fs for dashed line and $\delta\tau = 100$ fs for solid line. It is noticed that as $\delta\tau$ increases, the peak-to-background contrast ratio of the interferograms diminishes, as anticipated. Interestingly, the phase of the fringe beating also changes sensitively to produce a variety of interferograms including asymmetric ones. $\delta\tau$ expresses the unbalance dispersion effects between the two arms. A simple realistic example is an interferometer having an effective thickness of quartz or glass that differs significantly (many mm to a few cm) between its

two arms. Changing the thickness in one arm will control the degree of imbalance in the dispersion effects [21]. Physically, $\delta\tau$ corresponds to the separation of the peaks of the third and fourth terms of Eq. (2.11), i.e., the separation between the ω_2 only interferogram and the ω_3 only interferogram. Furthermore the fluctuations in $\delta\tau$ require phase-dependent fluctuations (otherwise $\delta\tau$ cannot change), which may be due to, for example, unbalance amplitude (thermal) fluctuations in air or the optics between the two arms of the Michelson interferometer.

2.1.2 FLPB in a Doppler-broadened System

The beat signal can be calculated from a different viewpoint. Under the Doppler-broadened limit (i.e., $k_1 u \to \infty$), we have

$$\int_{-\infty}^{+\infty} \mathrm{d}\boldsymbol{v} w(v) \exp[-\mathrm{i}\theta_{\mathrm{I}}(\boldsymbol{v})] \approx \frac{2\sqrt{\pi}}{\boldsymbol{k}_1 u}\delta(t_1 + t_2 + t_3 - \xi_1 t_2), \tag{2.15}$$

$$\int_{-\infty}^{+\infty} \mathrm{d}\boldsymbol{v} w(\boldsymbol{v}) \exp[-\mathrm{i}\theta_{\mathrm{II}}(\boldsymbol{v})] \approx \frac{2\sqrt{\pi}}{\boldsymbol{k}_1 u}\delta(t_1 + t_2 + t_3 - \xi_2 t_2). \tag{2.16}$$

Here, $\xi_1 = k_2/k_1, \xi_2 = k_3/k_1$. We assume $\xi_1 > 1, \xi_2 > 1$. When we substitute Eqs. (2.15) and (2.16) into Eqs. (2.7) and (2.8) we obtain $\mathrm{I}(\tau, \boldsymbol{r}) \propto \langle |P^{(3)}|^2 \rangle = \langle |P^{(\mathrm{I})} + P^{(\mathrm{II})}|^2 \rangle$.

We first consider the case that the beams 2 and 3 are narrow band so that $\alpha_2, \alpha_3 << \Gamma_{20}, \Gamma_{30}$ and $\Gamma_{20}|\tau|, \Gamma_{30}|\tau| >> 1$. Performing the tedious integration, the beat signal intensity is

$$\begin{aligned} I(\tau, \boldsymbol{r}) &\propto \langle |P^{(3)}|^2 \rangle \\ &\propto B_5 + |\eta|^2 B_6 + |B_{12}|^2 \exp(-2\alpha_2|\tau|) + |\eta B_{13}|^2 \exp(-2\alpha_3|\tau - \delta\tau|) + \\ &\quad \exp(-\alpha_2|\tau| - \alpha_3|\tau - \delta\tau|) \times \{\eta B_{12}^* B_{13} \exp[-\mathrm{i}\Delta\boldsymbol{k} \cdot \boldsymbol{r} - \mathrm{i}(\omega_3 - \omega_2)\tau + \\ &\quad \mathrm{i}\omega_3 \delta\tau] + \eta^* B_{12} B_{13}^* \exp[\mathrm{i}\Delta\boldsymbol{k} \cdot \boldsymbol{r} + \mathrm{i}(\omega_3 - \omega_2)\tau - \mathrm{i}\omega_3 \delta\tau]\}, \end{aligned} \tag{2.17}$$

where $B_{12} = \dfrac{(\xi_1 - 1)(\Gamma_{10}^2 + \Delta_1^2)^2}{(\Gamma_{20}^a - \Gamma_{10})^2 + (\Delta_2^a)^2}, B_{13} = \dfrac{(\xi_2 - 1)(\Gamma_{10}^2 + \Delta_1^2)^2}{(\Gamma_{30}^a - \Gamma_{10})^2 + (\Delta_3^a)^2}; \Gamma_{20}^a = \Gamma_{20} + \xi_1\Gamma_{10}, \Gamma_{30}^a = \Gamma_{30} + \xi_2\Gamma_{10}, \Delta_2^a = \Delta_2 + \xi_1\Delta_1, \Delta_3^a = \Delta_3 + \xi_2\Delta_1$. This equation is consistent with Eq. (2.11).

We now consider the case that beams 2 and 3 are broadband so that $\alpha_2, \alpha_3 >> \Gamma_{10}, \Gamma_{20}, \Gamma_{30}$.

(i) $\tau > \delta\tau, \alpha_2|\tau| >> 1, \alpha_3|\tau| >> 1$

$$\begin{aligned} I(\tau, \boldsymbol{r}) \propto \langle |P^{(3)}|^2 \rangle &= B_{14} + |\eta|^2 B_{15} + |B_{16}|^2 \exp[-2(\Gamma_{20}^a - \Gamma_{10})|\tau|] + \\ &\quad |\eta B_{17}|^2 \exp[-2 \times (\Gamma_{30}^a - \Gamma_{10})|\tau - \delta\tau|] + \\ &\quad B_{16} B_{17} \exp[-(\Gamma_{20}^a - \Gamma_{10})|\tau| - (\Gamma_{30}^a - \Gamma_{10})|\tau - \end{aligned}$$

$$\delta\tau|]\{\eta\exp[-\mathrm{i}\Delta\boldsymbol{k}\cdot\boldsymbol{r}-\mathrm{i}(\Omega_3-\Omega_2)\tau-\mathrm{i}(\xi_2-\xi_1)\Delta_1\tau+\mathrm{i}\xi_2\Delta_1\delta\tau]+\eta^*\exp[\mathrm{i}\Delta\boldsymbol{k}\cdot\boldsymbol{r}+\mathrm{i}(\Omega_3-\Omega_2)\tau+\mathrm{i}(\xi_2-\xi_1)\Delta_1\tau-\mathrm{i}\xi_2\Delta_1\delta\tau]\}, \tag{2.18}$$

where

$$B_{14}=\frac{(\xi_1-1)[\alpha_2^2+(\Delta_2^a)^2-2\mathrm{i}\alpha_2\Delta_2^a]}{2(\Gamma_{20}^a-\Gamma_{10})^2[\alpha_2^2+(\Delta_2^a)^2]},$$
$$B_{15}=\frac{(\xi_2-1)[\alpha_3^2+(\Delta_3^a)^2-2\mathrm{i}\alpha_3\Delta_3^a]}{2(\Gamma_{30}^a-\Gamma_{10})^2[\alpha_3^2+(\Delta_3^a)^2]},$$
$$B_{16}=\frac{2(\xi_1-1)\alpha_2\tau}{\alpha_2^2+(\Delta_2^a)^2},$$
$$B_{17}=\frac{2(\xi_2-1)\alpha_3(\tau-\delta\tau)}{\alpha_3^2+(\Delta_3^a)^2}.$$

Equation (2.18) indicates that the temporal modulation frequency of the beat signal equals $\Omega_3-\Omega_2$ when $\Delta_1=\delta\tau=0$. The overall accuracy of using FLPB with broadband lights to measure the energy-level difference between two excited states is limited by the homogeneous linewidth. This equation is analogous to Eq. (2.11).

(ii) $\tau<0$

$$I(\tau,\boldsymbol{r})\propto\langle|P^{(3)}|^2\rangle=B_{14}+|\eta|^2B_{15}+|B_{18}|^2\exp(-2\alpha_2|\tau|)+|\eta B_{19}|^2\exp(-2\alpha_3|\tau-\delta\tau|)+\exp(-\alpha_2|\tau|-\alpha_3|\tau-\delta\tau|)\{\eta B_{18}^*B_{19}\exp[-\mathrm{i}\Delta\boldsymbol{k}\cdot\boldsymbol{r}-\mathrm{i}(\omega_3-\omega_2)\tau+\mathrm{i}\omega_3\delta\tau]+\eta^*B_{18}B_{19}^*\exp[\mathrm{i}\Delta k\cdot r+\mathrm{i}(\omega_3-\omega_2)\tau-\mathrm{i}\omega_3\delta\tau]\}, \tag{2.19}$$

where

$$B_{18}=\frac{\xi_1-1}{(\alpha_2-\mathrm{i}\Delta_2^a)^2},$$
$$B_{19}=\frac{\xi_2-1}{(\alpha_3-\mathrm{i}\Delta_3^a)^2}.$$

This equation is consistent with Eq. (2.10).

(iii) $0<\tau<\delta\tau$ and $\alpha_2|\tau|\gg1$

$$I(\tau,\boldsymbol{r})\propto\langle|P^{(3)}|^2\rangle=B_{14}+|\eta|^2B_{15}+|B_{16}|^2\exp[-2(\Gamma_{20}^a-\Gamma_{10})|\tau|]+|\eta B_{19}|^2\times\exp(-2\alpha_3|\tau-\delta\tau|)+B_{16}\exp[-2(\Gamma_{20}^a-\Gamma_{10})|\tau|-\alpha_3|\tau-\delta\tau|]\{\eta B_{19}\exp[-\mathrm{i}\Delta k\cdot\boldsymbol{r}-\mathrm{i}(\omega_3-\omega_2)\tau+\mathrm{i}\omega_3\delta\tau-\mathrm{i}(\Delta_1+\Delta_2)\tau]+\eta^*B_{19}^*\exp[\mathrm{i}\Delta\boldsymbol{k}\cdot r+\mathrm{i}(\omega_3-\omega_2)\tau-\mathrm{i}\omega_3\delta\tau+\mathrm{i}(\Delta_1+\Delta_2)\tau]\}. \tag{2.20}$$

This equation is analogous to Eq. (2.12).

2.1.3 Photon-echo

It is interesting to understand the underlying physics in FLPB with broadband nontransform limited quasi-cw (noisy) lights [19, 20]. Much attention has been paid to the study of various ultrafast phenomena by using incoherent light sources recently [21 – 24]. For the phase matching condition $k_2 - k_2' + k_1$ and $k_3 - k_3' + k_1$ two sum-frequency trilevel echoes exist for the perturbation the chains (I) and (Ⅱ), respectively.

The chaotic field is a complex Gaussian stochastic process. Under the Doppler-broadened limit (i.e., $k_1 u \to \infty$), If assuming that the beams 2 and 3 are broadband so that $\alpha_2, \alpha_3 >> \Gamma_{20}, \Gamma_{30}$, then we have

$$\langle u_i(t_1) u_i^*(t_2) \rangle = \exp(-\alpha_i |t_1 - t_2|) \approx \frac{2}{\alpha_i} \delta(t_1 - t_2). \tag{2.21}$$

When we substitute Eqs. (2.8) and (2.21) into Eq. (2.16), we obtain as follows:

(i) $\tau > \delta\tau$,

$$\begin{aligned} I(\tau, \boldsymbol{r}) \propto \langle |P^{(3)}|^2 \rangle = {} & A_1 + |\eta|^2 A_2 + |A_3|^2 \exp[-2(\Gamma_{20}^a - \Gamma_{10})|\tau|] + \\ & |\eta A_4|^2 \exp[-2 \times (\Gamma_{30}^a - \Gamma_{10})|\tau - \delta\tau|] + A_3 A_4 \exp[-(\Gamma_{20}^a - \Gamma_{10})|\tau| - \\ & (\Gamma_{30}^a - \Gamma_{10})|\tau - \delta\tau|] \{\eta \exp[-\mathrm{i}\Delta \boldsymbol{k} \cdot \boldsymbol{r} - \mathrm{i}(\Omega_3 - \Omega_2)\tau - \\ & \mathrm{i}(\xi_2 - \xi_1)\Delta_1 \tau + \mathrm{i}\xi_2 \Delta_1 \delta\tau] + \eta^* \exp[\mathrm{i}\Delta \boldsymbol{k} \cdot \boldsymbol{r} + \mathrm{i}(\Omega_3 - \Omega_2)\tau + \\ & \mathrm{i}(\xi_2 - \xi_1)\Delta_1 \tau - \mathrm{i}\xi_2 \Delta_1 \delta\tau]\}, \end{aligned} \tag{2.22}$$

where

$$\begin{aligned} A_1 &= \frac{\xi_1 - 1}{4[\alpha_2(\Gamma_{20}^a - \Gamma_{10})]^2} \\ A_2 &= \frac{\xi_2 - 1}{4[\alpha_3(\Gamma_{30}^a - \Gamma_{10})]^2} \\ A_3 &= \frac{(\xi_1 - 1)\tau}{\alpha_2}, \\ A_4 &= \frac{(\xi_2 - 1)(\tau - \delta\tau)}{\alpha_3}. \end{aligned}$$

This equation is consistent with Eq. (2.18).

(ii) $0 < \tau < \delta\tau$

$$I(\tau, \boldsymbol{r}) \propto \langle |P^{(3)}|^2 \rangle = A_1 + |\eta|^2 A_2 + |A_3|^2 \exp[-2(\Gamma_{20}^a - \Gamma_{10})|\tau|].$$

Photon-echo only exists for the perturbation the chain (I).

(iii) $\tau < 0$

$$I(\tau, \boldsymbol{r}) \propto \langle |P^{(3)}|^2 \rangle = A_1 + |\eta|^2 A_2. \tag{2.23}$$

In this case, photon-echo doesn't exist for the perturbation chains (I) and (Ⅱ). The requirement for the existence of a τ-dependent beat signal for $\tau < 0$ is that the phase-correlated subpulses in the beams 2 and 3 are overlapped temporally. Since beams 2 and 3 are mutually coherent, the temporal behavior of the beat signal should coincide with the case when the beams 2 and 3 are nearly monochromatic [13, 18]. Therefore, this case is analogous to Eq. (2.10).

We have assumed that the laser sources are chaotic field in the above calculation. A chaotic field, which is used to describe a multimode laser source, is characterized by the fluctuation of both the amplitude and the phase of the field. Another commonly used stochastic model is a phase-diffusion model, which is used to describe an amplitude-stabilized laser source. This model assumes that the amplitude of the laser field is a constant, while its phase fluctuates as a random process.

We substitute Eqs. (2.21) and (2.23) into Eq. (2.16), we obtain as follows:
(i) $\tau > \delta\tau$

$$\begin{aligned} I(\tau, \boldsymbol{r}) \propto \langle |P^{(3)}|^2 \rangle = {} & |A_3|^2 \exp[-2(\Gamma_{20}^a - \Gamma_{10})|\tau|] + \\ & |\eta A_4|^2 \exp[-2(\Gamma_{30}^a - \Gamma_{10})|\tau - \delta\tau|] + \\ & A_3 A_4 \times \exp[-(\Gamma_{20}^a - \Gamma_{10})|\tau| - \\ & (\Gamma_{30}^a - \Gamma_{10})|\tau - \delta\tau|]\{\eta \exp[-\mathrm{i}\Delta\boldsymbol{k} \cdot \boldsymbol{r} - \mathrm{i}(\Omega_3 - \Omega_2)\tau - \\ & \mathrm{i}(\xi_2 - \xi_1)\Delta_1\tau + \mathrm{i}\xi_2\Delta_1\delta\tau] + \eta^* \exp[\mathrm{i}\Delta\boldsymbol{k} \cdot \boldsymbol{r} + \\ & \mathrm{i}(\Omega_3 - \Omega_2)\tau + \mathrm{i}(\xi_2 - \xi_1)\Delta_1\tau - \mathrm{i}\xi_2\Delta_1\delta\tau]\}. \end{aligned} \tag{2.24}$$

(ii) $0 < \tau < \delta\tau$

$$I(\tau, r) \propto \langle |P^{(3)}|^2 \rangle = |A_3|^2 \exp[-2(\Gamma_{20}^a - \Gamma_{10})|\tau|]. \tag{2.25}$$

Photon-echo only exists for the perturbation the chain (I).
(iii) $\tau < 0$

$$I(\tau, \boldsymbol{r}) \propto \langle |P^{(3)}|^2 \rangle = 0. \tag{2.26}$$

In this case, photon-echo doesn't exist for the perturbation the chains (I) and (Ⅱ).

Relation (2.24) consists of three terms. The first term for two-photon transition from $|0\rangle$ to $|2\rangle$ is dependent on the $u_2(t)$ fourth-order coherence function, while the second term for two-photon transition from $|0\rangle$ to $|3\rangle$ is dependent on the $u_3(t)$ fourth-order coherence functions. The first and second terms indicate an exponential decay of the beat signal as $|\tau|$ increases. The third term depending on the $u_2(t)$ and $u_3(t)$ second-order coherence functions, which is determined by the laser line shape, gives rise to the modulation of the beat signal. This case is consistent with results of the second-order coherence function theory $|\langle P^{(3)} \rangle|^2$ [10, 18]. The constant background contribution has been ignored in their analysis. Therefore, the fourth-order coherence function theory $\langle |P^{(3)}|^2 \rangle$ of chaotic field is of vital importance in FLPB.

The Gaussian-amplitude field has a constant phase but its real amplitude undergoes Gaussian fluctuations. If the lasers have Lorentzian line shape, the fourth-order coherence function is [6, 7]

$$\begin{aligned}\langle u_i(t_1)u_i(t_2)u_i(t_3)u_i(t_4)\rangle = {} & \langle u_i(t_1)u_i(t_3)\rangle\langle u_i(t_2)u_i(t_4)\rangle + \\ & \langle u_i(t_1)u_i(t_4)\rangle\langle u_i(t_2)u_i(t_3)\rangle + \\ & \langle u_i(t_1)u_i(t_2)\rangle\langle u_i(t_3)u_i(t_4)\rangle. \end{aligned} \tag{2.27}$$

When we substitute Eqs. (2.21) and (2.25) into Eq. (2.16) we obtain as follows:

(i) $\tau > \delta\tau$

$$\begin{aligned} I(\tau,\boldsymbol{r}) \propto \langle|P^{(3)}|^2\rangle = {} & A_1 + |\eta|^2 A_2 + A_5\exp[-2(\Gamma_{20}^a - \Gamma_{10})|\tau|] + \\ & |\eta A_6|^2\exp[-2(\Gamma_{30}^a - \Gamma_{10}) \times |\tau - \delta\tau|] + \\ & A_7\exp[-(\Gamma_{20}^a - \Gamma_{10})|\tau| - (\Gamma_{30}^a - \Gamma_{10})|\tau - \delta\tau|]\{\eta\exp[-\mathrm{i}\Delta\boldsymbol{k}\cdot\boldsymbol{r} - \\ & \mathrm{i}(\Omega_3 - \Omega_2)\tau - \mathrm{i}(\xi_2 - \xi_1)\Delta_1\tau + \mathrm{i}\xi_2\Delta_1\delta\tau] + \\ & \eta^*\exp[\mathrm{i}\Delta\boldsymbol{k}\cdot\boldsymbol{r} + \mathrm{i}(\Omega_3 - \Omega_2)\tau + \mathrm{i}(\xi_2 - \xi_1)\Delta_1\tau - \mathrm{i}\xi_2\Delta_1\delta\tau]\}, \end{aligned} \tag{2.28}$$

where

$$\begin{aligned} A_5 &= \frac{4(\xi_1 - 1)^2\tau^2}{\alpha_2^2} + \frac{\xi_1 - 1}{(\alpha_2\Delta_2^a)^2}, \\ A_6 &= \frac{4(\xi_2 - 1)^2(\tau - \delta\tau)^2}{\alpha_3^2} + \frac{\xi_2 - 1}{(\alpha_3\Delta_3^a)^2}, \\ A_7 &= \frac{(\xi_1 - 1)(\xi_2 - 1)}{\alpha_2\alpha_3}\tau(\tau - \delta\tau). \end{aligned}$$

(ii) $0 < \tau < \delta\tau$

$$I(\tau,\boldsymbol{r}) \propto \langle|P^{(3)}|^2\rangle = A_1 + |\eta|^2 A_2 + A_5\exp[-2(\Gamma_{20}^a - \Gamma_{10})|\tau|]. \tag{2.29}$$

Photon-echo only exists for the perturbation the chain (I).

(iii) $\tau < 0$

$$I(\tau,\boldsymbol{r}) \propto \langle|P^{(3)}|^2\rangle = A_1 + |\eta|^2 A_2. \tag{2.30}$$

In this case, photon-echo doesn't exist for the perturbation chains (I) and (Ⅱ).

Relation (2.28) consists of five terms. The first and third terms for two-photon transition from $|0\rangle$ to $|2\rangle$ are dependent on the $u_2(t)$ fourth-order coherence function, while the second and fourth terms for two-photon transition from $|0\rangle$ to $|3\rangle$ are dependent on the $u_3(t)$ fourth-coherence function. The first and second terms originating from the amplitude fluctuation of the Gaussian-amplitude field are independent of the relative time-delay between the beams 2 and 3. The third and fourth terms indicate an exponential decay of the beat signal as $|\tau|$ increases. The fifth term depending on the $u_2(t)$ and $u_3(t)$ second-order coherence functions, which is determined by the laser line shape, gives

rise to the modulation of the beat signal. Equation (2.26) also indicates that beat signal oscillates not only temporally with a period $2\pi/|\Omega_3 - \Omega_2| = 25$ fs but also spatially with a period $2\pi/\Delta\boldsymbol{k} = 0.28$ mm along the direction $\Delta\boldsymbol{k}$, which is almost perpendicular to the propagation direction of the beat signal. The three-dimensional interferogram of the beat signal intensity $I(\tau, r)$ versus time delay τ and transverse distance $\boldsymbol{r}$ has the larger constant background caused by the intensity fluctuation of the Gaussian-amplitude field in Fig. 2.4 (a), (b), and the parameters are $\Omega_3 - \Omega_2 = 254$ ps^{-1}, $\Delta k = 22.22$ mm^{-1}, $\eta = 1, \xi_i = 1.5, \Delta_1 = 0, A_i = 0.6, \Gamma^a_{20} - \Gamma_{10} = 12.5$ ps^{-1}, $\Gamma^a_{30} - \Gamma_{10} = 14.5$ ps^{-1}; while $\delta\tau = 0$ fs for (a) and $\delta\tau = 43$ fs for (b). At zero relative time delay ($\tau = 0$), the twin beams originating from the same source enjoy perfect overlap at the sample of their corresponding noise patterns in Fig. 2.4 (a). This gives maximum interferometric contrast. As $|\tau|$ is increased, the interferometric contrast diminishes on the time scale that reflects material memory, usually much longer than the correlation time of the light [24]. The contrast ratio is seen to diminish and the symmetry of the interferogram is destroyed in Fig. 2.4 (b).

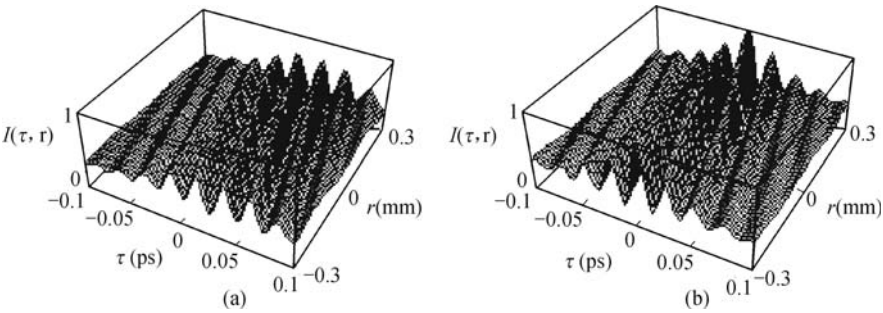

Fig. 2.4. A three-dimensional interferogram of the beat signal intensity $I(\tau, r)$ versus time delay τ and transverse distance r for the Gaussian-amplitude field. The parameters are $\Omega_3 - \Omega_2 = 254$ ps^{-1}, $\Delta k = 22.22$ mm^{-1}, $\Gamma^a_{20} - \Gamma_{10} = 12.5$ ps^{-1}, $\Gamma^a_{30} - \Gamma_{10} = 14.5$ ps^{-1}, $\eta = 1, \xi_i = 1.5, \Delta_1 = 0, A_i = 0.6$; while $\delta\tau = 0$ fs for (a) and $\delta\tau = 43$ fs for (b). Adopted from Ref. [22].

It is important to note that these three types of fields can have the same spectral density and thus the same second-order coherence function. The fundamental differences in statistics of these fields are manifest only in the higher-order coherence functions. The term "higher order" refers to all orders larger than the second. In this section, different stochastic models of the laser field only affect the fourth-order coherence function. Figure 2.5 presents the beat signal intensity versus relative time delay. The three curves represent the chaotic field (solid line), phase-diffusion field (dashed line), and Gaussian-amplitude field (dotted line). The polarization beat signal is shown to be particularly sensitive to the statistical properties of Markovian stochastic light fields with arbitrary bandwidth. This is quite different from fourth-order partial-coherence effects in the formation of integrated-intensity gratings with

pulsed light sources [25]. Their results proved to be insensitive to the specific radiation models. The constant background of the beat signal for a Gaussian-amplitude field or a chaotic field is much larger than that of the signal for a phase-diffusion field in Fig. 2.5. The physical explanation for this is that the Gaussian-amplitude field undergoes stronger intensity fluctuations than a chaotic field. On the other hand, the intensity (amplitude) fluctuations of the Gaussian-amplitude field or the chaotic field are always much larger than the pure phase fluctuations of the phase-diffusion field.

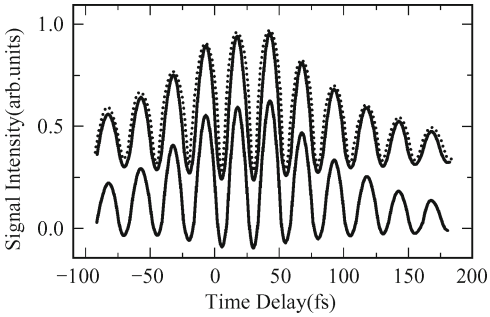

Fig. 2.5. The beat signal intensity versus relative time delay. The three curves represent the chaotic field (solid line), phase-diffusion field (dashed line), and Gaussian-amplitude field (dotted line). The parameters are $\Omega_3 - \Omega_2 = 254\ \mathrm{ps}^{-1}, \Delta k = 0, \eta = 1, \xi_i = 1.5, \Delta_1 = 0, A_i = 0.6, \delta\tau = 43\ \mathrm{fs}, \Gamma^a_{20} - \Gamma_{10} = 2.5\ \mathrm{ps}^{-1}$ and $\Gamma^a_{30} - \Gamma_{10} = 2.9\ \mathrm{ps}^{-1}$.

We discuss the difference between the FLPB and the UMS [17] with self-diffraction geometry from a physical viewpoint. The frequency and wave vector of the DeBeer's UMS signal are $\omega_{s_1} = 2\omega_1 - \omega_1, \omega_{s_2} = 2\omega_2 - \omega_2$ and $\boldsymbol{k}_{s_1} = 2\boldsymbol{k'}_1 - \boldsymbol{k}_1, \boldsymbol{k}_{s_2} = 2\boldsymbol{k'}_2 - \boldsymbol{k'}_2$, respectively, which means that a photon is absorbed from each of two mutually correlated pump beams. On the other hand, the frequency and wave vector of the FLPB signal are $\omega_{s_1} = \omega_2 - \omega_2 + \omega_1, \omega_{s_2} = \omega_3 - \omega_3 + \omega_1$, and $\boldsymbol{k}_{s_1} = \boldsymbol{k}_2 - \boldsymbol{k'}_2 + \boldsymbol{k'}_1, \boldsymbol{k}_{s_2} = \boldsymbol{k}_3 - \boldsymbol{k'}_3 + \boldsymbol{k}_1$, respectively, therefore photons are absorbed from and emitted to the mutually correlated beams 2 and 3, respectively. This difference between the FLPB and DeBeer's UMS has profound influence on the field-correlation effects. We note that the role of two pump beams are interchangeable in the DeBeer's UMS, this interchangeable feature also makes the second-order coherence function theory failure in the DeBeer's UMS. In virtue of $\langle u(t_1)u(t_2)\rangle = 0$, the absolute square of the stochastic average of the polarization $|\langle P^{(3)}\rangle|^2$ cannot be used to describe the temporal behavior of DeBeer's UMS. Our fourth-order theory $\langle |P^{(3)}|^2\rangle$ is of vital importance in DeBeer's UMS.

The main purpose of above discussion is that we reveal an important fact that the amplitude fluctuation plays a critical role in the temporal behavior of FLPB signals. Furthermore, the different roles of the phase fluctuation and amplitude fluctuation have been pointed out in the time domain. This is quite different from the time delayed FWM with incoherent light in a two-

level system [19]. For the latter case, the phase fluctuation of the light field is crucial. Therefore, the FLPB is analogous to Raman-enhanced polarization beats [24–30]. The amplitude fluctuation of the light field is also crucial in the Raman-enhanced polarization beats. On the other hand, because of $\langle u_i(t)\rangle = 0$ and $\langle u_i^*(t)\rangle = 0$, the absolute square of the stochastic average of the polarization $|\langle P^{(3)}\rangle|^2$, which involves second-order coherence function of $u_i(t)$, cannot be used to describe the temporal behavior of the FLPB [18]. The fourth-order theory $\langle |P^{(3)}|^2\rangle$ reduces to the second-order theory $|\langle P^{(3)}\rangle|^2$ in the case that the laser pulse width is much longer than the laser coherence time [25]. The second-order coherence function theory is valid when we are only interested in the τ-dependent part of the beating signal. Therefore, the fourth-order coherence function theory is of vital importance in FLPB. The application of these results to the FLPB experiment yielded a better fit to data than an expression involving only second-order coherence. We present experimental results for the atomic response in four-level polarization beats with phase-conjugation geometry using multimode laser fields. However, it is more difficult to get a clear picture of physical origins of effects in each type of fluctuating field in the experiment. We intend to rely on the cumulant expansion formulation. According to this theory, the fourth order correlation function generally reads as

$$\begin{aligned}\langle u_i(t)\ u_i\ (t+\tau_1)u_i^*(t+\tau_2)u_i^*(t+\tau_3)\rangle \\ = \langle u_i(t)u_i^*(t+\tau_2)\rangle\langle u_i(t+\tau_1)u_i^*(t+\tau_3)\rangle + \\ \langle u_i(t)u_i^*(t+\tau_3)\rangle\langle u_i(t+\tau_1)u_i^*(t+\tau_2)\rangle + \\ f(\tau_1,\tau_2,\tau_3)\ldots\ldots \quad (i=2,3),\end{aligned} \tag{2.31}$$

where $f(\tau_1,\tau_2,\tau_3)$ vanishes when either τ_1, τ_2, or τ_3 is larger than the correlation time τ_c. For instance this description applies to both chaotic and phase diffusion models. Departure of a specific process from gaussian statistics is contained in $f(\tau_1,\tau_2,\tau_3)$. This approach is well suited to problems which involve intricate time integrations. Indeed one easily expresses the non-gaussian contribution in powers of τ_c and it is straightforward to disclose possible sensitivity to statistics.

2.1.4 Experiment and Result

We performed the FLPB in sodium vapor, where the ground state $3S_{1/2}$, the intermediate state $3P_{1/2}$, and two excited states $5S_{1/2}$ and $4D_{3/2}$ formed a four-level system. Three dye lasers (DL1, DL2, and DL3) pumped by the second harmonic of a Quanta-Ray YAG laser, were used to generate frequencies at ω_1, ω_2, and ω_3. DL1 had linewidth 0.01 nm and pulse width 10 ns. DL2 and DL3 had linewidth 1 nm and pulse width 10 ns. DL1 was tuned to 589.6 nm, the wavelength of the $3S_{1/2} - 3P_{1/2}$ transition; DL2 was tuned to 615.4

nm, the wavelength of the $3P_{1/2} - 5S_{1/2}$ transition; while DL3 was tuned to 568.2 nm, the wavelength of the $3P_{1/2} - 4D_{3/2}$ transition. A beam splitter was used to combine the ω_2 and ω_3 components derived from DL2 and DL3, respectively, for beams 2 and 3, which intersected in the oven containing the Na vapor. The time delay τ between beams 2 and 3 could be varied. Beam 1, which propagated along the direction opposite to that of beam 2, was derived from DL1. All the incident beams were linearly polarized in the same direction. The beat signal had the same polarization as the incident beams, propagated along a direction almost opposite to that of beam 3. It was detected by a photodiode.

We first performed a degenerate FWM experiment with beams 1, 2, and 3, consisting of the ω_1 frequency component. From the degenerate FWM spectrum we tuned ω_1 to the resonant frequency Ω_1. We then performed the first nondegenerate FWM experiment with beams 2 and 3 consisting of only ω_2 frequency component. We measured the nondegenerate FWM spectrum, by scanning ω_2, which shows a resonant profile due to two-photon transition (Fig. 2.6), and the solid curve is the

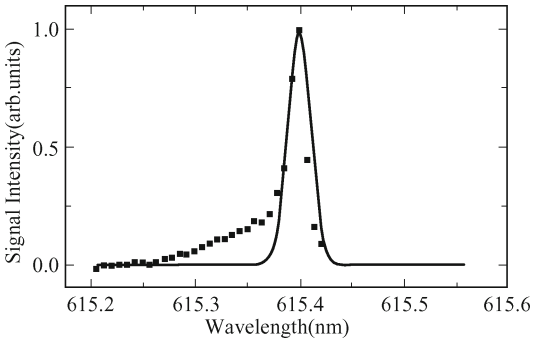

Fig. 2.6. Spectrum of FWM when beams 2 and 3 consist of only ω_2 in which center wavelength is 615.4 nm. The solid curve is the theoretical curve with $\alpha_2 = 2.5$ ps^{-1} and $\omega_2 = 3\,063$ ps^{-1}.

Theoretical curve given by the power spectral density

$$S_1(\omega) = \frac{\frac{2\alpha_2}{\pi}}{4\alpha_2^2 + (\omega - \omega_2)^2},$$

with $\alpha_2 = 2.5$ ps^{-1} and $\omega_2 = 3063$ ps^{-1}. From this spectrum ω_2 was tuned to the resonant frequency Ω_2, whose center wavelength is 615.4 nm. Furthermore, the relation of the FWM signal intensity versus relative time delay is showed in Fig. 2.7, the solid curve is the fourth-order theory curve given by the Autocorrelation intensity $I_1 = B_1 + |B_3|^2 \exp(-2\alpha_2|\tau|)$ of DL2 with $\alpha_2 = 2.5$ ps^{-1} and $B_i = 0.6$, and the dashed curve is the second-order theory curve. [10, 18]. We also performed the second two-photon nondegenerate FWM experiment in which beams 2 and 3 consisted of only ω_3 frequency

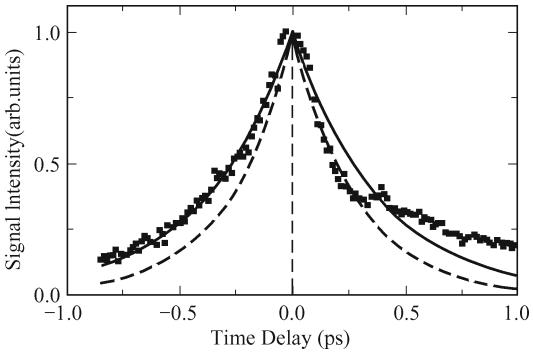

Fig. 2.7. The FWM signal intensity versus relative time delay when beams 2 and 3 consist of only ω_2. The square is experimental data; the solid curve is a fourth-order theory curve with $\alpha_2 = 2.5\ \mathrm{ps}^{-1}$ and $B_i = 0.6$; the dashed curve is a second-order theory curve.

component. Figure 2.8 presents the spectrum of the FWM, and the solid curve is the theoretical curve given by the power spectral density

$$S_2(\omega) = \frac{2\alpha_3/\pi}{4\alpha_3^2 + (\omega - \omega_3)^2},$$

with $\alpha_3 = 2.9\ \mathrm{ps}^{-1}$ and $\omega_3 = 3317\ \mathrm{ps}^{-1}$. From the FWM spectrum we tune ω_3 to the resonant frequency Ω_3, whose center wavelength is 568.2 nm. Figure 2.9 denotes the relation of the signal intensity versus relative time delay, the solid curve is the fourth-order theory curve given by the autocorrelation intensity $I_2 = |\eta|^2 B_2 + |\eta B_4|^2 \exp(-2\alpha_3|\tau - \delta\tau|)$ of DL3 with $\alpha_3 = 2.9\ \mathrm{ps}^{-1}, \delta\tau = 43$ fs, $B_i = 0.6$ and $\eta = 1$, and the dashed curve is the second-order theory curve. [10,18] Note that the fourth-order theory yields a much better fit in the wings of experimental data. After that, we performed the FLPB experiment

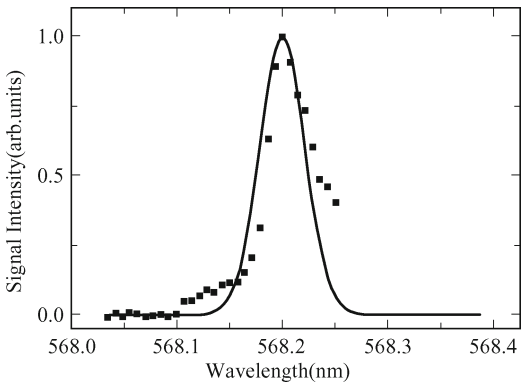

Fig. 2.8. Spectrum of FWM when beams 2 and 3 consist of only ω_3 in which center wavelength is 568.2 nm. The solid curve is the theoretical curve with $\alpha_3 = 2.9\ \mathrm{ps}^{-1}$ and $\omega_3 = 3317\ \mathrm{ps}^{-1}$.

by measuring the beat signal intensity as a function of the relative time delay when beams 2 and 3 consist of both frequencies ω_2 and ω_3. Figure 2.10 presents the result of the beat experiment in which τ is varied for a range of 362 fs, the solid curve is the theoretical curve given by Eq. (2.10) with $\alpha_2 = 2.5\ \mathrm{ps}^{-1}, \alpha_3 = 2.9\ \mathrm{ps}^{-1}, \omega_3 - \omega_2 = 2.54 \times 10^{14}\mathrm{s}^{-1}, \omega_3 = 3317\ \mathrm{ps}^{-1}, \Delta k = 0, \delta\tau = 43\ \mathrm{fs}, B_i = 0.6$ and $\eta = 1$, and the beat signal intensity modulates sinusoidally with period 24.74 fs. The modulation frequency can be obtained more directly by making a Fourier transformation of FLPB data. Figure 2.11 presents the Fourier spectrum of experimental data in which τ is varied for a range of 362 fs. Then we obtain the modulation frequency $2.54 \times 10^{14}\mathrm{s}^{-1}$ corresponding to the beating between the resonant frequencies of transitions from $3P_{1/2}$ to $5S_{1/2}$ and from $3P_{1/2}$ to $4D_{3/2}$

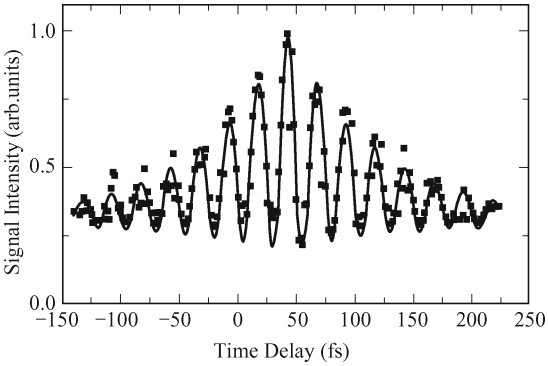

Fig. 2.9. FWM signal intensity versus relative time delay when beams 2 and 3 consist of only ω_3. The square is experimental data; the solid curve is the fourth-order theory curve with $\alpha_3 = 2.9\ \mathrm{ps}^{-1}, \delta\tau = 43\ \mathrm{fs}, \alpha_3 = 2.9\ \mathrm{ps}^{-1}, B_i = 0.6$ and $\eta = 1$; the dashed curve is the second-order theory curve.

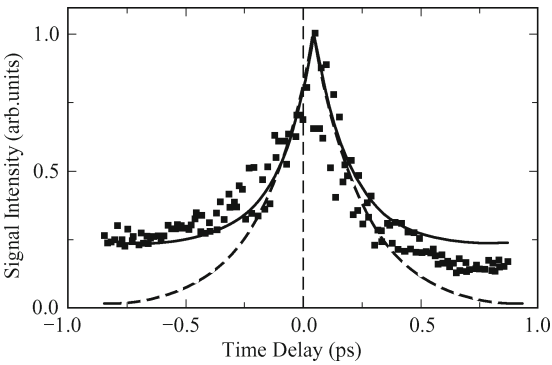

Fig. 2.10. The beat signal intensity versus relative time delay. The square is an experimental result; the solid curve is a theoretical curve given by Eq. (2.10) with $\alpha_2 = 2.5\ \mathrm{ps}^{-1}, \alpha_3 = 2.9\ \mathrm{ps}^{-1}, \omega_3 - \omega_2 = 2.54 \times 10^{14}\mathrm{s}^{-1}, \omega_3 = 3317\ \mathrm{ps}^{-1}, \Delta k = 0, \delta\tau = 43\ \mathrm{fs}, B_i = 0.6$ and $\eta = 1$.

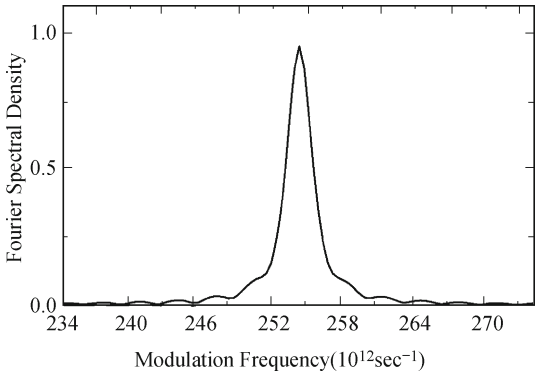

Fig. 2.11. The Fourier spectrum of experimental data in which τ is varied for a range of 362 fs.

The temporal behavior of FLPB signals is quite asymmetric with the maximum of signals shifted from $\tau = 0$. We attribute this asymmetry to the difference in the zero time delay between beams 2 and 3 for the ω_2 and ω_3 frequency components. To confirm this, we measured FWM signals when beams 2 and 3 only consisted of only one frequency component. Figures 2.7 and 2.9 present the results when the frequencies of beams 2 and 3 are ω_2 and ω_3, respectively. The difference in the zero-time delay is obvious in these figures. It is due to the large difference between wavelengths of DL2 and DL3 so that the dispersion of optical components becomes important. This can be understood as follows. Consider the case that the optical paths between 2 and 3 are equal for ω_2 component. Owing to the difference between the zero time delays for the ω_2 and ω_3 frequency components, the optical paths between beams 2 and 3 will be different by $c\delta\tau$ for the ω_3 component.

As the result, there is an extra phase factor $\omega_3\delta\tau$ for the ω_3 frequency component. For an optical glass with refractive index $n \approx 1.5$, the refractive index at $\lambda_3 = 568.2$ nm is larger than that at $\lambda_2 = 615.4$ nm by approximately 0.0006. A 43 fs delay between ω_2 and ω_3 corresponds to the propagation of beams in the glass (mainly the prism in the optical delay line) for a distance of about 2.5 cm. It is worth mentioning that asymmetric behaviors of polarization beat signals due to unbalanced dispersion effects of optical components between the two arms of an interferometer do not affect the overall accuracy in case using FLPB to measure the energy-level difference. By contrast, ultrashort pulses of equivalent bandwidth are not immune to such dispersive effects (even when balanced) because the transform limited light pulse is in fact temporally broadened (it is chirped) and this has drastic effects on its time resolution (the auto-correlation). In this sense, the FLPB with broadband noisy light has an advantage [21].

2.2 Ultrafast Sum-frequency Polarization Beats in Twin Markovian Stochastic Correlation

Research on the ultrafast phenomena is characterized by mixture of techniques and instrumentation of varied nature. To our knowledge the shortest pulses generated directly by a laser oscillator is shorter than 5.4 fs (Sub-two-cycle pulses) [31, 32]. A laser-based sampling system, consisting of a few-femtosecond visible light pulse and a synchronized sub-femtosecond soft X-ray pulse, allows them to trace these dynamics directly in the time domain with attosecond resolution [33, 34]. For over a decade, the ultra-short time resolution of material dynamics has been accomplished by the interferometric probing of wave mixing with broadband, non-transform limited noisy light (one less direct method). The time resolution is determined by the ultrafast correlation time of the noisy light and not by its temporal envelope, which is typically a few nanoseconds [35 – 41]. Such a "noisy" light source is usually derived from a dye laser modified to permit oscillation over almost the entire bandwidth of the broadband source. The typical bandwidth of the noisy light is about 100 cm^{-1}, and has a correlation time of 100 fs (HWHM) [35]. In fact, the multimode broadband light has an autocorrelation time similar to the autocorrelation time of a transform limited femtosecond laser pulse of the equivalent bandwidth although the broadband light can, in principle, be cw. Nevertheless, these two light sources are different in two fundamental ways. First the broadband source, though pulsed, is effectively nearly continuous (or quasi-cw) as well as more energetic than the femtosecond source, which is a true ultrashort pulse in time. A second fundamental distinction between two kinds of sources concerns the concept of "cross-color" coherence. While both sources may share identically broad spectra, the fields from a noisy source possess random relative phases among the available colors. There is no cross-color coherence; the field correlators are "color locked." A femtosecond pulse, whether chirped or truly transform limited, consists of fields characterized by nonrandom relative phases among the colors. The fundamental difference is that the transform limited femtosecond laser pulse is phase coherent over its spectrum while broadband light is phase random over its spectrum. Invariably the noisy light source is split into twin beams to polarize the sample. Ultrafast time resolution is achieved as the time separation of twin noisy beams is interferometrically tuned on the femtosecond to picosecond time scale. The polarization of the ensemble carries the imprint of the noisy field which it retains for the coherence time of the polarized sample. The stored polarization is probed by the delayed twin beam which recognizes its own noise pattern imprinted in the material coherence with good interferometric contrast as long as the coherence can survive in the presence of phase disrupting dynamics of the system [36].

We also have investigated the higher-order stochastic correlation effects of Markovian field in femtosecond difference-frequency polarization beats

(FDPB) [42 – 46]. In this section we shall systematically study ASPB in the twin Markovian stochastic correlation. The difference between ASPB and the first polarization beat experiment of Rothenberg and Grischkowsky [43] is that in ASPB the signal is modulated not in real time but rather as a function of the delay between two pump beams. ASPB is also related to the coherent control that has been used to control the ionization rate of an atom [47], the dissociation rate of a molecule [48], and the direction of the current generated in a semiconductor [49]. One achieves control by varying the relative phase of the two fields such that the induced transition amplitudes interfere constructively or destructively. The common point of ASPB and coherent control is that both methods involve two fields to induce two-pathway excitation. Physical processes are manipulated by variation of the phase of fields. The difference between them is that the coherent control describes a quantum interference between transition probability amplitudes, whereas ASPB originates from the interference between macroscopic polarizations, which is classic in nature.

In this section, we study ASPB theoreticallies in a Doppler-broadened three-level atomic system. As we mentioned above, ASPB is based on the interference between one-photon and two-photon processes simultaneously induced by time-delayed correlated fluctuating twin fields. Inasmuch as the one-photon degenerate FWM (DFWM) of ASPB is similar to the case of FDPB [28], here we shall mainly concentrate on two-photon nondegenerate FWM (NDFWM) in ASPB. In the case of broadband incident beams, unlike the corresponding one-photon resonant DFWM, the dephasing and rephrasing processes in an inhomogeneously broadened system cause the maximum of the two-photon resonant NDFWM signal to shift from zero time delay. If we assume that the incident fields are weak and have finite bandwidths, in the extremely Doppler-broadened limit an analytic closed form for the second-order or fourth-order Markovian stochastic correlation of ASPB can be obtained.

2.2.1 Basic Theory

ASPB is a polarization beat phenomenon [13, 14] originating from the interference between two-pathway excitations simultaneously induced by time-delayed correlated fluctuating twin fields, while the cascade three-level ASPB comes from the sum-frequency polarization interference between one-photon and two-photon processes in physics. Let us mainly consider a Doppler-broadened ladder three-level atomic system [see Fig. 2.12 (a)] with a ground state $|0\rangle$, an intermediate state $|1\rangle$ and an excited state $|2\rangle$. States between $|0\rangle$ and $|1\rangle$ and between $|1\rangle$ and $|2\rangle$ are coupled by dipolar transition with resonant frequencies Ω_1 and Ω_2, respectively, while states between $|0\rangle$ and $|2\rangle$ are dipolar forbidden. We consider in this cascade three-level system a

double-frequency time-delay FWM experiment in which beams 1 and 2 consist of two frequency components ω_1 and ω_2, while a beam 3 has frequency ω_3 (see Fig. 2.13). We assume that $\omega_1 \approx \Omega_1(\omega_3 \approx \Omega_1)$ and $\omega_2 \approx \Omega_2$, therefore $\omega_1(\omega_3)$ and ω_2 will drive the transitions from $|0\rangle$ to $|1\rangle$ and from $|1\rangle$ to $|2\rangle$, respectively. There are two distinct processes involved in this double-frequency time-delay FWM. First the ω_1 frequency component of twin composite beams 1 and 2 induces population gratings of states $|0\rangle$ and $|1\rangle$, which are probed by the beam 3 of frequency ω_3. This is a one-photon resonant DFWM and the signal (beam 4) has frequency ω_3. Second, the beam 3 and ω_2 frequency component of the beam 1 induce a two-photon coherence between $|0\rangle$ and $|2\rangle$, which is then probed by the ω_2 frequency component of the beam 2. This is a two-photon NDFWM with a resonant intermediate state and the frequency of the signal equals ω_3 again. Similarly, we also can consider the sum-frequency polarization interference between two one-photon processes in a V three-level Doppler-broadened atomic system [see Fig. 2.12(b)]. Comparing with the cascade three-level ASPB, two of them will share same four density operator pathways of one-photon DFWM processes.

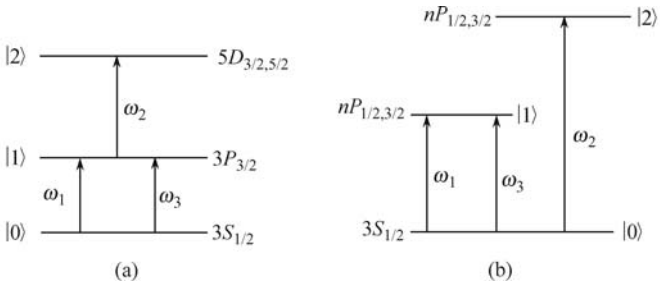

Fig. 2.12. Cascading three-level for (a) and V three-level for (b) configurations of the sodium atom to be treated by ASPB.

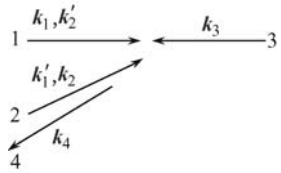

Fig. 2.13. Schematic diagram of the phase-conjugation sum-frequency geometry of ASPB.

Twin composite stochastic fields of the beam 1, E_{p1}, and the beam 2, E_{p2}, can be written as

$$\begin{aligned} E_{p1} &= A_1(\boldsymbol{r},t)\exp(-\mathrm{i}\omega_1 t) + A_2'(\boldsymbol{r},t)\exp(-\mathrm{i}\omega_2 t) \\ &= \varepsilon_1 u_1(t)\exp[\mathrm{i}(\boldsymbol{k}_1\cdot\boldsymbol{r}-\omega_1 t)] + \\ &\quad \varepsilon_2' u_2(t-\tau)\exp[\mathrm{i}(\boldsymbol{k}_2'\cdot\boldsymbol{r}-\omega_2 t+\omega_2\tau)], \end{aligned} \tag{2.32}$$

$$\begin{aligned} E_{P2} &= A_1'(\boldsymbol{r},t)\exp(-\mathrm{i}\omega_1 t) + A_2(\boldsymbol{r},t)\exp(-\mathrm{i}\omega_2 t) \\ &= \varepsilon_1' u_1(t-\tau)\exp[\mathrm{i}(\boldsymbol{k}_1'\cdot\boldsymbol{r} - \omega_1 t + \omega_1\tau)] + \\ &\quad \varepsilon_2 u_2(t)\exp[\mathrm{i}(\boldsymbol{k}_2\cdot\boldsymbol{r} - \omega_2 t)]. \end{aligned} \tag{2.33}$$

Here, $A_i(\boldsymbol{r},t) = \varepsilon_i u_i(t)\exp[\mathrm{i}\boldsymbol{k}_i\cdot\boldsymbol{r}(t)]$, $A_i'(\boldsymbol{r},t) = \varepsilon_i' u_i(t-\tau)\exp[\mathrm{i}\boldsymbol{k}_i'\cdot\boldsymbol{r}(t) + \omega_i\tau]$; $\varepsilon_i, \boldsymbol{k}_i(\varepsilon_i', \boldsymbol{k}_i')$ are the constant field amplitude and the wave vector of the ω_i component in the beam 1 (beam 2), respectively. $u_i(t)$ is a dimensionless statistical factor that contains phase and amplitude fluctuations. The $u_i(t)$ is taken to be a complex ergodic stochastic function of t, which obey complex circular Gaussian statistics in the chaotic field. τ is a variable relative time delay between the prompt (unprime) and delayed (prime) fields. To accomplish this the frequency component ω_1 and ω_2 lights are split and recombined to provide two double-frequency pulses in such a way that the ω_1 component is delayed by τ in beam 2 and the ω_2 component delayed by the same amount in the beam 1 (Fig. 2.13). The time delay τ is introduced in both beams, which is quite different with that of FDPB [44, 45].

On the other hand, the beam 3 is assumed to be a quasimonochromatic light, the complex electric fields of beam 3 can be written as

$$E_{P3} = A_3(\boldsymbol{r},t)\exp(-i\omega_3 t) = \varepsilon_3 u_3(t)\exp[\mathrm{i}(\boldsymbol{k}_3\cdot\boldsymbol{r} - \omega_3 t)]. \tag{2.34}$$

Here, ω_3, ε_3, and $\boldsymbol{k}_3$ are the frequency, the field amplitude and the wave vector of beam 3, respectively. Since ω_1 and ω_3 come from the same laser source (i.e., $\omega_1 = \omega_3$), we have $u_3(t) \approx 1$ for the quasimonochromatic light.

We only retain the resonant dipole interaction term in the calculation of the signal; this is known as the rotating wave approximation (RWA). Because of the selectivity imposed by the RWA, each pulse interaction contributes in a unique way to the phase matching direction of the nonlinear signal. We shall employ perturbation theory to calculate the density matrix elements by the following perturbation chains,

$$(\mathrm{I})\ \rho_{00}^{(0)} \xrightarrow{A_1} \rho_{10}^{(1)} \xrightarrow{(A_1')^*} \rho_{00}^{(2)} \xrightarrow{A_3} \rho_{10}^{(3)}, \tag{2.35}$$

$$(\mathrm{II})\ \rho_{00}^{(0)} \xrightarrow{(A_1')^*} (\rho_{10}^{(1)})^* \xrightarrow{A_1} \rho_{00}^{(2)} \xrightarrow{A_3} \rho_{10}^{(3)}, \tag{2.36}$$

$$(\mathrm{III})\ \rho_{00}^{(0)} \xrightarrow{A_1} \rho_{10}^{(1)} \xrightarrow{(A_1')^*} \rho_{11}^{(2)} \xrightarrow{A_3} \rho_{10}^{(3)}, \tag{2.37}$$

$$(\mathrm{IV})\ \rho_{00}^{(0)} \xrightarrow{(A_1')^*} (\rho_{10}^{(1)})^* \xrightarrow{A_1} \rho_{11}^{(2)} \xrightarrow{A_3} \rho_{10}^{(3)}, \tag{2.38}$$

$$(\mathrm{V})\ \rho_{00}^{(0)} \xrightarrow{A_3} \rho_{10}^{(1)} \xrightarrow{A_2'} \rho_{20}^{(2)} \xrightarrow{(A_2)^*} \rho_{10}^{(3)}. \tag{2.39}$$

One-photon and two-photon FWM signals are induced by ω_1 and ω_2 frequency components of twin beams 1 and 2. Now, we consider the other pos-

sible density operator pathways:

$$(\text{VI})\ \rho_{00}^{(0)} \xrightarrow{A_3} \rho_{10}^{(1)} \xrightarrow{(A_1')^*} \rho_{00}^{(2)} \xrightarrow{A_1} \rho_{10}^{(3)}, \tag{2.40}$$

$$(\text{VII})\ \rho_{00}^{(0)} \xrightarrow{(A_1')^*} (\rho_{10}^{(1)})^* \xrightarrow{A_3} \rho_{00}^{(2)} \xrightarrow{A_1} \rho_{10}^{(3)}, \tag{2.41}$$

$$(\text{VIII})\ \rho_{00}^{(0)} \xrightarrow{A_3} \rho_{10}^{(1)} \xrightarrow{(A_1')^*} \rho_{11}^{(2)} \xrightarrow{A_1} \rho_{10}^{(3)}, \tag{2.42}$$

$$(\text{IX})\ \rho_{00}^{(0)} \xrightarrow{(A_1')^*} (\rho_{10}^{(1)})^* \xrightarrow{A_3} \rho_{11}^{(2)} \xrightarrow{A_1} \rho_{10}^{(3)}, \tag{2.43}$$

where the population grating induced by beam 3 and ω_1 frequency component of beams 2 is responsible for the generation of the FWM signal. These gratings have much smaller fringe spacings which equal approximately one half of the wavelengths of the incident lights ($E_{p2}\lambda_i/[2\sin(\theta/2)] \xrightarrow{\theta\approx 180^\circ} \lambda_i/2$). For a Doppler-broadened system, the gratings will be washed out by the atomic motion. Therefore, it is appropriate to neglect the FWM signal from these density operator pathways. The stricter requirements on the phase matching also make this process unimportant.

In this section, Chains (I)–(IV) correspond to the one-photon DFWM processes of V or cascade three-level atomic system, while the Chain (V) corresponds to the two-photon NDFWM process of cascade three-level atomic system. We obtain the third-order off-diagonal density matrix element $\rho_{10}^{(3)}$ which has wave vector $\boldsymbol{k}_1 - \boldsymbol{k}_1' + \boldsymbol{k}_3$ or $\boldsymbol{k}_2' - \boldsymbol{k}_2 + \boldsymbol{k}_3$, $\rho^{(3)} = \rho^{(\text{I})} + \rho^{(\text{II})} + \rho^{(\text{III})} + \rho^{(\text{IV})} + \rho^{(\text{V})}$. Here $\rho^{(\text{I})}, \rho^{(\text{II})}, \rho^{(\text{III})}, \rho^{(\text{IV})}$ and $\rho^{(\text{V})}$ corresponding to $\rho_{10}^{(3)}$ of the perturbation the chain (I), (II), (III), (IV), and (V), respectively, are

$$\begin{aligned}\rho^{(\text{I})} = &\left(\frac{\mathrm{i}\mu_1}{\hbar}\right)^3 \exp(-\mathrm{i}\omega_3 t) \int_0^\infty \mathrm{d}t_3 \int_0^\infty \mathrm{d}t_2 \int_0^\infty \mathrm{d}t_1 \times \\ &H_3(t_3)H_2(t_2)H_1(t_1)A_1(\boldsymbol{r}, t - t_1 - t_2 - t_3) \times \\ &[A_1'(\boldsymbol{r}, t - t_2 - t_3)]^* A_3(\boldsymbol{r}, t - t_3),\end{aligned} \tag{2.44}$$

$$\begin{aligned}\rho^{(\text{II})} = &\left(\frac{\mathrm{i}\mu_1}{\hbar}\right)^3 \exp(-\mathrm{i}\omega_3 t) \int_0^\infty \mathrm{d}t_3 \int_0^\infty \mathrm{d}t_2 \int_0^\infty \mathrm{d}t_1 \times \\ &H_3(t_3)H_2(t_2)[H_1(t_1)]^* A_1(\boldsymbol{r}, t - t_2 - t_3) \times \\ &[A_1'(\boldsymbol{r}, t - t_1 - t_2 - t_3)]^* A_3(\boldsymbol{r}, t - t_3),\end{aligned} \tag{2.45}$$

$$\begin{aligned}\rho^{(\text{III})} = &\left(\frac{\mathrm{i}\mu_1}{\hbar}\right)^3 \exp(-\mathrm{i}\omega_3 t) \int_0^\infty \mathrm{d}t_3 \int_0^\infty \mathrm{d}t_2 \int_0^\infty \mathrm{d}t_1 \times \\ &H_3(t_3)H_4(t_2)H_1(t_1)A_1(\boldsymbol{r}, t - t_1 - t_2 - t_3) \times \\ &[A_1'(\boldsymbol{r}, t - t_2 - t_3)]^* A_3(\boldsymbol{r}, t - t_3),\end{aligned} \tag{2.46}$$

$$\rho^{(\mathrm{IV})} = \left(\frac{\mathrm{i}\mu_1}{\hbar}\right)^3 \exp(-\mathrm{i}\omega_3 t) \int_0^\infty \mathrm{d}t_3 \int_0^\infty \mathrm{d}t_2 \int_0^\infty \mathrm{d}t_1 \times H_3(t_3)H_4(t_2)[H_1(t_1)]^* A_1(\boldsymbol{r}, t-t_2-t_3) \times [A_1'(\boldsymbol{r}, t-t_1-t_2-t_3)]^* A_3(\boldsymbol{r}, t-t_3), \tag{2.47}$$

$$\rho^{(\mathrm{V})} = \left(\frac{\mathrm{i}\mu_1}{\hbar}\right)\left(\frac{\mathrm{i}\mu_2}{\hbar}\right)^2 \exp(-\mathrm{i}\omega_3 t) \int_0^\infty \mathrm{d}t_3 \int_0^\infty \mathrm{d}t_2 \int_0^\infty \mathrm{d}t_1 \times H_3(t_3)H_5(t_2)H_3(t_1)A_3(\boldsymbol{r}, t-t_1-t_2-t_3) \times A_2'(\boldsymbol{r}, t-t_2-t_3)[A_2(\boldsymbol{r}, t-t_3)]^*. \tag{2.48}$$

Here, $H_1(t) = \exp[-(\Gamma_{10} + \mathrm{i}\Delta_1)t], H_2(t) = \exp(-\Gamma_0 t), H_3(t) = \exp[-(\Gamma_{10} + \mathrm{i}\Delta_3)t], H_4(t) = \exp(-\Gamma_1 t), H_5(t) = \exp[-(\Gamma_{20} + \mathrm{i}\Delta_2 + \mathrm{i}\Delta_3)t]; \mu_1(\mu_2)$ is the dipole-moment matrix element between $|0\rangle$ and $|1\rangle(|1\rangle$ and $|2\rangle); \Gamma_0(\Gamma_1)$ is the population relaxation rate of state $|0\rangle(|1\rangle); \Gamma_{10}(\Gamma_{20})$ is the transverse relaxation rate of the transition from $|0\rangle$ to $|1\rangle(|0\rangle$ to $|2\rangle)$, which contains material dephasing dynamics; $\Delta_1 = \Omega_1 - \omega_1, \Delta_2 = \Omega_2 - \omega_2, \Delta_3 = \Omega_1 - \omega_3$.

The nonlinear polarization $P^{(3)}$ responsible for phase-conjugate FWM signals is given by averaging over the velocity distribution function $W(\boldsymbol{v})$. Thus

$$P^{(3)} = N\mu_1 \int_{-\infty}^{\infty} \mathrm{d}\boldsymbol{v} w(\boldsymbol{v}) \rho_{10}^{(3)}(\boldsymbol{v}).$$

Here, $\boldsymbol{v}$ is the atomic velocity, N is the density of atoms. For a Doppler-broadened atomic system, we have $w(\boldsymbol{v}) = \dfrac{1}{\sqrt{\pi}u} \exp[-(\boldsymbol{v}/u)^2]$. Here, $u = \sqrt{2k_B T/m}$ with m the mass of an atom, k_B is Boltzmann's constant and T the absolute temperature. In general, the total third-order polarization $P^{(3)}$ is supposition of the DFWM and NDFWM polarizations $P^{(3)} = P^{(\mathrm{I})} + P^{(\mathrm{II})} + P^{(\mathrm{III})} + P^{(\mathrm{IV})} + P^{(\mathrm{V})}$, where

$$P^{(\mathrm{I})} = S_1(\boldsymbol{r}) \exp[-\mathrm{i}(\omega_3 t + \omega_1 \tau)] \int_{-\infty}^{+\infty} \mathrm{d}\boldsymbol{v} w(\boldsymbol{v}) \int_0^\infty \mathrm{d}t_3 \int_0^\infty \mathrm{d}t_2 \int_0^\infty \mathrm{d}t_1 \times \exp[-\mathrm{i}\theta_{\mathrm{I}}(\boldsymbol{v})] H_1(t_1) \times H_2(t_2)H_3(t_3) \times u_1(t-t_1-t_2-t_3)u_1^*(t-t_2-t_3-\tau), \tag{2.49}$$

$$P^{(\mathrm{II})} = S_1(\boldsymbol{r}) \exp[-\mathrm{i}(\omega_3 t + \omega_1 \tau)] \int_{-\infty}^{+\infty} \mathrm{d}\boldsymbol{v} w(\boldsymbol{v}) \int_0^\infty \mathrm{d}t_3 \int_0^\infty \mathrm{d}t_2 \int_0^\infty \mathrm{d}t_1 \times \exp[-\mathrm{i}\theta_{\mathrm{II}}(\boldsymbol{v})] H_1^*(t_1) \times H_2(t_2)H_3(t_3) \times u_1(t-t_2-t_3)u_1^*(t-t_1-t_2-t_3-\tau), \tag{2.50}$$

$$P^{(\mathrm{III})} = S_1(\boldsymbol{r}) \exp[-\mathrm{i}(\omega_3 t + \omega_1 \tau)] \int_{-\infty}^{+\infty} \mathrm{d}\boldsymbol{v} w(\boldsymbol{v}) \int_0^\infty \mathrm{d}t_3 \int_0^\infty \mathrm{d}t_2 \int_0^\infty \mathrm{d}t_1 \times \exp[-\mathrm{i}\theta_{\mathrm{I}}(\boldsymbol{v})] H_1(t_1) \times H_4(t_2)H_3(t_3) \times u_1(t-t_1-t_2-t_3)u_1^*(t-t_2-t_3-\tau), \tag{2.51}$$

$$P^{(\mathrm{IV})} = S_1(\boldsymbol{r})\exp[-\mathrm{i}(\omega_3 t + \omega_1\tau)]\int_{-\infty}^{+\infty}\mathrm{d}\boldsymbol{v}w(\boldsymbol{v})\int_0^\infty \mathrm{d}t_3\int_0^\infty \mathrm{d}t_2\int_0^\infty \mathrm{d}t_1 \times \exp[-\mathrm{i}\theta_{\mathrm{II}}(\boldsymbol{v})]H_1^*(t_1)\times H_4(t_2)H_3(t_3)\times u_1(t-t_2-t_3)u_1^*(t-t_1-t_2-t_3-\tau), \tag{2.52}$$

$$P^{(\mathrm{V})} = S_2(\boldsymbol{r})\exp[-\mathrm{i}(\omega_3 t - \omega_2\tau)]\int_{-\infty}^{+\infty}\mathrm{d}\boldsymbol{v}w(\boldsymbol{v})\int_0^\infty \mathrm{d}t_3\int_0^\infty \mathrm{d}t_2\int_0^\infty \mathrm{d}t_1 \times \exp[-\mathrm{i}\theta_{\mathrm{III}}(\boldsymbol{v})]H_3(t_1)\times H_5(t_2)H_3(t_3)\times u_2(t-t_2-t_3-\tau)u_2^*(t-t_3). \tag{2.53}$$

Here,

$$S_1(\boldsymbol{r}) = -\mathrm{i}\hbar N\left(\frac{\mu_1}{\hbar}\right)^4\varepsilon_1(\varepsilon_1')^*\varepsilon_3\exp[\mathrm{i}(\boldsymbol{k}_1-\boldsymbol{k}_1'+\boldsymbol{k}_3)\cdot\boldsymbol{r}],$$
$$S_2(\boldsymbol{r}) = -\mathrm{i}\hbar N\left(\frac{\mu_1}{\hbar}\right)^2\left(\frac{\mu_2}{\hbar}\right)^2\varepsilon_2'(\varepsilon_2)^*\varepsilon_3\exp[\mathrm{i}(\boldsymbol{k}_2'-\boldsymbol{k}_2+\boldsymbol{k}_3)\cdot\boldsymbol{r}];$$
$$\theta_{\mathrm{I}}(\boldsymbol{v}) = \boldsymbol{v}\cdot[\boldsymbol{k}_1(t_1+t_2+t_3)-\boldsymbol{k}_1'(t_2+t_3)+\boldsymbol{k}_3t_3],$$
$$\theta_{\mathrm{II}}(\boldsymbol{v}) = \boldsymbol{v}\cdot[-\boldsymbol{k}_1'(t_1+t_2+t_3)+\boldsymbol{k}_1(t_2+t_3)+\boldsymbol{k}_3t_3],$$
$$\theta_{\mathrm{III}}(\boldsymbol{v}) = \boldsymbol{v}\cdot[\boldsymbol{k}_3(t_1+t_2+t_3)+\boldsymbol{k}_2'(t_2+t_3)-\boldsymbol{k}_2t_3].$$

In general, the ASPB (at the intensity level) can be viewed as built of the sum of four contributions: (i) τ-independent part, (ii) the purely resonant, (iii) the purely nonresonant, and (iv) the resonant-resonant, nonresonant-nonresonant or resonant-nonresonant three types of cross-terms contributions. For the ultrashort femtosecond pulsed excitation with homodyne detection, anharmonicity effects are cancelled (due to loss of phase information) [36]. Furthermore, unlike heterodyned signals, all the cross terms that complicate the homodyne (quadrature) signal are absent. One must introduce a second (harmonic) Raman resonance to be able to discriminate between the direct and cascaded events. In contrast, in the noisy light interferometric experiment, multiple harmonic resonances produce new frequency components and cross terms, yet one cannot distinguish between the direct and the cascaded events. In the absence of inhomogeneity, the presence of (diagonal) anharmonicity allows these pathways to become distinct.

2.2.2 Second-order Stochastic Correlation of ASPB

For the macroscopic system where phase matching takes place this signal must be drawn from the $P^{(3)}$ developed on one "atom" multiplied by the $(P^{(3)})^*$ that is developed on another "atom" which must be located elsewhere in space (with summation over all such pairs) [35–41, 46]. For homodyne detection the ASPB signal is proportional to the average of the absolute square of $P^{(3)}$ over the random variable of the stochastic process $\langle|P^{(3)}|^2\rangle$,

which involves fourth- and second-order coherence function of $u_i(t)$ in phase–conjugation geometry. The UMS in self-diffraction geometry is related to the sixth-order coherence function of the incident fields [8, 42].

In the case that we are only interested in the τ-dependent part of the ASPB signal, the ASPB signal intensity can be well approximated by the absolute square of the non-trivial stochastic average of the polarization $|\langle P^{(3)}\rangle|^2$, which involves second-order coherence function of $u_i(t)$ [44 – 46]. Using Eq. (2.10) the stochastic average of the polarization then

$$\langle P^{(3)}\rangle = \langle P^{(\mathrm{I})}\rangle + \langle P^{(\mathrm{II})}\rangle + \langle P^{(\mathrm{III})}\rangle + \langle P^{(\mathrm{IV})}\rangle + \langle P^{(\mathrm{V})}\rangle, \tag{2.54}$$

where

$$\begin{aligned}\langle P^{(\mathrm{I})}\rangle = {} & S_1(\boldsymbol{r})\exp[-\mathrm{i}(\omega_3 t+\omega_1\tau)]\int_{-\infty}^{+\infty}\mathrm{d}\boldsymbol{v}w(\boldsymbol{v})\int_0^\infty \mathrm{d}t_3\times\\ & \int_0^\infty \mathrm{d}t_2\int_0^\infty \mathrm{d}t_1\exp[-\mathrm{i}\theta_{\mathrm{I}}(\boldsymbol{v})]\times\\ & H_1(t_1)H_2(t_2)H_3(t_3)\exp(-\alpha_1|t_1-\tau|),\end{aligned} \tag{2.55}$$

$$\begin{aligned}\langle P^{(\mathrm{II})}\rangle = {} & S_1(\boldsymbol{r})\exp[-i(\omega_3 t+\omega_1\tau)]\int_{-\infty}^{+\infty}\mathrm{d}\boldsymbol{v}w(\boldsymbol{v})\int_0^\infty \mathrm{d}t_3\times\\ & \int_0^\infty \mathrm{d}t_2\int_0^\infty \mathrm{d}t_1\exp[-\mathrm{i}\theta_{\mathrm{II}}(\boldsymbol{v})]\times\\ & H_1^*(t_1)H_2(t_2)H_3(t_3)\exp(-\alpha_1|t_1+\tau|),\end{aligned} \tag{2.56}$$

$$\begin{aligned}\langle P^{(\mathrm{III})}\rangle = {} & S_1(\boldsymbol{r})\exp[-\mathrm{i}(\omega_3 t+\omega_1\tau)]\int_{-\infty}^{+\infty}\mathrm{d}\boldsymbol{v}w(\boldsymbol{v})\int_0^\infty \mathrm{d}t_3\times\\ & \int_0^\infty \mathrm{d}t_2\int_0^\infty \mathrm{d}t_1\exp[-\mathrm{i}\theta_{\mathrm{I}}(\boldsymbol{v})]\times\\ & H_1(t_1)H_4(t_2)H_3(t_3)\exp(-\alpha_1|t_1-\tau|),\end{aligned} \tag{2.57}$$

$$\begin{aligned}\langle P^{(\mathrm{IV})}\rangle = {} & S_1(\boldsymbol{r})\exp[-\mathrm{i}(\omega_3 t+\omega_1\tau)]\int_{-\infty}^{+\infty}\mathrm{d}\boldsymbol{v}w(\boldsymbol{v})\int_0^\infty \mathrm{d}t_3\times\\ & \int_0^\infty \mathrm{d}t_2\int_0^\infty \mathrm{d}t_1\exp[-\mathrm{i}\theta_{\mathrm{II}}(\boldsymbol{v})]\times\\ & H_1^*(t_1)H_4(t_2)H_3(t_3)\exp(-\alpha_1|t_1+\tau|),\end{aligned} \tag{2.58}$$

$$\begin{aligned}\langle P^{(\mathrm{V})}\rangle = {} & S_2(\boldsymbol{r})\exp[-\mathrm{i}(\omega_3 t-\omega_2)\tau]\int_{-\infty}^{+\infty}\mathrm{d}\boldsymbol{v}w(\boldsymbol{v})\int_0^\infty \mathrm{d}t_3\times\\ & \int_0^\infty \mathrm{d}t_2\int_0^\infty \mathrm{d}t_1\exp[-\mathrm{i}\theta_{\mathrm{III}}(\boldsymbol{v})]\times\\ & H_3(t_1)H_5(t_2)H_3(t_3)\exp(-\alpha_2|t_2+\tau|).\end{aligned} \tag{2.59}$$

We discuss the ASPB in a Doppler-broadened system. After performing the tedious integral in Eqs. (2.55) – (2.59) over t_1, t_2, and t_3 we obtain for

(i) $\tau > 0$

$$\langle P^{(3)}\rangle = S_1(\boldsymbol{r})\exp(-\mathrm{i}\omega_3 t)\int_{-\infty}^{+\infty}\mathrm{d}\boldsymbol{v}w(\boldsymbol{v})\frac{L_1(\boldsymbol{v})+L_2(\boldsymbol{v})}{\Gamma_{10}-\alpha_1+\mathrm{i}(\Delta_1+\boldsymbol{k}_1\cdot\boldsymbol{v})}\times \left\{\frac{[2\Gamma_{10}+\mathrm{i}(\boldsymbol{k}_1-\boldsymbol{k}_1')\cdot\boldsymbol{v}]\exp(-\alpha_1|\tau|-\mathrm{i}\omega_1\tau)}{\Gamma_{10}+\alpha_1-\mathrm{i}(\Delta_1+\boldsymbol{k}_1'\cdot\boldsymbol{v})}-\right. \left.\frac{2\alpha_1\exp[-\Gamma_{10}|\tau|-\mathrm{i}(\Omega_1+\boldsymbol{k}_1\cdot\boldsymbol{v})\tau]}{\Gamma_{10}+\alpha_1+\mathrm{i}(\Delta_1+\boldsymbol{k}_1\cdot\boldsymbol{v})}\right\}+S_2(\boldsymbol{r})\exp(-\mathrm{i}\omega_3 t)\times \int_{-\infty}^{+\infty}\mathrm{d}\boldsymbol{v}w(\boldsymbol{v})\frac{L_3(\boldsymbol{v})\exp(-\alpha_2|\tau|+\mathrm{i}\omega_2\tau)}{\Gamma_{20}+\alpha_2+\mathrm{i}[\Delta_2+\Delta_3+(\boldsymbol{k}_2'+\boldsymbol{k}_3)\cdot\boldsymbol{v}]}. \tag{2.60}$$

(ii) $\tau < 0$

$$\langle P^{(3)}\rangle = S_1(\boldsymbol{r})\exp(-\mathrm{i}\omega_3 t)\int_{-\infty}^{+\infty}\mathrm{d}\boldsymbol{v}w(\boldsymbol{v})\frac{L_1(\boldsymbol{v})+L_2(\boldsymbol{v})}{\Gamma_{10}-\alpha_1-\mathrm{i}(\Delta_1+\boldsymbol{k}_1'\cdot\boldsymbol{v})}\times \left\{\frac{[2\Gamma_{10}+\mathrm{i}(\boldsymbol{k}_1-\boldsymbol{k}_1')\cdot\boldsymbol{v}]\exp(-\alpha_1|\tau|-\mathrm{i}\omega_1\tau)}{\Gamma_{10}+\alpha_1+\mathrm{i}(\Delta_1+\boldsymbol{k}_1\cdot\boldsymbol{v})}-\right. \left.\frac{2\alpha_1\exp[-\Gamma_{10}|\tau|-\mathrm{i}(\Omega_1+\boldsymbol{k}_1'\cdot\boldsymbol{v})\tau]}{\Gamma_{10}+\alpha_1-\mathrm{i}(\Delta_1+\boldsymbol{k}_1'\cdot\boldsymbol{v})}\right\}\times\{\exp(-\alpha_2|\tau|+\mathrm{i}\omega_2\tau)- \left.\frac{2\alpha_2\exp\{-\Gamma_{20}|\tau|+\mathrm{i}[\Omega_2+\Delta_3+(\boldsymbol{k}_2'+\boldsymbol{k}_3)\cdot\boldsymbol{v}]\tau\}}{\Gamma_{20}+\alpha_2+\mathrm{i}[\Delta_2+\Delta_3+(\boldsymbol{k}_2'+\boldsymbol{k}_3)\cdot\boldsymbol{v}]}\right\}. \tag{2.61}$$

Here,

$$L_1(\boldsymbol{v}) = \frac{1}{[\Gamma_0+\mathrm{i}(\boldsymbol{k}_1-\boldsymbol{k}_1')\cdot\boldsymbol{v}]\{\Gamma_{10}+\mathrm{i}[\Delta_3+(\boldsymbol{k}_1-\boldsymbol{k}_1'+\boldsymbol{k}_3)\cdot\boldsymbol{v}]\}}, \tag{2.62}$$

$$L_2(\boldsymbol{v}) = \frac{1}{[\Gamma_1+\mathrm{i}(\boldsymbol{k}_1-\boldsymbol{k}_1')\cdot\boldsymbol{v}]\{\Gamma_{10}+\mathrm{i}[\Delta_3+(\boldsymbol{k}_1-\boldsymbol{k}_1'+\boldsymbol{k}_3)\cdot\boldsymbol{v}]\}}, \tag{2.63}$$

$$L_3(\boldsymbol{v}) = \frac{1}{[\Gamma_{10}+\mathrm{i}(\Delta_3+\boldsymbol{k}_3\cdot\boldsymbol{v})]\{\Gamma_{10}+\mathrm{i}[\Delta_3+(\boldsymbol{k}_2'-\boldsymbol{k}_2+\boldsymbol{k}_3)\cdot\boldsymbol{v}]\}}. \tag{2.64}$$

In general the temporal behavior of broadband two-photon NDFWM signals is complicated, which is asymmetric about $\tau = 0$. However, the situation becomes simpler when the laser linewidths are much narrower than the homogeneous linewidths of the transitions (i.e., $\alpha_1 << \Gamma_{10}$ and $\alpha_2 << \Gamma_{20}$). In this homogeneous broadening dominant case, after tail approximation (i.e., $\Gamma_{10}|\tau| >> 1$ and $\Gamma_{20}|\tau| >> 1$) we have for both $\tau > 0$ and $\tau < 0$,

$$\langle P^{(3)}\rangle = S_1(\boldsymbol{r})\exp(-\mathrm{i}\omega_3 t)\{B_1\exp(-\alpha_1|\tau|-\mathrm{i}\omega_1\tau)+ \eta B_2\exp[-\alpha_2|\tau|-\mathrm{i}(\Delta\boldsymbol{k}\cdot\boldsymbol{r}-\omega_2\tau)]\}. \tag{2.65}$$

Here, ratio of associated Rabi frequencies for NDFWM and DFWM processes $\eta = \dfrac{\mu_2^2}{\mu_1^2}\left[\dfrac{\varepsilon_2'(\varepsilon_2)^*}{\varepsilon_1(\varepsilon_1')^*}\right]$; spatial modulation factor $\Delta\boldsymbol{k} = (\boldsymbol{k}_1-\boldsymbol{k}_1')-(\boldsymbol{k}_2'-\boldsymbol{k}_2)$;

The constants B_i mainly depend on the laser linewidths and relaxation rate of the transition in this work. B_1 and B_2 are τ-independent factors which equal:

$$B_1 = \int_{-\infty}^{+\infty} \mathrm{d}\boldsymbol{v} w(\boldsymbol{v}) \frac{[2\Gamma_{10} + \mathrm{i}(\boldsymbol{k}_1 - \boldsymbol{k}_1') \cdot \boldsymbol{v}][L_1(\boldsymbol{v}) + L_2(\boldsymbol{v})]}{[\Gamma_{10} + \mathrm{i}(\Delta_1 + \boldsymbol{k}_1 \cdot \boldsymbol{v})][\Gamma_{10} - \mathrm{i}(\Delta_1 + \boldsymbol{k}_1' \cdot \boldsymbol{v})]}, \tag{2.66}$$

$$B_2 = \int_{-\infty}^{+\infty} \mathrm{d}\boldsymbol{v} w(\boldsymbol{v}) \frac{L_3(\boldsymbol{v})}{\Gamma_{20} + \mathrm{i}[\Delta_2 + \Delta_3 + (\boldsymbol{k}_2' + \boldsymbol{k}_3) \cdot \boldsymbol{v}]}. \tag{2.67}$$

According to Eq. (2.66), we first consider the case that $\omega_1(\omega_3)$ is tuned to within the Doppler linewidth of the $|0\rangle - |1\rangle$ transition, i.e., $\Delta_1 \leqslant k_1 u$. In this case, only atoms with velocity (along the $\boldsymbol{z}$ axis) $v \approx \Delta_1/k_1$ are resonant with beam 3. This group of atoms will interact further with the beam 1 and contribute to the two-photon NDFWM signal in Eq. (2.67). The condition for the two-photon transition is $(\omega_1 + k_1 v) + (\omega_2 - k_2 v) = \Omega_1 + \Omega_2$, i.e., $\Delta_1 + \Delta_2 = k_1(1-\xi_2)v$; therefore, we have $\Delta_1 + \Delta_2 = (1-\xi_2)\Delta_1$. The NDFWM spectrum is Doppler free because only atoms in a specific velocity group contribute to NDFWM signals. As we discuss below (the second term of Eq. (2.80)), in the extremely Doppler-broadened limit the Doppler-free linewidth equals approximately $2(\sqrt{2}-1)^{1/2}\Gamma_{20}^a$. A similar situation in the two-photon absorption with resonant intermediate state has been discussed by Bjorkholm and Liao [50]. We then consider the off-resonant Doppler-broadened NDFWM. In this case ω_1 is tuned to the wing of the Doppler-broadened line of the one-photon transition from $|0\rangle$ to $|1\rangle$ (i.e., $\Delta_1 \geqslant k_1 u, \Gamma_{10}$). We have

$$\langle P^{(V)} \rangle \approx -\frac{1}{\sqrt{\pi}\Delta_1^2} S_2(\boldsymbol{r}) \exp[-\alpha_2|\tau| - \mathrm{i}(\omega_3 t - \omega_2 \tau)] \times \int_{-\infty}^{+\infty} \mathrm{d}x \frac{\exp(-x^2)}{\Gamma_{20} + \mathrm{i}[\Delta_2 + \Delta_1 - k_1 u(1-\xi_2)x]}.$$

Here $x = \dfrac{v}{u}$. So the NDFWM signal has resonance at $\Delta_1 + \Delta_2 = 0$. The residual Doppler-broadened linewidth is approximately $2k_1 u(1-\xi_2)$. If the Doppler effect is neglected, we have

$$B_1 \approx \frac{2\Gamma_{10}(\Gamma_0 + \Gamma_1)}{(\Gamma_{10} + \mathrm{i}\Delta_3)(\Gamma_{10}^2 + \Delta_1^2)\Gamma_0\Gamma_1},$$

$$B_2 \approx \frac{1}{(\Gamma_{10} + \mathrm{i}\Delta_3)^2[\Gamma_{20} + \mathrm{i}(\Delta_2 + \Delta_3)]}.$$

According to Eq. (2.65), the τ-dependence of the ASPB (τ-independence is absent in second-order stochastic correlation $|\langle P^{(3)} \rangle|^2$) signal intensity is

$$I(\tau, \boldsymbol{r}) \propto |\langle P^{(3)} \rangle|^2 \propto |B_1|^2 \exp(-2\alpha_1|\tau|) + |\eta B_2|^2 \exp(-2\alpha_2|\tau|) + \exp[-(\alpha_1 + \alpha_2)|\tau|] \times$$

$$\{B_1^*\eta B_2 \exp[-\mathrm{i}(\Delta\boldsymbol{k}\cdot\boldsymbol{r}-(\omega_2+\omega_1)\tau)]+ B_1\eta^* B_2^* \exp[\mathrm{i}(\Delta\boldsymbol{k}\cdot\boldsymbol{r}-(\omega_2+\omega_1)\tau)]\}. \tag{2.68}$$

In this equation, the ASPB signal depends only on the laser characteristics, and exhibits a damping oscillation with frequency $\omega_2+\omega_1$ and damping rate $\alpha_1+\alpha_2$ for both $\tau>0$ and $\tau<0$. The theoretical limit at which the modulation frequency can be measured is determined by the laser linewidths (i.e., $\pi(\alpha_1+\alpha_2)$). For narrow-band laser sources the modulation frequency can be measured with great accuracy. Therefore, the precision of using ASPB to measure $\Omega_2+\Omega_1$ is determined by how well ω_3 and ω_2 can be tuned to Ω_1 and Ω_2, respectively. The beam 3 and the ω_1 component of the twin composite beams 1 and 2 originate from the same laser source (i.e., $\omega_1=\omega_3$). Similarly to the general saturated-absorption spectroscopy, one-photon resonant DFWM can provide a Doppler-free spectrum with a peak located at $\Delta_1=\Delta_3=0$ [51]. When ω_1 is set to the center of the Doppler profile, as discussed in Section 2.2.2, ω_2 can also be tuned to Ω_2 with the Doppler-free accuracy.

However, as the laser bandwidth is comparable with the homogeneous linewidth of the transition in Eqs. (2.60) and (2.61), the one-photon resonant term (The factor $\exp(-\Gamma_{10}|\tau|-i\Omega_1\tau)$ reflects the free evolution of one-photon resonance) and two photon resonant term (The factor $\exp(-\Gamma_{20}|\tau|+\mathrm{i}\Omega_2\tau)$ reflects the free evolution of two-photon coherence resonance) become important. When the laser sources are broadband so that $\alpha_1 >> \Gamma_{10}$ and $\alpha_2 >> \Gamma_{20}$ (inhomogeneous broadening dominant case), the ASPB beat signal rises to its maximum quickly and then decays with time constant mainly determined by the transverse relaxation times of the atomic system.

(i) $\tau<0, \alpha_1|\tau| >> 1$ and $\alpha_2|\tau| >> 1$

$$\langle P^{(3)}\rangle = S_1(\boldsymbol{r})\exp(-\mathrm{i}\omega_3 t)\{B_3\exp(-\Gamma_{10}|\tau|-\mathrm{i}\Omega_1\tau)+ \eta B_4\exp[-\Gamma_{20}|\tau|-\mathrm{i}(\Delta\boldsymbol{k}\cdot\boldsymbol{r}-(\Omega_2+\Delta_3)\tau)]\}. \tag{2.69}$$

Here, B_3 and B_4 still are τ-independent factors which equal

$$B_3=\int_{-\infty}^{+\infty}\mathrm{d}\boldsymbol{v}w(\boldsymbol{v})\frac{2\alpha_1[L_1(\boldsymbol{v})+L_2(\boldsymbol{v})]\exp[\mathrm{i}(\boldsymbol{k}_1'\cdot\boldsymbol{v})|\tau|]}{\alpha_1^2+(\Delta_1+\boldsymbol{k}_1'\cdot\boldsymbol{v})^2}, \tag{2.70}$$

$$B_4=\int_{-\infty}^{+\infty}\mathrm{d}\boldsymbol{v}w(\boldsymbol{v})\frac{2\alpha_2 L_3(\boldsymbol{v})\exp\{-\mathrm{i}[(\boldsymbol{k}_2'+\boldsymbol{k}_3)\cdot\boldsymbol{v}]|\tau|\}}{\alpha_2^2+[\Delta_2+\Delta_3+(\boldsymbol{k}_2'+\boldsymbol{k}_3)\cdot\boldsymbol{v}]^2}. \tag{2.71}$$

If the Doppler effect is neglected, we have

$$B_3\approx\frac{2\alpha_1(\Gamma_0+\Gamma_1)}{(\Gamma_{10}+\mathrm{i}\Delta_3)(\alpha_1^2+\Delta_1^2)\Gamma_0\Gamma_1}$$

$$B_4\approx\frac{2\alpha_2}{(\Gamma_{10}+\mathrm{i}\Delta_3)^2[\alpha_2^2+(\Delta_2+\Delta_3)^2]}.$$

According to Eq. (2.69), the ASPB signal intensity is

$$I(\tau,\boldsymbol{r}) \propto |\langle P^{(3)}\rangle|^2 \propto |B_3|^2\exp(-2\Gamma_{10}|\tau|) + |\eta B_4|^2\exp(-2\Gamma_{20}|\tau|) + \exp[-(\Gamma_{10}+\Gamma_{20})|\tau|]\{B_3^*\eta B_4 \times \exp[-\mathrm{i}(\Delta\boldsymbol{k}\cdot\boldsymbol{r} - (\Omega_2+\Omega_1+\Delta_3)\tau)] + B_3\eta^* B_4^*\exp[\mathrm{i}(\Delta\boldsymbol{k}\cdot\boldsymbol{r} - (\Omega_2+\Omega_1+\Delta_3)\tau)]\}. \quad (2.72)$$

(ii) $\tau > 0$ and $\alpha_1|\tau| >> 1$

$$I(\tau,\boldsymbol{r}) \propto |\langle P^{(3)}\rangle|^2 \propto |B_5|^2\exp(-2\Gamma_{10}|\tau|) + |\eta B_6|^2\exp(-2\alpha_2|\tau|) + \exp[-(\Gamma_{10}+\alpha_2)|\tau|]\{B_5^*\eta B_6 \times \exp[-\mathrm{i}(\Delta\boldsymbol{k}\cdot\boldsymbol{r} - (\omega_2+\Omega_1)\tau)] + B_5\eta^* B_6^*\exp[\mathrm{i}(\Delta\boldsymbol{k}\cdot\boldsymbol{r} - (\omega_2+\Omega_1)\tau)]\}. \quad (2.73)$$

For simplicity, we neglect the Doppler effect in B_5 and B_6,

$$B_5 = -\frac{2\alpha_1(\Gamma_0+\Gamma_1)}{(\alpha_1^2+\Delta_1^2)\Gamma_0\Gamma_1},$$
$$B_6 = \frac{1}{(\Gamma_{10}+\mathrm{i}\Delta_3)[\alpha_2+\mathrm{i}(\Delta_2+\Delta_3)]}.$$

According to Eqs. (2.72) or (2.73), the ASPB signal exhibits a damping oscillation with frequency $\Omega_2+\Omega_1$ or $\omega_2+\Omega_1$ and a damping rate $\Gamma_{10}+\Gamma_{20}$ or $\Gamma_{10}+\alpha_2$ when $\alpha_2|\tau| >> 1$ or $\alpha_1|\tau| >> 1$, respectively. If we tune the frequency of the beam 3 to the center of the Doppler profile (i.e., $\Delta_3 = 0$), then the modulation frequency of Eq. (2.71) will correspond directly to sum-frequency beating between the resonant frequencies of the cascading three level system. As the modulation frequency can be measured with an accuracy given by $\pi\ (\Gamma_{10}+\Gamma_{20})$ approximately. For Eq. (2.72) the modulation frequency $\omega_2+\Omega_1$ can also be measured with great accuracy $\pi(\Gamma_{10}+\alpha_2)$. In this case, the precision of using the ASPB to measure $\Omega_2+\Omega_1$ is determined by how well ω_2 can be tuned to Ω_2. the ASPB with broadband light is again a Doppler-free spectroscopy. It needs to be mentioned that the crossed correlation with a decay factor $\exp[-(\Gamma_{10}+\alpha_2)|\tau|]$ produced from twin composite stochastic fields displays features on the time scale significantly shorter than the autocorrelation with a decay factor $\exp(-2\Gamma_{10}|\tau|)$ produced from single color stochastic fields in Eq. (2.72).

For the sake of analytical simplicity, the total polarization of beat signals can be calculated from a different viewpoint. Under the Doppler-broadened limit (i.e., $k_3u \to \infty$), we have

$$\int_{-\infty}^{+\infty} \mathrm{d}\boldsymbol{v}w(\boldsymbol{v})\exp[-\mathrm{i}\theta_{\mathrm{I}}(\boldsymbol{v})] \approx \frac{2\sqrt{\pi}}{k_3u}\delta(t_3-\xi_1t_1), \quad (2.74)$$

$$\int_{-\infty}^{+\infty} \mathrm{d}\boldsymbol{v}w(\boldsymbol{v})\exp[-\mathrm{i}\theta_{\mathrm{II}}(v)] \approx \frac{2\sqrt{\pi}}{k_3u}\delta(t_3+\xi_1t_1), \quad (2.75)$$

$$\int_{-\infty}^{+\infty} \mathrm{d}\boldsymbol{v}w(\boldsymbol{v})\exp[-\mathrm{i}\theta_{\mathrm{III}}(v)] \approx \frac{2\sqrt{\pi}}{k_3u}\delta[t_3+t_1-(\xi_2-1)t_2]. \quad (2.76)$$

Here, we assume $\xi_2 > 1, \xi_1 = k_1/k_3, \xi_2 = k_2/k_3$. When we substitute Eqs. (2.53) and (2.74)–(2.76) into Eqs. (2.55)–(2.59), we obtain the stochastic averaging of the total third-order polarization

$$\begin{aligned}\langle P^{(3)}\rangle = \langle P^{(\mathrm{I})} + P^{(\mathrm{III})} + P^{(\mathrm{V})}\rangle = \frac{2\sqrt{\pi}}{k_3 u} S_1(\boldsymbol{r}) \exp[-\mathrm{i}(\omega_3 t + \omega_1 \tau)] \times \\ \int_0^\infty \mathrm{d}t_1 \left\{ \left(\frac{1}{\Gamma_0} + \frac{1}{\Gamma_1} \right) \times \exp[-(\Gamma_{10}^a + \mathrm{i}\Delta_1^a) t_1 - \alpha_1 |t_1 - \tau|] \right\} + \\ \frac{2\sqrt{\pi}}{k_3 u} S_2(\boldsymbol{r}) \exp[-\mathrm{i}(\omega_3 t - \omega_2 \tau)] \times \int_0^\infty \mathrm{d}t_3 \int_0^\infty \mathrm{d}t_1 \times \\ \exp\left[-\frac{\Gamma_{20}^a + \mathrm{i}\Delta_2^a}{\xi_2 - 1} (t_1 + t_3) - \alpha_2 \left| \frac{t_1 + t_3}{\xi_2 - 1} + \tau \right| \right]. \end{aligned} \tag{2.77}$$

Here, $\Gamma_{10}^a = \Gamma_{10} + \xi_1 \Gamma_{10}, \Delta_1^a = \Delta_1 + \xi_1 \Delta_3, \Gamma_{20}^a = \Gamma_{20} + (\xi_2 - 1)\Gamma_{10}$, and $\Delta_2^a = \Delta_2 + \xi_2 \Delta_3$. It should be noted that because of the δ functions in Eq. (2.75), we have $P^{(\mathrm{II})} = P^{(\mathrm{IV})} = 0$ since $t_1, t_3 > 0$. The integral in Eq. (2.77) can be performed easily, from which we obtain the second-order stochastic averaging of the polarization for an extremely Doppler-broadened system, i.e.,

(i) $\tau > 0$

$$\begin{aligned}\langle P^{(3)}\rangle = \frac{2\sqrt{\pi}}{k_3 u} S_1(\boldsymbol{r}) \left(\frac{1}{\Gamma_0} + \frac{1}{\Gamma_1} \right) \exp[-\mathrm{i}(\omega_3 t + \omega_1 \tau)] \times \\ \left\{ \frac{(\Gamma_{10}^a + \mathrm{i}\Delta_1^a + \alpha_1) \exp(-\alpha_1 |\tau|)}{(\Gamma_{10}^a + \mathrm{i}\Delta_1^a)^2 - \alpha_1^2} - 2\alpha_1 \exp[-(\Gamma_{10}^a + \mathrm{i}\Delta_1^a)|\tau|] \right\} + \\ \frac{2\sqrt{\pi}}{k_3 u} S_2(\boldsymbol{r}) \exp[-\mathrm{i}(\omega_3 t - \omega_2 \tau)] \frac{(\xi_2 - 1)^2 \exp(-\alpha_2 |\tau|)}{(\Gamma_{20}^a + \mathrm{i}\Delta_2^a + \alpha_2)^2}. \end{aligned} \tag{2.78}$$

(ii) $\tau < 0$

$$\begin{aligned}\langle P^{(3)}\rangle = \frac{2\sqrt{\pi}}{k_3 u} S_1(\boldsymbol{r}) \left(\frac{1}{\Gamma_0} + \frac{1}{\Gamma_1} \right) \exp[-\mathrm{i}(\omega_3 t + \omega_1 \tau)] \frac{\exp(-\alpha_1 |\tau|)}{\alpha_1 + \Gamma_{10}^a + \mathrm{i}\Delta_1^a} + \\ \frac{2\sqrt{\pi}}{k_3 u} S_2(\boldsymbol{r}) \times \exp[-\mathrm{i}(\omega_3 t - \omega_2 \tau)] \left\{ \frac{(\xi_2 - 1)^2 \exp(-\alpha_2 |\tau|)}{[\alpha_2 - (\Gamma_{20}^a + \mathrm{i}\Delta_2^a)]^2} + \right. \\ \frac{|\tau|[\alpha_2^2 - (\Gamma_{20}^a + \mathrm{i}\Delta_2^a)^2] - 2(\Gamma_{20}^a + \mathrm{i}\Delta_2^a)}{[\alpha_2^2 - (\Gamma_{20}^a + \mathrm{i}\Delta_2^a)^2]^2} \times \\ \left. 2\alpha_2 (\xi_2 - 1)^2 \exp[-(\Gamma_{20}^a + \mathrm{i}\Delta_2^a)|\tau|] \right\}. \end{aligned} \tag{2.79}$$

Figure 2.14 presents spectra for one-photon DFWM ($\tau > 0$). The graphs are normalized within each set. The lineshape is sensitive to the $\Gamma_{10}^a \tau$ variation for the twin field correlation. When twin field become almost uncorrelated (larger $\Gamma_{10}^a \tau$ case), the weak damping oscillation in frequency space with a modulation period $2\pi/\tau$ is shown in Fig. 2.14.

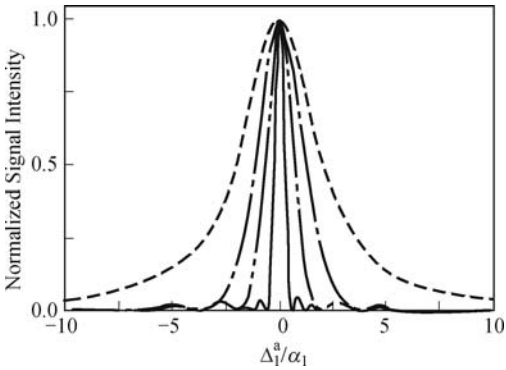

Fig. 2.14. Normalized one-photon DFWM signal intensity versus Δ_1^a/α_1. $\alpha_1/\Gamma_{10}^a = 1, \Gamma_0/\Gamma_{10}^a = 10^{-4}, \Gamma_1/\Gamma_{10}^a = 3.35 \times 10^{-4}$. $\Gamma_{10}^a\tau = 0$ (dash-dotted curve), 1.5 (dotted curve), 3 (dashed curve), 10 (solid curve).

When the broadband laser frequency is "off resonant" from atomic transition (some frequency within the bandwidth of the noisy light may still act), the DFWM and NDFWM signal exhibit hybrid radiation-matter detuning terahertz damping oscillation in Figs. 2.15 and 2.16, respectively. This is similar to radiation difference oscillation or Rabi detuning oscillation. The Rabi detuning oscillations and the radiation difference oscillation are exactly synonymous. More specifically, these two parts of the first term in Eq. (2.78) or two parts of the second term (40) interfere and give rise to a modulation of the signal intensity versus $\Gamma_{10}^a\tau$ when $\tau > 0$ for DFWM in Fig. 2.15, or $\Gamma_{20}^a\tau$ when $\Gamma_{10}^a\tau$ for NDFWM in Fig. 2.16, respectively. The complicated modulation frequency of radiation-matter detuning beats dramatically depends on Δ_1^a (Fig. 2.15) or Δ_2^a (Fig. 2.16), respectively.

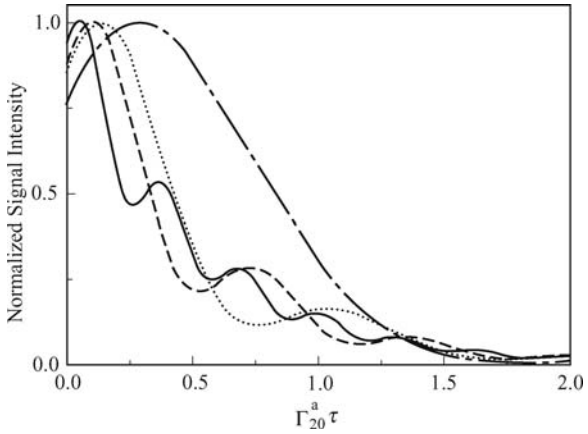

Fig. 2.15. Normalized one-photon DFWM signal intensity versus $\Gamma_{10}^a\tau$ with $\Delta_1^a/\alpha_1 = 3$ (dash-dotted curve), 7 (dotted curve), 10 (dashed curve), 20 (solid curve). $\alpha_1/\Gamma_{10}^a = 1, \Gamma_0/\Gamma_{10}^a = 10^{-4}$ and $\Gamma_1/\Gamma_{10}^a = 3.35 \times 10^{-4}$. Adopted from Ref. [31].

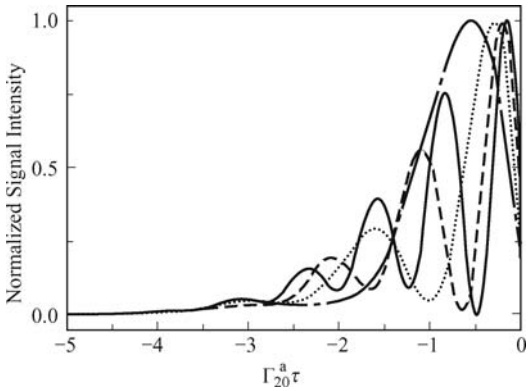

Fig. 2.16. Normalized two-photon NDFWM signal intensity versus $\Gamma^a_{20}\tau$ with $\alpha_2/\Gamma^a_{20} = 1, \Delta^a_2/\alpha_2 = 2$ (dash-dotted curve), 4 (dotted curve), 6 (dashed curve), 8 (solid curve). Adopted from Ref. [31].

We first consider the situation when laser linewidths are much narrower than homogeneous linewidths of transitions (i.e., $\alpha_1 << \Gamma_{10}$ and $\alpha_2 << \Gamma_{20}$). In homogeneous broadening dominant limit, after tail approximation (i.e., $\Gamma_{10}|\tau| >> 1$ and $\Gamma_{20}|\tau| >> 1$) we have for both $\tau > 0$ and $\tau < 0$,

$$\langle P^{(3)}\rangle = \frac{2\sqrt{\pi}}{k_3 u} S_1(\boldsymbol{r}) \exp(-\mathrm{i}\omega_3 t) \left\{ \frac{\exp\left(-\alpha_1|\tau| - \mathrm{i}\omega_1\tau\right)}{\Gamma^a_{10} + \mathrm{i}\Delta^a_1} \left(\frac{1}{\Gamma_0} + \frac{1}{\Gamma_1}\right) + \frac{\eta(\xi_2 - 1)^2 \exp(-\alpha_2|\tau| - \mathrm{i}\Delta\boldsymbol{k}\cdot\boldsymbol{r} + \mathrm{i}\omega_2\tau)}{(\Gamma^a_{20} + \mathrm{i}\Delta^a_2)^2} \right\}. \tag{2.80}$$

Therefore, the second-order correlation ASPB signal intensity is

$$\begin{aligned} I(\tau, \boldsymbol{r}) &\propto |\langle P^{(3)}\rangle|^2 \\ &\propto \frac{\exp(-2\alpha_1|\tau|)}{(\Gamma^a_{10})^2 + (\Delta^a_1)^2} \left(\frac{1}{\Gamma_0} + \frac{1}{\Gamma_1}\right)^2 + \frac{(\xi_2 - 1)^4 |\eta|^2 \exp(-2\alpha_2|\tau|)}{[(\Gamma^a_{20})^2 + (\Delta^a_2)^2]^2} + \\ &\quad (\xi_2 - 1)^2 \exp[-(\alpha_1 + \alpha_2)|\tau|]\{q \exp[-\mathrm{i}(\Delta\boldsymbol{k}\cdot\boldsymbol{r} - (\omega_2 + \omega_1)\tau)] + \\ &\quad q^* \exp[\mathrm{i}(\Delta\boldsymbol{k}\cdot\boldsymbol{r} - (\omega_2 + \omega_1)\tau)]\}, \end{aligned} \tag{2.81}$$

$$q = \left(\frac{1}{\Gamma_0} + \frac{1}{\Gamma_1}\right) \frac{\eta}{(\Gamma^a_{10} - \mathrm{i}\Delta^a_1)(\Gamma^a_{20} + \mathrm{i}\Delta^a_2)^2}. \tag{2.82}$$

Therefore, the one-photon DFWM signal (the first term of Eq. (2.81)) has resonance at $\Delta^a_1 = 0$ with linewidth $2\Gamma^a_{10}$, while the two-photon NDFWM signal has resonance at $\Delta^a_2 = 0$ with linewidth $2(\sqrt{2} - 1)^{1/2}\Gamma^a_{20}$. The ASPB with narrow band light is again a Doppler-free precision spectroscopy. This result is consistent with Eq. (2.68). The second-order correlation ASPB signal intensity also is modulated with the frequency $\omega_2 + \omega_1$ as τ is varied.

We now consider the temporal behavior of the second-order ASPB signal intensity when laser beams are broadband so that $\alpha_1 >> \Gamma_{10}$ and $\alpha_2 >> \Gamma_{20}$.

In this case, the ASPB signal rises to its maximum quickly and then decays with time constant mainly determined by the transverse relaxation times of the system. Although the ASPB signal modulation is complicated in general, at the tail of the signal (i.e., $\alpha_1|\tau| >> 1$ or $\alpha_2|\tau| >> 1$) we have:

(i) $\tau < 0$ and $\alpha_2|\tau| >> 1$

$$I(\tau, \boldsymbol{r}) \propto |\langle P^{(3)}\rangle|^2 \propto |B_7|^2 \exp(-2\alpha_1|\tau|) + |\eta B_8|^2 \exp(-2\Gamma_{20}^a|\tau|) + \exp[-(\alpha_1 + \Gamma_{20}^a)|\tau|]\{B_7^*\eta B_8 \exp[-\mathrm{i}(\Delta\boldsymbol{k}\cdot\boldsymbol{r} - (\Omega_2 + \omega_1 + \xi_2\Delta_3)\tau)] + B_7\eta^* B_8^* \exp[\mathrm{i}(\Delta\boldsymbol{k}\cdot\boldsymbol{r} - (\Omega_2 + \omega_1 + \xi_2\Delta_3)\tau)]\}. \tag{2.83}$$

(ii) $\tau > 0$ and $\alpha_1|\tau| >> 1$

$$I(\tau, \boldsymbol{r}) \propto |\langle P^{(3)}\rangle|^2 \propto |B_9|^2 \exp(-2\Gamma_{10}^a|\tau|) + |\eta B_{10}|^2 \exp(-2\alpha_2|\tau|) + \exp[-(\Gamma_{10}^a + \alpha_2)|\tau|]\{B_9^*\eta B_{10} \exp[-\mathrm{i}(\Delta\boldsymbol{k}\cdot\boldsymbol{r} - (\omega_2 + \Omega_1 + \xi_1\Delta_3)\tau)] + B_9\eta^* B_{10}^* \exp[\mathrm{i}(\Delta\boldsymbol{k}\cdot\boldsymbol{r} - (\omega_2 + \Omega_1 + \xi_1\Delta_3)\tau)]\}. \tag{2.84}$$

Here,

$$B_7 = \left(\frac{1}{\Gamma_0} + \frac{1}{\Gamma_1}\right)\frac{1}{\alpha_1 + \Gamma_{10}^a + \mathrm{i}\Delta_1^a},$$

$$B_8 = 2\alpha_2(\xi_2 - 1)^2\frac{|\tau|[\alpha_2^2 - (\Gamma_{20}^a + \mathrm{i}\Delta_2^a)^2] - 2(\Gamma_{20}^a + \mathrm{i}\Delta_2^a)}{[\alpha_2^2 - (\Gamma_{20}^a + \mathrm{i}\Delta_2^a)^2]^2};$$

$$B_9 = \left(\frac{1}{\Gamma_0} + \frac{1}{\Gamma_1}\right)\frac{2\alpha_1}{\alpha_1^2 - (\Gamma_{10}^a + \mathrm{i}\Delta_1^a)^2},$$

$$B_{10} = \frac{(\xi_2 - 1)^2}{(\Gamma_{20}^a + \mathrm{i}\Delta_2^a + \alpha_2)^2}.$$

Relation (2.83) or (2.84) consists of three terms. In Eq. (2.83), the first term with factor $\exp(-2\alpha_1|\tau|)$ and second term with factor $\exp(-2\Gamma_{20}^a|\tau|)$ are one-photon nonresonance DFWM and two-photon resonance NDFWM auto-correlation terms, respectively, while the third term is one-photon nonresonance DFWM and two-photon resonance NDFWM cross-correlation terms; In Eq. (2.84), the first term with factor $\exp(-2\Gamma_{10}^a|\tau|)$ and second term with factor $\exp(-2\alpha_2|\tau|)$ are one-photon resonance DFWM and two-photon non-resonance NDFWM auto-correlation terms, respectively, while the third term is one-photon resonance DFWM and two-photon nonresonance NDFWM cross-correlation term. Ulness et al. [38] directly observed the resonant–nonresonant cross-term contribution to coherent Raman scattering of quasi-continuous-wave noisy light in molecular liquids.

Equations (2.83) and (2.84) are basically consistent with Eqs. (2.72) and (2.73) which all show resonant and nonresonant terms cross interference and give rise to modulation frequencies $\Omega_2 + \omega_1$ and $\omega_2 + \Omega_1$, respectively. It is interesting that the broadband $\tau < 0$ result in Eqs. (2.72) and (2.73) is different with that of the femtosecond difference-frequency polarization beats

[44, 45]. In the FDPB, the requirement for the existence of a τ-dependent beat signal for $\tau < 0$ is that the phase-correlated subpulses in beams 1 and 2 are overlapped temporally. Since beams 1 and 2 are mutually coherent, the temporal behavior of beat signals should coincide with the case when the beams 1 and 2 are nearly monochromatic in the FDPB [28].

It is interesting to understand the underlying physics in the ASPB with broadband nontransform limited quasi-cw (noisy) lights [19]. Much attention has been paid to the study of various ultrafast phenomena by using incoherent light sources recently [35 – 41]. The beams 1 and 2 have broadband linewidths so the beams can be modeled as a sequence of short, phase-incoherent subpulses of duration τ_c, where τ_c is the laser coherence time [19]. For the phase matching condition $\boldsymbol{k}_1 - \boldsymbol{k}_1' + \boldsymbol{k}_3$ the three-pulse stimulated photon-echo exists for the perturbation chains (I) and (Ⅲ). For the phase matching condition $\boldsymbol{k}_2' - \boldsymbol{k}_2 + \boldsymbol{k}_3$ the sum-frequency trilevel echo exists for the perturbation the chain (V) [52]. The broadband limit ($\tau_c \approx 0$) corresponds to "white" noise, noise characterized by a δ-function correlation time or it possesses a constant spectrum. So the second-order correlation function can be approximated as Eq. (2.21) by a δ function.

Under the Doppler-broadened limit (i.e., $k_3 u \to \infty$) and laser broadband limit (i.e., $\alpha_i \to \infty$) approximations, we substitute Eqs. (2.74), (2.76), and (2.46) into Eqs. (2.55), (2.57), and (2.59) we obtain as follows,

$$\begin{aligned}\langle P^{(\mathrm{I})} \rangle = {} & \frac{4\sqrt{\pi}}{k_3 u \alpha_1} S_1(\boldsymbol{r}) \exp[-\mathrm{i}(\omega_3 t + \omega_1 \tau)] \times \\ & \int_0^\infty \mathrm{d}t_3 \int_0^\infty \mathrm{d}t_2 \int_0^\infty \mathrm{d}t_1 \delta(t_3 - \xi_1 t_1) \delta(t_1 - \tau) \times \\ & \exp[-(\Gamma_{10} + \mathrm{i}\Delta_3) t_3 - \Gamma_0 t_2 - (\Gamma_{10} + \mathrm{i}\Delta_1) t_1], \end{aligned} \tag{2.85}$$

$$\begin{aligned}\langle P^{(\mathrm{Ⅲ})} \rangle = {} & \frac{4\sqrt{\pi}}{k_3 u \alpha_1} S_1(\boldsymbol{r}) \exp[-\mathrm{i}(\omega_3 t + \omega_1 \tau)] \times \\ & \int_0^\infty \mathrm{d}t_3 \int_0^\infty \mathrm{d}t_2 \int_0^\infty \mathrm{d}t_1 \delta(t_3 - \xi_1 t_1) \delta(t_1 - \tau) \times \\ & \exp[-(\Gamma_{10} + \mathrm{i}\Delta_3) t_3 - \Gamma_1 t_2 - (\Gamma_{10} + \mathrm{i}\Delta_1) t_1], \end{aligned} \tag{2.86}$$

$$\begin{aligned}\langle P^{(\mathrm{V})} \rangle = {} & \frac{4\sqrt{\pi}}{k_3 u \alpha_2} S_2(\boldsymbol{r}) \exp[-\mathrm{i}(\omega_3 t - \omega_2) \tau] \times \\ & \int_0^\infty \mathrm{d}t_3 \int_0^\infty \mathrm{d}t_2 \int_0^\infty \mathrm{d}t_1 \delta[t_3 + t_1 - (\xi_2 - 1) t_2] \delta(t_2 + \tau) \times \\ & \exp[-(\Gamma_{10} + \mathrm{i}\Delta_3)(t_1 + t_3) - (\Gamma_{20} + \mathrm{i}\Delta_2 + \mathrm{i}\Delta_3) t_2]. \end{aligned} \tag{2.87}$$

Equation (2.87) can be explained as follows (see Eq. (2.48) also): The optical polarization induced by A_3 at time $t - t_1 - t_2 - t_3$ exhibits damping oscillation in a time interval t_1 with decay rate Γ_{10} and frequency Δ_3 in rotating frame. It then interacts with A_2' at time $t - t_2 - t_3$; as a result, a two-photon coherence from $|0\rangle$ to $|2\rangle$ is induced. The two-photon coherence

undergoes damping oscillation with decay rate Γ_{20} and frequency $\Delta_2 + \Delta_3$. After time t_2, beam 2 probes the two-photon coherence at time $t - t_3$ and induces a polarization that is responsible for NDFWM signals. We are interested in NDFWM signals at time t, which is t_3 after the application of beam 2. Here again the polarization exhibits damping oscillation in the time interval t_3 with decay rate Γ_{10} and frequency Δ_3. Now, as a result of the distribution of resonant frequencies in an inhomogeneously broadened system, the dipoles induced by A_3 at $t-t_1-t_2-t_3$ will soon run out of phase with one another. The dephased dipoles can be rephased after the application of beam 2, and the sum-frequency trilevel echo will appear [52]. From Eq. (2.87), the sum-frequency trilevel echo occurs at time t when $t_3+t_1 = (\xi_2-1)t_2$. Because $t_3 \geqslant 0, t_1 \leqslant (\xi_2 - 1)t_2$ is required. We consider the case that beams 1 and 2 have broadband linewidths so beams can be modeled as a sequence of short, phase-incoherent subpulses of duration τ_c, where τ_c is the laser coherence time. Although NDFWM signals can be generated by any pair of subpulses in beams 1 and 2, only those pairs that are phase correlated give rise to the τ-dependence of NDFWM signals. When the beam 1 is delayed with respect to the beam 2 by E_{p2}, the time duration t_2 between the phase-correlated subpulses in beams 1 and 2 should be equal to$-\tau$. The total third-order polarization is the accumulation of the polarization induced at different times. Because the sum-frequency trilevel echo occurs only when $t_1 \leqslant (\xi_2 - 1)t_2$, or $t_1 \leqslant -(\xi_2-1)\tau$ in our case, the integration of t_1 in Eq. (2.87) is restricted to a region from 0 to $-(\xi_2-1)\tau$. The increase of the integration region of t_1 with $|\tau|$ leads to the initial increase of resonant NDFWM signals [see the second term of Eq. (2.83)]. After that, the decay of the two-photon coherence becomes dominant; as a result, the NDFWM signal decays with further increasing $|\tau|$. This process is different from that of the incoherent-light three-pulse stimulated photon echo [28], for which the maximum of resonant DFWM signals occurs at $\tau \approx 0$ [see the first term of Eq. (2.84)].

The ASPB signal intensity is:

(i) $\tau < 0$ and $\alpha_2 \to \infty$

$$I(\tau, \boldsymbol{r}) \propto |\langle P^{(3)}\rangle|^2 \propto |B_7|^2 \exp(-2\alpha_1|\tau|) + |\eta B_{11}|^2 \exp(-2\Gamma^a_{20}|\tau|) + \exp[-(\alpha_1 + \Gamma^a_{20})|\tau|]\{B^*_7 \eta B_{11} \exp[-\mathrm{i}(\Delta\boldsymbol{k}\cdot\boldsymbol{r} - (\Omega_2 + \omega_1 + \xi_2\Delta_3)\tau)] + B_7\eta^* B^*_{11} \exp[\mathrm{i}(\Delta\boldsymbol{k}\cdot\boldsymbol{r} - (\Omega_2 + \omega_1 + \xi_2\Delta_3)\tau)]\}. \quad (2.88)$$

(ii) $\tau > 0$ and $\alpha_1 \to \infty$

$$I(\tau, \boldsymbol{r}) \propto |\langle P^{(3)}\rangle|^2 \propto |B_{12}|^2 \exp(-2\Gamma^a_{10}|\tau|) + |\eta B_{10}|^2 \exp(-2\alpha_2|\tau|) + \exp[-(\Gamma^a_{10} + \alpha_2)|\tau|]\{B^*_{12}\eta B_{10} \exp[-\mathrm{i}(\Delta\boldsymbol{k}\cdot\boldsymbol{r} - (\omega_2 + \Omega_1 + \xi_1\Delta_3)\tau)] + B_{12}\eta^* B^*_{10} \exp[\mathrm{i}(\Delta\boldsymbol{k}\cdot\boldsymbol{r} - (\omega_2 + \Omega_1 + \xi_1\Delta_3)\tau)]\}. \quad (2.89)$$

Here, $B_{11} = \dfrac{2(\xi_2 - 1)|\tau|}{\alpha_2}, B_{12} = \left(\dfrac{1}{\Gamma_0} + \dfrac{1}{\Gamma_1}\right)\dfrac{2}{\alpha_1}$.

As we mentioned above, in the case of broadband incident beams, unlike the corresponding one-photon resonant DFWM [the first term of Eq. (2.83)

or (2.89)], the dephasing and rephrasing processes in an inhomogeneously broadened system cause the maximum of two-photon resonant NDFWM [the second term of Eq. (2.82) or (2.88)] signals to shift from zero time delay.

2.2.3 Fourth-order Stochastic Correlation of ASPB

For the macroscopic system where phase matching takes place this signal must be drawn from the $P^{(3)}$ developed on one chromophore multiplied by the$(P^{(3)})^*$ that is developed on another chromophore which must be located elsewhere in space (with summation over all such pairs) [35 – 41]. In general, the signal is homodyne (quadrature) detected. This means that the signal at the detector is derived from the squared modulus of the sum of all of the fields that are generated from the huge number of polarized chromophores in the interaction volume. The sum over chromophores leads to the phase-matching condition at the signal level and its square modulus (the homodyne detected signal) is fully dominated by the bichromophoric cross terms. Thus the quadrature detected signal is effectively built from the products of all polarization fields derived from all pairs of chromophores. This bichromophoric model is particularly important to the noisy light spectroscopies where the stochastic averaging at the signal level must be carried out [35 – 41].

It is important to note that these three types of Markovian stochastic fields can have the same spectral density and thus the same second-order coherence function. The fundamental differences in the statistics of these fields are manifest only in the higher-order coherence functions. The term "higher order" refers to all orders larger than the second. In this section, different stochastic models of the noisy laser field only affect the fourth-order coherence function.

The ASPB signal is proportional to the average of the absolute square of $P^{(3)}$ over the random variable of the stochastic process, so that the signal intensity

$$\begin{aligned} I(\tau, \boldsymbol{r}) &\propto \langle |P^{(3)}|^2 \rangle = \langle P^{(3)} (P^{(3)})^* \rangle \\ &= \langle (P^{(\mathrm{I})} + P^{(\mathrm{II})} + P^{(\mathrm{III})} + P^{(\mathrm{IV})} + P^{(\mathrm{V})}) \\ &\quad [(P^{(\mathrm{I})})^* + (P^{(\mathrm{II})})^* + (P^{(\mathrm{III})})^* + (P^{(\mathrm{IV})})^* + (P^{(\mathrm{V})})^*] \rangle \end{aligned}$$

contains $5 \times 5 = 25$ different terms in the fourth- and second-order coherence function of $u_i(t)$ in phase conjugation geometry. While the ASPB signal intensity in self-diffraction geometry is related to the sixth-order coherence function of the incident fields [42]. We first assumed that the laser sources are chaotic fields. A chaotic field, which is used to describe a multimode laser source, is characterized by the fluctuation of both the amplitude and phase of the field. The random functions $u_i(t)$ of the complex noisy fields are taken to obey complex circular Gaussian statistics with its fourth-order coherence function satisfying [6, 7] Eq. (2.9).

All higher order coherence functions can be expressed in terms of products of second-order coherence functions. Thus any given $2n$ order coherence function may be decomposed into the sum of $n!$ terms, each consisting of the products of n second-order coherence function.

For simplicity, we neglect the Doppler effect. We first consider the case that the laser source is a narrow band so that $\alpha_1, \alpha_2 << \Gamma_{10}, \Gamma_{20}$ (homogeneous broadening dominant case). The composite noisy beam 1 (beam 2) is treated as one whose spectrum is simply a sum of two Lorentzians. According to Eq. (2.9) and tail approximation (i.e., $\Gamma_{10}|\tau| >> 1$ and $\Gamma_{20}|\tau| >> 1$), the ASPB signal intensity in fourth-order stochastic correlation then becomes for both $\tau > 0$ and $\tau < 0$,

$$\begin{aligned} I(\tau, \boldsymbol{r}) \propto \langle |P^{(3)}|^2 \rangle \propto B_{13} + |\eta|^2 B_{14} + |B_{15}|^2 \exp(-2\alpha_1|\tau|) + \\ |\eta B_{16}|^2 \exp(-2\alpha_2|\tau|) + \exp[-(\alpha_1 + \alpha_2)|\tau|] + \\ \{\eta B_{17} \exp[-\mathrm{i}(\Delta \boldsymbol{k} \cdot \boldsymbol{r} - (\omega_2 + \omega_1)\tau)] + \\ \eta^* B_{17}^* \exp[\mathrm{i}(\Delta \boldsymbol{k} \cdot \boldsymbol{r} - (\omega_2 + \omega_1)\tau)]\}. \end{aligned} \tag{2.90}$$

Here,

$$\begin{aligned} B_{13} &= \frac{\Gamma_{10} + \Gamma_{20}}{2\Gamma_{10}(\Gamma_{10}^2 - \Delta_3^2)^2[(\Delta_2 + \Delta_3)^2 - \Gamma_{20}^2]}, \\ B_{15} &= \frac{\Gamma_{10}(\Gamma_0 + \Gamma_1)}{(\Gamma_{10} + \mathrm{i}\Delta_3)(\Gamma_{10}^2 - \Delta_1^2)\Gamma_0\Gamma_1}, \\ B_{16} &= \frac{1}{(\Gamma_{10} + \mathrm{i}\Delta_3)^2[\mathrm{i}(\Delta_2 + \Delta_3) - \Gamma_{20}]}, \\ B_{17} &= \frac{\Gamma_0 + \Gamma_1}{\Gamma_0\Gamma_1(\Gamma_{10} - \mathrm{i}\Delta_3)(\Delta_3^2 - \Gamma_{10}^2)(\mathrm{i}\Delta_1 + \Gamma_{10})(\mathrm{i}\Delta_2 + \mathrm{i}\Delta_3 - \Gamma_{20})}, \\ B_{14} &= \frac{2\alpha_1\Gamma_{10}^2}{(\Gamma_{10}^2 + \Delta_1^2)^2(\Gamma_0^2 - 4\alpha_1^2)(\Gamma_1^2 - 4\alpha_1^2)} \left[\frac{(\Gamma_0 + \Gamma_1)^2 - 16\alpha_1^2}{2\alpha_1(\Gamma_{10}^2 + \Delta_3^2)} - \right. \\ &\quad \left. \frac{(2\Gamma_0 + \Gamma_1)(\Gamma_1^2 - 4\alpha_1^2)}{(\Gamma_0 + \Gamma_{10})\Gamma_{10}\Gamma_0(\Gamma_0 + \Gamma_1)} - \frac{(\Gamma_0 + 2\Gamma_1)(\Gamma_0^2 - 4\alpha_1^2)}{(\Gamma_1 + \Gamma_{10})\Gamma_{10}\Gamma_1(\Gamma_0 + \Gamma_1)}\right]. \end{aligned}$$

The constants B_i mainly depend on typical parameters: a short correlation of the light, rapid dephasing rate, and a relatively long excited-state lifetime.

Relation (2.90) consists of five terms. The first and third terms are dependent on the $u_1(t)$ fourth-order coherence function for the nonresonant DFWM, while the second and fourth terms are dependent on the $u_2(t)$ fourth-order coherence functions for the nonresonant NDFWM. The first and second terms originating from the amplitude fluctuation of the chaotic field are independent of the relative time-delay τ. The third and fourth terms indicate an exponential decay of the ASPB signal as $|\tau|$ increases. The fifth term depending on the $u_1(t)$ or $u_2(t)$ second-order coherence functions gives nonresonant DFWM and nonresonant NDFWM cross interference with a modulation frequency $\omega_2 + \omega_1$ and a decaying rate $\alpha_1 + \alpha_2$.

Equation (2.90) indicates that ASPB signal oscillates not only temporally but also spatially with a period $2\pi/\Delta\boldsymbol{k}$ along the direction $\Delta\boldsymbol{k}$, which is almost perpendicular to the propagation direction of beat signals, here $\Delta\boldsymbol{k} \approx 2\pi|\lambda_1 - \lambda_2|\theta/\lambda_2\lambda_1, \theta$ is the angle between beam 1 and beam 2. Physically, the polarization-beat model assumes that both the pump beams are plane waves. Therefore, DFWM and NDFWM, which propagate along $\boldsymbol{k}_{s_1} = \boldsymbol{k}_1 - \boldsymbol{k}_1' + \boldsymbol{k}_3$ and $\boldsymbol{k}_{s_2} = \boldsymbol{k}_2' - \boldsymbol{k}_2 + \boldsymbol{k}_3$, respectively, are plane waves also. Since DFWM and NDFWM propagate along a slightly different direction, the interference between them leads to the spatial oscillation, which should be detected by a pinhole detector. Equation (2.90) also indicates that ASPB signal modulates temporally with a frequency $\omega_2 + \omega_1$ as τ is varied. In this case that ω_1 and ω_2 are tuned to the resonant frequencies of the transitions from $|0\rangle$ to $|1\rangle$ and from $|1\rangle$ and $|2\rangle$, respectively, then the modulation frequency equals $\Omega_2+\Omega_1$. In the other words, we can obtain sum-frequency beating between the resonant frequencies of a cascade three-level system. A Doppler-free precision can be achieved in the measurement of $\Omega_2 + \Omega_1$ [13, 14].

We now consider the case that the laser sources are broadband so that $\alpha_1, \alpha_2 >> \Gamma_{10}, \Gamma_{20} >> \Gamma_0, \Gamma_1$. In inhomogeneous broadening case, the ASPB signal rises to its maximum quickly and then decays with time constant mainly determined by the transverse relaxation times of the atomic system.

(i) $\tau < 0, \alpha_1|\tau| >> 1$ and $\alpha_2|\tau| >> 1$

$$\begin{aligned} I(\tau, \boldsymbol{r}) \propto \langle |P^{(3)}|^2 \rangle \propto B_{13} + |\eta|^2 B_{14} + |B_{18}|^2 \exp(-2\Gamma_{10}|\tau|) + \\ |\eta B_{19}|^2 \exp(-2\Gamma_{20}|\tau|) + \exp[-(\Gamma_{10} + \Gamma_{20})|\tau|] \times \\ \{\eta B_{17} \exp[-\mathrm{i}(\Delta\boldsymbol{k} \cdot \boldsymbol{r} - (\Omega_2 + \Omega_1 + \Delta_3)\tau)] + \\ \eta^* B_{17}^* \exp[\mathrm{i}(\Delta\boldsymbol{k} \cdot \boldsymbol{r} - (\Omega_2 + \Omega_1 + \Delta_3)\tau)]\}. \end{aligned} \tag{2.91}$$

(ii) $\tau > 0$ and $\alpha_1|\tau| >> 1$

$$\begin{aligned} I(\tau, \boldsymbol{r}) \propto \langle |P^{(3)}|^2 \rangle \propto B_{13} + |\eta|^2 B_{14} + |B_{18}|^2 \exp(-2\Gamma_{10}|\tau|) + \\ |\eta B_{16}|^2 \exp(-2\alpha_2|\tau|) + \exp[-(\Gamma_{10} + \alpha_2)|\tau|] \times \\ \{\eta B_{17} \exp[-\mathrm{i}(\Delta\boldsymbol{k} \cdot \boldsymbol{r} - (\omega_2 + \Omega_1)\tau)] + \\ \eta^* B_{17}^* \exp[\mathrm{i}(\Delta\boldsymbol{k} \cdot \boldsymbol{r} - (\omega_2 + \Omega_1)\tau)]\}. \end{aligned} \tag{2.92}$$

Here,

$$B_{18} = \frac{2\alpha_1(\Gamma_0 + \Gamma_1)}{(\Gamma_{10} + \mathrm{i}\Delta_3)(\Gamma_{10} + \mathrm{i}\Delta_1)^2\Gamma_0\Gamma_1},$$
$$B_{19} = \frac{2\alpha_2}{(\mathrm{i}\Delta_3^2 - \Gamma_{10}^2)[\alpha_2^2 + (\Delta_2 + \Delta_3)^2]}.$$

The crossed correlation with a decay factor $\exp[-(\Gamma_{10} + \alpha_2)|\tau|]$ produced from twin composite stochastic fields display features on the time scale significantly shorter than the autocorrelation with a decay factor $\exp(-2\Gamma_{10}|\tau|)$ produced from single color stochastic fields in Eq. (2.92).

The ASPB signal can be calculated in the extremely Doppler broadened limit. We can obtain the stochastic averaging of the mod square of the total third-order polarization

$$\mathrm{I}(\tau, r) \propto \langle |P^{(3)}|^2 \rangle = \langle |P^{(\mathrm{I})} + P^{(\mathrm{III})} + P^{(\mathrm{V})}|^2 \rangle. \tag{2.93}$$

We first consider the case that the laser sources are narrow band so that $\alpha_1 << \Gamma_{10}$ and $\alpha_2 << \Gamma_{20}$. In homogeneous broadening case, after tail approximation (i.e., $\Gamma_{10}|\tau| >> 1$ and $\Gamma_{20}|\tau| >> 1$) we have the for both $\tau > 0$ and $\tau < 0$.

$$\begin{aligned} P_{R1} = N\alpha_R I(\tau, \boldsymbol{r}) \propto \langle |P^{(3)}|^2 \rangle \propto |\eta|^2 B_{20} + B_{21} + |B_{22}|^2 \exp(-2\alpha_1|\tau|) + \\ |\eta B_{23}|^2 \times \exp(-2\alpha_2|\tau|) + \exp[-(\alpha_1 + \alpha_2)|\tau|] \times \\ \{B_{22}^* \eta B_{23} \exp[-\mathrm{i}(\Delta \boldsymbol{k} \cdot \boldsymbol{r} - (\omega_2 + \omega_1)\tau)] + \\ B_{22}\eta^* B_{23}^* \exp[\mathrm{i}(\Delta \boldsymbol{k} \cdot \boldsymbol{r} - (\omega_2 + \omega_1)\tau)]\}. \end{aligned} \tag{2.94}$$

Here,

$$\begin{aligned} B_{20} &= \frac{(\xi_2 - 1)^3}{2} \left\{ \frac{\Gamma_{10}(\xi_2 - 1) + [\Gamma_{10}(\xi_2^2 - 1) + \Gamma_{20}](\xi_2 - 2)}{\Gamma_{10}(\Gamma_{20}^a - \Gamma_{10})^4} \right\}, \\ B_{21} &= \frac{1}{\Gamma_0(\Gamma_0 + 2\alpha_2)[(\Gamma_{20}^a)^2 + (\Delta_2^a)^2]}, \\ B_{22} &= \frac{\Gamma_0 + \Gamma_1}{\Gamma_0 \Gamma_1 (\Gamma_{10}^a + \mathrm{i}\Delta_1^a)}, \\ B_{23} &= \frac{(\xi_1 - 1)^2}{(\mathrm{i}\Delta_2 + \mathrm{i}\Delta_3 \xi_2 - \Gamma_{20}^a + \Gamma_{10})^2}. \end{aligned}$$

This equation is consistent with Eq. (2.90).

We now consider the case that the laser sources are broadband so that $\alpha_1, \alpha_2 >> \Gamma_{10}, \Gamma_{20}$. In inhomogeneous broadening case, the ASPB signal rises to its maximum quickly and then decays with time constant mainly determined by the transverse relaxation times of the system. Although the ASPB signal modulation is complicated in general, at the tail of the signal (i.e., $\alpha_1|\tau| >> 1$ or $\alpha_2|\tau| >> 1$) we have:

(i) $\tau < 0$ and $\alpha_2|\tau| >> 1$

$$\begin{aligned} I(\tau, \boldsymbol{r}) \propto \langle |P^{(3)}|^2 \rangle \propto B_{24} + |\eta|^2 B_{25} + B_{26} \exp(-2\alpha_1|\tau|) + \\ |\eta|^2 B_{25} \exp(-2\Gamma_{20}^a|\tau|) + \exp[-(\alpha_1 + \Gamma_{20}^a)|\tau|] \times \\ \{\eta B_{27} \exp[-\mathrm{i}(\Delta \boldsymbol{k} \cdot \boldsymbol{r} - (\Omega_2 + \omega_1 + \xi_2 \Delta_3)\tau)] + \\ \eta^* B_{27}^* \exp[\mathrm{i}(\Delta \boldsymbol{k} \cdot \boldsymbol{r} - (\Omega_2 + \omega_1 + \xi_2 \Delta_3)\tau)]\}. \end{aligned} \tag{2.95}$$

(ii) $\tau > 0$ and $\alpha_1|\tau| >> 1$

$$\begin{aligned} I(\tau, \boldsymbol{r}) \propto \langle |P^{(3)}|^2 \rangle \propto B_{24} + |\eta|^2 B_{25} + B_{26} \exp(-2\Gamma_{10}^a|\tau|) + \\ |\eta|^2 B_{25} \exp(-2\alpha_2|\tau|) + \exp[-(\Gamma_{10}^a + \alpha_2)|\tau|] \times \\ \{\eta B_{27} \exp[-\mathrm{i}(\Delta \boldsymbol{k} \cdot \boldsymbol{r} - (\omega_2 + \Omega_1 + \xi_1 \Delta_3)\tau)] + \\ \eta^* B_{27}^* \exp[\mathrm{i}(\Delta \boldsymbol{k} \cdot \boldsymbol{r} - (\omega_2 + \Omega_1 + \xi_1 \Delta_3)\tau)]\}. \end{aligned} \tag{2.96}$$

Here,

$$B_{24} = \frac{9(\xi_2 - 1)^2}{4\alpha_2^2 \Gamma_{10} \Gamma_{20}^a},$$
$$B_{25} = \frac{4(\xi_2 - 1)^4}{[(\Delta_2 + \Delta_3)^2 - \alpha_2^2]\alpha_2^2},$$
$$B_{26} = \frac{(\Gamma_0 + \Gamma_1)^2}{\Gamma_0^2 \Gamma_1^2 [(\Delta_1^a)^2 + \alpha_1^2]},$$
$$B_{27} = \frac{2|\tau|\alpha_2(\xi_2 - 1)[(\Delta_2^a)^2 + \alpha_2^2](\Gamma_0 + \Gamma_1)}{(\alpha_2 - \mathrm{i}\Delta_2^a)^4 \Gamma_0 \Gamma_1 (\alpha_1 - \mathrm{i}\Delta_1^a)}.$$

Relations (2.95) and (2.96) all consist of five terms. The first and third terms are dependent on the $u_1(t)$ fourth-order coherence function for DFWM, while the second and fourth terms are dependent on the $u_2(t)$ fourth-order coherence functions for NDFWM. The first and second terms originating from the amplitude fluctuation of the chaotic field are independent of the relative time-delay τ. The third and fourth terms indicate an exponential decay of the ASPB signal as $|\tau|$ increases. The fifth term depending on the $u_1(t)$ or $u_2(t)$ second-order coherence functions gives rise to the sum-frequency modulation of ASPB signals. Equation (2.95) shows nonresonant DFWM and resonant NDFWM cross interference and gives rise to modulation frequencies $\Omega_2 + \omega_1$, while Eqation (2.96) shows resonant DFWM and nonresonant NDFWM cross interference and gives rise to modulation frequencies $\omega_2 + \Omega_1$. In this case, the precision of using ASPB to measure $\Omega_2 + \Omega_1$ is determined by how well ω_1 or ω_2 can be tuned to Ω_1 or Ω_2, respectively. ASPB with broadband light is again a Doppler-free precision spectroscopy.

The chaotic field fourth-order correlation ASPB signal can be calculated under Doppler and broadband limit. The broadband limit ($\tau_c \approx 0$) corresponds to "white" noise, noise characterized by a δ-function correlation time or, alternatively, it possesses a constant spectrum. Under the extremely Doppler-broadened limit (i.e., $k_3 u \to \infty$) and laser broadband limit (i.e., $\alpha_i \to \infty$) approximations, we obtain the stochastic averaging of the mod square of the total third-order polarization as follows:

(i) $\tau < 0$ and $\alpha_2 \to \infty$

$$\begin{aligned} I(\tau, \boldsymbol{r}) \propto \langle |P^{(3)}|^2 \rangle \propto |B_{28}|^2 + |\eta B_{29}|^2 + B_{26} \exp(-2\alpha_1|\tau|) + \\ |\eta B_{30}|^2 \exp(-2\Gamma_{20}^a|\tau|) + \exp[-(\alpha_1 + \Gamma_{20}^a)|\tau|] \times \\ \{B_{26}^{\frac{1}{2}} \eta B_{30} \exp[-\mathrm{i}(\Delta \boldsymbol{k} \cdot \boldsymbol{r} - (\Omega_2 + \omega_1 + \xi_2 \Delta_3)\tau)] + \\ B_{26}^{\frac{1}{2}} \eta^* B_{30}^* \exp[\mathrm{i}(\Delta \boldsymbol{k} \cdot \boldsymbol{r} - (\Omega_2 + \omega_1 + \xi_2 \Delta_3)\tau)]\}. \end{aligned} \tag{2.97}$$

(ii) $\tau > 0$ and $\alpha_1 \to \infty$

$$\begin{aligned} I(\tau, \boldsymbol{r}) \propto \langle |P^{(3)}|^2 \rangle \propto |B_{28}|^2 + |\eta B_{29}|^2 + |B_{31}|^2 \exp(-2\Gamma_{10}^a|\tau|) + \\ |\eta|^2 B_{25} \exp(-2\alpha_2|\tau|) + \exp[-(\Gamma_{10}^a + \alpha_2)|\tau|] \times \end{aligned}$$

$$\{B_{31}\eta B_{25}^{\frac{1}{2}} \exp[-\mathrm{i}(\Delta\boldsymbol{k}\cdot\boldsymbol{r} - (\omega_2 + \Omega_1 + \xi_1\Delta_3)\tau)] + B_{31}\eta^* B_{25}^{\frac{1}{2}} \exp[\mathrm{i}(\Delta\boldsymbol{k}\cdot\boldsymbol{r} - (\omega_2 + \Omega_1 + \xi_1\Delta_3)\tau)]\}. \tag{2.98}$$

Here,

$$B_{28} = \frac{\Gamma_0^2 + 6\Gamma_0\Gamma_1 + \Gamma_1^2}{4\Gamma_0\Gamma_1(\Gamma_0 + \Gamma_1)\Gamma_{10}^a},$$
$$B_{29} = \frac{(\xi_2 - 1)^2}{4\Gamma_{20}^a[(\xi_2 - 1)\Gamma_0 + \Gamma_{20}]},$$
$$B_{30} = \frac{2|\tau|}{\alpha_2}(\xi_2^2 + 1)^{1/2},$$
$$B_{31} = \frac{(\Gamma_0 + \Gamma_1)^2}{\Gamma_0^2\Gamma_1^2}.$$

The crossed correlation with a decay factor $\exp[-(\alpha_1 + \Gamma_{20}^a)|\tau|]$ produced from twin composite stochastic fields display features on the time scale significantly shorter than the autocorrelation with a decay factor $\exp(-2\Gamma_{20}^a|\tau|)$ produced from single color stochastic fields in Eq. (2.97). By contrast, the crossed correlation with a decay factor $\exp[-(\Gamma_{10}^a + \alpha_2)|\tau|]$ produced from twin composite stochastic fields display features on the time scale significantly shorter than the autocorrelation with a decay factor $\exp(-2\Gamma_{10}^a|\tau|)$ produced from single color stochastic fields in Eq. (2.98).

We have assumed that the laser sources are chaotic field in the above calculation. A chaotic field, which is used to describe a multimode laser source, is characterized by the fluctuation of both the amplitude and the phase of the field. Another commonly used stochastic model is a phase-diffusion model, which is used to describe an amplitude-stabilized laser source. This model assumes that the amplitude of laser fields is a constant, while its phase fluctuates as a random process caused by spontaneous emission. If the lasers have Lorentzian line shape, the fourth-order coherence function are [6, 7].

$$\begin{aligned}\langle u_i(t_1)\, u_i\,(t_2)u_i^*(t_3)u_i^*(t_4)\rangle &= \exp[-\alpha_i(|t_1 - t_3| + |t_1 - t_4| + |t_2 - t_3| + |t_2 - t_4|)] \times \\ &\quad \exp[\alpha_i(|t_1 - t_2| + |t_3 - t_4|)].\end{aligned} \tag{2.99}$$

The fourth-order correlation ASPB signal of a phase-diffusion model can be calculated under Doppler (i.e., $\boldsymbol{k}_3 u \to \infty$) and broadband limit (i.e., $\alpha_i \to \infty$). We can obtain the stochastic averaging of the mod square of the total third-order polarization in the limit of pure inhomogeneous broadening approximations, as follows:

(i) $\tau < 0, \alpha_1 \to \infty$ and $\alpha_2 \to \infty$

$$I(\tau, \boldsymbol{r}) \propto \langle |P^{(3)}|^2 \rangle \propto B_{26} \exp(-2\alpha_1|\tau|) + |\eta B_{32}|^2 \exp(-2\Gamma_{20}^a|\tau|) + \exp[-(\alpha_1 + \Gamma_{20}^a)|\tau|] \Big\{ B_{26}^{\frac{1}{2}} \eta B_{32} \exp[-\mathrm{i}(\Delta \boldsymbol{k} \cdot \boldsymbol{r} - (\Omega_2 + \omega_1 + \xi_2 \Delta_3)\tau)] + B_{26}^{\frac{1}{2}} \eta^* B_{32}^* \exp[\mathrm{i}(\Delta \boldsymbol{k} \cdot \boldsymbol{r} - (\Omega_2 + \omega_1 + \xi_2 \Delta_3)\tau)] \Big\}. \tag{2.100}$$

(ii) $\tau > 0, \alpha_1 \to \infty$ and $\alpha_2 \to \infty$

$$I(\tau, \boldsymbol{r}) \propto \langle |P^{(3)}|^2 \rangle \propto B_{33} \exp(-2\Gamma_{10}^a|\tau|) + |\eta|^2 B_{25} \exp(-2\Gamma_{20}^a|\tau|) + \exp[-(\Gamma_{10}^a + \Gamma_{20}^a)|\tau|] \Big\{ B_{33}^{\frac{1}{2}} \eta B_{25}^{\frac{1}{2}} \exp[-\mathrm{i}(\Delta \boldsymbol{k} \cdot \boldsymbol{r} - (\Omega_2 + \Omega_1(\xi_2 + \xi_1)\Delta_3)\tau)] + B_{33}^{\frac{1}{2}} \eta^* B_{25}^{\frac{1}{2}} \exp[\mathrm{i}(\Delta \boldsymbol{k} \cdot \boldsymbol{r} - (\Omega_2 + \Omega_1 + (\xi_2 + \xi_1)\Delta_3)\tau)] \Big\}. \tag{2.101}$$

Here,

$$B_{32} = \frac{2|\tau|}{\alpha_2}(\xi_2 - 1),$$
$$B_{33} = \frac{(\Gamma_0 + \Gamma_1)^2}{\alpha^2 \Gamma_0^2 \Gamma_1^2}.$$

Relations (2.100) and (2.101) all consist of three terms. The first term is dependent on the $u_1(t)$ fourth-order coherence function for DFWM, while the second term is dependent on the $u_2(t)$ fourth-order coherence functions for NDFWM. The first and second terms indicate an exponential decay of beat signals as $|\tau|$ increases. The third term depending on the $u_1(t)$ and $u_2(t)$ second-order coherence functions gives rise to the sum-frequency modulation of ASPB signals. This case is somehow similar to the results of the second-order stochastic correlation of ASPB in Section 2.2.2, in which the τ-independent part contribution has been ignored. Therefore, the fourth-order stochastic correlation of chaotic fields is of vital importance in ASPB. Equation (2.100) shows a nonresonant DFWM and a resonant NDFWM cross interference and gives a rise to modulation frequencies $\Omega_2 + \omega_1$, while Eq. (2.101) shows a resonant DFWM and a resonant NDFWM cross interference and gives rise to modulation frequencies $\Omega_2 + \Omega_1$.

The Gaussian-amplitude field has a constant phase but its real amplitude undergoes Gaussian fluctuations. If the lasers have Lorentzian line shape, the fourth-order coherence function is [6, 7]

$$\begin{aligned} &\langle u_i(t_1) u_i(t_2) u_i(t_3) u_i(t_4) \rangle \\ &\quad = \langle u_i(t_1) u_i(t_3) \rangle \langle u_i(t_2) u_i(t_4) \rangle + \langle u_i(t_1) u_i(t_4) \rangle \langle u_i(t_2) u_i(t_3) \rangle + \\ &\quad \langle u_i(t_1) u_i(t_2) \rangle \langle u_i(t_3) u_i(t_4) \rangle. \end{aligned} \tag{2.102}$$

The fourth-order correlation ASPB signal of Gaussian-amplitude model can be calculated under Doppler (i.e., $k_3 u \to \infty$) and broadband limit (i.e., $\alpha_i \to \infty$). We can obtain the stochastic averaging of the mod square of the total third-order polarization in the limit of pure inhomogeneous broadening, as follows:

(i) $\tau < 0, \alpha_1 \to \infty$ and $\alpha_2 \to \infty$

$$\begin{aligned} I(\tau, \boldsymbol{r}) \propto \langle |P^{(3)}|^2 \rangle \propto |B_{28}|^2 + \left[\frac{|\eta|^2(\xi_2 - 1)}{\alpha_2^2 (\Gamma_{20}^a)^2} + |\eta B_{29}|^2 \right] + \\ B_{33} \exp(-2\Gamma_{10}^a |\tau|) + |\eta B_{32}|^2 \exp(-2\Gamma_{20}^a |\tau|) + \\ \exp[-(\Gamma_{10}^a + \Gamma_{20}^a)|\tau|] \{ B_{33}^{\frac{1}{2}} \eta B_{32} \exp[-\mathrm{i}(\Delta \boldsymbol{k} \cdot \boldsymbol{r} - \\ (\Omega_2 + \Omega_1 + (\xi_2 + \xi_1)\Delta_3)\tau)] + B_{33}^{\frac{1}{2}} \eta^* B_{32}^* + \\ \exp[\mathrm{i}(\Delta \boldsymbol{k} \cdot \boldsymbol{r} - (\Omega_2 + \Omega_1 + (\xi_2 + \xi_1)\Delta_3)\tau)] \}. \end{aligned} \tag{2.103}$$

(ii) $\tau > 0, \alpha_1 \to \infty$ and $\alpha_2 \to \infty$

$$\begin{aligned} I(\tau, \boldsymbol{r}) \propto \langle |P^{(3)}|^2 \rangle \propto \left[|B_{28}|^2 + \frac{\xi_1 - 1}{\alpha_1^2 (\Gamma_{10}^a)^2} \right] + |\eta B_{29}|^2 + \\ B_{33} \exp(-2\Gamma_{10}^a |\tau|) + |\eta B_{32}|^2 \exp(-2\Gamma_{20}^a |\tau|) + \\ \exp[-(\Gamma_{10}^a + \Gamma_{20}^a)|\tau|] \{ B_{33}^{\frac{1}{2}} \eta B_{32} \exp[-\mathrm{i}(\Delta \boldsymbol{k} \cdot \boldsymbol{r} - \\ (\Omega_2 + \Omega_1 + (\xi_2 + \xi_1)\Delta_3)\tau)] + B_{33}^{\frac{1}{2}} \eta^* B_{32}^* \\ \exp[\mathrm{i}(\Delta \boldsymbol{k} \cdot \boldsymbol{r} - (\Omega_2 + \Omega_1 + (\xi_2 + \xi_1)\Delta_3)\tau)] \}. \end{aligned} \tag{2.104}$$

Relations (2.103) and (2.104) all consist of five terms. The first and third terms are dependent on the $u_1(t)$ fourth-order coherence function for the DFWM, while the second and fourth terms are dependent on the $u_2(t)$ fourth-order coherence functions for NDFWM. The first and second terms originating from the amplitude fluctuation of the Gaussian-amplitude field are independent of the relative time-delay τ. The third and fourth terms indicate an exponential decay of the ASPB signal as $|\tau|$ increases. The fifth term depending on the $u_1(t)$ and $u_2(t)$ second-order coherence functions gives rise to the sum-frequency modulation of ASPB signals. Equations (2.103) and (2.104) all shows a one-photon resonant DFWM and a two-photon resonant NDFWM cross interference with a modulation frequency $\Omega_2 + \Omega_1 + (\xi_2 + \xi_1)\Delta_3$. The overall accuracy of using the ASPB with broadband lights to measure the sum-frequency of energy-levels $\Omega_2 + \Omega_1$ is limited by the homogeneous linewidths $\pi(\Gamma_{10}^a + \Gamma_{20}^a)$ [13, 14].

Figure 2.17 indicates that homodyne detected ASPB signal oscillates not only temporally with an ultrafast period $2\pi/|\Omega_2 + \Omega_1| = 900$ as [Fig. 2.12 (a)] but also spatially with a period $\Omega_2 + \Omega_1 2\pi/\Delta k = 0.124$ mm along the direction $\Delta \boldsymbol{k}$, which is almost perpendicular to the propagation direction of ASPB signals. The three-dimensional plot (time-spatial interferogram) of the ASPB

signal intensity $I(\tau, r)$ versus time delay τ and transverse distance r has the larger constant background caused by the intensity fluctuation of the chaotic field. At zero relative time delay ($\tau = 0$), the twin beams originating from the same source enjoy perfect overlap at the sample of their corresponding noise patterns. This gives maximum interferometric contrast. As $|\tau|$ is increased, the interferometric contrast diminishes on the time scale that reflects material no frictional memory, usually much longer than the correlation time of the light [41]. The advantage of the ASPB is that the ultrafast modulation period $2\pi/|\Omega_2 + \Omega_1| = 900$ as with a Doppler-free precision can still be improved, because the energy-level interval between ground state $|0\rangle$ and excited state $|2\rangle$ can be widely separated. The experiment of the ASPB is now underway in our group.

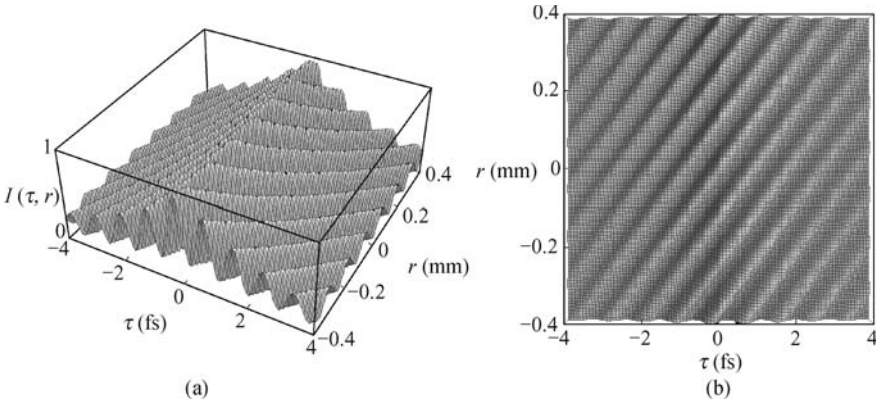

Fig. 2.17. (a) A three dimensional plot (time-spatial interferogram) of the ASPB signal intensity $I(\tau, r)$ versus time delay τ and transverse position $\boldsymbol{r}$ for the chaotic field. The intensity (displayed on the vertical axis) has been normalized to unit. The parameters are $\Omega_2 + \Omega_1 = 6.978$ fs^{-1}, $\Delta k = 50.84$ mm^{-1}, $\alpha_1 = 0.136$ fs^{-1}, $\alpha_2 = 0.19$ fs^{-1}, $\Gamma_{10}^a = 1.35\times10^{-2}$ fs^{-1}, $\Gamma_{20}^a = 1.45\times10^{-2}$ fs^{-1}, $\Gamma_0 = 1.35\times10^{-3}$ fs^{-1}, $\Gamma_1 = 1.45 \times 10^{-3}$ fs^{-1}, $\eta = 1, \xi_i = 1.5, \Delta_i = 0, B_i = 0.4$. (b) A projection of the three-dimensional interferogram of the ASPB.

Figure 2.18 presents the ASPB signal intensity versus relative time delay. The three curves represent the chaotic field (dashed line), phase-diffusion field (dotted line), and Gaussian-amplitude field (solid line). The sum-frequency polarization beat signal is shown to be particularly sensitive to the statistical properties of Markovian stochastic light fields with arbitrary bandwidth. This is quite different from fourth-order partial-coherence effects in the formation of integrated-intensity gratings with pulsed light sources [25]. Their results proved to be insensitive to specific radiation models. The τ-independent contribution of ASPB signals for a Gaussian-amplitude field or a chaotic field is much larger than that of signals for a phase-diffusion field in Fig. 2.18. The physical explanation for this is that the Gaussian-amplitude field undergoes stronger intensity fluctuations than a chaotic field. On the other hand,

the intensity (amplitude) fluctuations of the Gaussian-amplitude field or the chaotic field are always much larger than the pure phase fluctuations of the phase-diffusion field. In Fig. 2.18, the field correlation has weakly influenced on ASPB signals when the laser has a narrow bandwidth. In contrast, the sensitivities of the ASPB signal intensity to three Markovian stochastic models increase as time delay is increased when the laser has broadband linewidth.

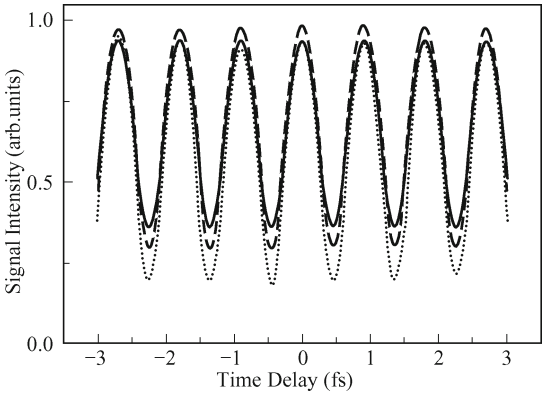

Fig. 2.18. The ASPB signal intensity versus relative time delay. The three curves represent the chaotic field (dashed line), phase-diffusion field (dotted line), and Gaussian-amplitude field (solid line). The parameters are taken as $\Omega_2 + \Omega_1 = 6.978\ \text{fs}^{-1}, \boldsymbol{r} = 0, \eta = 1, \xi_i = 1.5, \Delta_i = 0, B_i = 0.4, \Gamma_{10}^a = 1.35 \times 10^{-2}\ \text{fs}^{-1}, \Gamma_{20}^a = 1.45 \times 10^{-2}\ \text{fs}^{-1}, \Gamma_0 = 1.35 \times 10^{-3}\ \text{fs}^{-1}, \Gamma_1 = 1.45 \times 10^{-3}\ \text{fs}^{-1}$, while $\alpha_1 = 2.715 \times 10^{-5}\ \text{fs}^{-1}, \alpha_2 = 3.793 \times 10^{-5}\ \text{fs}^{-1}$ for (a) and $\alpha_1 = 0.2715\ \text{fs}^{-1}, \alpha_2 = 0.3793\ \text{fs}^{-1}$ for (b).

The main purpose of the above discussion is that we reveal an important fact that the amplitude fluctuation plays a critical role in the temporal behavior of ASPB signals. Furthermore, the different roles of the phase fluctuation and amplitude fluctuation have been pointed out in the time domain. This is quite different from the time delayed FWM with incoherent light in a two-level system [19]. For the latter case, the phase fluctuation of the light field is crucial. But the ASPB is analogous to Raman enhanced polarization beats [26, 46]. The amplitude fluctuation of the light field is also crucial in the Raman enhanced polarization beats. On the other hand, due to $\langle u_i(t) \rangle = 0$ and $\langle u_i^*(t) \rangle = 0$, the absolute square of the stochastic average of the polarization $|\langle P^{(3)} \rangle|^2$, which involves second-order coherence function of $u_i(t)$, cannot be used to describe the temporal behavior of the ASPB [45]. The second-order coherence function theory is valid when we are only interested in the τ-dependent part of the attosecond sum-frequency beating signal. In this point, it is somehow similar to the four-order stochastic correlation of the phase-diffusion model. Inasmuch as the one-photon DFWM of the ASPB is similar to the case of the FDPB [28], here we shall mainly concentrate on the two-photon NDFWM in the ASPB. In the case of broadband incident

beams, unlike the corresponding one-photon resonant DFWM, the dephasing and rephrasing processes in an inhomogeneously broadened system cause the maximum of two-photon resonant NDFWM signals to shift from zero time delay. Figure 2.19 denotes the comparisons of two-photon NDFWM autocorrelation signal intensities for three Markovian stochastic models and second-order correlation approximation treatments. The maximum of the two-photon resonant NDFWM autocorrelation signal occurs at $\tau = -1/\Gamma_{20}^{a} = -2.63$ fs in the extremely Doppler-broadened limit, which is quite different with that of FDPB [45]. The application of higher-order stochastic correlation results to the FDPB experiment yielded a better fit to data than an expression involving only second-order coherence [12, 22]. Therefore, the fourth-order coherence function theory is of vital importance in ASPB.

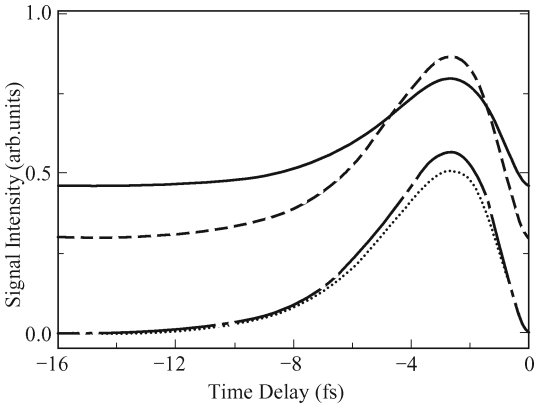

Fig. 2.19. Two-photon resonant NDFWM auto-correlation signal versus relative time delay when beams 1 and 2 consist of only ω_2 frequency component. The four curves represent the fourth-order correlation for chaotic field (dashed line), phase-diffusion field (dotted line), Gaussian-amplitude field (solid line), and the second-order auto-correlation curve (dashed dot line), respectively. The parameters are taken as, $\Gamma_{20}^{a} = 0.38$ fs^{-1}, $\Gamma_1 = 1.45 \times 10^{-3}$ fs^{-1}, $\xi_i = 1.5$, $\Delta_i = 0$, $B_i = 0.4$ and $\eta = 1$.

Next, we discuss the difference between ASPB and sum-frequency UMS [42] with self-diffraction geometry from a physical viewpoint. The frequencies and wave vectors of sum-frequency UMS signals are $\omega_{s_1} = 2\omega_1 - \omega_1, \omega_{s_2} = 2\omega_2 - \omega_2$ and $\boldsymbol{k}_{s_1} = 2\boldsymbol{k}_1 - \boldsymbol{k}_1', \boldsymbol{k}_{s_2} = 2\boldsymbol{k}_2' - \boldsymbol{k}_2$, respectively, which means that a photon is absorbed from each of two mutually correlated fluctuating pump beams. On the other hand, the frequencies and wave vectors of ASPB signals are $\omega_{s_1} = \omega_1 - \omega_1 + \omega_3, \omega_{s_2} = \omega_2 - \omega_2 + \omega_3$ and $\boldsymbol{k}_{s_1} = \boldsymbol{k}_1 - \boldsymbol{k}_1' + \boldsymbol{k}_3, \boldsymbol{k}_{s_2} = \boldsymbol{k}_2' - \boldsymbol{k}_2 + \boldsymbol{k}_3$, respectively. Therefore photons are absorbed from and emitted to the mutually correlated fluctuating twin beams 1 and 2, respectively. This difference between the ASPB and UMS has profound influence on field-correlation effects. We note that the role of beams 1 and 2 is interchangeable in the UMS, this interchangeable feature also makes the second-order co-

herence function theory failure in the UMS. Due to $\langle u(t_1)u(t_2)\rangle = 0$, the absolute square of the stochastic average of the polarization $|\langle P^{(3)}\rangle|^2$ cannot be used to describe the temporal behavior of the sum-frequency UMS [44]. Our fourth-order correlation treatment also is of vital importance in the sum-frequency UMS.

It turns out that for every conventional high-resolution nonlinear spectroscopy — purely frequency domain or purely time domain — one can design its complete time-frequency interferometric spectroscopic counterpart [39]. The stochastic correlation spectroscopy of broad-band quasi-cw (nontransform limited) noisy light can be considered as one that is intermediate in nature between steady state spectroscopy and the pure time resolved techniques [35 – 41]. For the frequency-domain techniques (such as saturated-absorption spectroscopy and two-photon absorption spectroscopy), the spectral resolution is determined by the laser linewidth. Therefore, narrow-band cw laser sources are usually required. A common feature of these time-domain techniques is that the temporal resolution is determined by laser's pulse width. More specifically, excitation laser's pulses must have a spectral width larger than energy-level splittings so energy sublevels can be excited simultaneously. The disadvantage of this quantum beat technique is that it will be inefficient and, therefore, impractical to excite two transitions simultaneously with an extremely broadband light when the sum $\Omega_2 + \Omega_1$ of energy-level resonant frequencies is large. However, the ASPB can overcome this difficulty because we can excite the two transitions separately with two lasers that have bandwidths much narrower than the energy-level splitting. The phase coherent control of light beams in the ASPB is subtle. We consider the case that twin fields have narrow bandwidths. If time delay τ between twin noisy fields, which come from a single source, is shorter than coherence time τ_c of the laser (i.e., $\alpha_i|\tau| << 1$), the relative phase between twin fields will be well defined. The interference between one-photon nonresonant DFWM and two-photon nonresonant NDFWM causes the ASPB signal intensity to modulate with frequency $\omega_2 + \omega_1$ as is τ varied. In contrast, the relative phase between twin fields will fluctuate randomly if $\alpha_i|\tau| >> 1$. In this case, the temporal and spatial modulation of the ASPB signal intensity disappears. Now we consider the case that twin beams have broadband linewidths. As mentioned above, a broadband laser can be modeled as a sequence of short, phase-incoherent subpulses of duration τ_c . Consider the DFWM or NDFWM from the ω_1 or ω_2 frequency component of twin beams 1 and 2, respectively. The DFWM or NDFWM, which is related to the three-pulse simulated photon-echo or the sum-frequency trilevel echo, respectively, originates from the interaction of atoms with phase-correlated subpulses in twin beams 1 and 2, which are separated by $|\tau|$. The homodyne detected ASPB interestingly shows the cross interference of resonant and nonresonant terms in broadband linewidths. Moreover, the broadband multimode light are tailored in a controllable fashion by dispersion [21]. The dispersion effects of polarization beats can also be exactly balanced between the two arms [46].

By contrast, ultrashort pulses of equivalent bandwidth are not immune to such dispersive effects (even when balanced) because the transform limited ultrashort pulse is in fact temporally broadened (it is chirped) and this has drastic effects on its time resolution (the auto-correlation). In this sense, the ASPB with twin Markovian stochastic fields has an advantage.

The one-photon Doppler-free DFWM or NDFWM occurs when two overlapping counterpropagating beams are both resonant with the same velocity atom group [28]. If the beam 3 and ω_1 component of the beam 1 (Figs. 2.12 and 2.13) have the same laser source frequency, they will only satisfy the condition of simultaneously being resonant with the gas when they are both resonant with the zero-velocity group (except crossover resonance case). Only those atoms whose velocities are centered on $\boldsymbol{k}_1 \cdot \boldsymbol{v} \approx 0$ are effective in generating a conjugate signal. Therefore, as in the case of saturated absorption spectroscopy [53], we have a one-photon Doppler-free DFWM spectrum with a peak located at $\Delta_1 = 0$ [51]. We then fix the frequency of the beam 3 and perform one-photon NDFWM experiment with beams 1 and 2 consisting of the ω_2 frequency component [28]. Since only atoms whose velocities are $\boldsymbol{k}_1 \cdot \boldsymbol{v} \approx 0$ interact with the beam 3, the condition that beams 1 and 2 interact with the same group of atoms is $\Delta_2 = 0$. Here again, one-photon NDFWM signals are Doppler free because only atoms in a specific velocity group contribute to NDFWM signals. The one-photon Doppler free NDFWM spectrum is somehow similar to the following case (the general saturated absorption), but they are different. If there is just a tiny frequency offset between the pump and probe, then they will satisfy the condition of simultaneous resonance when they are resonant with a nonzero particular velocity group whose first-order Doppler shift is half the tiny offset in frequencies. That is to say, a moving atom can only be in resonance with both lasers if its resonance frequency is halfway between the two lasers, because then there is a velocity at which the Doppler shifts compensate the difference in the frequency between the lasers [53].

Finally, the Doppler-free absorption of two photons can be illustrated as follows. If the atom has a velocity component in the direction of the laser beams, the resonance condition changes to $(E_f - E_i)/\hbar = \omega_1 + \omega_2 - \boldsymbol{v} \cdot (\boldsymbol{k}_1 + \boldsymbol{k}_2)$ [54]. If both waves are of the same frequency ω and counterpropagating, the wave vectors are opposite to each other. This implies that the velocity-dependent term in the resonance condition vanishes. All atoms with $(E_f - E_i)/\hbar = 2\omega$ are in resonance. These more restrictive condition results in the line narrowing, and the fact that all atoms can be excited at the same frequency, gives the enhancement in the cross section over the Doppler-broadened single-beam case. If the laser is detuned from resonance by $|\Delta| = (E_f - E_i)/\hbar - 2\omega$ then the zero-velocity group is out of resonance with any combination of photons from two lasers. If $\Delta > 0$, the $z$axis direction laser is on resonance with an atom having $v = -c|\Delta|/2\omega$ and $-z$ axis direction laser is on resonance with an atom having $v = c|\Delta|/2\omega$. By contrast, if $\Delta < 0$, the z axis direction laser is on resonance with an atom

having $v = c|\Delta|/2\omega$ and $-z$ axis direction laser is on resonance with an atom having $v = -c|\Delta|/2\omega$. Thus, when the laser is detuned from the resonance frequency only two particular velocity groups are in resonance, whereas when the laser is on the exact resonance frequency, all the velocity groups are on resonance for absorbing one photon from pump and one from the probe. The lineshape of the same frequency two-photon absorption is the sum of the broad Doppler-broadened background $(I_1^2 + I_2^2)\delta\omega_i/\delta\omega_D$. (here, $\delta\omega_D$ Doppler broadening, I_i laser intensity) from two-photon absorption in each of beams and the sharp Doppler-free line $(I_1 + I_2)^2 N$. If the two lasers have the same intensity, the integral of Doppler-free signals should be at least twice that of the Doppler-broadened one. Since the enhancement of Doppler-free signals increases proportionally to the uncollimated helium beam Doppler width, the observed enhancement of the Doppler-free signal over the Doppler-broadened one was a few hundred to one [55]. As we mentioned in Section 2.2.2, one-photon resonant DFWM can provide a Doppler-free spectrum with peak located at $\Delta_1 = 0$. When ω_1 is set to the center of the Doppler profile, then only atoms whose velocities are $\boldsymbol{k}_1 \cdot \boldsymbol{v} \approx 0$ interact with the beam 3. This group of atoms will interact with the beam 1 of frequency ω_2 and contribute to different frequency two-photon NDFWM signals. Since only atoms in a specific velocity group contribute the signal, the different frequency two-photon NDFWM spectrum is also Doppler-free. Combining the capability of the high accuracy in measuring the ASPB modulation frequency, a Doppler-free precision can be achieved in the measurement of $\Omega_2 + \Omega_1$. Figure 2.20 shows the Fourier spectrum of the data in which τ is varied for a range of 300 fs. We can obtain the modulation frequency $\Omega_2 + \Omega_1 = 6.97833 \times 10^{15}\mathrm{s}^{-1}$ corresponding to the sum of resonant frequencies of transitions from $3S_{1/2}$ to $3P_{3/2}$ and from $3P_{3/2}$ to $5D_{3/2,5/2}$ [Fig. 2.12 (a)].

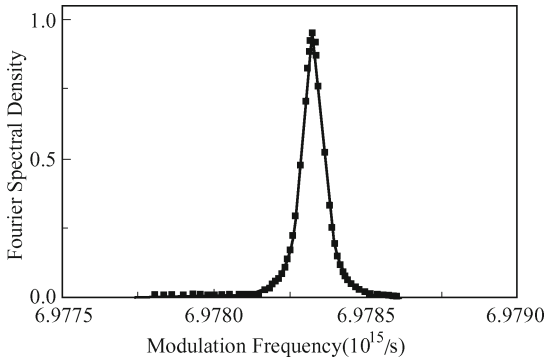

Fig. 2.20. The Fourier spectrum of ASPB given by Eq. (2.93) with $\alpha_1 = 2.715 \times 10^{-5}$ fs^{-1}, $\alpha_2 = 3.793 \times 10^{-5}$ fs^{-1}, $\omega_2 + \omega_1 = 6.9783$ fs^{-1}, $r = 0, B_i = 0.4, |\tau| \leqslant 150$ fs, and $\eta = 1$.

In conclusion, we have adopted chaotic, phase-diffusion, and Gaussian-amplitude field models to study the FLPB with broadband noisy light. The

polarization beat signal is shown to be particularly sensitive to the field statistics. Different stochastic models of laser fields only affect the fourth-order coherence functions. The constant background of the beat signal originates from the amplitude fluctuation of Markovian stochastic fields. The Gaussian-amplitude field shows fluctuations larger than the chaotic field, which again exhibits fluctuations much larger than for the phase-diffusion field with pure phase fluctuations caused by spontaneous emission. We have considered the cases that pump beams have either narrow band or broadband linewidth and found that for both cases a Doppler-free precision in the measurement of the energy-level difference between two states, which are dipolar forbidden from the ground state can be achieved. On the other hand, the new phenomenon of phase-conjugation sum-frequency attosecond beats by twin composite stochastic fields has been documented, and its origins explained. As a Doppler-free attosecond ultrafast modulation process, in principle, it can be extended to any sum-frequency of energy-levels.

References

[1] Ryan R E, Bergeman T H. Handle effect in nonmonochromatic laser light. Phys Rev A, 1991, 43: 6142 – 6155.

[2] Chen C, Elliott D S, Hamilton M W. Two-photon absorption from the real Gaussian field. Phys Rev Lett, 1992, 68: 3531 – 3534.

[3] Walser R, Ritsch H, Zoller P, et al. Laser-noise-induced population fluctuations in two-level systems: complex and real Gaussian driving fields. Phys Rev A, 1992, 45: 468 – 476.

[4] Anderson M H, Vemuri G, Cooper J, et al. Experimental study of absorption and gain by two-level atoms in a time-delayed non-Markovian optical field. Phys Rev A, 1993, 47: 3202 – 3209.

[5] Ryan R E, Westling L A, Blumel R, et al. Two-photon spectroscopy: a technique for characterizing diode-laser noise. Phys Rev A, 1995, 52: 3157 – 3169.

[6] Georges A T. Resonance fluorescence in Markovian stochastic fields. Phys Rev A, 1980, 21: 2034 – 2049.

[7] Bratfalean R, Ewart P. Spectral line shape of nonresonant four-wave mixing in Markovian stochastic fields. Phys Rev A, 1997, 56: 2267 – 2279.

[8] Ma H, Araujo C B de. Interference between third- and fifth-order polarizations in semiconductor doped glasses. Phys Rev Lett, 1993, 71: 3649 – 3652.

[9] Ma H, Acioli L H, Gomes A S L, et al. Method to determine the phase dispersion of the third-order susceptibility. Opt Lett, 1991, 16: 630 – 632.

[10] Zhang Y P, Sun L Q, Tang T T, et al. Effects of field correlation on polarization beats. Phys Rev A, 2000, 61: 053819.

[11] Zhang Y P, Tang T T, Li S, et al. Theoretical study of the fifth-order polarization beats in a four-level system. Acta Physica Sinica, 1999, 48: 1452 – 1458.

[12] Zhang Y P, Sun L Q, Tang T T, et al. Fourth-order interference on polarization beats in a four-level system J Opt Soc Am B, 2000, 17: 690 – 696.

[13] Zhang Y P, Tang T T, Sun L Q, et al. Effects of fourth-order coherence on ultrafast modulation spectroscopy. Phys Rev A, 2000, 61: 023809.

[14] Zhang Y P, Araujo C B de, et al. Higher-order correlation on polarization beats in Markovian stochastic fields. Phys Rev A, 2001, 63: 043802.

[15] Zhang Y P, Sun L Q, Tang T. T, et al. Fourth-order interference on polarization beats with phase-conjugation geometry. Chin Phys Lett, 2000, 17: 206 – 208.

[16] Zhang Y P, Tang T T, Fu P M. Asymmetric behavior of the polarization beats signal in a four-level system. Acta Physica Sinica, 1999, 48: 242 – 248.

[17] DeBeer D, Wagenen L G Van, Beach R. et al. Ultrafast modulation spectroscopy. Phys Rev Lett, 1986, 56:1128 – 1131.

[18] Fu P M, Mi X, Yu Z H, et al. Ultrafast modulation spectroscopy in a cascade three-level system. Phys Rev A, 1995, 52: 4867 – 4870.

[19] Morita N, Yajima T. Ultrahigh-time-resolution coherent transient spectroscopy with incoherent light. Phys Rev A, 1984, 30: 2525 – 2536.

[20] Asaka S, Nakatsuka M, Fujiwara M, et al. Accumulated photon echoes with incoherent light in Nd+3-doped silicate glass. Phys Rev A, 1984, 29: 2286 – 2289.

[21] DeMott D C, Ulness D J, Albrecht A C. Femtosecond temporal probes using spectrally tailored noisy quasi-cw laser light. Phys Rev A, 1997, 55: 761 – 771.

[22] Zhang Y P, Gan C L, Farooqi S M, et al. Four-level polarization beats with broadband noisy light. J Opt Soc Am B, 2002, 19: 1204 – 1215.

[23] Kirkwood J C, Albrecht A C. Down-conversion of electronic frequencies and their dephasing dynamics: interferometric four-wave-mixing spectroscopy with broadband light. Phys Rev A, 2000, 61:033802.

[24] Kirkwood J C, Albrecht A C, Ulness D J. Fifth-order nonlinear Raman processes in molecular liquids using quasi-cw noisy light. I Theory J Chem Phys, 1999, 111: 253 – 271.

[25] Trebino R, Gustafson E K, Siegman A E. Fourth-order partial-coherence effects in the formation of integrated-intensity gratings with pulsed light sources. J Opt Soc Am B, 1986, 3: 1295 – 1304.

[26] Zhang Y P, Hou X, Lu K Q, et al. Sixth-order correlation on Raman-enhanced polarization beats with phase-conjugation geometry. Opt Commun, 2000, 184: 265 – 276.

[27] Zhang Y P, Wu H C, Wang P F, et al. Phase fluctuations on Raman-enhanced nondegenerate four-wave mixing. Chinese Physics, 2000, 9: 599 – 605.

[28] Zhang Y P, Lu K Q, Li C S, et al. Correlation effects of chaotic and phase-diffusion fields on polarization beats in a V-type three-level system. J Mod Optic, 2001, 48: 549 – 564.

[29] Zhang Y P, Lu K Q, Wu H C, et al. Nonlinear effects of third- and fifth-order in polarization beats. Chinese Physics, 2000,9: 606 – 610.

[30] Zhang Y P, Hou X, Lu K Q, et al. Raman-enhanced polarization beats with phase-conjugation geometry. Chinese Physics, 2000, 9: 905 – 909.

[31] Zhang Y P, Gan C L, Ping S J, et al. Ultrafast sum-frequency polarization beats in twin Markovian stochastic correlation. J Mod Optics, 2002,52: 2013 – 2047.

[32] Morgner U, Kartner F X, Cho S H, et al. Sub-two-cycle pulses from a Kerr-lens mode-locked Ti : sapphire laser. Opt Lett, 1999, 24: 411 – 413.

[33] Drescher M, Hentschel M, Kienberger R, et al. Time-resolved atomic inner-shell spectroscopy. Nature, 2002, 419: 803 – 807.

[34] Hentschel M, Kienberger R, Spielmann Ch, et al. Attosecond metrology. Nature, 2001, 414: 509 – 513.

[35] Kirkwood J C, Albrecht A C, Ulness D J, et al. Fifth-order nonlinear Raman processes in molecular liquids using quasi-cw noisy light. Ⅱ Experiment Chem Phys, 1999, 111: 272 – 280.

[36] Kirkwood J C and Albrecht A C. Multi-dimensional time-resolved coherent Raman six-wave mixing: a comparison of the direct and cascaded processes with femtosecond excitation and noisy light interferometry. J Raman Spectrosc, 2000, 31: 107 – 124.

[37] Ulness D J, Kirkwood J C, and Albrecht A C. Raman scattering from a Brownian oscillator with nonohmic Drude dissipation: Applications to continuous wave, impulsive, and noisy excitation. J Chem Phys, 1998, 109: 4478 – 4486.

[38] Ulness D J, Stimson M J, Kirkwood J C, et al. Direct observation of the resonant-non-resonant cross-term contribution to coherent Raman scattering of quasi-continuous-wave noisy light in molecular liquids. J Raman Spectrosc, 1997, 28: 917 – 925.

[39] Ulness D J, Stimson M J, Kirkwood J C, et al. Interferometric down-conversion of high-frequency molecular vibrations with time-frequency-resolved coherent Raman scattering using quasi-CW noisy light: C-H stretching modes of chloroform and benzene. J Phys Chem, 1997, 101: 4587 – 4591.

[40] Ulness D J and Albrecht A C. Four-wave mixing in a Bloch two-level system with incoherent laser light having a Lorentzian spectral density: Analytic solution and a diagrammatic approach. Phys Rev A, 1996, 53: 1081 – 1095.

[41] Kirkwood J C, Albrecht A C, Ulness D J, et al. Coherent Raman scattering with incoherent light for a multiply resonant mixture: A factorized time correlator diagram analysis. Phys Rev A, 1998,58: 4910 – 4925.

[42] DeBeer D, Usadi E, Hartmann S R. Attosecond beats in sodium vapor. Phys Rev Lett, 1988, 60: 1262 – 1266.

[43] Rothenberg J E and Grischkowsky D. Observation of a 1.9-psec polarization beat. Opt Lett, 1985, 10: 22 – 24.

[44] Fu P M, Yu Z H, Mi X, et al. Doppler-free ultrafast modulation spectroscopy with phase-conjugation geometry. Phys Rev A, 1994, 50: 698 – 708.

[45] Fu P M, Wang Y B, Jiang Q, et al. Ultrafast modulation spectroscopy in cascading three-level and four-level systems. J Opt Soc Am B, 2001, 18: 370 – 378.

[46] Zhang Y P, Gan C L, Lu K Q, et al. Raman-enhanced polarization beats in Markovian stochastic fields. Opt Commun, 2002, 205: 163 – 186.

[47] Chen C, Yin Y Y, and Elliott D S. Interference between optical-transitions. Phys Rev Lett, 1990, 64: 507 – 510.

[48] Kleiman V D, Zhu L, Allen J, et al. Coherent control over the photodissociation of CH3I. Chem Phys, 1995, 103: 10800 – 10803.

[49] Dupont E, Corkum P B, Liu H, et al. Phase-controlled currents in semiconductors. Phys Rev Lett, 1995, 74: 3596 – 3599.

[50] Bjorkholm J E and Liao P F. Line-shape and strength of 2-photon absorption in an atomic vapor with a resonant or nearly resonant intermediate state. Phys Rev A, 1976, 14: 751 – 760.

[51] Liao P F, Bloom D M, and Economou N P. Cw optical wavefront conjugation by saturated absorption in atomic sodium vapor. Appl Phys Lett, 1978, 32: 813 – 815.

[52] Mossberg T W, Kachru R, Hartmann S R, et al. Echoes in gaseous media-generalized theory of rephasing phenomena. Phys Rev A, 1979, 20: 1976 – 1996.

[53] Levenson M D. Introduction to Nonlinear Laser Spectroscopy. New York: Academic, 1982.

[54] Demtroder W. Laser Spectroscopy. New York: Springer-Verlag, 1982.

[55] Bergeson S D, Baldwin K G, Lucatorto T B, et al. Doppler-free two-photon spectroscopy in the vacuum ultraviolet: helium 1(1)S-2(1)S transition. J Opt Soc Am B, 2000, 17: 1599 – 1606.

3 Raman, Rayleigh and Brillouin-enhanced FWM Polarization Beats

Based on color-locking noisy field correlation, the Raman, Raman and Rayleigh, Rayleigh and Brillouin, coexisting Raman, Rayleigh and Brillouin-enhanced polarization beats have been investigated. Roles of amplitude fluctuations and phase fluctuations have been pointed out in attosecond sum-frequency polarization beats (ASPB). The different roles of amplitude fluctuations and phase fluctuations have been pointed out in both time- and frequency-domains. The Raman, Rayleigh and Brillouin-enhanced four-wave mixing processes strongly compete with each other in the ASPB. The heterodyne detected signal of ASPB potentially offers rich dynamic information about the homogeneous broadening material phase of the third-order nonlinear susceptibility.

3.1 Attosecond Sum-frequency Raman-enhanced Polarization Beats Using Twin Phase-sensitive Color Locking Noisy Lights

Raman-enhanced polarization beats (REPB) are one interesting way to study the stochastic properties of light [1 – 10]. Previous extensive noisy light based coherent Raman scattering (CRS) often called coherent anti-Stokes Raman scattering or coherent Stokes Raman scattering (CSRS) yield both Raman frequencies via radiation difference oscillations [4] and dephasing times in the interferometric time domains. Unlike in the REPB, in those spectroscopies the presence of one monochromatic beam is essential [5 – 8]. Markovian stochastic processes are ubiquitous in all branches of science. Unlike non-Markovian fluctuations, which arise from atom's memory of its past, the atomic response to Markovian stochastic optical fields is now largely well understood [11 – 14]. When the laser field is sufficiently intense that many photon interactions occur, the laser spectral bandwidth or spectral shape, obtained from the second-order correlation function, is inadequate to characterize the field. Rather than using higher-order correlation functions explicitly, the chaotic field, the phase-diffusion field, and the Gaussian-amplitude field, are considered.

The characteristics of the interferogram of the REPB are a result of two main components: material response (resonant term) and light response (nonresonant term) along with the interplay between two responses. We have developed a unified theory which involves sixth- and fourth-order coherence-functions, and obtained an analytic closed form for attosecond polarization beats [15 – 19]. The difference-frequency homodyne detected polarization beats in femtosecond scale have known well [20 – 22]. In general, polarization beats may or may not contain resonances. Nonresonant terms are always present. Interference between resonant and nonresonant polarizations is present. Cross terms between them appear when homodyne detected. Beat signals can appear at all orders of the incident field [but only at odd orders for achiral isotropic media (gases, liquid, amorphous solids)]. At even order, the polarization (signals) field must oscillate at a new frequency not present in the incident field. At odd order, the polarization field may contain frequency components of the incident field but usually produces a new color. Cross-section is quadratic in concentration for homodyne detection; linear for heterodyne detection. Unlike heterodyned signals, homodyne (quadrature) detection signals contain all possible cross terms between polarizations. Phase-matching must be implemented through experimental design of the REPB.

Polarization beat is closely related to quantum beats, Raman quantum beats [9], or CRS. CRS is a powerful tool for studying the vibrational or rotational mode of a molecule. Specifically, in the Raman-enhanced nondegenerate four-wave mixing (RENFWM) the Raman vibration is excited by the simultaneous presence of two incident beams whose frequency difference equals the Raman excitation frequency, and the RENFWM signal is the result of this resonant excitation. In contrast, Rayleigh-type nondegenerate FWM (NDFWM) is a nonresonant process with no energy transfer between lights and medium when the frequency difference between two incident beams equals zero. Rayleigh-type NFWM appears as a special case of the RENFWM with zero frequency resonance, the difference between them is essential. The resonant structure in the Rayleigh-type NFWM spectrum is the result of induced moving grating. The lineshape of the Rayleigh-type NFWM is always symmetric [23]. In contrast, the RENFWM spectrum is generally normal asymmetric due to the interference between the resonant signal and the nonresonant background [24].

This section addresses the role of noise in incident fields on the nature of wave-mixing signals in time- and frequency-domains. This important topic has been already treated extensively in the literature, including the introduction of a new diagrammatic technique (called factorized time correlator diagrams) [1 – 8]. They have treated the higher order noise correlators when circular Gaussian statistics apply. There should be two classes of such two component beams. In one class components are derived from separate lasers, and their mixed (cross) correlators should vanish. In the second case, two components are derived from a single laser source whose spectral output is

doubly peaked. This can be created from a single dye laser in which two different dyes in solution together are amplified [5–8]. This section deals only with the first class. That is to say, we are considering only the class of two-color beams in which each color is derived from a separate broadband laser source. The doubled peaked beams 1 and 2 [Fig. 3.1 (a)] are paired and correlated, but each of the peaks is uncorrelated. Beam3, having one of peaks (from a same broadband laser source)found in twin beams 1 and 2 is dependent and correlated to twin beams 1 and 2. In any case, the literature has already explored both theoretically and experimentally the use of such multicolor noisy light in FWM. Interestingly, that work only treats the second class of multicolored beams (a single laser source for the multipeaked "tailored" light) in difference-frequency self-diffraction geometry [5–8]. Also that work did not treat the REPB with sum- and difference-frequency phase-conjugation geometry using three types of noisy models. Furthermore its beam 3 was not noisy (it was "monochromatic").

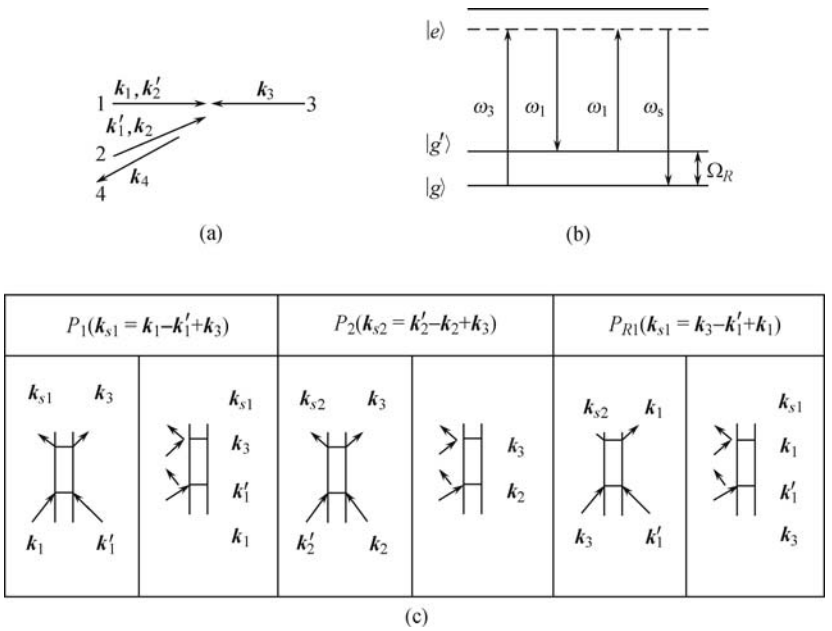

Fig. 3.1. (a) Phase-conjugation geometry of the attosecond REPB; (b) Level configuration of P_{R1}; (c) Double-sided Feynman diagrams representing the Liouville pathways for P_1 and P_2, respectively.

3.1.1 Basic Theory of Attosecond Sum-frequency REPB

REPB is a third-order nonlinear polarization beat phenomenon. The polarization beat is based on the interference at the detector between FWM signals,

which originate from macroscopic polarizations excited simultaneously in the homogeneous [9, 10] or inhomogeneous [15] broadening sample. It critically requires that all the polarizations have the same frequency. The basic geometry is shown in Fig. 3.1(a). Twin beams 1 and 2 consist of two central circular frequency components ω_1 and ω_3, a small angle exists between them. Beam 3 with central circular frequency ω_3 is almost propagating along the opposite direction of beam 1. In an optical Kerr medium (no thermal grating effects), the nonlinear interaction of beams 1 and 2 with the medium gives rise to two molecular-reorientational gratings, i.e., ω_1 and ω_3 will induce their own nonresonant static gratings G1 and G2, respectively. Two FWM signals are the results of the diffraction of beam 3 by G1 and G2, respectively. Now, if $|\omega_1 - \omega_3|$ is near the Raman resonant frequency Ω_R [Fig. 3.1 (b)], a large angle resonant moving grating formed by the interference of beams 2 and 3, will excite the Raman-active vibrational mode of the medium and enhance the FWM signal of G1 (i.e., RENFWM). Finally, polarization beats originate from the interference between macroscopic polarizations from the RENFWM process and the ω_3 degenerate FWM (DFWM) process. The beat signal (beam 4) is along the opposite direction of beam 2 approximately.

In a typical experiment, the ω_1 and ω_3 two-color light sources enter a dispersion-compensated Michelson interferometer to generate identical twin composite beams. Twin composite stochastic fields of beam 1, $E_{p1}(\boldsymbol{r}, t)$, and beam 2, $E_{p2}(\boldsymbol{r}, t)$ for homodyne detection scheme of the attosecond sum-frequency REPB, can be written as

$$\begin{aligned} E_{p1} &= E_1(\boldsymbol{r}, t) + E_2'(\boldsymbol{r}, t) = A_1(\boldsymbol{r}, t)\exp(-\mathrm{i}\omega_1 t) + A_2'(\boldsymbol{r}, t)\exp(-\mathrm{i}\omega_3 t) \\ &= \varepsilon_1 u_1(t)\exp[\mathrm{i}(\boldsymbol{k}_1 \cdot \boldsymbol{r} - \omega_1 t)] + \\ &\quad \varepsilon_2' u_3(t-\tau)\exp[\mathrm{i}(\boldsymbol{k}_2' \cdot \boldsymbol{r} - \omega_3 t + \omega_3 \tau)], \end{aligned} \tag{3.1}$$

$$\begin{aligned} E_{p2} &= E_1'(\boldsymbol{r}, t) + E_2(\boldsymbol{r}, t) = A_1'(\boldsymbol{r}, t)\exp(-\mathrm{i}\omega_1 t) + A_2(\boldsymbol{r}, t)\exp(-\mathrm{i}\omega_3 t) \\ &= \varepsilon_1' u_1(t-\tau)\exp[\mathrm{i}(\boldsymbol{k}_1' \cdot \boldsymbol{r} - \omega_1 t + \omega_1 \tau)] + \\ &\quad \varepsilon_2 u_3(t)\exp[\mathrm{i}(\boldsymbol{k}_2 \cdot \boldsymbol{r} - \omega_3 t)]. \end{aligned} \tag{3.2}$$

Here, $\varepsilon_i, \boldsymbol{k}_i(\varepsilon_i', \boldsymbol{k}_i')$ are the constant field amplitude and the wave vector of the ω_i component in beam 1 (beam 2), respectively. $u_i(t)$ is a dimensionless statistical factor that contains phase and amplitude fluctuations. The $u_i(t)$ is taken to be a complex ergodic stochastic function of t, which obey complex circular Gaussian statistics in the chaotic field. τ is a variable relative time delay between the prompt (unprime) and delayed (prime) fields. To accomplish this the frequency component ω_1 and ω_3 lights are split and recombined to provide two double-frequency pulses in such a way that the ω_1 component is delayed by τ in beam 2 and the ω_3 component delayed by the same amount in the beam 1 [Fig. 3.1 (a)]. The time delay τ is introduced in both composite beams, which is quite different with that of difference-frequency REPB. On the other hand, the complex electric fields of beam 3 can be written as

$$E_3(\boldsymbol{r}, t) = A_3(\boldsymbol{r}, t)\exp(-\mathrm{i}\omega_3 t) = \varepsilon_3 u_3(t)\exp[\mathrm{i}(\boldsymbol{k}_3 \cdot \boldsymbol{r} - \omega_3 t)]. \tag{3.3}$$

Here, ω_3, ε_3, and $\boldsymbol{k}_3$ are the frequency, the field amplitude and the wave vector of the field, respectively.

In general different colors of twin composite noisy light beams correlate at different delay times because they have been delayed in the dispersed beam relative to the undispersed beam except balanced. This is analogous to the stretching of short pulses by transmission through a dispersive medium (chirp). In fact, identical physical processes are responsible for chirp in coherent short pulses and the correlation functions of broadband fields. Considering the situation in which the double frequencies noisy field derived from separate lasers with a finite bandwidth is split into twin replicas; then ω_1 or ω_3 frequency component of one twin composite beam is transmitted through a dispersive medium so that it is no longer identical to that of the other twin composite beam. Two autocorrelation processes corresponding to RENFWM process and ω_3 DFWM process, respectively, are differently stretched in τ because each color component between twin composite beams 1 and 2 is maximally correlated at different delay times, whereas all color components in beam 1 or 2 are maximally correlated at the same delay time. The phases of chirped correlation functions exhibit a time dependence that is similar to time-dependent phases of chirped coherent short pulses. Unchirped (transform-limited) correlation functions and short pulses have phases that are independent of time. An important practical distinction between short pulses and noisy-light correlation functions is that the chirping of correlation functions in the double-frequency noisy-light interferometry can occur only after the double-frequency noisy field is split into beams 1 and 2, and then only if there is a difference between the dispersion in the paths traveled by ω_1 or ω_3 frequency component of beams 1 and 2, but a short pulse is chirped as it propagates through any dispersive medium between the source and the sample. That is to say, ultrashort pulses of equivalent bandwidth are not immune to such dispersive effects (even when balanced) because the transform limited light pulse is in fact temporally broadened (it is chirped) and this has drastic effects on its time resolution (the auto-correlation). In this sense, the sum-frequency REPB with double-frequency noisy light has an advantage.

The order parameters Q_1 and Q_2 of two nonresonant static gratings induced by beams 1 and 2 satisfy the following equations:

$$\frac{\mathrm{d}Q_1}{\mathrm{d}t} + \gamma Q_1 = \chi\gamma E_1(\boldsymbol{r}, t)[E_1'(\boldsymbol{r}, t)]^*, \tag{3.4}$$

$$\frac{\mathrm{d}Q_2}{\mathrm{d}t} + \gamma Q_2 = \chi\gamma E_2'(\boldsymbol{r}, t)[E_2(\boldsymbol{r}, t)]^*. \tag{3.5}$$

Here γ and χ are the relaxation rate and the nonlinear susceptibility of two static gratings, respectively. The optical Kerr effect for the liquid CS_2 has at least two components, i.e., a relatively long "Debye" component and a shorter "interaction-induced" component.

We consider a large angle resonant moving grating formed by the interference of beams 2 and 3, and the order parameter Q_{R1} satisfies the following

equation:

$$\frac{\mathrm{d}Q_{R1}}{\mathrm{d}t} + (\gamma_R - \mathrm{i}\Delta)Q_{R1} = \frac{\mathrm{i}\alpha_R}{4\hbar}[A_1'(\boldsymbol{r},t)]^* A_3(\boldsymbol{r},t). \tag{3.6}$$

Here, $\Delta = |\omega_1 - \omega_3| - \Omega_R$ is the frequency detuning; Ω_R and γ_R are the resonant frequency and the relaxation rate of the Raman mode, respectively. α_R is a parameter denoting the strength of the Raman interaction.

The induced three third-order nonlinear polarizations which are responsible for FWM signals are

$$\begin{aligned} P_1 &= Q_1(\boldsymbol{r},t)E_3(\boldsymbol{r},t) \\ &= \chi\gamma\varepsilon_1(\varepsilon_1')^*\varepsilon_3 \exp\{\mathrm{i}[(\boldsymbol{k}_1 - \boldsymbol{k}_1' + \boldsymbol{k}_3)\cdot\boldsymbol{r} - \omega_3 t - \omega_1\tau]\} \times \\ &\quad \int_0^\infty u_1(t-t')u_1^*(t-t'-\tau)u_3(t)\exp(-\gamma t')\mathrm{d}t', \end{aligned} \tag{3.7}$$

$$\begin{aligned} P_2 &= Q_2(\boldsymbol{r},t)E_3(\boldsymbol{r},t) \\ &= \chi\gamma\varepsilon_2'(\varepsilon_2)^*\varepsilon_3 \exp\{\mathrm{i}[(\boldsymbol{k}_2' - \boldsymbol{k}_2 + \boldsymbol{k}_3)\cdot\boldsymbol{r} - \omega_3 t + \omega_3\tau]\} \times \\ &\quad \int_0^\infty u_3^*(t-t')u_3(t-t'-\tau)u_3(t)\exp(-\gamma t')\mathrm{d}t', \end{aligned} \tag{3.8}$$

$$\begin{aligned} P_{R1} &= \frac{1}{2}N\alpha_R Q_{R1}(\boldsymbol{r},t)E_1(\boldsymbol{r},t)\exp[\mathrm{i}(\omega_1-\omega_3)t - i\omega_1\tau] \\ &= \mathrm{i}\chi_R\gamma_R\varepsilon_1(\varepsilon_1')^*\varepsilon_3 \times \exp\{\mathrm{i}[(\boldsymbol{k}_1 - \boldsymbol{k}_1' + \boldsymbol{k}_3)\cdot\boldsymbol{r} - \omega_3 t - \omega_1\tau]\} \times \\ &\quad \int_0^\infty u_1(t)u_1^*(t-t'-\tau)u_3(t-t')\exp[-(\gamma_R - \mathrm{i}\Delta)t']\mathrm{d}t', \end{aligned} \tag{3.9}$$

with $\chi_R = N\alpha_R^2/8\hbar\gamma_R$ and N the density of molecules. The third-order nonlinear polarizations P_1, P_{R1} (with Lorentzian lineshape for the Raman mode) and P_2 have the same frequency $\omega_3, P_1 + P_{R1}$, and P_2 correspond to RENFWM process and ω_3 DFWM process, which have the wave vectors $\boldsymbol{k}_1 - \boldsymbol{k}_1' + \boldsymbol{k}_3$ and $\boldsymbol{k}_2' - \boldsymbol{k}_2 + \boldsymbol{k}_3$, respectively [Fig. 3.1 (c)]. Physically, RENFWM is similar to the corresponding CSRS. Unlike CSRS no coherence spike appears at $\tau = 0$ [Fig. 3.2 (a)]. As the laser linewidth α_1/γ_R increases, the maximum is more close to $\tau = 0$, and the τ-independent nonresonant background is increased. Moreover, the RENFWM [$\langle P_{R1}P_{R1}^*\rangle$ (interference from purely Raman-resonant signals); $\langle P_1 P_{R1}^*\rangle$ and $\langle P_1^* P_{R1}\rangle$ (interference between the Raman-resonant signal and the nonresonant background)] of REPB exhibits hybrid radiation-matter detuning terahertz damping oscillation with a frequency close to Δ, which originate from $\sin(\Delta\tau)$ and $\cos(\Delta\tau)$ factors for $\tau < 0$ [Fig. 3.2 (b)]. The maximum of the temporal profile for the RENFWM is shifted to $\tau = 0$ as the frequency detuning Δ/γ_R increases.

Specifically, according to P_1 and P_{R1} [Fig. 3.1(b)], there exists integration effect in the establishment of order parameters Q_1 and Q_{R1}. However, as mentioned in [23], whether the gratings are washed out due to the phase fluctuation of the interference patterns [i.e.,$A_1(t-t')[A_1'(t-t')]^*$ and $[A_1'(t-t')]^* A_3(t-t')$ in Eqs. (3.7) and (3.9)] depends on the ratio between

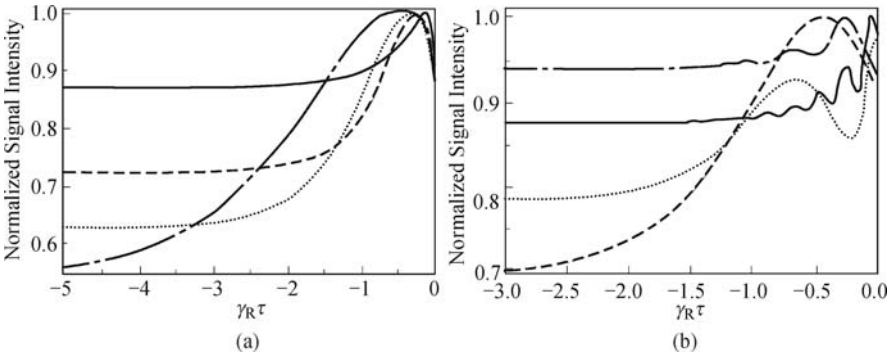

Fig. 3.2. Normalized RENFWM signal intensity versus time delay $\gamma_R\tau$ for $\chi/\chi_R = 0.05, \gamma/\gamma_R = 4$, and $\alpha_3/\gamma_R = 0.1$. $\Delta/\gamma_R = 0, \alpha_1/\gamma_R = 0.5$ (dash-dotted curve), 2 (dotted curve), 5 (dashed curve), 20 (solid curve) for (a); while $\alpha_1/\gamma_R = 2, \Delta/\gamma_R = 1$ (dash-dotted curve), 3 (dotted curve), 15 (dashed curve), 30 (solid curve) for (b). Adopted from Ref. [19].

a $\alpha_1(\alpha_3)$ and $\gamma(\gamma_R)$. The problem is complicated further by the fact that the effect of field correlation on the order parameters Q_1 and Q_{R1} are different. In particular, as we increase the time delay, the phase fluctuation of the interference pattern between $A_1(t-t')$ and $A_1'(t-t')$ components of beams 1 and 2, respectively, affect the establishment of Q_1 directly. In contrast, since Q_{R1} is induced by $A_1'(t-t')$ and $A_3(t-t')$ components of beams 2 and 3, respectively, the integration effect will not lead directly to the τ dependence of Q_{R1}. The field-correlation effect here is due to the coincidence of intensity spikes between Q_{R1} and beam 1 instead. The RENFWM is also influenced by the interference between signals originating from Q_1 and Q_{R1}. The degree of the interference is reflected in the parameter $\xi(\tau) = I_{res.}(\Delta = 0)/I_{nonres.}$, which is defined as the ratio between the intensity of the resonant signal at $\Delta = 0$ and the nonresonant background.

The resonant signal and the nonresonant background of the RENFWM originate from the order parameters Q_{R1} and Q_1, respectively. According to Eqs. (3.7) and (3.9), integration effects are involved in the establishment of order parameters of the gratings. We first consider the case when $\gamma, \gamma_R >> \alpha_1, \alpha_3$. In this case, the material gratings have very short relaxation times; therefore, they can respond to the phase fluctuations of the fields almost immediately. More specifically, $A_1(t-t')[A_1'(t-t')]^*$ and $[A_1'(t-t')]^* A_3(t-t')$ in Eqs. (3.7) and (3.9) are slowly varying functions in comparison with $\exp(-\gamma t')$ and $\exp(-\gamma_R t')$ which have a peak at $t' = 0$, and therefore can be approximated as and $A_1(t)[A_1'(t)]^*$ and $[A_1'(t)]^* A_3(t)$, respectively. We have P_1 and P_{R1} proportional to $\chi\gamma A_1(t)[A_1'(t)]^* A_3(t) \int_0^\infty \exp(-\gamma t')\mathrm{d}t'$ and $\chi_R\gamma_R A_1(t)[A_1'(t)]^* A_3(t) \int_0^\infty \exp[-(\gamma_R - \mathrm{i}\Delta)t']\mathrm{d}t'$. The above equations in-

dicate that the RENFWM spectrum is independent of τ and the relaxation rate γ plays uncritical role here. Although the phases of P_1 and P_{R1} fluctuate randomly, the relative phase between them is fixed; therefore, we have $\xi(\tau) \approx (\chi_R/\chi)^2$ due to the interference between P_1 and P_{R1}. Moreover, due to the interference between the resonant signal and the nonresonant background, the RENFWM spectrum with narrow-band driving fields is asymmetric and the peak does not correspond to the exact Raman resonance.

Next, considering the broadband case (i.e.,$\gamma, \gamma_R << \alpha_1, \alpha_3$), the effect of integration is to wash out the gratings. At zero time delay no washout takes place in the establishment of Q_1 because the phase factor ϕ_1 of $A_1(t - t')[A_1'(t - t')]^*$ is stationary. On the other hand, the phase factor ϕ_{R1} of $[A_1'(t-t')]^* A_3(t-t')$ is a random variable which fluctuates with a characteristic time scale $(\alpha_1+\alpha_3)^{-1}$. Because of the integration effect, the fast random fluctuation of ϕ_{R1} leads to the reduction of the amplitude of Q_{R1}. Therefore, the RENFWM spectrum is dominated by a large nonresonant background when $\tau = 0$, and $\xi(0) \approx \chi_R^2 \gamma_R/\chi^2(\alpha_1 + \alpha_3)$, which is independent of γ. The RENFWM spectrum in the limit of $\alpha_i\,|\tau| << 1$ is quite different. Similar to Q_{R1}, Q_1 is now induced by mutually incoherent fields. If $\alpha_1 \approx \alpha_3$ replaced by α, then the influences of the integration effect on Q_1 and Q_{R1} are equal. Furthermore, the relative phase between P_1 and P_{R1} is a stochastic variable. Since there is no interference between them, we have $\xi(\tau \to \infty) \approx \chi_R^2 \gamma_R/\chi^2\gamma$ instead of $\xi(\tau) \approx (\chi_R/\chi)^2$. The interesting thing is that, when $\gamma_R/\gamma \approx 1$, we have $\xi(\tau \to \infty) \approx (\chi_R/\chi)^2$ for the broadband case, which is the same as that for the narrow-band case. In general, comparing to the narrow-band case $(\gamma, \gamma_R >> \alpha_1, \alpha_3)$ the RENFWM spectrum exhibits a larger nonresonant background. Besides, the linewidth (full width at half maximum) of the Raman resonant signal increases from $2\gamma_R$ to $2(\alpha_1 + \alpha_3)$. We then increase τ that beams 1 and 2 become uncorrelated. In this case, the randomization of ϕ_1 washes out the ω_1 molecular-reorientational grating. In contrast, Raman-active mode is nearly independent of τ because the τ-dependent part is much smaller than the τ-independent part when beams 1 and 2 have broadband linewidths. The implication of this is that the ratio between the Raman resonant signal and the nonresonant background increases as τ increased. Since $\gamma, \gamma_R << \alpha_1, \alpha_3$ the nonresonant background is suppressed drastically and the RENFWM spectrum depends on the ratio between the relaxation rates γ_R and γ. However, the relative phase between P_1 and P_{R1} is now a stochastic variable. Due to the randomization of the relative phase between the Raman resonant term and the nonresonant background the interference between them disappears almost completely. As a result, the RENFWM spectrum exhibits a symmetric line shape (Fig. 3.3). As γ_R/γ is increased further so that $\gamma_R/\gamma > 1$, the ratio between the resonant and the nonresonant signal can even be enhanced in the comparison with the narrow band case. So there is the exact advantage of using the REPB with twin color-locking noisy lights to measure the resonant frequency of the Raman active mode.

3.1.2 Homodyne Detection of Sum-frequency REPB

We have the total third-order polarization $P^{(3)} = P_1 + P_2 + P_{R1}$. For the macroscopic system where phase matching takes place this signal must be drawn from the $P^{(3)}$ developed on one chromophore multiplied by the $(P^{(3)})^*$ that is developed on another chromophore, which must be located elsewhere in space (with summation over all such pairs) [1–8]. The bichromophoric model is particularly important to the noisy light spectroscopies where the stochastic averaging at the signal level must be carried out [1–8]. The sum-frequency REPB signal is proportional to the average of the absolute square of $P^{(3)}$ over the random variable of the stochastic process, so that the signal

$$I(\Delta,\tau)\propto\langle\left|P^{(3)}\right|^2\rangle=\langle P^{(3)}(P^{(3)})^*\rangle=\langle(P_1+P_2+P_{R1})[(P_1)^*+(P_2)^*+(P_{R1})^*]\rangle$$

contains $3\times 3 = 9$ different terms in the sixth-, fourth- and second-order coherence function of $u_i(t)$ in phase conjugation geometry. In general, the REPB of the homodyne detection (at the intensity level) can be viewed as built of the sum of three contributions: (i) τ-independent or dependent nonresonant auto-correlation terms of ω_3 molecular-reorientational grating, which include $u_3(t)$ sixth-order Markovian stochastic correlation functions; (ii) τ-independent or dependent auto-correlation terms (i.e., RENFWM) of ω_1 nonresonant molecular-reorientational grating and $\omega_3-\omega_1\approx\Omega_R$ Raman resonant vibrational mode, which include $u_1(t)$ fourth-order and $u_3(t)$ second-order Markovian stochastic correlation functions; (iii) τ-dependent cross-correlation terms between RENFWM and ω_3 DFWM processes, which include $u_3(t)$ fourth-order and $u_1(t)$ second-order Markovian stochastic correlation functions. Different Markovian stochastic models of the laser field only affect the sixth- or fourth-, not second-order correlation functions.

We first assumed that laser sources are chaotic fields. A chaotic field, which is used to describe a multimode laser source, is characterized by the fluctuation of both the amplitude and the phase of fields. The random function $u_i(t)$ of complex noisy fields is taken to obey complex Gaussian statistics with its sixth- and fourth-order coherence function satisfying [11, 12]

$$\begin{aligned}&\langle u_i(t_1)u_i(t_2)u_i(t_3)u_i^*(t_4)u_i^*(t_5)u_i^*(t_6)\rangle\\&\quad=\langle u_i(t_1)u_i^*(t_4)\rangle\langle u_i(t_2)u_i(t_3)u_i^*(t_5)u_i^*(t_6)\rangle+\\&\qquad\langle u_i(t_1)u_i^*(t_5)\rangle\times\langle u_i(t_2)u_i(t_3)u_i^*(t_4)u_i^*(t_6)\rangle+\\&\qquad\langle u_i(t_1)u_i^*(t_6)\rangle\times\langle u_i(t_2)u_i(t_3)u_i^*(t_4)u_i^*(t_5)\rangle,\quad(i=1,2,3)\end{aligned}\tag{3.10}$$

$$\begin{aligned}&\langle u_i(t_1)u_i(t_2)u_i^*(t_3)u_i^*(t_4)\rangle\\&\quad=\langle u_i(t_1)u_i^*(t_3)\rangle\langle u_i(t_2)u_i^*(t_4)\rangle+\langle u_i(t_1)u_i^*(t_4)\rangle\langle u_i(t_2)u_i^*(t_3)\rangle.\end{aligned}\tag{3.11}$$

All higher order coherence functions can be expressed in terms of products of second-order coherence functions. Thus any given $2n$ order coherence function may be decomposed into the sum of $n!$ terms, each consisting of the products of n second-order coherence function.

Furthermore assuming that laser sources have Lorentzian line shape, then we have

$$\langle u_i(t_1)\, u_i^*(t_2)\rangle = \exp\left(-\alpha_i |t_1 - t_2|\right). \tag{3.12}$$

Here, $\alpha_i = \dfrac{1}{2}\delta\omega_i, \delta\omega_i$ is the linewidth of the laser with frequency ω_i.

The composite noisy beam 1 (beam 2) is treated as one whose spectrum is simply a sum of two Lorentzians. The high-order decay cross-correlation terms are reasonably neglected in our treatment. After performing the tedious integration we obtain for:

(i) $\tau > 0$

$$\begin{aligned} I(\Delta,\tau) \propto B_1 + \left[\chi^2 + \frac{\chi_R^2\gamma_R^2\gamma_R'}{(\gamma_R+\alpha_1)(\gamma_R'^2+\Delta^2)} + \frac{2\chi\chi_R\gamma_R\Delta}{\gamma_R'^2+\Delta^2}\right]\exp(-2\alpha_1|\tau|) + \\ \frac{\eta^2\chi^2(4\gamma^2+5\gamma\alpha_3+2\alpha_3^2)}{(\gamma+\alpha_3)(\gamma+2\alpha_3)} \times \exp(-2\alpha_3|\tau|) + \frac{2\eta\chi}{\gamma+2\alpha_3} \times \\ \left\{\left[2\chi(\gamma+\alpha_3) + \frac{\gamma\chi_R\gamma_R\Delta}{(2\alpha_3-\gamma_R')^2+\Delta^2} - \frac{\gamma\chi_R\gamma_R\Delta}{\gamma_R'^2+\Delta^2}\right]\times\right. \\ \cos[\Delta\boldsymbol{k}\cdot\boldsymbol{r} - (\omega_1+\omega_3)\tau] + \left[\frac{\gamma\chi_R\gamma_R\gamma_R'}{\gamma_R'^2+\Delta^2} - \frac{\gamma\chi_R\gamma_R(2\alpha_3-\gamma_R')}{(2\alpha_3-\gamma_R')^2+\Delta^2}\right]\times \\ \left.\sin[\Delta\boldsymbol{k}\cdot\boldsymbol{r} - (\omega_1+\omega_3)\tau]\right\}\exp[-(\alpha_1+\alpha_3)|\tau|]. \end{aligned} \tag{3.13}$$

(ii) $\tau < 0$

$$\begin{aligned} I(\Delta,\tau) \propto B_1 + \left\{\chi^2 + \frac{\chi_R^2\gamma_R^2(2\alpha_1-\gamma_R')}{(\alpha_1-\gamma_R)[(2\alpha_1-\gamma_R')^2+\Delta^2]} - \right. \\ \left.\frac{2\chi\chi_R\gamma_R\Delta}{(\gamma_R'-2\alpha_1)^2+\Delta^2}\right\}\exp(-2\alpha_1|\tau|) + \frac{\eta^2\chi^2(4\gamma-3\alpha_3)}{\gamma-\alpha_3} \times \\ \exp(-2\alpha_3|\tau|) + \frac{6\eta^2\chi^2\gamma^2\alpha_3^2}{(\gamma^2-\alpha_3^2)(\gamma^2-4\alpha_3^2)}\exp(-2\gamma|\tau|) + \chi_R^2\gamma_R^2 \times \\ \left\{\frac{\gamma_R'-2\gamma_R}{(\gamma_R'-2\gamma_R)^2+\Delta^2}\left(\frac{1}{\alpha_1-\gamma_R} + \frac{\eta_2^2}{\alpha_3-\gamma_R}\right) + \right. \\ \frac{\gamma_R'}{\gamma_R'^2+\Delta^2}\left(\frac{1}{\alpha_1+\gamma_R} + \frac{\eta_2^2}{\alpha_3+\gamma_R}\right) - \\ \left.\frac{2(1+\eta_2^2)[\gamma_R'^2+\Delta^2-(\alpha_1+\alpha_3)^2]}{(\gamma_R'^2+\Delta^2)[(\gamma_R'-2\gamma_R)^2+\Delta^2]}\right\}\exp(-2\gamma_R|\tau|) + \\ 4\eta\left\{\left[\chi^2 - \frac{\chi\chi_R\gamma_R\Delta}{(2\alpha_1-\gamma_R')^2+\Delta^2}\right]\cos[\Delta\boldsymbol{k}\cdot\boldsymbol{r} - (\omega_1+\omega_3)\tau] - \end{aligned}$$

$$\left.\frac{\chi\chi_R\gamma_R(2\alpha_1-\gamma'_R)}{(2\alpha_1-\gamma'_R)^2+\Delta^2}\sin[\Delta\boldsymbol{k}\cdot\boldsymbol{r}-(\omega_1+\omega_3)\tau]\right\}\times \exp[-(\alpha_1+\alpha_3)\,|\tau|]. \tag{3.14}$$

Here, $\eta_1=\varepsilon_2/\varepsilon'_1,\eta_2=\varepsilon'_2/\varepsilon_1,\eta=\varepsilon'_2\varepsilon_2/\varepsilon'_1\varepsilon_1;\Delta\boldsymbol{k}=(\boldsymbol{k}_1-\boldsymbol{k}'_1)-(\boldsymbol{k}'_2-\boldsymbol{k}_2)$; $\gamma'_R=\alpha_1+\alpha_3+\gamma_R$; and

$$B_1=\chi^2\gamma\left[\frac{1}{\gamma+2\alpha_1}+\frac{\eta^2(2\gamma+\alpha_3)}{(\alpha_3+\gamma)(2\alpha_3+\gamma)}\right]+\frac{\chi_R^2\gamma_R\gamma'_R}{\gamma'^2_R+\Delta^2}- 2\chi_R\chi\gamma_R\gamma\Delta\frac{(\gamma'_R+\gamma+2\alpha_1)(\gamma'_R+\gamma)+2\alpha_1\gamma'_R+\Delta^2}{(\gamma+2\alpha_1)(\gamma'^2_R+\Delta^2)[(\gamma'_R+\gamma)^2+\Delta^2]}.$$

The sum-frequency REPB is generally different for $\tau>0$ and $\tau<0$. However, as $|\tau|\to\infty$, Eq. (3.13) is identical to Eq. (3.14). Physically, when $|\tau|\to\infty$, beams 1 and 2 are mutually incoherent. Therefore whether τ is positive or negative does not affect the sum-frequency REPB. Different Markovian stochastic models of laser fields only affect the sixth- or fourth-, not second-order correlation functions. The interferometric contrast ratio of interferogram mainly determined the cross-correlation between RENFWM and ω_3 DFWM processes is equally sensitive to the amplitude and phase fluctuations of chaotic fields. The constant term $\chi_R^2\gamma_R\gamma'_R/(\gamma'^2_R+\Delta^2)$ in relations (3.13) and (3.14), which is independent of the relative time-delay between twin beams 1 and 2, originates from the phase fluctuation of chaotic fields, while the purely decay terms including these factors $\exp(-2\alpha_1\,|\tau|),\exp(-2\alpha_3\,|\tau|),\exp(-2\gamma\,|\tau|)$ and $\exp(-2\gamma_R\,|\tau|)$ in relations (3.13) and (3.14) come from amplitude fluctuation of chaotic fields. Physically, the chaotic field has the property of photon bunching, which can affect any multiphoton process when the higher-order correlation function of the field plays an important role.

Equations (3.13) and (3.14) generally indicate not only the characteristic of twin laser fields, but also a molecule vibrational property. Specifically, the temporal behaviors of the sum-frequency REPB intensities mainly reflect the characteristics of twin composite laser fields for $\tau>0$, and molecule vibrational property for $\tau<0$. The sum-frequency REPB signal versus τ typically shows the attosecond scale modulation with a sum-frequency $\omega_3+\omega_1$ and a damping rate $\alpha_1+\alpha_3$. If we employ sum-frequency REPB in attosecond scale to measure the modulation frequency $\omega_d=\omega_3+\omega_1$, the accuracy can be improved by measuring as many cycles of the attosecond modulation as possible. Since the amplitude of the attosecond modulation decays with a time constant $(\alpha_1+\alpha_3)^{-1}$ as $|\tau|$ increases, the maximum domain of time delay $|\tau|$ should equal approximately $2(\alpha_1+\alpha_3)^{-1}$. We obtain the theoretical limit of the uncertainty of the modulation frequency measurement $\Delta\omega_d$ which is $\Delta\omega_d\approx\pi(\alpha_1+\alpha_3)$, i.e., in the modulation frequency measurement the theoretical limit of the accuracy is related to the decay time constant of the beat signal modulation amplitude.

Equations (3.13) and (3.14) indicate that beat signal oscillates not only temporally but also spatially with a period $2\pi/\Delta k$ along the direction $\Delta\boldsymbol{k}$,

which is almost perpendicular to the propagation direction of the beat signal. Here $\Delta k \approx 2\pi\,|\lambda_1 - \lambda_3|\,\theta/\ \lambda_3\lambda_1, \theta$ is the angle between beam 1 and beam 2. Physically, the polarization-beat model assumes that the twin composite beams are plane waves. Therefore, RENFWM and ω_3 DFWM signals, which propagate along $\boldsymbol{k}_1 - \boldsymbol{k}_1' + \boldsymbol{k}_3$ and $\boldsymbol{k}_2' - \boldsymbol{k}_2 + \boldsymbol{k}_3$, respectively, are plane waves also. Since FWM signals propagate along the slightly different direction, the interference between them leads to the spatial oscillation. To observe the spatial modulation of the beat signal the dimension of the detector should be smaller than 0.6 mm, which should be detected by the pinhole detector. The finite thickness of the sample has a catastrophic effect on the correlation of counter-propagating color-locked noisy fields. Although transverse modulation of attosecond REPB signals is considered, the effect of signal integration in the longitudinal direction is reasonably neglected here.

It is interesting to understand the underlying physics in the REPB with incoherent lights. Much attention has been paid to the study of various ultrafast phenomena by using incoherent light sources recently [25–27]. The REPB with incoherent lights is related to the three-pulse Raman echoes. It is different from the conventional true Raman echo, which is a seventh order process or the Raman pseudo-echo which is a fifth order process [27]. For the sake of analytical simplicity, the second-order correlation of broadband noisy light can be treated as δ-functions in time. Then we have

$$\exp(-\alpha_i\,|t_1 - t_2|) \approx \frac{2}{\alpha_i}\delta\,(t_1 - t_2)\,, \quad i = 1, 2, 3. \tag{3.15}$$

When we substitute Eqs. (3.10)–(3.12) and (3.15) into $I(\Delta,\tau) \propto \langle \left| P^{(3)} \right|^2 \rangle$, we obtain, for:

(i) $\tau > 0$

$$\begin{aligned} I(\Delta,\tau) \propto B_2 + \left[\chi^2 + \frac{\chi_R^2\gamma_R^2}{\alpha_3(\alpha_1+\gamma_R)} - \frac{2\chi\chi_R\gamma_R\Delta}{\gamma_R'^2+\Delta^2}\right]\exp(-2\alpha_1\,|\tau|) + \\ \frac{\eta^2\chi^2(\gamma^3+2\alpha_3^3+5\gamma^2\alpha_3+5\alpha_3^2\gamma)}{\alpha_3(\gamma+\alpha_3)(\gamma+2\alpha_3)} \times \exp(-2\alpha_3\,|\tau|) + \\ \frac{2\eta\chi}{\gamma+2\alpha_3}\left\{\left[2\chi(\gamma+\alpha_3) + \frac{\gamma\chi_R\gamma_R\Delta}{(2\alpha_3-\gamma_R')^2+\Delta^2} - \frac{\gamma\chi_R\gamma_R\Delta}{\gamma_R'^2+\Delta^2}\right] \times \right. \\ \cos[\Delta\boldsymbol{k}\cdot\boldsymbol{r} - (\omega_1+\omega_3)\tau] + \left[\frac{\gamma\chi_R\gamma_R\gamma_R'}{\gamma_R'^2+\Delta^2} - \frac{\gamma\chi_R\gamma_R(2\alpha_3-\gamma_R')}{(2\alpha_3-\gamma_R')^2+\Delta^2}\right] \times \\ \left.\sin[\Delta\boldsymbol{k}\cdot\boldsymbol{r} - (\omega_1+\omega_3)\tau]\right\}\exp[-(\alpha_1+\alpha_3)\,|\tau|]. \end{aligned} \tag{3.16}$$

(ii) $\tau < 0$

$$\begin{aligned} I(\Delta,\tau) \propto B_2 + \left\{\chi^2 - \frac{\chi_R^2\gamma_R^2}{\alpha_3(\alpha_1-\gamma_R)} - \frac{2\chi\chi_R\gamma_R\Delta}{(\gamma_R'-2\alpha_1)^2+\Delta^2}\right\}\exp(-2\alpha_1\,|\tau|) + \\ \frac{\eta^2\chi^2[3\alpha_3(\alpha_3-\gamma)-\gamma^2]}{\alpha_3(\alpha_3-\gamma)}\exp(-2\alpha_3\,|\tau|) + \frac{2\eta^2\chi^2\gamma^2}{\alpha_3^2-\gamma^2}\exp(-2\gamma\,|\tau|) + \end{aligned}$$

$$\frac{2\chi_R^2\gamma_R^2\alpha_1}{\alpha_3(\alpha_1^2-\gamma_R^2)}\exp(-2\gamma_R|\tau|)+4\eta\left\{\left[\chi^2-\frac{\chi\chi_R\gamma_R\Delta}{(\alpha_1-\alpha_3)^2+\Delta^2}\right]\times\right.$$
$$\cos[\Delta\boldsymbol{k}\cdot\boldsymbol{r}-(\omega_1+\omega_3)\tau]-\frac{\chi\chi_R\gamma_R(\alpha_1-\alpha_3)}{(\alpha_1-\alpha_3)^2+\Delta^2}\times$$
$$\left.\sin[\Delta\boldsymbol{k}\cdot\boldsymbol{r}-(\omega_1+\omega_3)\tau]\right\}\exp[-(\alpha_1+\alpha_3)|\tau|]. \tag{3.17}$$

Here, $B_2=\chi^2\gamma^2\left[\frac{1}{2\alpha_1\gamma}+\frac{\eta^2(3\gamma+\alpha_3)}{2\alpha_3\gamma(\alpha_3+\gamma)}\right]+\frac{\chi_R^2\gamma_R}{\alpha_1}-\frac{4\chi\gamma\chi_R\gamma_R\Delta}{\alpha_1[(\gamma_R'+\gamma)^2+\Delta^2]}$.

Equations (3.16) and (3.17) are analogous to Eqs. (3.13) and (3.14), respectively. The three-order polarizations [see Eqs. (3.7)–(3.9)], which involves the integration of t' from 0 to ∞, are the accumulation of the polarization induced at a different time. In broadband linewidth and $\gamma \geqslant \gamma_R$ case, the modulation frequency of the femtosecond difference-frequency REPB corresponds to Raman resonant frequency Ω_R directly, and the symmetric lineshape [24] of the RENFWM is also good for tuning $\omega_3-\omega_1$ to Ω_R. Specifically, the relative phase between P_1 and P_{R1} is now a stochastic variable. Due to the randomization of the relative phase between the Raman resonant term from P_{R1} and the nonresonant background from P_1 the interference between them disappears almost completely. As a result, The RENFWM spectrum exhibits a symmetric line shape (Fig. 3.3).

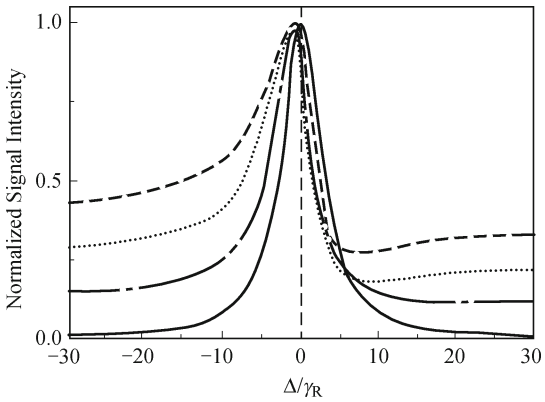

Fig. 3.3. Normalized RENFWM signal intensity versus Δ/γ_R for $\chi/\chi_R = 0.5, \alpha_3/\gamma_R = 0.1, \alpha_1/\gamma_R = 2$, and $\gamma_R\tau = 10, \gamma/\gamma_R = 0.001$ (solid curve), 1 (dashed curve), 4 (dotted curve), 100 (dash-dotted curve).

We have assumed that the laser sources are chaotic field in the above calculation. A chaotic field, which is used to describe a multimode laser source, is characterized by the fluctuation of both the amplitude and the phase of the field. Another commonly used stochastic model is a phase-diffusion model, which is used to describe an amplitude-stabilized laser source. This model assumes that the amplitude of the laser field is a constant, while its phase

fluctuates as a random process. If the lasers have Lorentzian line shape, the sixth-and fourth-order coherence function is [15, 16]

$$\begin{aligned}&\langle u_i(t_1)u_i(t_2)u_i(t_3)u_i^*(t_4)u_i^*(t_5)u_i^*(t_6)\rangle\\&\quad=\exp[-\alpha_i(|t_1-t_4|+|t_1-t_5|+|t_1-t_6|+|t_2-t_4|+|t_2-t_5|+\\&\quad\quad|t_2-t_6|+|t_3-t_4|+|t_3-t_5|+|t_3-t_6|)]\exp[\alpha_i(|t_1-t_2|+\\&\quad\quad|t_1-t_3|+|t_2-t_3|+|t_4-t_5|+|t_4-t_6|+|t_5-t_6|)],\end{aligned}\tag{3.18}$$

$$\begin{aligned}&\langle u_i(t_1)u_i(t_2)u_i^*(t_3)u_i^*(t_4)\rangle\\&\quad=\exp[-\alpha_i(|t_1-t_3|+|t_1-t_4|+|t_2-t_3|+|t_2-t_4|)]\times\\&\quad\quad\exp[\alpha_i(|t_1-t_2|+|t_3-t_4|)].\end{aligned}\tag{3.19}$$

After substituting Eqs. (3.12), (3.18), and (3.19) into $I(\Delta,\tau)\propto\langle\left|P^{(3)}\right|^2\rangle$, we obtain as follows:

(i) $\tau>0$

$$\begin{aligned}I(\Delta,\tau)\propto B_3+\frac{4\chi_R\chi\gamma_R\alpha_1\Delta-2\chi_R\chi\gamma_R\Delta(\gamma+2\alpha_1)}{(\gamma+2\alpha_1)(\gamma_R'^2+\Delta^2)}+\frac{2\eta\chi\gamma\chi_R\gamma_R\alpha_3}{\gamma_R'^2+\Delta^2}\times\\\left\{\left[\frac{\chi(\gamma_R'^2+\Delta^2)}{\gamma\chi_R\gamma_R\alpha_3}-\frac{\Delta}{\gamma\alpha_3}+\left[\frac{\gamma_R'}{\gamma\alpha_3}-\right.\right.\right.\\\frac{(\gamma_R'-\mathrm{i}\Delta)(2\alpha_3-\gamma_R'+\mathrm{i}\Delta)(\gamma_R'+\gamma-\mathrm{i}\Delta)}{[(2\alpha_3-\gamma_R')^2+\Delta^2][(\gamma_R'+\gamma)^2+\Delta^2]}-\\\left.\left.\left.\frac{(\gamma_R'+\mathrm{i}\Delta)(2\alpha_3-\gamma_R'-\mathrm{i}\Delta)(\gamma_R'+\gamma+\mathrm{i}\Delta)}{[(2\alpha_3-\gamma_R')^2+\Delta^2][(\gamma_R'+\gamma)^2+\Delta^2]}\right]\times\right.\\\left.\sin[\Delta\boldsymbol{k}\cdot\boldsymbol{r}-(\omega_1+\omega_3)\tau]\right\}\exp\left[-(\alpha_1+\alpha_3)|\tau|\right].\end{aligned}\tag{3.20}$$

(ii) $\tau<0$

$$\begin{aligned}I(\Delta,\tau)\propto B_3+2\mathrm{i}\alpha_1\chi\gamma\chi_R\gamma_R\times\\\left\{\frac{(2\alpha_1-\gamma_R'-\mathrm{i}\Delta)(\gamma_R'+\mathrm{i}\Delta)(\gamma_R'+\gamma+\mathrm{i}\Delta)}{[(2\alpha_1-\gamma_R')^2+\Delta^2](\gamma_R'^2+\Delta^2)[(\gamma_R'+\gamma)^2+\Delta^2]}-\right.\\\frac{(2\alpha_1-\gamma_R'+\mathrm{i}\Delta)(\gamma_R'-\mathrm{i}\Delta)(\gamma_R'+\gamma-\mathrm{i}\Delta)}{[(2\alpha_1-\gamma_R')^2+\Delta^2](\gamma_R'^2+\Delta^2)[(\gamma_R'+\gamma)^2+\Delta^2]}+\\\left.\frac{2\mathrm{i}\Delta}{\gamma(2\alpha_1+\gamma)[(2\alpha_1-\gamma_R')^2+\Delta^2]}\right\}+\left\{\left[2\chi^2\eta-\right.\right.\\\left.\left.\frac{4\eta\chi\chi_R\gamma_R\alpha_3\Delta}{(2\alpha_3+\gamma)[(\alpha_1-3\alpha_3-\gamma_R-\gamma)^2+\Delta^2]}\right]\times\right.\end{aligned}$$

$$\cos[\Delta\boldsymbol{k}\cdot\boldsymbol{r}-(\omega_1+\omega_3)\tau]-\frac{2\eta\chi\gamma\chi_R\gamma_R(2\alpha_1-\gamma'_R)}{(2\alpha_3+\gamma)[(2\alpha_1-\gamma'_R)^2+\Delta^2]}\times$$
$$\sin[\Delta\boldsymbol{k}\cdot\boldsymbol{r}-(\omega_1+\omega_3)\tau]\Bigg\}\exp[-(\alpha_1+\alpha_3)\,|\tau|]. \tag{3.21}$$

After that, based on phase-diffusion model, we consider the three-pulse Raman echo when the laser sources have a broadband linewidth. Substituting Eqs. (3.12), (3.15), (3.18) and (3.19) into $I(\Delta,\tau)\propto\langle\left|P^{(3)}\right|^2\rangle$, we obtain for:

(i) $\tau>0$

$$\begin{aligned}I(\Delta,\tau)\propto B_4+\frac{2\eta\chi\gamma\chi_R\gamma_R\alpha_3}{\gamma'^2_R+\Delta^2}\Bigg\{\Bigg[&\frac{\chi(\gamma'^2_R+\Delta^2)}{\gamma\chi_R\gamma_R\alpha_3}-\frac{\Delta}{\gamma\alpha_3}+\\&\frac{\mathrm{i}(\gamma'_R-\mathrm{i}\Delta)(2\alpha_3-\gamma'_R+\mathrm{i}\Delta)}{[(2\alpha_3-\gamma'_R)^2+\Delta^2][(\gamma'_R+\gamma)^2+\Delta^2]}\times\\&(\gamma'_R+\gamma-\mathrm{i}\Delta)-\frac{\mathrm{i}(\gamma'_R+\mathrm{i}\Delta)(2\alpha_3-\gamma'_R-\mathrm{i}\Delta)(\gamma'_R+\gamma+\mathrm{i}\Delta)}{[(2\alpha_3-\gamma'_R)^2+\Delta^2][(\gamma'_R+\gamma)^2+\Delta^2]}\Bigg]\times\\&\cos[\Delta\boldsymbol{k}\cdot\boldsymbol{r}-(\omega_1+\omega_3)\tau]+\Bigg[\frac{\gamma'_R}{\gamma\alpha_3}-\\&\frac{(\gamma'_R-\mathrm{i}\Delta)(2\alpha_3-\gamma'_R+\mathrm{i}\Delta)(\gamma'_R+\gamma-\mathrm{i}\Delta)}{[(2\alpha_3-\gamma'_R)^2+\Delta^2][(\gamma'_R+\gamma)^2+\Delta^2]}-\\&\frac{(\gamma'_R+\mathrm{i}\Delta)(2\alpha_3-\gamma'_R-\mathrm{i}\Delta)(\gamma'_R+\gamma+\mathrm{i}\Delta)}{[(2\alpha_3-\gamma'_R)^2+\Delta^2][(\gamma'_R+\gamma)^2+\Delta^2]}\Bigg]\times\\&\sin[\Delta\boldsymbol{k}\cdot\boldsymbol{r}-(\omega_1+\omega_3)\tau]\}\exp[-(\alpha_1+\alpha_3)\,|\tau|].\end{aligned} \tag{3.22}$$

(ii) $\tau<0$

$$\begin{aligned}I(\Delta,\tau)\propto B_4+\Bigg\{&\left[2\chi^2\eta-\frac{4\eta\chi\chi_R\gamma_R\alpha_3\Delta}{(2\alpha_3+\gamma)[(\alpha_1-3\alpha_3-\gamma_R-\gamma)^2+\Delta^2]}\right]\times\\&\cos[\Delta\boldsymbol{k}\cdot\boldsymbol{r}-(\omega_1+\omega_3)\tau]-\frac{2\eta\chi\gamma\chi_R\gamma_R(2\alpha_1-\gamma'_R)}{(2\alpha_3+\gamma)[(2\alpha_1-\gamma'_R)^2+\Delta^2]}\times\\&\sin[\Delta\boldsymbol{k}\cdot\boldsymbol{r}-(\omega_1+\omega_3)\tau]\Bigg\}\exp[-(\alpha_1+\alpha_3)\,|\tau|].\end{aligned} \tag{3.23}$$

Here,

$$B_3=\chi^2\gamma\left(\frac{1}{\gamma+2\alpha_1}+\frac{\eta^2}{2\alpha_3+\gamma}\right)+\frac{\chi_R^2\gamma_R\gamma'_R}{\gamma'^2_R+\Delta^2},$$
$$B_4=\frac{\chi^2\gamma^2(1+\eta^2)}{2\alpha_3\gamma}+\frac{\chi_R^2\gamma_R}{\alpha_1}-\frac{4\chi_R\chi\gamma\gamma_R\Delta}{\alpha_1[(\gamma'_R+\gamma)^2+\Delta^2]}.$$

The high-order decay cross-correlation terms are reasonably neglected in our above treatment. Equations (3.22) and (3.23) are analogous to Eqs. (3.20) and (3.21), respectively. Equations (3.20) and (3.22) indicate that when $\tau > 0$, the temporal behavior of the beat signal intensity reflects mainly the characteristic of the lasers. When $\tau < 0$, Eqs. (3.21) and (3.23) are mainly determined by a molecule vibrational property. Equations (3.20) – (3.23) are remarkably different from the result based on a chaotic model. Equations (3.20) – (3.23) are short of the purely auto-correlation decay terms including these factors $\exp(-2\alpha_1|\tau|), \exp(-2\alpha_3|\tau|), \exp(-2\gamma|\tau|)$, and $\exp(-2\gamma_R|\tau|)$, which are shown to be particularly insensitive to phase fluctuations of Markovian stochastic light fields. The drastic difference of the results also exists in the higher-order correlation on difference-frequency REPB when three Markovian stochastic models are employed.

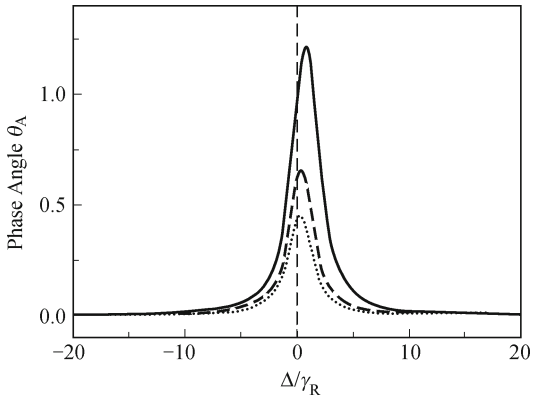

Fig. 3.4. Phase angle θ_A versus frequency detuning Δ/γ_R. The three curves represent $\chi/\chi_R = 0.3$(solid curve),$\chi/\chi_R = 0.6$ (dashed curve), and $\chi/\chi_R = 0.9$ (dotted curve).

The Raman-enhanced nonlinear polarization and the corresponding susceptibility have the relation $P_A = P_1 + P_{R1} = S(\boldsymbol{r})\chi_A$. Based on the cross-correlation terms of the Raman REPB, we can obtain the expression of the Raman-enhanced susceptibility χ_A for $\tau < 0$ different from that for $\tau > 0$ because of the interplay between the material and the light responses. We decompose the nonlinear susceptibilities χ_A into a real and an imaginary part, i.e., $\chi_A = \chi'_A + i\chi''_A$. On the other hand, χ_A can be expressed as $|\chi_A| \exp i\theta_A = |\chi_A| \cos\theta_A + i|\chi_A| \sin\theta_A$ with θ_A given by $\theta_A(\Delta_2) = \tan^{-1}(\chi''_A/\chi'_A)$. The phase dispersions θ_A are greatly modified by the color-locked noisy field with both linewidth α_i and time delay τ for $\tau < 0$, but only with α_i for $\tau > 0$. Figure 3.4 shows the phase dispersion of Raman-enhanced FWM including the influence of the color-locked noisy field for $\tau > 0$. In Fig. 3.4 the phase angle θ_A shows the absorption-like shape. When χ/χ_R increase, it becomes more symmetrical at $\Delta = 0$ and the value decreases more drastically. In the cw limit $(\alpha_i = 0), \chi_A$ for $\tau < 0$ and $\tau > 0$ become same, i.e.,

$\chi_A = \chi - \chi_R\gamma_R/(\Delta_2 + i\gamma_R)$. $\chi'_A(\Delta)$ is neither an odd nor an even function due to χ term, and $\chi''_A(\Delta)$ is an even function. So θ_A shows the asymmetric absorption-like line shape.

A direct comparison between a solid curve and a dashed curve in Fig. 3.5 indicates a drastic difference between them. In the case of $\alpha_1, \alpha_3 << \gamma, \gamma_R$, the phase-diffusion model predicts a damping oscillation of attosecond sum-frequency REPB signals around a constant value. We can understand this phenomenon as follows. The interference pattern of the $\omega_1(\omega_3)$ component of twin composite beams 1 and 2 will be in constant motion with a characteristic time constant $\alpha_1^{-1}(\alpha_3^{-1})$ when $|\tau|$ is much longer than the laser coherence time τ_c. In the case of $\alpha_1, \alpha_3 << \gamma, \gamma_R$, the relaxation time of the molecular-reorientational grating is so short that the induced gratings G1 and G2 always follow the interference pattern, and therefore the beat signal will never decay. On the other hand, the relative phase between G1 and G2 fluctuates randomly, which makes spatial interference between them impossible. In this case, the beat signal intensity is simply the summation of the signal intensity originating from G1 and G2. In contrast, the fringes of G1 and G2 are stable when $|\tau| < \tau_c$. The constructive or destructive interference between G1 and G2 enhances or reduces the beat signal and gives rise to the oscillation of the beat signal intensity as τ varies. We note that the main difference between the phase-diffusion model and the chaotic model is that amplitude fluctuation exists in the latter case. When $|\tau| < \tau_c$, the coincidence of intensity spikes of two composite beams gives an additional enhancement of beat signals for the chaotic model [24].

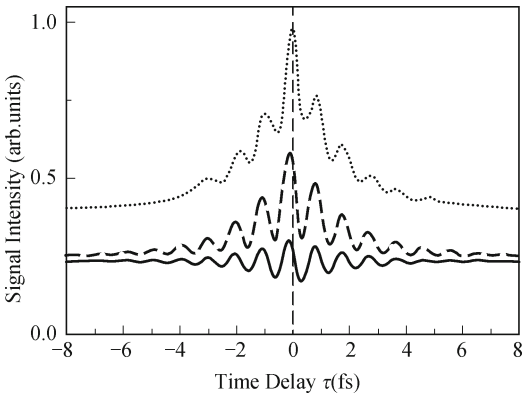

Fig. 3.5. The attosecond sum-frequency REPB signal intensity versus relative time delay. The three curves represent the chaotic field (dashed line), phase-diffusion field (solid line), and Gaussian-amplitude field (dotted line). The parameters are $\omega_1 = 3.237$ fs$^{-1}, \omega_3 = 3.358$ fs$^{-1}, r = 0, \eta_1 = \eta_2 = 1, \Delta = 0, \chi/\chi_R = 0.5, \gamma_R = 5 \times 10^{-5}$ fs$^{-1}, \gamma = 2 \times 10^{-4}$ fs$^{-1}, \Delta k = 10.58$ mm$^{-1}, \alpha_1 = 0.278$ fs^{-1}, and $\alpha_3 = 0.299$ fs^{-1}.

The Gaussian-amplitude field has a constant phase but its real amplitude undergoes Gaussian fluctuations. If the lasers have Lorentzian line shape, the

sixth- and fourth-order coherence function is [11, 12]

$$\begin{aligned}
&\langle u_i(t_1)u_i(t_2)u_i(t_3)u_i(t_4)u_i(t_5)u_i(t_6)\rangle \\
&\quad = \langle u_i(t_1)u_i(t_4)\rangle\langle u_i(t_2)u_i(t_3)u_i(t_5)u_i(t_6)\rangle + \\
&\quad\quad \langle u_i(t_1)u_i(t_5)\rangle\langle u_i(t_2)u_i(t_3)u_i(t_4)u_i(t_6)\rangle + \\
&\quad\quad \langle u_i(t_1)u_i(t_6)\rangle\langle u_i(t_2)u_i(t_3)u_i(t_4)u_i(t_5)\rangle + \\
&\quad\quad \langle u_i(t_1)u_i(t_2)\rangle\langle u_i(t_3)u_i(t_4)u_i(t_5)u_i(t_6)\rangle + \\
&\quad\quad \langle u_i(t_1)u_i(t_3)\rangle \times \langle u_i(t_2)u_i(t_4)u_i(t_5)u_i(t_6)\rangle, \qquad (3.24)
\end{aligned}$$

$$\begin{aligned}
&\langle u_i(t_1)u_i(t_2)u_i(t_3)u_i(t_4)\rangle \\
&\quad = \langle u_i(t_1)u_i(t_3)\rangle\langle u_i(t_2)u_i(t_4)\rangle + \langle u_i(t_1)u_i(t_4)\rangle \times \\
&\quad\quad \langle u_i(t_2)u_i(t_3)\rangle + \langle u_i(t_1)u_i(t_2)\rangle\langle u_i(t_3)u_i(t_4)\rangle. \qquad (3.25)
\end{aligned}$$

Based on the Gaussian-amplitude field, the high-order decay cross-correlation terms have been reasonably neglected. After substituting Eqs. (3.12), (3.24), and (3.25) into $I(\Delta,\tau) \propto \langle \left|P^{(3)}\right|^2\rangle$, we obtain as follows:

(i) $\tau > 0$

$$\begin{aligned}
I(\Delta,\tau) \propto\; & B_5 - 2[\chi^2 + \frac{\chi_R^2\gamma_R^2\gamma_R'}{(\gamma_R+\alpha_1)(\gamma_R'^2+\Delta^2)} - \frac{2\chi\chi_R\gamma_R\Delta}{\gamma_R'^2+\Delta^2}]\exp(-2\alpha_1|\tau|) + \\
& \frac{\eta^2\chi^2(11\gamma^2+14\gamma\alpha_3+4\alpha_3^2)}{(\gamma+\alpha_3)(\gamma+2\alpha_3)}\exp(-2\alpha_3|\tau|) + \frac{2\eta\chi}{\gamma+2\alpha_3}\times \\
& \left\{\left[\chi(3\gamma+2\alpha_3) + \frac{\gamma\chi_R\gamma_R\Delta}{(2\alpha_3-\gamma_R')^2+\Delta^2} + \frac{\chi_R\gamma_R\Delta(2\alpha_3-\gamma)}{\gamma_R'^2+\Delta^2}\right]\times\right. \\
& \cos[\Delta\boldsymbol{k}\cdot\boldsymbol{r} - (\omega_1+\omega_3)\tau] + \left[\frac{\chi_R\gamma_R\gamma_R'(\gamma-2\alpha_3)}{\gamma_R'^2+\Delta^2} - \right. \\
& \left.\left.\frac{\gamma\chi_R\gamma_R(2\alpha_3-\gamma_R')}{(2\alpha_3-\gamma_R')^2+\Delta^2}\right]\times\sin[\Delta\boldsymbol{k}\cdot\boldsymbol{r} - (\omega_1+\omega_3)\tau]\right\}\times \\
& \exp[-(\alpha_1+\alpha_3)|\tau|]. \qquad (3.26)
\end{aligned}$$

(ii) $\tau < 0$

$$\begin{aligned}
I(\Delta,\tau) \propto\; & B_5 + 2\left\{\chi^2 + \frac{\chi_R^2\gamma_R^2(2\alpha_1-\gamma_R')}{(\alpha_1-\gamma_R)[(2\alpha_1-\gamma_R')^2+\Delta^2]} + \frac{2\chi\chi_R\gamma_R\Delta}{(\gamma_R'-2\alpha_1)^2+\Delta^2}\right\}\times \\
& \exp(-2\alpha_1|\tau|) + 10\eta^2\chi^2\exp(-2\alpha_3|\tau|) + \frac{12\eta^2\chi^2\gamma^2\alpha_3^2}{(\gamma^2-\alpha_3^2)(\gamma^2-4\alpha_3^2)}\times \\
& \exp(-2\gamma|\tau|) + 2\chi_R^2\gamma_R^2\left\{\frac{\gamma_R'-2\gamma_R}{[(\gamma_R'-2\gamma_R)^2+\Delta^2](\alpha_1-\gamma_R)} + \right. \\
& \left.\frac{\gamma_R'}{(\gamma_R'^2+\Delta^2)(\alpha_1+\gamma_R)} - \frac{2[\gamma_R^2+\Delta^2-(\alpha_1+\alpha_3)^2]}{(\gamma_R'^2+\Delta^2)[(\gamma_R'-2\gamma_R)^2+\Delta^2]}\right\}\times
\end{aligned}$$

$$\exp(-2\gamma_R|\tau|) + 4\eta\Bigg\{\left[3\chi^2 - \frac{2\chi\chi_R\gamma_R\Delta}{(2\alpha_1-\gamma_R')^2+\Delta^2}\right]\times$$
$$\cos[\Delta\boldsymbol{k}\cdot\boldsymbol{r} - (\omega_1+\omega_3)\tau] - \frac{\chi\chi_R\gamma_R(2\alpha_1-\gamma_R')}{(2\alpha_1-\gamma_R')^2+\Delta^2}\times$$
$$\sin[\Delta\boldsymbol{k}\cdot\boldsymbol{r} - (\omega_1+\omega_3)\tau]\Bigg\}\exp[-(\alpha_1+\alpha_3)|\tau|] +$$
$$\frac{4\eta\chi\chi_R\gamma_R\alpha_3}{(2\alpha_3+\gamma)(2\alpha_3-\gamma)}\times\Bigg\{\Bigg[\frac{\Delta(2\alpha_3+\gamma)}{(\gamma_R'-\gamma-2\gamma_R)^2+\Delta^2} -$$
$$\frac{\Delta(2\alpha_3-\gamma)}{(\gamma_R'-2\gamma_R)^2+\Delta^2} + \frac{\Delta(2\alpha_3-\gamma)}{(\gamma_R'+\gamma)^2+\Delta^2} - \frac{\Delta(2\alpha_3+\gamma)}{\gamma_R'^2+\Delta^2}\Bigg]\times$$
$$\cos[\Delta\boldsymbol{k}\cdot\boldsymbol{r} - (\omega_1+\omega_3)\tau - \mathrm{i}\Delta\tau] + \Bigg[\frac{(\gamma_R'-\gamma-2\gamma_R)(2\alpha_3+\gamma)}{(\gamma_R'-\gamma-2\gamma_R)^2+\Delta^2} -$$
$$\frac{(\gamma_R'-2\gamma_R)(2\alpha_3-\gamma)}{(\gamma_R'-2\gamma_R)^2+\Delta^2} - \frac{(\gamma_R'+\gamma)(2\alpha_3-\gamma)}{(\gamma_R'+\gamma)^2+\Delta^2} + \frac{\gamma_R'(2\alpha_3+\gamma)}{\gamma_R'^2+\Delta^2}\Bigg]\times$$
$$\sin[\Delta\boldsymbol{k}\cdot\boldsymbol{r} - (\omega_1+\omega_3)\tau - \mathrm{i}\Delta\tau]\Bigg\}\exp[-(\gamma+\gamma_R)|\tau|]. \tag{3.27}$$

Here,

$$B_5 = \chi^2\gamma\left[\frac{1}{\gamma+2\alpha_1} + \frac{\eta^2(3\gamma+\alpha_3)}{(\alpha_3+\gamma)(2\alpha_3+\gamma)}\right] + \frac{\chi_R^2\gamma_R\gamma_R'}{\gamma_R'^2+\Delta^2} -$$
$$2\chi_R\chi\gamma_R\gamma\Delta\frac{(\gamma_R'+\gamma+2\alpha_1)(\gamma_R'+\gamma)+2\alpha_1\gamma_R'+\Delta^2}{(\gamma+2\alpha_1)(\gamma_R'^2+\Delta^2)[(\gamma_R'+\gamma)^2+\Delta^2]}.$$

Equations (3.26) and (3.27) generally indicate not only the characteristic of twin laser fields, but also a molecule vibrational property. Specifically, the temporal behaviors of the sum-frequency REPB intensities mainly reflect the characteristics of twin composite laser fields for $\tau > 0$, and material vibrational property for $\tau < 0$. Based on the Gaussian-amplitude field, the resonant cross-correlation between the Raman-active vibrational mode and the molecular-reorientational grating (i.e., a factor $\exp[-(\gamma+\gamma_R)|\tau|]$) are shown in Eq. (3.27) for $\tau < 0$. The τ independent constant background of the Gaussian-amplitude field is slightly larger than that of the chaotic field (i.e., $B_5 > B_1$), which originates from the amplitude fluctuation of the Markovian stochastic field.

After that, based on Gaussian-amplitude field, we consider the three-pulse Raman echo when laser sources have a broadband linewidth (noisy light). Substituting Eqs. (3.12), (3.15), (3.24), and (3.25) into $I(\Delta,\tau) \propto \langle|P^{(3)}|^2\rangle$, we obtain as follows:

(i) $\tau > 0$

$$I(\Delta,\tau) \propto B_6 + 2\left\{\chi^2 - \frac{\chi_R^2\gamma_R^2}{(\gamma_R+\alpha_1)\alpha_3} - \frac{2\chi\chi_R\gamma_R\Delta}{\gamma_R'^2+\Delta^2}\right\}\exp(-2\alpha_1|\tau|) + \left\{\frac{\eta^2\chi^2(\gamma^3+5\gamma^2\alpha_3+5\gamma\alpha_3^2+2\alpha_3^3)}{\alpha_3(\gamma+\alpha_3)(\gamma+2\alpha_3)} + \eta^2\chi^2\left[\frac{2\gamma+2\alpha_3}{\gamma+2\alpha_3} + \frac{\gamma^2}{\alpha_3(\gamma+\alpha_3)}\right]\right\}\exp(-2\alpha_3|\tau|) + \frac{2\eta\chi}{\gamma+2\alpha_3}\left\{\left[\chi(3\gamma+2\alpha_3) + \frac{\gamma\chi_R\gamma_R\Delta}{(2\alpha_3-\gamma_R')^2+\Delta^2} - \frac{\chi_R\gamma\gamma_R\Delta(5\alpha_3+2\gamma)}{\alpha_3(\gamma_R'^2+\Delta^2)}\right]\cos[\Delta\boldsymbol{k}\cdot\boldsymbol{r} - (\omega_1+\omega_3)\tau] + \left[\frac{\chi_R\gamma\gamma_R\gamma_R'(2\gamma+5\alpha_3)}{\alpha_3\gamma_R'^2+\Delta^2} - \frac{\gamma\chi_R\gamma_R(2\alpha_3-\gamma_R')}{(2\alpha_3-\gamma_R')^2+\Delta^2}\right]\times \sin[\Delta\boldsymbol{k}\cdot\boldsymbol{r} - (\omega_1+\omega_3)\tau]\right\}\exp[-(\alpha_1+\alpha_3)|\tau|]. \tag{3.28}$$

(ii) $\tau < 0$

$$I(\Delta,\tau) \propto B_6 + 2\left\{\chi^2 - \frac{\chi_R^2\gamma_R^2}{(\alpha_1-\gamma_R)\alpha_3} - \frac{2\chi\chi_R\gamma_R\Delta}{(\gamma_R'-2\alpha_1)^2+\Delta^2}\right\}\times \exp(-2\alpha_1|\tau|) + \frac{\eta^2\chi^2(10\gamma\alpha_3+10\alpha_3^2-2\gamma^2)}{\alpha_3(\alpha_3-\gamma)}\times \exp(-2\alpha_3|\tau|) + \frac{4\eta^2\chi^2\gamma^2}{\alpha_3^2-\gamma^2}\exp(-2\gamma|\tau|) + \frac{4\chi_R^2\gamma_R^2\alpha_1}{\alpha_3(\alpha_1^2-\gamma_R^2)}\times \exp(-2\gamma_R|\tau|) + 4\eta\left\{\left[\chi^2 - \frac{\chi\chi_R\gamma_R\Delta}{(2\alpha_1-\gamma_R')^2+\Delta^2}\right]\times \cos[\Delta\boldsymbol{k}\cdot\boldsymbol{r} - (\omega_1+\omega_3)\tau] - \frac{\chi\chi_R\gamma_R(2\alpha_1-\gamma_R')}{(2\alpha_1-\gamma_R')^2+\Delta^2}\times \sin[\Delta\boldsymbol{k}\cdot\boldsymbol{r} - (\omega_1+\omega_3)\tau]\right\}\exp[-(\alpha_1+\alpha_3)|\tau|]. \tag{3.29}$$

Here,

$$B_6 = \chi^2\gamma^2\left[\frac{1}{2\alpha_1\gamma} + \frac{\eta^2(3\gamma+\alpha_3)}{2\alpha_3\gamma(2\alpha_3+\gamma)} + \frac{\eta^2}{\alpha_3(\alpha_3+\gamma)}\right] + \frac{\chi_R^2\gamma_R}{\alpha_1} - \frac{4\chi_R\gamma\chi\gamma_R\Delta}{\alpha_1[(\gamma_R'+\gamma)^2+\Delta^2]}.$$

Equations (3.28) and (3.29) are analogous to Eqs. (3.26) and (3.27), respectively.

The attosecond sum-frequency REPB indicates that beat signal oscillates not only temporally but also spatially along the direction $\Delta \boldsymbol{k}$, which is almost perpendicular to the propagation direction of the beat signal. Three normalized three-dimensional interferograms of the signal intensity $I(\tau, \Delta)$ versus time delay τ and frequency detuning Δ, $I(\tau, r)$ versus time delay τ and transverse position r, and $I(\Delta, r)$ versus frequency detuning Δ and transverse position r, respectively, have a smaller constant background caused by the intensity fluctuation of the narrowband (0.01 nm) chaotic field in Fig. 3.6. At zero relative time delay ($\tau = 0$), twin beams originating from the same source enjoy perfect overlap at the sample of their corresponding noise patterns in Figs. 3.6(a) and (b).

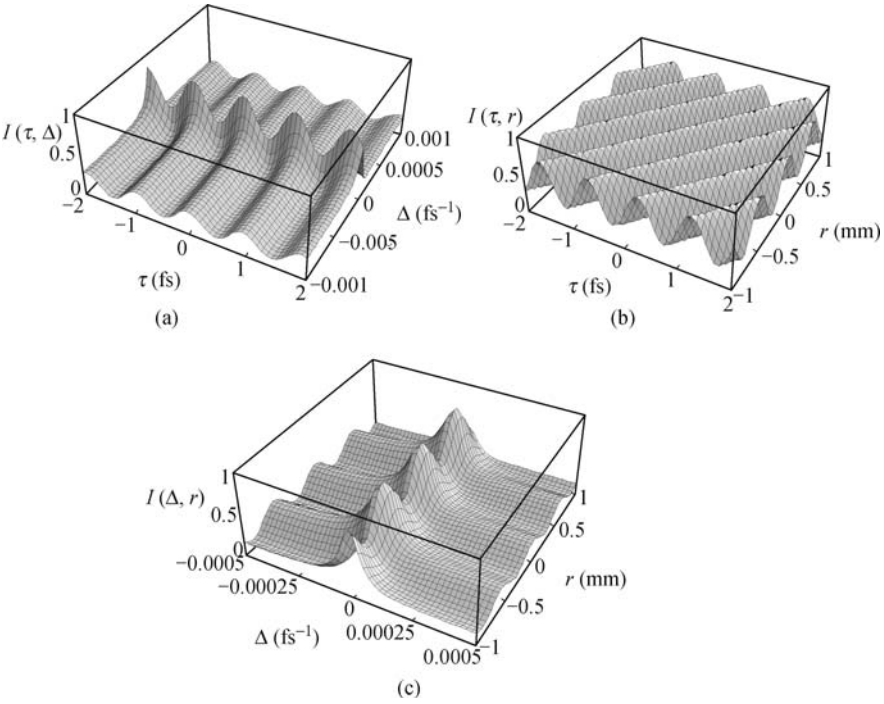

Fig. 3.6. Three normalized three-dimensional interferograms of the signal intensity $I(\tau, \Delta)$ versus time delay τ and frequency detuning Δ, $I(\tau, r)$ versus time delay τ and transverse position r and $I(\Delta, r)$ versus frequency detuning Δ and transverse position r, respectively. The parameters are $\omega_1 = 3.237$ fs^{-1}, $\omega_3 = 3.358$ fs^{-1}, $\alpha_1 = 2.78 \times 10^{-5}$ fs^{-1}, $\alpha_3 = 2.99 \times 10^{-5}$ fs^{-1}, $\chi/\chi_R = 0.5$, $\gamma_R = 5 \times 10^{-5}$ fs^{-1}, $\gamma = 2 \times 10^{-4}$ fs^{-1}, $\eta_1 = \eta_2 = 1$, $\Delta k = 10.58$ mm^{-1}; while $r = 0$ for (a), $\Delta = 0$ for (b), and $\tau = 0$ for (c).

This gives maximum interferometric contrast. As $|\tau|$ is increased, the interferometric contrast diminishes on the time scale that reflects material

memory, usually much longer than the correlation time of the noisy light. The pure auto-correlation decay terms of the Raman-active vibrational mode, the molecular-reorientational grating, and laser fields for the attosecond sum-frequency REPB originated from the amplitude fluctuation of Markovian stochastic fields.

It is important to note that these three types of Markovian stochastic fields can have the same spectral density and thus the same second-order coherence function. The fundamental differences in the statistics of these fields are manifest only in higher-order coherence functions [21, 22]. The term "higher order" refers to all orders larger than the second. In this section, different stochastic models of laser fields only affect the sixth- and fourth-order coherence functions in frequency- and time-domains. At a fixed large time delay (i.e., $\tau = 500$ fs), Fig. 3.7 give RENFWM spectrums for three Markovian stochastic fields using laser linewidths 0.01 nm and 0.1 nm, respectively. Comparing to the narrowband case [Fig. 3.7 (a)], Fig. 3.7 (b) shows a much larger nonresonant Δ-independent background. On the other hand, Fig. 3.5 presents the attosecond sum-frequency REPB versus relative time delay with fixed frequency detuning (i.e., $\Delta = 0$). Due to the interference of $\cos[\Delta\boldsymbol{k}\cdot\boldsymbol{r} - (\omega_1+\omega_3)\tau]$ and $\sin[\Delta\boldsymbol{k}\cdot\boldsymbol{r} - (\omega_1+\omega_3)\tau]$ factors of Eqs. 3.13, 3.14, 3.16, 3.17 (for chaotic field), Eqs. 3.20 – 3.23 (for phase-diffusion field), and Eqs. 3.26 – 3.29 (for Gaussian-amplitude field), the temporal behavior of the attosecond sum-frequency REPB is asymmetric with the maximum of the beat signal shifted from $\tau = 0$ (Fig. 3.5). Whereas in the limit of $\Delta \to \infty$, the term with $\sin[\Delta\boldsymbol{k}\cdot\boldsymbol{r} - (\omega_1+\omega_3)\tau]$ factor will disappear, then the beat signal exhibits a symmetric behavior. The peak-to-background contrast ratio of the chaotic field is larger than that of the Gaussian-amplitude field or the phase-diffusion field in Figs. 3.5 and 3.28. Furthermore, the contrast ratio of the phase-diffusion field is slightly larger than that of the Gaussian-amplitude field. The physical explanation for this is that the signal contrast

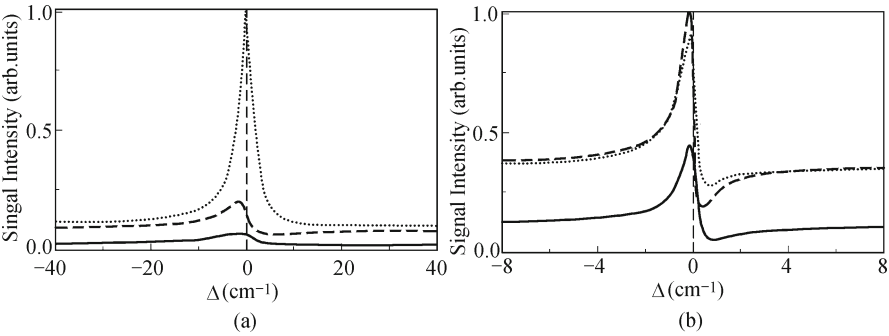

Fig. 3.7. RENFWM spectrum with fixed time delay. The three curves represent the chaotic field (dashed line), phase-diffusion field (solid line), and Gaussian-amplitude field (dotted line). The parameters are $\chi/\chi_R = 0.5, \gamma_R = \gamma = 5\times10^{-5}$ fs$^{-1}, \tau = 500$ fs; while $\alpha_1 = 2.78\times10^{-5}$ fs$^{-1}, \gamma_R' = 1.077\times10^{-4}$ fs^{-1} for (a), and $\alpha_1 = 2.78\times10^{-4}$ fs$^{-1}, \gamma_R' = 6.27\times10^{-4}$ fs^{-1} for (b).

ratio is equally sensitive to the amplitude and phase fluctuations of Markovian stochastic fields. The polarization beat signal is shown to be particularly sensitive to statistical properties of Markovian stochastic light fields with arbitrary bandwidth. The Δ- or τ-independent constant background of the beat signal for Gaussian-amplitude field or chaotic field is much larger than that of the signal for a phase-diffusion field in Figs. 3.5 and 3.7. The physical explanation for this is that the Gaussian-amplitude field undergoes stronger intensity fluctuations than a chaotic field. On the other hand, the intensity (amplitude) fluctuations of Gaussian-amplitude fields or chaotic fields are always much larger than the pure phase fluctuations of phase-diffusion fields.

Next, we discuss the chromophore $P^{(3)}$ difference between the sum-frequency REPB with a phase-conjugation geometry and the sum-frequency ultrafast modulation spectroscopy (UMS) [15] with a self-diffraction geometry from a physical viewpoint. The frequencies and wave vectors of sum-frequency UMS signals are $\omega_{s_1} = 2\omega_1 - \omega_1, \omega_{s_2} = 2\omega_2 - \omega_2$ and $\boldsymbol{k}_{s_1} = 2\boldsymbol{k}_1 - \boldsymbol{k}_1', \boldsymbol{k}_{s_2} = 2\boldsymbol{k}_2' - \boldsymbol{k}_2$, respectively, which means that a photon is absorbed from each of the two mutually correlated fluctuating pump beams. On the other hand, the frequencies and wave vectors of the sum-frequency REPB signal are $\omega_{s_1} = \omega_1 - \omega_1 + \omega_3, \omega_{s_2} = \omega_3 - \omega_3 + \omega_3$ and $\boldsymbol{k}_{s_1} = \boldsymbol{k}_1 - \boldsymbol{k}_1' + \boldsymbol{k}_3, \boldsymbol{k}_{s_2} = \boldsymbol{k}_2' - \boldsymbol{k}_2 + \boldsymbol{k}_3$, respectively [Fig. 3.1(c)], therefore photons are absorbed from and emitted to the mutually correlated fluctuating twin beams 1 and 2, respectively. This difference between the REPB and the UMS has profound influence on field-correlation effects. We note that the role of beams 1 and 2 are interchangeable in the UMS, this interchangeable feature also makes the second-order coherence function theory failure in the UMS. Due to $\langle u(t_1)u(t_2)\rangle = 0$, the absolute square of the stochastic average of the polarization $|\langle P^{(3)}\rangle|^2$ cannot be used to describe the temporal behavior of the sum-frequency UMS [20]. Our higher-order correlation (intensity correlation) treatment also is of vital importance in the sum-frequency UMS. Moreover, because of $\langle u_i(t)\rangle = 0$ and $\langle u_i^*(t)\rangle = 0$, the absolute square of the stochastic average of the polarization $|\langle P^{(3)}\rangle|^2$, which involves second-order coherence function of $u_i(t)$, cannot be used to describe the temporal behavior of the attosecond sum-frequency REPB. The sixth-order correlation theory $\langle |P^{(3)}|^2\rangle$ reduces to the second-order correlation theory $|\langle P^{(3)}\rangle|^2$ in the case that the laser pulse width is much longer than the laser coherence time. The second-order coherence function theory is valid when we are only interested in the τ-dependent part of beating signals [20]. Therefore, the sixth-order coherence function theory is of vital importance in the sum-frequency REPB. The application of higher-order results to the difference-frequency REPB experiment yielded a better fit to data than an expression involving only second-order coherence. Apparently, the nature of Markovian fields has a more drastic effect on the outcome of the experiment than the underlying molecular nonlinearity. Since real laser fields are unlikely to behave like the pure three field classes, a complicated superposition of various types of responses is to be expected. In a Kerr medium carbon

disulfide with the 655.7 cm^{-1} vibrational mode, the sum-frequency REPB experiment is now underway in our group (The key question is the design of a dispersion-compensated Michelson interferometer delay line in attosecond scale).

3.1.3 Heterodyne Detection of Difference-frequency REPB

Since optical fields oscillate too quickly for direct detection, they must be measured "in quadrature"-as photons. There are two ways to achieve quadrature. One is homodyne detection in which the new polarizations is measured at its quadrature, $(P_1+P_{R1})[(P_1)^*+(P_{R1})^*]$. These signals must be proportional to $\left|\chi^{(3)}\right|^2$. Thus, $I_{\mathrm{hom}\,odyne} \propto \left|\chi^{(3)}\right|^2$ and all phase information in $\chi^{(3)}$ is lost. The second way to achieve quadrature is to introduce another polarization, P_2', (called a reference signal) designed in frequency and wave vector to conjugate (go into quadrature) in its complex representation with the new polarization of interest. Thus, in the heterodyne case, the signal photons are derived from $(P_1+P_2'+P_{R1})[(P_1)^*+(P_2')^*+(P_{R1})^*]$ or $I_{heterodyne} \propto \chi^{(3)}$ (the signal is linear rather than quadratic). In heterodyne detected $(3+1)$ wave mixing, phase information is retained and one can take a full measure of the complex susceptibility, including its phase. The phase of the complex induced polarization, $P'^{(3)}$, determines how its energy will partition between Class I (the absorbed or emitted active spectroscopy) and Class II (the passive spectroscopy with a new launched field) spectroscopies [3].

We demonstrated a phase-sensitive method for studying the RENFWM. The reference signal is another FWM signal, which propagates along the same optical path as the RENFWM signal. This method is used for studying the phase dispersion of the third-order susceptibility $\chi^{(3)}$ and for the optical heterodyne detection of the RENFWM signal. Based on three types of models described above, subtle Markovian field correlation effects will be investigated in the heterodyne detection of the femtosecond difference-frequency REPB. Compare with the above homodyne detection scheme of the attosecond sum-frequency REPB, the composite twin beams 1 and 2 for the heterodyne detection scheme of the femtosecond difference-frequency REPB also originate from the same color locking noisy lights. The complex electric fields of beam 1, E_{p1}', and beam 2, E_{p2}', instead of E_{p1} and E_{p2}, respectively, can be written as:

$$\begin{aligned} E_{p1}' &= E_1(\boldsymbol{r},t)+F_2(\boldsymbol{r},t) = A_1(\boldsymbol{r},t)\exp(-\mathrm{i}\omega_1 t)+B_2(\boldsymbol{r},t)\exp(-\mathrm{i}\omega_2 t) \\ &= \varepsilon_1 u_1(t)\exp[\mathrm{i}(\boldsymbol{k}_1\cdot\boldsymbol{r}-\omega_1 t)]+\varepsilon_2 u_2(t)\exp[\mathrm{i}(\boldsymbol{k}_2\cdot\boldsymbol{r}-\omega_2 t)], \end{aligned} \tag{3.30}$$

$$\begin{aligned} E_{P2}' &= E_1'(\boldsymbol{r},t)+F_2'(\boldsymbol{r},t) = A_1'(\boldsymbol{r},t)\exp(-\mathrm{i}\omega_1 t)+B_2'(\boldsymbol{r},t)\exp(-\mathrm{i}\omega_2 t) \\ &= \varepsilon_1' u_1(t-\tau)\exp[\mathrm{i}(\boldsymbol{k}_1'\cdot\boldsymbol{r}-\omega_1 t+\omega_1\tau)]+\varepsilon_2' u_2(t-\tau)\times \\ &\quad \exp[\mathrm{i}(\boldsymbol{k}_2'\cdot\boldsymbol{r}-\omega_2 t+\omega_2\tau)]. \end{aligned} \tag{3.31}$$

Compared with beam 1 (E'_{p1}) case, the frequency components ω_1 and ω_2 of beam 2 (E'_{p2}) are relatively delayed by an interferometric time τ in the heterodyne detection. Specifically, there is a $\omega_2 = \omega_3$ in the above homodyne detection scheme of the attosecond sum-frequency REPB.

The order parameter Q'_2 of nonresonant static grating induced by ω_2 frequency components of beams 1 and 2 satisfy the following equation

$$\frac{\mathrm{d}Q'_2}{\mathrm{d}t} + \gamma Q'_2 = \chi\gamma F_2(\boldsymbol{r}, t)[F'_2(\boldsymbol{r}, t)]^*. \tag{3.32}$$

The induced third-order nonlinear polarization P'_2 of ω_2 component which is responsible for the FWM signal is

$$\begin{aligned} P'_2 &= Q'_2(\boldsymbol{r}, t)E_3(\boldsymbol{r}, t) \\ &= \chi\gamma\varepsilon_2(\varepsilon'_2)^*\varepsilon_3 \exp\{\mathrm{i}[(\boldsymbol{k}_2 - \boldsymbol{k}'_2 + \boldsymbol{k}_3)\cdot\boldsymbol{r} - \omega_3 t - \omega_2\tau]\} \times \\ &\quad \int_0^\infty u_2(t-t')u_2^*(t-t'-\tau)u_3(t)\exp(-\gamma t')\mathrm{d}t'. \end{aligned} \tag{3.33}$$

Polarization beat is based on the interference at the detector between FWM signals, which originate from the macroscopic polarizations excited simultaneously in the sample. It prefers that all the polarizations have the same frequency. The frequencies of $u_1(t), P'_2$, and P_{R1} are ω_3, while P_{R2} and P_{R3} have frequencies $\omega_1 - \omega_2 + \omega_3$ and $\omega_2 - \omega_1 + \omega_3$, respectively. Furthermore, due to the phase mismatching, FWM signals from P_{R2} and P_{R3} are usually much smaller than that from P_1, P'_2, and P_{R1}. So we have the total third-order polarization $P'^{(3)} = P_1 + P'_2 + P_{R1}$. The third-order nonlinear polarizations $P_1 + P_{R1}$ and P'_2 correspond to RENFWM process and ω_2 NDFWM process which have wave vectors $\boldsymbol{k}_1 - \boldsymbol{k}'_1 + \boldsymbol{k}_3$ and $\boldsymbol{k}_2 - \boldsymbol{k}'_2 + \boldsymbol{k}_3$, respectively. Difference-frequency REPB signals are proportional to the average of the absolute square of $P^{'(3)}$ over the random variable of the stochastic process, so that the signal intensity $I(\Delta, \tau) \propto |P^{'(3)}(P^{'(3)})^*\rangle = \langle(P_1 + P'_2 + P_3)[(P_1)^* + (P'_2)^* + (P_{R1})^*]\rangle$ contains $3 \times 3 = 9$ different terms in the fourth- and second-order coherence function of $u_1(t)$ in phase-conjugation geometry, where $\langle P_1 P_1^*\rangle, \langle P'_2 P'^*_2\rangle, \langle P'_{R1} P'^*_{R1}\rangle, \langle P_1 P'^*_{R1}\rangle$, and $\langle P_1^* P_{R1}\rangle$ are include the $u_1(t)$ or $u_2(t)$ fourth-order coherence functions; while $\langle P_1 P_2^*\rangle, \langle P_1^* P'_2\rangle, \langle P'_2 P^*_{R1}\rangle$, and $\langle P'^*_2 P_{R1}\rangle$ are include the $u_i(t)$ second-order coherence functions. In general, the REPB of heterodyne detection (at the intensity level) can be viewed as built of the sum of three contributions

$$I(\Delta, \tau) \propto I_{P'_2} + I_{P_1, P_{R1}} + I_{P'_2, P_1, P_{R1}},$$

where $I_{P'_2} = \langle P'_2 P'^*_2\rangle, I_{P_1, P_{R1}} = \langle P_1 P_1^*\rangle + \langle P_{R1} P^*_{R1}\rangle + \langle P_1 P^*_{R1}\rangle + \langle P_1^* P_{R1}\rangle$, and $I_{P'_2, P_1, P_{R1}} = \langle P_1 P'^*_2\rangle + \langle P_1^* P'_2\rangle + \langle P'_2 P^*_{R1}\rangle + \langle P'^*_2 P_{R1}\rangle$: (i) the nonresonant auto-correlation term $I_{P'_2}$ of ω_2 molecular-reorientational grating, which include $u_2(t)$ fourth-order and $u_3(t)$ second-order Markovian stochastic correlation functions; (ii) the autocorrelation term $I_{P1, P_{R1}}$ (i.e., RENFWM) of ω_1

nonresonant molecular-reorientational grating and $\omega_3 - \omega_1 \approx \omega_R$ Raman resonant vibrational mode, which include $u_1(t)$ fourth-order and $u_3(t)$ second-order Markovian stochastic correlation functions; (iii) the cross-correlation term $I_{P_2',P_1,P_{R1}}$ between $I_{P_2'}$ and $I_{P_1,P_{R1}}$, which include $u_1(t), u_2(t)$ and $u_3(t)$ second-order Markovian stochastic correlation functions.

Based on the chaotic field, we first have difference-frequency REPB signals in heterodyne detection, for:

(i) $\tau > 0$

$$
\begin{aligned}
I(\Delta,\tau) \propto\; & I_{P_2'} + \frac{\chi^2\gamma}{\gamma+2\alpha_1} + \frac{\chi_R^2\gamma_R\gamma_R'}{\gamma_R'^2+\Delta^2} - \\
& \frac{2\chi\gamma\chi_R\gamma_R\Delta(\Delta^2+2\gamma\alpha_1+\gamma^2+4\gamma_R'\alpha_1+2\gamma_R'\gamma+\gamma_R'^2)}{(\gamma+2\alpha_1)(\gamma_R'^2+\Delta^2)[(\gamma_R'+\gamma)^2+\Delta^2]} + \\
& \left[\chi^2 + \frac{\chi_R^2\gamma_R^2\gamma_R' - 2\chi\chi_R\gamma_R\Delta(\gamma_R+\alpha_1)}{(\gamma_R+\alpha_1)(\gamma_R'^2+\Delta^2)}\right]\exp(-2\alpha_1|\tau|) + \\
& 2\left|\chi^{(3)}\right|\chi\eta\exp[-(\alpha_1+\alpha_2)|\tau|]\times \\
& \cos[-\Delta\boldsymbol{k}\cdot\boldsymbol{r} + (\omega_1-\omega_2)\tau - \theta_R]. \qquad (3.34)
\end{aligned}
$$

(ii) $\tau < 0$

$$
\begin{aligned}
& I(\Delta,\tau) \\
\propto\; & I_{P_2'} + \frac{\chi^2\gamma}{\gamma+2\alpha_1} + \frac{\chi_R^2\gamma_R\gamma_R'}{\gamma_R'^2+\Delta^2} - \\
& \frac{2\chi\gamma\chi_R\gamma_R\Delta(\Delta^2+2\gamma\alpha_1+\gamma^2+4\gamma_R'\alpha_1+2\gamma_R'\gamma+\gamma_R'^2)}{(\gamma+2\alpha_1)(\gamma_R'^2+\Delta^2)[(\gamma_R'+\gamma)^2+\Delta^2]} + \\
& \left[\chi^2 + \frac{\chi_R^2\gamma_R^2\gamma_R' - 2\chi\chi_R\gamma_R\Delta(\gamma_R+\alpha_1)}{(\gamma_R+\alpha_1)(\gamma_R'^2+\Delta^2)}\right]\exp(-2\alpha_1|\tau|) + \\
& 4\chi_R\alpha_1\left\{\chi\gamma_R' \times \frac{2\gamma_R\Delta\cos(\Delta|\tau|) + [(\alpha_1+\alpha_3)^2 - \gamma_R^2 + \Delta^2]\sin(\Delta|\tau|)}{(\gamma_R'^2+\Delta^2)[(\alpha_1+\alpha_3-\gamma_R)^2+\Delta^2]} + \right. \\
& \chi_R\gamma_R^2\Delta\left[\frac{[\gamma_R^2 - \alpha_1^2 + \Delta^2 - 2(\gamma_R+\alpha_1)\alpha_3 - 3\alpha_3^2]\sin(\Delta|\tau|)}{(\gamma_R'^2+\Delta^2)[(\gamma_R-\alpha_1+\alpha_3)^2+\Delta^2][(\gamma_R-\alpha_1-\alpha_3)^2+\Delta^2]} - \right. \\
& \left.\left.\frac{[\gamma_R'^2 + (\gamma_R-\alpha_1+\alpha_3)(\gamma_R-\alpha_1-\alpha_3) + \gamma_R'\Delta]\cos(\Delta|\tau|)}{(\gamma_R'^2+\Delta^2)[(\gamma_R-\alpha_1+\alpha_3)^2+\Delta^2][(\gamma_R-\alpha_1-\alpha_3)^2+\Delta^2]}\right]\right\}\times \\
& \exp(-\gamma_R'|\tau|) + A\sin[-\Delta\boldsymbol{k}\cdot\boldsymbol{r} + (\omega_1-\omega_2)\tau + \Delta|\tau|] + \\
& 2\left|\chi^{(3)}\right|\chi\eta\exp[-(\alpha_1+\alpha_2)|\tau|]\times\cos[-\Delta\boldsymbol{k}\cdot\boldsymbol{r} + (\omega_1-\omega_2)\tau - \theta_R]. \qquad (3.35)
\end{aligned}
$$

Here,

$$
A = \exp\left[-(\alpha_2+\alpha_3+\gamma_R)|\tau|\right]\frac{2\chi_R\chi\gamma\eta\gamma_R[\alpha_1^2 - (\alpha_3+\gamma_R)^2 - \Delta^2]}{4\Delta^2(\alpha_3+\gamma_R)^2 + [\alpha_1^2 - (\alpha_3+\gamma_R)^2 + \Delta^2]^2},
$$

$$I_{P_2'} = (\chi\gamma\eta)^2 \left[\frac{1}{\gamma(\gamma + 2\alpha_2)} + \frac{\exp(-2\alpha_2 |\tau|)}{\gamma^2}\right]$$

for the chaotic field. The third-order susceptibility for the RENFWM consists of a Raman-resonant term and a nonresonant term that originates from the ω_1 molecular-reorientational grating, i.e.,

$$\chi^{(3)} = \chi - \frac{\chi_R \gamma_R}{\Delta + i\gamma_R'}.$$

We express $\chi^{(3)}$ as $|\chi^{(3)}| \exp(\mathrm{i}\theta_R)$, with θ_R given by

$$\theta_R = \tan^{-1}\left[\frac{\chi_R \gamma_R \gamma_R'}{\chi(\gamma_R'^2 + \Delta^2 - \chi_R \Delta \gamma_R')}\right].$$

We decompose the nonlinear susceptibility $\chi^{(3)}$ into a real and an imaginary part, i.e.,

$$\chi^{(3)} = \chi' + i\chi'',$$

with $\chi' = \chi - \dfrac{\chi_R \gamma_R \Delta}{\Delta^2 + \gamma_R'^2}, \chi'' = \chi_R - \dfrac{\gamma_R' \gamma_R}{\Delta^2 + \gamma_R'^2}$.

Equations (3.34) and (3.35) indicate that the difference-frequency REPB signal of heterodyne detection is modulated with a frequency $\omega_1 - \omega_2$ as τ is varied. The phase of the signal oscillation depends on the phase θ_R of the nonlinear susceptibility. Two-color difference-frequency REPB signals can also be employed for optical heterodyne detection to yield the real and the imaginary parts of the nonlinear susceptibility. We assume that $I_{P_2'} >> I_{P_1,P_{R1}}$ at intensity level ($\eta\chi >> |\chi^{(3)}|$ at field level), so the reference signal that originates from the ω_2 frequency component of twin beams 1 and 2 is much larger than the RENFWM signal that originates from the ω_1 frequency component of twin beams 1 and 2. In this case we first have, from Eq (3.34),

$$I(\tau > 0) \propto I_{P_2'} + 2\left|\chi^{(3)}\right| \chi\eta \exp[-(\alpha_1 + \alpha_2)|\tau|] \cos[-\Delta\boldsymbol{k}\cdot\boldsymbol{r} + (\omega_1 - \omega_2)\tau - \theta_R].$$

If we adjust the time delay τ and $\boldsymbol{r}$ such that $-\Delta\boldsymbol{k}\cdot\boldsymbol{r} + (\omega_1 - \omega_2)\tau = 2n\pi$, then

$$I(\tau > 0) \propto I_{P_2'}/\chi + 2\eta \exp[-(\alpha_1 + \alpha_2)|\tau|]\chi'.$$

However, if $-\Delta\boldsymbol{k}\cdot\boldsymbol{r} + (\omega_1 - \omega_2)\tau = (2n - 1/2)\pi$, we have

$$I(\tau > 0) \propto I_{P_2'}/\chi + 2\eta \exp[-(\alpha_1 + \alpha_2)|\tau|]\chi''.$$

Secondly, we have from Eq (3.35),

$$I(\tau < 0) \propto I_{P_2'} + A\sin[-\Delta\boldsymbol{k}\cdot\boldsymbol{r} + (\omega_1 - \omega_2)\tau + \Delta|\tau|] + 2\left|\chi^{(3)}\right| \chi\eta \exp[-(\alpha_1 + \alpha_2)|\tau|] \cos[-\Delta\boldsymbol{k}\cdot\boldsymbol{r} + (\omega_1 - \omega_2)\tau - \theta_R].$$

If we adjust the time delay τ and $\boldsymbol{r}$ (if $\Delta|\tau| \approx 0$) such that $-\Delta k \cdot r + (\omega_1 - \omega_2) = 2n\pi$, then $I(\tau < 0) \propto I_{p_2}/\chi + 2\eta \exp[-(\alpha_1 + \alpha_2)|\tau|]\chi'$. However, if $-\Delta k \cdot r + (\omega_1 - \omega_2)\tau = (2n - 1/2)\pi$, we have $I(\tau < 0) \propto I_{P_2'}/\chi + A/\chi + 2\eta \exp[-(\alpha_1 + \alpha_2)\,|\tau|]\chi''$. In summary, by changing the time delay τ between twin beams 1 and 2 (If $\boldsymbol{r} = 0$) we can obtain the real [the dashed line of Fig. 3.8 (a)] and imaginary [the dashed line of Fig. 3.8 (b)] parts of $\chi^{(3)}$.

Based on the phase-diffusion field, we then have difference-frequency REPB signals in heterodyne detection, for:

(i) $\tau > 0$

$$
\begin{aligned}
I(\Delta,\tau) \propto\; & I_{P_2'} + \frac{\chi^2\gamma}{\gamma + 2\alpha_1} + \frac{\chi_R\gamma_R(\gamma_R'\chi_R - 2\Delta\chi)}{\gamma_R'^2 + \Delta^2} + \\
& \frac{4\chi\chi_R\gamma_R\Delta\alpha_1}{(\gamma + 2\alpha_1)[(\gamma_R' + \gamma)^2 + \Delta^2]} + \\
& \left\{ \frac{2\alpha_1\chi^2}{2\alpha_1 + \gamma} - \frac{4\chi\chi_R\gamma_R\Delta\alpha_1}{(2\alpha_1 + \gamma)[(\gamma_R' + \gamma)^2 + \Delta^2]} \right\} \times \\
& \exp[-(2\alpha_1 + \gamma)\,|\tau|] + 2\left|\chi^{(3)}\right| \chi\eta \exp[-(\alpha_1 + \alpha_2)\,|\tau|] \times \\
& \cos[-\Delta\boldsymbol{k} \cdot \boldsymbol{r} + (\omega_1 - \omega_2)\tau - \theta_R]. \qquad (3.36)
\end{aligned}
$$

(ii) $\tau < 0$

$$
\begin{aligned}
& I(\Delta,\tau) \\
& \propto I_{P_2'} + \frac{\chi^2\gamma}{\gamma + 2\alpha_1} + \frac{\chi_R^2\gamma_R\gamma_R'}{\gamma_R'^2 + \Delta^2} + \frac{4\chi\chi_R\gamma_R\Delta\alpha_1}{(\gamma + 2\alpha_1)[(2\alpha_1 - \gamma_R')^2 + \Delta^2][(\gamma_R' + \gamma)^2 + \Delta^2]} \times \\
& \frac{1}{(\gamma_R'^2 + \Delta^2)}[5\gamma_R'^4 + 8\gamma_R'^3\gamma - 2\gamma_R'\gamma(\gamma^2 - 4\Delta^2) + 4\alpha_1^2(2\gamma_R' + \gamma)^2 + \Delta^4 - \\
& 10\gamma_R'^2\Delta^2 - 2\alpha_1(4\gamma_R'^3 - \gamma^3 - 2\gamma\Delta^2 + 6\gamma\gamma_R'^2) + 2\gamma_R'^2(\gamma^2 - 2\Delta^2)] + \\
& \left\{ \frac{2\alpha_1\chi^2}{2\alpha_1 + \gamma} - \frac{4\chi\chi_R\gamma_R\Delta\alpha_1}{(2\alpha_1 + \gamma)[(2\alpha_1 - \gamma_R')^2 + \Delta^2]} \right\} \times \\
& \exp[-(2\alpha_1 + \gamma)\,|\tau|] + 4\chi\chi_R\gamma_R\alpha_1 \left[\frac{\gamma_R'(2\alpha_1 + \gamma_R' + \gamma_m)\sin(\Delta\,|\tau|)}{(\gamma_R'^2 + \Delta^2)[(2\alpha_1 + \gamma_R' + \gamma_m)^2 + \Delta^2]} + \right. \\
& \left. \frac{\Delta(2\alpha_1 + 2\gamma_R' + \gamma_m)\cos(\Delta\,|\tau|)}{(\gamma_R'^2 + \Delta^2)[(2\alpha_1 + \gamma_R' + \gamma_m)^2 + \Delta^2]} \right] \exp(-\gamma_R'\,|\tau|) + \\
& A\sin[-\Delta\boldsymbol{k} \cdot \boldsymbol{r} + (\omega_1 - \omega_2)\tau + \Delta\,|\tau|] + \\
& 2\left|\chi^{(3)}\right| \chi\eta \exp[-(\alpha_1 + \alpha_2)\,|\tau|] \cos[-\Delta\boldsymbol{k} \cdot \boldsymbol{r} + (\omega_1 - \omega_2)\tau - \theta_R]. \qquad (3.37)
\end{aligned}
$$

Here,

$$
I_{P_2'} = (\chi\gamma\eta)^2 \left\{ \frac{1}{\gamma(\gamma + 2\alpha_2)} - \frac{2\alpha_2^2}{\gamma^2(4\alpha_2^2 - \gamma^2)} \exp(-2\gamma\,|\tau|) + \right.
$$

$$\left.\frac{6\alpha_2^2-\alpha_2\gamma}{\gamma^2(4\alpha_2^2-\gamma^2)}\exp[-(2\alpha_2+\gamma)\,|\tau|]\right\}$$

for the phase-diffusion field. The high-order decay terms are reasonably neglected in $\tau<0$ case. If $I_{P_2'}>>I_{P_1,P_{R1}}$, we have

$$I(\tau>0)\propto I_{P_2'}+2\left|\chi^{(3)}\right|\chi\eta\exp[-(\alpha_1+\alpha_2)\,|\tau|]\cos[-\Delta\boldsymbol{k}\cdot\boldsymbol{r}+(\omega_1-\omega_2)\tau-\theta_R]$$

from Eq. (3.36), and

$$I(\tau<0)\propto I_{P_2'}+A\sin[-\Delta\boldsymbol{k}\cdot\boldsymbol{r}+(\omega_1-\omega_2)\tau+\Delta\,|\tau|]+ 2\left|\chi^{(3)}\right|\chi\eta\exp[-(\alpha_1+\alpha_2)\,|\tau|]\cos[-\Delta\boldsymbol{k}\cdot\boldsymbol{r}+(\omega_1-\omega_2)\tau-\theta_R]$$

from Eq. (3.37), respectively. Except the reference signal $I_{P_2'}$, the heterodyne detection signal is the same as that of the heterodyne detected chaotic field case. By changing the time delay τ between twin beams 1 and 2 (If $\boldsymbol{r}=0$) we can obtain the real [the solid line of Fig. 3.8 (a)] and imaginary [the solid line of Fig. 3.7 (b)] parts of $\chi^{(3)}$ for the phase-diffusion field. Due to the absence of the amplitude fluctuation, the solid curves of Fig. 3.7 have the smallest Δ-independent constant background.

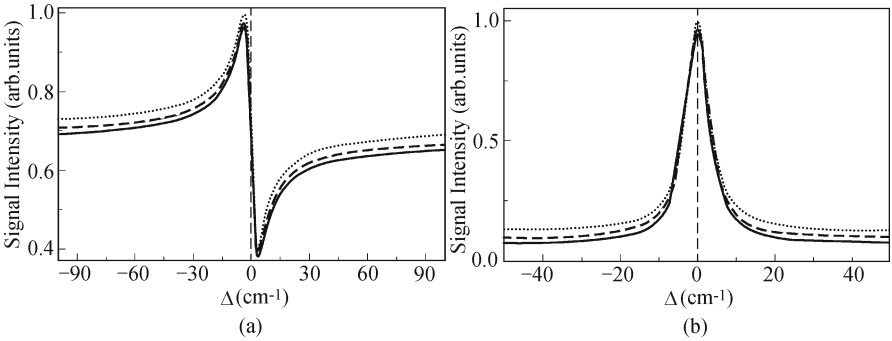

Fig. 3.8. The heterodyne detection spectra of the difference-frequency REPB with (a) $-\Delta\boldsymbol{k}\cdot\boldsymbol{r}+(\omega_1-\omega_2)\tau=0$ and (b) $-\Delta\boldsymbol{k}\cdot\boldsymbol{r}+(\omega_1-\omega_2)\tau=-\pi/2$. Theoretical curves represent the chaotic field (dashed line), phase-diffusion field (solid line), and Gaussian-amplitude field (dotted line) with parameters $\gamma_R'=1.077\times10^{-4}$ fs^{-1}, $\alpha_1=2.78\times10^{-5}$ fs^{-1}, $\alpha_2=2.75\times10^{-5}$ fs^{-1}, $\chi/\chi_R=0.5$, $\Delta,\Delta k=1.449$ mm^{-1}, $r=0$, $\omega_1-\omega_2=0.0166$ fs^{-1}, and $\eta=3$.

Based on the real Gaussian field, we finally have difference-frequency REPB signals in heterodyne detection as follows:

(i) $\tau>0$

$$I(\Delta,\tau)\propto I_{P_2'}+\frac{\chi^2\gamma}{\gamma+2\alpha_1}+\frac{\chi_R^2\gamma_R\gamma_R'}{\gamma_R'^2+\Delta^2}- \frac{2\chi\gamma\chi_R\gamma_R\Delta(\Delta^2+2\gamma\alpha_1+\gamma^2+4\gamma_R'\alpha_1+2\gamma_R'\gamma+\gamma_R'^2)}{(\gamma+2\alpha_1)(\gamma_R'^2+\Delta^2)[(\gamma_R'+\gamma)^2+\Delta^2]}+$$

$$\left[\chi^2+\frac{2\chi_R^2\gamma_R^2\gamma_R'-2\chi\chi_R\gamma_R\Delta(\gamma_R+\alpha_1)}{(\gamma_R+\alpha_1)(\gamma_R'^2+\Delta^2)}-\frac{2\chi\chi_R\gamma_R\Delta}{(\gamma_R'-2\alpha_1)^2+\Delta^2}\right]\times$$

$$\exp(-2\alpha_1|\tau|)+\left\{\frac{\chi^2\gamma}{2\alpha_1+\gamma}+\frac{4\chi\chi_R\gamma_R\Delta\alpha_1}{(2\alpha_1+\gamma)[(2\alpha_1-\gamma_R')^2+\Delta^2]}\right\}\times$$

$$\exp[-(2\alpha_1+\gamma)|\tau|]+2\left|\chi^{(3)}\right|\chi\eta\exp[-(\alpha_1+\alpha_2)|\tau|]\times$$

$$\cos[-\Delta\boldsymbol{k}\cdot\boldsymbol{r}+(\omega_1-\omega_2)\tau-\theta_R]. \tag{3.38}$$

(ii) $\tau<0$

$$I(\Delta,\tau)\propto I_{P_2'}+\frac{\chi^2\gamma}{\gamma+2\alpha_1}+\frac{\chi_R^2\gamma_R\gamma_R'}{\gamma_R'^2+\Delta^2}-$$

$$\frac{2\chi\gamma\chi_R\gamma_R\Delta(\Delta^2+2\gamma\alpha_1+\gamma^2+4\gamma_R'\alpha_1+2\gamma_R'\gamma+\gamma_R'^2)}{(\gamma+2\alpha_1)(\gamma_R'^2+\Delta^2)[(\gamma_R'+\gamma)^2+\Delta^2]}+$$

$$\left\{\chi^2+\frac{\chi_R^2\gamma_R^2\gamma_R'-4\chi\chi_R\gamma_R\Delta(\gamma_R+\alpha_1)}{(\gamma_R+\alpha_1)(\gamma_R'^2+\Delta^2)}+\right.$$

$$\left.\frac{2\chi_R^2\gamma_R^2(2\alpha_1-\gamma_R')}{(\alpha_1-\gamma_R)[(2\alpha_1+\gamma_R')^2+\Delta^2]}\right\}\exp(-2\alpha_1|\tau|)+$$

$$\frac{(\alpha_1+\alpha_3-\gamma_R)(\gamma_R'^2+\Delta^2)+\gamma_R'[(\alpha_1+\alpha_3-\gamma_R)^2+\Delta^2]-2[\Delta^2+\gamma_R'^2-(\alpha_1+\alpha_3)^2](\alpha_1+\gamma_R)}{(\alpha_1+\gamma_R)(\gamma_R'^2+\Delta^2)[(\alpha_1+\alpha_3-\gamma_R)^2+\Delta^2]}\times$$

$$\exp(-2\gamma_R|\tau|)-2\alpha_1\chi_R^2\gamma_R^2\left\{\frac{\exp[-(\gamma_R-\mathrm{i}\Delta)|\tau|]}{[\alpha_1^2-(\alpha_3+\gamma_R-\mathrm{i}\Delta)^2](\alpha_1+\alpha_3-\gamma_R-\mathrm{i}\Delta)}+\right.$$

$$\left.\frac{\exp[-(\gamma_R+\mathrm{i}\Delta)|\tau|]}{[\alpha_1^2-(\alpha_3+\gamma_R+\mathrm{i}\Delta)^2](\alpha_1+\alpha_3-\gamma_R+\mathrm{i}\Delta)}\right\}+$$

$$A\sin[-\Delta\boldsymbol{k}\cdot\boldsymbol{r}+(\omega_1-\omega_2)\tau+\Delta|\tau|]+2\left|\chi^{(3)}\right|\chi\eta\times$$

$$\exp[-(\alpha_1+\alpha_2)|\tau|]\cos[-\Delta\boldsymbol{k}\cdot\boldsymbol{r}+(\omega_1-\omega_2)\tau-\theta_R]. \tag{3.39}$$

Here, $I_{P_2'}=(\chi\gamma\eta)^2\left\{\frac{1}{\gamma(\gamma+2\alpha_2)}+\frac{\exp(-2\alpha_2|\tau|)}{\gamma^2}+\frac{\exp[-(2\alpha_2+\gamma)|\tau|]}{\gamma(\gamma+2\alpha_2)}\right\}$ for the real Gaussian field. The high-order decay terms are reasonably neglected in $\tau<0$ case. If the reference signal is much larger than the RENFWM signal (i.e., $I_{P_2'}>>I_{P_1,P_{R1}}$), except $u_1(t)$ the heterodyne detection signal is also the same as that of the heterodyne detected chaotic field case. By changing the time delay τ between twin beams 1 and 2 (If $\boldsymbol{r}=0$) we can obtain the real [the dotted line of Fig. 3.8 (a)] and imaginary [the dotted line of Fig. 3.8 (b)] parts of $\chi^{(3)}$ for the Gaussian-amplitude field. Due to the larger amplitude fluctuation, the dotted curves of Fig. 3.8 have the largest Δ-independent constant background.

Based on three stochastic models, the subtle Markovian field correlation effects have been investigated in the homodyne detected attosecond sum-frequency REPB and the heterodyne detected of femtosecond difference-frequency REPB. Different roles of the amplitude fluctuations and the phase fluctuations can be understood in time- and frequency-domains. The physical explanation for this is that the Gaussian-amplitude field undergoes stronger intensity fluctuations than a chaotic field. On the other hand, the intensity

(amplitude) fluctuations of the Gaussian-amplitude field or the chaotic field are always much larger than the pure phase fluctuations of the phase-diffusion field.

Based on the polarization interference between nonresonant FWM and Raman resonant FWM processes, we can employ the femtosecond difference-frequency REPB to obtain the real and the imaginary parts of the Raman resonance (Fig. 3.8). In the heterodyne detection of femtosecond difference-frequency REPB, we purposely introduce the nonresonant FWM signal by adding another component of noisy light with the frequency ω_2 to twin composite beams 1 and 2. The relative phase between the reference signal and RENFWM signal is determined by time delay τ between twin composite beams 1 and 2. Compared with the optical heterodyne detection Raman-induced Kerr effect method, because the polarizations of incident beams can be adjusted independently REPB is more convenient for studying various components of the fourth-rank tensor of third-order susceptibility. The REPB has also been employed for studying the phase dispersion of $\chi^{(3)}$. Although this method is similar to the method of Ma et al., [9] we show that for Raman resonance one can obtain the phase dispersion of $\chi^{(3)}$ by simply measuring the phase change of the FWM signal modulation as ω_3 is varied (Fig. 3.8). Generally speaking, this method can be applied to study the phase dispersion of $\chi^{(3)}$ in the attosecond sum-frequency REPB.

In conclusion, the homodyne detected attosecond sum-frequency REPB and the heterodyne detected femtosecond difference-frequency REPB are investigated using chaotic field, phase-diffusion, and Gaussian-amplitude models with color locking noisy light. The REPB is shown to be particularly sensitive to statistical properties of Markovian stochastic light fields in both time- and frequency-domains. The interferometric contrast ratio is equally sensitive to the amplitude and phase fluctuations of Markovian stochastic fields. The constant background of beat signals originates from the amplitude fluctuation. The Gaussian-amplitude field shows fluctuations larger than the chaotic field, which again exhibits fluctuations much larger than for the phase-diffusion field with pure phase fluctuations caused by spontaneous emission. It is found that the sum-frequency beat signal oscillates not only temporally with a period of 953 as but also spatially with a period of 0.6 mm. When the beating frequency between ω_3 and ω is off resonant from the Raman mode, the RENFWM signal exhibits terahertz damping oscillation as the time delay increases. The REPB in the heterodyne detection scheme has also been employed to obtain the real and imaginary parts of the Raman resonance.

3.2 Competition Between Raman and Rayleigh-enhanced Four-Wave Mixings in Attosecond Polarization Beats

Phase locking ultrashort-pulse nonlinear optical spectroscopy has proved to be a valuable technique for investigating the dynamics of a wealth of mechanisms in condensed matters. Four-wave mixing (FWM) is a third-order nonlinear optical process [28]. Using a femtosecond time-resolved FWM, valuable information on the dephasing dynamics in semiconductors and molecular materials has been obtained. The time resolution of this method is limited by the pulse width. However, the ultrafast dephasing phenomena can also be studied by the time-delayed FWM with incoherent light [25]. This technique is intrinsically related to the optical coherent transient spectroscopy with an advantage that the time resolution is determined by the correlation time τ_c of the color locking noisy light source. Since the relaxation time is deduced from the FWM spectrum, the measurement is not limited by the laser pulse width [25].

Laser-induced gratings have received considerable attention because of their potential applications in spectroscopy and phase conjugation. When two pump beams with the same frequency interfere in liquids, the optical Kerr effect [29] results in the generation of a molecular-reorientation grating. Moreover, if the absorption coefficient of a sample at the pump beam frequency is not zero, the molecular-reorientation grating is usually accompanied by an undesired thermal grating [30]. In this case, FWM signals can be the Bragg reflection of the probe beam by the molecular-reorientation grating and the thermal grating induced by two pump beams [31].

In Raman-enhanced FWM [32], the Raman vibration is excited by the simultaneous presence of two incident beams whose frequency difference equals the Raman excitation frequency, and the Raman-enhanced FWM signal is the result of this resonant excitation. In contrast, Rayleigh-enhanced FWM [32] is a non-resonant process with no energy transfer between the lights and the medium when the frequency difference between two incident beams equals zero. The resonant structure in Rayleigh-enhanced FWM spectrum is the result of induced moving grating. The Raman or Rayleigh-enhanced FWM may be superior to all other CRS techniques [32, 33]. They possess features of non-resonant background suppression, excellent spatial signal resolution, free choice of interaction volume and simple optical alignment. Moreover, phase matching can be achieved for a very wide frequency range from many hundreds to thousands of cm^{-1}.

In this section, based on the field-correlation of color-locking twin noisy lights, the Raman and Rayleigh-enhanced FWM, and the homodyne, heterodyne detection of pure Raman, pure Rayleigh, and coexistence of Raman and Rayleigh ASPB have been investigated, respectively. Raman and Rayleigh-enhanced FWM compete with each other in the coexistence of Raman and Rayleigh ASPB. An analytic closed form of results is obtained. Characteris-

tics of the interferogram of the Raman and Rayleigh-enhanced ASPB are a result of two main components: the material response and the light response along with the interplay between the two responses.

The section is organized as follows. Section 3.2.1 presents the basic theory of field-correlation effects on the Raman and Rayleigh-enhanced FWM. We give the three schemes of the pure Raman ASPB, the pure Rayleigh ASPB, and the coexisting Raman and Rayleigh ASPB. Section 3.2.2 presents the Rayleigh and Raman-enhanced FWM in three Markovian stochastic models. In addition, a time-delayed method to suppress the background is mentioned in a Kerr medium and an absorbing medium. Section 3.2.3 gives the Raman and Rayleigh-enhanced nonlinear susceptibility with cw laser beams. In Sections 3.2.4 and 3.2.5 the homodyne and heterodyne detection of three types of the ASPB are shown. Section 3.2.6 gives discussion and conclusion.

3.2.1 Basic Theory

The Raman and Rayleigh ASPB are the third-order nonlinear polarization beat phenomenon. It requires that all the polarizations have the same frequency.

The basic geometry is shown in Fig. 3.9. Twin beams 1 and 2 consist of two frequency components ω_1 and ω_2, a small angle exists between them. Beam 3 with frequency ω_3 is almost propagating along the opposite direction of beam 1. Twin composite stochastic fields of beam 1, $E_{p1}(\boldsymbol{r},t)$, and beam 2, $E_{p2}(\boldsymbol{r},t)$ for homodyne detection scheme, can be written as

$$\begin{aligned}
E_{p1} &= E_1(\boldsymbol{r},t) + E_2'(\boldsymbol{r},t) = A_1(\boldsymbol{r},t)\exp(-\mathrm{i}\omega_1 t) + A_2'(\boldsymbol{r},t)\exp[-\mathrm{i}\omega_2(t-\tau)] \\
&= \varepsilon_1 u_1(t)\exp[\mathrm{i}(\boldsymbol{k}_1\cdot\boldsymbol{r}-\omega_1 t)] + \varepsilon_2' u_2(t-\tau)\exp[\mathrm{i}(\boldsymbol{k}_2'\cdot\boldsymbol{r}-\omega_2 t+\omega_2\tau)], \\
E_{p2} &= E_1'(\boldsymbol{r},t) + E_2(\boldsymbol{r},t) = A_1'(\boldsymbol{r},t)\exp[-\mathrm{i}\omega_1(t-\tau)] + A_2(\boldsymbol{r},t)\exp(-\mathrm{i}\omega_2 t) \\
&= \varepsilon_1' u_1(t-\tau)\exp[\mathrm{i}(\boldsymbol{k}_1'\cdot\boldsymbol{r}-\omega_1 t+\omega_1\tau)] + \\
&\quad \varepsilon_2 u_2(t)\exp[\mathrm{i}(\boldsymbol{k}_2\cdot\boldsymbol{r}-\omega_2 t)].
\end{aligned} \tag{3.40}$$

Here, $\varepsilon_i, \boldsymbol{k}_i(\varepsilon_i', \boldsymbol{k}_i')$ are the constant field amplitude and the wave vector of the ω_i component in beams 1 and 2, respectively. $u_i(t)$ is a dimensionless statistical factor that contains phase and amplitude fluctuations. It is taken to be a complex ergodic stochastic function of t, which obey complex circular Gaussian statistics in a chaotic field. τ is a variable relative time delay between the prompt (unprime) and delayed (prime) fields. To accomplish this the frequency component ω_1 and ω_2 lights are split and recombined to provide two double-frequency pulses in such a way that the ω_1 component is delayed by τ in beam 2 and the ω_2 component delayed by the same amount in the beam 1 (Fig. 3.9). The time delay τ is introduced in both composite beams, which is quite different with that of femtosecond difference-frequency polarization beats [17]. On the other hand, the complex electric fields of the beam 3 can be

written as $E_3(\boldsymbol{r},t) = A_3(\boldsymbol{r},t)\exp(-\mathrm{i}\omega_3 t) = \varepsilon_3 u_3(t)\exp[\mathrm{i}(\boldsymbol{k}_3\cdot\boldsymbol{r}-\omega_3 t)]$. Here, ω_3, ε_3, and $\boldsymbol{k}_3$ are the frequency, the field amplitude and the wave vector of the field, respectively.

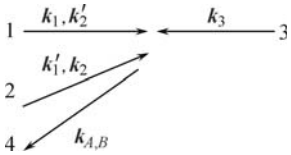

Fig. 3.9. Phase-conjugation geometry of the ASPB.

In an absorbing medium, the nonlinear interaction of beams 1 and 2 with the medium gives rise to the molecular-reorientation gratings and the thermal gratings, i.e., $\omega_{1,2}$ will induce their own non-resonant static molecular-reorientation gratings $G_{M1,2}$ and the rmal gratings $G_{T1,2}$. FWM signals are results of the diffraction of the beam 3 by these four gratings, respectively. The order parameters Q_{M1}, Q_{T1}, Q_{M2}, and Q_{T2} of four non-resonant static gratings satisfy the following equations [29, 30]:

$$\begin{cases} \mathrm{d}Q_{M1}/\mathrm{d}t + \gamma_M Q_{M1} = \chi_M\gamma_M E_1(\boldsymbol{r},t)[E_1'(\boldsymbol{r},t)]^*, \\ \mathrm{d}Q_{T1}/\mathrm{d}t + \gamma_T Q_{T1} = \chi_T\gamma_T E_1(\boldsymbol{r},t)[E_1'(\boldsymbol{r},t)]^*, \\ \mathrm{d}Q_{M2}/\mathrm{d}t + \gamma_M Q_{M2} = \chi_M\gamma_M E_2'(\boldsymbol{r},t)[E_2(\boldsymbol{r},t)]^*, \\ \mathrm{d}Q_{T2}/\mathrm{d}t + \gamma_T Q_{T2} = \chi_T\gamma_T E_2'(\boldsymbol{r},t)[E_2(\boldsymbol{r},t)]^*. \end{cases} \tag{3.41}$$

Here $\gamma_{M,T}$ and $\chi_{M,T}$ are the relaxation rate and the nonlinear susceptibility of the molecular-reorientation grating and thermal grating, respectively.

Now if the frequency difference $\Delta_1 = \omega_3 - \omega_1$ is much smaller than $\Delta_1' = \omega_3 - \omega_2$ (i.e., $\Delta_1 << \Delta_1'$ and $\Delta_1 \approx 0$) and the frequency detuning $\Delta_2 = \Delta_1' - \Omega_R$ is near zero, the coexisting Raman and Rayleigh modes of the medium enhance FWM signals. Here Ω_R is the Raman resonant frequency. Specifically, on one hand, two resonant moving gratings, G_{RM} and G_{RT} with large angle formed by the interference between the ω_1 frequency component of the beam 2 and the ω_3 frequency component of the beam 3, will excite the Rayleigh mode of the medium and enhance FWM signals corresponding to G_{M1} and G_{T1} (i.e., Rayleigh-enhanced FWM). On the other hand, one large resonant moving grating, G_R formed by the interference between the ω_2 frequency component of the beam 2 and the ω_3 frequency component of the beam 3, will excite the Raman mode of the medium and enhance FWM signals corresponding to G_{M2} and G_{T2} (i.e., Raman-enhanced FWM). The order parameters Q_R, Q_{RT}, and Q_{RM} satisfy the following equations:

$$\begin{cases} \mathrm{d}Q_R/\mathrm{d}t + (\gamma_R - \mathrm{i}\Delta_2)Q_R = \chi_R\gamma_R[E_2(\boldsymbol{r},t)]^* E_3(\boldsymbol{r},t), \\ \mathrm{d}Q_{RM}/\mathrm{d}t + \gamma_M Q_{RM} = \chi_M\gamma_M[E_1'(\boldsymbol{r},t)]^* E_3(\boldsymbol{r},t), \\ \mathrm{d}Q_{RT}/\mathrm{d}t + \gamma_T Q_{RT} = \chi_T\gamma_T[E_1'(\boldsymbol{r},t)]^* E_3(\boldsymbol{r},t). \end{cases} \tag{3.42}$$

Based on Eqs. (3.41) and (3.42) shown above, the induced seven third-

order nonlinear polarizations which are responsible for FWM signals are

$$P_{M1} = Q_{M1}(\boldsymbol{r},t)E_3(\boldsymbol{r},t) = \chi_M\gamma_M S_1(\boldsymbol{r})\varepsilon_1(\varepsilon_1')^*\varepsilon_3 \times \int_0^\infty u_1(t-t')u_1^*(t-t'-\tau)u_3(t)\exp(-\gamma_M t')\mathrm{d}t', \tag{3.43}$$

$$P_{T1} = Q_{T1}(\boldsymbol{r},t)E_3(\boldsymbol{r},t) = \chi_T\gamma_T S_1(\boldsymbol{r})\varepsilon_1(\varepsilon_1')^*\varepsilon_3 \times \int_0^\infty u_1(t-t')u_1^*(t-t'-\tau)u_3(t)\exp(-\gamma_T t')\mathrm{d}t', \tag{3.44}$$

$$P_{M2} = Q_{M2}(\boldsymbol{r},t)E_3(\boldsymbol{r},t) = \chi_M\gamma_M S_2(\boldsymbol{r})(\varepsilon_2)^*\varepsilon_2'\varepsilon_3 \times \int_0^\infty u_2^*(t-t')u_2(t-t'-\tau)u_3(t)\exp(-\gamma_M t')\mathrm{d}t', \tag{3.45}$$

$$P_{T2} = Q_{T2}(\boldsymbol{r},t)E_3(\boldsymbol{r},t) = \chi_T\gamma_T S_2(\boldsymbol{r})(\varepsilon_2)^*\varepsilon_2'\varepsilon_3 \times \int_0^\infty u_2^*(t-t')u_2(t-t'-\tau)u_3(t)\exp(-\gamma_T t')\mathrm{d}t', \tag{3.46}$$

$$P_R = Q_R(\boldsymbol{r},t)E_2'(\boldsymbol{r},t) = \mathrm{i}\chi_R\gamma_R S_2(\boldsymbol{r})(\varepsilon_2)^*\varepsilon_3\varepsilon_2' \times \int_0^\infty u_2^*(t-t')u_3(t-t')u_2(t-\tau)\exp[-(\gamma_R-\mathrm{i}\Delta_2)t']\mathrm{d}t', \tag{3.47}$$

$$P_{RM} = Q_{M1}(\boldsymbol{r},t)E_1(\boldsymbol{r},t) = \chi_M\gamma_M S_1(\boldsymbol{r})(\varepsilon_1')^*\varepsilon_3\varepsilon_1 \times \int_0^\infty u_1^*(t-t'-\tau)u_3(t-t')u_1(t)\exp[-(\gamma_M-\mathrm{i}\Delta_1)t']\mathrm{d}t', \tag{3.48}$$

$$P_{RT} = Q_{T1}(\boldsymbol{r},t)E_1(\boldsymbol{r},t) = \chi_T\gamma_T S_1(\boldsymbol{r})(\varepsilon_1')^*\varepsilon_3\varepsilon_1 \times \int_0^\infty u_1^*(t-t'-\tau)u_3(t-t')u_1(t)\exp[-(\gamma_T-\mathrm{i}\Delta_1)t']\mathrm{d}t'. \tag{3.49}$$

Here, $S_1(\boldsymbol{r}) = \exp\{\mathrm{i}[(\boldsymbol{k}_1-\boldsymbol{k}_1'+\boldsymbol{k}_3)\cdot\boldsymbol{r}-\omega_3 t-\omega_1\tau]\}$ and $S_2(\boldsymbol{r}) = \exp\{\mathrm{i}[(\boldsymbol{k}_2'-\boldsymbol{k}_2+\boldsymbol{k}_3)\cdot\boldsymbol{r}-\omega_3 t+\omega_2\tau]\}$. Therefore, polarization $P_A = P_{M2}+P_{T2}+P_R$ corresponding to the Raman-enhanced FWM process with phase-matching condition $\boldsymbol{k}_2'-\boldsymbol{k}_2+\boldsymbol{k}_3$ and $P_B = P_{M1}+P_{T1}+P_{RM}+P_{RT}$ corresponding to the Rayleigh-enhanced FWM process with phase-matching condition $\boldsymbol{k}_1-\boldsymbol{k}_1'+\boldsymbol{k}_3$. Both FWM signals have the same frequency, i.e., ω_3. As a result, ASPB originates from the interference between macroscopic polarizations from Rayleigh-enhanced FWM and Raman-enhanced FWM signals. The beat signal (beam 4) is along the opposite direction of the beam 2 approximately [9].

Furthermore, if the ω_1, ω_2, and ω_3 frequency components of the beams only satisfy the excitation condition of Rayleigh mode where $\Delta_1 << \Delta_1'$ and $\Delta_1 \approx 0$, the Raman-enhanced FWM polarization P_A converts into the FWM polarization $P_C = P_{M2}+P_{T2}$ and we have the pure Rayleigh ASPB based on the interference at the detector between FWM signals resulted from P_B and P_C. Similarly, we can have the pure Raman ASPB resulted from P_A and

$P_D = P_{M1} + P_{T1}$ if only the excitation condition of Raman mode is satisfied and the Rayleigh-enhanced FWM polarization P_B converts into the FWM polarization P_D.

To be brief, with the geometry shown in Fig. 3.9, under the excitation condition of Raman mode the beams $\boldsymbol{k}_2$ and $\boldsymbol{k}_2'$ generate Raman-enhanced FWM (P_A); under the excitation condition of Rayleigh mode the beams $\boldsymbol{k}_1$ and $\boldsymbol{k}_1'$ generate Rayleigh-enhanced FWM (P_B). When only one condition is satisfied, we obtain pure Raman ASPB ($P_A + P_D = P_{M2} + P_{T2} + P_R + P_{M1} + P_{T1}$) or Rayleigh ASPB ($P_B + P_C = P_{M1} + P_{T1} + P_{RM} + P_{RT} + P_{M2} + P_{T2}$). However, when both the excitation conditions are fulfilled, Raman and Rayleigh-enhanced FWM interact with each other to generate the coexisting Raman and Rayleigh ASPB ($P_A + P_B = P_{M2} + P_{T2} + P_R + P_{M1} + P_{T1} + P_{RM} + P_{RT}$).

3.2.2 Stochastic Correlation Effects of Rayleigh and Raman-enhanced FWM

We have the total third-order polarization $P_A(P_B)$ for the Raman-(Rayleigh-) enhanced FWM. For the macroscopic system where phase matching takes place the signal must be drawn from the $P_A(P_B)$ developed on one "atom" multiplied by the P_A^* (P_B^*) that is developed on another "atom" which must be located elsewhere in space (with summation over all such pairs). For homodyne detection the Raman (Rayleigh-) enhanced FWM signal is proportional to the average of the absolute square of $P_A(P_B)$ over the random variable of the stochastic process. We can have

$$\begin{aligned}
\langle |P_A|^2 \rangle = {} & \langle P_{M2} P_{M2}^* \rangle + \langle P_{M2} P_{T2}^* \rangle + \langle P_{M2} P_R^* \rangle + \langle P_{T2} P_{M2}^* \rangle + \langle P_{T2} P_{T2}^* \rangle + \\
& \langle P_{T2} P_R^* \rangle + \langle P_R P_{M2}^* \rangle + \langle P_R P_{T2}^* \rangle + \langle P_R P_R^* \rangle, \\
\langle |P_B|^2 \rangle = {} & \langle P_{M1} P_{M1}^* \rangle + \langle P_{M1} P_{T1}^* \rangle + \langle P_{M1} P_{RM}^* \rangle + \langle P_{M1} P_{RT}^* \rangle + \\
& \langle P_{T1} P_{M1}^* \rangle + \langle P_{T1} P_{T1}^* \rangle + \langle P_{T1} P_{RM}^* \rangle + \langle P_{T1} P_{RT}^* \rangle + \\
& \langle P_{RM} P_{M1}^* \rangle + \langle P_{RM} P_{T1}^* \rangle + \langle P_{RM} P_{RM}^* \rangle + \langle P_{RM} P_{RT}^* \rangle + \\
& \langle P_{RT} P_{M1}^* \rangle + \langle P_{RT} P_{T1}^* \rangle + \langle P_{RT} P_{RM}^* \rangle + \langle P_{RT} P_{RT}^* \rangle.
\end{aligned}$$

They involves fourth- and second-order coherence functions of $u_i(t)$. For example, one term of $\langle |P_A|^2 \rangle$ is

$$\begin{aligned}
\langle P_R P_{M2}^* \rangle = {} & \mathrm{i} \chi_R \gamma_R \chi_M \gamma_M (\varepsilon_2)^* \varepsilon_3 \varepsilon_2' S_2(\boldsymbol{r}) \varepsilon_2 (\varepsilon_2')^* (\varepsilon_3)^* S_2^*(\boldsymbol{r}) \times \\
& \int_0^\infty dt' \int_0^\infty ds' \langle u_2(t-\tau) u_2(t-s') u_2^*(t-t') u_2^*(t-s'-\tau) \rangle \\
& \langle u_3(t-t') u_3^*(t) \rangle \times \exp[-(\gamma_R - \mathrm{i}\Delta_2)t' - \gamma_M s'].
\end{aligned}$$

The fourth- and second-order coherence functions of $u_i(t)$ included in this equation are $\langle u_2(t-\tau) u_2(t-s') u_2^*(t-t') u_2^*(t-s'-\tau) \rangle$ and $\langle u_3(t-t') u_3^*(t) \rangle$, respectively.

In an optical Kerr medium there is no thermal effect, we assume $\chi_T = 0$. The optical Kerr effect for the liquid CS_2, for example, has at least two components, i.e., a relatively long "Debye" component and a shorter "interaction-induced" component. Here for simplicity, we only consider the field correlation effects in a medium which has single relaxation rate γ_M.

We first consider Raman-enhanced FWM. After performing the tedious integration, in the case of broadband linewidth ($\gamma_M, \gamma_R << \alpha_2, \alpha_3$), we can obtain as follows:

$$\tau > 0$$
$$I_A(\Delta_2, \tau) \propto \langle P_A P_A^* \rangle = L_1(n_1)\chi_M^2 + L_2\chi_R^2 - 2L_3\chi_M\chi_R. \tag{3.50}$$

$$\tau < 0$$
$$I_A(\Delta_2, \tau) \propto L_1(n_1)\chi_M^2 + L_2\chi_R^2 - 2\Bigg\{L_3 - \frac{4\alpha_1\gamma_R[2\alpha_3\Delta_2\cos\Delta_2\tau + (\alpha_1^2 - \alpha_3^2 + \Delta_2^2)\sin\Delta_2\tau]\exp(\alpha_1+\alpha_3)\tau}{\alpha_1^4 - 2\alpha_1^2(\alpha_3^2 - \Delta_2^2) + (\alpha_3^2 + \Delta_2^2)^2}\Bigg\} \times \chi_M\chi_R. \tag{3.51}$$

Here, $L_1(n_1) = \gamma_M[1 + n_1\exp(-2\alpha_1|\tau|)]/2\alpha_1 + \exp(-2\alpha_1|\tau|)$, $L_2 = \gamma_R(\alpha_1 + \alpha_3)/[(\alpha_1+\alpha_3)^2 + \Delta_2^2]$, and $L_3 = 2\gamma_R\Delta_2\exp(-2\alpha_1|\tau|)/[(\alpha_1-\alpha_3)^2 + \Delta_2^2]$. n_1 in the function $L_1(n_1)$ equals $0, -1, 2$ for the CFM, PDM and GAM, respectively. The terms $L_1(n)\chi_M^2$ and $L_2\chi_R^2$ in Eqs. (3.50) and (3.51) are the autocorrelation terms of the non-resonant background and the resonant signal, respectively. Other terms with the factor $\chi_M\chi_R$ are cross-correlation terms between them. Obviously, the above two equations show that the Raman-enhanced FWM spectrum is asymmetrical about $\tau = 0$. Since the autocorrelation terms are the same for $\tau > 0$ and $\tau < 0$, the temporal asymmetry is induced by cross-correlation terms. Moreover, when $\Delta_2 \neq 0, I(\Delta_2, \tau)$ for $\tau < 0$ exhibits hybrid-radiation-matter-detuning damping oscillations with a frequency close to Δ_2 that originate from $\cos\Delta_2\tau$ and $\sin\Delta_2\tau$ factors of interference term for $\tau < 0$ [see Eq. 3.51 and the dashed curve in Fig. 3.10 (a)]. On the other hand, we define a parameter $R = I(\Delta_2 \to \infty)/[I(\Delta_2 = 0) - I(\Delta_2 \to \infty)]$ as the ratio between the non-resonant background and the resonant signal. When $\tau = 0$ and $\alpha_2 = \alpha_3$ we obtain $R = \chi_M^2(\gamma_M + 2\alpha_2)/\chi_R^2\gamma_R >> 1$ in the limit of broadband linewidth. Thus the resonant signal at $\tau = 0$ is obscured by the huge non-resonant background [the solid curve in Fig. 3.10 (a)]. However, when $\alpha_2|\tau| >> 1$, the resonant signal and the non-resonant background become comparable, and we have $R = \chi_M^2\gamma_M/\chi_R^2\gamma_R$, which equals 1 if $\chi_R = \chi_M, \gamma_R = \gamma_M$, as shown by the dashed and dotted curve in Fig. 3.10(a). Therefore, the huge non-resonant background can be effectively suppressed with large time delay.

Next,we consider the Raman-enhanced FWM with narrow-band linewidth

$(\gamma_M, \gamma_R >> \alpha_2, \alpha_3)$. We have

$$I_A(\Delta_2) \approx n_2 \left(\chi_M^2 + \chi_R^2 \frac{\gamma_R^2}{\gamma_R^2 + \Delta_2^2} - 2\chi_M \chi_R \frac{\gamma_R \Delta_2}{\gamma_R^2 + \Delta_2^2} \right). \tag{3.52}$$

Here, n_2 equals 2, 1, 3 for the CFM, PDM, and GAM, respectively. We can see that autocorrelation terms are even functions while the cross-correlation term is odd function. Therefore, the spectral asymmetry of Raman-enhanced FWM results from interference between the resonant signal and the non-resonant background (Fig. 3.10). Moreover, the interference term has contribution to neither the resonant signal nor non-resonant background. The ratio between the resonant signal and the non-resonant background is almost independent of the delay time τ and we have $R = (\chi_M/\chi_R)^2 = 1$ if $\chi_M = \chi_R$, as shown in Fig. 3.10 (b).

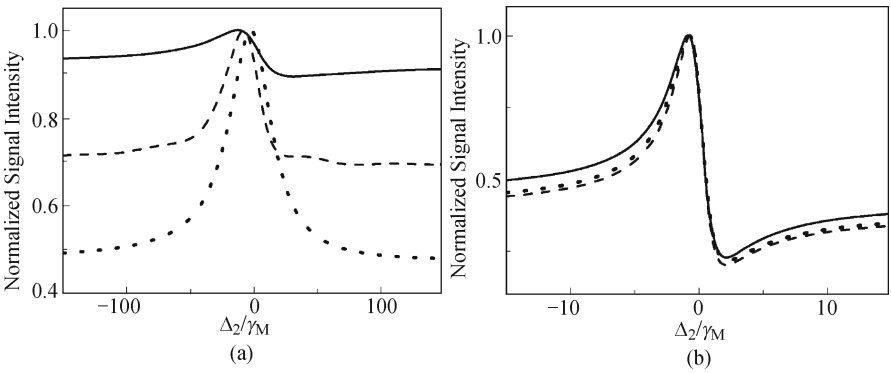

Fig. 3.10. The Raman-enhanced FWM spectra of the GAM versus Δ_2/γ_M for $\chi_M/\chi_R = 1, \alpha_3/\alpha_1 = 1, \alpha_1\tau = 0$ (solid curve), -1 (dashed curve), -10 (dotted curve), (a) $\gamma_M/\alpha_1 = 0.1, \gamma_R/\alpha_1 = 0.1$, (b) $\gamma_M/\alpha_1 = 5, \gamma_R/\alpha_1 = 5$. Adopted from Ref. [20].

In general, the Raman-enhanced FWM of Kerr medium exhibits spectral and temporal asymmetry and hybrid-radiation-matter-detuning damping oscillations with a frequency close to Δ_2 that originate from $\cos\Delta_2\tau$ and $\sin\Delta_2\tau$ factors for $\tau < 0$ due to the interference between the non-resonant background of the molecular-reorientation grating and the resonant signal of the Raman-active mode. In addition, on one hand, in the case of narrowband linewidth the ratio between the resonant signal and the non-resonant background is almost independent of the delay time τ. On the other hand, the huge non-resonant background can be effectively suppressed with large time delay.

The Rayleigh-enhanced FWM expressions and spectra versus Δ_1/γ_M have been studied under narrowband and broadband line width condition before [32]. In contrast to the Raman-enhanced FWM, since the interference term between the molecular-reorientation grating and the Rayleigh moving grating

is even function of Δ_1, the spectra of the Rayleigh-enhanced FWM are symmetrical about $\Delta_1 = 0$ (Fig. 3.11). In addition, Rayleigh moving grating does not have the exclusive relaxation rate but Debye relaxation rate γ_M instead, which is different from Raman moving grating. On the other hand, in the case of the narrowband linewidth, though the Rayleigh-enhanced FWM signal intensity of GAM is the largest while that of PDM is the smallest and that of CFM is moderate, the spectra of the three models are different drastically [Fig. 3.11 (a)]. On the other hand, under broadband line width condition, when $\tau = 0$ the spectra of the three models have the same point that the non-resonant background is so larger than the resonant signal that the contribution from molecular-reorientation grating dominates the FWM spectra and obscure the valuable information of the spectra, the difference value of the signals intensity at $\Delta_1 = 0$ among the three models get smaller than those of Fig. 3.11 (a), as shown in Fig. 3.11 (b). However, when $\alpha_1\tau >> 1$ the resonant signal, and the non-resonant background become comparable, and

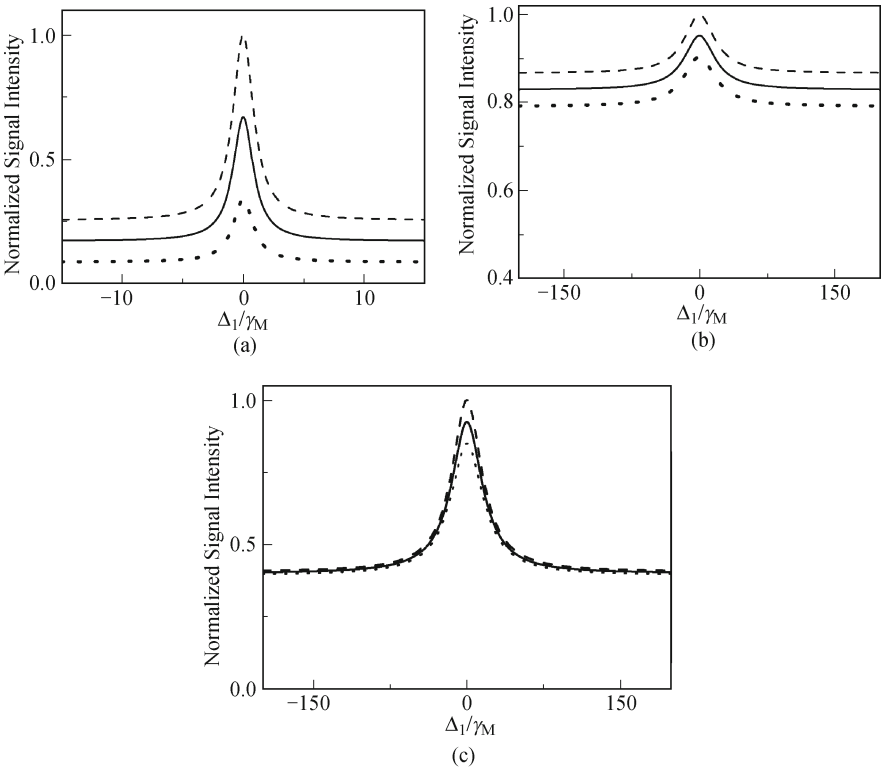

Fig. 3.11. The Rayleigh-enhanced FWM spectra in a Kerr medium with a single relaxation rate of molecular-reorientation grating for $\alpha_3/\alpha_1 = 1$, (a) $\gamma_M/\alpha_1 = 100, \tau = 0$; (b) $\gamma_M/\alpha_1 = 0.1, \tau = 0$; (c) $\gamma_M/\alpha_1 = 0.1, \alpha_1\tau = -0.3\Delta$. The three curves represent the CFM (solid curve), PDM (dashed curve) and GAM (dotted curve), respectively.

the PDM and GAM results are the same as that of the CFM, as shown in Fig. 3.11 (c). Therefore, the differences among CFM, PDM, and GAM are drastic with narrowband linewidth, while get similar with broadband linewidth. Also, in this case the huge non-resonant background can be effectively suppressed with large time delay.

Typically, we assume, in absorbing medium the relaxation time of a thermal grating is on the order of a microsecond, while the relaxation time of the molecular-reorientation grating is a few hundreds femtosecond, the reduction factor is about 10^{-6}. Therefore, the difference in the temporal behavior of the Raman and Rayleigh-enhanced FWM for $\gamma_M >> \alpha_1, \alpha_3$ and $\gamma_T << \alpha_1, u_1(t)$ can be employed for the suppression of non-resonant thermal background in an absorbing medium.

We have discussed the Raman-enhanced FWM spectra at fixed time delay in the Kerr medium, now we turn our attention to the dependence of the Raman-enhanced signal intensity on the time delay when the frequencies of the incident beams are fixed. Figure 3.12 shows the temporal behavior of the Raman-enhanced FWM signal intensity for GAM. Here no coherence spike appears at $\tau = 0$ and the signal intensity decay with different rate for $\tau > 0$ and $\tau < 0$. As the laser linewidth α_2 increases, the maximum is closer to $\tau = 0$, and the τ-independent background increases, as shown in Fig.3.12 (a). Moreover, there only exist the hybrid-radiation-matter-detuning damping oscillations for $\tau < 0$ and the maximum of the profile is shifted to $\tau = 0$ as Δ_2 increases, as shown in Fig. 3.12 (b). In fact, when $\tau < 0$, the Raman mode and beam 1 are mutually correlated and the Raman-enhanced FWM signal intensity depends on the coherence time of the pump beams and the relaxation time of the Raman mode, while when $\tau > 0$ it only depends on

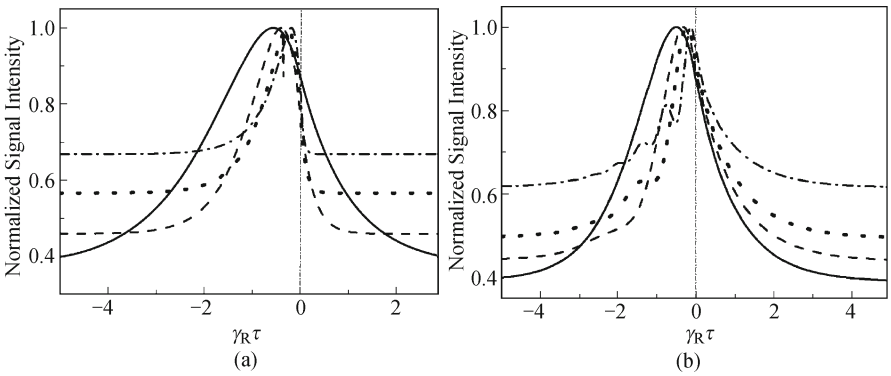

Fig. 3.12. The Raman-enhanced FWM signal intensity of the GAM versus $I(\tau, r)$ in an absorbing medium for (a) $\chi_M/\chi_R = 0.05, \gamma_M/\gamma_R = 4, \chi_T/\chi_R = 0.05, \gamma_T/\gamma_R = 1 \times 10^{-6}, \alpha_3/\gamma_R = 0.1, \Delta_2 = 0, \alpha_2/\gamma_R = 0.5$ (solid curve), $\alpha_2/\gamma_R = 2$ (dashed curve), $\alpha_2/\gamma_R = 5$ (dotted curve), $\alpha_2/\gamma_R = 10$ (dot-dashed curve); (b) $\chi_M/\chi_R = 0.05, \gamma_M/\gamma_R = 4, \chi_T/\chi_R = 0.05, \gamma_T/\gamma_R = 1 \times 10^{-6}, \alpha_3/\gamma_R = 0.1, \alpha_2/\gamma_R = 0.5, \Delta_2/\gamma_R = 1$ (solid curve), $\Delta_2/\gamma_R = 3$ (dashed curve), $\Delta_2/\gamma_R = 5$ (dotted curve), $\Delta_2/\gamma_R = 10$ (dot-dashed curve).

the laser coherence time. The temporal asymmetry and the hybrid-radiation-matter-detuning damping oscillation are induced by such mutual correlation. As the pump laser linewidth increases, the mutual correlation gets weak and the τ-independent background increases.

For simplicity, in the limit of $\gamma_R, \gamma_M >> \alpha_1, \alpha_3 >> \gamma_T$ we have

$$I_A(\Delta_2, \tau) \propto [1 + n_3 \exp(-2\alpha_2|\tau|)] \left(\chi_M^2 - \frac{2\gamma_R \Delta_2}{\gamma_R^2 + \Delta_2^2} \chi_M \chi_R + \frac{\gamma_R^2}{\gamma_R^2 + \Delta_2^2} \chi_R^2 \right) + \frac{\gamma_T \chi_T^2}{2\alpha_2} + \exp(-2\alpha_2|\tau|) \left(2\chi_M \chi_T - \frac{2\gamma_R \Delta_2}{\gamma_R^2 + \Delta_2^2} \chi_T \chi_R + \chi_T^2 \right). \quad (3.53)$$

Here, n_3 equals 1, 0, 2 for CFM, PDM, and GAM, respectively. Suppose that the thermal grating is much efficient than the molecular-reorientation grating so that $\chi_T^2 >> \chi_M^2, \chi_R^2$, then we have $I_A(\Delta_2) \propto \chi_T^2$ at zero time delay. Hence, the Raman-enhanced FWM spectrum is dominated by the non-resonant thermal background, as shown in Fig. 3.13 (a). On the other hand, under the condition $(\chi_T/\chi_M)^2(\gamma_T/2\alpha_1) << 1$, the thermal background can be eliminated completely when the relative time delay is much longer than the laser coherence time. In this limit, the theoretical Raman-enhanced FWM spectra show the normal asymmetry due to the interference between the Raman-resonant term and the non-resonant background originating solely from the molecular-reorientation grating, as shown in Fig. 3.13 (b). Furthermore, from Eq. (3.53) we can see that the time-delayed method to suppress the thermal background is useful for all the three Markovian stochastic models. However, if $(\chi_T/\chi_M)^2(\gamma_T/2\alpha_1) \approx 1$, the residue contribution from the thermal grating due to the second term cannot be neglected even when $|\tau| \to \infty$. Our numerical results are given in Fig. 3.13 (c).

Physically, the establishment of $Q_{M2}(\boldsymbol{r}, t)$ and $Q_{T2}(\boldsymbol{r}, t)$ are dependent on the delay time τ directly while that of $Q_R(\boldsymbol{r}, t)$ is almost independent of delay time τ. Moreover, we define the coherent time of the pump beams as T_c, the decay time of the thermal grating as T_t, and the relaxation time of the molecular-reorientation grating as T_M. For most liquids T_t is of the order of microseconds, while T_M is only a few picoseconds. We choose the laser linewidth such that $T_M < T_c << T_t$. When $\tau >> T_c$, the interference patterns of the pump beams fluctuate with a characteristic time scale $(\alpha_2 + \alpha_3)^{-1}$. Thus the thermal grating is washed out due to integration effect on the phase fluctuation, while the molecular-reorientation grating with short relaxation time can respond to the phase fluctuation of the fields almost immediately. Therefore, thermal gratings can be effectively suppressed with large τ, while the Bragg-reflection signal from the molecular-reorientation grating can still be observed. It should be noted that if the pump beams are derived from a pulse laser with a pulse width $T_p << T_t$,the condition for the suppression of thermal gratings should be replaced by $T_p >> T_c$. That is to say, because of the finite interaction time between the laser and the material, the role of the relaxation time should be replaced by the laser pulse width.

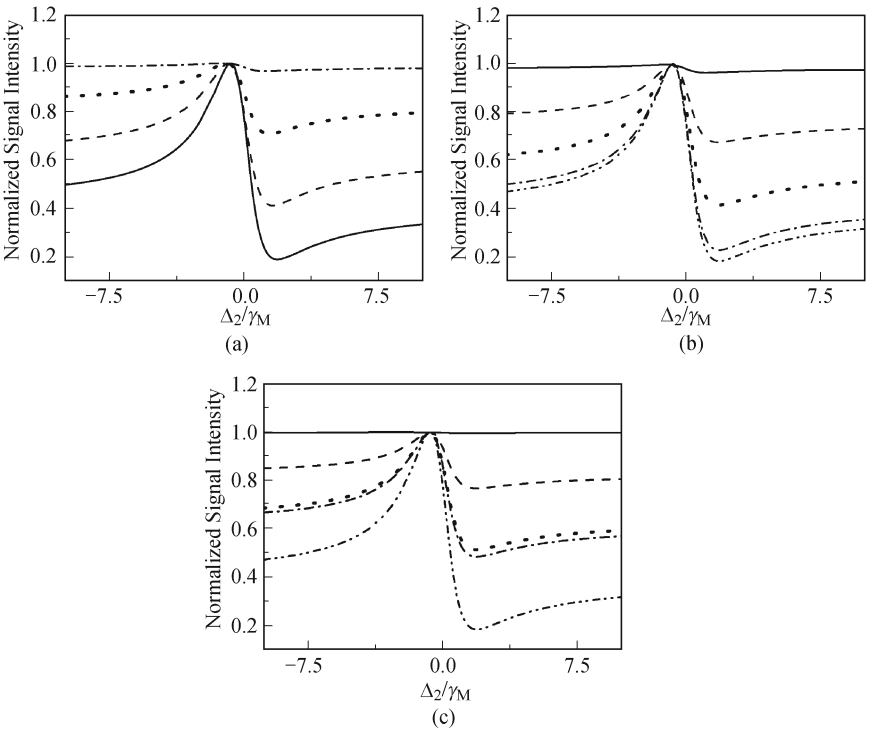

Fig. 3.13. The Raman-enhanced FWM spectra of the GAM versus Δ_2/γ_M in an absorbing medium for (a) $\alpha_3/\alpha_1 = 1, \gamma_T/\alpha_1 = 1 \times 10^{-5}, \gamma_M/\alpha_1 = \gamma_R/\alpha_1 = 10, \alpha_1\tau = 0, \chi_M/\chi_R = 1, \chi_T/\chi_R = 0$ (solid curve), $\chi_T/\chi_R = 1.5$ (dashed curve), $\chi_T/\chi_R = 5$ (dotted curve), $\chi_T/\chi_R = 50$ (dot-dashed curve); (b) $\alpha_3/\alpha_1 = 1, \gamma_T/\alpha_1 = 1 \times 10^{-5}, \gamma_M/\alpha_1 = \gamma_R/\alpha_1 = 10, \chi_M/\chi_R = 1, \chi_T/\chi_R = 50, \alpha_1\tau = 0$ (solid curve), $\alpha_1\tau = 3.3$ (dashed curve), $\alpha_1\tau = 4$ (dotted curve), $\alpha_1\tau = 5$ (dot-dashed curve), $\chi_T/\chi_R = 0, \alpha_1\tau = 5$ (dot-dot-dashed curve); (c) $\alpha_3/\alpha_1 = 1, \gamma_T/\alpha_1 = 1 \times 10^{-5}, \gamma_M/\alpha_1 = \gamma_R/\alpha_1 = 10, \chi_M/\chi_R = 1, \chi_T/\chi_R = 500, \alpha_1\tau = 0$ (solid curve), $\alpha_1\tau = 5.5$ (dashed curve), $\alpha_1\tau = 7$ (dotted curve), $\alpha_1\tau = 10$ (dot-dashed curve), $\chi_T/\chi_R = 0$ and $\alpha_1\tau = 10$ (dot-dot-dashed curve).

Then we consider the difference among the three Markovian stochastic models. Form Eq. (3.53), we can see that in the limit of $\gamma_R, \gamma_M >> \alpha_1$, $\alpha_3 >> \gamma_T$ APD is short of the amplitude decay factor $\exp(-2\alpha_2\tau)$ while the amplitude decay factor of GAM is two times of that of CFM. Thus the signal intensity of GAM is largest of all and that of PDM is smallest [see Fig. 3.14(a)]. However, on one hand, if the thermal grating is much efficient than the molecular-reorientation grating, the same large thermal background obscures the different amplitude decay of the three models [see Fig. 3.14 (b)]. On the other hand, the difference of the three models can also be eliminated by the time delay method, as shown in Fig. 3.14(c) and Fig. 3.15.

For Rayleigh-enhanced FWM, the thermal effect of an absorbing medium can be suppressed by a time-delayed method. Physically, the resonant signal

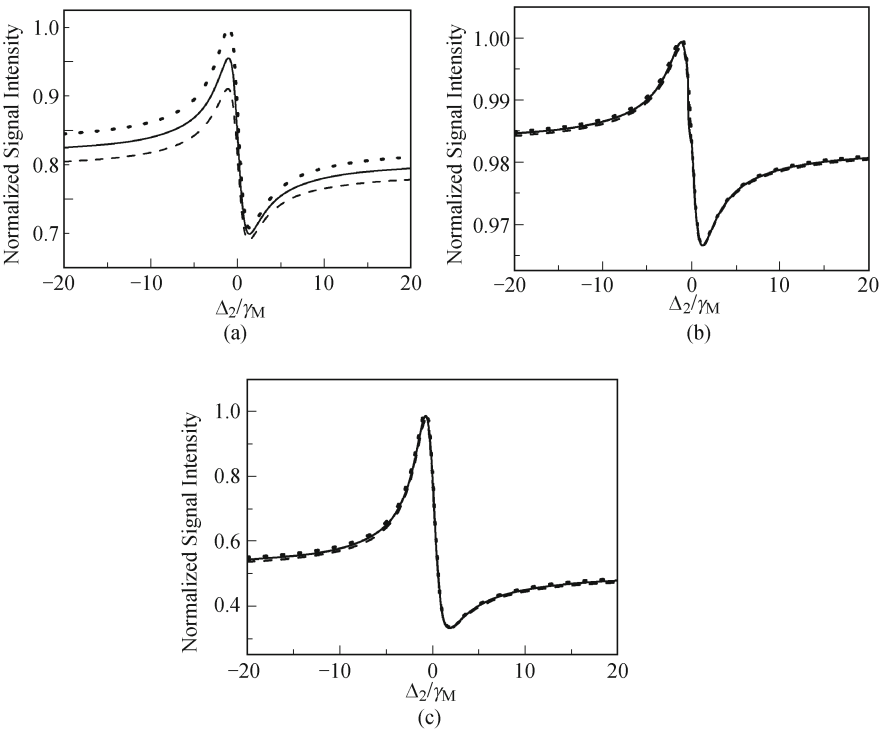

Fig. 3.14. The Raman-enhanced FWM spectra versus Δ_2/γ_R in an absorbing medium for (a) $\gamma_M/\alpha_1 = 10, \gamma_R/\alpha_1 = 10, \gamma_T/\alpha_1 = 1 \times 10^{-5}, \alpha_3/\alpha_1 = 1, \chi_M/\chi_R = 1, \chi_T/\chi_R = 5, \tau = 0$, (b) $\gamma_M/\alpha_1 = 10, \gamma_R/\alpha_1 = 10, \gamma_T/\alpha_1 = 1 \times 10^{-5}, \alpha_3/\alpha_1 = 1, \chi_M/\chi_R = 1, \chi_T/\chi_R = 50, \tau = 0$, (c) $\gamma_M/\alpha_1 = 10, \gamma_R/\alpha_1 = 10, \gamma_T/\alpha_1 = 1 \times 10^{-5}, \alpha_3/\alpha_1 = 1, \chi_M/\chi_R = 1, \chi_T/\chi_R = 5, \gamma_R\tau = 2$. The three curves represent the CFM (solid curve), PDM (dashed curve) and GAM (dotted curve), respectively.

originate from the order parameters both $Q_{RM}(\boldsymbol{r}, t)$ and $Q_{RT}(\boldsymbol{r}, t)$, while the non-resonant background come from both $Q_{M1}(\boldsymbol{r}, t)$ and $Q_{T1}(\boldsymbol{r}, t)$. The establishment of order parameters of the gratings involves integration effects. On the other hand, the fact that the effects of field correlation on the order parameters $Q_{RM}(\boldsymbol{r}, t)(Q_{RT}(\boldsymbol{r}, t))$ and $Q_{M1}(\boldsymbol{r}, t)(Q_{T1}(\boldsymbol{r}, t))$ are different. $Q_{RM}(\boldsymbol{r}, t)(Q_{RT}(\boldsymbol{r}, t))$ is induced by beams 2 and 3, the phase factor of $[E_1'(\boldsymbol{r}, t)]^* E_3(\boldsymbol{r}, t)$ is a random variable. Due to the integration effect, the fast random fluctuation of phase leads to the reduction of the amplitude which is almost independent of delay time τ. In contrast, since $Q_{M1}(\boldsymbol{r}, t)(Q_{T1}(\boldsymbol{r}, t))$ is induced by beams 1 and 2, the incident laser fields is coherent when $\tau = 0$ while incoherent when $\alpha_i\tau >> 1$, the establishment of gratings is dependent on the delay time τ directly. In particular, we consider the condition $\gamma_M >> \alpha_{1,3} >> \gamma_T$. On one hand the incident fields have broadband line width compared to thermal grating when $\alpha_{1,3} >> \gamma_T$. The effect of integration is to wash out the thermal grating with large time delay while no washout

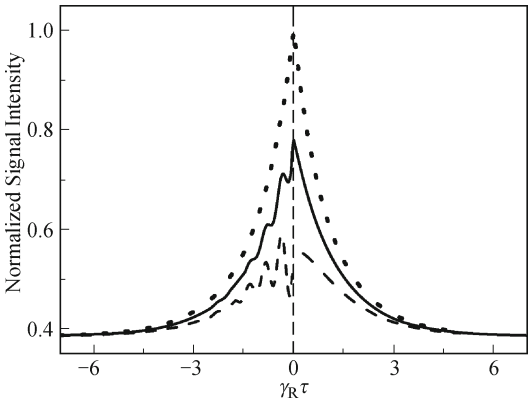

Fig. 3.15. The Raman-enhanced FWM spectra versus $\tau\gamma_R$ for $\chi_M/\chi_R = 0.05, \gamma_M/\gamma_R = 1, \chi_T/\chi_R = 0.1, \gamma_T/\gamma_R = 0.000001, \alpha_3/\gamma_R = 0.1, \alpha_1/\gamma_R = 0.4, \Delta_2/\gamma_R = 13$. The three curves represent the chaotic field (solid curve), phase-diffusion field (dashed curve), Gaussian-amplitude field (dotted curve).

takes place when $\tau = 0$. On the other hand the fields have narrowband line width compared to molecular-reorientation grating when $\gamma_M >> \alpha_{1,3}$. In this case the material gratings have very short relaxation times and respond to the phase fluctuation of the fields almost immediately. Therefore, although the phase of P_{M1} and P_{RM} fluctuate randomly, the relative phase between them is fixed. The ratio between the non-resonant background induced by molecular-reorientation grating and the resonant signal is almost independent of τ.

3.2.3 The Raman and Rayleigh-enhanced Nonlinear Susceptibility in cw Limit

For simplicity, with cw laser beams we can assume that $u_i(t) = 1$ in Eqs. (3.43) – (3.44). Under such condition the Raman-enhanced nonlinear polarization

$$P_A = P_{M2} + P_{T2} + P_R = S_2(\boldsymbol{r}) \left(\chi_M + \chi_T - \frac{\chi_R \gamma_R}{\Delta_2 + \mathrm{i}\gamma_R} \right) \tag{3.54}$$

can be obtained. Therefore, the third-order susceptibility for Raman-enhanced FWM consists of a Raman-resonant term and a non-resonant background that originates from the molecular-reorientation grating and the thermal grating. i.e.,

$$\chi_A = \chi_M + \chi_T - \frac{\chi_R \gamma_R}{\Delta_2 + \mathrm{i}\gamma_R}. \tag{3.55}$$

We decompose the nonlinear susceptibility χ_A into a real and an imaginary part, i.e., $\chi_A = \chi'_A + \mathrm{i}\chi''_A$, with $\chi'_A = \chi_M + \chi_T - \chi_R \gamma_R \Delta_2 / (\Delta_2^2 + \gamma_R^2)$ and

$\chi''_A = \chi_R\gamma_R^2/(\Delta_2^2+\gamma_R^2)$. The real and imaginary parts are odd and even functions, respectively. We express χ_A as $|\chi_A|\exp i\theta_A = |\chi_A|\cos\theta_A + i|\chi_A|\sin\theta_A$, with θ_A given by $\theta_A(\Delta_2) = \tan^{-1}(\chi''_A/\chi'_A)$. We can see in Fig. 3.16 (a) the phase angle θ_A becomes more asymmetrical about $\Delta_2 = 0$ and the value changes more drastically when χ_M/χ_R and χ_T/χ_R decrease.

Similarly, we can obtain the Rayleigh-enhanced nonlinear polarization with cw laser beams, i.e.,

$$\begin{aligned} P_B &= P_{M1} + P_{T1} + P_{RM} + P_{RT} \\ &= S_1(\boldsymbol{r})\left(\chi_M + \chi_T + \frac{\chi_M\gamma_M}{\gamma_M - \mathrm{i}\Delta_1} + \frac{\chi_T\gamma_T}{\gamma_T - \mathrm{i}\Delta_1}\right). \end{aligned} \tag{3.56}$$

Therefore, the third-order susceptibility for the Rayleigh-enhanced FWM consists of a Rayleigh-resonant term and a non-resonant background that originates from the molecular-reorientation grating and the thermal grating, i.e.,

$$\chi_B = \chi_M + \chi_T + \frac{\chi_M\gamma_M}{\gamma_M - \mathrm{i}\Delta_1} + \frac{\chi_T\gamma_T}{\gamma_T - \mathrm{i}\Delta_1}. \tag{3.57}$$

We decompose the nonlinear susceptibility χ_B into a real and an imaginary part, i.e., $\chi_B = \chi'_B + i\chi''_B$, with $\chi'_B = \chi_M + \chi_T + \gamma_M^2\chi_M/(\gamma_M^2 + \Delta_1^2) + \gamma_T^2\chi_T/(\gamma_T^2 + \Delta_1^2)$ and $\chi''_B = \chi_M\gamma_M\Delta_1/(\gamma_M^2 + \Delta_1^2) + \chi_T\gamma_T\Delta_1/(\gamma_T^2 + \Delta_1^2)$. In contrast of Raman-enhanced nonlinear susceptibility χ_A, the real and imaginary parts are even and odd functions, respectively. We express χ_B as $|\chi_B|\exp\mathrm{i}\theta_B = |\chi_B|\cos\theta_B + \mathrm{i}|\chi_B|\sin\theta_B$, with θ_B given by $\theta_B(\Delta_1) = \tan^{-1}(\chi''_B/\chi'_B)$. From Fig. 3.16(b) we can see that $\theta_B(\Delta_1)$ is an odd function and the value changes more drastically when χ_T/χ_M decreases.

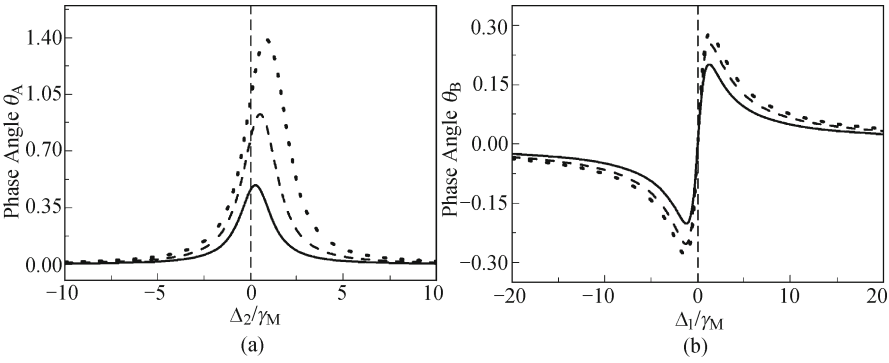

Fig. 3.16. (a) The phase angle θ_A versus frequency detuning Δ_2/γ_R for $\chi_M/\chi_R = \chi_T/\chi_R = 1$ (solid curve), $\chi_M/\chi_R = \chi_T/\chi_R = 0.5$ (dashed curve), $\chi_M/\chi_R = \chi_T/\chi_R = 0.3$(dotted curve); (b) Phase angle θ_B versus frequency detuning Δ_1/γ_M for $\gamma_T/\gamma_M = 1\times10^{-6}\chi_T/\chi_M = 1$ (solid curve), $\chi_T/\chi_M = 0.5$ (dashed curve), $\chi_T/\chi_M = 0.3$ (dotted curve).

Figure 3.17 shows the phase dispersion of the Raman and Rayleigh-enhanced FWM including the influence of the color-locked noisy field for

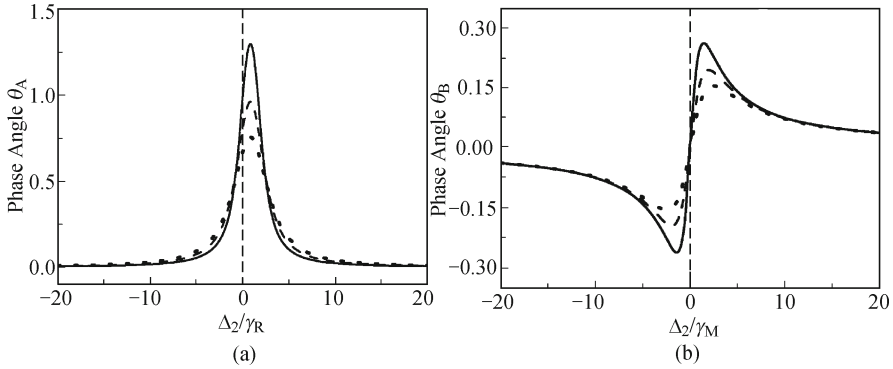

Fig. 3.17. (a) The phase angle θ_A versus frequency detuning Δ_2/γ_R for $\alpha_2/\gamma_R = 1, \alpha_2/\gamma_R = 0.5, \alpha_2/\gamma_R = 0$. The three curves represent $\alpha_2/\gamma_R = 0$ (solid curve), $\alpha_2/\gamma_R = 0.5$ (dashed curve), and $\alpha_2/\gamma_R = 1$ (dotted curve); (b) the phase angle θ_B versus frequency detuning Δ_1/γ_M for $\gamma_T/\gamma_M = 1 \times 10^{-6}$ $\alpha_1/\gamma_M = 1, \alpha_1/\gamma_M = 0.5, \alpha_1/\gamma_M = 0$. The three curves represent $\alpha_1/\gamma_M = 0$ (solid curve), $\alpha_1/\gamma_M = 0.5$ (dashed curve), and $\alpha_1/\gamma_M = 1$ (dotted curve).

$\tau > 0$. In Fig. 3.17(a), the phase angle θ_A shows the absorption-like shape. On the other hand, in Fig. 3.17(b), we can see the phase angle θ_B shows the dispersion-like shape. In the cw limit $(\alpha_i = 0), \chi_A(\chi_B)$ for $\tau < 0$ and $\tau > 0$ become same, i.e., $\chi_A = \chi_M + \chi_T - \chi_R\gamma_R/(\Delta_2 + i\gamma_R)$ and $\chi_B = \chi_M + \chi_T + \chi_M\gamma_M/(\gamma_M - \mathrm{i}\Delta_1) + \chi_T\gamma_T/(\gamma_T - i\Delta_1)$. $\chi'_A(\Delta_2)$ is neither an odd nor an even function, and $\chi''_A(\Delta_2)$ is an even function. So θ_A shows the asymmetric absorption-like line shape. $\theta_B(\Delta_1)$ is an odd function (dispersion-like shape) for even function $\chi'_B(\Delta_1)$ and odd function $\chi''_B(\Delta_1)$. Comparison with the broadband $(\alpha_i/\gamma_M >> 1, \alpha_i/\gamma_T >> 1)$, the dispersion and absorption under narrowband condition are independent on the linewidth α_i and time delay τ, which correspond to the nonmodified nonlinear dispersion and absorption of the material. In Fig. 3.17, θ_A and θ_B decrease and the line shape becomes broad versus increasing linewidth, which shows the influence of the field-correlation of the color-locked noisy light. Thus, by virtue of the ultrafast modulation processes within the femtosecond regime, one can optimize the nonlinear susceptibilities and obtain the efficient nonlinear optical signals, which have potential applications in achieving better nonlinear optical materials and opt-electronic devices.

3.2.4 Homodyne Detection of ASPB

For the macroscopic system where phase matching takes place this signal must be drawn from the total third-order polarization $P^{(3)}$ developed on one chromophore multiplied by the $(P^{(3)})^*$ that is developed on another chromophore which must be located elsewhere in space (with summation over

all such pairs). The bichromophoric model is particularly important to the noisy light spectroscopies where the stochastic averaging at the signal level must be carried out. The ASPB signal is proportional to the average of the absolute square of $P^{(3)}$ over the random variable of the stochastic process, so that the signal $I(\Delta_i, \tau) \propto \langle |P^{(3)}|^2 \rangle = \langle P^{(3)}(P^{(3)})^* \rangle$ contains different terms in the fourth- and second-order coherence function of $u_i(t)$ in phase conjugation geometry. In general, the ASPB of homodyne detection (at the intensity level) can be viewed as built of the sum of three contributions: (i) the τ-independent or dependent auto-correlation terms of ω_1 component, which include $u_1(t)$ fourth-order and $u_3(t)$ two-order Markovian stochastic correlation functions; (ii) the τ-independent or dependent auto-correlation terms of ω_2 component, which include $u_2(t)$ fourth-order and $u_3(t)$ two-order Markovian stochastic correlation functions; (iii) the τ-dependent cross-correlation terms between ω_1 and ω_2 components, which include $u_1(t), u_2(t)$ and $u_3(t)$ second-order Markovian stochastic correlation functions. Different Markovian stochastic models of the laser field only affect the fourth-, not second-order correlation functions

For the Raman ASPB, we have the total third-order polarization $P^{(3)} = P_A + P_D = (P_{M2} + P_{T2} + P_R) + (P_{M1} + P_{T1})$. Therefore, the homodyne-detection signal $I(\Delta_2, \tau)$ contains $5 \times 5 = 25$ different terms which include the non-resonant terms of the ω_1 molecular-reorientation and thermal gratings, terms of the ω_2 molecular-reorientation and thermal gratings and Raman resonant mode, and the cross-correlation terms between FWM and Raman-enhanced FWM.

The composite noisy beam 1 (beam 2) is treated as one whose spectrum is simply a sum of two Lorentzians. The high-order decay cross-correlation terms are reasonably neglected in our treatment. After performing the tedious integration from Eqs. (3.43)–(3.47), in the limit $\gamma_M, \gamma_R >> \alpha_1, \alpha_2$, $\alpha_3 >> \gamma_T$ we obtain

$$\begin{aligned} I_{ASPB}(\Delta_2, \tau) \propto \eta^2 \exp(-2\mathrm{i}\Delta\boldsymbol{k} \cdot \boldsymbol{r}) \{ & [1 + n_4 \exp(-2\alpha_2|\tau|)]\, L_5 + L_6 \} + \\ & \left\{ [1 + n_4 \exp(-2\alpha_1|\tau|)] \times \chi_M^2 + L_7 \right\} + \\ & \eta L_8 \{ \exp[\mathrm{i}\Delta\boldsymbol{k} \cdot \boldsymbol{r} - \mathrm{i}(\omega_1 + \omega_2)|\tau|] \chi_A^* + \\ & \exp[-\mathrm{i}\Delta\boldsymbol{k} \cdot \boldsymbol{r} + \mathrm{i}(\omega_1 + \omega_2)|\tau|] \chi_A \}\,. \end{aligned} \tag{3.58}$$

Here,

$$\begin{aligned} L_5 &= \chi_M^2 - 2\gamma_R \Delta_2 \chi_M \chi_R / (\gamma_R^2 + \Delta_2^2) + \gamma_R^2 \chi_R^2 / (\gamma_R^2 + \Delta_2^2), \\ L_6 &= \exp(-2\alpha_2|\tau|)[2\chi_M \chi_T - 2\gamma_R \Delta_2 \chi_T \chi_R / (\gamma_R^2 + \Delta_2^2) + \chi_T^2], \\ L_7 &= \exp(-2\alpha_1|\tau|)(2\chi_M \chi_T + \chi_T^2), \\ L_8 &= (\chi_M + \chi_T) \exp[-(\alpha_1 + \alpha_2)|\tau|], \\ \chi_A &= \chi_M + \chi_T - \chi_R \gamma_R / (\Delta_2 + i\gamma_R), \\ \eta &= \varepsilon_2'(\varepsilon_2)^* / \varepsilon_1(\varepsilon_1')^*, \\ \Delta\boldsymbol{k} &= (\boldsymbol{k}_1 - \boldsymbol{k}_1') - (\boldsymbol{k}_2' - \boldsymbol{k}_2), \end{aligned}$$

and n_4 equals 1, 0, 2 for the CFM, PDM, and GAM, respectively.

First for CFM, the Raman ASPB versus τ shows the attosecond scale modulation with a sum frequency $\omega_1 + \omega_2$ and damping rates α_1 and α_2 [see Fig. 3.18]. The constant term $\gamma_R^2\chi_R^2/(\gamma_R^2 + \Delta_2^2)$ in Eq. 3.58, which is independent of the relative time-delay between twin beams 1 and 2, originates from the phase fluctuation of the chaotic fields, while the purely decay terms including these factors $\exp(-2\alpha_1|\tau|), \exp(-2\alpha_2|\tau|)$ come from amplitude fluctuation of the chaotic fields.

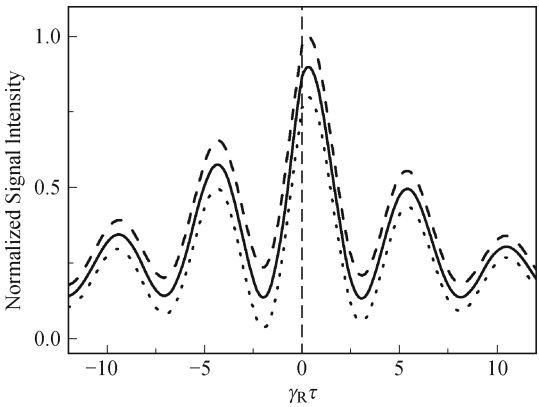

Fig. 3.18. The Raman ASPB signal intensity versus $\gamma_R\tau$ for $\chi_M/\chi_R = 0.2$, $\gamma_M/\gamma_R = 1, \chi_T/\chi_R = 1, \gamma_T/\gamma_R = 1 \times 10^{-6}, \alpha_2/\gamma_R = 0.05, \alpha_1/\gamma_R = \alpha_3/\gamma_R = 0.1, \Delta_2 = 0, r = 0, \omega_1/\alpha_2 = 11.99, \omega_2/\alpha_2 = 12.75$ and $\eta = 1$. The three curves represent the chaotic field (solid curve), Gaussian-amplitude field (dashed curve), and phase-diffusion field (dotted curve).

Secondary for PDM the temporal behavior of the beat signal only reflects the characteristic of the lasers. The result is remarkably different from that based on a chaotic model. It is short of the purely auto-correlation decay terms including these factors $\exp(-2\alpha_1|\tau|)$ and $\exp(-2\alpha_2|\tau|)$, which are shown to be particularly insensitive to the phase fluctuation of the Markovian stochastic light fields. The drastic difference of the results also exists in the higher-order correlation on Rayleigh ASPB when three Markovian stochastic models are employed [32].

Third for GAM, contrast to CFM and PDM, the decay term includes the factors $2\exp(-2\alpha_1|\tau|)$ and $2\exp(-2\alpha_2|\tau|)$. The τ-dependent term of Gaussian-amplitude field is larger than that of the chaotic field and the phase-diffusion field (Fig. 3.18), which originates from the amplitude fluctuation of the Markovian stochastic field. The physical explanation for this is that the Gaussian-amplitude field undergoes stronger intensity fluctuations than a chaotic field. On the other hand, the intensity (amplitude) fluctuations of the Gaussian-amplitude field or the chaotic field are always much larger than the pure phase fluctuations of the phase-diffusion field.

For the Rayleigh ASPB, we have the total third-order polarization $P^{(3)} =$

$P_B+P_C=(P_{M1}+P_{RM}+P_{T1}+P_{RT})+(P_{M2}+P_{T2})$. Therefore, the homodyne-detection signal $I(\Delta_1,\tau)$ contains $6\times6=36$ different terms which include the non-resonant terms of the ω_2 molecular-reorientation and thermal gratings, terms of the ω_1 molecular-reorientation and thermal gratings and Rayleigh resonant mode, and the cross-correlation terms between FWM and Rayleigh-enhanced FWM.

After performing the tedious integration of Eqs. (3.43 – 3.46, 3.48, 3.49), in the limit $\gamma_M,\gamma_R >> \alpha_1,\alpha_2,\alpha_3 >> \gamma_T$, we can obtain

$$\begin{aligned} I_{ASPB}(\Delta_1,\tau) \propto & \{[1+n_4\exp(-2\alpha_1|\tau|)]L_9+L_{10}\}+ \\ & \eta^2\exp(-2\mathrm{i}\Delta\boldsymbol{k}\cdot\boldsymbol{r})\left\{[1+n_4\exp(-2\alpha_2|\tau|)]\chi_M^2+L_{11}\right\}+ \\ & \eta L_8\left\{\exp[\mathrm{i}\Delta\boldsymbol{k}\cdot\boldsymbol{r}-\mathrm{i}(\omega_1+\omega_2)|\tau|]\chi_B+\right. \\ & \left.\exp[-\mathrm{i}\Delta\boldsymbol{k}\cdot\boldsymbol{r}+\mathrm{i}(\omega_1+\omega_2)|\tau|]\chi_B^*\right\}. \end{aligned} \tag{3.59}$$

Here, $L_9=[1+3\gamma_M^2/(\gamma_M^2+\Delta_1^2)]\chi_M^2, L_{10}=\exp(-2\alpha_1|\tau|)\{[1+\gamma_M^2/(\gamma_M^2+\Delta_1^2)]2\chi_M\chi_T+\chi_T^2\}, L_{11}=\exp(-2\alpha_2|\tau|)(2\chi_M\chi_T+\chi_T^2)$, and $\chi_B=\chi_M+\chi_T+\chi_M\gamma_M/(\gamma_M-i\Delta_1)$.

Similarly with the Raman ASPB, first for the CFM, under such condition the Rayleigh ASPB shows the attosecond scale modulation with a sum frequency $\omega_1+\omega_2$ and damping rates α_1 and α_2 [see Fig. 3.19]. On the other hand, since Rayleigh-enhance FWM exhibits spectral symmetry, which is different from the Raman-enhance FWM, Eq. (3.59) also shows symmetry about Δ_1.

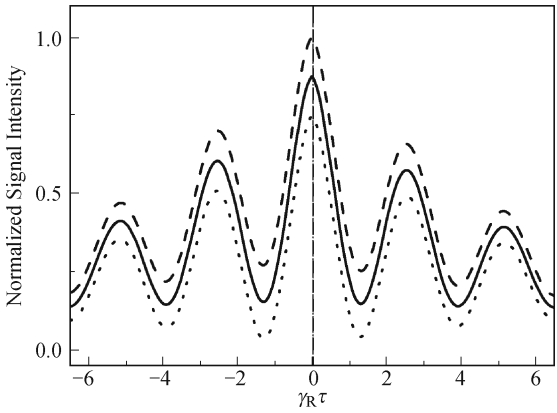

Fig. 3.19. The Rayleigh ASPB signal intensity versus $\gamma_M\tau$ for $\chi_M/\chi_T=1,\gamma_T/\gamma_M=1\times10^{-6},\alpha_1/\gamma_M=\alpha_2/\gamma_M=\alpha_3/\gamma_M=0.1,\Delta_1=0,r=0,\omega_1/\alpha_1=12.08,\omega_2/\alpha_1=11.99$ and $\eta=1$. The three curves represent the chaotic field (solid curve), Gaussian-amplitude field (dashed curve), and phase-diffusion field (dotted curve).

Similarly, secondary for the PDM, equation (3.59) of the PDM is insensitive to the intensity fluctuation (amplitude fluctuation) and is short of decay terms $\exp(-2\alpha_1|\tau|)$ and $\exp(-2\alpha_2|\tau|)$, which is remarkably different from

the result based on a chaotic model. It indicates that the τ-independent term $3\gamma_M^2/(\gamma_M^2+\Delta_1^2)$ comes from the phase fluctuation.

Third for GAM due to the amplitude fluctuation of the Markovian stochastic field, Rayleigh ASPB of the GAM has the τ-dependent factors $2\exp(-2\alpha_1|\tau|)$ and $2\exp(-2\alpha_2|\tau|)$ which is larger than that of the CFM and PDM.

We find that as the Rayleigh-mode detuning $\Delta_1 = 0$, the temporal behavior of the Rayleigh ASPB is symmetric with the maximum of the beat signal at $\tau = 0$ (Fig. 3.19), while as the Raman-mode detuning $\Delta_2 = 0$, that of the Raman ASPB is asymmetric with the maximum of the beat signal shifted from $\tau = 0$ (Fig. 3.18). In fact it is induced by phase shift of Raman phase-angle θ_A and Rayleigh phase-angle θ_B, respectively. When $\Delta_1 = \Delta_2 = 0$, we have $\theta_A \neq 0$ and $\theta_B = 0$, as shown in Fig. 3.16.

For the coexisting of the Raman and Rayleigh ASPB, we have the total third-order polarization $P^{(3)} = P_A + P_B = P_{M2} + P_{T2} + P_R + P_{M1} + P_{RM} + P_{T1} + P_{RT}$. Therefore, the homodyne-detection signal $I(\Delta_1, \tau) \propto \langle (P_A + P_B)(P_A^* + P_B^*)\rangle$ contains $7 \times 7 = 49$ different terms which include the terms of the ω_2 molecular-reorientation and thermal gratings and Raman resonant mode, the terms of the ω_1 molecular-reorientation and thermal gratings and Rayleigh resonant mode, and the cross-correlation terms between Raman-enhanced and Rayleigh-enhanced FWM

By virtue of the result of the integration in pure Raman and pure Rayleigh ASPB shown above, in the limit $\gamma_M, \gamma_R >> \alpha_1, \alpha_2, \alpha_3 >> \gamma_T$ we obtain

$$\begin{aligned} I_{ASPB}(\Delta_1, \Delta_2, \tau) \propto \eta^2 \exp(-2\mathrm{i}\Delta\boldsymbol{k}\cdot\boldsymbol{r})\left\{[1 + n_4\exp(-2\alpha_2|\tau|)]\, L_5 + L_6\right\} + \\ \left\{[1 + n_4\exp(-2\alpha_1|\tau|)] \times L_9 \;\; + L_{10}\right\} + \\ \eta\exp[-(\alpha_1+\alpha_2)|\tau|]\left\{\exp[\mathrm{i}\Delta\boldsymbol{k}\cdot\boldsymbol{r} - \mathrm{i}(\omega_1+\omega_2)|\tau|]\chi_A^*\chi_B + \right. \\ \left. \exp[-\mathrm{i}\Delta\boldsymbol{k}\cdot\boldsymbol{r} + \mathrm{i}(\omega_1+\omega_2)|\tau|]\chi_A\chi_B^*\right\}. \end{aligned} \tag{3.60}$$

First for the CFM, we can see that Raman and Rayleigh-enhanced FWM auto-correlation terms coexist and they interfere with each other and generate the ASPB. The auto-correlation terms decay with a time constant α_1^{-1} and α_2^{-1} while the cross-correlation term is modulated with a sum frequency $\omega_1 + \omega_2$ and a damping rate $\alpha_1 + \alpha_2$. The interferometric contrast ratio of interferogram mainly determined the cross-correlation between Raman and Rayleigh-enhanced FWM processes is equally sensitive to the amplitude and phase fluctuations of the chaotic fields. Physically, the chaotic field has the property of photon bunching, which can affect any multi-photon process when the higher-order correlation function of the field plays an important role.

Secondary for PDM, in the case of $\gamma_M >> \alpha_1, \alpha_2, \alpha_3 >> \gamma_T$ of PDM, both the Raman and Rayleigh-enhanced FWM auto-correlation terms in Eq. (3.60) are short of the purely decay factors $\exp(-2\alpha_1|\tau|)$ and $\exp(-2\alpha_2|\tau|)$. The phase-diffusion model predicts the ASPB signal has a damping oscillation of the attosecond sum-frequency around a constant value (Fig. 3.20). We can understand this phenomenon as follows. The interference pattern of

the $\omega_1(\omega_2)$ component of the twin composite beams 1 and 2 will be in constant motion with a characteristic time constant $\alpha_1^{-1}(\alpha_2^{-1})$ when $|\tau|$ is much longer than the laser coherence time τ_c. On the other hand, the relaxation time of the molecular-reorientation grating is so short that the induced gratings $G_{M1}(G_{T1}, G_{RM}, G_{RT})$ and $G_{M2}(G_{T2}, G_R)$ always follow the interference pattern, and therefore the beat signal will never decay. Furthermore, the relative phase between $G_{M1}(G_{T1}, G_{RM}, G_{RT})$ and $G_{M2}(G_{T2}, G_R)$ fluctuates randomly, which makes spatial interference between them impossible. In this case the beat signal intensity is simply the summation of the signal intensity originating from $G_{M1}(G_{T1}, G_{RM}, G_{RT})$ and $G_{M2}(G_{T2}, G_R)$. In contrast, the fringes of $G_{M1}(G_{T1}, G_{RM}, G_{RT})$ and $G_{M2}(G_{T2}, G_R)$ are stable when $|\tau| < \tau_c$. The constructive or destructive interference between $G_{M1}(G_{T1}, G_{RM}, G_{RT})$ and $G_{M2}(G_{T2}, G_R)$ enhances or reduces the beat signal and gives rise to the oscillation of the beat signal intensity as τ varies. We note that the main difference between the phase-diffusion model and the chaotic model is that amplitude fluctuation exists in the latter case. When $|\tau| < \tau_c$, the coincidence of the intensity spikes of the two composite beams gives an additional enhancement of the beat signal for the chaotic model (see Fig. 3.20).

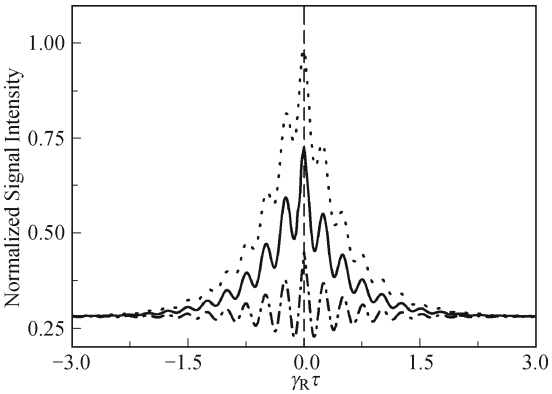

Fig. 3.20. The coexisting of Raman and Rayleigh ASPB signal intensity versus $\alpha_1\tau$ for $\chi_M/\chi_R = 10, \gamma_M/\alpha_1 = \gamma_R/\alpha_1 = 10, \chi_T/\chi_R = 1, \gamma_T/\alpha_1 = 1 \times 10^{-5}, \alpha_2/\alpha_1 = \alpha_3/\alpha_1 = 1, \Delta_1 = \Delta_2 = 0, r = 0, \omega_1/\alpha_1 = 12.08$ and $\omega_2/\alpha_1 = 12.75, \eta = 0.3$.The three curves represent the chaotic field (solid curve), Gaussian-amplitude field (dotted curve), and phase-diffusion field (dot-dashed curve).

Third for GAM, apparently, the τ-dependent term $2\exp(-2\alpha_1|\tau|)$ and $2\exp(-2\alpha_2|\tau|)$ of Gaussian-amplitude field is larger than that of the chaotic field and the phase-diffusion field and the signal intensity of $\tau = 0$ for GAM is largest of three models (Fig. 3.20). However, Eq. (3.60) shows that the τ-independent terms of three models are the same and do not include the factor χ_T. On the other hand, though the polarization beat signal is shown to be particularly sensitive to the statistical properties of Markovian stochastic light fields with arbitrary bandwidth, different Markovian stochastic models

of the laser field only affect the fourth-, not second-order correlation functions. The cross-correlation terms between Raman and Rayleigh-enhanced polarization of three models are the same. Therefore, Fig. 3.20 shows that ASPB signal intensities in CFM, PDM and GAM versus τ oscillate with the same frequency $\omega_1 + \omega_2$ and have the same background.

Next, we discuss the chromophore $P^{(3)}$ difference between the ASPB with a phase-conjugation geometry and the sum-frequency UMS [25] with a self-diffraction geometry from a physical viewpoint. The frequencies and wave vectors of the sum-frequency UMS signal are $\omega_A = 2\omega_2 - \omega_2, \omega_B = 2\omega_1 - \omega_1$ and $\boldsymbol{k}_A = 2\boldsymbol{k}_2 - \boldsymbol{k}_2', \boldsymbol{k}_B = 2\boldsymbol{k}_1' - \boldsymbol{k}_1$, respectively, which means that a photon is absorbed from each of the two mutually correlated fluctuating pump beams. On the other hand, the frequencies and wave vectors of the ASPB signal are $\omega_A = \omega_2 - \omega_2 + \omega_3, \omega_B = \omega_1 - \omega_1 + \omega_3$ and $\boldsymbol{k}_A = \boldsymbol{k}_1 - \boldsymbol{k}_1' + \boldsymbol{k}_3, \boldsymbol{k}_B = \boldsymbol{k}_2' - \boldsymbol{k}_2 + \boldsymbol{k}_3$, respectively (Fig. 3.9), therefore photons are absorbed from and emitted to the mutually correlated fluctuating twin beams 1 and 2, respectively. This difference between the ASPB and the UMS has profound influence on the field-correlation effects. We note that the role of beams 1 and 2 are interchangeable in the UMS, this interchangeable feature also makes the second-order coherence function theory failure in the UMS. Due to $\langle u(t_1)u(t_2)\rangle = 0$, the absolute square of the stochastic average of the polarization $|\langle P^{(3)}\rangle|^2$ cannot be used to describe the temporal behavior of the sum-frequency UMS [25]. Our higher-order correlation (intensity correlation) treatment also is of vital importance in the sum-frequency UMS. Moreover, because of $\langle u_i(t)\rangle = 0$ and $\langle u_i^*(t)\rangle = 0$, the absolute square of the stochastic average of the polarization $|\langle P^{(3)}\rangle|^2$, which involves second-order coherence function of $u_i(t)$, cannot be used to describe the temporal behavior of the ASPB. The sixth-order correlation theory $\langle |P^{(3)}|^2\rangle$ reduces to the second-order correlation theory $|\langle P^{(3)}\rangle|^2$ in the case that the laser pulse width is much longer than the laser coherence time. The second-order coherence function theory is valid when we are only interested in the τ-dependent part of the beating signal [14]. Therefore, the fourth-order coherence function theory is of vital importance in ASPB. The application of higher-order results to the difference-frequency polarization beat experiment yielded a better fit to the data than an expression involving only second-order coherence [9]. Apparently the nature of the Markovian field has a more drastic effect on the outcome of the experiment than the underlying molecular nonlinearity. Since real laser fields are unlikely to behave like the pure three field classes, a complicated superposition of various types of responses is to be expected.

3.2.5 Heterodyne Detection of ASPB

Since optical fields oscillate too quickly for direct detection and they must be measured "in quadrature"-as photons. One common measurement tech-

niques, such as FWM measured at its quadrature $I_A = P_A P_A^*$ or $I_B = P_B P_B^*$, yield only absolute values of the nonlinear susceptibility $|\chi_A|^2$ or $|\chi_B|^2$. Thus, all phase information in the nonlinear susceptibility is lost. The second way to achieve quadrature is the phase-sensitive method used for optical heterodyne detection. We introduce another reference FWM signal designed in frequency and wave vector (see Fig. 3.9) to conjugate (go into quadrature) in its complex representation with the new polarization of interest. Both the measured signal and the reference signal have the same frequency, thus, they interfere directly at the detector and generate ASPB by changing the relative time delay τ between the measured beam and the reference beam. In other words the total signal is modulated by the time delay. In the heterodyne case that the reference signal is larger than the measured signal, the phase information is retained and one can take a full measure of the complex susceptibility through adjusting the time delay τ. The phase of the complex induced polarization determines how its energy will partition between Class I (the absorbed or emitted active spectroscopy) and Class II (the passive spectroscopy with a new launched field) spectroscopy.

For the Raman-enhanced FWM signal with polarization P_A, we introduce the reference FWM signal with polarization P_D. Thus the Raman ASPB signal is proportional to the average of the absolute square of $P_A + P_D$ over the random variable of the stochastic process, so that the signal intensity $I(\Delta_2, \tau) \propto \langle |P_A + P_D|^2 \rangle = \langle (P_A + P_D)(P_A^* + P_D^*) \rangle = \langle P_A P_A^* \rangle + \langle P_D P_D^* \rangle + \langle P_A P_D^* \rangle + \langle P_D P_A^* \rangle$ contains $5 \times 5 = 25$ different terms in the fourth- and second-order coherence function of $u_i(t)$ in phase conjugation geometry. In general, the Raman ASPB (at the intensity level) can be viewed as built of the sum of three contributions: (i) the τ-independent or dependent auto-correlation terms $I_A(\Delta_2, \tau) = \langle P_A P_A^* \rangle$ (i.e., Raman-enhanced FWM) of ω_2 nonresonant molecular-reorientation and thermal gratings, and Δ_2 Raman resonant mode, which include the $u_2(t)$ fourth-order and the $u_3(t)$ second-order Markovian stochastic correlation functions; (ii) the τ-independent or dependent nonresonant auto-correlation terms $I_D(\tau) = \langle P_D P_D^* \rangle$ of ω_1 molecular-reorientation and thermal gratings, which include $u_1(t)$ fourth-order and $u_3(t)$ second-order Markovian stochastic correlation functions; (iii) the τ-dependent cross-correlation terms $I_{A,D}(\Delta_2, \tau) = \langle P_A P_D^* \rangle + \langle P_D P_A^* \rangle$ between Raman-enhanced FWM and NDFWM processes, which include $u_1(t)$, $u_2(t)$ and $u_3(t)$ second-order Markovian stochastic correlation functions. Different Markovian stochastic models of the laser field only affect the fourth-, not second-order correlation functions. Therefore, the cross-correlation terms are the same for three Markovian stochastic models. Furthermore, by virtue of the cross-correlation term $I_{A,D}(\Delta_2, \tau)$ we can obtain the third-order susceptibilities for the Raman-enhanced FWM $\chi_A = \chi_M + \chi_T - \chi_R \gamma_R / [\Delta_2 + \mathrm{i}(\alpha_2 + \alpha_3 + \gamma_R)]$ and for the reference NDFWM $\chi_D = \chi_M + \chi_T$ theoretically. The real and imaginary parts of χ_A are odd and even functions, i.e., $\chi_A' = \chi_M + \chi_T - \chi_R \gamma_R \Delta_2 / [\Delta_2^2 + (\alpha_2 + \alpha_3 + \gamma_R)^2]$ and $\chi_A'' = \chi_R \gamma_R (\alpha_2 + \alpha_3 + \gamma_R) / [\Delta_2^2 + (\alpha_2 + \alpha_3 + \gamma_R)^2]$, respectively.

In heterodyne detection, we assume $I_D(\tau) >> I_A(\Delta_2, \tau)$ that at intensity level, in other words, we let $\eta << 1$, thus we have $I \propto I_D(\tau) + I_{A,D}(\Delta_2, \tau)$. For simply, in the limit of $\gamma_R, \gamma_M >> \alpha_1, \alpha_2, \alpha_3 >> \gamma_T$ and based on the chaotic, the phase-diffusion and the real Gaussian fields, we have the Raman ASPB signals, respectively,

$$\begin{aligned} &\gamma_R, \gamma_M >> \alpha_1, \alpha_2, \alpha_3 >> \gamma_T, \\ &I_{ASPB}(\Delta_2, \tau) \propto \left\{[1 + n_4 \exp(-2\alpha_1|\tau|)]\chi_M^2 + L_7\right\} + \\ &\qquad \eta L_8 \left\{\exp[\mathrm{i}\Delta\boldsymbol{k}\cdot\boldsymbol{r} - \mathrm{i}(\omega_1+\omega_2)|\tau|]\chi_A^* + \right. \\ &\qquad \left. \exp[-\mathrm{i}\Delta\boldsymbol{k}\cdot\boldsymbol{r} + \mathrm{i}(\omega_1+\omega_2)|\tau|]\chi_A\right\}. \end{aligned} \tag{3.61}$$

We express χ_A as $|\chi_A|\exp(i\theta_A) = |\chi_A|\cos\theta_A + i\,|\chi_A|\sin\theta_A$, with θ_A (see Fig. 3.16). Therefore, we have

$$I_{ASPB}(\Delta_2, \tau) \propto I_D(\tau) + 2L_8\eta|\chi_A|\cos[-\Delta\boldsymbol{k}\cdot\boldsymbol{r} + (\omega_1+\omega_2)|\tau| + \theta_A]. \tag{3.62}$$

Equation (3.62) indicates that the reference FWM signal $I_D(\tau)$ and the factor $2L_8\eta$ are independent of Δ_2, while the heterodyne signal is modulated with a sum-frequency $\omega_1 + \omega_2$ as τ is varied, in addition, the phase of the oscillation depends on the phase θ_A of the measured third-order susceptibility χ_A. If we adjust the time delay τ such that $-\Delta\boldsymbol{k}\cdot\boldsymbol{r} + (\omega_1+\omega_2)|\tau| = 2n\pi$, then

$$I_{ASPB}(\Delta_2, \tau) \propto I_D(\tau) + 2L_8\eta|\chi_A|\cos\theta_A \propto I_D(\tau) + 2L_4\eta\chi_A'. \tag{3.63}$$

However, if $-\Delta\boldsymbol{k}\cdot\boldsymbol{r} + (\omega_1+\omega_2)|\tau| = (2n-1/2)\pi$, we have

$$I_{ASPB}(\Delta_2, \tau) \propto I_D(\tau) + 2L_8\eta|\chi_A|\sin\theta_A \propto I_D(\tau) + 2L_4\eta\chi_A''. \tag{3.64}$$

In other words, by changing the time delay τ between beams 1 and 2 we can obtain the real and the imaginary parts of the Raman-enhanced susceptibility χ_A.

The heterodyne detection spectra versus Δ_2/γ_R of the Raman ASPB is shown in Fig.3.21. We can see that the spectra have the profile of the real and imaginary parts of the Raman resonance with comparable backgrounds. On the other hand, the spectra of the CFM, PDM, and GAM are the same as those of cw beam, as shown in Fig.3.21. However, the background of the three Markovian models is smaller than that of the cw beam due to the phase fluctuation.

For the Rayleigh-enhanced FWM signal with polarization P_B, we introduce the reference FWM signal with polarization P_C. Thus the Rayleigh ASPB signal is proportional to the average of the absolute square of $P_B + P_C v$, so that the signal intensity $I(\Delta_1, \tau) \propto \langle|P_B + P_C|^2\rangle = \langle(P_B + P_C)(P_B^* + P_C^*)\rangle$ contains $6 \times 6 = 36$ different terms where $I_B(\Delta_1, \tau) = \langle P_B P_B^*\rangle$ and $I_C(\tau) = \langle P_C P_C^*\rangle$ include the $u_1(t)$ and the $u_2(t)$ fourh-order Markovian stochastic correlation functions, respectively, while $I_{B,C}(\Delta_1, \tau) = \langle P_B P_C^*\rangle + \langle P_B P_C^*\rangle$

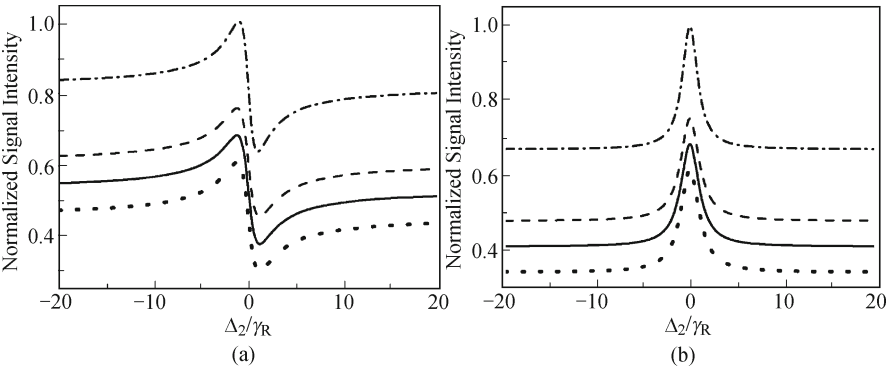

Fig. 3.21. The heterodyne detection spectra versus Δ_2/γ_R of the Raman ASPB with (a) $\tau = (-2\pi + \Delta\boldsymbol{k}\cdot\boldsymbol{r})/(\omega_1+\omega_2)$ for the real part of χ_A, while with (b) $\tau = (-2\pi+\pi/2+\Delta\boldsymbol{k}\cdot\boldsymbol{r})/(\omega_1+\omega_2)$ for the imaginary part of χ_A. The other parameters are for $\chi_M/\chi_R = 0.1, \gamma_M/\alpha_1 = \gamma_R/\alpha_1 = 10, \chi_T/\chi_R = 0.1, \gamma_T/\alpha_1 = 1\times10^{-5}, \alpha_2/\alpha_1 = \alpha_3/\alpha_1 = 1, \eta = 0.1$. Theoretical curves are shown in CFM (solid curve), PDM (dotted curve), GAM (dashed curve), and the model with cw laser beams (dot-dashed curve).

include $u_i(t)$ second-order Markovian stochastic correlation functions. We know that different Markovian stochastic models of the laser field only affect the fourth-, not second-order correlation functions. Therefore, the cross-correlation terms $I_{B,C}(\Delta_1,\tau)$ are the same for three Markovian stochastic models, from which we can obtain the third-order susceptibilities for the Rayleigh-enhanced FWM $\chi_B = \chi_M + \chi_T + \chi_M\gamma_M/[(\alpha_1+\alpha_3+\gamma_M) - \mathrm{i}\Delta_1] + \chi_T\gamma_T/[(\alpha_1+\alpha_3+\gamma_T) - \mathrm{i}\Delta_1]$ and for the reference NDFWM $\chi_C = \chi_M + \chi_T$ theoretically. The real and imaginary parts of χ_B are even and odd functions, i.e., $\chi'_B = \chi_M + \chi_T + \gamma_M(\alpha_1+\alpha_3+\gamma_M)\chi_M/[(\alpha_1+\alpha_3+\gamma_M)^2+\Delta_1^2] + \gamma_T(\alpha_1+\alpha_3+\gamma_T)\chi_T/[(\alpha_1+\alpha_3+\gamma_T)^2+\Delta_1^2]$ and $\chi''_B = \chi_M\gamma_M\Delta_1/[(\alpha_1+\alpha_3+\gamma_M)^2+\Delta_1^2] + \chi_T\gamma_T\Delta_1/[(\alpha_1+\alpha_3+\gamma_T)^2+\Delta_1^2]$, respectively.

In heterodyne detection, we assume $I_C(\tau) >> I_B(\Delta_1,\tau)$ at intensity level, in other words, we let $\eta >> 1$, thus we have $I(\Delta_1,\tau) \propto I_C(\tau) + I_{B,C}(\Delta_1,\tau)$. Under the condition of $\gamma_M >> \alpha_1,\alpha_2,\alpha_3 >> \gamma_T$ we have the Rayleigh ASPB signals for the three Markovian models, respectively, i.e.,

$$\begin{aligned} I_{ASPB}(\Delta_1,\tau) \propto \eta^2\exp(-2\mathrm{i}\Delta\boldsymbol{k}\cdot\boldsymbol{r})\left\{[1+n_4\exp(-2\alpha_2|\tau|)]\chi_M^2 \quad + L_{11}\right\} + \\ \eta L_8\left\{\exp[\mathrm{i}\Delta\boldsymbol{k}\cdot\boldsymbol{r} - \mathrm{i}(\omega_1+\omega_2)|\tau|]\chi_B + \exp[-\mathrm{i}\Delta\boldsymbol{k}\cdot\boldsymbol{r} + \right. \\ \left.\mathrm{i}(\omega_1+\omega_2)|\tau|]\chi_B^*\right\}. \end{aligned} \tag{3.65}$$

We express χ_B as $|\chi_B|\exp(\mathrm{i}\theta_B) = |\chi_B|\cos\theta_B + \mathrm{i}\,|\chi_B|\sin\theta_B$, with θ_B (see Fig. 3.18). From Eqs. (3.65) we have

$$I_{ASPB}(\Delta_1,\tau) \propto I_C(\tau) + 2L_8\eta|\chi_B|\cos[\Delta\boldsymbol{k}\cdot\boldsymbol{r} - (\omega_1+\omega_2)|\tau| + \theta_B]. \tag{3.66}$$

Equation (3.66) indicates that the reference FWM signal $I_C(\tau)$ and the factor $2L_8\eta$ are independent of Δ_1. The heterodyne signal is modulated with

a sum-frequency $\omega_1+\omega_2$ as τ is varied, in addition, the phase of the oscillation depends on the phase θ_B of the measured third-order susceptibility χ_B. If we adjust the time delay τ such that $\Delta\boldsymbol{k}\cdot\boldsymbol{r}-(\omega_1+\omega_2)|\tau|=2n\pi$, then

$$I_{ASPB}(\Delta_1,\tau)\propto I_C(\tau)+2L_8\eta|\chi_B|\cos\theta_B\propto I_C+2L_4\eta\chi'_B. \tag{3.67}$$

However, if $\Delta\boldsymbol{k}\cdot\boldsymbol{r}-(\omega_1+\omega_2)|\tau|=(2n-1/2)\pi$, we have

$$I_{ASPB}(\Delta_1,\tau)\propto I_C(\tau)+2L_8\eta|\chi_B|\sin\theta_B\propto I_C(\tau)+2L_4\eta\chi''_B. \tag{3.68}$$

In other words, by changing the time delay τ between beams 1 and 2 we can obtain the real and the imaginary parts of the Rayleigh-enhanced susceptibility χ_B.

Figure 3.22 shows the heterodyne detection spectra versus Δ_1/γ_M of the Rayleigh ASPB. We can see that the spectra have the profile of the real and imaginary parts of the Rayleigh resonance with comparable backgrounds. It is clear that the curves represent the even function for the real part and the odd function for the imaginary part of χ_B, which is just opposite to those of the Raman-enhanced susceptibility χ_A (see Fig. 3.21). On the other hand, similarly, for heterodyne signal of Rayleigh ASPB the spectra of cw beams are the same as those of CFM, PDM and GAM. However, the spectra of cw beams have the largest background while the spectra of PDM have the smallest background due to the absence of the amplitude fluctuation.

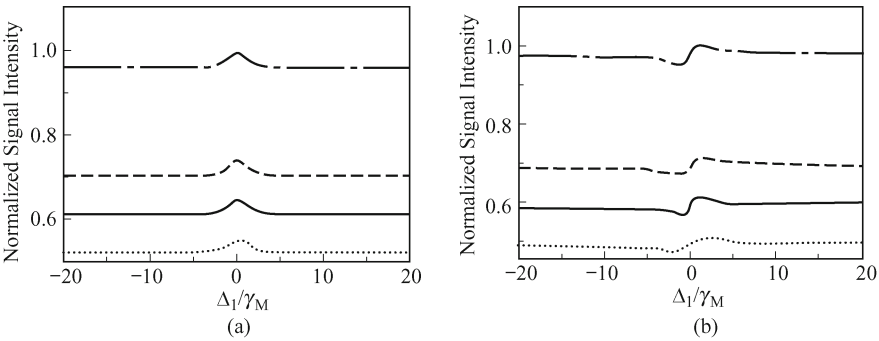

Fig. 3.22. The heterodyne detection spectra versus Δ_1/γ_M of the Rayleigh ASPB with (a) $\tau=(-2\pi+\Delta\boldsymbol{k}\cdot\boldsymbol{r})/(\omega_1+\omega_2)$ for the real part of χ_B, while with (b) $\tau=(-2\pi+\pi/2+\Delta\boldsymbol{k}\cdot\boldsymbol{r})/(\omega_1+\omega_2)$ for the imaginary part of χ_B. The other parameters are for $\chi_M/\chi_T=1,\gamma_M/\alpha_1=10,\gamma_T/\alpha_1=1\times10^{-5},\alpha_2/\alpha_1=\alpha_3/\alpha_1=1,\eta=10$. Theoretical curves are shown in CFM (solid curve), PDM (dotted curve), GAM (dashed curve) and the model with cw laser beams (dot-dashed curve).

The Raman and Rayleigh-enhanced FWM can coexist in the same experiment system. In fact, they can be considered as the reference signal mutually. Thus, the coexisting of Raman and Rayleigh ASPB signal is proportional to the average of the absolute square of P_A+P_B, so that the signal intensity $I(\Delta_1,\Delta_2,\tau)\propto\langle|P_A+P_B|^2\rangle$ contains $7\times7=49$ different terms where

$I_{A,B}(\Delta_1, \Delta_2, \tau) = \langle P_A P_B^* \rangle + \langle P_A P_B^* \rangle$ include $u_i(t)$ second-order Markovian stochastic correlation functions. The cross-correlation terms are the same for three Markovian stochastic models but more complex than that of the pure Rayleigh and Raman ASPB. It consists of the third-order susceptibilities for the Rayleigh and Raman-enhanced FWM, i.e., χ_A and χ_B.

In heterodyne detection, we assume $I_C(\tau) >> I_B(\Delta_1, \tau)$ at intensity level, in other words, we let $\eta >> 1$, thus we have $I(\Delta_1, \tau) \propto I_C(\tau) + I_{B,C}(\Delta_1, \tau)$. Under the condition of $\gamma_M >> \alpha_1, \alpha_2, \alpha_3 >> \gamma_T$ we have the Rayleigh ASPB signals for the three Markovian models, respectively, i.e.

Under the condition of $\gamma_R, \gamma_M >> \alpha_1, \alpha_2, \alpha_3 >> \gamma_T$ and $\eta >> 1$ we have the coexisting Raman and Rayleigh ASPB signals for the three Markovian models, respectively, i.e.,

$$I_{ASPB}(\Delta_1, \Delta_2, \tau) \propto \eta^2 \exp(-2\mathrm{i}\Delta\boldsymbol{k} \cdot \boldsymbol{r}) \{[1 + n_4 \exp(-2\alpha_2|\tau|)] L_5 + L_6\} + \eta \exp[-(\alpha_1 + \alpha_2)|\tau|] \times \{\exp[\mathrm{i}\Delta\boldsymbol{k} \cdot \boldsymbol{r} - \mathrm{i}(\omega_1 + \omega_2)|\tau|] \times \chi_A^* \chi_B + \exp[-\mathrm{i}\Delta\boldsymbol{k} \cdot \boldsymbol{r} + i(\omega_1 + \omega_2)|\tau|] \chi_A \chi_B^*\}. \quad (3.69)$$

Therefore, from Eq. (3.69) we have

$$I(\Delta_1, \Delta_2, \tau) \propto I_A(\Delta_2, \tau) + 2\eta \exp[-(\alpha_1 + \alpha_2)|\tau|] |\chi_A||\chi_B| \times \cos[\Delta\boldsymbol{k} \cdot \boldsymbol{r} - (\omega_1 + \omega_2)|\tau| - \theta_A + \theta_B]. \quad (3.70)$$

Here, $I_A(\Delta_2, \tau) = \eta^2 \exp(-2\mathrm{i}\Delta\boldsymbol{k} \cdot \boldsymbol{r}) \{[1 + n_4 \exp(-2\alpha_2|\tau|)] L_5 + L_6\}$. Equation (3.70) indicates that the reference Raman-enhanced FWM signal $I_A(\Delta_2, \tau)$, the factor $2\eta \exp[-(\alpha_1 + \alpha_2)|\tau|]|\chi_A|$ and θ_A are independent of Δ_1. If we adjust the time delay τ such that $\Delta\boldsymbol{k} \cdot \boldsymbol{r} - (\omega_1 + \omega_2)|\tau| - \theta_A = 2n\pi$ [Fig. 3.23 (a, c)], then

$$I(\Delta_1, \Delta_2, \tau) \propto I_A(\Delta_2, \tau) + 2\eta \exp[-(\alpha_1 + \alpha_2)|\tau|] |\chi_A||\chi_B| \cos\theta_B = I_A(\Delta_2, \tau) + 2\eta \exp[-(\alpha_1 + \alpha_2)|\tau|] |\chi_A| \chi_B'. \quad (3.71)$$

However, if $\Delta\boldsymbol{k} \cdot \boldsymbol{r} - (\omega_1 + \omega_2)|\tau| - \theta_A = (2n - 1/2)\pi$ [see Fig. 3.23 (b,d)], we have

$$I(\Delta_1, \Delta_2, \tau) \propto I_A(\Delta_2, \tau) + 2\eta \exp[-(\alpha_1 + \alpha_2)|\tau|] |\chi_A||\chi_B| \sin\theta_B = I_A(\Delta_2, \tau) + 2\eta \exp[-(\alpha_1 + \alpha_2)|\tau|] |\chi_A| \chi_B''. \quad (3.72)$$

In other words, by changing the time delay τ between beams 1 and 2 we can obtain the real and the imaginary parts of the Rayleigh-enhanced susceptibility χ_B. Figure 3.23 (a, b) show the heterodyne detection spectra versus Δ_1/γ_M of the coexisting Raman and Rayleigh ASPB with large η. They are the same as Fig. 3.22 and only the reference backgrounds are different. Therefore, the spectra show the profile of the real and imaginary parts of the Rayleigh-enhanced susceptibility. Similarly, under the condition of $\gamma_R, \gamma_M >> \alpha_1, \alpha_2, \alpha_3 >> \gamma_T$ and $\eta << 1$ we have the coexisting Raman

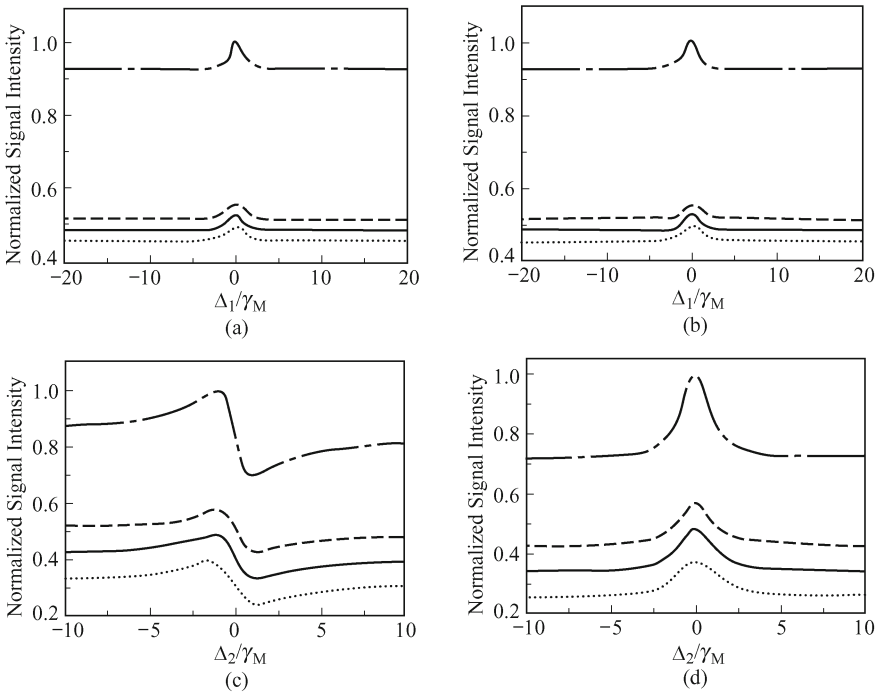

Fig. 3.23. The heterodyne detection spectra versus Δ_1/γ_M of the coexisting ASPB for $\chi_M/\chi_R = 0.1, \gamma_M/\alpha_1 = \gamma_R/\alpha_1 = 10, \chi_T/\chi_R = 0.1, \gamma_T/\alpha_1 = 1 \times 10^{-5}, \alpha_2/\alpha_1 = \alpha_3/\alpha_1 = 1$, (a) $\eta = 10, \Delta_2/\gamma_R = 10, \tau = (2n\pi + \Delta\boldsymbol{k}\cdot\boldsymbol{r})/(\omega_1+\omega_2)$ for the real part of χ_B, (b) $\eta = 10, \Delta_2/\gamma_R = 10, \tau = (2n\pi + \pi/2 + \Delta\boldsymbol{k}\cdot\boldsymbol{r})/(\omega_1+\omega_2)$ for the imaginary part of χ_B, (c) $\eta = 0.1, \Delta_1/\gamma_R = 1, \tau = (2n\pi + \Delta\boldsymbol{k}\cdot\boldsymbol{r})/(\omega_1+\omega_2)$ for the real part of χ_A, (d) $\eta = 0.1, \Delta_1/\gamma_R = 1, \tau = (2n\pi + \Delta\boldsymbol{k}\cdot\boldsymbol{r})/(\omega_1+\omega_2)$ for the imaginary part ofχ_A. Here $n = -10\ 000$.

and Rayleigh ASPB signals for the three Markovian models, respectively, i.e.,

$$I(\Delta_1,\Delta_2,\tau) \propto \{[1+n_4\exp(-2\alpha_1|\tau|)]L_9 + L_{10}\} + \eta\exp[-(\alpha_1+\alpha_2)|\tau|] \times \{\exp[\mathrm{i}\Delta\boldsymbol{k}\cdot\boldsymbol{r} - \mathrm{i}(\omega_1+\omega_2)|\tau|]\chi_A^*\chi_B + \exp[-\mathrm{i}\Delta\boldsymbol{k}\cdot\boldsymbol{r} + \mathrm{i}(\omega_1+\omega_2)|\tau|]\chi_A\chi_B^*\}\,. \tag{3.73}$$

From Eq. (3.73), we have

$$I(\Delta_1,\Delta_2,\tau) \propto I_B(\Delta_1,\tau) + 2\eta\exp[-(\alpha_1+\alpha_2)|\tau|]|\chi_B||\chi_A| \times \cos[\Delta\boldsymbol{k}\cdot\boldsymbol{r} - (\omega_1+\omega_2)|\tau| - \theta_A + \theta_B]. \tag{3.74}$$

Here, $I_B\,(\Delta_1,\tau) = [1+n_4\exp(-2\alpha_1|\tau|)]L_9 + L_{10}$. The reference Rayleigh-enhanced FWM signal $I_B(\Delta_1,\tau)$, the factor $2\eta\exp[-(\alpha_1+\alpha_2)|\tau|]|\chi_B|$ and θ_B are independent of Δ_2. If we adjust the time delay τ such that $\Delta\boldsymbol{k}\cdot\boldsymbol{r} -$

$(\omega_1+\omega_2)|\tau|+\theta_B = 2n\pi$ [see Fig. 3.23(c) and Fig. 3.24(a)–(c)], then

$$\begin{aligned} I(\Delta_1,\Delta_2,\tau) &\propto I_B(\Delta_1,\tau)+2\eta\exp[-(\alpha_1+\alpha_2)|\tau|]|\chi_B||\chi_A|\cos\theta_A \\ &= I_B(\Delta_1,\tau)+2\eta\exp[-(\alpha_1+\alpha_2)|\tau|]|\chi_B|\chi'_A. \end{aligned} \tag{3.75}$$

However, if $\Delta\boldsymbol{k}\cdot\boldsymbol{r}-(\omega_1+\omega_2)|\tau|+\theta_B=(2n+1/2)\pi$ [see Fig. 3.23 (d) and Fig. 3.24 (d)–(f)], we have

$$\begin{aligned} I(\Delta_1,\Delta_2,\tau) &\propto I_B(\Delta_1,\tau)+2\eta\exp[-(\alpha_1+\alpha_2)|\tau|]|\chi_B||\chi_A|\sin\theta_A \\ &= I_B(\Delta_1,\tau)+2\eta\exp[-(\alpha_1+\alpha_2)|\tau|]|\chi_B|\chi''_A. \end{aligned} \tag{3.76}$$

In other words, by changing the time delay τ between beams 1 and 2 we can obtain the real and the imaginary parts of the Raman-enhanced susceptibility χ_A. Figure 3.23 (c), (d) shows the heterodyne detection spectra versus Δ_2/γ_R of the coexisting Raman and Rayleigh ASPB with small η. They are the same as Fig. 3.21 and only the reference backgrounds are different. Therefore, the spectra show the profile of the real and imaginary parts of the Raman-enhanced susceptibility. In addition, Fig. 3.24 shows the spectra versus Δ_1/γ_R and Δ_2/γ_R. The spectra mainly show the profile of Rayleigh-enhanced FWM

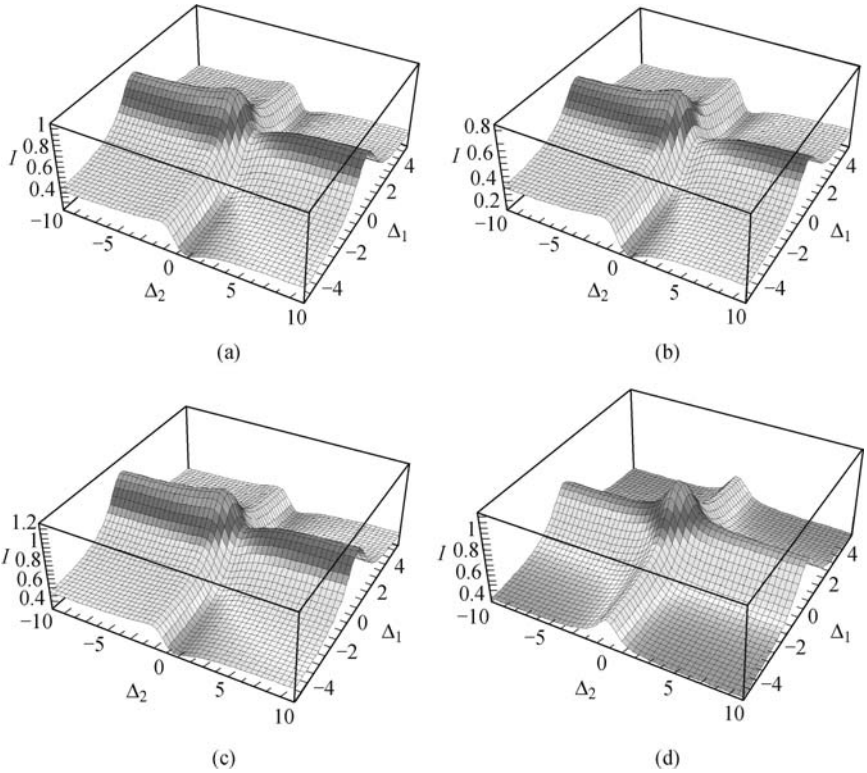

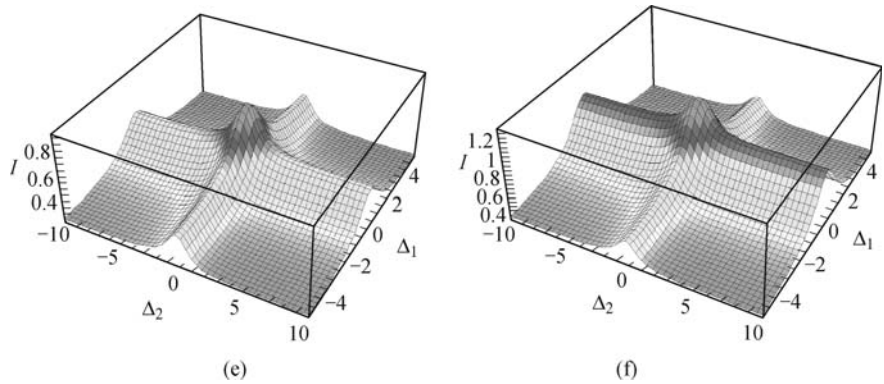

Fig. 3.24. The heterodyne detection spectra versus Δ_1/γ_R and Δ_2/γ_R of the coexisting ASPB for $\eta = 0.1, \chi_M/\chi_R = 0.1, \gamma_M/\alpha_1 = \gamma_R/\alpha_1 = 10, \chi_T/\chi_R = 0.1, \gamma_T/\alpha_1 = 1 \times 10^{-5}, \alpha_2/\alpha_1 = \alpha_3/\alpha_1 = 1$ with $\tau = (2n\pi - \Delta\boldsymbol{k}\cdot\boldsymbol{r} - \theta_B)/(\omega_1 + \omega_2)$ and $(2n\pi + \pi/2 - \Delta\boldsymbol{k}\cdot\boldsymbol{r} - \theta_B)/(\omega_1 + \omega_2)$ for $\tau > 0$ for the real and imaginary part of χ_A. Theoretical curves represent the (a) and (d) CFM, (b) and (e) PDM, (c) and (f) GAM. Here $n = -10\ 000$. Adopted from Ref. [20].

signal versus Δ_1/γ_R. As $\Delta_1/\gamma_R = -5$ and τ satisfies the condition of $\Delta\boldsymbol{k}\cdot\boldsymbol{r} - (\omega_1 + \omega_2)|\tau| + \theta_B = 2n\pi$, the spectra versus Δ_2/γ_R show the real part of the Raman-enhanced susceptibility, while as $\Delta_1/\gamma_R = -5$ and τ satisfies the condition of $\Delta\boldsymbol{k}\cdot\boldsymbol{r} - (\omega_1 + \omega_2)|\tau| + \theta_B = 2n\pi + \pi/2$, the spectra versus Δ_2/γ_R show the imaginary part of the Raman-enhanced susceptibility.

3.2.6 Discussion and Conclusion

Based on three stochastic models, the subtle Markovian, field-correlation effects have been investigated in Raman and Rayleigh-enhanced FWM, homodyne and heterodyne-detected ASPB. All of these can be understood in the time and frequency domains.

The ASPB with double-frequency color-locking noisy light has an advantage [21]. Based on three stochastic models, the subtle Markovian field correlation effects have been investigated in the homodyne or heterodyne detected ASPB. The physical explanation for this is that the Gaussian-amplitude field undergoes stronger intensity fluctuations than a chaotic field. On the other hand, the intensity (amplitude) fluctuations of the Gaussian-amplitude field or the chaotic field are always much larger than the pure phase fluctuations of the phase-diffusion field. In fact, the difference of the spectra of the three Markovian stochastic models of the laser field can be controlled. Specifically: (i) at zero delay time it shows the drastic difference for three Markovian stochastic fields, while the PDM and GAM results are the same as those of the CFM in the limit of $|\tau| \to \infty$. It means that the fluctuation of both the amplitude and the phase of the field have no effect in the limit of $|\tau| \to \infty$.

(ii) Under narrowband linewidth ($\alpha_i << \gamma_M, \gamma_T$), the difference value of the signal intensity at $\Delta_{1,2} = 0$ among the three models is dramatic. However, it becomes smaller under broadband linewidth ($\alpha_i >> \gamma_M, \gamma_T$). That is to say, stochastic correlation effects are sensitive to narrowband linewidth. (iii) As χ_T is small, the difference of the spectra of the three models is drastically, while the non-resonant thermal background is much larger than the resonant signal that the contribution from thermal grating dominates the FWM spectra and obscure the difference of the spectra of the three models.

Both Raman and Rayleigh-enhanced FWM are proposed for studying ultrafast processes. In contrast to the conventional time-domain technique, they are frequency-domain techniques, the time resolution is independent of the incident laser pulse width. Therefore, the Raman and Rayleigh-enhanced FWM can be employed for the measurement of ultrafast longitudinal relaxation time in the frequency-domain [6]. Based on the field-correlation effects, this technique can be applied even to an absorbing medium if a time-delayed method. There are two mechanisms involved. First, the nonlinear interaction of beams 1 and 2 with the same frequencies gives rise to the static gratings (molecular-reorientation and thermal gratings). The FWM signal is the result of the diffraction of beam 3 by the grating. Second, beams 2 and 3 with different frequencies build up the moving gratings (Raman and Rayleigh modes). If the grating lifetime is larger than the time it needs to move over one spatial period, then destructive interference occurs during engraving and erases the grating.

Physically, for the coexisting Rayleigh and Raman-enhanced FWM processes, the resonant signals originate from the order parameters $Q_{RM,RT,R}(\boldsymbol{r}, t)$ while the non-resonant background come from both $Q_{M1,2}(\boldsymbol{r}, t)$ and $Q_{T1,2}(\boldsymbol{r}, t)$. The establishment of order parameters of the gratings involves integration effects. In the broadband case (i.e., $\alpha_{1,2,3} >> \gamma_T, \gamma_M, \gamma_R$), the effect of integration is to wash out the gratings. At zero time delay no washout takes place in the establishment of $Q_{M1,2}(\boldsymbol{r}, t)$ and $Q_{T1,2}(\boldsymbol{r}, t)$ because the phase factor $\boldsymbol{\phi}_{1,2}$ of $A_{1,2}(t - t')[A_{1,2}(t - t' - \tau)]^*$ is stationary. On the other hand, the phase factors $\boldsymbol{\phi}_{3a}$ of $A_3(t - t')[A_1(t - t' - \tau)]^*$ and $\boldsymbol{\phi}_{3b}$ of $A_3(t - t')[A_2(t - t')]^*$ are random variable which fluctuate with characteristic time scales $(\alpha_1 + \alpha_3)^{-1}$ and $(\alpha_2 + \alpha_3)^{-1}$, respectively. Because of the integration effect, the fast random fluctuation of $\boldsymbol{\phi}_{3a,b}$ leads to the reduction of the amplitude of $Q_{RM,RT,R}(r, t)$. Therefore, the coexisting Rayleigh and Raman-enhanced FWM spectra are dominated by a large non-resonant background when $\tau = 0$. However, the coexisting Rayleigh and Raman-enhanced FWM spectra are quite different in the limit of $\alpha|\tau| >> 1$. Similar to $Q_{RM,RT,R}(\boldsymbol{r}, t), Q_{M1,2}(\boldsymbol{r}, t)$ and $Q_{T1,2}(\boldsymbol{r}, t)$ is now induced by mutually incoherent fields. If $\alpha_{1,2} = \alpha_3$, then the influences of the integration effect on them are equal [see Fig. 3.10(b)]. Thus, the non-resonant backgrounds are suppressed effectively. We now consider the case when $\gamma_T, \gamma_M, \gamma_R >> \alpha_{1,2,3}$. In this case, the gratings have quite short relaxation times, therefore, they can respond to the phase fluctuations of the fields almost immediately.

More specifically, $A_{1,2}(t-t')[A_{1,2}(t-t'-\tau)]^*, A_3(t-t')[A_1(t-t'-\tau)]^*$ and $A_3(t-t')[A_2(t-t')]^*$ are slowly varying functions in comparison with $\exp(-\gamma_{M,T,R}t')$ which have a peak at $t'=0$, and therefore can be approximated as $A_{1,2}(t)[A_{1,2}(t)]^*, A_3(t)[A_1(t)]^*$ and $A_3(t)[A_2(t)]^*$, respectively. We have $P_{M1,2}(\boldsymbol{r},t) \propto \chi_M \gamma_M A_{1,2}(t)[A_{1,2}(t)]^* A_3(t) \int_0^\infty \exp(-\gamma_M t')\mathrm{d}t'$, $P_{T1,2}(\boldsymbol{r},t) \propto \chi_T \gamma_T A_{1,2}(t)[A_{1,2}(t)]^* A_3(t) \int_0^\infty \exp(-\gamma_T t')\mathrm{d}t'$, $P_{RM,RT}(\boldsymbol{r},t) \propto \chi_{M,T}\gamma_{M,T} A_1(t)[A_1(t)]^* A_3(t) \int_0^\infty \exp[-(\gamma_{M,T} - \mathrm{i}\Delta_1)t']\mathrm{d}t'$ and $P_R(\boldsymbol{r},t) \propto \chi_R \gamma_R A_2(t)[A_2(t)]^* A_3(t) \int_0^\infty \exp[-(\gamma_R - \mathrm{i}\Delta_2)t']\mathrm{d}t'$. The above equation indicates that the Rayleigh and Raman-enhanced FWM spectra are independent of τ.

The Raman-enhanced FWM the Raman vibration is excited by the simultaneous presence of two incident beams whose frequency difference equals the Raman excitation frequency and the Raman-enhanced FWM signal is the result of this resonant excitation. In contrast, the Rayleigh-enhanced FWM process is a nonresonant process and a frequency-domain nonlinear laser spectroscopy with high frequency resolution determined by the laser linewidth. Moreover, the Rayleigh-enhanced FWM is a non-resonant process with no energy transfer between the lights and the medium when the frequency difference between two incident beams equals zero. The resonant structure in the Rayleigh-enhanced FWM spectrum is the result of induced moving grating. This difference is also reflected in their line shapes. Specifically, unlike the Raman-enhanced FWM spectrum, which is asymmetric due to the interference between the resonant signal and the nonresonant background, the lineshape of the Rayleigh-enhanced FWM is always symmetric.

In this section, we employ the ASPB to obtain the real and the imaginary parts of the competition Raman and Rayleigh resonance (see Fig. 3.23) based on the polarization interference between coexistence of the Raman and Rayleigh-enhanced FWM processes. Specifically, since Raman and Rayleigh-enhanced FWM signals propagate along the same optical path, in the heterodyne detection of ASPB, we purposely introduce them as the reference signals of each other. Our method is based on polarization interference between two competition Raman and Rayleigh-enhanced FWM processes. The detuning Δ_1 and Δ_2 control the intensity and phase angle of the Rayleigh and Raman-enhanced susceptibilities χ_B and χ_A, respectively. We need scanning one detuning to show the phase dispersion of χ_B or χ_A with proper time delay, while the other one only to change the reference background. If Δ_1 or Δ_2 change large enough, the value of θ_B or θ_A will equal zero and the coexisting Raman and Rayleigh ASPB will convert into the pure Raman or Rayleigh ASPB.

One possible experimental candidate for the proposed system is the sample of benzene in which oxazine dye is dissolved. The strong vibration mode of benzene is at $\Omega_R = 992\ \mathrm{cm}^{-1}$. The Raman mode can be activated in benzene.

In addition, the static molecular-reorientation grating and the corresponding Rayleigh mode also exist in such material. On the other hand, the oxazine dye introduces the static thermal grating and the corresponding Rayleigh mode. Therefore, we can study the competition of Raman and Rayleigh-enhanced FWM and ASPB mediated by thermal effects.

Such an experiment can be done by using three nanosecond dye lasers (color-locking) or femtosecond ultrashort lasers (phase-locking) D1, D2, and D3. D1 and D2 are used to generate frequencies at ω_1 and ω_2, respectively. A beam splitter is used to combine the ω_1 and ω_2 components for the pump beams. Beam 1 and beam 2 intersected in the sample with a small angle between them. The relative time delay between beams 1 and 2 can be varied by an optical delay line controlled by a stepping motor. Beam 3, used as the probe beam and originating from D3 with frequency ω_3, propagating along the direction opposite that of beam 1.

More specifically, (i) for the coexisting Raman and Rayleigh ASPB, D1, D2, and D3 have the wavelengths $\lambda_1 = 561$ nm, $\lambda_2 = 532$ nm and $\lambda_3 = 561$ nm, respectively. Thus, the Raman mode is activated by the interaction of beam 3 and ω_2 component of beam 2. As a result, Raman-enhanced FWM is generated. On the other hand, the Rayleigh-enhanced FWM is generated due to the interaction of beam 3 and ω_1 component of beam 2. Both ω_1 and ω_2 frequencies can be varied. (ii) For the Raman ASPB, D1, D2, and D3 have the wavelength $\lambda_1 = 565$ nm, $\lambda_2 = 532$ nm and $\lambda_3 = 561$ nm, respectively. Thus only the Raman mode is activated by the interaction of beam 3 and ω_2 component of beam 2. As a result, Raman-enhanced FWM is generated accompanying NFWM resulting from diffraction by the static molecular-reorientation and thermal gratings due to the interaction of beam 3 and ω_1 component of beam 2. The ω_2 frequency can be varied. (iii) For the Rayleigh ASPB, D1, D2, and D3 have the wavelength $\lambda_1 = 561$ nm, $\lambda_2 = 565$ nm and $\lambda_3 = 561$ nm, respectively. Thus only the Rayleigh-enhanced FWM is generated due to the interaction of the beam 3 and ω_1 component of the beam 2, while NFWM due to the interaction of the beam 3 and ω_2 component of the beam 2 is generated used as reference signal. The ω_1 frequency can be varied.

In addition, there exist two types of polarization configurations: (i) Beam 1 was polarized along the x direction and beams 2 and 3 were polarized along the y direction. The FWM signal, which was polarized along the x direction, propagated along a direction almost opposite that of beam 2 (see Fig. 3.9). In such case no thermal grating is generated because the two pump beams 1 and 2 are perpendicular to each other. (ii) Beams 1, 2, and 3 were polarized along the x direction. The FWM signal was polarized along the x direction. Here, both thermal grating and molecular-reorientation grating are induced. The non-resonant background can be suppressed dramatically by increasing the relative time-delay (successfully controlling field correlation). There still exists the residual non-resonant background due to the molecular-reorientation grating. In this work [case (ii)], we consider the influence of the

thermal grating to the coexisting Raman and Rayleigh-enhanced FWM and the time-delayed method to suppress the thermal non-resonant background.

In summary, based on color-locking noisy field correlation, the subtle Markovian field correlation effects in three stochastic models have been investigated in studying the Raman and Rayleigh-enhanced FWM. One interesting feature in field-correlation effects is that Rayleigh-enhanced FWM exhibits spectral symmetry, while Raman-enhanced FWM exhibits spectral asymmetry due to the interference between the resonant mode and the non-resonant background. We also note that Raman-enhanced FWM exhibits temporal asymmetry with hybrid radiation-matter detuning terahertz damping oscillation. In addition, a time-delayed method to suppress the background is mentioned in a Kerr medium and an absorbing medium. On the other hand, based on the three stochastic models, homodyne (quadratic) and heterodyne (linear) detection of the Raman ASPB, the Rayleigh ASPB and the coexisting Raman and Rayleigh ASPB have also been investigated, respectively.

3.3 Coexisting Brillouin, Rayleigh and Raman-enhanced Four-Wave Mixings

When the frequency difference between two incident beams equals the acoustic photon resonance in the thicker sample, coherent Raman methods are applied to Brillouin spectroscopy to obtain Brillouin-enhanced FWM. The Raman, Rayleigh and Brillouin-enhanced FWMs are superior to all other CRS techniques. They possess the features of non-resonant background suppression, excellent spatial signal resolution, free choice of interaction volume and simple optical alignment [23].

Polarization beat between two excitation pathways is related to recent studies on the quantum interference. The pure Raman, pure Rayleigh, or the coexisting Raman and Rayleigh ASPB is the interesting way to study the stochastic properties of light [5]. Based on the field-correlation of color-locking twin noisy lights, homodyne and heterodyne detections of these ASPB have also been exhibited to study the characteristics of the dispersion and absorption of the resonant Raman and Rayleigh-enhanced FWM [18].

The disadvantage of noisy light with color-locking is that neither frequency nor time features can be directly probed without some data analysis. When the laser field is sufficiently intense, the laser spectral bandwidth or spectral shape obtained from the second-order correlation function is then inadequate to characterize the field. Rather than using higher-order correlation functions explicitly, three different models for Markovian fields are considered [11].

Based on the field-correlation of color-locking twin noisy lights, the coexisting Raman, Rayleigh and Brillouin-enhanced FWMs are considered in this section and they will compete with each other. We also obtain the phase

dispersion of the coexisting Raman, Rayleigh and Brillouin-enhanced third-order susceptibility. The phase angles of the third-order susceptibilities have been studied using the phase-sensitive detection. The heterodyne detected signal of ASPB potentially offers rich dynamic information about the homogeneous broadening material phase of the third-order nonlinear susceptibility.

3.3.1 Basic Theory

We first pay attention to the pure Rayleigh-enhanced FWM. The basic geometry is shown in Fig. 3.9. The beams 1 and 2 only have the frequency component ω_1, a small angle exists between them. Beam 3 with frequency ω_3 is almost propagating along the opposite direction of the beam 1. Here we define the frequency difference $\Delta_1 = \omega_3 - \omega_1$, if the condition satisfy $\Delta_1 \approx 0$, the frequency components of the beams are fitted to the Rayleigh mode. The beam composite stochastic fields of the beam 1 and 2, $E_1(\boldsymbol{r}, t)$ and $E_1'(\boldsymbol{r}, t)$ for homodyne detection scheme and the complex electric fields of the beam 3 can be written as

$$E_1(\boldsymbol{r}, t) = A_1(\boldsymbol{r}, t)\exp(-\mathrm{i}\omega_1 t) = \varepsilon_1 u_1(t)\exp[\mathrm{i}(\boldsymbol{k}_1 \cdot \boldsymbol{r} - \omega_1 t)], \tag{3.77a}$$

$$\begin{aligned} E_1'(\boldsymbol{r}, t) &= A_1'(\boldsymbol{r}, t)\exp[-\mathrm{i}\omega_1(t-\tau)] \\ &= \varepsilon_1' u_1(t-\tau)\exp[\mathrm{i}(\boldsymbol{k}_1' \cdot \boldsymbol{r} - \omega_1 t + \omega_1 \tau)], \end{aligned} \tag{3.77b}$$

$$E_3(\boldsymbol{r}, t) = A_3(\boldsymbol{r}, t)\exp(-\mathrm{i}\omega_3 t) = \varepsilon_3 u_3(t)\exp[\mathrm{i}(\boldsymbol{k}_3 \cdot \boldsymbol{r} - \omega_3 t)]. \tag{3.77c}$$

Here, $\varepsilon_i, \boldsymbol{k}_i(\varepsilon_i', \boldsymbol{k}_i')$ are the constant field amplitude and the wave vector of the ω_i component in beams 1, 2, and 3. $u_i(t)$ is a dimensionless statistical factor that contains phase and amplitude fluctuations. It is taken to be a complex ergodic stochastic function of t, which obey complex circular Gaussian statistics in chaotic field. τ is a variable relative time delay between the prompt (unprime) and delayed (prime) fields. In an absorbing medium, the nonlinear interaction of beams 1 and 2 with the medium can enhance the molecular-reorientation gratings and the thermal gratings, i.e., ω_1 will induce their own non-resonant static molecular-reorientation gratings G_{M1} and thermal gratings G_{T1}. FWM signals are the results of the diffraction of the beam 3 by these two gratings, respectively. Two non-resonant moving gratings, G_{RM} and G_{RT} with large angle formed by the interference between the ω_1 frequency component of the beam 2 and the ω_3 frequency component of the beam 3 excite the Rayleigh mode of the medium, will diffract the ω_1 frequency component of the beam 1 to obtain the Rayleigh third-order polarizations P_{RM} and P_{RT}. Such polarizations enhance the FWM signals induced by G_{M1} and G_{T1}. The order parameters Q_{M1}, Q_{T1} of two non-resonant static gratings and Q_{RM}, Q_{RT} of the Rayleigh non-resonant moving gratings satisfy the following equations [23]:

$$\mathrm{d}Q_{M1}/\mathrm{d}t + \gamma_M Q_{M1} = \chi_M \gamma_M E_1(\boldsymbol{r}, t)[E_1'(\boldsymbol{r}, t)]^*, \tag{3.78a}$$

$$\mathrm{d}Q_{T1}/\mathrm{d}t + \gamma_T Q_{T1} = \chi_T \gamma_T E_1(\boldsymbol{r},t)[E_1'(\boldsymbol{r},t)]^*, \tag{3.78b}$$

$$\mathrm{d}Q_{RM}/\mathrm{d}t + \gamma_M Q_{RM} = \chi_M \gamma_M [E_1'(\boldsymbol{r},t)]^* E_3(\boldsymbol{r},t), \tag{3.79a}$$

$$\mathrm{d}Q_{RT}/\mathrm{d}t + \gamma_T Q_{RT} = \chi_T \gamma_T [E_1'(\boldsymbol{r},t)]^* E_3(\boldsymbol{r},t). \tag{3.79b}$$

Here $\gamma_{M,T}$ and $\chi_{M,T}$ are the relaxation rate and the nonlinear susceptibility of the molecular-reorientation grating and thermal grating, respectively. The induced third-order nonlinear polarizations which are responsible for the pure Rayleigh-enhanced FWM signals are

$$P_{M1} = Q_{M1}(\boldsymbol{r},t)E_3(\boldsymbol{r},t) = \chi_M \gamma_M S_1(\boldsymbol{r})\varepsilon_1(\varepsilon_1')^*\varepsilon_3 \times \int_0^\infty u_1(t-t')u_1^*(t-t'-\tau)u_3(t)\exp(-\gamma_M t')\mathrm{d}t', \tag{3.80}$$

$$P_{T1} = Q_{T1}(\boldsymbol{r},t)E_3(\boldsymbol{r},t) = \chi_T \gamma_T S_1(\boldsymbol{r})\varepsilon_1(\varepsilon_1')^*\varepsilon_3 \times \int_0^\infty u_1(t-t')u_1^*(t-t'-\tau)u_3(t)\exp(-\gamma_T t')\mathrm{d}t', \tag{3.81}$$

$$P_{RM} = Q_{M1}(\boldsymbol{r},t)E_1(\boldsymbol{r},t) = \chi_M \gamma_M S_1(\boldsymbol{r})(\varepsilon_1')^*\varepsilon_3\varepsilon_1 \times \int_0^\infty u_1^*(t-t'-\tau)u_3(t-t')u_1(t)\exp[-(\gamma_M - \mathrm{i}\Delta_1)t']\mathrm{d}t', \tag{3.82}$$

$$P_{RT} = Q_{T1}(\boldsymbol{r},t)E_1(\boldsymbol{r},t) = \chi_T \gamma_T S_1(\boldsymbol{r})(\varepsilon_1')^*\varepsilon_3\varepsilon_1 \times \int_0^\infty u_1^*(t-t'-\tau)u_3(t-t')u_1(t)\exp[-(\gamma_T - \mathrm{i}\Delta_1)t']\mathrm{d}t'. \tag{3.83}$$

Here $S_1(\boldsymbol{r}) = \exp\{\mathrm{i}[(\boldsymbol{k}_1 - \boldsymbol{k}_1' + \boldsymbol{k}_3)\cdot\boldsymbol{r} - \omega_3 t - \omega_1\tau]\}$. So the polarization of Rayleigh-enhanced FWM process is $P_{A1} = P_{M1} + P_{RM} + P_{T1} + P_{RT}$ with phase matching condition $\boldsymbol{k}_{S1} = \boldsymbol{k}_1 - \boldsymbol{k}_1' + \boldsymbol{k}_3$.

We consider the Rayleigh and Brillouin-enhanced FWM. In the Rayleigh mode, when Δ_1 tunes towards the acoustic phonon resonance, the resonant moving grating G_{Br} can be formed by the interference between the ω_1 frequency component of beam 2 and the ω_3 frequency component of beam 3. Since the moving speed just matches the sound-wave velocity, this resonant moving grating G_{Br} excites the Brillouin mode of the medium and diffracts the ω_1 frequency component of beam 1 to obtain the Brillouin third-order polarization P_{Br}. Such polarization enhances the FWM signals corresponding to G_{RM}, G_{RT}, G_{M1} and G_{T1}. The order parameter $Q_{Br}(\boldsymbol{r},t) = Q_{Br}\exp[-\mathrm{i}(\boldsymbol{k}_1' - \boldsymbol{k}_3)\cdot\boldsymbol{r}]$, which reflects the diversification of medium density, satisfy the following equations [34–37]:

$$\mathrm{d}^2Q_{Br}/\mathrm{d}t^2 + \gamma_{Br}\mathrm{d}Q_{Br}/\mathrm{d}t + \nu_{Br}^2 Q_{Br} = \chi_b[E_2'(\boldsymbol{r},t)]^* E_3(\boldsymbol{r},t). \tag{3.84a}$$

Based on Eqs. (3.80)–(3.83) shown above, we can obtain

$$P_{Br} = \int_0^\infty \frac{\chi_b \gamma_{Br}^2}{\nu_{Br}^2 - \Delta_1^2 - \mathrm{i}\Delta_1\gamma_{Br}}\varepsilon_1\varepsilon_2^*\varepsilon_3 S_1(\boldsymbol{r})u_1^*(t-\tau)u_3(t)u_1(t)\mathrm{d}t. \tag{3.84b}$$

Here, ν_{Br} and γ_{Br} are the Brillouin frequency and linewidth, respectively, and χ_b is a constant. So the polarization of Rayleigh and Brillouin-enhanced FWM processes is $P_{A2} = P_{A1} + P_{Br} = P_{M1} + P_{RM} + P_{T1} + P_{RT} + P_{Br}$ with phase matching condition $\boldsymbol{k}_{S1} = \boldsymbol{k}_1 - \boldsymbol{k}_1' + \boldsymbol{k}_3$.

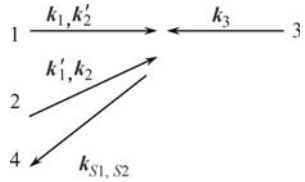

Fig. 3.25. The phase-conjugation geometries of the coexisting Raman, Rayleigh, and Brillouin ASPB. E_1 (E_1') and E_2' (E_2) are the fields with frequency ω_1 and ω_2 in beam 1 (beam 2), respectively. E_3 with frequency ω_3 is the field in beam 3. The enhanced FWM signals or the generated ASPB signals in beam 4 propagate almost along the opposite direction of beam 2.

In Fig. 3.25, if beams 1 and 2 have the frequency component ω_2 which can induce another two non-resonant static molecular-reorientation gratings G_{M2} and thermal gratings G_{T2}. FWM signals are the results of the diffraction of beam 3 by such two gratings. On the other hand, if the frequency detuning $\Delta_2 = \Delta_1' - \Omega_R(\Delta_1' = \omega_3 - \omega_2)$ is near zero, here Ω_R is the Raman resonant frequency, the ω_2 frequency component of beam 2 and the ω_3 frequency component of beam 3 excite the Raman mode of the medium to create the Raman resonant grating G_R. It diffracts the ω_2 frequency component of beam 1 to obtain the Raman third-order polarization P_R. Such polarization enhances FWM signals corresponding to G_{M2} and G_{T2}. The order parameters Q_{M2}, Q_{T2} of two non-resonant static gratings and Q_R of the Raman resonant moving grating satisfies the following equations [31]:

$$\mathrm{d}Q_{M2}/\mathrm{d}t + \gamma_M Q_{M2} = \chi_M \gamma_M E_2'(\boldsymbol{r},t)[E_2(\boldsymbol{r},t)]^*, \tag{3.85a}$$

$$\mathrm{d}Q_{T2}/\mathrm{d}t + \gamma_T Q_{T2} = \chi_T \gamma_T E_2'(\boldsymbol{r},t)[E_2(\boldsymbol{r},t)]^*, \tag{3.85b}$$

$$\mathrm{d}Q_R/\mathrm{d}t + (\gamma_R - \mathrm{i}\Delta_2)Q_R = \chi_R \gamma_R [E_2(\boldsymbol{r},t)]^* E_3(\boldsymbol{r},t). \tag{3.85c}$$

Here the beam stochastic fields of beam 1 and 2 can be expressed as: $E_{p1} = E_2'(\boldsymbol{r},t) = A_2'(\boldsymbol{r},t)\exp[-\mathrm{i}\omega_2(t-\tau)] = \varepsilon_2' u_2(t-\tau)\exp[\mathrm{i}(\boldsymbol{k}_2' \cdot \boldsymbol{r} - \omega_2 t + \omega_2\tau)]$, $E_{p2} = E_2(\boldsymbol{r},t) = A_2(\boldsymbol{r},t)\exp(-\mathrm{i}\omega_2 t) = \varepsilon_2 u_2(t)\exp[\mathrm{i}(\boldsymbol{k}_2 \cdot \boldsymbol{r} - \omega_2 t)]$.

The induced third-order nonlinear polarizations which are responsible for the pure Raman-enhanced FWM signals are

$$P_{M2} = Q_{M2}(\boldsymbol{r},t)E_3(\boldsymbol{r},t) = \chi_M \gamma_M S_2(\boldsymbol{r})(\varepsilon_2)^* \varepsilon_2' \varepsilon_3 \times \int_0^\infty u_2^*(t-t')u_2(t-t'-\tau)u_3(t)\exp(-\gamma_M t')\mathrm{d}t', \tag{3.86}$$

$$P_{T2} = Q_{T2}(\boldsymbol{r},t)E_3(\boldsymbol{r},t) = \chi_T \gamma_T S_2(\boldsymbol{r})(\varepsilon_2)^* \varepsilon_2' \varepsilon_3 \times \int_0^\infty u_2^*(t-t')u_2(t-t'-\tau)u_3(t)\exp(-\gamma_T t')\mathrm{d}t', \tag{3.87}$$

$$P_R = Q_R(\boldsymbol{r},t)E_2'(\boldsymbol{r},t) = \mathrm{i}\chi_R\gamma_R S_2(\boldsymbol{r})(\varepsilon_2)^*\varepsilon_3\varepsilon_2' \times \int_0^\infty u_2^*(t-t')u_3(t-t')u_2(t-\tau)\exp[-(\gamma_R - \mathrm{i}\Delta_2)t']\mathrm{d}t'. \quad (3.88)$$

Here, $S_2(\boldsymbol{r}) = \exp\{\mathrm{i}[(\boldsymbol{k}_2' - \boldsymbol{k}_2 + \boldsymbol{k}_3)\cdot\boldsymbol{r} - \omega_3 t + \omega_2\tau]\}$, and the polarization of Raman-enhanced FWM process is $P_B = P_{M2} + P_{T2} + P_R$ with phase matching condition $\boldsymbol{k}_{S2} = \boldsymbol{k}_2' - \boldsymbol{k}_2 + \boldsymbol{k}_3$.

Here we focus on the coexisting Raman, Rayleigh and Brillouin-enhanced FWM. Now the beams 1 and 2 both consist of the frequency components ω_1 and ω_2, if the two conditions are satisfied simultaneously: the frequency difference $\Delta_1 = \omega_3 - \omega_1$ is much smaller than $\Delta_1' = \omega_3 - \omega_2$ (i.e., $\Delta_1 << \Delta_1'$ and $\Delta_1 \approx 0$) and the frequency detuning $\Delta_2 = \Delta_1' - \Omega_R$ is near zero, the coexisting Raman, Rayleigh and Brillouin modes of medium enhance FWM signals. Therefore, polarization $P_B = P_{M2} + P_{T2} + P_R$ corresponds to the Raman-enhanced FWM process with phase-matching condition $\boldsymbol{k}_{S2}$ and $P_{A2} = P_{M1} + P_{T1} + P_{RM} + P_{RT} + P_{Br}$ corresponds to the Rayleigh and Brillouin-enhanced FWM process with phase-matching condition $\boldsymbol{k}_{S1}$. Both FWM signals have the same frequency, i.e., ω_3. As a result, the FWM signals originate from the interference between the macroscopic polarizations from the Raman-enhanced FWM, the Rayleigh and Brillouin-enhanced FWM signals. The FWM signal (beam 4) is along the opposite direction of beam 2 approximately.

To some extent, the Raman and Brillouin-enhanced FWMs are both the resonant process with energy transfer between the lights and the medium. While because the frequency difference (which is tuned towards the acoustic phonon resonance) between two incident beams of the Brillouin-enhanced FWM is so small that the Rayleigh-enhanced FWM which possesses the zero frequency difference and the Brillouin-enhanced FWM always coexist during the experiment. Hence, we investigate the Rayleigh and Brillouin-enhanced FWM as a whole.

3.3.2 Homodyne Detection of ASPB

For the Rayleigh-enhanced FWM signal, we obtain the total third-order polarization $P^{(3)} = P_{A1} + P_C = (P_{M1} + P_{RM} + P_{T1} + P_{RT}) + (P_{M2} + P_{T2})$, where the reference polarization $P_C = P_{M2} + P_{T2}$ with a frequency ω_1 (which only excite the nonresonant reference signals and do not satisfy the Raman resonant excitation condition) have the phase matching condition $\boldsymbol{k}_{S2} = \boldsymbol{k}_2' - \boldsymbol{k}_2 + \boldsymbol{k}_3$. So the homodyne-detection ASPB signal $I(\Delta_1,\tau) = \langle|P_{A1} + P_C|^2\rangle$ contains $6\times 6 = 36$ different terms. For Rayleigh and Brillouin-enhanced FWMs, there exists one more polarization — the Brillouin polarization. Here we suppose that the Rayleigh and Brillouin polarizations have the same phase angle and they have no interaction between them, so we have the total third-order polarization $P^{(3)} = P_{A2} + P_C = (P_{M1} + P_{RM} + P_{T1} + P_{RT} + P_{Br}) + (P_{M2} + P_{T2})$.

Therefore, the homodyne-detection beat signal $I(\Delta_1, \tau) \propto \langle |P_{A2} + P_C|^2 \rangle$ contains $7 \times 7 = 49$ different terms which include the nonresonant terms of the ω_2 and ω_1 molecular-reorientation and thermal gratings and the Rayleigh and Brillouin resonant mode as the autocorrelation terms, and the cross-correlation terms between FWM and Rayleigh and Brillouin-enhanced FWM. Here,

$$\begin{aligned}
&\langle |P_{A2}|^2 \rangle \\
&\quad = \langle P_{M1} P_{M1}^* \rangle + \langle P_{M1} P_{T1}^* \rangle + \langle P_{M1} P_{RM}^* \rangle + \langle P_{M1} P_{RT}^* \rangle + \langle P_{M1} P_{Br}^* \rangle + \\
&\qquad \langle P_{T1} P_{M1}^* \rangle + \langle P_{T1} P_{T1}^* \rangle + \langle P_{T1} P_{RM}^* \rangle + \langle P_{T1} P_{RT}^* \rangle + \langle P_{T1} P_{Br}^* \rangle + \\
&\qquad \langle P_{RM} P_{M1}^* \rangle + \langle P_{RM} P_{T1}^* \rangle + \langle P_{RM} P_{RM}^* \rangle + \langle P_{RM} P_{RT}^* \rangle + \langle P_{RM} P_{Br}^* \rangle + \\
&\qquad \langle P_{RT} P_{M1}^* \rangle + \langle P_{RT} P_{T1}^* \rangle + \langle P_{RT} P_{RM}^* \rangle + \langle P_{RT} P_{RT}^* \rangle + \langle P_{RT} P_{Br}^* \rangle + \\
&\qquad \langle P_{Br} P_{M1}^* \rangle + \langle P_{Br} P_{T1}^* \rangle + \langle P_{Br} P_{RM}^* \rangle + \langle P_{Br} P_{RT}^* \rangle + \langle P_{Br} P_{Br}^* \rangle. \qquad (3.89)
\end{aligned}$$

They involves fourth- and second-order coherence functions of $u_i(t)$. For example, the first term of $\langle |P_{A2}|^2 \rangle$ is

$$\begin{aligned}
&\langle P_{RM} P_{M1}^* \rangle \\
&\quad = \mathrm{i} \chi_M^2 \gamma_M^2 (\varepsilon_1)^* \varepsilon_3 \varepsilon_1' S_1(\boldsymbol{r}) \varepsilon_1 (\varepsilon_1')^* (\varepsilon_3)^* S_1^*(\boldsymbol{r}) \times \\
&\qquad \int_0^\infty \mathrm{d}t' \int_0^\infty \mathrm{d}s' \langle u_1(t-\tau) u_1(t-s') u_1^*(t-t') u_1^*(t-s'-\tau) \rangle \\
&\qquad \langle u_3(t-t') u_3^*(t) \rangle \times \exp[-(\gamma_M - i\Delta_1)t' - \gamma_M s']. \qquad (3.90)
\end{aligned}$$

The fourth- and second-order coherence functions of $u_i(t)$ included in this equation are $\langle u_1(t-\tau) u_1(t-s') u_1^*(t-t') u_1^*(t-s'-\tau) \rangle$ and $\langle u_3(t-t') u_3^*(t) \rangle$, respectively.

If the laser sources have Lorentzian line shape, we have the second-order coherence function $\langle u_i(t_1) u_i^*(t_2) \rangle = \exp(-\alpha_i |t_1 - t_2|)$ (i.e., $\langle |u_i(t)|^2 \rangle = 1$ when $t = t_1 = t_2$). Here $\alpha_i = \delta\omega_i/2$, $\delta\omega_i$ is the line width of the laser with frequency ω_i. On the other hand, if assuming that the laser sources have Gaussian line shape, then we have $\langle u_i(t_1) u_i^*(t_2) \rangle = \exp\{-[\alpha_i(t_1 - t_2)/2\sqrt{\ln 2}]^2\}$. Here, we only consider the former. In fact, the form of the second-order coherence function shown above, which is determined by the laser line shape, is general feature of the stochastic models [11].

Here we also give the other two terms:

$$\langle |P_C|^2 \rangle = \langle P_{M2} P_{M2}^* \rangle + \langle P_{M2} P_{T2}^* \rangle + \langle P_{T2} P_{M2}^* \rangle + \langle P_{T2} P_{T2}^* \rangle, \qquad (3.91)$$

$$\begin{aligned}
&\langle P_{A2} P_C^* \rangle + \langle P_{A2}^* P_C \rangle \\
&\quad = \langle P_{M1} P_{M2}^* \rangle + \langle P_{T1} P_{M2}^* \rangle + \langle P_{RM} P_{M2}^* \rangle + \langle P_{RT} P_{M2}^* \rangle + \\
&\qquad \langle P_{Br} P_{M2}^* \rangle + \langle P_{M1} P_{T2}^* \rangle + \langle P_{T1} P_{T2}^* \rangle + \langle P_{RM} P_{T2}^* \rangle + \\
&\qquad \langle P_{RT} P_{T2}^* \rangle + \langle P_{Br} P_{T2}^* \rangle + \langle P_{M2} P_{M1}^* \rangle + \langle P_{T2} P_{M1}^* \rangle + \\
&\qquad \langle P_{M2} P_{RM}^* \rangle + \langle P_{M2} P_{RT}^* \rangle + \langle P_{M2} P_{Br}^* \rangle + \langle P_{T2} P_{M1}^* \rangle + \\
&\qquad \langle P_{T2} P_{T1}^* \rangle + \langle P_{T2} P_{RM}^* \rangle + \langle P_{T2} P_{RT}^* \rangle + \langle P_{T2} P_{Br}^* \rangle. \qquad (3.92)
\end{aligned}$$

The atomic response to Markovian stochastic optical fields is well understood [11]. There are three different Markovian fields: (a) the chaotic field, (b) the phase-diffusion field, and (c) the Gaussian-amplitude field. The chaotic field undergoes both amplitude and phase fluctuations and corresponds to a multimode laser field with a large number of uncorrelated modes, or a single-mode laser emitting light below threshold. Since a chaotic field does not possess any intensity stabilization mechanism, the field can take on any value in a two-dimensional region of the complex plane centered about the origin [11]. For the purpose of further investigations of the field-correlation, the three different Markovian noise stochastic models are considered: the chaotic field model (CFM), the phase-diffusion field model (PDM), the Gaussian-amplitude field model (GAM). In this case, $u_1(t)$ has Gaussian statistics with its fourth-order coherence function satisfying

$$\begin{aligned}&\langle u_i(t_1)u_i(t_2)u_i^*(t_3)u_i^*(t_4)\rangle_{CFM}\\&\quad=\exp[-\alpha_i(|t_1-t_3|+|t_2-t_4|)]+\exp[-\alpha_i(|t_1-t_4|+|t_2-t_3|)].\end{aligned}$$

The phase-diffusion field undergoes only phase fluctuations and corresponds to an intensity-stabilized single-mode laser field. The phase of the laser field, however, has no natural stabilizing mechanism. The fourth-order coherence function can be written as

$$\begin{aligned}&\langle u_i(t_1)u_i(t_2)u_i^*(t_3)u_i^*(t_4)\rangle_{PDM}\\&\quad=\exp[-\alpha_i(|t_1-t_3|+|t_1-t_4|+|t_2-t_3|+|t_2-t_4|)]\\&\qquad\exp[\alpha_i(|t_1-t_2|+|t_3-t_4|)]\\&\quad=\frac{\langle u_i(t_1)u_i^*(t_3)\rangle\langle u_i(t_2)u_i^*(t_4)\rangle\langle u_i(t_1)u_i^*(t_4)\rangle\langle u_i(t_2)u_i^*(t_3)\rangle}{\langle u_i(t_1)u_i^*(t_2)\rangle\langle u_i(t_3)u_i^*(t_4)\rangle}.\end{aligned}\tag{3.93}$$

The Gaussian-amplitude field undergoes only amplitude fluctuations. There is no such obvious natural source for a real Gaussian field. However, one can generate it through intentionally modulating the cw laser with the acousto-optic modulator. We do consider the Gaussian-amplitude field for two reasons. First, it allows us to isolate those effects due solely to amplitude fluctuations and second, it is an example of a field that undergoes stronger amplitude (intensity) fluctuations than a chaotic field. The fourth-order coherence function of $u(t)$ satisfies

$$\begin{aligned}&\langle u_i(t_1)u_i(t_2)u_i(t_3)u_i(t_4)\rangle_{GAM}\\&\quad=\langle u_i(t_1)u_i(t_2)u_i(t_3)u_i(t_4)\rangle_{CFM}+\langle u_i(t_1)u_i(t_2)\rangle\langle u_i(t_3)u_i(t_4)\rangle\\&\quad=\exp[-\alpha_i(|t_1-t_3|+|t_2-t_4|)]+\exp[-\alpha_i(|t_1-t_4|+|t_2-t_3|)]+\\&\qquad\exp[-\alpha_i(|t_1-t_2|+|t_3-t_4|)].\end{aligned}\tag{3.94}$$

By comparing the results for the chaotic and the Gaussian-amplitude fields we can determine the effect of increasing amplitude fluctuations [11].

From Fig. 3.26, we give the simulation of Rayleigh and Brillouin ASPBs intensity $I(\Delta_1, \tau) = \langle |P_{A1} + P_C|^2 \rangle$, the three stochastic models have the similar oscillation curve, the GAM field has the highest background, and the PDM field has the lowest background.

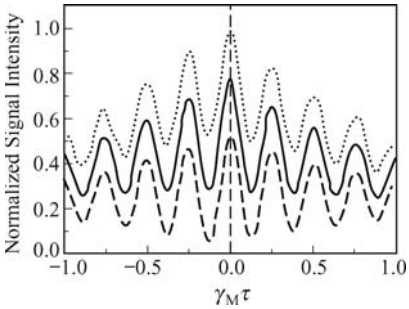

Fig. 3.26. The Rayleigh and Brillouin ASPB signal versus $\gamma_M \tau$ for $\chi_M/\chi_T = 10, \gamma_T/\gamma_M = 2 \times 10^{-6}, \Delta_1 = 0, r = 0, \omega_1/\gamma_M = 12.7450, \omega_2/\gamma_M = 12.0781, \alpha_1/\gamma_M = \alpha_2/\gamma_M = \alpha_3/\gamma_M = 1, \gamma_{Br}/\gamma_M = 0.05, \nu_{Br}/\gamma_M = 0.33, \chi_b/\chi_T = 3.33$ and $\eta = 1$. Three curves are shown in CFM (solid curve), GAM (dotted curve), and PDM (dashed curve).

For the coexisting of Raman, Rayleigh, and Brillouin ASPBs, we have the total third-order polarization $P^{(3)} = P_B + P_{A2} = (P_{M2} + P_{T2} + P_R) + (P_{M1} + P_{RM} + P_{T1} + P_{RT} + P_{Br})$. Therefore, the homodyne-detection signal $I(\Delta_1, \tau) \propto \langle (P_B + P_{A2})(P_B^* + P_{A2}^*) \rangle$ contains $8 \times 8 = 64$ different terms which include the Rayleigh and Brillouin resonant mode as autocorrelation terms and the cross-correlation terms between Raman, Rayleigh, and Brillouin-enhanced FWMs. Here $\langle |P_{A2}|^2 \rangle$ maintains the same as the Rayleigh and Brillouin mode. The other two terms are

$$\langle |P_B|^2 \rangle \tag{3.95}$$

$$= \langle P_{M2} P_{M2}^* \rangle + \langle P_{M2} P_{T2}^* \rangle + \langle P_{M2} P_R^* \rangle + \langle P_{T2} P_{M2}^* \rangle + \langle P_{T2} P_{T2}^* \rangle + \langle P_{T2} P_R^* \rangle + \langle P_R P_{M2}^* \rangle + \langle P_R P_{T2}^* \rangle + \langle P_R P_R^* \rangle, \tag{3.96}$$

$$\begin{aligned} &\langle P_{A2} P_B^* \rangle + \langle P_{A2}^* P_B \rangle \\ &= \langle P_{M1} P_{M2}^* \rangle + \langle P_{T1} P_{M2}^* \rangle + \langle P_{RM} P_{M2}^* \rangle + \langle P_{RT} P_{M2}^* \rangle + \langle P_{Br} P_{M2}^* \rangle + \\ &\quad \langle P_{M1} P_{T2}^* \rangle + \langle P_{T1} P_{T2}^* \rangle + \langle P_{RM} P_{T2}^* \rangle + \langle P_{RT} P_{T2}^* \rangle + \langle P_{Br} P_{T2}^* \rangle + \\ &\quad \langle P_{M1} P_R^* \rangle + \langle P_{T1} P_R^* \rangle + \langle P_{RM} P_R^* \rangle + \langle P_{RT} P_R^* \rangle + \langle P_{Br} P_R^* \rangle + \\ &\quad \langle P_{M2} P_{M1}^* \rangle + \langle P_{T2} P_{M1}^* \rangle + \langle P_{M2} P_{RM}^* \rangle + \langle P_{M2} P_{RT}^* \rangle + \langle P_{M2} P_{Br}^* \rangle + \\ &\quad \langle P_{T2} P_{M1}^* \rangle + \langle P_{T2} P_{T1}^* \rangle + \langle P_{T2} P_{RM}^* \rangle + \langle P_{T2} P_{RT}^* \rangle + \langle P_{T2} P_{Br}^* \rangle + \\ &\quad \langle P_R P_{M1}^* \rangle + \langle P_R P_{T1}^* \rangle + \langle P_R P_{RM}^* \rangle + \langle P_R P_{RT}^* \rangle + \langle P_R P_{Br}^* \rangle. \end{aligned} \tag{3.97}$$

The coexisting Raman and Rayleigh-enhanced FWM has been considered in the previous work [18]. Though the polarization beat signal is shown to be particularly sensitive to the statistical properties of the Markovian stochastic

light fields with arbitrary bandwidth, different Markovian stochastic models of the laser field only influence the fourth-, not second-order correlation functions. That means only the auto-correlation terms will be effected by three different Markovian stochastic models and the cross-correlation terms have nothing to do with three stochastic models. Here the cross-correlation terms between Raman, Rayleigh and Brillouin-enhanced polarization of three models are the same. Therefore, Fig. 3.27 shows that ASPB signal intensities in CFM, PDM, and GAM versus τ. Signals have the same oscillation characteristics that they oscillate with the same frequency $\omega_1 + \omega_2$, which is similar to that of coexisting Raman and Rayleigh ASPBs [20].

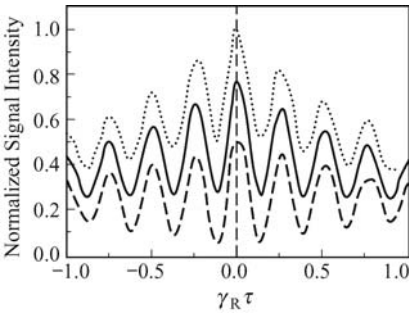

Fig. 3.27. Raman, Rayleigh, and Brillouin ASPB signals versus $\gamma_R \tau$ with the same parameters as in Fig 3.26.

3.3.3 Heterodyne Detection of ASPB

Now we try to do some discussions on the heterodyne detection of ASPB, to obtain information on the third-order susceptibility. We take the Rayleigh and Brillouin ASPB for example: the intensity of beat signal consist of three parts: the auto-correlation term $|P_{A2}|^2$ of the Rayleigh and Brillouin ASPB, the auto-correlation ter, $|P_C|^2$ of the beam ω_2, and the cross-correlation term $\langle P_{A2} P_C^* \rangle + \langle P_{A2}^* P_C \rangle$. The susceptibility of the Rayleigh and Brillouin ASPB is contained in two parts, i.e., $|P_{A2}|^2$ and $\langle P_{A2} P_C^* \rangle + \langle P_{A2}^* P_C \rangle$. The third-order susceptibility $\boldsymbol{\chi}_{A2}$ in $|P_{A2}|^2$ appears in the form of the $|\chi_{A2}|^2$ without phase characteristics. Only in $\langle P_{A2} P_C^* \rangle + \langle P_{A2}^* P_C \rangle$ term there exists phase characteristics of $\boldsymbol{\chi}_{A2}$ of the Rayleigh and Brillouin resonant modes. We can scan the frequency difference Δ_1, but both $|P_{A2}|^2$ and $\langle P_{A2} P_C^* \rangle + \langle P_{A2}^* P_C \rangle$ have our scanning parameter. To avoid the Δ_1 influence on $|P_{A2}|^2$, we can make the field E_1 intensity much weaker, and P_{A2} will be too weak to be considered. In this case, we can obtain the phase dispersion information in the cross-correlation term $\langle P_{A2} P_C^* \rangle + \langle P_{A2}^* P_C \rangle$.

Rayleigh and Brillouin ASPB signals are proportional to the average of the absolute square of $P_{A2} + P_C$, so that the signal intensity $I(\Delta_1, \tau) \propto$

$\langle |P_{A2}+P_C|^2\rangle = \langle (P_{A2}+P_C)(P^*_{A2}+P^*_C)\rangle$ contains $7\times 7 = 49$ different terms. $I_{A2}\left(\Delta_1,\tau\right) = \langle P_{A2}P^*_{A2}\rangle$ and $I_C\left(\tau\right) = \langle P_C P^*_C\rangle$ include the $u_1(t)$ and the $u_2(t)$ fourth-order Markovian stochastic correlation functions, respectively, while $I_{A2,C}\left(\Delta_1,\tau\right) = \langle P_{A2}P^*_C\rangle + \langle P^*_{A2}P_C\rangle$ include $u_i(t)$ second-order Markovian stochastic correlation functions. In order to get the information about the Rayleigh and Brillouin susceptibility, we need to detect the Rayleigh and Brillouin ASPB signal intensity.

We know that different Markovian stochastic models of the laser field only affect the fourth, not second-order correlation functions. Therefore, the cross-correlation terms $I_{A2,C}\left(\Delta_1,\tau\right)$ are the same for three Markovian stochastic models. We can obtain the third-order susceptibilities for Rayleigh and Brillouin-enhanced FWM,

$$\begin{aligned}\chi_{A2} = {} & \chi_M + \chi_T + \chi_M\gamma_M/[(\alpha_1+\alpha_3+\gamma_M) - \mathrm{i}\Delta_1] + \\ & \chi_T\gamma_T/[(\alpha_1+\alpha_3+\gamma_T) - \mathrm{i}\Delta_1] + \\ & \chi_b\gamma^2_{Br}/(\nu^2_{Br} - \Delta^2_1 - \mathrm{i}\Delta_1\gamma_{Br}).\end{aligned} \tag{3.98}$$

The real and imaginary parts of χ_{A2} are even and odd functions, respectively, i.e.,

$$\begin{aligned}\chi'_{A2} = {} & \chi_M + \chi_T + \gamma_M(\alpha_1+\alpha_3+\gamma_M)\chi_M/[(\alpha_1+\alpha_3+\gamma_M)^2 + \Delta^2_1] + \\ & \gamma_T(\alpha_1+\alpha_3+\gamma_T)\chi_T/[(\alpha_1+\alpha_3+\gamma_T)^2 + \Delta^2_1] + \\ & \chi_b\gamma^2_{Br}(\nu^2_{Br} - \Delta^2_1)/[(\nu^2_{Br} - \Delta^2_1)^2 + (\Delta_1\gamma_{Br})^2]\end{aligned}$$

and

$$\begin{aligned}\chi''_{A2} = {} & \chi_M\gamma_M\Delta_1/[(\alpha_1+\alpha_3+\gamma_M)^2 + \Delta^2_1] + \\ & \chi_T\gamma_T\Delta_1/[(\alpha_1+\alpha_3+\gamma_T)^2 + \Delta^2_1] + \\ & \chi_b\gamma^3_{Br}\Delta_1/[(\nu^2_{Br} - \Delta^2_1)^2 + (\Delta_1\gamma_{Br})^2].\end{aligned}$$

In heterodyne detection, assuming $I_C(\tau) >> I_{A2}(\Delta_1,\tau)$ at intensity level, we obtain $I(\Delta_1,\tau) \propto I_C(\tau) + I_{A2,C}(\Delta_1,\tau)$. Under the condition of $\gamma_M >> \alpha_1,\alpha_2,\alpha_3 >> \gamma_T$ we have Rayleigh and Brillouin ASPB signals for three Markovian models, respectively, i.e.,

$$\begin{aligned}\chi_{A2} = {} & \chi_M + \chi_T + \chi_M\gamma_M/[(\alpha_1+\alpha_3+\gamma_M) - \mathrm{i}\Delta_1] + \\ & \chi_T\gamma_T/[(\alpha_1+\alpha_3+\gamma_T) - \mathrm{i}\Delta_1] + \\ & \chi_b\gamma^2_{Br}/(\nu^2_{Br} - \Delta^2_1 - \mathrm{i}\Delta_1\gamma_{Br}).\end{aligned} \tag{3.99}$$

We express χ_{A2} as $|\chi_{A2}|\exp(\mathrm{i}\theta_{A2}) = |\chi_{A2}|\cos\theta_{A2} + \mathrm{i}\,|\chi_{A2}|\sin\theta_{A2}$. From Eq. (3.98) we have

$$\begin{aligned}\chi_{A2} = {} & \chi_M + \chi_T + \chi_M\gamma_M/[(\alpha_1+\alpha_3+\gamma_M) - \mathrm{i}\Delta_1] + \\ & \chi_T\gamma_T/[(\alpha_1+\alpha_3+\gamma_T) - \mathrm{i}\Delta_1].\end{aligned} \tag{3.100}$$

Here, $L_1 = (\chi_M + \chi_T)\exp[-(\alpha_1+\alpha_2)|\tau|]$, $L_2 = [1+3\gamma_M^2/(\gamma_M^2+\Delta_1^2)]\chi_M^2$, $L_3 = \exp(-2\alpha_1|\tau|)\{[1+\gamma_M^2/(\gamma_M^2+\Delta_1^2)]2\chi_M\chi_T+\chi_T^2\}$, $L_4 = \exp(-2\alpha_2|\tau|)(2\chi_M\chi_T+\chi_T^2)$, $\eta = \varepsilon_2'(\varepsilon_2)^*/\varepsilon_1(\varepsilon_1')^*$, spatial modulation frequency $\Delta\boldsymbol{k} = (\boldsymbol{k}_1 - \boldsymbol{k}_1') - (\boldsymbol{k}_2' - \boldsymbol{k}_2)$, and n_a equals 1, 0, 2 for the CFM, PDM, and GAM, respectively.

Equation (3.99) indicates that the reference FWM signal $I_C(\tau)$ and the factor $u_1(t)$ are independent of Δ_1. The heterodyne signal is modulated with a sum-frequency $\omega_1+\omega_2$ as τ is varied, in addition, the phase of the oscillation depends on the phase θ_{A2} of the measured third-order susceptibility χ_{A2}. If adjusting the time delay τ to satisfy the condition $\Delta\boldsymbol{k}\cdot\boldsymbol{r}-(\omega_1+\omega_2)|\tau| = 2n\pi$, we obtain the real part of χ_{A2},

$$I_{ASPB}(\Delta_1,\tau) \propto I_C(\tau) + 2L_1\eta|\chi_{A2}|\cos\theta_{A2} \propto I_C + 2L_1\eta\chi_{A2}'. \tag{3.101}$$

On the other hand, if $\Delta\boldsymbol{k}\cdot\boldsymbol{r} - (\omega_1+\omega_2)|\tau| = (2n-1/2)\pi$, we have the imaginary part of χ_{A2},

$$I_{ASPB}(\Delta_1,\tau) \propto I_C(\tau) + 2L_1\eta|\chi_{A2}|\sin\theta_{A2} \propto I_C(\tau) + 2L_1\eta\chi_{A2}''. \tag{3.102}$$

Raman, Rayleigh, and Brillouin ASPB signals are proportional to the average of the absolute square of $P_B + P_{A2}$, the signal intensity $I(\Delta_1,\Delta_2,\tau) \propto \langle|P_B+P_{A2}|^2\rangle$ contains $8\times 8 = 64$ different terms where $I_{A2,B}(\Delta_1,\Delta_2,\tau) = \langle P_{A2}P_B^*\rangle + \langle P_{A2}^*P_B\rangle$ include $u_i(t)$ second-order Markovian stochastic correlation functions. The cross-correlation terms are the same for three Markovian stochastic models but more complex than that of pure Rayleigh and Raman ASPBs. In heterodyne detection, we can control the laser field intensity to either make $I_B(\Delta_2,\tau) >> I_{A2}(\Delta_1,\tau)$ (i.e. $\eta >> 1$) to obtain $I \propto I_B(\Delta_2,\tau) + I_{A2,B}(\Delta_1,\Delta_2,\tau)$ for studying the phase dispersion of the Rayleigh and Brillouin-enhanced third-order susceptibility χ_{A2} (see Fig. 3.28) or make $I_B(\Delta_2,\tau) << I_{A2}(\Delta_1,\tau)$ ($\eta << 1$) to obtain $I \propto I_{A2}(\Delta_1,\tau) + I_{A2,B}(\Delta_1,\Delta_2,\tau)$ for studying the phase dispersion of the Raman-enhanced third-order susceptibility χ_B (see Fig. 3.29).

Under the condition of $\gamma_R,\gamma_M >> \alpha_1,\alpha_2,\alpha_3 >> \gamma_T$ and $\eta >> 1$ we have the coexisting Raman, Rayleigh, and Brillouin ASPB signals for three Markovian models, respectively, i.e.,

$$\begin{aligned} I_{ASPB}(\Delta_1,\Delta_2,\tau) \propto \eta^2\exp(-2\mathrm{i}\Delta\boldsymbol{k}\cdot\boldsymbol{r})\{[1+n_a\exp(-2\alpha_2|\tau|)]L_5 + L_6\} + \\ \eta\exp[-(\alpha_1+\alpha_2)|\tau|]\times \\ \{\exp[\mathrm{i}\Delta\boldsymbol{k}\cdot\boldsymbol{r} - \mathrm{i}(\omega_1+\omega_2)|\tau|]\chi_B^*\chi_{A2} + \\ \exp[-\mathrm{i}\Delta\boldsymbol{k}\cdot\boldsymbol{r} + \mathrm{i}(\omega_1+\omega_2)|\tau|]\chi_B\chi_{A2}^*\}. \end{aligned} \tag{3.103}$$

Here,

$$\begin{aligned} L_5 &= \chi_M^2 - 2\gamma_R\Delta_2\chi_M\chi_R/(\gamma_R^2+\Delta_2^2) + \gamma_R^2\chi_R^2/(\gamma_R^2+\Delta_2^2), \\ L_6 &= \exp(-2\alpha_2|\tau|)[2\chi_M\chi_T - 2\gamma_R\Delta_2\chi_T\chi_R/(\gamma_R^2+\Delta_2^2) + \chi_T^2], \\ L_7 &= \exp(-2\alpha_1|\tau|)(2\chi_M\chi_T + \chi_T^2), \end{aligned}$$

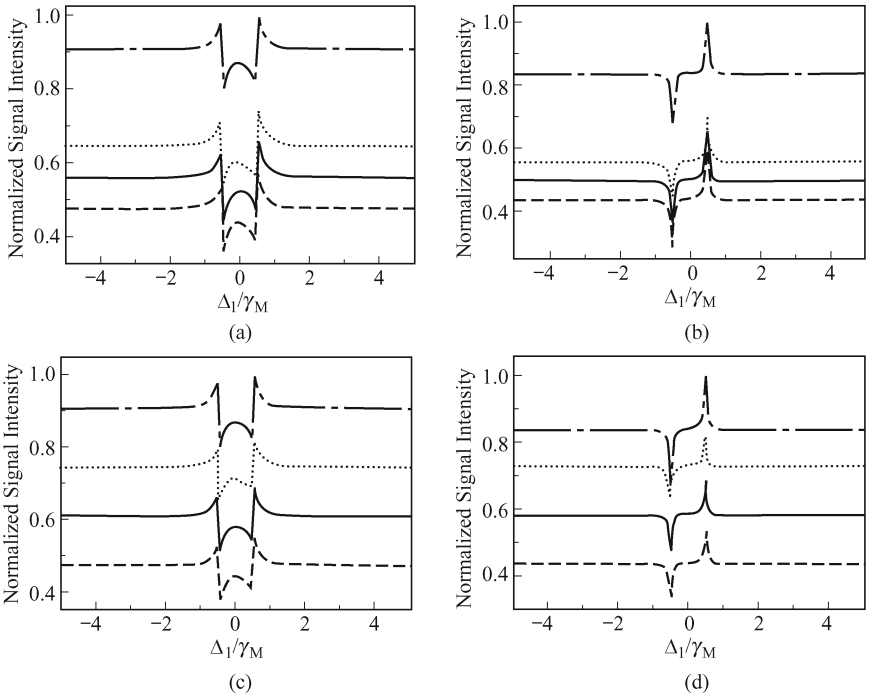

Fig. 3.28. The heterodyne detection spectra versus Δ_1/γ_M of the coexisting Raman, Rayleigh and Brillouin ASPB with (a) $\tau = (2\pi + \Delta\boldsymbol{k}\cdot\boldsymbol{r})/(\omega_1+\omega_2)$ for the real part of χ_{A2}, while with (b) $\tau = (2\pi + \pi/2 + \Delta\boldsymbol{k}\cdot\boldsymbol{r})/(\omega_1+\omega_2)$ for the imaginary part of χ_{A2} when $\tau > 0$; (c) $\tau = (-2\pi + \Delta\boldsymbol{k}\cdot\boldsymbol{r})/(\omega_1+\omega_2)$ for the real part of χ_{A2}, while with (d) $\tau = (-2\pi + \pi/2 + \Delta\boldsymbol{k}\cdot\boldsymbol{r})/(\omega_1+\omega_2)$ for the imaginary part of χ_{A2} when $\tau < 0$. The other parameters are for $\chi_M/\chi_T = 1000, \gamma_T/\gamma_M = 1, \alpha_1/\gamma_M = \alpha_2/\gamma_M = \alpha_3/\gamma_M = 1, \omega_1/\gamma_M = 127450, \omega_2/\gamma_M = 120781, \gamma_{Br}/\gamma_M = 0.1, \nu_{Br}/\gamma_M = 0.5, \chi_b/\chi_T = 10, \eta = 10$. Theoretical curves are shown in CFM (dashed curve), PDM (dotted curve), GAM (dot-dashed curve) and the model with cw laser beams (dot-dot-dashed curve). Adopted from Ref. [21].

and the third-order Raman-enahnced susceptibility

$$\chi_B = \chi_M + \chi_T - \chi_R\gamma_R/(\Delta_2 + \mathrm{i}\gamma_R).$$

Therefore, from Eq. (3.102) we have

$$I(\Delta_1,\Delta_2,\tau) \propto I_B(\Delta_2,\tau) + 2\eta\exp[-(\alpha_1+\alpha_2)|\tau|]|\chi_B||\chi_{A2}| \times \cos[\Delta\boldsymbol{k}\cdot\boldsymbol{r} - (\omega_1+\omega_2)|\tau| - \theta_B + \theta_{A2}]. \quad (3.104)$$

Here, $I_B(\Delta_2,\tau) = \eta^2\exp(-2\mathrm{i}\Delta\boldsymbol{k}\cdot\boldsymbol{r})\{[1+n_a\exp(-2\alpha_2|\tau|)]L_5 + L_6\}$, the factor $2\eta\exp[-(\alpha_1+\alpha_2)|\tau|]|\chi_B|$ and θ_B are independent of Δ_1. If we adjust the time delay τ such that $\Delta\boldsymbol{k}\cdot\boldsymbol{r} - (\omega_1+\omega_2)|\tau| - \theta_B = 2n\pi$ [Fig. 3.28 (a),

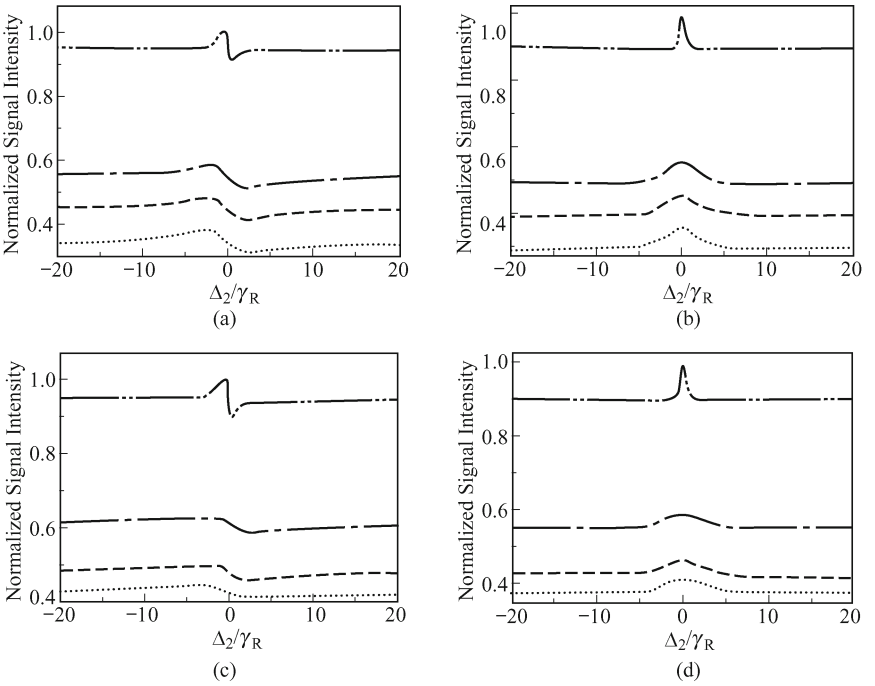

Fig. 3.29. The heterodyne detection spectra versus Δ_2/γ_R of coexisting Raman, Rayleigh, and Brillouin ASPBs for (a) the real part of χ_B, while with (b) the imaginary part of χ_B when $\tau > 0$. (c) The real part of χ_B, while with (d) the imaginary part of χ_B when $\tau < 0$. Other parameters are for $\chi_M/\chi_T = 1, \gamma_T/\gamma_M = 1 \times 10^{-6}, \gamma_{Br}/\gamma_M = 0.05, \nu_{Br}/\gamma_M = 0.33, \chi_b/\chi_T = 3.33, \eta = 0.1$. Theoretical curves are shown in CFM (dashed curve), PDM (dotted curve), GAM (dot-dashed curve), and the model with cw laser beams (dot-dot-dashed curve).

(c)], then

$$I(\Delta_1, \Delta_2, \tau) \propto I_B(\Delta_2, \tau) + 2\eta \exp[-(\alpha_1 + \alpha_2)|\tau|]|\chi_B||\chi_{A2}| \cos\theta_{A2}$$
$$= I_B(\Delta_2, \tau) + 2\eta \exp[-(\alpha_1 + \alpha_2)|\tau|]|\chi_B|\chi'_{A2}. \quad (3.105)$$

However, if $\Delta \boldsymbol{k} \cdot \boldsymbol{r} - (\omega_1 + \omega_2)|\tau| - \theta_B = (2n - 1/2)\pi$ [Fig. 3.28 (b) and (d)], we have

$$I(\Delta_1, \Delta_2, \tau) \propto I_B(\Delta_2, \tau) + 2\eta \exp[-(\alpha_1 + \alpha_2)|\tau|]|\chi_B||\chi_{A2}| \sin\theta_{A2}$$
$$= I_B(\Delta_2, \tau) + 2\eta \exp[-(\alpha_1 + \alpha_2)|\tau|]|\chi_B|\chi''_{A2}. \quad (3.106)$$

In other words, by changing the time delay τ between beams 1 and 2 we can obtain the real and the imaginary parts of Rayleigh and Brillouin-enhanced susceptibilities. Figure 3.28 (a) – (d) shows the heterodyne detection spectra versus Δ_1/γ_M of the coexisting Raman, Rayleigh and Brillouin ASPB with large η. Therefore, the spectra show the characteristics of the dispersion and

absorption of the resonant Rayleigh and Brillouin-enhanced susceptibility. From Fig 3.28 (a, c), two Brillouin resonance humps stand on the both sides of Rayleigh resonance hump. By choosing proper parameters, two Brillouin resonance humps have been enhanced and the Rayleigh resonance hump becomes weaker, now the apex of the Rayleigh resonance hump is just below that of the Brillouin mode.

Similarly, under the condition of $\gamma_R, \gamma_M >> \alpha_1, \alpha_2, \alpha_3 >> \gamma_T$ and $\eta << 1$ we have the coexisting Raman, Rayleigh and Brillouin ASPB signals for three Markovian models,respectively, i.e.,

$$\begin{aligned} I(\Delta_1, \Delta_2, \tau) \propto & \{[1 + n_a \exp(-2\alpha_1|\tau|)]L_2 + L_3\} + \\ & \eta \exp[-(\alpha_1 + \alpha_2)|\tau|] \times \\ & \{\exp[\mathrm{i}\Delta\boldsymbol{k} \cdot \boldsymbol{r} - \mathrm{i}(\omega_1 + \omega_2)|\tau|]\chi_B^* \chi_{A2} + \\ & \exp[-\mathrm{i}\Delta\boldsymbol{k} \cdot \boldsymbol{r} + \mathrm{i}(\omega_1 + \omega_2)|\tau|]\chi_B \chi_{A2}^*\}. \end{aligned} \tag{3.107}$$

From Eq. (3.106) we have

$$\begin{aligned} I(\Delta_1, \Delta_2, \tau) \propto & I_{A2}(\Delta_1, \tau) + 2\eta \exp[-(\alpha_1 + \alpha_2)|\tau|]|\chi_B||\chi_{A2}| \times \\ & \cos[\Delta\boldsymbol{k} \cdot \boldsymbol{r} - (\omega_1 + \omega_2)|\tau| - \theta_B + \theta_{A2}]. \end{aligned} \tag{3.108}$$

Here, $I_{A2}(\Delta_1, \tau) = [1 + n_a \exp(-2\alpha_1|\tau|)]L_2 + L_3$, the factor $2\eta \exp[-(\alpha_1 + \alpha_2)|\tau|]|\chi_{A2}|$ and θ_{A2} are independent of Δ_2. If we adjust the time delay τ such that $\Delta\boldsymbol{k} \cdot \boldsymbol{r} - (\omega_1 + \omega_2)|\tau| + \theta_{A2} = 2n\pi$ [Fig. 3.28 (a, c)], then

$$\begin{aligned} I(\Delta_1, \Delta_2, \tau) &\propto I_{A2}(\Delta_1, \tau) + 2\eta \exp[-(\alpha_1 + \alpha_2)|\tau|]|\chi_{A2}||\chi_B| \cos\theta_B \\ &= I_{A2}(\Delta_1, \tau) + 2\eta \exp[-(\alpha_1 + \alpha_2)|\tau|]|\chi_{A2}|\chi_B'. \end{aligned} \tag{3.109}$$

However, if $\Delta\boldsymbol{k} \cdot \boldsymbol{r} - (\omega_1 + \omega_2)|\tau| + \theta_{A2} = (2n + 1/2)\pi$ [Fig. 3.29 (b, d)], we have

$$\begin{aligned} I(\Delta_1, \Delta_2, \tau) &\propto I_{A2}(\Delta_1, \tau) + 2\eta \exp[-(\alpha_1 + \alpha_2)|\tau|]|\chi_{A2}||\chi_B| \sin\theta_B \\ &= I_{A2}(\Delta_1, \tau) + 2\eta \exp[-(\alpha_1 + \alpha_2)|\tau|]|\chi_{A2}|\chi_B''. \end{aligned} \tag{3.110}$$

Similarly, by changing the time delay τ between beams 1 and 2 we can obtain real and imaginary parts of the Raman-enhanced susceptibility χ_B. Figure 3.29 (a – d) shows the characteristics of the dispersion and absorption of the resonant Raman-enhanced FWM.

In Figs. 3.28 and 3.29, we can see that three CFM, PDM, GAM models have the same profiles, which is similar as the model with cw laser beam. On the other hand, in the coexisting Raman, Rayleigh and Brillouin ASPB, both the Raman-enhanced susceptibility and Rayleigh and Brillouin-enhanced susceptibility still hold their inherent characteristics in the heterodyne-detected ASPB, showing the similar curves as that in the pure Raman mode and the Rayleigh and Brillouin mode.

In the above discussion, we individually obtain the real and imaginary parts of the Rayleigh and Brillouin susceptibility (see Fig. 3.28) and the Raman susceptibility (Fig. 3.29) . In fact, the conditions for the excited Raman,

Rayleigh and Brillouin-enhanced FWM can be simultaneously satisfied in one experiment system and the Raman, Rayleigh, and Brillouin-enhanced FWMs are mixed and interfere with each other. Each of them can be considered as the reference signal of each other. Next we will consider the spectra versus Δ_1/γ_R and Δ_2/γ_R. Figure 3.30 gives the three-dimensional diagram of the coexisting Raman susceptibility, Rayleigh and Brillouin susceptibilities in ASPB. We can see two resonance humps of the Rayleigh and Brillouin ASPB versus Δ_1/γ_R. As τ satisfies the condition of $\Delta\boldsymbol{k}\cdot\boldsymbol{r}-(\omega_1+\omega_2)|\tau|+\theta_{A2}=2n\pi$, the spectra versus Δ_2/γ_R shows the real part of the Raman-enhanced susceptibility [Fig. 3.30 (a)], however, when $\Delta\boldsymbol{k}\cdot\boldsymbol{r}-(\omega_1+\omega_2)|\tau|+\theta_{A2}=2n\pi+\pi/2$, the spectra versus Δ_2/γ_R show the imaginary part of the Raman-enhanced susceptibility [Fig. 3.30 (b)].

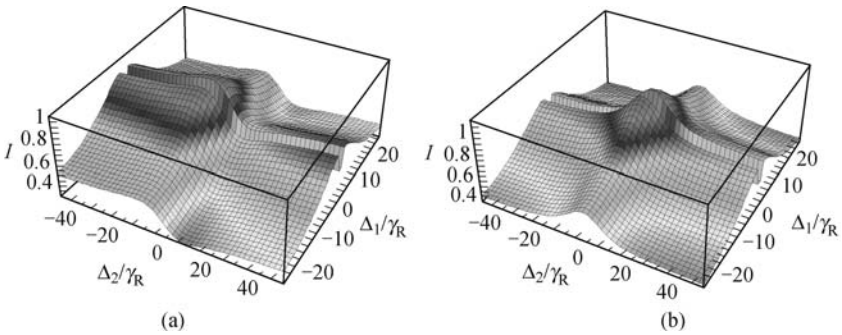

Fig. 3.30. The heterodyne detection spectra versus Δ_1/γ_R and Δ_2/γ_R of coexisting ASPBs for $\eta = 0.1, \chi_M/\chi_R = 0.1, \gamma_R/\gamma_M = 1, \chi_T/\chi_R = 0.1, \gamma_T/\gamma_M = 1\times10^{-6}, \alpha_1/\gamma_M = \alpha_2/\gamma_M = \alpha_3/\gamma_M = 1, \gamma_{Br}/\gamma_M = 0.05, \nu_{Br}/\gamma_M = 0.3, \chi_b/\chi_T = 3$ with (a) $\tau = (2n\pi - \Delta\boldsymbol{k}\cdot\boldsymbol{r} - \theta_B)/(\omega_1+\omega_2)$ for the real part and (b) $\tau = (2n\pi+\pi/2-\Delta\boldsymbol{k}\cdot\boldsymbol{r}-\theta_B)/(\omega_1+\omega_2)$ for the imaginary part of χ_B, respectively. Adopted from Ref. [21].

On the other hand, as is known we can not directly obtain the pure Brillouin-enhanced FWM, but with the proper value of time delay τ in beat signal intensity, we could get it if removing the Rayleigh-enhanced FWM signal intensity from the coexisting Brillouin- and Rayleigh-enhanced ASPBs. i.e., with $\langle|P_{A2}+P_C|^2\rangle - \langle|P_{A1}+P_C|^2\rangle$, we can get the information of the Brillouin-enhanced susceptibility χ_{Br}. It means by changing the time delay τ between beams 1 and 2, we can obtain real and imaginary parts of the Brillouin-enhanced susceptibility χ_{Br}. Figure 3.31 shows the profile of the real and imaginary parts of χ_{Br}. The CFM, PDM, GAM are the same as that in cw limit, but only their backgrounds are different. On the other hand, the Brillouin-mode susceptibility has the similar absorption-like shape and dispersion-like shape as the Rayleigh-mode susceptibility, whose real part of the susceptibility is an even function and the imaginary part is an odd function. In Fig. 3.31 (a, c), the dispersion-like shape of Brillouin-mode susceptibility has two resonant peaks which are near the zero point. And in Rayleigh

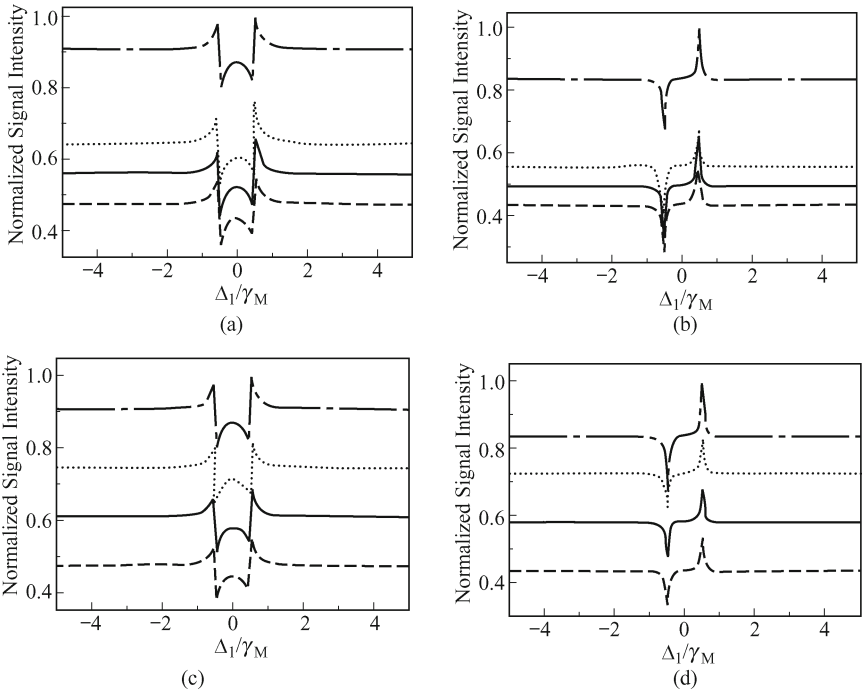

Fig. 3.31. The heterodyne detection spectra versus Δ_1/γ_M of the Brillouin-enhanced ASPB with (a) $\tau = (2\pi + \Delta\boldsymbol{k}\cdot\boldsymbol{r})/(\omega_1+\omega_2)$ for the real part of χ_{Br}, while with (b) $\tau = (2\pi + \pi/2 + \Delta\boldsymbol{k}\cdot\boldsymbol{r})/(\omega_1+\omega_2)$ for the imaginary part of χ_{Br} when $\tau > 0$; (c) $\tau = (-2\pi + \Delta\boldsymbol{k}\cdot\boldsymbol{r})/(\omega_1+\omega_2)$ for the real part of χ_{Br}, while with (d) $\tau = (-2\pi + \pi/2 + \Delta\boldsymbol{k}\cdot\boldsymbol{r})/(\omega_1+\omega_2)$ for the imaginary part of χ_{Br} when $\tau < 0$. Other parameters are for $\chi_M/\chi_T = 1000, \gamma_T/\gamma_M = 5, \alpha_1/\gamma_M = \alpha_2/\gamma_M = \alpha_3/\gamma_M = 1, \omega_1/\gamma_M = 127450, \omega_2/\gamma_M = 120781, \gamma_{Br}/\gamma_M = 10, \nu_{Br}/\gamma_M = 2, \chi_{Br}/\chi_T = 0.1, \eta = 10$. Theoretical curves are shown in CFM (solid curve), PDM (dashed curve), GAM (dot curve) and the model with cw laser beams (dot-dashed curve).

and Brillouin-mode susceptibilities, the two Brillouin resonant peaks are in the bound of Rayleigh resonant peaks, The separation of these two Brillouin resonance peaks can be controlled by the parameters ν_{Br} and γ_{Br}, respectively.

Figures 3.32 (a) and 3.33 (a) show the real and imaginary part of susceptibilities of the Raman mode in the pure Raman ASPB, while Figs. 3.34 (a) and 3.35 (a) show those of the susceptibility of Rayleigh mode in the pure Rayleigh ASPB. We can see the dispersion-like profile for the real part and the absorption-like profile for the imaginary part of these modes. For the coexisting Raman and Rayleigh [Figs. 3.32 (b) – 3.35 (b)] ASPB and the coexisting Raman, Rayleigh, and Brillouin ASPBs [see Figs. 3.32 (c) – 3.35 (c)], different τ can give each curve with different backgrounds. No matter how τ changes, the curves have the similar profile as the curve of cw laser beams.

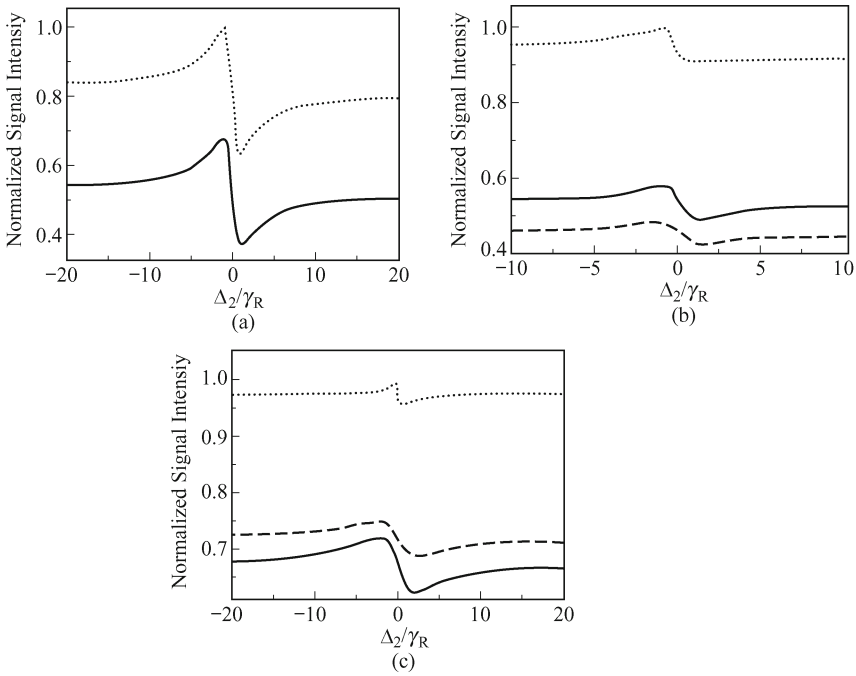

Fig. 3.32. The heterodyne detection spectra versus Δ_2/γ_R of (a) the pure Raman ASPB, (b) the coexisting Raman and Rayleigh ASPBs and (c) the coexisting Raman, Rayleigh and Brillouin ASPB with $\tau = (\pm 2\pi + \Delta \boldsymbol{k} \cdot \boldsymbol{r})/(\omega_1 + \omega_2)$ for the real part of χ_B. The parameters are $\chi_M/\chi_T = 1, \gamma_T/\gamma_M = 1 \times 10^{-6}, \alpha_1/\gamma_M = \alpha_2/\gamma_M = \alpha_3/\gamma_M = 1, \omega_1/\gamma_M = 127\ 450, \omega_2/\gamma_M = 119\ 924, \eta = 0.1, \gamma_{Br}/\gamma_M = 0.05, \nu_{Br}/\gamma_M = 0.3, \chi_b/\chi_T = 3, \chi_R/\chi_T = 5$. Theoretical curves are shown in the model when $\tau > 0$ (solid curve), $\tau < 0$ (dashed curve) and the model with cw laser beams (dotted curve).

Let us turn to the coexisting Rayleigh and Brillouin susceptibility. In the coexisting Raman, Rayleigh, and Brillouin-enhanced ASPBs, the curves of the real part of susceptibility [see Fig. 3.34 (c)] are still even function-like,

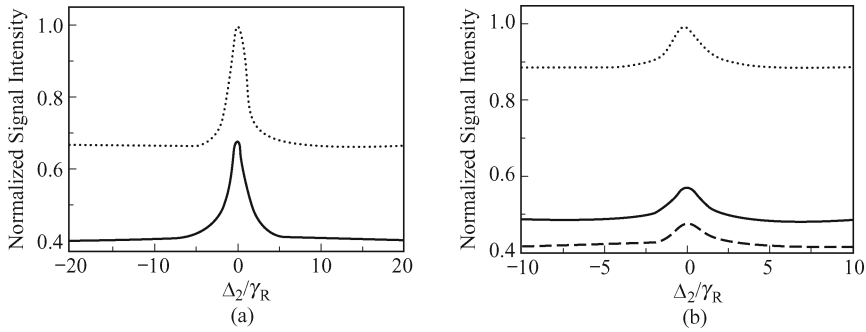

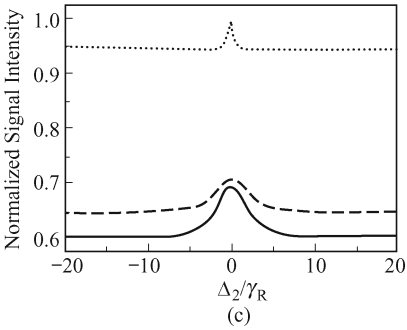

Fig. 3.33. The heterodyne detection spectra versus Δ_2/γ_R of (a) the pure Raman ASPB (b) the coexisting Raman and Rayleigh ASPB and (c) the coexisting of Raman, Rayleigh, and Brillouin ASPBs with $\tau = (\pm 2\pi + \pi/2 + \Delta \boldsymbol{k} \cdot \boldsymbol{r})/(\omega_1 + \omega_2)$ for the imaginary part of χ_B. The parameters are the same as in Fig. 3.32. Theoretical curves are shown in the model when $\tau > 0$ (solid curve), $\tau < 0$ (dashed curve) and the model with cw laser beams (dotted curve).

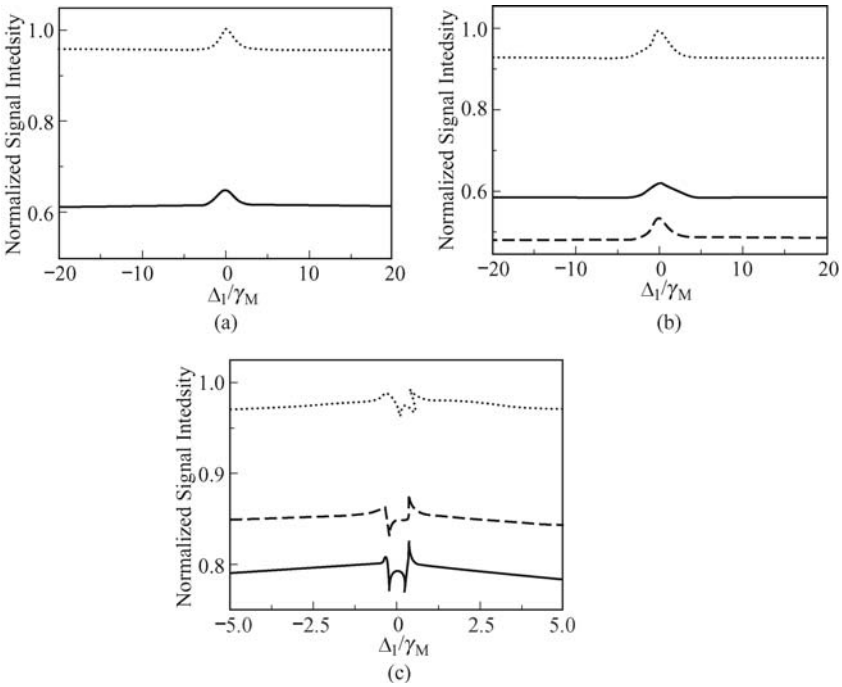

Fig. 3.34. The heterodyne detection spectra with $\tau = (\pm 2\pi + \Delta \boldsymbol{k} \cdot \boldsymbol{r})/(\omega_1 + \omega_2)$ versus Δ_1/γ_M of (a) the pure Rayleigh ASPB (b) coexisting Raman and Rayleigh ASPBs for the real part of χ_{A1} and (c) the coexisting Raman, Rayleigh and Brillouin ASPB for the real part of χ_{A2}. The parameters are $\chi_M/\chi_T = 1, \gamma_T/\gamma_M = 1 \times 10^{-6}, \alpha_1/\gamma_M = \alpha_2/\gamma_M = \alpha_3/\gamma_M = 1, \gamma_{Br}/\gamma_M = 0.05, \nu_{Br}/\gamma_M = 0.3, \chi_b/\chi_T = 3, \chi_R/\chi_T = 5, \omega_1/\gamma_M = 127\ 450, \omega_2/\gamma_M = 119\ 924, \eta = 10$. Theoretical curves are shown in the model when $\tau > 0$ (solid curve), $\tau < 0$ (dashed curve) and the model with cw laser beams (dotted curve).

but there are two more Brillouin resonance humps on the both sides of the lower Rayleigh resonance hump [Fig. 3.34 (a), (b)]. The separation of the two Brillouin resonance humps can be controlled by the value of ν_{Br} and γ_{Br}. As increasing ν_{Br} and γ_{Br}, the distance between two Brillouin resonance humps increases. For imaginary part of susceptibility [see Fig. 3.35(c)], there are peak and valley near zero, which reflects the characteristics of the Brillouin-enhanced FWM, the curves are still odd function-like, similar as the pure Raman, and the coexisting Raman and Rayleigh case [see Fig. 3.35 (a, b)].

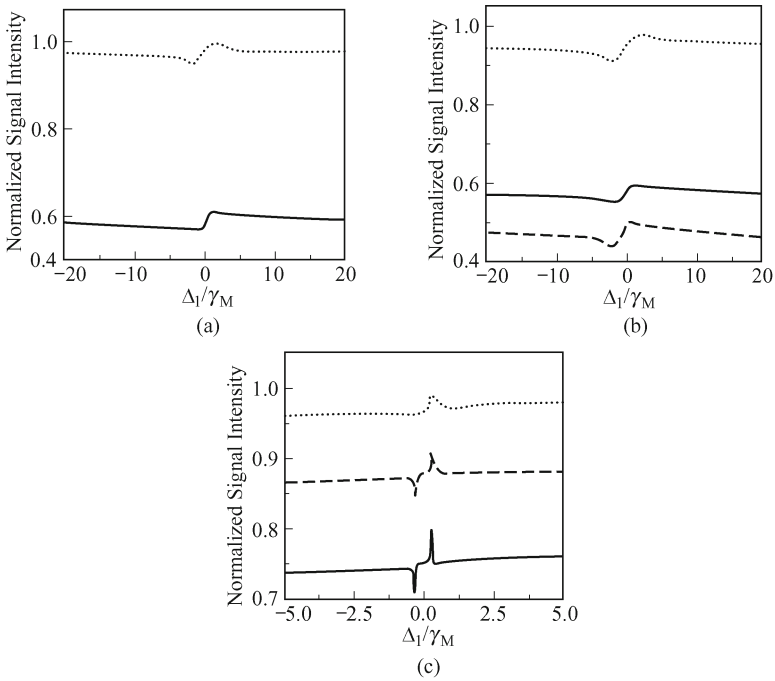

Fig. 3.35. The heterodyne detection spectra with $\tau = (\pm 2\pi + \pi/2 + \Delta \boldsymbol{k} \cdot \boldsymbol{r})/(\omega_1 + \omega_2)$ versus Δ_1/γ_M of (a) the pure Rayleigh ASPB (b) the coexisting Raman and Rayleigh ASPB for the real part of χ_{A1} and (c) coexisting Raman, Rayleigh, and Brillouin ASPBs for the real part of χ_{A2}. The parameters are the same as in Fig. 3.34. Theoretical curves are shown in the model when $\tau > 0$ (solid curve), $\tau < 0$ (dashed curve) and the model with cw laser beams (dotted curve).

3.3.4 Phase Angle

We first consider the phase angle of Raman susceptibility χ_B [19]. Under cw laser condition for simplicity, we decompose the nonlinear susceptibility χ_B into a real and imaginary part, i.e., $\chi_B = \chi'_B + \mathrm{i}\chi''_B$, with $\chi'_B = \chi_M + \chi_T - \chi_R\gamma_R\Delta_2/(\Delta_2^2 + \gamma_R^2)$ and $\chi''_B = \chi_R\gamma_R^2/(\Delta_2^2 + \gamma_R^2)$.$\chi'_B(\Delta_2)$ is nei-

ther an odd nor an even function due to the terms χ_M and χ_T.$\chi''_B(\Delta_2)$ is an even function. We can obtain phase angle θ_B with $|\chi_B|\exp \mathrm{i}\theta_B = |\chi_B|\cos\theta_B + \mathrm{i}|\chi_B|\sin\theta_B$ and $\theta_B(\Delta_2) = \tan^{-1}(\chi''_B/\chi'_B)$. From the formula above, as decreasing $\chi_M + \chi_T, \chi'_B = \chi_M + \chi_T - \chi_R\gamma_R\Delta_2/(\Delta_2^2 + \gamma_R^2)$ can get close to $\chi'_B = -\chi_R\gamma_R\Delta_2/(\Delta_2^2 + \gamma_R^2)$, which is an odd function. While as increasing $\chi_M + \chi_T, \theta_B$ turn to an even function, and we have $\chi'_B = \chi_M + \chi_T$ which is independent of Δ_2, shown in Fig. 3.36 (a). In Fig. 3.36 (a), we can see that the phase angle θ_B becomes more symmetrical with $\Delta_2 = 0$ when χ_M/α_1 and χ_T/α_1 increase. Similarly, the phase angle θ_B in coexisting Raman, Rayleigh, and Brillouin ASPBs in Fig. 3.36 (b) shows the similar characteristics as that in Fig. 3.36 (a). On the other hand, the laser linewidth also affects the phase angle versus Δ_2. As increasing the laser linewidth, the value of the phase angle decreases but the symmetry of phase angle has little influence, as shown in Fig. 3.36 (c, d). In fact, comparing with the broadband ($\alpha_i/\gamma_M >> 1, \alpha_i/\gamma_T >> 1$), the dispersion and absorption under narrowband limit are independent of the linewidth α_i and time delay τ, which correspond to the non-modified nonlinear dispersion and absorption of the material.

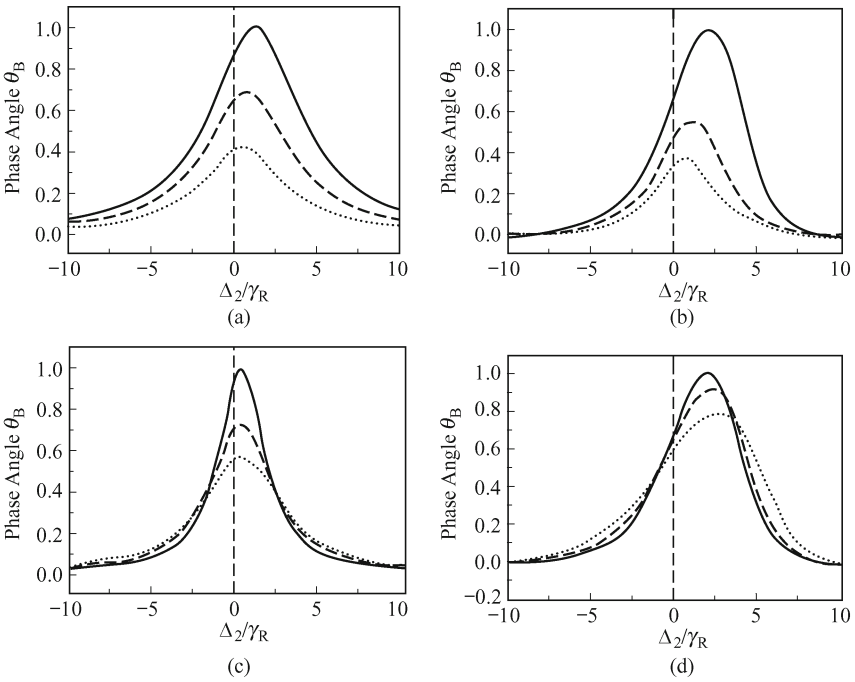

Fig. 3.36. The phase angle θ_B in the pure Raman enhanced FWM versus Δ_2/γ_R for (a) $\chi_M/\chi_R = \chi_T/\chi_R = 0.2$ (solid curve), 0.3 (dashed curve), and 0.5 (dotted curve), and for (c) $\alpha_1/\gamma_M = \alpha_2/\gamma_M = \alpha_3/\gamma_M = 0.3$ (solid curve), 0.6 (dashed curve), and 0.9 (dotted curve). θ_B in coexisting Raman, Rayleigh, and Brillouin-enhanced FWMs versus Δ_2/γ_R for (b) $\chi_M/\chi_R = \chi_T/\chi_R = 0.3$ (solid curve), 0.6 (dashed curve), and 0.9 (dotted curve), and for (d) $\alpha_1/\gamma_M = \alpha_2/\gamma_M = \alpha_3/\gamma_M = 0.9$ (solid curve), 1.2 (dashed curve), and 2 (dotted curve).

Then we focus on the phase angle $\theta_{A1}(\Delta_1)$ of Rayleigh susceptibility χ_{A1} i.e., $\chi_{A1} = |\chi_{A1}| \exp \mathrm{i}\theta_{A1} = \chi'_{A1} + \mathrm{i}\chi''_{A1}$, with $\chi'_{A1} = \chi_M + \chi_T + \gamma_M^2 \chi_M/(\gamma_M^2 + \Delta_1^2) + \gamma_T^2 \chi_T/(\gamma_T^2 + \Delta_1^2), \chi''_{A1} = \chi_M \gamma_M \Delta_1/(\gamma_M^2 + \Delta_1^2) + \chi_T \gamma_T \Delta_1/(\gamma_T^2 + \Delta_1^2)$, and $\theta_{A1}(\Delta_1) = \tan^{-1}(\chi''_{A1}/\chi'_{A1})$. From the expressions we can see that the real part of Rayleigh susceptibility is an even function and the imaginary part is an odd function, so the phase angle is an odd function. When we increase χ_T/χ_M, the value of $\theta_{A1}(\Delta_1)$ versus Δ_1 in the pure Rayleigh ASPB is reduced [see Fig. 3.37 (a)]. Similarly, for the phase angle $\theta_{A2}(\Delta_1)$ of Rayleigh and Brillouin susceptibility $\chi_{A2} = \chi'_{A2} + \mathrm{i}\chi''_{A2} = |\chi_{A2}| \exp \mathrm{i}\theta_{A2}$, we also obtain the even function $\chi'_{A2} = \chi_M + \chi_T + \gamma_M^2 \chi_M/(\gamma_M^2 + \Delta_1^2) + \gamma_T^2 \chi_T/(\gamma_T^2 + \Delta_1^2) + \chi_b \gamma_{Br}^2 (\nu_{Br}^2 - \Delta_1^2)/[(\nu_{Br}^2 - \Delta_1^2)^2 + (\Delta_1 \gamma_{Br})^2]$ and the odd function $\chi''_{A2} = \chi_M \gamma_M \Delta_1/(\gamma_M^2 + \Delta_1^2) + \chi_T \gamma_T \Delta_1/(\gamma_T^2 + \Delta_1^2) + \chi_b \gamma_{Br}^3 \Delta_1/[(\nu_{Br}^2 - \Delta_1^2)^2 + (\Delta_1 \gamma_{Br})^2]$. We can find two sharp peaks near $\Delta_1 = 0$ induced by the Brillouin resonance for $\theta_{A2}(\Delta_1)$ in the Rayleigh and Brillouin ASPB [Fig. 3.37 (b)] and in the Raman, Rayleigh and Brillouin ASPB [Fig. 3.37 (c)]. The distance between two sharp peaks is proportional to the value of ν_{Br} and γ_{Br} of Brillouin mode. On the other hand, when we reduce α_1 and α_3, the value of the phase angle θ_{A1}, θ_{A2} increase [see Fig. 3.37 (d–f)], which shows the influence of the field-correlation of the color-locked noisy light. Thus, by virtue of the ultrafast modulation processes within the attosecond regime, one can optimize the nonlinear susceptibilities and obtain the efficient nonlinear optical signals, which have potential applications in achieving better nonlinear optical materials and opt-electronic devices.

3.3.5 Discussion and Conclusion

Based on three stochastic models, the subtle Markovian field-correlation effects have been investigated in Raman, Rayleigh, and Brillouin-enhanced FWMs, homodyne and heterodyne-detected ASPB. All of these can be understood for time and frequency domains. Raman or Brillouin-enhanced FWMs are both the resonant third-order nonlinear processes. The Raman grating and Brillouin grating are created by the ω_2 frequency component of beam 2 and the ω_3 frequency component of beam 3 in Fig. 3.31. Specifically, the Raman vibration mode is excited by the simultaneous presence of two incident beams whose frequency difference equals the Raman resonant excitation frequency. In the Brillouin-enhanced FWM, the Brillouin mode is excited by the simultaneous presence of two incident beams whose frequency difference equals the phonon resonant frequency. In contrast, the Rayleigh-enhanced FWM is a non-resonant process which is excited when frequency difference between two incident beams equals zero, and there is no energy transfer between the lights and the medium.

Here we employ the ASPB to obtain real and imaginary parts of susceptibilities based on the polarization interference among coexisting Raman,

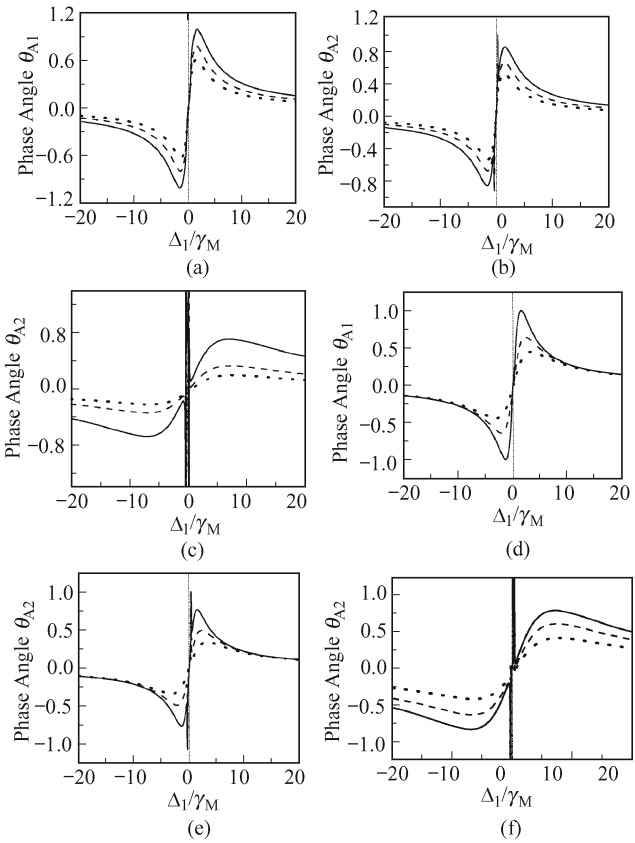

Fig. 3.37. The phase angle θ_{A1} in the pure Rayleigh-enhanced FWM versus Δ_1/γ_M for (a) $\chi_T/\chi_M = 0.1$ (solid curve), 0.5 (dashed curve), and 1 (dotted curve), and for (d) $\alpha_1/\gamma_M = \alpha_3/\gamma_M = 0.1$ (solid curve), 0.5 (dashed curve), and 1 (dotted curve); the phase angle θ_{A2} in coexisting Rayleigh and Brillouin-enhanced FWMs versus Δ_1/γ_M for (b) $\chi_T/\chi_M = 0.1$ (solid curve), 0.5 (dashed curve), and 1 (dotted curve) and for (e) $\alpha_1/\gamma_M = \alpha_3/\gamma_M = 0.1$ (solid curve), 0.5 (dashed curve), and 1 (dotted curve); the phase angle θ_{A2} in coexisting Raman, Rayleigh, and Brillouin-enhanced FWMs versus Δ_1/γ_M for (c) $\chi_M/\chi_R = 0.05$ (solid curve), 0.1 (dashed curve), and 0.3 (dotted curve), and for (f) $\alpha_1/\gamma_M = \alpha_2/\gamma_M = \alpha_3/\gamma_M = 0.1$ (solid curve), 0.5 (dashed curve), and 1 (dotted curve).

Rayleigh and Brillouin-enhanced FWM processes by the detuning Δ_1 and Δ_2. Similarly, we can obtain the phase angle of χ_{A1}, χ_{A2}, and χ_B, respectively. If Δ_1 or Δ_2 is large enough, the value of θ_{A2} or θ_B will equal zero, respectively, and coexisting Raman, Rayleigh, and Brillouin ASPBs will convert into the pure Raman or Rayleigh and Brillouin ASPB.

The experiment can be done by using three nanosecond dye lasers (color-locking) or femtosecond ultrashort lasers (phase-locking) D1, D2, and D3. The carbon disulfide (CS2) with $\Omega_R = 655.7\ \mathrm{cm}^{-1}$ vibrational mode was

contained in a sample cell with thickness 10 mm. The laser had linewidth 0.01 nm and pulse width 5ns. Here the Brillouin frequency is 0.3 cm^{-1}. The thickness of the sample in this experiment is thicker than the sample of the pre-experiment of the Raman and Rayleigh. D1 and D2 are used to generate frequencies at ω_1 and ω_2, respectively. A beam splitter is used to combine ω_1 and ω_2 components for the pump beams. Beam 1 and beam 2 intersected in the sample with a small angle between them. The relative time delay between beams 1 and 2 can be varied by an optical delay line controlled by a stepping motor. Beam 3, used as the probe beam and originating from D3 with frequency ω_3, propagating along the direction opposite that of beam 1.

More specifically, (i) for the coexisting Rayleigh and Brillouin ASPB, D1, D2, and D3 have the wavelengths $\lambda_1 = 561$ nm, $\lambda_2 = 565$ nm and $\lambda_3 = 561$ nm, respectively. Thus only Rayleigh and Brillouin-enhanced FWMs are generated due to the interaction of beam 3 and ω_1 component of beam 2, while FWM due to the interaction of beam 3 and ω_2 component of beam 2 is generated used as a reference signal. The ω_1 frequency can be varied. (ii) For the coexisting of Raman, Rayleigh, and Brillouin ASPBs, D1, D2, and D3 have the wavelength $\lambda_1 = 561$ nm, $\lambda_2 = 532$ nm and $\lambda_3 = 561$ nm, respectively. Thus, the Raman-enhanced mode (Raman resonant moving grating G_R) is excited by the interaction of beam 3 and ω_2 component of beam 2. On the other hand, the Rayleigh and Brillouin-enhanced mode (two Rayleigh non-resonant moving gratings G_{RM} and G_{RT}, and Brillouin resonant moving grating G_{BR}) is generated due to the interaction of beam 3 and ω_1 component of beam 2. As a result, Raman, Rayleigh, and Brillouin-enhanced FWMs are generated by the diffractions of the ω_2 component, and ω_1 component of beam 1 by Raman grating G_R, and the Rayleigh and Brillouin gratings G_{RM}, G_{RT} and G_{BR}, respectively.

In summary, based on three stochastic models, coexisting Raman, Rayleigh, and Brillouin-enhanced ASPBs is detected by homodyne and heterodyne methods, respectively. The subtle Markovian field correlation effects in three stochastic models have been investigated.The heterodyne detected signal of ASPB potentially offers rich dynamic information about the homogeneous broadening material phase of the third-order nonlinear susceptibility.

References

[1] Ulness D J. On the role of classical field time correlations in noisy light spectroscopy: Color locking and a spectral filter analogy. J Phys Chem A, 2003, 107: 8111 – 8123.

[2] Kirkwood J C, Albrecht A C. Multi-dimensional time-resolved coherent Raman six-wave mixing: a comparison of the direct and cascaded processes with femtosecond excitation and noisy light interferometry. J Raman Spectrosc, 2000, 31: 107 – 124.

[3] Kirkwood J C, Ulness D J, Albrecht A C. On the classification of the electric field spectroscopies: Application to Raman scattering. J Phys Chem A, 2000,

104: 4167 – 4173.

[4] Dugan M A, Albrecht A C. Radiation-matter oscilations and spectral-line narrowing in field-correlated 4-wave-mixing .I Theory Phys Rev A, 1991, 43: 3877 – 3921.

[5] DeMott D C, Ulness D J, Albrecht A C. Femtosecond temporal probes using spectrally tailored noisy quasi-cw laser light. Phys Rev A, 1997, 55: 761 – 771.

[6] Ulness D J, Albrecht A C. Theory of time-resolved coherent Raman scattering with spectrally tailored noisy light. J Raman Spectrosc, 1997, 28: 571 – 578.

[7] Stimson M J, Ulness D J, Albrecht A C. Time-resolved coherent Raman spectroscopy controlled by spectrally tailored noisy light. J Raman Spectrosc, 1997, 28: 579 – 587.

[8] Stimson M J, Ulness D J, Kirkwood J C, et al. Noisy-light correlation functions by frequency resolved optical gating. J Opt Soc Am B, 1998, 15: 505 – 514.

[9] Ma H, Gomes A S L, de Araujo C B. Raman-assisted polarization beats in time-delayed four-wave mixing. Opt Lett,1992, 17: 1052 – 1054.

[10] Mi X, Yu Z H, Jiang Q, et al. Phase-sensitive detection of Raman-enhanced nondegenerate four-wave mixing. J Opt Soc Am B, 2000, 17: 1543 – 1547.

[11] Zhang Y P, Hou X, Lu K Q, et al. Sixth-order correlation on Raman-enhanced polarization beats with phase-conjugation geometry. Opt Commun, 2000, 184: 265 – 276.

[12] Zhang Y P, Gan C L, Lu K Q, et al. Raman-enhanced polarization beats in Markovian stochastic fields. Opt Commun, 2002, 205: 163 – 186.

[13] Georges A T. Resonance fluorescence in Markovian stochastic fields. Phys Rev A, 1980, 21: 2034 – 2049.

[14] Bratfalean R, Ewart P. Spectral line shape of nonresonant four-wave mixing in Markovian stochastic fields. Phys Rev A, 1997, 56: 2267 – 2279.

[15] Ryan R E, Westling L A, Blumel R, et al. Two-photon spectroscopy: A technique for characterizing diode-laser noise. Phys Rev A, 1995, 52: 3157 – 3169.

[16] Chen C, Elliott D S, Hamilton M W. Two-photon absorption from the real Gaussian field. Phys Rev Lett, 1992, 68: 3531 – 3534.

[17] DeBeer D, Usadi E, Hartmann S R. Attosecond beats in sodium vapor. Phys Rev Lett, 1988, 60: 1262 – 1265.

[18] Bogdanov V L, Evdokimov A B, Lukomskil G V, et al. Subfemtosecond beats in an interference of the fields of Rayleigh scattering and four-wave mixing. JETP Lett, 1989, 49: 157 – 161.

[19] Zhang Y P, Gan C L, Song J P, et al. Attosecond sum-frequency Raman-enhanced polarization beating by use of twin phase-sensitive color locking noisy light beams. J Opt Soc Am B, 2005, 22: 694 – 711.

[20] Gan C L, Zhang Y P, Nie Z Q, et al. Competition between Raman and Rayleigh-enhanced four-wave mixings in attosecond polarization beats. Phys Rev A, 2009, 79: 023802.

[21] Zhao Y, Nie Z Q, Zhang Y P, et al. Coexisting Brillouin, Rayleigh, and Raman-enhanced four-wave mixings. Opt Soc Am B, 2010, 27: 863 – 875.

[22] Fu P M, Mi X, Yu Z H, et al. ultrafast modulation spectroscopy in a cascade 3-level system. Phys Rev A, 1995, 52: 4867 – 4870.

[23] Zhang Y P, Sun L Q, Tang T T, et al. Effects of field correlation on polarization beats. Phys Rev A, 2000, 61: 053819.

[24] Zhang Y P, Sun L Q, Tang T T, et al. Fourth-order interference on polarization beats in a four-level system. J Opt Soc Am B, 2000, 17: 690 – 696.

[25] Zhang Y P, Tang T T, Sun L Q, et al. Effects of fourth-order coherence on ultrafast modulation spectroscopy. Phys Rev A, 2000, 61: 023809.

[26] Zhang Y P, de Araujo C B, Eyler E E. Higher-order correlation on polarization beats in Markovian stochastic fields. Phys Rev A, 2001, 63: 043802.

[27] Zhang Y P, Lu K Q, Li C S, et al. Correlation effects of chaotic and phase-diffusion fields on polarization beats in a V-type three-level system. J Mod Opt, 2001, 48: 549 – 564.

[28] Zhang Y P, Gan C L, Farooqi S M, et al. Four-level polarization beats with broadband noisy light. J Opt Soc Am B, 2002, 19: 1204 – 1215.

[29] Fu P M, Jiang Q, Mi X, et al. Rayleigh-Type Nondegenerate Four-Wave Mixing: Ultrafast Measurement and Field Correlation. Phys Rev Lett, 2002, 88: 113902.

[30] Yu Z H, Mi X, Jiang Q, et al. Field-correlation effects on Raman-enhanced nondegenerate four-wave mixing. Phys Rev A, 1997, 55: 2334 – 2339.

[31] Morita N, Yajima T. Ultrahigh-time-resolution coherent transient spectroscopy with incoherent light. Phys Rev A, 1984, 30: 2525 – 2530.

[32] Bout D V, Berg M. Ultrafast Raman echo experlments in liquids. J Raman Spectrosc, 1995, 26: 503 – 511.

[33] Tokmakoff A, Fleming G R. Two-dimensional Raman spectroscopy of the intermolecular modes of liquid CS2. J Chem Phys, 1997, 106: 2569 – 2582.

[34] Jacobson A G, Shen Y R. Coherent Brillouin spectroscopy. Appl Phys Lett, 1979, 34: 464 – 467.

[35] Skeldon M D, Narum P, Boyd R W. Non-frequency-shifted, high-fidelity phase conjugation with aberrated pump waves by Brillouin-enhanced four-wave mixing. Opt Lett, 1987, 12: 343 – 345.

[36] Narum P, Boyd R W. Non-frequency shifted phase conjugation by Brillouin-enhanced four-wave mixing. IEEE J Quantum Electron., 1987, 23: 1211 – 1216.

[37] Randall C J, Albritton J R. Chaotic Nonlinear Stimulated Brillouin Scattering. Phys Rev Lett, 1984, 52: 1887 – 1890.

4 Multi-Dressing Four-Wave Mixing Processes in Confined and Non-confined Atomic System

Other than generating various four-wave mixing (FWM) processes, multi-level atomic system can also be used to generate co-existing FWM and six-wave mixing (SWM) processes with specially-designed spatial patterns and phase-watching conditions for laser beams. Making use of electro magnetically induced transparency (EIT) windows, and induced atomic coherence, the FWM and SWM signals can be made to be very efficient and pass through the dense atomic medium. When the relative phase between different multi-wave mixing processes is tuned, frequency, spatial, and temporal interferences can occur between two different wave-mixing processes. In such cases, FWM and SWM signals are modulated with the phase difference. In this chapter, using phase-control between FWM and SWM channels in a four-level atomic system, we describe temporal and spatial interference between these two high-order nonlinear optical processes. Efficient and co-existing FWM and SWM signals are produced in the same EIT window via atomic coherence. On the other hand, we present the interplay between FWM, SWM, and eight-wave mixing (EWM) resulting from atomic coherence in multi-level atomic systems. FWM with three kinds of dual-dressed schemes (nested, sequential, and parallel schemes), SWM with the quadruply nested dressed, and EWM with the parallel combination of two nested dressed schemes coexisting synchronously in a multi-dressed EIT system were well described. At last, we also investigated the coexisting FWM, SWM and EWM in ultra-thin, micrometer and long cells. Investigations of these multi-dressing schemes and interactions are very useful to understand and control the generated high-order nonlinear optical signals.

4.1 Temporal and Spatial Interference Between Four-Wave Mixing and Six-Wave Mixing Channels

For more than two decades, the interaction of coherent light with matter, and the "control" of matter using light, has been a prominent scientific theme. When two transition paths exist between an initial state and a final state,

the total transition probability can be either enhanced or suppressed, depending on the relative phase between two transition amplitudes [1 – 6]. Such the quantum coherent control technique has been used to control the transition probability in atoms [1], photo-electron angular distribution [6], phase-controlled current in semiconductors [2], and various chemical reactions [4, 7, 8]. Recently, destructive interference due to two intrinsic four-wave mixing (FWM) processes was used to understand the bi-photon generation in a two-level atomic system [9].

Here, we experimentally demonstrate a new type of phase-controlled, spatial-temporal coherent interference between two different high-order nonlinear wave-mixing [i.e., FWM and six-wave mixing (SWM)] processes in a four-level, inverted-Y system in rubidium atoms. By making use of atomic coherence induced by laser fields among different energy levels, SWM signals can be greatly enhanced and even made to be in the same order of magnitude as co-existing FWM signals [10, 11]. With a specially-designed spatial configuration for laser beams for phase matching and an appropriate optical delay introduced in one of the pump laser beams, we can have a controllable phase difference between dominant FWM and SWM processes. When this relative phase is varied, temporal, as well as spatial, interference can be observed. One of the interesting features is that the interference in the time domain is in the femtosecond time scale, corresponding to the optical transition frequency excited by the delayed pump laser beam. Understanding the mechanism for efficient generations of high-order nonlinear optical processes and interplays between them, especially with the ability to control these processes with a controllable phase difference, can have broad impacts in many fields of science including coherent control for chemical reactions [4, 7, 8], stable 2D-soliton generation for optical communications [12], high-precision spectroscopy [13], nonlinear spectroscopy, and quantum information processing [9, 14 – 16]

Let us consider a four-level inverted Y-type atomic system as shown in Fig. 4.1(b). The four relevant energy levels are $5S_{1/2}, F = 2(|0\rangle), 5S_{1/2}, F = 3(|3\rangle), 5P_{3/2}(|1\rangle)$, and $5D_{5/2}(|2\rangle)$ in ^{85}Rb. In the three-level ladder-type subsystem $(|0\rangle - |1\rangle - |2\rangle)$, as shown in Fig. 4.1 (a), if a strong coupling beam E_2 (frequency $\omega_2, \boldsymbol{k}_2$, and Rabi frequency G_2) couples to the upper transition and a weak probe beam E_1 (frequency $\boldsymbol{k}_1$, and Rabi frequency G_1) interacts with the lower transition, and they propagate in the opposite direction through the atomic medium, an electromagnetically induced transparency (EIT) window will be created for the probe field due to two-photon, Doppler-free configuration in the Doppler-broadened medium [17]. When another coupling laser beam E_2' (frequency $\omega_2, \boldsymbol{k}_2'$, and G_2') is also applied to the upper transition [Fig. 4.1 (a)], a FWM signal will be generated with frequency ω_1 in the created EIT window of the ladder subsystem. Such a FWM (E_F) process can be described by using a perturbative the chain: $\rho_{00}^{(0)} \xrightarrow{\omega_1} \rho_{10}^{(1)} \xrightarrow{\omega_2} \rho_{20}^{(2)} \xrightarrow{-\omega_2} \rho_{10}^{(3)}$ [10]. If we align coupling and probe laser beams in a spatial pattern, as shown in Fig. 4.1 (c), the generated FWM signal (ω_3 E_F) will have a small

angle θ from $\boldsymbol{k}_1$, satisfying the phase-matching condition $\boldsymbol{k}_F = \boldsymbol{k}_1 + \boldsymbol{k}_2 - \boldsymbol{k}_2'$. The FWM efficiency depends on the intensities of all the laser beams involved. Next, let us turn our attention to Fig. 4.1 (b), where coupling beam E_2' is blocked and two pump beams $E_3(\omega_3, \boldsymbol{k}_3$, and $G_3)$ and $E_3'(\omega_3, \boldsymbol{k}_3'$, and $G_3')$ are applied on transition $|3\rangle$–$|1\rangle$. The laser beams are carefully aligned in the square-box pattern [10], as shown in Fig. 4.1 (c). In this case, the FWM channel in the ladder subsystem is turned off (without E_2'), and the FWM process in the $\wedge$-type subsystem ($|0\rangle - |1\rangle - |3\rangle$) is not efficient (not observable in the experiment) since no EIT window exists for this configuration (probe and pump beams counter-propagate) [17]. From phase-matching condition ($\boldsymbol{k}_S = \boldsymbol{k}_1 + \boldsymbol{k}_3 - \boldsymbol{k}_3' + \boldsymbol{k}_2 - \boldsymbol{k}_2$), efficient SWM signals can be generated via either $\rho_{00}^{(0)} \xrightarrow{\omega_1} \rho_{10}^{(1)} \xrightarrow{\omega_2} \rho_{20}^{(2)} \xrightarrow{-\omega_2} \rho_{10}^{(3)} \xrightarrow{-\omega_3} \rho_{30}^{(4)} \xrightarrow{\omega_3} \rho_{10}^{(5)}$ or $\rho_{00}^{(0)} \xrightarrow{\omega_1} \rho_{10}^{(1)} \xrightarrow{-\omega_3} \rho_{30}^{(2)} \xrightarrow{\omega_3} \rho_{10}^{(3)} \xrightarrow{\omega_2} \rho_{20}^{(4)} \xrightarrow{-\omega_2} \rho_{10}^{(5)}$, which are both in the direction of θ angle from $\boldsymbol{k}_1$ [denoted as $\boldsymbol{k}_S$ and E_S with frequency ω_1 in Figs. 4.1 (b) and (c)], and these SWM signals also fall into the same EIT window as the FWM signal in the ladder subsystem. In the generated FWM and SWM signal beams, the coherence lengths are given by $l_F = 2c/[n(\omega_2/\omega_1)\,|\omega_2 - \omega_1|\,\theta^2]$ and $l_S = 2c/[n(\omega_3/\omega_1)\,|\omega_3 - \omega_1|\,\theta^2]$, respectively, with n being the refractive index at the frequency ω_1. In the experiment, θ is very small (0.3^0) so that l_F and l_S are much larger than the interaction length L, so the phase-mismatch effect can be neglected.

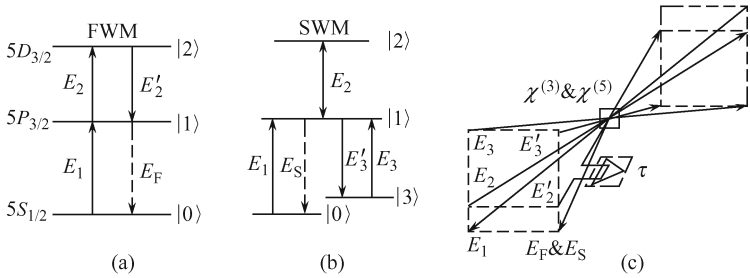

Fig. 4.1. Atomic levels and laser beam arrangements for generating co-existing FWM (a) and SWM (b) processes in the same EIT window. The dash-dotted lines are the generated FWM (E_F) and SWM (E_S) signals. (c) Spatial beam (square-box) geometry used in the experiment, τ is a time delay through a precision translation stage for beam E_2'. The probe beam E_1 propagates in the opposite direction from the coupling and pump beams with small angles.

Now, we add the coupling beam E_2' back into the upper transition, but keep its power to be adjustable. When the power of E_2' is same as the power of E_2, the FWM process in the ladder subsystem is very efficient, and it dominates over the SWM processes, so only this FWM signal can be observed. Typically, the lower-order nonlinear optical processes always overpower the higher-order ones (normally by several orders of magnitude [18]), which is the reason why co-existing FWM and SWM processes were not well studied

in the atomic systems previously. However, in the current case as the power of E_2' decreases, the FWM signal reduces rapidly and the relative strengths of the SWM signal increases, until the SWM signal dominates when E_2' is reduced to zero. By carefully adjusting the power of E_2' relative toE_2, the SWM signals are made to be in the same strength as the FWM signal, as shown in Fig .4.2 (a), and both fall in the same EIT window [Fig. 4.2 (b)]. Since $G_2' << G_2$ when SWM signals get to be the same order as the FWM, the SWM processes with E_2' replacing E_2 in Fig. 4.1 (b) can be negligible. Notice that E_2' only involves in the FWM process, so it can be used to tune not only the relative strength of the FWM and SWM processes, but also the relative phase between these two nonlinear wave-mixing processes, since E_2' is split from the E_2 laser beam and delayed with a precision (nanometer resolution) computer-controlled translation stage.

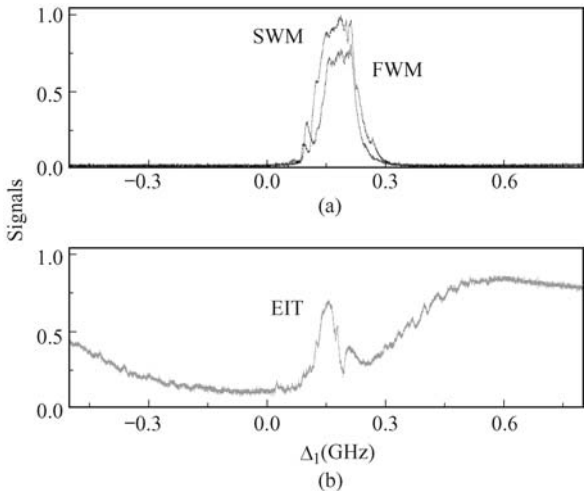

Fig. 4.2. Measured EIT-assisted FWM [solid line of (a)] and SWM [dashed line of (a)] signal intensities, and the corresponding probe beam transmission (b) for selected atomic density (0.2×1012 cm^{-3}) versus probe detuning Δ_1. The experimental parameters are $G_1 = 2\pi \times 15$ MHz, $G_2 = 2\pi \times 60$ MHz, $G_2' = 2\pi \times 19$ MHz, $G_3 = G_3' = 2\pi \times 87$ MHz, $\Delta_3 = 0$, and $\Delta_2 = 170$ MHz. Adopted from Ref. [16].

The experiment was done with ^{85}Rb atoms in an atomic vapor cell of 5 cm long, which is wrapped in μ-metal for magnetic shielding and heated to 60°C. The probe beam E_1 is from an extended-cavity diode laser (ECDL) at 780.23 nm. The coupling beams E_2 and E_2' are split from another ECDL at 775.98 nm. The beam E_2' is delayed by an amount τ using a computer-controlled stage. The pump beams E_3 and E_3' are split from a cw Ti: Sapphire laser at 780.24 nm. The CCD and an avalanche photodiode (APD) are set at an angle θ from the probe beam (with a beam splitter) to measure the dominant FWM and SWM signals. The transmitted probe beam is simultaneously monitored by a silicon photodiode. The powers and frequency detunings of the coupling

beams $E_2(E_2')$ are 40 mW (4 mW) and 170 MHz, and those of the pump beams $E_3(=E_3')$ are 67 mW and 0 MHz, respectively. Since the angles between the laser beams in the square-box pattern are very small (0.3°) the optical alignments of the laser beams are quite tedious and challenging

Under the current conditions of $G_3, G_3' > G_2 >> G_2', G_1$, and neglecting other multi-wave mixing processes either very weak or propagating in other directions, the total detected intensity at angleθ is given by the co-existing FWM (E_F) and SWM (E_S) signal as

$$I(\tau, r) \propto |\chi^{(3)}|^2 + |\eta\chi^{(5)}|^2 + 2\eta|\chi^{(3)}||\chi^{(5)}|\cos(\varphi_3 - \varphi_5 + \varphi), \tag{4.1}$$

where $\eta = \varepsilon_2\varepsilon_3\varepsilon_3'/\varepsilon_2', \chi^{(3)} = -\mathrm{i}\mu_1^2\mu_2^2 N/\{\varepsilon_0\hbar^3 d_1 d_2[d_1 + (G_3 + G_3')^2/d_3]\} = |\chi^{(3)}|\exp(\mathrm{i}\varphi_3), \Omega_R, \chi^{(5)} = 2\mathrm{i}\mu_1^2\mu_2^2\mu_3^2 N/(\varepsilon_0\hbar^5 d_1^3 d_2 d_3) = |\chi^{(5)}|\exp(\mathrm{i}\varphi_5), d_1 = \Gamma_{10} + \mathrm{i}\Delta_1, d_3 = \Gamma_{30} + \mathrm{i}(\Delta_1 - \Delta_3)$ with $\Delta_i = \Omega_i - \omega_i, \varphi = \Delta\boldsymbol{k}\cdot\boldsymbol{r} - \omega_2\tau$ and $\Delta\boldsymbol{k} = \boldsymbol{k}_F - \boldsymbol{k}_S = (\boldsymbol{k}_2 - \boldsymbol{k}_2') - (\boldsymbol{k}_3 - \boldsymbol{k}_3')$. μ_1, μ_2 and μ_3 are the dipole moments of the transitions $|0\rangle - |1\rangle, |1\rangle - |2\rangle$ and $|3\rangle - |1\rangle$, respectively, and $\varepsilon_2, \varepsilon_2', \varepsilon_3, \varepsilon_3'$ are the respective amplitudes of the fields.

From Eq. (4.1), it is clear that the total signal has not been only spatial interference with a period of $2\pi/\Delta k$, but also an ultrafast time oscillation with a period of $2\pi/\omega_2$, which form a spatial–temporal interferogram. With a plane-wave approximation and the square-box configuration for the laser beams with small angles [Fig. 4.1(c)], the spatial interference occurs in the plane perpendicular to the propagation direction.

Figure 4.3 depicts a typical three-dimensional interferogram pattern [Fig. 4.3 (a)] and their projections on time [Fig. 4.3 (c)] and space [Fig. 4.3 (d)] planes. Figure 4.3 (b) presents a theoretical simulation for the total intensity with appropriate parameters. The temporal oscillation period is $2\pi/\omega_2 = 2.588$ fs, which corresponds to the $5P_{3/2}$ to $5D_{5/2}$ transition frequency of $\Omega_2 = 2.427\ \mathrm{fs}^{-1}$ in ^{85}Rb. Such measurement of atomic transition frequency in optical wavelength range is Doppler free and can be used as a tool for precision frequency measurement. If this technique is used on a transition with the larger energy difference, sub-femtosecond time resolution can be achieved by scanning translation stage in nanometer precision. The spatial interference is determined by the value of $\Delta k \approx 2\pi\,|\lambda_2 - \lambda_3|\,\theta/\lambda_2\lambda_3$. In our experimental situation, we have $2\pi/\Delta k = 3.3$ mm along the direction of Δk, which gives a little more than one interference fringe, as shown in Fig. 4.3 (d). When the phase delay is varied on E_2' beam, the spatial interference pattern can be changed from destructive to constructive at the center of the beam profile ($r = 0$) [19]. The solid curves in Fig. 4.3 (c) and Fig. 4.3 (d) are theoretical calculations from the full density-matrix equations, which fit well with the experimentally measured results.

To see how well the transition frequency Ω_2 can be determined from such time interference fringe, we need to consider two cases. When the laser linewidths are much narrower than the homogeneous linewidths of the transitions, the phase fluctuations of the laser fields will limit the range of the time delay, which puts an upper bound on the accuracy of the modulation

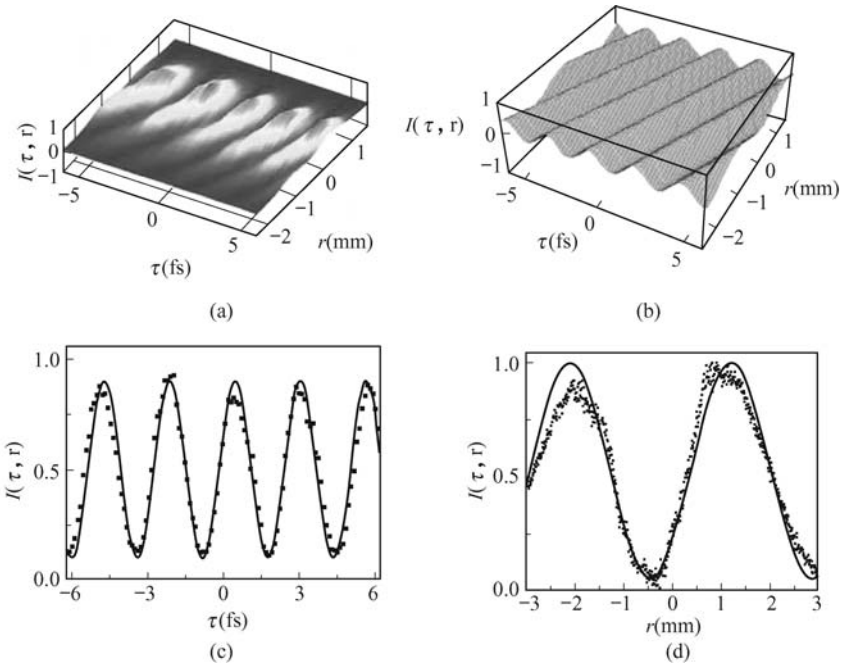

Fig. 4.3. (a) A three-dimensional spatial-temporal interferogram of the FWM and SWM signal intensity $I(\tau, r)$ versus time-delay τ and transverse position r. (b) The theoretically simulated result from Eq. (6.1). (c) Cross section of the spatial-temporal interferogram on time plane ($r = 0$) (square points are experimental data, and the solid curve is the theoretically simulated result). (d) Measured (square points) and calculated (solid curve) cross section of the spatial-temporal interferogram on a space plane ($\tau = 0$), respectively. The signal intensity is normalized to 1. The parameters are $\Omega_2 = 2.427$ fs^{-1}, $\Delta k = 1.\ 9$ mm^{-1}, and $\eta = 1.5$.

frequency measurement. In such case, the accuracy of measuring modulation frequency is determined by the laser linewidths. This measurement depends on how well ω_2 can be tuned to the transition frequency Ω_2, and is Doppler-free, which can be useful in optical spectroscopy and precision measurements. In the other case, when the laser bandwidths are larger than the atomic decay rates, the modulation frequency corresponds directly to the resonant frequency Ω_2. The accuracy in the modulation frequency measurement will then be determined by the homogeneous linewidths of the atomic transitions, even in the Doppler-broadened atomic medium, which is applicable to transitions between metastable states.

Figure 4.4 (a) shows the temporal interference with a much longer time delay in beam E_2', which makes the spatial-temporal interferogram to be dominated by the temporal component. By fitting the interference fringe [Fig. 4.4 (b)], the period is determined to be 2.588 fs. Using Fourier transformation of the interferogram data (with a time delay change of 50 ps), as shown in Fig. 4.4 (c), the modulation frequency is determined to be 2.427 $\pm$0.004 fs^{-1},

which corresponds to the resonant frequency of the transition from $5P_{3/2}$ to $5D_{5/2}$ in ^{85}Rb. Of course, what we present here is simply a proof of principle demonstration with laser linewidths of about 1 MHz and such measurement technique can surely be further improved.

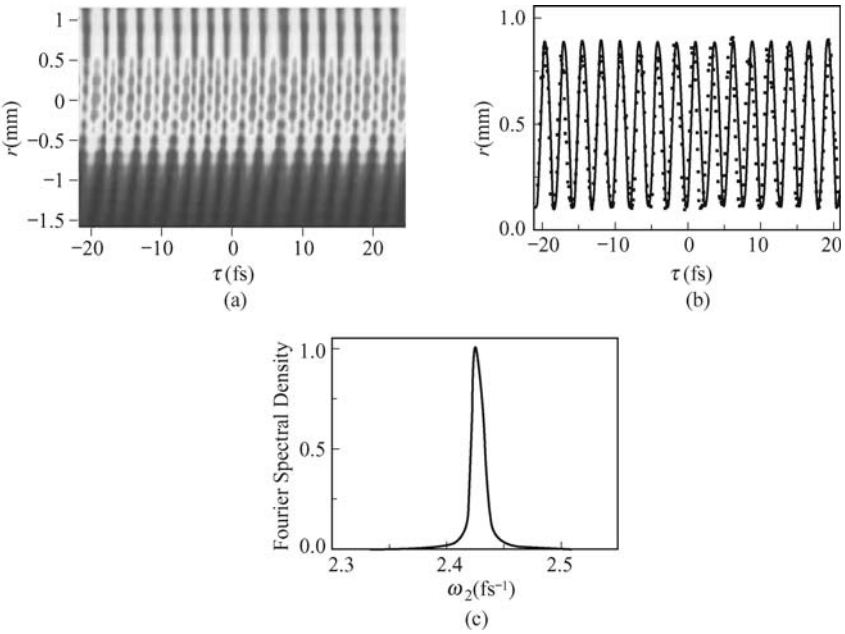

Fig. 4.4. The spatial-temporal interferogram (a) versus τ and r, $\Omega_2 = 2.427$ fs^{-1}, $\Delta k = 1.\ 9$ mm^{-1}, and $\eta = 1.5$. The theoretically simulated results from Eq. (4.1) are plotted in (b) (solid line) together with the measured data (dots). (c) Fourier spectrum of the beat signal.

A few points are worth mentioning here. First, our experimental results indicate that we cannot only enhance SWM to be in the same order of intensity as the co-existing FWM signal, but also manipulate their spatial and temporal behaviors by controlling the phase delay in one of the laser beams. Such spatial-temporal interferogram between FWM and SWM signals was generated with three independent laser sources. Second, by adjusting the power of the E_2' beam, the relative strengths of the FWM and SWM signals can be easily adjusted. In the case of making $E_S << E_F$ (letting $E_2' \rightarrow E_2$ in power), Eq. (4.1) can serve as a heterodyne detection method to determine the ratio of high-order nonlinear susceptibilities ($\chi^{(5)}/\chi^{(3)}$). Since $\chi^{(3)}$ can be easily measured [20], the $\chi^{(5)}$ coefficient in such an atomic medium can then be determined. Third, the technique used here can be easily transferred to solid materials, on which EIT and FWM processes can be easily obtained. Fourth, with controlled FWM and SWM processes and enhanced efficiency via atomic coherence, and the opened EIT window, three-photon entanglement or correlated triplet photons [14] can be generated for testing

fundamental quantum mechanics and quantum information processing [14, 15].

Efficient FWM and SWM processes have been shown to co-exist in the four-level inverted-Y atomic system. By adjusting the intensity and time delay of one of the coupling beams (E_2'), the relative strength and spatial-temporal interferences between the FWM and SWM channels can be controlled. The generated spatial-temporal interferogram in femtosecond time scale can be used to determine the optical transition frequency with a Doppl er-free precision. Such manipulations of high-order nonlinear optical processes and their interplays in multi-level atomic systems can have potential applications in coherence quantum control, nonlinear optical spectroscopy, precision measurements, and quantum information processing.

4.2 Intermixing Between Four-Wave Mixing and Six-Wave Mixing in a Four-level Atomic System

Multiwave mixing due to atomic coherence and polarization beat (PB) in multi-level atomic systems has attracted a lot of attention recently [20 – 25]. PB originates from the interference between the macroscopic polarizations that are excited simultaneously in the medium [23 – 25]. An important application of electromagnetically induced transparency (EIT) [20, 21] is its ability to enhance the efficiencies of nonlinear optical processes. Two of the interesting nonlinear optical processes are FWM and six-wave mixing (SWM), which normally have high efficiencies in closely-cycled four-level systems such as double-Λ system [26 – 28]. Recently, SWM processes were observed in closed four-level atomic systems [27]. Such high-order SWM process is often obscured by sequential or parallel cascade third-order FWM processes that compete with the direct process and give similar time domain behavior, though they probe different overtone vibration dynamics [29]. Garrett *et al.* also explored the two-photon plus three-photon resonant FWM and SWM involving stimulated hyper Raman generation as opposed to pause cognate generation [30].

Although triple resonance spectroscopy has been reported previously by fluorescence detection [31], the current method is a coherence phenomenon, where atomic coherence is induced among different energy levels. Due to the parametric nature of this process, the signal is coherent radiation. Comparing with the earlier FWM [24, 25] or SWM work [27], our system has some substantial advantages as following: (i) the coherent interplay between the SWM and FWM processes through the EIT windows has been considered (EIT window-opened or enhanced nonlinear optical processes, which are otherwise closed); (ii) the evolution pathways of the dressed FWM have also been identified and studied [32]; (iii) quantum interference (QI) between two FWM channels, or between one FWM and one SWM channels leads to sub-

stantial suppression and enhancement of the dressed FWM signals; (iv) PB of coexisting FWM and SWM results in the acquirement of the fifth-order nonlinear response.

4.2.1 Interplay Between FWM and SWM

In order to understand such interplay between FWM and SWM in a folded four-level system, we present both the steady state analysis without time delay and the non-steady state analysis with time delay.

We consider a folded four-level system (Fig. 4.5), in which states between $|0\rangle$ and $|1\rangle, |1\rangle$ and $|2\rangle$, and $|2\rangle$ and $|3\rangle$ are dipole allowed transitions with resonant frequencies Ω_1, Ω_2 and Ω_3 and dipole moments μ_1, μ_2 and μ_3, respectively. As shown in Fig. 4.5 (d), beam 2 includes three color-locked fields, $E_2(\omega_2, \boldsymbol{k}_2,$ and Rabi frequency $G_2), E_3(\omega_3, \boldsymbol{k}_3,$ and Rabi frequency $G_3)$, and E_3' $(\omega_3, \boldsymbol{k}_3',$ and Rabi frequency $G_3')$, and beam 3 has one locked field, $E_2'(\omega_2, \boldsymbol{k}_2',$ and Rabi frequency $G_2')$. A small angle exists between these two beams. Beam 1 is a monochromatic field $E_1(\omega_1, \boldsymbol{k}_1,$ and Rabi frequency $G_1)$ which propagates along the opposite direction of beam 2. Assuming near resonance so that E_1 drives the transition from $|0\rangle$ to $|1\rangle$ while E_2 drives the transition from $|1\rangle$ to $|2\rangle$ simultaneously, which induce atomic coherence between $|0\rangle$ and $|2\rangle$ through two-photon excitation [30]. This established atomic coherence is probed by E_2' in beam 3 and, as a result, a FWM signal of frequency ω_1 (beam 4) is generated almost opposite to the direction of beam 3, i.e., $\rho_{00}^{(0)} \xrightarrow{\omega_1} \rho_{10}^{(1)} \xrightarrow{\omega_2} \rho_{20}^{(2)} \xrightarrow{-\omega_2} \rho_{10}^{(3)}$ (I). Next, we apply two coupling laser fields with same frequency $\omega_3(\approx \Omega_3)$, both of which propagate along beam 2, to drive the transition $|2\rangle$ to $|3\rangle$. The strong coupling fields E_3 and E_3' create dressed atomic states $|+\rangle$ and $|-\rangle$ from the level $|2\rangle$ [Fig. 4.5 (c)], which are the coherent superpositions of the states $|2\rangle$ and $|3\rangle$. Physically, in the dressed-state picture, suppression and enhancement of the dressed FWM signals are due to destructive and constructive interference between the two FWM channels: $\rho_{00}^{(0)} \xrightarrow{\omega_1} \rho_{10}^{(1)} \xrightarrow{\omega_2} \rho_{+0}^{(2)} \xrightarrow{-\omega_2} \rho_{10}^{(3)}$ (FWM^+) and $\rho_{00}^{(0)} \xrightarrow{\omega_1} \rho_{10}^{(1)} \xrightarrow{\omega_2} \rho_{-0}^{(2)} \xrightarrow{-\omega_2} \rho_{10}^{(3)}$ (FWM^-), respectively. On the other hand, in the bare-state picture, the simultaneous interactions of atoms with E_1 of beam 1, as well as E_2 and E_3' of beam 2, can induce atomic coherence between $|0\rangle$ and $|3\rangle$ through resonant two-photon or resonant three-photon transition [30] under particular conditions [Fig. 4.5 (b)]. This induced atomic coherence is then probed by E_3 of beam 2 and E_2' of beam 3 and, as a result, a SWM signal of frequency ω_1 (beam 4) is generated almost opposite to the direction of beam 3, i.e., $\rho_{00}^{(0)} \xrightarrow{\omega_1} \rho_{10}^{(1)} \xrightarrow{\omega_2} \rho_{20}^{(2)} \xrightarrow{-\omega_3} \rho_{30}^{(3)} \xrightarrow{\omega_3} \rho_{20}^{(4)} \xrightarrow{-\omega_2} \rho_{10}^{(5)}$ (II) [Fig. 4.5 (e)]. The phase evolution is illustrated by the Feynman diagram shown in Fig. 4.5 (e). Such Feynman diagram provides a convenient approach to keep

track of possible quantum mechanical path to a given order of electric field in a perturbative expansion of the optical Bloch equations. QI and PB lead to interplay between these SWM and FWM processes. The specific evolution pathways of the dressed FWM can be controlled by the coupling field.

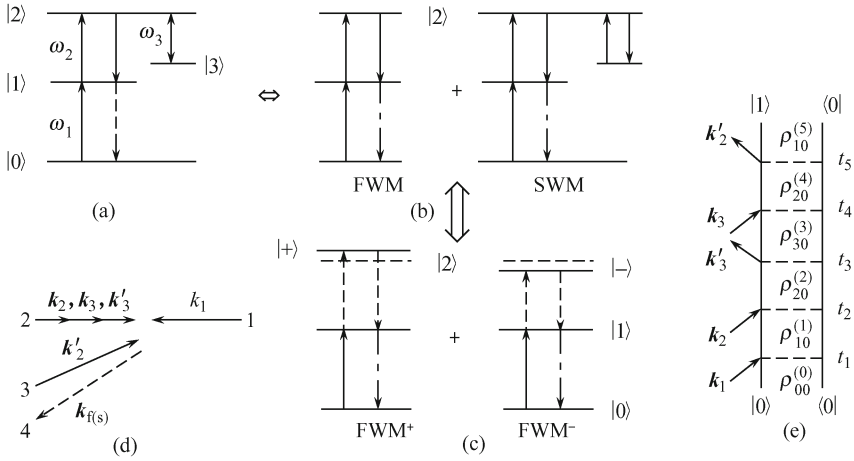

Fig. 4.5. Ladder diagrams representing the dressed FWM evolution pathways, and the interplay between SWM and FWM via atomic coherence: (a) the dressed FWM, (b) FWM+SWM, (c) FWM^{+}+FWM^{-}, (d) Phase-conjugation geometry, (e) SWM double-sided Feynman diagram. The solid and dashed vertical arrows represent ket-side interactions. The dash-dotted arrows are the emitted FWM or SWM signal. The primed vectors are with time delay τ.

The Rabi frequencies are defined as $G_i = \varepsilon_i \mu_i/\hbar, G_i' = \varepsilon_i' \mu_i/\hbar, \alpha = G_1 G_2 (G_2')^*$ and $\beta = G_1 G_2 (G_3')^* G_3 (G_2')^* (G_3 \approx G_3' \approx G)$; while the noisy fields are $E_i = \varepsilon_i u_i(t) \mathrm{e}^{\mathrm{i}\boldsymbol{k}_i \cdot \boldsymbol{r} - \mathrm{i}\omega_i t}$ and $E_i' = \varepsilon_i' u_i(t-\tau) \mathrm{e}^{\mathrm{i}(\boldsymbol{k}_i' \cdot \boldsymbol{r} - \omega_i t + \omega_i \tau)}$ (τ is a time delay). $\varepsilon_i, \boldsymbol{k}_i (\varepsilon_i', \boldsymbol{k}_i')$ are the constant field amplitude and the wave vector. $u_i(t) (u_1 \approx 1)$ is a dimensionless statistical factor that contains phase and amplitude fluctuations (i.e., $u_i(t) = \varepsilon_i(t) \exp[i\theta_i(t)]$, here $\varepsilon_i(t)$ contains pure amplitude fluctuation, while $\Omega_R \theta_i(t)$ contains pure phase fluctuation). The $u_i(t)$ is taken to be a complex ergodic stochastic function of t, which obeys complex circular Gaussian statistics in the chaotic field. Γ_{10}, Γ_{20} and Γ_{30} are the transverse relaxation rates between states $|0\rangle$ and $|1\rangle, |0\rangle$ and $|2\rangle, |0\rangle$ and $|3\rangle$, respectively. The detuning factors are defined as $\Delta_1 = \Omega_1 - \omega_1, \Delta_2 = \Omega_2 - \omega_2, \Delta_3 = \Omega_3 - \omega_3, \Delta_a = \Delta_1 + \Delta_2, \Delta_b = \Delta_a - \Delta_3, d_1 = \Gamma_{10} + \mathrm{i}\Delta_1, d_2 = \Gamma_{20} + \mathrm{i}\Delta_a, d_3 = \Gamma_{30} + \mathrm{i}\Delta_b$. The FWM and SWM phase matching conditions are $\boldsymbol{k}_f = \boldsymbol{k}_1 + \boldsymbol{k}_2 - \boldsymbol{k}_2'$ and $\boldsymbol{k}_s = \boldsymbol{k}_1 + \boldsymbol{k}_2 - \boldsymbol{k}_3' + \boldsymbol{k}_3 - \boldsymbol{k}_2'$, respectively.

The nonlinear polarization responsible for the dressed FWM signal is proportional to the off-diagonal density matrix element ρ_{10}'. We will assume, as usual, that G_1, G_2, and G_2' are weak, whereas the coupling field G can be of arbitrary magnitude. Thus ρ_{10}' needs to be calculated to the order

$G_1G_2G_2'$, but to all orders in G. Without the coupling field G, by virtue of the Liouville pathway (I), we obtain $\rho_{10}^{(3)} = -\mathrm{i}\alpha \mathrm{e}^{\mathrm{i}\boldsymbol{k}_f\cdot\mathbf{r}}/(d_1^2 d_2)$, here $\rho_{10}^{(3)}$ is the density-matrix element of the pure FWM. In the presence of the coupling field G, the two-photon atomic coherence $\rho_{20}^{(2)}$ can be obtained by solving the coupling equations:

$$\begin{cases} \dfrac{\partial \rho_{20}^{(2)}}{\partial t} = -d_2\rho_{20}^{(2)} + \mathrm{i}G_2\mathrm{e}^{\mathrm{i}\boldsymbol{k}_2\cdot\mathbf{r}}\rho_{10}^{(1)} + \mathrm{i}G_3\mathrm{e}^{\mathrm{i}\boldsymbol{k}_3\cdot\mathbf{r}}\rho_{30}, \\ \dfrac{\partial \rho_{30}}{\partial t} = -d_3\rho_{30} + \mathrm{i}(G_3')^*\mathrm{e}^{-\mathrm{i}\boldsymbol{k}_3\cdot\mathbf{r}}\rho_{20}^{(2)}. \end{cases} \tag{4.2}$$

In the steady-state case $\partial\rho_{20}^{(2)}/\partial t = \partial\rho_{30}/\partial t = 0$ and zero time delay $\tau = 0$, we can obtain $\rho_{20}^{(2)} = \mathrm{i}G_2 e^{\mathrm{i}\boldsymbol{k}_2\cdot\mathbf{r}} d_3\rho_{10}^{(1)}/[d_2d_3 + |G|^2]$ from Eq. (4.2). We can also get $\rho_{10}^{(1)} = \mathrm{i}G_1\mathrm{e}^{\mathrm{i}\boldsymbol{k}_1\cdot\mathbf{r}}/d_1$ and $\rho_{10}^{(3)} = \mathrm{i}(G_2')^*\mathrm{e}^{-\mathrm{i}\boldsymbol{k}_2'\cdot\mathbf{r}}\rho_{20}^{(2)}/d_1$ via the FWM the chain (I). Thus, the dressed FWM density-matrix element is $\rho_{10}' = \dfrac{-\mathrm{i}\alpha d_3\mathrm{e}^{\mathrm{i}\boldsymbol{k}_f\cdot\mathbf{r}}}{d_1^2(d_2d_3 + G^2)}$. Note that ρ_{10}' is not a purely third-order nonlinearity ($\rho_{10}^{(3)}$), instead it denotes the dressed FWM, including fifth-order nonlinear responses.

Under assumption $\zeta >> 1(\zeta = G^2/\psi, \psi = \Gamma_{20}\Gamma_{30}, \Gamma' = \Gamma_{20} + \Gamma_{30})$, the dressed FWM intensity becomes sum of two separate FWMs $|\rho_{10}'|^2 \approx \left|\rho_+^{(3)}\right|^2 + \left|\rho_-^{(3)}\right|^2$, here $\rho_+^{(3)} = \dfrac{-\mathrm{i}\alpha\mathrm{e}^{\mathrm{i}\boldsymbol{k}_f\cdot\mathbf{r}}}{d_1^2[\mathrm{i}(\Delta_1 + \Delta_{2+}) + \Gamma']}, \rho_-^{(3)} = \dfrac{-\mathrm{i}\alpha\mathrm{e}^{\mathrm{i}\boldsymbol{k}_f\cdot\mathbf{r}}}{d_1^2[\mathrm{i}(\Delta_1 + \Delta_{2-}) + \Gamma']}, \Delta_{2\pm} = \Delta_2 \pm \Delta_{AT}/2 = \Delta_2 \pm [G(G^2 + 2\Gamma_{30}\Gamma')^{1/2} - \Gamma_{30}^2]^{1/2}$ and Δ_{AT} is the three-photon resonant Autler-Townes (AT) splitting. In the limit of $G >> \Gamma_{20}$ & $\Gamma_{30}, \Delta_{AT} \approx 2G$ and the linewidths of these two separate FWMs are approximately to be Γ'. When the coupling field becomes large enough ($G \to \infty$), two FWM peaks will diminish and disappear completely $\rho_+^{(3)} \approx \rho_-^{(3)} \approx 0$. There exists QI between FWM^+ and FWM^- channels which leads to the suppression and enhancement of the dressed FWM signal

Under condition $\zeta << 1, \rho_{10}'$ becomes sum of FWM and SWM

$$\rho_{10}' \approx \rho_{10}^{(3)} + \rho_{10}^{(5)} = \frac{-\mathrm{i}\alpha\mathrm{e}^{\mathrm{i}\boldsymbol{k}_f\cdot\mathbf{r}}}{d_1^2 d_2}\left(1 - \frac{G^2}{d_2d_3}\right). \tag{4.3}$$

The dressed FWM process converts to a coherent superposition of signals from FWM and SWM in the weak coupling field limit. The first term in the above equation corresponds to the two-photon resonant FWM (third-order response, linewidth $2\Gamma_{20}$) described by the perturbation the chain (I), while the second term corresponds to a three-photon resonant SWM (fifth-order response, linewidth $2\Gamma_{30}$) described by the perturbation the chain (II). The indistinguishable FWM and SWM processes lead to QI between them. The interference signal of FWM and SWM is $\left|\rho_{10}^{(3)} + \rho_{10}^{(5)}\right|^2 \propto 1 - 2G^2(\psi -$

$\Delta_a\Delta_b)/(\Gamma'_{20}\Gamma'_{30})(\Gamma'_{20} = \Delta_a^2 + \Gamma_{20}^2, \Gamma'_{30} = \Delta_b^2 + \Gamma_{30}^2, \Gamma''_{30} = \Delta_3^2 + \Gamma_{30}^2)$. At exact two-photon resonance (i.e., $\Delta_a = 0$), the signal intensity becomes $1 - 2G^2\psi/(\Gamma_{20}^2\Gamma''_{30})$, which shows the absorption-like effect, related to the imaginary part of the dressed FWM (Fig. 4.6). Due to the multiple resonance and the reduced linear absorption by double EIT (standard $|0\rangle \xrightarrow{\omega_1} |1\rangle \xrightarrow{\omega_2} |2\rangle$ ladder-type EIT and $|1\rangle \xrightarrow{\omega_2} |2\rangle \xrightarrow{-\omega_3} |3\rangle$ Λ-type EIT with condition $\Delta_1 = -\Delta_2 = -\Delta_3$), the generation of the SWM signal is quite efficient. Such reduced linear absorption can open the nonlinear window, which is generally closed due to strong absorption [32]. It can be proven easily that the ratio between the SWM and FWM signal intensities at resonance is approximately $I_S/I_F \approx \zeta^2$ (Fig. 4.6, right inset). When the coupling field is weak enough ($\zeta \approx 0$), ρ'_{10} completely evolves into $\rho_{10}^{(3)}$ (i.e., $\rho'_{10} \approx \rho_{10}^{(3)}$). On the other hand, we can also obtain the atomic coherence $\rho_{10}^{(5)}$ with three-photon resonance via SWM Liouville pathway (Ⅱ) $\rho_{10}^{(5)} = \mathrm{i}\beta \mathrm{e}^{\mathrm{i}\boldsymbol{k}_s\cdot\mathbf{r}}/(d_1^2 d_2^2 d_3)$. At the value $\zeta \approx 1.6$ ($\Delta_1 = \Delta_2 = \Delta_3 = 0$), we have $\rho'_{10} \approx \rho_{10}^{(5)}$.

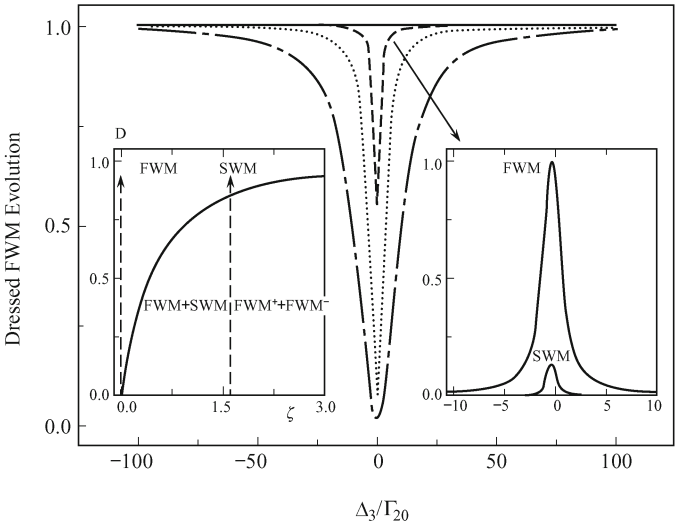

Fig. 4.6. The dressed FWM signal intensity evolution (normalized by no coupling field case) at exact two-photon resonance with parameters $\Delta_a = 0$, $\Gamma_{20} = \Gamma_{30}$ for $G/\Gamma_{20} = 0$ (solid curve, FWM), 0.6 (dashed curve, FWM+SWM), 1.6 (dotted curve, SWM) and 3 (dotted-dashed curve, FWM^++FWM^-). The suppression depth versus ζ (left insert plot shows the specific evolution pathways: two FWM and SWM turning points, and two FWM+SWM and FWM^++FWM^- interference regions). The right inset shows a comparison of FWM and SWM of the dashed curve.

Next, we discuss competition between FWM and SWM in the dressed FWM spectrum. The dressed FWM evolution pathways can be controlled by the coupling field: FWM^++$\mathrm{FWM}^-(\zeta >> 1) \leftrightarrow$ SWM ($\zeta \approx 1.6$) $\leftrightarrow$

FWM+SWM ($\zeta << 1$) $\leftrightarrow$ FWM ($\zeta \approx 0$). When state $|2\rangle$ is coupled to state $|3\rangle$ by the coupling field, QI between two dressed FWM channels via the common state, or FWM and SWM channels, leads to suppression and enhancement of the dressed FWM signal. The physical origin of this beat is an interference between indistinguishable quantum-mechanical pathways, and such QI can lead to the cancellation of spontaneous emission [22, 33]. Specifically, the $|+\rangle$ and $|-\rangle$ dressed states are very close (small than the linewidth) and can be excited simultaneously. The spontaneous emission from the pair of dressed states ($|+\rangle$ and $|-\rangle$) to lower state ($|1\rangle$) can be reduced or even cancelled under certain condition. The dressed FWM signal intensity is suppressed when the frequency of the coupling field is scanned across the resonance (Fig. 4.6). There exists the maximum suppression at double EIT condition $\Delta_1 = -\Delta_2 = -\Delta_3$. We can easily obtain the suppressed depth of the dip and linewidth in the spectrum as $D = 1 - (\zeta + 1)^{-2}$ and $w = 2\Gamma_{30}(1 + \zeta)$, respectively, which in the limit of $\zeta << 1$ become $D = 0$ and $w = 2\Gamma_{30}$. Since Γ_{20} can be obtained directly from the FWM spectrum of I_F, both G and Γ_{30} can be deduced through D and w. In the limit of $G >> \Gamma_{20}$ & Γ_{30}, G can also be obtained by the AT splitting $2G$. So the transition dipole moment between two highly-excited states can finally be obtained via $G = \varepsilon_3\mu_3/\hbar$. Recently, the power-dependent AT splitting of lines in the upper-level fluorescence excitation spectrum has been used as a spectroscopic tool for the measurement of transition dipole moments [31]. Compared to their method, our technique has the following advantages: (i) Due to the drive-back prime beams (including two-color $-\omega_2$ and $-\omega_3$), our signal is a well directed and strong coherent light beam; (ii) the coupling field in our scheme can be below saturation, so that transitions with small dipole moments can be studied; (iii) our method can measure the transition dipole moment between $|2\rangle$ and $|3\rangle$, which has such long radiative lifetime that a direct detection of the fluorescence is difficult.

Now, we consider the competition of the dispersion and absorption contributions to the dressed signal intensity (The suppression and enhancement mainly originate from the absorption and dispersion of the dressed FWM, respectively). The intensity of light is proportional to $|\chi'|^2$ (the nonlinear response of noise-free dressed FWM: Re $\chi' = (\Delta_b G^2 - \Delta_a \Gamma'_{30})/A$, Im $\chi' = -(\Gamma_{20}\Gamma'_{30}+\Gamma_{30}|G|^2)/A$, $R =$ Re χ'/Im χ', here $A = \Gamma'_{20}\Gamma'_{30}+2(\psi-\Delta_a\Delta_b)G^2+G^4$). We discuss R under $\zeta << 1$ condition (Re $\chi' \approx$ Re χ_F + Re $\chi_S \approx$ Re $\chi_F$and Im $\chi' \approx$ Im χ_F + Im $\chi_S \approx$ Im χ_F): (i) In the limit of $\Delta_a = 0$, the simplified ratio is $R \approx \Delta_3 G^2/(\Gamma_{20}\Gamma''_{30}) << 1$, which means that the contributions of the real parts of FWM and SWM are negligible, most of the signal intensity comes from the contribution of the imaginary part of FWM [the dotted curve of Fig. 4.7 (a)]; (ii) Under $\Delta_a >> \Gamma_{20}$, the ratio becomes $R \approx \Delta_a/\Gamma_{20} >> 1$. It means that contributions of the imaginary parts of FWM and SWM are neglectable. The signal intensity mostly comes from the contribution of the real part of FWM [the solid curve of Fig. 4.7 (a)].

The suppression and enhancement of the dressed FWM mainly originate

from the absorption and dispersion of FWM, respectively. When we increase the coupling field G, the contribution of SWM then becomes dominant (Re χ_S and Im χ_S present same order of contribution) [Fig. 4.7 (b)]. Figure 4.7 (a) shows dramatic suppression from Im χ_F, while Fig. 4.7 (b) shows dramatic enhancement from Re χ_S. Therefore, there exists a strong competition between FWM and SWM in the dressed FWM spectrum. Multidimensional solitons and light condensates have been predicted in a double-Λ EIT system with competitive and giant χ_F and χ_S of opposite signs [12].

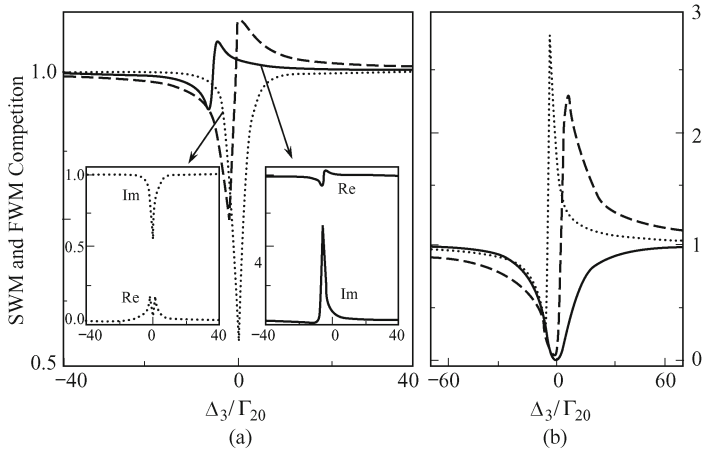

Fig. 4.7. The competition between absorption and dispersion of FWM and SWM (normalized by no coupling field case) with parameters $\Gamma_{20} = \Gamma_{30}$ for $\Delta_a/\Gamma_{20} = 0$ (dotted curve), -1.5 (dashed curve), -6 (solid curve). (a) $G/\Gamma_{20} = 0.6$ and (b) 3 for FWM+SWM and FWM$^+$+FWM$^-$ interference regions, respectively. The insert plots show a comparison of $(\text{Re}\ \chi')^2 = \text{Re}$ and $(\text{Im}\chi')^2 = \text{Im}$. The dotted Re curve and solid Im curve have been scaled by a factor 10 and 100, respectively.

We now discuss the controllable intra- or inter-atomic polarization interference (PI). In a Doppler broadened system, the induced polarization is sensitive to the atomic velocity, and interference exists between nonlinear polarizations of atoms with different velocity motions. This interference can have a strong impact on the FWM or SWM spectra. To investigate it, instead of calculating $\langle \left| P^{(n)} \right|^2 \rangle$ with inter-atomic PI and correlation, we can sum up the signal intensity of each atom motion, i.e., $N\mu_1 \int_{-\infty}^{+\infty} \mathrm{d}\nu w(\boldsymbol{\nu}) \langle \left| \rho_{10}^{(n)}(v) \right|^2 \rangle$ without inter-atomic PI and correlation. The role of induced PI can be clarified by studying the real and imaginary parts of $\rho_{10}^{(n)}(v)$. The imaginary part Im $\rho_{10}^{(n)}$ shows a dispersion lineshape, which leads to $\int_{-\infty}^{+\infty} \mathrm{d}\nu w(\boldsymbol{\nu})$ Im $\rho_{10}^{(n)} = 0$, therefore only the real part Re $\rho_{10}^{(n)}$ contributes to the FWM and SWM signals. Since Re $\rho_{10}^{(n)}$ changes sign on the wings of both the $v < 0$ and $v > 0$ sides, destructive PI occurs between atoms, thereby suppressing the total

polarization of the dressed FWM. The degree of destructive interference depends on $\boldsymbol{k}_2/\boldsymbol{k}_1$. Specifically, the destructive interference between polarizations of atoms with different velocities causes broadening of the dressed FWM linewidth. The coupling field G_3 can control the degree of destructive interference, thus reducing the linewidth. Furthermore, PB originates from the interference between the macroscopic polarizations simultaneously excited in at least two distinct resonances [22 – 25]. In contrast, the induced PI originates from the interference between polarizations induced in the same transition with a Doppler-shift frequency, also can be controlled by the coupling field (Fig. 4.6).

4.2.2 Discussion

Higher-order time-resolved nonlinear optical processes can often be obscured by sequential or parallel cascade lower order processes that compete with the direct event and give similar time domain behaviors [29]. Unlike the direct fifth-order case, cascade third-order processes must simultaneously satisfy two related phase-matching conditions. There exist sequential cascade FWM processes in our folded four-level system [28], which can obscure the direct SWM process, i.e., (a) $\rho_{00}^{(0)} \xrightarrow{\omega_1} \rho_{10}^{(1)} \xrightarrow{\omega_2} \rho_{20}^{(2)} \xrightarrow{-\omega_3} \rho_{30}^{(3)} \xrightarrow{-\omega_m} \rho_{00}^{(0)} (\boldsymbol{k}_m = \boldsymbol{k}_1 + \boldsymbol{k}_2 - \boldsymbol{k}_3'$ and $\omega_m = \omega_1 + \omega_2 - \omega_3)$, and (b) $\rho_{00}^{(0)} \xrightarrow{\omega_m} \rho_{30}^{(1)} \xrightarrow{\omega_3} \rho_{20}^{(2)} \xrightarrow{-\omega_2} \rho_{10}^{(3)} \xrightarrow{-\omega_{sc}} \rho_{00}^{(0)}$ $(\boldsymbol{k}_{sc} = \boldsymbol{k}_m + \boldsymbol{k}_3 - \boldsymbol{k}_2'$ and $\omega_{sc} = \omega_m + \omega_3 - \omega_2 = \omega_1)$. The direct three-photon SWM signal with frequency ω_1 will be emitted along the direction $\boldsymbol{k}_1 + \boldsymbol{k}_2 - \boldsymbol{k}_3' + \boldsymbol{k}_3 - \boldsymbol{k}_2'$, while two sequential cascade FWM signals propagate along the directions of $\boldsymbol{k}_m$ and $\boldsymbol{k}_{sc}$, respectively. Due to the weak population of state $|3\rangle$ and the optical pumping of the strong coupling field G_3, the direct fifth-order process shows the much stronger behavior than the cascade third-order processes in our folded four-state system. In principle, there also exist other possible SWM pathways: $\rho_{00}^{(0)} \xrightarrow{\omega_1} \rho_{10}^{(1)} \xrightarrow{\omega_2} \rho_{20}^{(2)} \xrightarrow{-\omega_2} \rho_{10}^{(3)} \xrightarrow{\omega_2} \rho_{20}^{(4)} \xrightarrow{-\omega_2} \rho_{10}^{(5)}$ and $\rho_{00}^{(0)} \xrightarrow{\omega_1} \rho_{10}^{(1)} \xrightarrow{-\omega_1} \rho_{00}^{(2)} \xrightarrow{\omega_1} \rho_{10}^{(3)} \xrightarrow{-\omega_1} \rho_{00}^{(4)} \xrightarrow{\omega_1} \rho_{10}^{(5)}$. However, these SWM processes have much smaller contributions and will not be discussed here.

4.3 Coexistence of Four-Wave, Six-Wave and Eight-Wave Mixing Processes in Multi-dressed Atomic Systems

Highly efficient multi-wave mixing processes with coherently prepared states have been the subjects of intensive research activities in the past few decades. Efficient four-wave mixing (FWM) [26, 34 – 36], six-wave mixing (SWM) [27,

37], and eight-wave mixing (EWM) [27] have been individually studied in multi-level atomic systems. By choosing appropriate atomic level schemes and driving fields, one can generate controllable nonlinearities with very interesting applications in designing novel nonlinear optical devices. This motivates the studies of enhanced higher-order nonlinear wave-mixing processes. Since higher-order nonlinear optical processes are usually much smaller in amplitude than lower-order ones [18], the interplay between nonlinear optical processes of different orders, if exists, is usually very difficult to observe experimentally. However, co-existing higher-order processes can become comparable or even greater in amplitude than the lower-order wave-mixing processes by means of atomic coherence and multi-photon interference [37]. As already proposed in the literature, the co-existing third- and fifth-order nonlinearities have important applications in 2D soliton formation and liquid-like surface tension [12, 38], so the co-existing third-, fifth-, and seventh-order nonlinearities will have applications in similar physical situations, or at least be important to such applications.

A phenomenon that has attracted much attention in recent years is electromagnetically induced transparency (EIT) [17, 21]. The existence of a dark state is the basis of EIT which reduces linear absorption and enhances FWM processes [26, 34, 35] via atomic coherence in multi-level atomic systems. Dark resonances arise from the quantum superposition states that are decoupled from coherent and dissipative interactions. Lukin *et al.* [17] studied interaction of dark resonances and predicted the splitting of dark states by changing the strength of the dressing laser beam in a four-level atomic system. Later the doubly-dressed states were observed in cold atoms, and the triple-peak absorption spectrum exhibits a constructive interference between the excitation paths of the two closely spaced, doubly dressed states [39]. In this study, we present two kinds of doubly-dressing schemes, in which constructive interference occurs between two FWM excitation paths of the doubly-dressed states in an open five-level system. The high-order multi-photon interference and light-induced atomic coherence are very important in nonlinear wave-mixing processes and might be used to open and optimize multi-channel nonlinear optical processes in multi-level atomic systems that are otherwise prohibited by the strong absorption [37]. As a simple example, in the conventional EIT-based FWM, a strong coupling laser beam induces transparency for the generated FWM signal [26, 34, 35]. By contrast, in the doubly-dressed FWM and singly-dressed SWM the dressing fields do not directly create an EIT window at the frequency ω_1 of the FWM and SWM signals.

Several features in this work are distinctly different and advantageous over the previously reported multi-wave mixing processes [26, 27, 34 – 37]. First, there exist co-existing FWM, SWM and EWM processes in an open five-level system, which is good for studying the interplay between nonlinear optical processes of different orders. In most of the previously studied multi-level atomic systems, especially the close-cycled ones [26, 27, 34, 35], the FWM,

SWM, and EWM processes cannot coexist, and different order nonlinearities can only be observed individually under different laser configurations, which is fundamentally different from the current study. Second, two kinds of doubly-dressing schemes (parallel and nested types) are considered to generate co-existing FWM, SWM, and EWM signals. The coherent interactions of doubly-dressed states created by two dressing fields have been studied in detail, which can result in dramatic enhancements of multi-wave mixing signals. Moreover, such coherent interactions between two dressing processes in nested type are much stronger than that in parallel type. Thus, by virtue of controlling the singly- or doubly-dressed multi-wave mixing signal, one can obtain the nonlinear susceptibilities of desired order, which can be very important for certain applications. Third, large third-, fifth-and seventh-order nonlinear responses can be obtained by controlling the coherent phases of the polarization beats between these FWM, SWM, and EWM signals. Investigations of such intermixing and interplay between different types of nonlinear wave-mixing processes will help us to understand and optimize the generated high-order multi-channel nonlinear optical signals.

4.3.1 Parallel and Nested Dressing Schemes

With the basic system [see Fig. 4.8 (a)] of three energy levels ($|0\rangle, |1\rangle$, and $|2\rangle$) and three laser fields ($\varepsilon_2, \varepsilon_2'$, and ε_1), a FWM signal at frequency ω_1 will be generated [37]. By adding another energy level (either $|3\rangle$ or $|4\rangle$) and another laser field (ε_3 or ε_3' for level $|3\rangle$, or ε_4 or ε_4' for level $|4\rangle$), the original energy level ($|1\rangle$ or $|2\rangle$) will be dressed to produce two dressed states. Such four-level system with a dressing field will modify the original FWM process (called singly-dressed FWM with notation $\rho_{FiSj}^{(3)}$) and generate SWM signals ($\rho_{Si}^{(5)}$). If two energy levels ($|3\rangle$ and $|4\rangle$) are both added with two additional fields, the original FWM system is said to be doubly dressed (denoted as $\rho_{Fij}^{(3)}$), which can generate not only SWM signals ($\rho_{Si}^{(5)}$), but also EWM ($\rho_{Ei}^{(7)}$). One can consider such system first as a four-level system ($|0\rangle, |1\rangle, |2\rangle$ and $|3\rangle$) which generates SWM, and then by adding another level ($|4\rangle$) and a field ε_4, this four-level atomic system is (singly) dressed again to give a singly-dressed SWM signal ($\rho_{Sij}^{(5)}$), which will have contributions from EWM under certain conditions. Note that $\rho_{Fij}^{(3)}$ and $\rho_{Sij}^{(5)}$ are not purely third-order and fifth-order nonlinearities, instead they are the doubly-dressed FWM and singly-dressed SWM, respectively, including higher-order nonlinear responses. The main purpose of using such doubly-dressed schemes is to generate efficient EWM and, at the same time, to allow us to control the relative strengths of various wave-mixing processes. So the high-order nonlinear optical processes can be enhanced, manipulated, and studied in detail.

For a five-level atomic system as shown in Fig. 4.8 (a), states $|i-1\rangle$ to

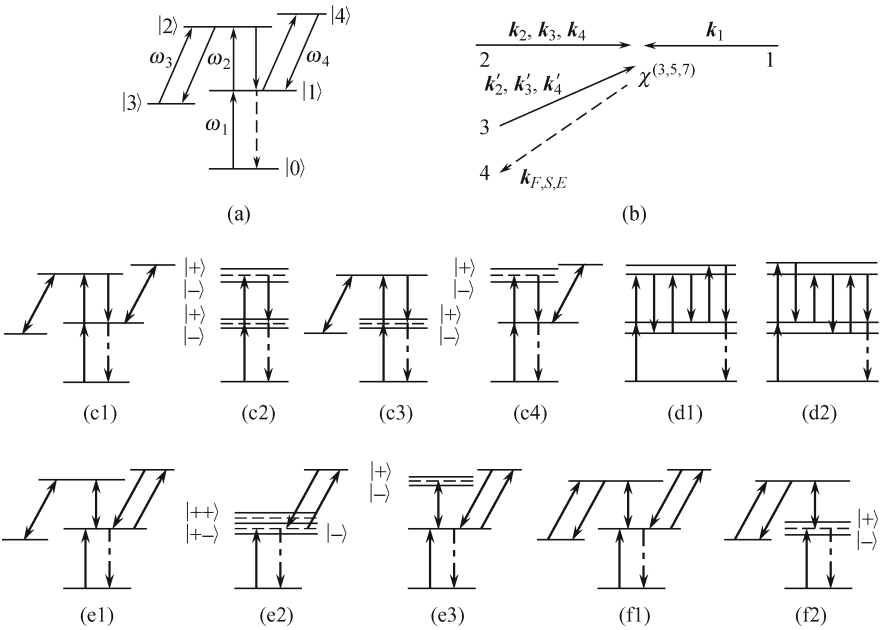

Fig. 4.8. (a) The energy-level diagram for co-existing FWM, SWM, and EWM in an open five-level system. (b) Phase-conjugate schematic diagram of phase-matched multi-wave mixing. (c1) Five-level atomic system with blocking fields ε_3' and ε_4', doubly-dressed FWM (parallel type) (c2) and singly-dressed SWM (c3, c4) in the dressed-state picture. (d1) and (d2) Two five-level atomic systems for EWM. (e1) Five-level at omic system with blocking fields ε_2' and ε_3', doubly-dressed FWM (nested type) (e2) and singly-dressed SWM (e3) in the dressed-state picture. (f1) Five-level atomic system with blocking fields ε_2' and ε_4', singly-dressed SWM (f2) in the dressed-state picture. The $|+\rangle$ and $|-\rangle$ correspond to the primarily-dressed states, the $|++\rangle$ and $|+-\rangle$ are the secondarily-dressed states around the primarily-dressed state $|+\rangle$.

$|i\rangle (i = 1, 2, 3, 4)$ are coupled by laser fields ε_i and $\varepsilon_i'(\omega_i, \boldsymbol{k}_i(\boldsymbol{k}_i')$ with Rabi frequency $G_i(G_i'))$. The Rabi frequencies are defined as $G_i = \varepsilon_i \mu_{ij}/\hbar$ and $G_i' = \varepsilon_i' \mu_{ij}/\hbar$, respectively, where μ_{ij} is the transition dipole moment between level i and level j. Fields ε_i and ε_i' with the same frequency and different time delays (ε_i' is delayed by time τ) propagate along beams 2 and 3 with a small angle [Fig. 4.8 (b)], while a weak probe field ε_1 (beam 1) propagates along the opposite direction of beam 2. There exist three cases of blocking fields, i.e., blocking ε_3' and ε_4' [Fig. 4.8 (c1)], blocking ε_2' and ε_3' [Fig. 4.8 (e1)], or blocking ε_2' and ε_4' [Fig. 4.8 (f1)] as given in Table 4.1. Table 4.1 gives all possible phase-matched Liouville pathways for coexisting FWM, SWM, and EWM processes under certain conditions. Specifically, we consider two types of doubly-dressed FWM schemes involved in this system, as shown in Fig. 4.8 (c2, e2), we refer to them as parallel and nested dressing schemes, respectively. The FWM process will be dressed by either two synchronous fields

Table 4.1 Phase-matching conditions and the perturbation chains of co-existing EWM, dressed SWM and doubly dressed FWM.

Blocked beams	Doubly dressed FWM F_{ij}	Dressed SWM S_{ij}	EWM E_1
$\boldsymbol{k}_3', \boldsymbol{k}_4'$	$\boldsymbol{k}_{F1} = \boldsymbol{k}_1 + \boldsymbol{k}_2 - \boldsymbol{k}_2'(F_{11}, F_{12})$	$\boldsymbol{k}_{S1}^{(1)} = \boldsymbol{k}_1 + \boldsymbol{k}_2 - \boldsymbol{k}_2' + \boldsymbol{k}_3 - \boldsymbol{k}_3(S_{11}, S_{12})$ $\boldsymbol{k}_{S2,3}^{(1)} = \boldsymbol{k}_1 + \boldsymbol{k}_2 - \boldsymbol{k}_2' + \boldsymbol{k}_4 - \boldsymbol{k}_4(S_{21}, S_{32})$	$\boldsymbol{k}_{E1,2}^{(1)} = \boldsymbol{k}_1 + \boldsymbol{k}_2 - \boldsymbol{k}_2' + \boldsymbol{k}_3 - \boldsymbol{k}_3 + \boldsymbol{k}_4 - \boldsymbol{k}_4(E_1, E_2)$
$\boldsymbol{k}_2', \boldsymbol{k}_3'$	$\boldsymbol{k}_{F2} = \boldsymbol{k}_1 + \boldsymbol{k}_4 - \boldsymbol{k}_4'(F_{21}, F_{22})$	$\boldsymbol{k}_{S2,3}^{(2)} = \boldsymbol{k}_1 + \boldsymbol{k}_2 - \boldsymbol{k}_2 + \boldsymbol{k}_4 - \boldsymbol{k}_4'(S_{21}, S_{32})$	$\boldsymbol{k}_{E1,2}^{(2)} = \boldsymbol{k}_1 + \boldsymbol{k}_2 - \boldsymbol{k}_2 + \boldsymbol{k}_3 - \boldsymbol{k}_3 + \boldsymbol{k}_4 - \boldsymbol{k}_4'(E_1, E_2)$
$\boldsymbol{k}_2', \boldsymbol{k}_4'$	None	$\boldsymbol{k}_{S1}^{(2)} = \boldsymbol{k}_1 + \boldsymbol{k}_2 - \boldsymbol{k}_2 + \boldsymbol{k}_3 - \boldsymbol{k}_3'(S_{11}, S_{12})$	$\boldsymbol{k}_{E1,2}^{(3)} = \boldsymbol{k}_1 + \boldsymbol{k}_2 - \boldsymbol{k}_2 + \boldsymbol{k}_3 - \boldsymbol{k}_3' + \boldsymbol{k}_4 - \boldsymbol{k}_4(E_1, E_2)$
FWM F_i,SWM S_i and EWM E_i chains		$F_1 : \rho_{00}^{(0)} \xrightarrow{\omega_1} \rho_{10}^{(1)} \xrightarrow{\omega_2} \rho_{20}^{(2)} \xrightarrow{-\omega_2} \rho_{10}^{(3)}$ $F_2 : \rho_{00}^{(0)} \xrightarrow{\omega_1} \rho_{10}^{(1)} \xrightarrow{\omega_4} \rho_{40}^{(2)} \xrightarrow{-\omega_4} \rho_{10}^{(3)}$ $S_1 : \rho_{00}^{(0)} \xrightarrow{\omega_1} \rho_{10}^{(1)} \xrightarrow{\omega_2} \rho_{20}^{(2)} \xrightarrow{-\omega_3} \rho_{30}^{(3)} \xrightarrow{\omega_3} \rho_{20}^{(4)} \xrightarrow{-\omega_2} \rho_{10}^{(5)}$ $S_2 : \rho_{00}^{(0)} \xrightarrow{\omega_1} \rho_{10}^{(1)} \xrightarrow{\omega_2} \rho_{20}^{(2)} \xrightarrow{-\omega_2} \rho_{10}^{(3)} \xrightarrow{\omega_4} \rho_{40}^{(4)} \xrightarrow{-\omega_4} \rho_{10}^{(5)}$ $S_3 : \rho_{00}^{(0)} \xrightarrow{\omega_1} \rho_{10}^{(1)} \xrightarrow{\omega_4} \rho_{40}^{(2)} \xrightarrow{-\omega_4} \rho_{10}^{(3)} \xrightarrow{\omega_2} \rho_{20}^{(4)} \xrightarrow{-\omega_2} \rho_{10}^{(5)}$ $E_1 : \rho_{00}^{(0)} \xrightarrow{\omega_1} \rho_{10}^{(1)} \xrightarrow{\omega_2} \rho_{20}^{(2)} \xrightarrow{-\omega_3} \rho_{30}^{(3)} \xrightarrow{\omega_3} \rho_{20}^{(4)} \xrightarrow{-\omega_2} \rho_{10}^{(5)} \xrightarrow{\omega_4} \rho_{40}^{(6)} \xrightarrow{-\omega_4} \rho_{10}^{(7)}$ $E_2 : \rho_{00}^{(0)} \xrightarrow{\omega_1} \rho_{10}^{(1)} \xrightarrow{\omega_4} \rho_{40}^{(2)} \xrightarrow{-\omega_4} \rho_{10}^{(3)} \xrightarrow{\omega_2} \rho_{20}^{(4)} \xrightarrow{-\omega_3} \rho_{30}^{(5)} \xrightarrow{\omega_3} \rho_{20}^{(6)} \xrightarrow{-\omega_2} \rho_{10}^{(7)}$	
Doubly dressed FWM F_{ij}, Dressed SWM S_{ij} chains		$F_{11} : \rho_{00}^{(0)} \xrightarrow{\omega_1} \rho_{10}^{(1)} \xrightarrow{\omega_2} \rho_{(G_3\pm)0}^{(2)} \xrightarrow{-\omega_2} \rho_{(G_4\pm)0}^{(3)}$ $F_{12} : \rho_{00}^{(0)} \xrightarrow{\omega_1} \rho_{(G_4\pm)0}^{(1)} \xrightarrow{\omega_2} \rho_{(G_3\pm)0}^{(2)} \xrightarrow{-\omega_2} \rho_{10}^{(3)}$ $F_{21} : \rho_{00}^{(0)} \xrightarrow{\omega_1} \rho_{(G_3\pm G_2\pm)0}^{(1)} \xrightarrow{\omega_4} \rho_{40}^{(2)} \xrightarrow{-\omega_4} \rho_{10}^{(3)}$ $F_{22} : \rho_{00}^{(0)} \xrightarrow{\omega_1} \rho_{10}^{(1)} \xrightarrow{\omega_4} \rho_{40}^{(2)} \xrightarrow{-\omega_4} \rho_{(G_3\pm G_2\pm)0}^{(3)}$ $S_{11} : \rho_{00}^{(0)} \xrightarrow{\omega_1} \rho_{10}^{(1)} \xrightarrow{\omega_2} \rho_{20}^{(2)} \xrightarrow{-\omega_3} \rho_{30}^{(3)} \xrightarrow{\omega_3} \rho_{20}^{(4)} \xrightarrow{-\omega_2} \rho_{(G_4\pm)0}^{(5)}$ $S_{12} : \rho_{00}^{(0)} \xrightarrow{\omega_1} \rho_{(G_4\pm)0}^{(1)} \xrightarrow{\omega_2} \rho_{20}^{(2)} \xrightarrow{-\omega_3} \rho_{30}^{(3)} \xrightarrow{-\omega_3} \rho_{20}^{(4)} \xrightarrow{-\omega_2} \rho_{10}^{(5)}$ $S_{21} : \rho_{00}^{(0)} \xrightarrow{\omega_1} \rho_{10}^{(1)} \xrightarrow{\omega_2} \rho_{(G_3\pm)0}^{(2)} \xrightarrow{-\omega_2} \rho_{10}^{(3)} \xrightarrow{\omega_4} \rho_{40}^{(4)} \xrightarrow{-\omega_4} \rho_{10}^{(5)}$ $S_{32} : \rho_{00}^{(0)} \xrightarrow{\omega_1} \rho_{10}^{(1)} \xrightarrow{\omega_4} \rho_{40}^{(2)} \xrightarrow{-\omega_4} \rho_{10}^{(3)} \xrightarrow{\omega_2} \rho_{(G_3\pm)0}^{(4)} \xrightarrow{-\omega_2} \rho_{10}^{(5)}$	

[parallel type as shown in Fig. 4.8 (c2)] or two in-series fields [nested type as shown in Fig. 4.8 (e2)]. There exist coherent interactions of doubly dressed states created by two dressing fields. Moreover, both dressing schemes lead to multiple quantum superposition states that interact coherently, and can be used to mitigate decoherence effects [37, 39, 40]. Furthermore, such coherent interactions of doubly-dressed processes result in dramatic enhancements of multi-wave mixing signals.

The nonlinear polarizations, responsible for multi-wave mixing signals, are proportional to the off-diagonal density matrix elements $\rho_{10}^{(n)}$. We will assume, as usual, that G_1 is weak, whereas the laser fields $G_2, G_2', G_3, G_3', G_4$, and G_4' can be of arbitrary magnitudes. Thus, $\rho_{10}^{(n)}$ needs to be calculated to the lowest-order in G_1, but to all orders in other fields under various conditions.

When fields ε_3' and ε_4' are blocked, the simultaneous interactions of atoms with fields ε_1 and ε_2 will induce a substantial atomic coherence between $|0\rangle$ and $|2\rangle$ through resonant two-photon transition. This coherently prepared two-photon coherence is then probed by field ε_2' and, as a result, a FWM ($\rho_{F1}^{(3)}$) signal of frequency ω_1 in beams 4 is generated almost opposite to the direction of beams 3, satisfying phase-matching condition $\boldsymbol{k}_{F1} = \boldsymbol{k}_1 + \boldsymbol{k}_2 - \boldsymbol{k}_2'$. When two strong dressing fields ε_3 and ε_4 are used to drive the transitions $|2\rangle$ to $|3\rangle$ and $|1\rangle$ to $|4\rangle$, respectively, as shown in Fig. 4.8 (c1), there coexist two doubly-dressed FWM [$\rho_{F11}^{(3)}$ of the chain F_{11} and $\rho_{F12}^{(3)}$ of the chain F_{12} depicted in Fig. 4.8 (c2)], as well as four singly-dressed SWM [$\rho_{S11}^{(5)}$of S_{11} and $\rho_{S12}^{(5)}$ of S_{12} depicted in Fig. 4.8 (c3); $\rho_{S21}^{(5)}$ of S_{21} and $\rho_{S32}^{(5)}$ of S_{32} depicted in Fig. 4.8 (c4)], and two EWM [$\rho_{E1}^{(7)}$of E_1 and $\rho_{E2}^{(7)}$ of E_2 depicted in Fig. 4.8 (d1 – d2)] processes, satisfying the phase-matching directions for $\boldsymbol{k}_{F1}, \boldsymbol{k}_{S1}^{(1)}$ and $\boldsymbol{k}_{S2,3}^{(1)}, \boldsymbol{k}_{E1,2}^{(1)}$ respectively. $F_{\rm ij}$, $S_{\rm ij}$, and E_i represent doubly-dressed FWM, singly-dressed SWM, and EWM processes, respectively, as given in Table 4.1 Moreover, we have $\boldsymbol{k}^{(1)} = \boldsymbol{k}_{F1} = \boldsymbol{k}_{S1}^{(1)} = \boldsymbol{k}_{S2,3}^{(1)} = \boldsymbol{k}_{E1,2}^{(1)}$ in this interaction case (Table 4.1).

Specifically, the FWM process F_1 is generated by interactions of three fields $\varepsilon_1, \varepsilon_2$, and ε_2', which is parallelly dressed by ε_3 and ε_4 [Fig. 4.8 (c2)]. The SWM process S_1 is generated by interactions with one photon each from $\varepsilon_1, \varepsilon_2, \varepsilon_2'$, and two photons from the same field ε_3, which is dressed by ε_4 [Fig. 4.8 (c3)]. The SWM processes S2 and S3 are generated by interactions with one photon each from $\varepsilon_1, \varepsilon_2, \varepsilon_2'$, and two photons from the same field ε_4, which is dressed by ε_3 [Fig. 4.8 (c4)]. Similarly, EWM processes E1 and E2 can also exist at the same time with one photon each from ε_1, ε_2, ε_2', two photons from the same field ε_3, and two photons from the same field ε_4, as shown in Fig. 4.8 (d1) – (d2).

To better understand such phenomenon of interplay between coexisting EWM, dressed SWM and doubly-dressed FWM (parallel type) processes, we use the perturbation the chain expressions involving $\rho_{F1}^{(3)}, \rho_{S1}^{(5)}, \rho_{S2}^{(5)} (\rho_{S3}^{(5)})$ and $\rho_{E1}^{(7)}$ ($\rho_{E2}^{(7)}$) nonlinear wave-mixing processes for this case of blocking fields ε_3'

and ε_4'. Although, such perturbative approach makes significant approximations it shows a simple picture of the leading contributions from the complicated nonlinear optical processes. The simple FWM ($\rho_{F1}^{(3)}$) via Liouville pathway F_1 gives $\rho_{F1}^{(3)} = -G_a/d_1^2 d_2$, where $G_a = \mathrm{i}G_1 G_2 (G_2')^* \exp(\mathrm{i}\boldsymbol{k}^{(1)} \cdot \boldsymbol{r}), d_1 = \Gamma_{10} + \mathrm{i}\Delta_1$ and $d_2 = \Gamma_{20} + \mathrm{i}\Delta_2^a$ with $\Delta_i = \Omega_i - \omega_i$, $\Delta_2^a = \Delta_1 + \Delta_2$. Γ_{ij} is the decoherence rate between two relevant states. Similarly, we can easily obtain three SWM processes, $\rho_{S1}^{(5)} = G_a \left|G_3\right|^2 / (d_1^2 d_2^2 d_3)$ via the chain S_1 and $\rho_{S2}^{(5)} = \rho_{S3}^{(5)} = G_a \left|G_4\right|^2 / (d_1^3 d_2 d_4)$ via the chains S_2 and S_3, as well as EWM $\rho_{E1}^{(7)} = \rho_{E2}^{(7)} = -G_a \left|G_3\right|^2 \left|G_4\right|^2 / (d_1^3 d_2^2 d_3 d_4)$ via the chains E_1 and E_2, where $d_3 = \Gamma_{30} + i\Delta_3^a$ and $d_4 = \Gamma_{40} + \mathrm{i}\Delta_4^a$ with $\Delta_3^a = \Delta_2^a - \Delta_3, \Delta_4^a = \Delta_1 + \Delta_4$.

Two separate sub-processes for the dressing fields ε_3 and ε_4, "$\rho_{20}^{(2)} \xrightarrow{-\omega_3} \rho_{30}^{(3)} \xrightarrow{\omega_3} \rho_{20}^{(4)}$" and "$\rho_{10}^{(5)} \xrightarrow{\omega_4} \rho_{40}^{(6)} \xrightarrow{-\omega_4} \rho_{10}^{(7)}$", are parallelly existing in the EWM the Chain E_1. Such the mechanism can be called the parallel-dressing interaction. It means that the fields ε_3 and ε_4 dress the states $|2\rangle$ and $|1\rangle$ [Fig 4.8 (c2)], and affect the atomic coherences $\rho_{20}^{(2)}$ between $|0\rangle$ and $|2\rangle$, and $\rho_{10}^{(5)}$ between $|0\rangle$ and $|1\rangle$, respectively. So we have $\rho_{(G_3\pm)0}^{(2)}$ and $\rho_{(G_4\pm)0}^{(3)}$ in the doubly-dressed FWM the Chain F_{11} (Table 4.1). Specifically, in this interaction, due to parallel-dressing fields ε_3 and ε_4, the FWM (F_1) process will be dressed synchronously by both fields and a perturbative approach for such parallel-type, doubly-dressed interaction can be described by the following coupled equations:

$$\begin{cases} \dfrac{\partial \rho_{20}}{\partial t} = -d_2 \rho_{20} + \mathrm{i}G_2 \rho_{10} \exp(\mathrm{i}\boldsymbol{k}_2 \cdot \boldsymbol{r}) + \mathrm{i}G_3 \rho_{30} \exp(\mathrm{i}\boldsymbol{k}_3 \cdot \boldsymbol{r}) \\ \dfrac{\partial \rho_{30}}{\partial t} = -d_3 \rho_{30} + \mathrm{i}G_3^* \rho_{20} \exp(-\mathrm{i}\boldsymbol{k}_3 \cdot \boldsymbol{r}), \end{cases} \tag{4.4}$$

$$\begin{cases} \dfrac{\partial \rho_{10}}{\partial t} = -d_1 \rho_{10} + \mathrm{i}G_2'^* \rho_{20} \exp(-\mathrm{i}\boldsymbol{k}_2' \cdot \boldsymbol{r}) + \mathrm{i}G_4^* \rho_{40} \exp(-\mathrm{i}\boldsymbol{k}_4 \cdot \boldsymbol{r}) \\ \dfrac{\partial \rho_{40}}{\partial t} = -d_4 \rho_{40} + \mathrm{i}G_4 \rho_{10} \exp(\mathrm{i}\boldsymbol{k}_4 \cdot \boldsymbol{r}). \end{cases} \tag{4.5}$$

Equations (4.4) and (4.5) correspond to G_3 and G_4 dressing equations, respectively. The energy levels $|1\rangle$ and $|2\rangle$ of the chain F_1 are created as two parallel groups of dressed states $|+\rangle$ and $|-\rangle$, as shown in Fig. 4.8 (c2). In the steady state, Eqs. (4.4) and (4.5) can be solved together with the perturbation the chains F_1 and E_1 to give the strength of the parallel-dressing FWM of the chain F_{11},

$$\rho_{F11}^{(3)} = \frac{-G_a}{d_1(d_1 + |G_4|^2/d_4)(d_2 + |G_3|^2/d_3)} \tag{4.6}$$

In a special limit of $|G_4|^2 \ll \Gamma_{10}\Gamma_{40}$ and $|G_3|^2 \ll \Gamma_{20}\Gamma_{30}$, $\rho_{F11}^{(3)}$ can be

expanded to the lowest order to give

$$\begin{aligned}\rho_{F11}^{(3)} &\approx \frac{-G_a}{d_1^2 d_2} + \frac{G_a\left|G_3\right|^2}{d_1^2 d_2^2 d_3} + \frac{G_a|G_4|^2}{d_1^3 d_2 d_4} + \frac{-G_a\left|G_3\right|^2|G_4|^2}{d_1^3 d_2^2 d_3 d_4} \\ &= \rho_{F1}^{(3)} + \rho_{S1}^{(5)} + \rho_{S2}^{(5)} + \rho_{E1}^{(7)} \\ &= \rho_{F1S1}^{(3)} + \rho_{S21}^{(5)} = \rho_{F1S2}^{(3)} + \rho_{S11}^{(5)}, \end{aligned} \tag{4.7}$$

where $\rho_{F1S1}^{(3)} = -G_a(1-\left|G_3\right|^2/d_3d_2)/(d_1^2d_2) = \rho_{F1}^{(3)}+\rho_{S1}^{(5)}, \rho_{S21}^{(5)} = G_a|G_4|^2(1-\left|G_3\right|^2/d_2d_3)/(d_1^3d_2d_4) = \rho_{S2}^{(5)} + \rho_{E1}^{(7)}$, $\rho_{F1S2}^{(3)} = -G_a(1-\left|G_4\right|^2/d_1d_4)/(d_1^2d_2) = \rho_{F1}^{(3)} + \rho_{S2}^{(5)}$ and $\rho_{S11}^{(5)} = G_a|G_3|^2(1-\left|G_4\right|^2/d_1d_4)/(d_1^2d_2^2d_3) = \rho_{S1}^{(5)} + \rho_{E1}^{(7)}$. Note again that $\rho_{Fij}^{(3)}$, $\rho_{Sij}^{(5)}$ are not pure third- and fifth-order nonlinear responses. These symbols are used here denote the dressed FWM and SWM, respectively. Expansions of Eq. (4.7) indicate that the doubly-dressed FWM process converts to a coherent superposition of signals from FWM (F_1), SWM (S_1), SWM (S_2), and EWM (E_1) ($\rho_{F1}^{(3)} + \rho_{S1}^{(5)} + \rho_{S2}^{(5)} + \rho_{E1}^{(7)}$), or dressed FWM and dressed SWM ($\rho_{F1S1}^{(3)}+\rho_{S21}^{(5)}$) or ($\rho_{F1S2}^{(3)}+\rho_{S11}^{(5)}$) in this weak dressing field limit. That is to say, $\rho_{F11}^{(3)}$ includes third-, fifth- and seventh-order nonlinear optical responses. Hence, the dressed SWM response of $\rho_{S11}^{(5)}(\rho_{S21}^{(5)})$ can be obtained by homodyne beat detection with the dressed FWM signal $\rho_{F1S2}^{(3)}$ ($\rho_{F1S1}^{(3)}$) as the strong local oscillator [25]. Similarly, we can get doubly-dressed FWM of the chain $F_{12}, \rho_{F12}^{(3)} \approx \rho_{F1}^{(3)} + \rho_{S1}^{(5)} + \rho_{S3}^{(5)} + \rho_{E2}^{(7)} = \rho_{F1S1}^{(3)} + \rho_{S32}^{(5)} = \rho_{F1S3}^{(3)} + \rho_{S12}^{(5)}$ in Table 4.1.

When the fields ε_2' and ε_3' are blocked [as shown in Fig. 4.8 (e1)], there coexist two doubly-dressed FWM [$\rho_{F21}^{(3)}$ of the chain F_{21} and $\rho_{F22}^{(3)}$ of the chain F_{22} depicted in Fig. 4.8 (e2)], two singly-dressed SWM [$\rho_{S21}^{\prime(5)}$ of S_{21} and $\rho_{S32}^{\prime(5)}$ of S_{32} depicted in Fig. 4.8 (e3)] and two EWM [$\rho_{E1}^{\prime(7)}$ of E_1 and $\rho_{E2}^{\prime(7)}$ of E_2 depicted in Fig. 4.8 (d1 – d2)] processes, satisfying the phase-matching conditions $\boldsymbol{k}_{F2}, \boldsymbol{k}_{S2,3}^{(2)}$ and $\boldsymbol{k}_{E1,2}^{(2)}$ (additionally, $\boldsymbol{k}^{(2)} = \boldsymbol{k}_{F2} = \boldsymbol{k}_{S2,3}^{(2)} = \boldsymbol{k}_{E1,2}^{(2)}$). More specifically, the FWM process F_2 is generated by interactions of three fields ε_1, ε_4 and ε_4', which is sequentially dressed by ε_2 and ε_3 [Fig. 4.8 (e2)]. The SWM processes S_2 and S_3 are generated by interactions with one photon each from ε_1, $\varepsilon_4, \varepsilon_4'$, and two photons from the same field ε_2, which is dressed by ε_3 [Fig. 4.8 (e3)]. Similarly, EWM processes E_1 and E_2 can also exist at the same time with one photon each from ε_1, ε_4, ε_4', two photons from the same field ε_2, and two photons from the same field ε_3, as shown in Fig. 4.8 (d1 – d2).

The sub-chain "$\rho_{10}^{(1)} \xrightarrow{\omega_2} \rho_{20}^{(2)} \xrightarrow{-\omega_3} \rho_{30}^{(3)} \xrightarrow{\omega_3} \rho_{20}^{(4)} \xrightarrow{-\omega_2} \rho_{10}^{(5)}$" of the EWM the chain E_1 shows that the dressing process of the field ε_3, "$\rho_{20}^{(2)} \xrightarrow{-\omega_3} \rho_{30}^{(3)} \xrightarrow{\omega_3} \rho_{20}^{(4)}$", is nested in the dressing process of the field ε_2. Moreover, the dressing field ε_3 is based on the dressing field ε_2. If $\varepsilon_2 = 0$, the dressing effect of field ε_3 will disappear in expression $\rho_{F21}^{(3)}$. This doubly-

dressed mechanism is called the nested-dressing interaction. Both of fields ε_2 and ε_3 dress the same state $|1\rangle$ [Fig. 4.8 (e2)], and affect the atomic coherence $\rho_{10}^{(1)}$ between $|0\rangle$ and $|1\rangle$. So we have $\rho_{(G_3\pm G_2\pm)0}^{(1)}$ in the doubly-dressed FWM the chain F_{21} (Table 4.1).

In this case, the coherently prepared two-photon coherence between $|0\rangle$ and $|4\rangle$ created by fields ε_1 and ε_4 is probed by field ε_4' and, as a consequence, a FWM ($\rho_{F2}^{(3)}$) signal is generated. Such an FWM process will be dressed by two fields ε_2 and ε_3 in sequence, a perturbative approach for such the doubly-dressed interaction, which is termed as nested dressing interaction, can be described by Eq. (4.4) and the following equation:

$$\partial\rho_{10}/\partial t = -d_1\rho_{10} + \mathrm{i}G_2^*\rho_{20}\exp(-\mathrm{i}\boldsymbol{k}_2\cdot\boldsymbol{r}) + iG_1. \tag{4.8}$$

The FWM (F_2 process given in Table 4.1) is doubly dressed by fields G_2 and G_3. When one of dressing fields is tuned close to one of the primarily-dressed states $|+\rangle$ (or $|-\rangle$), the energy levels at level $|1\rangle$ of the chain F_2 are created as the secondarily-dressed states $|++\rangle$ and $|+-\rangle$ around the primarily-dressed state $|+\rangle$ [Fig. 4.8 (e2)] [39]. Coupling Eqs. (4.4) and (4.8) can be solved together with the perturbation chain F_2 and E_1 to give the doubly-dressed FWM of the chain F_{21},

$$\rho_{F21}^{(3)} = \frac{-G_b}{d_1 d_4\left[d_1 + \dfrac{|G_2|^2}{(d_2+|G_3|^2/d_3)}\right]}, \tag{4.9}$$

with $G_b = \mathrm{i}G_1(G_4')^*G_4\exp(\mathrm{i}\boldsymbol{k}^{(2)}\cdot\boldsymbol{r})$. Consequently, under the conditions $|G_2|^2 << \Gamma_{10}\Gamma_{20}$ and $|G_3|^2 << \Gamma_{20}\Gamma_{30}$, we can expand $\rho_{F21}^{(3)}$ (to the lowest orders) into

$$\begin{aligned}\rho_{F21}^{(3)} &\approx \frac{-G_b}{d_1^2 d_4} + \frac{G_b|G_2|^2}{d_1^3 d_2 d_4} + \frac{-G_b|G_2|^2|G_3|^2}{d_1^3 d_2^2 d_3 d_4} = \rho_{F2}^{(3)} + \rho_{S2}^{\prime(5)} + \rho_{E1}^{\prime(7)} \\ &= \rho_{F2S2}^{(3)} + \rho_{E1}^{\prime(7)} = \rho_{F2}^{(3)} + \rho_{S21}^{\prime(5)},\end{aligned} \tag{4.10}$$

where $\rho_{F2}^{(3)} = -G_b/(d_1^2 d_4), \rho_{S2}^{\prime(5)} = \rho_{S3}^{\prime(5)} = G_b|G_2|^2/(d_1^3 d_2 d_4), \rho_{E1}^{\prime(7)} = \rho_{E2}^{\prime(7)} = -G_b|G_2|^2|G_3|^2/(d_1^3 d_2^2 d_3 d_4), \rho_{F2S2}^{(3)} = -G_b(1-|G_2|^2/d_1 d_2)/(d_1^2 d_4) = \rho_{F2}^{(3)} + \rho_{S2}^{\prime(5)}$, and $\rho_{S21}^{\prime(5)} = G_b|G_2|^2(1-|G_3|^2/d_2 d_3)/(d_1^3 d_2 d_4) = \rho'^{(5)}_{S2} + \rho_{E1}^{\prime(7)}$. It should be pointed out that the nested-dressing FWM process converts to a coherent superposition of signals from FWM (F_2), SWM (S_2), and EWM (E_1) ($\rho_{F2}^{(3)} + \rho_{S2}^{\prime(5)} + \rho_{E1}^{\prime(7)}$), or dressed FWM and EWM ($\rho_{F2S2}^{(3)} + \rho_{E1}^{\prime(7)}$), or FWM and dressed SWM ($\rho_{F2}^{(3)} + \rho_{S21}^{\prime(5)}$) in the weak dressing field limit. Here, the prime indicates that such multi-wave mixing process is with the different phase-matched condition. Correspondingly, we can get doubly-dressed FWM of the Chain $F_{22}, \rho_{F22}^{(3)} \approx \rho_{F2}^{(3)} + \rho'^{(5)}_{S3} + \rho_{E2}^{\prime(7)} = \rho_{F2S3}^{(3)} + \rho_{E2}^{\prime(7)} = \rho_{F2}^{(3)} + \rho_{S32}^{\prime(5)}$ in Table 4.1. Note that $\rho_{F21}^{(3)}$ and $\rho_{F22}^{(3)}$ are not purely third-order nonlinearities, instead it denotes the doubly-dressed FWM, including fifth- and seventh-order

nonlinear optical responses. Thus, the EWM response of $\rho_{E1}^{\prime(7)}$ ($\rho_{E2}^{\prime(7)}$) can be obtained by homodyne beat detection with the dressed FWM signal $\rho_{F2S2}^{(3)}$ ($\rho_{F2S3}^{(3)}$) as the strong local oscillator [25]. Note again that $\rho_{S21}^{\prime(5)}$ and $\rho_{S32}^{\prime(5)}$ are not pure fifth-order nonlinear responses, and they are used to denote the dressed SWM processes, including seventh-order nonlinear optical response. Except parallel and nested interaction types of doubly dressing FWM mechanisms, the sequential dressing interaction scheme will be considered in our future work.

From Eqs. (4.6) and (4.9), we easily realize that there exist the dramatic difference between parallel-dressing and nested-dressing interactions. The coherent interaction between two dressing processes in nested type is much stronger than that in parallel type. On the other hand, the three-photon FWM and seven-photon EWM have the same sign, which is opposite with that of the five-photon SWM. In weak dressing field limit, Eqs. (4.7) and (4.10) clearly show the destructive interferences among these multi-photon processes.

When the fields ε_2' and ε_4' are blocked [as shown in Fig. 4.8 (f1)], there coexist two singly-dressed SWM [$\rho_{S11}^{\prime(5)}$of S_{11} and $\rho_{S12}^{\prime(5)}$ of S_{12} depicted in Fig. 4.8 (f2)] and two EWM [$\rho_{E1}^{\prime\prime(7)}$of E_1 and $\rho_{E2}^{\prime\prime(7)}$ of E_2 depicted in Fig. 4.8 (d1 – d2)] processes, satisfying the phase-matching directions $\boldsymbol{k}_{S1}^{(2)}$ and $\boldsymbol{k}_{E1,2}^{(3)}$($\boldsymbol{k}^{(3)} = \boldsymbol{k}_{S1}^{(2)} = \boldsymbol{k}_{E1,2}^{(3)}$). Here, the prime and double prime also indicate that such multi-wave mixing processes are with different phase-matched directions. The SWM process S_1 (see Table 4.1) is generated by interactions with one photon each from ε_1, ε_3, ε_3', and two photons from the same field $\Omega_R\varepsilon_2$, which is dressed by field ε_4 [Fig. 4.8 (f2)]. Similarly, EWM processes E_1 and E_2 can also exist at the same time with one photon each from ε_1, ε_3, ε_3', two photons from the same field ε_2, and two photons from the same field ε_4, as shown in Figs. 4.8 (d1) – (d2).

The sub-process for the dressing field ε_4, "$\rho_{10}^{(5)} \xrightarrow{\omega_4} \rho_{40}^{(6)} \xrightarrow{-\omega_4} \rho_{10}^{(7)}$", is existing in the EWM the chain E_1. It means that the field ε_4 dress the state $|1\rangle$ [Fig. 4.8 (c3)], and affect the atomic coherences $\rho_{10}^{(5)}$ between $|0\rangle$ and $|1\rangle$. So we have $\rho_{(G_4\pm)0}^{(5)}$ in the dressed SWM the chain S_{11} (Table 4.1).

The high-order atomic coherence plays a significant role for the enhancement of multi-wave mixing processes. In coherent SWM processes, the simultaneous interactions of atoms with fields ε_1, ε_2 and ε_3' generate atomic coherence between $|0\rangle$ and $|3\rangle$ through resonant three-photon interaction. Such coherently prepared three-photon coherence with wave vector $\boldsymbol{k}_{03} = \boldsymbol{k}_1 + \boldsymbol{k}_2 - \boldsymbol{k}_3'$ is then probed by fields ε_3 and ε_2 and, as a result, a SWM process $\rho_{S1}^{\prime(5)} = G_c\left|G_2\right|^2/(d_1^2 d_2^2 d_3)$ is generated with $G_c = \mathrm{i}G_1(G_3')^* G_3 \exp(\mathrm{i}\boldsymbol{k}^{(3)} \cdot \boldsymbol{r})$. Such SWM process is then perturbed by field ε_4. A perturbative approach for such interaction can be described by the following coupled equations:

$$\begin{cases} \dfrac{\partial \rho_{10}}{\partial t} = -d_1\rho_{10} + \mathrm{i}G_2^*\rho_{20}\exp(-\mathrm{i}\boldsymbol{k}_2\cdot\boldsymbol{r}) + \mathrm{i}G_4^*\rho_{40}\exp(-\mathrm{i}\boldsymbol{k}_4\cdot\boldsymbol{r}) \\ \dfrac{\partial \rho_{40}}{\partial t} = -d_4\rho_{40} + \mathrm{i}G_4\rho_{10}\exp(\mathrm{i}\boldsymbol{k}_4\cdot\boldsymbol{r}). \end{cases} \tag{4.11}$$

We can get $\rho_{10}^{(5)} = \mathrm{i}G_2^*\rho_{20}^{(4)}/(d_1 + |G_4|^2/d_4)$ from the coupling Eq. (4.11) of the Chain E_1 for ε_4 interaction terms. $\rho_{10}^{(1)} = \mathrm{i}G_1\exp(\mathrm{i}\boldsymbol{k}_1\cdot\boldsymbol{r})/d_1$, $\rho_{20}^{(2)} = \mathrm{i}G_2\exp(\mathrm{i}\boldsymbol{k}_2\cdot\boldsymbol{r})\rho_{10}^{(1)}/d_2$, $\rho_{30}^{(3)} = \mathrm{i}(G_3')^*\exp(-\mathrm{i}\boldsymbol{k}_3'\cdot\boldsymbol{r})\rho_{20}^{(2)}/d_3$, and $\rho_{20}^{(4)} = \mathrm{i}G_3\exp(\mathrm{i}\boldsymbol{k}_3\cdot\boldsymbol{r})\rho_{30}^{(3)}/d_2$ are also obtained from the chain S_1. Thus, we can get

$$\rho_{S11}^{\prime(5)} = \rho_{10}^{(5)} = \frac{G_c|G_2|^2}{d_1d_2^2d_3(d_1 + |G_4|^2/d_4)}. \tag{4.12}$$

Assuming $|G_4|^2 << \Gamma_{10}\Gamma_{40}$, then through power expansion, we obtain

$$\rho_{S11}^{\prime(5)} = \frac{G_c|G_2|^2}{d_1^2d_2^2d_3}\left(1 - \frac{|G_4|^2}{d_1d_4}\right). \tag{4.13}$$

The dressed SWM process approximately converts to a coherent superposition of signals from SWM ($\rho_{S1}^{\prime(5)}$) and EWM ($|G_4|^2$ term). Note again that $\rho_{S11}^{\prime(5)}$ include both fifth- and seventh-order nonlinear optical responses.

This open five-level atomic system with co-existing FWM, SWM and EWM is consist of four conventional EIT subsystems, i.e., $|0\rangle \to |1\rangle \to |2\rangle$ (ladder-type) with two counter-propagation beams ε_2 (or ε_2') and ε_1, $|0\rangle \to |1\rangle \to |4\rangle$ (ladder-type) with two counter-propagation beams ε_4 (or ε_4') and ε_1, $|1\rangle \to |2\rangle \to |3\rangle$ (Λ-type) with two co-propagation beams ε_2 (or ε_2') and ε_3 (or ε_3'), and $|2\rangle \to |1\rangle \to |4\rangle$ (V-type) with two co-propagation beams ε_2 (or ε_2') and ε_4 (or ε_4'). More explicitly, the two ladder-type EIT, one Λ-type EIT and one V-type EIT configurations all satisfy the two-photon Doppler-free condition in the Fig. 4.8 (b) [17].

4.3.2 Interplay Among Coexisting FWM, SWM and EWM Processes

One possible experimental candidate for the proposed system is ^{87}Rb atoms with states $|0\rangle = |5S_{1/2}\rangle, |1\rangle = |5P_{3/2}\rangle, |2\rangle = |5D_{3/2}\rangle, |3\rangle = |5P_{1/2}\rangle$ and $|4\rangle = |5D_{5/2}\rangle$ [Fig. 4.8 (a)]. The respective transitions are $|0\rangle \to |1\rangle$ at 780.2 nm ($\gamma_{10} \approx 5.89$ MHz, where γ_{ij} is term due to spontaneous emission (longitudinal relaxation rate) between states $|i\rangle$ and $|j\rangle$), $|1\rangle \to |2\rangle$ at 776.2 nm ($\gamma_{21} \approx 0.77$ MHz), $|2\rangle \to |3\rangle$ at 762.1 nm ($\gamma_{23} \approx 0.98$ MHz), $|0\rangle \to |3\rangle$ at 795.0 nm ($\gamma_{30} \approx 5.40$ MHz) and $|1\rangle \to |4\rangle$ at 776.0 nm ($\gamma_{41} \approx 0.79$ MHz). The transverse relaxation rate Γ_{ij} between states $|i\rangle$ and $|j\rangle$ can be obtained by $\Gamma_{ij} = (\Gamma_i + \Gamma_j)/2$ ($\Gamma_0 = 0$, $\Gamma_1 = \gamma_{10}$, $\Gamma_2 = \gamma_{21} + \gamma_{23}$, $\Gamma_3 = \gamma_{30}$ and

$\Gamma_4 = \gamma_{41}$). i.e., $\Gamma_{10} = \gamma_{10}/2 = 2.94$ MHz, $\Gamma_{20} = (\gamma_{21} + \gamma_{23})/2 = 0.88$ MHz, $\Gamma_{30} = \gamma_{30}/2 = 2.70$ MHz and $\Gamma_{40} = \gamma_{41}/2 = 0.40$ MHz. Thus, $\Gamma_{10}/\Gamma_{20} \approx 3.3$, $\Gamma_{30}/\Gamma_{20} \approx 3.0$, $\Gamma_{40}/\Gamma_{20} \approx 0.5$, $\Gamma_{30}/\Gamma_{10} \approx 0.9$, and $\Gamma_{40}/\Gamma_{10} \approx 0.1$.

We consider the interaction of the dual dressings and the interplay among coexisting FWM, SWM, and EWM processes. First, we consider the doubly-dressed FWM (parallel-dressing interaction) spectra versus Δ_1/Γ_{20} for the case with blocking fields ε_3' and ε_4' [Fig. 4.8 (c1, c2)]. In this type of doubly-dressed FWM, a dressing field G_4 creates dressed atomic states $|+\rangle$ and $|-\rangle$ from the unperturbed state $|1\rangle$ [the Autler-Townes (AT) splitting $\Delta_{G4} \approx 2\{G_4[G_4^2 + 2\Gamma_{40}(\Gamma_{10} + \Gamma_{40})]^{1/2} - \Gamma_{40}^2\}^{1/2}$ mainly results from G_4, i.e., outer peak pair of Fig. 4.9 (a) and inner peak pair of Fig. 4.9 (b)]. When the dressing field G_3 is tuned close to the unperturbed state $|2\rangle$, the AT splitting created by field G_3 can be approximated to be $\Delta_{G3} \approx 2\{G_3[G_3^2 + 2\Gamma_{30}(\Gamma_{20} + \Gamma_{30})]^{1/2} - \Gamma_{30}^2\}^{1/2}$ [i.e., inner peak pair of Fig. 4.9 (a) and outer peak pair of Fig. 4.9 (b)]. More specifically, Fig. 4.9 (a) presents the dependence of the doubly-dressed FWM (parallel-dressing interaction) signal intensity at exact resonance $\Delta_2 = \Delta_3 = \Delta_4 = 0$, and the separation Δ_{G3} between the two inner peaks increases versus increase of G_3 ($G_4 > G_3$). For further identifying this parallel dressing interaction, we change the laser detunings to different values [Fig. 4.9 (b) for $G_3 > G_4$]. Compared with the solid curve of Fig. 4.9 (b), the dashed and dotted curves of Fig. 4.9 (b) present left shift of inner peak pair and right shift of outer peak pair due to the two-photon $\Delta_1 + \Delta_4$ factor of G_4 dressing term and three-photon $\Delta_1 + \Delta_2 - \Delta_3$ factor of G_3 dressing term in Eq. (4.6), respectively. Two AT shift processes due to the G_3 and G_4 dressings are independent, so the interaction between them is weak at the larger Δ_3 and Δ_4 values. When Δ_3 and Δ_4 are close to zero, two AT shift processes depend each other and start to interact with each other [Fig. 4.9 (c – f)]. On the other hand, when the doubly-dressed FWM (parallel-dressing interaction) signal intensity versus both Δ_3 and Δ_4 is normalized by no dressing field ($G_3 = G_4 = 0$) case (i.e., $\rho_{F11}^{(3)}/\rho_{F1}^{(3)}$), the controllable enhancement and suppression of the doubly-dressed FWM can be obtained by adjusting laser frequencies and two dressing field intensities [Fig. 4.9 (c) with both weak enhancements, (d) with one weak enhancement and one weak suppression, (e) with one weak suppression and one strong suppression, (f) with both strong enhancements]. Notice that Fig. 4.9 (c) presents anomalous and normal dispersion-like effects along Δ_3 and Δ_4, which are determined by the factors d_3 and d_4 of G_3 and G_4 in the Eq. (4.6), respectively. Due to the induced resonances of two-photon $\Delta_1 + \Delta_2 + \Delta_{G3}/2 = 0$ [Fig. 4.10 (a)] and one-photon $\Delta_1 + \Delta_{G4}/2 = 0$ [Fig. 4.10 (b)], Fig. 4.9(f) shows strong enhancements of FWM versus Δ_3 and Δ_4.

Next, we consider the doubly-dressed FWM (nested-dressing interaction) spectra versus Δ_1/Γ_{20} for blocking fields ε_2' and ε_3' [Fig. 4.8 (e1, e2)]. There exists strong coherent interaction between inner G_2 and outer G_3 dressing processes. When $G_2 = 0$ or $\Delta_2 = \infty$, $\rho_{F21}^{(3)}$ (or $\rho_{F22}^{(3)}$) becomes purely third-

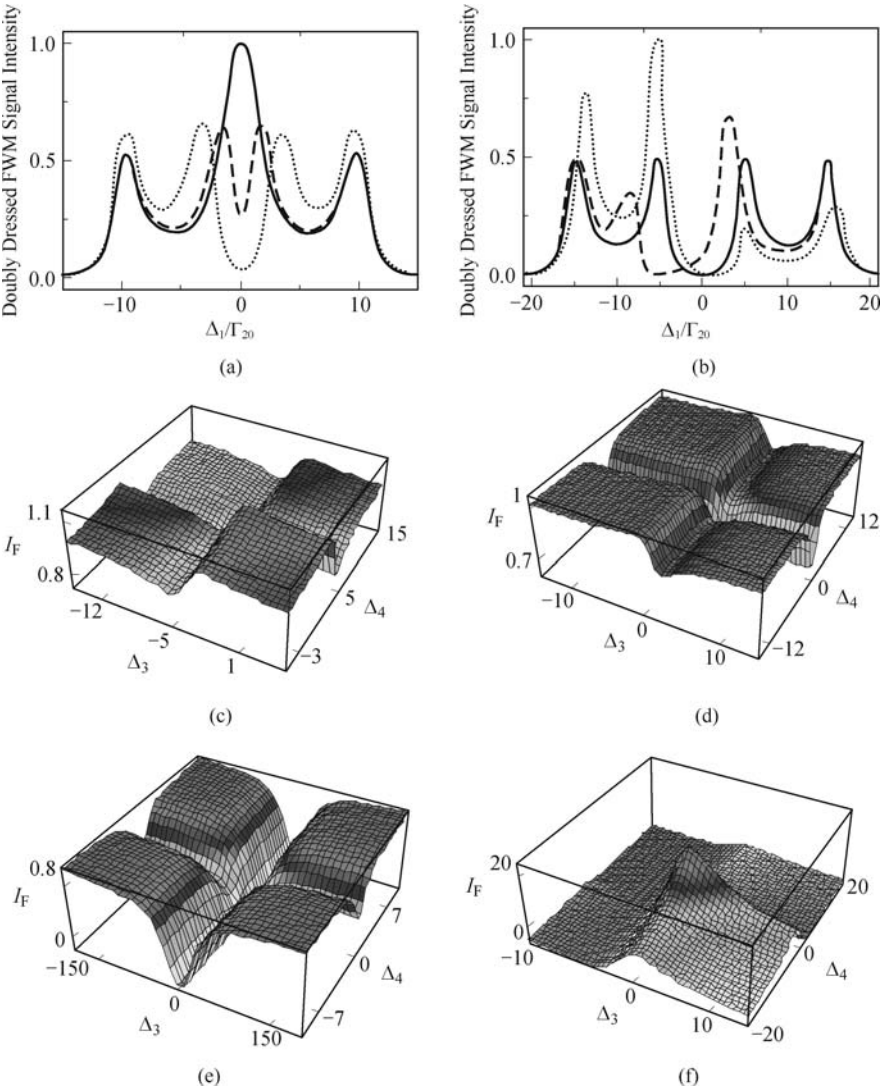

Fig. 4.9. (a) Doubly-dressed FWM (parallel type) signal intensities versus Δ_1/Γ_{20} ($\Gamma_{10}/\Gamma_{20} = 3.3, \Gamma_{30}/\Gamma_{20} = 3, \Gamma_{40}/\Gamma_{20} = 0.5, \Delta_2 = \Delta_3 = \Delta_4 = 0, G_4/\Gamma_{20} = 10$) for $G_3/\Gamma_{20} = 0$ (solid curve), 1.2 (dashed curve), and 3 (dotted curve); (b) [$G_3/\Gamma_{20} = 15, G_4/\Gamma_{20} = 5, \Delta_2 = 0, \Delta_3/\Gamma_{20} = 0$ and $\Delta_4/\Gamma_{20} = 0$ (solid curve), 0 and 5 (dashed curve), 2 and 0 (dotted curve)]. Doubly-dressed FWM signal intensity (normalized by the case with $G_3 = G_4 = 0$, i.e., $I_F = \rho^{(3)}_{F11}/\rho^{(3)}_{F1}$) versus Δ_3/Γ_{20} and Δ_4/Γ_{20} at (c) $G_3/\Gamma_{20} = G_4/\Gamma_{20} = 0.7$, $\Delta_1/\Gamma_{20} = -4, \Delta_2 = 0$; (d) $G_3/\Gamma_{20} = G_4/\Gamma_{20} = 0.5, \Delta_1 = 0, \Delta_2/\Gamma_{20} = 2$; (e), $G_4/\Gamma_{20} = 0.8, \Delta_1 = \Delta_2 = 0$; (f) $G_3/\Gamma_{20} = G_4/\Gamma_{20} = 5, \Delta_1/\Gamma_{30} = -4$, $\Delta_2 = 0$. Adopted from Ref. [36].

order nonlinearities. The primarily dressing field G_2 [$G_2 > G_3$ (where G_3 is the secondarily dressing field)] creates dressed atomic states $|+\rangle$ and $|-\rangle$

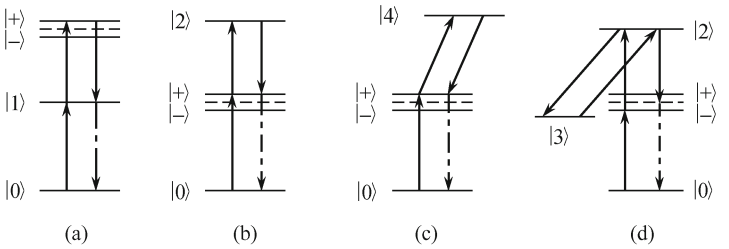

Fig. 4.10. Energy-level diagrams for induced enhancements of (a) two-photon resonant $\Delta_1 + \Delta_2 + \Delta_{G3}/2 = 0$ FWM, (b) one-photon resonant $\Delta_1 + \Delta_{G4}/2 = 0$ FWM, (c) two-photon resonant $|0\rangle \rightarrow |G_2+\rangle \rightarrow |4\rangle$ FWM, and (d) three-photon resonant $|0\rangle \rightarrow |-\rangle \rightarrow |2\rangle \rightarrow |3\rangle$ SWM, respectively.

from the unperturbed states $|1\rangle$ and $|2\rangle$ [solid curve in Fig. 4.11 (a)]. When the secondarily dressing field G_3 is tuned close to one of the primarily-dressed states $|+\rangle$ (or $|-\rangle$), basically the dressing field only couples the dressed state $|+\rangle$ (or $|-\rangle$) to the state $|3\rangle$ and leaves the other dressed state $|-\rangle$ (or $|+\rangle$) unperturbed [39]. Thus, when $\Delta_3 \approx \Delta_{G2}/2$, there exist the secondarily-dressed states $|-+\rangle$ and $|+-\rangle$ around the primarily-dressed state $|-\rangle$ [dashed curve in Fig. 4.11 (a)]; when $\Delta_3 \approx -\Delta_{G2}/2$ the secondarily-dressed states $|++\rangle$ and $|--\rangle$ (around the primarily-dressed state $|+\rangle$) can be generated (dotted curve in [Fig. 4.11 (a)]. Here, the separation between the two outer peaks [solid curve in Fig. 4.11 (a)] created by G_2 is given by $\Delta_{G2} \approx 2\{G_2[G_2^2 + 2\Gamma_{20}(\Gamma_{10} + \Gamma_{20})]^{1/2} - \Gamma_{20}^2\}^{1/2})$, while the change of the AT splitting between two inner peaks weakly depends on field G_2. More importantly, three FWM Liouville pathways for $\Delta_3 \approx -\Delta_{G2}/2$ ($\rho_{00}^{(0)} \xrightarrow{\omega_1} \rho_{(++)0}^{(1)} \xrightarrow{\omega_2} \rho_{20}^{(2)} \xrightarrow{-\omega_2} \rho_{(++)0}^{(3)}, \rho_{00}^{(0)} \xrightarrow{\omega_1} \rho_{(+-)0}^{(1)} \xrightarrow{\omega_2} \rho_{20}^{(2)} \xrightarrow{-\omega_2} \rho_{(+-)0}^{(3)}$, and $\rho_{00}^{(0)} \xrightarrow{\omega_1} \rho_{-0}^{(1)} \xrightarrow{\omega_2} \rho_{20}^{(2)} \xrightarrow{-\omega_2} \rho_{-0}^{(3)}$) interfere constructively (coherent interaction), leading to an enhanced FWM signal. Due to the decoherence of the Raman coherence ρ_{30}, the doubly-dressed four-level system also exhibits a constructive interference [39]. By contrast, the doubly-dressed system with a metastable excited state shows sharp dark resonance due to destructive interference between the secondarily-dressed states [17].

In Fig. 4.11 (b, c) the FWM (nested-dressing interaction) signal intensity with no dressing field ($G_2 = G_3 = 0$) is normalized to 1 (i.e., $\rho_{F21}^{(3)}/\rho_{F2}^{(3)}$). There are two groups (channels) of suppression and enhancement curves due to the primarily-dressed states $|G_3\pm\rangle$ created by G_3 ($G_3 > G_2$). Based on the same secondarily-dressed state $|G_2+\rangle$ created by G_2, the two-photon $\{|0\rangle \rightarrow |G_2+\rangle \rightarrow |4\rangle$ [Fig. 4.10 (c)]$\}$ resonant FWM signals (corresponding to each group of curves) are enhanced [Fig. 4.11 (c)]. Specifically, at exact resonance $\Delta_1 = 0$ we see that the FWM signal intensity is suppressed when the frequency of the dressing field G_2 is scanned across $\Delta_2 = \pm\Delta_{G3}/2$ [Fig. 4.11 (b)]. If G_2 increases, FWM signal has been strongly suppressed through two channels created by G_3 [Fig. 4.11 (b)]. On the other hand, the presence

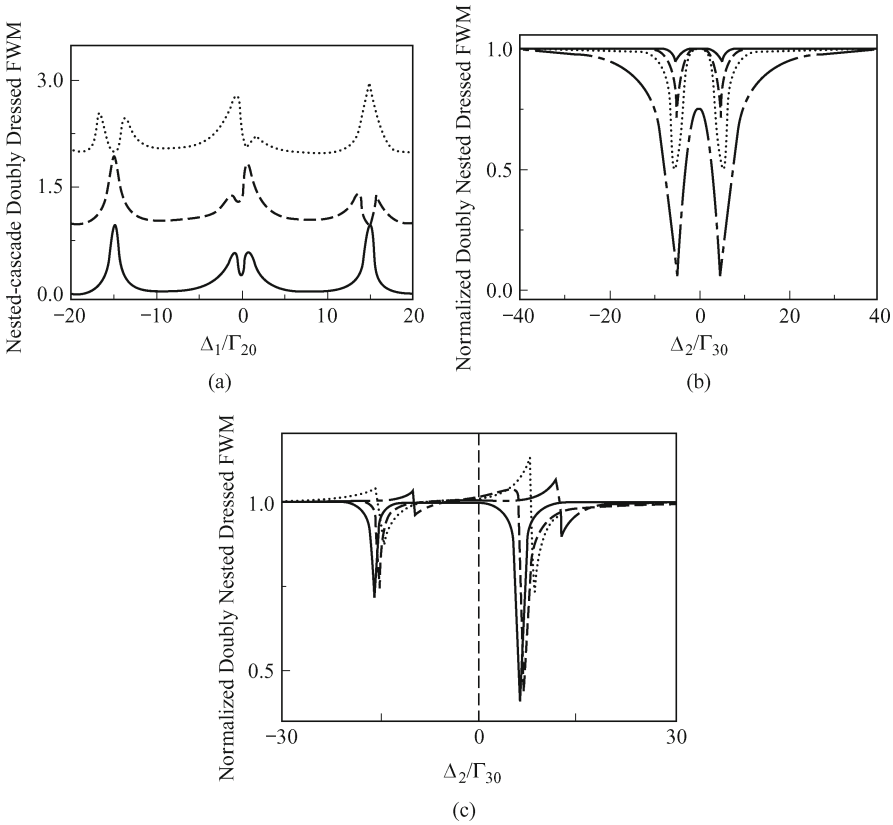

Fig. 4.11. (a) The doubly-dressed FWM (nested type) signal intensity versus Δ_1/Γ_{10} ($\Gamma_{20}/\Gamma_{10} = 0.3, \Gamma_{30}/\Gamma_{10} = 0.9, \Gamma_{40}/\Gamma_{10} = 0.1, G_2/\Gamma_{10} = 15, G_3/\Gamma_{10} = 1.5, \Delta_2 = \Delta_4 = 0$) for $\Delta_3/\Gamma_{10} = 10000$ (solid curve), 14.5 (dashed curve), and –14.5 (dotted curve), respectively. (b) Doubly-dressed FWM signal intensity (normalized by the signal with $G_3 = G_4 = 0$ case, i.e., $\rho_{F21}^{(3)}/\rho_{F2}^{(3)}$) versus Δ_2/Γ_{10} ($\Delta_1 = \Delta_2 = \Delta_4 = 0, G_3/\Gamma_{10} = 5$) for $G_2/\Gamma_{10} = 0.2$ (solid curve), 0.5 (dashed curve), 1 (dotted curve), 2 (dash-dotted curve), respectively; (c) at $G_2/\Gamma_{10} = 0.5, G_3/\Gamma_{10} = 10, \Delta_3/\Gamma_{10} = -10, \Delta_4 = 0$, for $\Delta_1/\Gamma_{10} = 0$ (solid curve), -0.5 (dashed curve), -2 (dotted curve), -6 (dash-dotted curve), respectively.

of the weak dressing field G_2 can either suppress or enhance the FWM signal when $\Delta_1 \neq 0$ [Fig. 4.11 (c)]. Due to $\Delta_3 < 0$, the amplitudes of enhancement and suppression of FWM's right channel for the dressed state $|G_3-\rangle$ are obviously larger than that of FWM's left channel for the dressed state $|G_3+\rangle$ [Fig. 4.11(c)]. Furthermore, the strongly enhanced dual-FWM channels can be opened simultaneously by the two strong dressing fields, which provide the energy for such large enhancement.

Finally, we investigate the dressed SWM spectrum versus Δ_4/Γ_{30}. Figure. 4.12 presents the enhancement of the dressed SWM signal intensity at different probe detunings. The SWM signal intensity with no dressing field

is normalized to 1 (i.e., $\rho'^{(5)}_{S11}/\rho'^{(5)}_{S1}$). When $G_4/\Gamma_{30} = 50$ the SWM signal is strongly enhanced by a factor of 700 in the presence of the dressing field when $\Delta_1/\Gamma_{30} = 50$ (the dotted curve in Fig. 4.12), which mainly results from the three-photon $\{|0\rangle \rightarrow |-\rangle \rightarrow |2\rangle \rightarrow |3\rangle$ [Fig. 4.10 (d)]$\}$ resonance. In other words, such huge enhancement of the signal is due to induced resonance by the strong coupling field. In general, the constructive and destructive interferences between the $|+\rangle$ and $|-\rangle$ SWM channels (Table 4.1) result in the enhancement and suppression of SWM signal, respectively. However, such enhancement mainly originates from the dispersion of SWM and EWM signals and their interference under the weak dressing field limit [21].

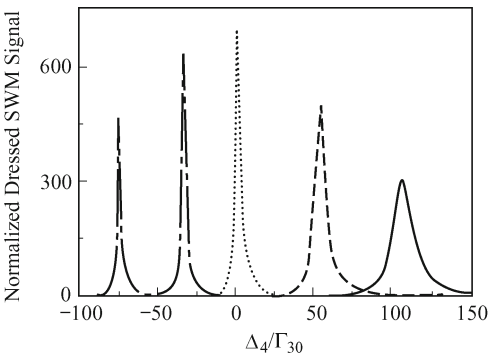

Fig. 4.12. The dressed SWM signal intensity (normalized by no dressing field case) versus $\Delta_4/\Gamma_{10}(\Gamma_{20}/\Gamma_{10} = 0.3,\ \Gamma_{30}/\Gamma_{10} = 0.9,\ \Gamma_{40}/\Gamma_{10} = 0.1,\ \Delta_2 = \Delta_3 = 0,\ G_4/\Gamma_{10} = 50)$ for $\Delta_1/\Gamma_{10} = 20$ (solid curve), $\Delta_1/\Gamma_{10} = 30$ (dashed curve), $\Delta_1/\Gamma_{10} = 50$ (dotted curve), $\Delta_1/\Gamma_{10} = 70$ (dash-dotted curve), $\Delta_1/\Gamma_{10} = 100$ (dash-dot-dotted curve), respectively.

4.4 Controlled Multi-Wave Mixing via Interacting Dark States in a Five-level System

Recently a great deal of attention has been paid to observe and understand the phenomenon of EIT and related effects in multi-level atomic systems [41] interacting with two or more electromagnetic fields. Investigations about interactions of doubly dressed states and corresponding effects on atomic systems have also attracted many researchers. The doubly dressed states were obtained in the inverted Y system [42] and double-Λ system [43]. In this work, we go further to theoretically study, in a five-level system with three possible dressing fields, three types of dual-dressing (nested and sequential) schemes and precisely predicted the splitting of dark states resulting in five absorption peaks.

On the other hand, highly efficient multi-wave mixing (MWM) processes with coherently prepared states have also been intensively studied in the

past few decades [44, 45]. Enhanced four-wave mixing (FWM) and efficient six-wave mixing (SWM) processes have been experimentally demonstrated in optically dressed systems [44, 45]. Moreover, eight-wave mixing (EWM) in a folded five-level atomic system has been observed recently [27]. In previously studied close-cycled (ladder-type, N-type, double-Λ-type and folded) systems, FWM, SWM, and EWM processes cannot coexist in a given configuration and different order nonlinearities can only be observed individually. In our recent studies, the third-order and fifth-order nonlinear processes coexist in an open (such as V-type, Y-type and inverted Y-type) atomic system were demonstrated, in which the coexisting SWM signal can become comparable or even greater than the companion FWM by manipulating the atomic coherence [16, 37]. After that, three kinds of doubly dressed FWM processes (in nested, parallel and sequential dressing schemes) were investigated [46]. Here, we present controlled MWM (FWM, SWM, and EWM) via interacting dark states in a five-level system [Fig. 4.13 (a)]. Specifically, there exists the intermixture among three dressing schemes (nested, parallel, and sequential dressing schemes) in FWM, the quadruple nested scheme in SWM, and the parallel combination of two nested schemes in EWM.

Several features of this work are distinctly different and gain an advantage over the previously reported MWM processes [46]. Firstly, multi-dressed FWM, SWM, and EWM processes coexist and compete in a five-level system because FWM is suppressed while SWM and EWM are enhanced by controlling the offsets of fields. Secondly, various multi-dressed types in FWM, SWM, EWM, and EIT are viewed as the combination of three basic dual-dressing types (nested, parallel and sequential dressing schemes) which is also separately investigated for better explanation of multi-dressing. Thirdly, we obtain triple Aulter-Townes (AT) splitting in the spectra of FWM signal, quadruple AT splitting in SWM signal, and two triply splitting in EIT. The spectra of AT splitting, suppression and enhancement of FWM and EWM signals are the superposition of two groups of the different AT splitting peaks. The interaction of multi-dressed states created by three dressing fields has been studied, which can result in the dramatic enhancement of MWM signals. Thus, by virtue of controlling the multi-dressed MWM signal, we can obtain the nonlinear susceptibility of the desired order.

4.4.1 Basic Theory

With the basic system [in Fig. 4.13 (a)] of three energy levels ($|0\rangle - |1\rangle - |2\rangle$) and three laser fields (the pumping beams E_2 (with frequency ω_2, wave vector $\boldsymbol{k}_2$, and Rabi frequency G_2), $E_2'(\omega_2, \boldsymbol{k}_2', G_2')$ and the probe beam $E_1(\omega_1, \boldsymbol{k}_1, G_1)$), a FWM signal at frequency ω_1 will be generated and propagates in the $\boldsymbol{k}_f = \boldsymbol{k}_1 + \boldsymbol{k}_2 - \boldsymbol{k}_2'$ direction depending on the phase-matching condition. By adding another energy level ($|4\rangle$) and another laser field $E_4(\omega_4, \boldsymbol{k}_4, G_4)$,

system $|4\rangle - |0\rangle - |1\rangle - |2\rangle$ is formed [37] and a small-angle grating in the atomic medium is established. E_4 interacts with the FWM process in the ladder system and generate SWM signals propagating along with the $\boldsymbol{k}_s(= \boldsymbol{k}_1 + \boldsymbol{k}_2 - \boldsymbol{k}_2' + \boldsymbol{k}_4 - \boldsymbol{k}_4)$ direction owing to the phase-matching condition. When the pumping beams $E_3(\omega_3, \boldsymbol{k}_3, G_3)$ is turned on, this five-level system also can generate EWM signal, which propagate in the same direction due to the phase-matching condition $\boldsymbol{k}_e = \boldsymbol{k}_1 + \boldsymbol{k}_2 - \boldsymbol{k}_2' + \boldsymbol{k}_3 - \boldsymbol{k}_3 + \boldsymbol{k}_4 - \boldsymbol{k}_4$. Simultaneously, there exists another SWM signal which satisfies the phase-matching condition $\boldsymbol{k}_{s1} = \boldsymbol{k}_1 + \boldsymbol{k}_2 - \boldsymbol{k}_2' + \boldsymbol{k}_3 - \boldsymbol{k}_3$. However, only SWM $\boldsymbol{k}_s(= \boldsymbol{k}_1 + \boldsymbol{k}_2 - \boldsymbol{k}_2' + \boldsymbol{k}_4 - \boldsymbol{k}_4)$ is discussed in the paper.

According to the description above, the Hamiltonian of this system can be written as

$$\begin{aligned} H_{int} = &- \hbar[\Delta_1|1\rangle\langle 1| + (\Delta_1 + \Delta_2)|2\rangle\langle 2| + (\Delta_1 - \Delta_3)|3\rangle\langle 3| + \Delta_4|4\rangle\langle 4|] - \\ &\hbar(G_1|1\rangle\langle 0| + G_4|4\rangle\langle 0| + (G_2 + G_2')|2\rangle\langle 1| + G_3|3\rangle\langle 1| + H.c.). \end{aligned}$$

Then the density-matrix equations which determine the evolution of the whole system can be obtained. As to a five-level system, there are 15 independent density-matrix equations without considering that $\rho_{00} + \rho_{11} + \rho_{22} + \rho_{33} + \rho_{44} = 1$. However, if we consider the probe field being weak enough, the number of the required equations will be reduced because some weak terms will be omitted in further derivation. Moreover, the perturbation the chain method, a suitable method for our special case and can remove density-matrixes which contribute little to MWM generation, is employed to calculate density-matrix related to MWM process. Finally only six equations can be useful for derivation is as follows:

$$\rho_{10}^{(r)} = -d_{10}\rho_{10}^{(r)} - \mathrm{i}G_4\mathrm{e}^{\mathrm{i}\boldsymbol{k}_4\cdot\boldsymbol{r}}\rho_{14}^{(r)} + \mathrm{i}(G_2')^*\mathrm{e}^{-\mathrm{i}\boldsymbol{k}_2'\cdot\boldsymbol{r}}\rho_{20}^{(r)} + \mathrm{i}G_3\mathrm{e}^{\mathrm{i}\boldsymbol{k}_3\cdot\boldsymbol{r}}\rho_{30}^{(r)} + \mathrm{i}G_1\mathrm{e}^{\mathrm{i}\boldsymbol{k}_1\cdot\boldsymbol{r}}\rho_{00}^{(r)}, \tag{4.14a}$$

$$\rho_{20}^{(r)} = -d_{20}\rho_{20}^{(r)} - \mathrm{i}G_1\mathrm{e}^{\mathrm{i}\boldsymbol{k}_1\cdot\boldsymbol{r}}\rho_{21}^{(r)} - \mathrm{i}G_4\mathrm{e}^{\mathrm{i}\boldsymbol{k}_4\cdot\boldsymbol{r}}\rho_{24}^{(r)} + \mathrm{i}G_2\mathrm{e}^{\mathrm{i}\boldsymbol{k}_2\cdot\boldsymbol{r}}\rho_{10}^{(r)}, \tag{4.14b}$$

$$\rho_{30}^{(r)} = -d_{30}\rho_{30}^{(r)} - \mathrm{i}G_1\mathrm{e}^{\mathrm{i}\boldsymbol{k}_1\cdot\boldsymbol{r}}\rho_{31}^{(r)} - \mathrm{i}G_4\mathrm{e}^{\mathrm{i}\boldsymbol{k}_4\cdot\boldsymbol{r}}\rho_{34}^{(r)} + \mathrm{i}G_3^*\mathrm{e}^{-\mathrm{i}\boldsymbol{k}_3\cdot\boldsymbol{r}}\rho_{10}^{(r)}, \tag{4.14c}$$

$$\rho_{14}^{(r)} = -d_{14}\rho_{14}^{(r)} + \mathrm{i}G_2^*\mathrm{e}^{-\mathrm{i}\boldsymbol{k}_2'\cdot\boldsymbol{r}}\rho_{24}^{(r)} + \mathrm{i}G_3\mathrm{e}^{\mathrm{i}\boldsymbol{k}_3\cdot\boldsymbol{r}}\rho_{34}^{(r)} - \mathrm{i}G_4^*\mathrm{e}^{-\mathrm{i}\boldsymbol{k}_4\cdot\boldsymbol{r}}\rho_{10}^{(r)}, \tag{4.14d}$$

$$\rho_{24}^{(r)} = -d_{24}\rho_{24}^{(r)} + \mathrm{i}G_2\mathrm{e}^{\mathrm{i}\boldsymbol{k}_2\cdot\boldsymbol{r}}\rho_{14}^{(r)} - \mathrm{i}G_4^*\mathrm{e}^{-\mathrm{i}\boldsymbol{k}_4\cdot\boldsymbol{r}}\rho_{20}^{(r)}, \tag{4.14e}$$

$$\rho_{34}^{(r)} = -d_{34}\rho_{34}^{(r)} + \mathrm{i}G_3^*\mathrm{e}^{-\mathrm{i}\boldsymbol{k}_3\cdot\boldsymbol{r}}\rho_{14}^{(r)} - \mathrm{i}G_4^*\mathrm{e}^{-\mathrm{i}\boldsymbol{k}_4\cdot\boldsymbol{r}}\rho_{30}^{(r)}, \tag{4.14f}$$

where $d_{10} = \Gamma_{10} + \mathrm{i}\Delta_1, d_{20} = \Gamma_{20} + \mathrm{i}(\Delta_1 + \Delta_2), d_{30} = \Gamma_{30} + \mathrm{i}(\Delta_1 - \Delta_3), d_{14} = \Gamma_{14} - \mathrm{i}(\Delta_1 - \Delta_4), d_{24} = \Gamma_{24} - \mathrm{i}(\Delta_1 + \Delta_2 - \Delta_4)$ and $d_{34} = \Gamma_{34} - \mathrm{i}(\Delta_1 - \Delta_3 - \Delta_4)$ with the frequency detuning $\Delta_i = \Omega_i - \omega_i$. Γ_{ij} is the transverse relaxation rate between states $|i\rangle$ and $|j\rangle$. Ω_i is the atomic resonance frequency. The Rabi frequencies are defined as $G_i = \varepsilon_i\mu_{ij}/\hbar$, where $\mu_{ij}$are the transition dipole moments between level $|i\rangle$ and level $|j\rangle$. Next we will apply modified density-matrix equations via perturbation chains to analyze the coexisting multi-dressed FWM, SWM, and EWM, respectively.

To better understand the interplay among coexisting FWM, SWM, and EWM processes, we use the perturbation the chain method to derive expressions of high-order density-matrix elements standing for FWM, SWM, and EWM processes. Although such approach makes significant approximations, it shows a simple but clear picture of which give leading contributions in the complicated nonlinear optical processes. Moreover, we approach the final complicated expressions by inserting the dressing field step by step. So the expression of the pure FWM without any dressing field of a ladder sub-system contained in the system we showed above are given clear derivation process using perturbation the chain method in the following.

Considering a sub-system consisting of states $|0\rangle, |1\rangle, |2\rangle$ and three laser beams E_1, E_2, and E_2', there are a simple FWM (ρ_{F1}) expressed as the FWM perturbation the chain (F1) $\rho_{00}^{(0)} \xrightarrow{\omega_1} \rho_{10}^{(1)} \xrightarrow{\omega_2} \rho_{20}^{(2)} \xrightarrow{-\omega_2} \rho_{10}^{(3)}$. Density-matrix elements in the chain denote the initial, intermediary and final states of the transition process of generating FWM. According to the physics of the perturbation the chain, as to certain element denoting a state, only the higher-order element in the chain can contribute to it, the other weak term can be neglected then. Consequently, simplified density matrix equations about $\rho_{10}^{(1)}, \rho_{20}^{(2)}$, and $\rho_{10}^{(3)}$ are

$$\rho_{10}^{(1)} = \mathrm{i}G_1 \mathrm{e}^{\mathrm{i}\boldsymbol{k}_1\cdot\boldsymbol{r}}/d_{10}, \tag{4.15a}$$

$$\rho_{20}^{(2)} = \mathrm{i}G_2 \mathrm{e}^{\mathrm{i}\boldsymbol{k}_2\cdot\boldsymbol{r}}\rho_{10}^{(1)}/d_{20}, \tag{4.15b}$$

$$\rho_{10}^{(3)} = \mathrm{i}G_2'^{*} \mathrm{e}^{-\mathrm{i}\boldsymbol{k}_2'\cdot\boldsymbol{r}}\rho_{20}^{(2)}/d_{10}. \tag{4.15c}$$

Substitute Eq. (4.15a) into Eq. (4.15b), and then the result substitute to Eq. (4.15c), we get

$$\rho_{F1} = \rho_{10}^{(3)} = -\mathrm{i}G_A \mathrm{e}^{\mathrm{i}\boldsymbol{k}_f\cdot\boldsymbol{r}}/d_{10}^2 d_{20}. \tag{4.16}$$

where $G_A = G_1 G_2 G_2'^{*}$. Let us talk about the case that an additional strong dressing field E_3 (connecting transition $|1\rangle$ and $|3\rangle$) are added in system $|0\rangle - |1\rangle - |2\rangle$. E_3 dresses level $|1\rangle$ and created two new states $|G_3+\rangle$ and $|G_3-\rangle$, and then the dressed FWM is denoted as the dressed perturbation the chain: (F2) $\rho_{00}^{(0)} \xrightarrow{\omega_1} \rho_{10}^{(1)} \xrightarrow{\omega_2} \rho_{20}^{(2)} \xrightarrow{-\omega_2} \rho_{G3\pm0}^{(3)}$, where the sub-script "1" of element $\rho_{10}^{(3)}$ is replaced by "$G_3\pm$". In the following we will see that the dressed state is actual the interference between the polarizations $\rho_{10}^{(3)}$ and $\rho_{10}^{(5)}$ which is generated by E_3 combining with FWM (F1). This lead us expanding $\rho_{G3\pm0}^{(3)}$ as sub-chain $\rho_{10}^{(3)} \xrightarrow{-\omega_3} \rho_{30}^{(4)} \xrightarrow{\omega_3} \rho_{10}^{(5)}$ and then the dressed FWM the chain transform into the SWM the chain (S1) $\rho_{00}^{(0)} \xrightarrow{\omega_1} \rho_{10}^{(1)} \xrightarrow{\omega_2} \rho_{20}^{(2)} \xrightarrow{-\omega_2}$ $\rho_{10}^{(3)} \xrightarrow{-\omega_3} \rho_{30}^{(4)} \xrightarrow{\omega_3} \rho_{10}^{(5)}$ which stand for the one which interfere with FWM (F1) and finally cause dressing states $|G_3\pm\rangle$. In the weak field approximation, terms containing weak field G_1 are all neglect in density matrix equation,

while terms containing strong field G_3 are saved. We do this also is guided by sub-chain $\rho_{10}^{(3)} \xrightarrow{-\omega_3} \rho_{30}^{(4)} \xrightarrow{\omega_3} \rho_{10}^{(5)}$, then the coupling equations are as follows $\dot{\rho}_{10}^{(3)} = -d_{10}\rho_{10}^{(3)} + \mathrm{i}G_2^* \mathrm{e}^{\mathrm{i}\boldsymbol{k}_2'\cdot\boldsymbol{r}}\rho_{20}^{(2)} + \mathrm{i}\mathrm{e}^{\mathrm{i}\boldsymbol{k}_3\cdot\boldsymbol{r}}G_3\rho_{30}, \dot{\rho}_{30} = -d_{30}\rho_{30} + \mathrm{i}G_3^*\mathrm{e}^{-\mathrm{i}\boldsymbol{k}_3\cdot\boldsymbol{r}}\rho_{10}^{(3)}$. Solve the above equations, we get

$$\rho_{G3\pm0}^{(3)} = \frac{\mathrm{i}G_2'^* \mathrm{e}^{\mathrm{i}\boldsymbol{k}_2'\cdot\boldsymbol{r}}}{d_{10} + |G_3|^2/d_{30}}\rho_{20}^{(2)}. \tag{4.17}$$

Combining Eqs. (4.15a) and (4.15b) with Eq. (4.17), the dressed FWM is finally obtained as

$$\rho_{F1}' = \rho_{10}^{(3)} = \frac{-\mathrm{i}G_A \mathrm{e}^{\mathrm{i}\boldsymbol{k}_f\cdot\boldsymbol{r}}}{d_{10}d_{20}} \frac{1}{d_{10} + |G_3|^2/d_{30}}. \tag{4.18}$$

We can see the factor d_{10} in ρ_{F1}' is modified by the G_3 dressing term in this singly dressed FWM [45]. More interesting, under the weak field limit ($|G_3|^2 << \Gamma_{10}\Gamma_{30}$), Eq. (4.18) can be expanded to be $\rho_{F1}' = \rho_{F1} + iG_A|G_3|^2\mathrm{e}^{\mathrm{i}\boldsymbol{k}_s\cdot\boldsymbol{r}}/(d_{10}^2 d_{20}d_{30}) = \rho_{F1} + \rho_{S1}$, here ρ_{S1} is the SWM expression which can be deduced via the chain S1. This means that the density-matrix element of the singly dressed FWM can be considered as a coherent superposition of one pure FWM (ρ_{F1}) process and one pure SWM (ρ_{S1}) process under the weak field limit. The enhancement and suppression of the FWM process consequently can be viewed as resulting from the constructive and destructive interference between these two processes, respectively. In addition, such the coherent superposition can be investigated the autoionization state of atoms by optics heterodyne between FWM and SWM. However, when the dressing field E_3 is strong enough, Eq. (4.17) cannot be series expanded. Here we believe the dressing field splits the level $|1\rangle$, and the enhancement and suppression of FWM process result from the constructive and destructive interferences between two dressed paths ($|0\rangle \to |G_3+\rangle \to |1\rangle$ and $|0\rangle \to |G_3-\rangle \to |1\rangle$), respectively.

Next let us discuss the dual-dressed scheme. It generally has three different types, namely the nested, sequential and parallel dressed schemes. Detailed analyses are as follows.

Here, besides the dressing field E_3, another strong field E_4 is turned on too, then a dual-dressed FWM is generating in this five-level system. The dressing fields E_3 and E_4 dress the levels $|0\rangle$ and $|1\rangle$, respectively. So they can act on two different transition processes, namely two different matrix density elements in perturbation the chain. For example, dual-dressed FWM expressed by (F3) $\rho_{00}^{(0)} \xrightarrow{\omega_1} \rho_{1G4\pm}^{(1)} \xrightarrow{\omega_2} \rho_{20}^{(2)} \xrightarrow{-\omega_2} \rho_{G3\pm0}^{(3)}$. Taking two subchains of dressing fields (D1) $\rho_{10}^{(1)} \xrightarrow{-\omega_4} \rho_{14}^{(2)} \xrightarrow{\omega_4} \rho_{10}^{(3)}$ and (D2) $\rho_{10}^{(5)} \xrightarrow{-\omega_3} \rho_{30}^{(6)} \xrightarrow{\omega_3} \rho_{10}^{(7)}$ to displace two matrix density elements $\rho_{1G4\pm}^{(1)}$ and $\rho_{G3\pm0}^{(3)}$, the EWM perturbation the chain (E1) $\rho_{00}^{(0)} \xrightarrow{\omega_1} \rho_{10}^{(1)} \xrightarrow{-\omega_4} \rho_{14}^{(2)} \xrightarrow{\omega_4} \rho_{10}^{(3)} \xrightarrow{\omega_2}$

$\rho_{20}^{(4)} \xrightarrow{-\omega_2} \rho_{10}^{(5)} \xrightarrow{-\omega_3} \rho_{30}^{(6)} \xrightarrow{\omega_3} \rho_{10}^{(7)}$ is obtained. This doubly dressing scheme is called as a parallel dressing scheme for the two dressing field are influence this process parallelly. According to the chain D1, we solve the coupling equations

$$\dot{\rho}_{10}^{(1)} = -d_{10}\rho_{10}^{(1)} - \mathrm{i}G_4\mathrm{e}^{\mathrm{i}\boldsymbol{k}_4\cdot\boldsymbol{r}}\rho_{14} + \mathrm{i}G_1\mathrm{e}^{\mathrm{i}\boldsymbol{k}_1\cdot\boldsymbol{r}}\rho_{00}^{(0)},$$
$$\dot{\rho}_{14} = -d_{14}\rho_{14} - \mathrm{i}G_4^*\mathrm{e}^{-\mathrm{i}\boldsymbol{k}_4\cdot\boldsymbol{r}}\rho_{10}^{(1)}$$

and obtain

$$\rho_{1G4\pm}^{(1)} = \frac{\mathrm{i}G_1\mathrm{e}^{\mathrm{i}\boldsymbol{k}_1\cdot\boldsymbol{r}}}{d_{10} + |G_4|^2/d_{14}}\rho_{00}^{(0)}. \tag{4.19}$$

According to the chain D2, we solve coupling equations

$$\dot{\rho}_{10}^{(3)} = -d_{10}\rho_{10}^{(3)} + \mathrm{i}G_2^*\mathrm{e}^{-\mathrm{i}\boldsymbol{k}_2'\cdot\boldsymbol{r}}\rho_{20}^{(2)} + \mathrm{i}G_3\mathrm{e}^{\mathrm{i}\boldsymbol{k}_3\cdot\boldsymbol{r}}\rho_{30},$$
$$\dot{\rho}_{30} = -d_{30}\rho_{30} + \mathrm{i}G_3^*\mathrm{e}^{-\mathrm{i}\boldsymbol{k}_3\cdot\boldsymbol{r}}\rho_{10}^{(3)},$$

and obtain

$$\rho_{G3\pm0}^{(3)} = \frac{\mathrm{i}G_2'^*\mathrm{e}^{-\mathrm{i}\boldsymbol{k}_2'\cdot\boldsymbol{r}}}{d_{10} + |G_3|^2/d_{30}}\rho_{20}^{(2)}. \tag{4.20}$$

From the chain (F3) and combining Eqs. (4.15b), (4.17) and (4.18), we can obtain

$$\rho_{F1}'' = \rho_{10}^{(3)} = \frac{-\mathrm{i}G_A\mathrm{e}^{\mathrm{i}\boldsymbol{k}_f\cdot\boldsymbol{r}}}{d_{20}}\frac{1}{d_{10} + |G_4|^2/d_{14}}\frac{1}{d_{10} + |G_3|^2/d_{30}}. \tag{4.21}$$

where d_{10} in two terms are modified parallelly. Under the weak limit ($|G_4|^2 << \Gamma_{10}\Gamma_{14}$), Equation (4.21) can be expanded as $\rho_{F1}' + G_A|G_4|^2/[d_{10}d_{14}d_{20}(d_{10}+|G_3|^2/d_{30})] = \rho_{F1}' + \rho_S'$. This means that the density-matrix element of the dual-dressed FWM can be considered as a coherent superposition of one single dressed FWM process and single dressed SWM process under the weak field limit. We can see that the dual-dressed FWM is actual the interference between the polarizations ρ_{F1}' and ρ_S'. In addition, under the weak field limit ($|G_3|^2 << \Gamma_{10}\Gamma_{30}$ and $|G_4|^2 << \Gamma_{10}\Gamma_{14}$), the parallel dual-dressed FWM (DDFWM) can be considered as a coherent superposition of signals from one FWM, two SWM and one EWM processes [46] according to its expression expansion.

In this part, we will talk about the dressing mechanism contained five-dressing fields based on the three basic dual-dressing types. We focus on investigating the two portions of the expression: one is the two dressing term which is a simply nested dressing scheme, the other contain three dressing fields of which the outer dressing terms of the nested dressing scheme is a sequential dressing scheme.

At first, let us consider the nested dressing scheme, which the dressing fields E_3 and E_4 perform their dressing effect in another manner denoted

as sub-chain (D3) $\rho_{10}^{(3)} \xrightarrow{-\omega_3} \rho_{30} \xrightarrow{\omega_4} \rho_{34} \xrightarrow{-\omega_4} \rho_{30} \xrightarrow{\omega_3} \rho_{10}^{(3)}$, in which the sub-chain "$\rho_{30} \xrightarrow{\omega_4} \rho_{34} \xrightarrow{-\omega_4} \rho_{30}$" induced by dressing field E_4 is nested into the sub-chains "$\rho_{10}^{(3)} \xrightarrow{-\omega_3} \rho_{30}$" and "$\rho_{30} \xrightarrow{\omega_3} \rho_{10}^{(3)}$" induced by dressing field E_3. That is why it is called as the nested-dressing scheme [37, 46] and $\rho_{10}^{(3)}$ in the chain (F1) can be modified as $\rho_{G3\pm G4\pm}^{(3)}$. Similarly, from the chain D3, we choose the following equations as the coupling equations: $\dot{\rho}_{10}^{(3)} = -d_{10}\rho_{10}^{(3)} + \mathrm{i}G_2^* \mathrm{e}^{-\mathrm{i}\boldsymbol{k}_2'\cdot\boldsymbol{r}}\rho_{20}^{(r)} + \mathrm{i}G_3\mathrm{e}^{\mathrm{i}\boldsymbol{k}_3\cdot\boldsymbol{r}}\rho_{30}, \dot{\rho}_{30} = -d_{30}\rho_{30} - \mathrm{i}G_4\mathrm{e}^{\mathrm{i}\boldsymbol{k}_4\cdot\boldsymbol{r}}\rho_{34} + \mathrm{i}G_3^*\mathrm{e}^{-\mathrm{i}\boldsymbol{k}_3\cdot\boldsymbol{r}}\rho_{10}^{(3)}, \dot{\rho}_{34} = -d_{34}\rho_{34} + \mathrm{i}G_4^*\mathrm{e}^{-\mathrm{i}\boldsymbol{k}_4\cdot\boldsymbol{r}}\rho_{30}$. Solving above equations, we get

$$\rho_{G3\pm G4\pm}^{(3)} = \frac{\mathrm{i}G_2'^*\mathrm{e}^{-\mathrm{i}\boldsymbol{k}_2'\cdot\boldsymbol{r}}}{d_{10} + \dfrac{|G_3|^2}{d_{30} + |G_4|^2/d_{34}}}\rho_{20}^{(2)}. \tag{4.22}$$

So, the single-photon term d_{10} is modified by G_3 which is called the inner dressing field) and then d_{30} is modified by the outer G_4 which is called the outer dressing field). From the expression we can see that G_4 term depend on G_3 term, they interact tightly.

Next we investigate the three dressing fields term. Here we assume E_2 is also strong enough to be a dressing field. It can dress the same level $|1\rangle$ and act on element $\rho_{14}^{(2)}$ together with E_3, which is denoted as $\rho_{(G2G3\pm)4}^{(2)}$. It expand as the sub-chain (D4) $\rho_{14}^{(2)} \xrightarrow{\omega_2} \rho_{24} \xrightarrow{-\omega_2} \rho_{14} \xrightarrow{-\omega_3} \rho_{34} \xrightarrow{\omega_3} \rho_{14}^{(2)}$ which is the adhesion of two sub-chains of the dressing fields $\rho_{14}^{(2)} \xrightarrow{\omega_2} \rho_{24} \xrightarrow{-\omega_2} \rho_{14}$ and $\rho_{14} \xrightarrow{-\omega_3} \rho_{34} \xrightarrow{\omega_3} \rho_{14}^{(2)}$. Here, the subscript "1" of "$\rho_{14}^{(2)}$" is replaced by $G_2G_3\pm$. By virtue of the sub-chain D4, we take coupling equations: $\dot{\rho}_{14}^{(2)} = -d_{14}\rho_{14}^{(2)} + \mathrm{i}G_2^*\mathrm{e}^{-\mathrm{i}\boldsymbol{k}_2'\cdot\boldsymbol{r}}\rho_{24} + \mathrm{i}G_3\mathrm{e}^{\mathrm{i}\boldsymbol{k}_3\cdot\boldsymbol{r}}\rho_{34} - \mathrm{i}G_4^*\mathrm{e}^{\mathrm{i}\boldsymbol{k}_4\cdot\boldsymbol{r}}\rho_{10}^{(1)}, \dot{\rho}_{24}^{(r)} = -d_{24}\rho_{24} + \mathrm{i}G_2\mathrm{e}^{\mathrm{i}\boldsymbol{k}_2\cdot\boldsymbol{r}}\rho_{14}^{(2)}, \dot{\rho}_{34} = -d_{34}\rho_{34} + \mathrm{i}G_3^*\mathrm{e}^{\mathrm{i}\boldsymbol{k}_3\cdot\boldsymbol{r}}\rho_{14}^{(2)}$.

Under the dipole moment approximation, we have

$$\rho_{(G2G3\pm)4}^{(2)} = \frac{-\mathrm{i}G_4^*\mathrm{e}^{\mathrm{i}\boldsymbol{k}_4\cdot\boldsymbol{r}}}{d_{14} + |G_2|^2/d_{24} + |G_3|^2/d_{34}}\rho_{10}^{(1)}. \tag{4.23}$$

Here, term d_{14} is modified by G_2 and G_3 terms sequentially. From the expression we can see that these two dressing terms can interact, but not firm as the nested scheme.

Here, we have known that the interaction between two dressing fields of the nested dressing scheme is strongest while the parallel dressing scheme is weakest and the sequential dressing scheme intermediate between them [36].

Based on the discussion above, let us talk about the five-dressing scheme in FWM process which can be viewed as the multiplication of two dressing term and three dressing term. When the dressing fields E_2, E_3 and E_4 are all turned on and strong enough, they dress the FWM process simultaneously and the created multi-dark states are interacting with each other.

Actually, it is denoted as the five-dressing FWM the chain (F4) $\rho_{00}^{(0)} \xrightarrow{\omega_1} \rho_A^{(1)} \xrightarrow{\omega_2} \rho_{20}^{(2)} \xrightarrow{-\omega_2} \rho_{G3\pm G4\pm}^{(3)}$, where $\rho_A^{(1)}$ represents the dressed sub-chain (D5) $\rho_{10}^{(1)} \xrightarrow{-\omega_4} \rho_{(G2G3\pm)4} \xrightarrow{\omega_4} \rho_{10}^{(1)}$. In D5, the sub-chain D4 (represented by $\rho_{(G2G3\pm)4}$) shows the sequential scheme, and then it is nested between sub-chains "$\rho_{10}^{(1)} \xrightarrow{-\omega_4} \rho_{14}$" and "$\rho_{14} \xrightarrow{\omega_4} \rho_{10}^{(1)}$". In addition, $\rho_A^{(1)}$ and $\rho_{G3\pm G4\pm}^{(3)}$ lie parallelly in the chain F4. We have kwon the expressions of $\rho_{G3\pm G4\pm}^{(3)}$ and $\rho_{(G2G3\pm)4}$, according to the sub-chain D5, we can obtain

$$\rho_A^{(1)} = \frac{\mathrm{i}G_1 \mathrm{e}^{\mathrm{i}\boldsymbol{k}_1\cdot\boldsymbol{r}}}{d_{10} + \dfrac{|G_4|^2}{d_{14} + |G_2|^2/d_{24} + |G_3|^2/d_{34}}} \rho_{00}^{(0)}. \tag{4.24}$$

So the "ω_1" single-photon term d_{10} is modified directly by G_4 term, while G_2 and G_3 terms synchronously modify the "$\omega_1 + \omega_4$" two-photon term d_{14}. The outer dressing terms of the nested dressing scheme in Eq. (4.24) is a sequential combination of G_2 and G_3 dressing term. Three dressing fields E_2, E_3, and E_4 in this combining form can induce second or triple AT splitting in spectra numerical simulation.

The density matrix elements for the five-dressing FWM, based on the discussion above, can be written as

$$\rho_{F1}''' = \rho_{10}^{(3)} = \frac{-\mathrm{i}G_A \mathrm{e}^{\mathrm{i}\boldsymbol{k}_f\cdot\boldsymbol{r}}}{d_{20}} \frac{1}{d_{10} + \dfrac{|G_3|^2}{d_{30} + |G_4|^2/d_{43}}} \times \frac{1}{d_{10} + \dfrac{|G_4|^2}{d_{41} + |G_2|^2/d_{42} + |G_3|^2/d_{43}}}. \tag{4.25}$$

Apparently, nested, parallel and sequential dressing schemes coexist in this five-dressing FWM process. Since the spectra of parallel dressing scheme can be considered as a superposition of two groups of the different peaks, we separately investigate the two dressing terms: $\rho_{A1} = 1/[d_{10} + |G_3|^2/(d_{30} + |G_4|^2/d_{43})]$ (two dressing fields term) and $\rho_{A2} = 1/[d_{10} + |G_4|^2/(d_{41} + |G_2|^2/d_{42} + |G_3|^2/d_{43})]$ (three dressing fields term). After then, ρ_{F1}''', which is proportional to the multiplication of ρ_{A1} and ρ_{A2} terms, is investigated. More interesting, in the weak fields limit ($|G_3|^2 \ll \Gamma_{14}\Gamma_{34}$, $|G_4|^2 \ll \Gamma_{10}\Gamma_{14}$ and $|G_2|^2 \ll \Gamma_{14}\Gamma_{24}$), ρ_{F1}''' can be expanded as

$$\rho_{10}^{(3)} = -\mathrm{i}G_A \left(1 - \frac{|G_4|^2}{d_{10}d_{14}} + \frac{|G_2|^2|G_4|^2}{d_{10}d_{14}^2 d_{24}} + \frac{|G_3|^2|G_4|^2}{d_{10}d_{14}^2 d_{34}}\right) \rho_{A2}/(d_{10}d_{20}). \tag{4.26}$$

We can see that the density matrix element representing the five-dressing FWM is the summation of one FWM (first term), one SWM (second term) and two EWM (third and fourth terms). Hence, under the weak-dressing field condition, the polarization state of generating five-dressing FWM can be viewed as the coherent superposition state of these states generating FWM, SWM and EWM. The relative FWM signal intensity is given by $I_F \propto |\rho'''_{F1}|^2$

There also exists four-dressing SWM in the five-level system, as shown in Fig. 4.13 (a). when E_3 is blocked, by means of the SWM perturbation the chain (S) $\rho_{00}^{(0)} \xrightarrow{\omega_1} \rho_{10}^{(1)} \xrightarrow{-\omega_4} \rho_{14}^{(2)} \xrightarrow{\omega_4} \rho_{10}^{(3)} \xrightarrow{\omega_2} \rho_{20}^{(4)} \xrightarrow{-\omega_2} \rho_{10}^{(5)}$, we can obtain the expression of pure SWM without any dressing field:

$$\rho_S = \rho_{10}^{(5)} = \mathrm{i}G_B \mathrm{e}^{\mathrm{i}\boldsymbol{k}_s \cdot \boldsymbol{r}} / d_{10}^3 d_{20} d_{14}, \tag{4.27}$$

where $G_B = G_A G_4 G_4^*$. When the strong dressing fields E_2, E_3, and E_4 dress the levels $|1\rangle$ and $|0\rangle$, they affect the atomic coherence $\rho_{10}^{(3)}$ in the form of sub-chain (D6) $\rho_{10}^{(3)} \xrightarrow{-\omega_3} \rho_{30} \xrightarrow{\omega_4} \rho_{34} \xrightarrow{\omega_3} \rho_{G2\pm4} \xrightarrow{-\omega_3} \rho_{34} \xrightarrow{-\omega_4} \rho_{30} \xrightarrow{\omega_3} \rho_{10}^{(3)}$. In D6, $\rho_{G2\pm4}$ induced by the dressing field E_2 is nested in $\rho_{34} \xrightarrow{\omega_3} \rho_{G2\pm4} \xrightarrow{-\omega_3} \rho_{34}$ induced by the dressing field E_3, which are then nested into "$\rho_{30} \xrightarrow{\omega_4} \rho_{34}$" and "$\rho_{34} \xrightarrow{-\omega_4} \rho_{30}$", and all are finally nested into "$\rho_{10}^{(3)} \xrightarrow{-\omega_3} \rho_{30}$" and "$\rho_{30} \xrightarrow{\omega_3} \rho_{10}^{(3)}$". Thus we can obtain

$$\rho''_S = \rho_{10}^{(5)} = \frac{\mathrm{i}G_B \mathrm{e}^{\mathrm{i}\boldsymbol{k}_S \cdot \boldsymbol{r}}}{d_{10}^2 d_{20} d_{14}} \frac{1}{d_{10} + \dfrac{|G_3|^2}{d_{30} + \dfrac{|G_4|^2}{d_{34} + \dfrac{|G_3|^2}{d_{14} + |G_2|^2 / d_{24}}}}}. \tag{4.28}$$

Here, term d_{10} which represents ω_1 single-photon process is dressed directly by the inner dressing field E_3 which involves in a two-photon term d_{30}, and then it is modified by the first outer dressing field E_4 which shows that two dressing fields entangle with each other in such a nested scheme. Again, the second outer dressing field E_3 affects the $|G_4|^2$ term, and finally $|G_3|^2$ term is modified by the third outer dressing field E_2. Hence, the chain D6 and the expression ρ''_S show that four-dressing fields are entangled with each other in such a quadruple nested scheme. The inner dressing field E_3 controls the SWM signal directly, while three outer dressing fields E_4, E_3 and E_2 affect the SWM signal indirectly. In the weak dressing fields limit ($|G_3|^2 << \Gamma_{10}\Gamma_{30}$), ρ''_S can be expanded to $\rho''_S = \rho_{10}^{\prime(5)} + \rho_{10}^{(7)}$, where $\rho_{10}^{\prime(5)} = \mathrm{i}\mathrm{e}^{\mathrm{i}\boldsymbol{k}_s \cdot \boldsymbol{r}} G_B / (d_{10}^2 d_{20} d_{14} B_1)$, $\rho_{10}^{(7)} = -\mathrm{i}\mathrm{e}^{\mathrm{i}\boldsymbol{k}_e \cdot \boldsymbol{r}} G_B |G_3|^2 / (d_{10}^4 d_{20} d_{14} B_1)$ and $B_1 = d_{30} + |G_4|^2 / \{d_{34} + [|G_3|^2 / (d_{14} + |G_2|^2 / d_{24})]\}$. Under the weak field condition, the four-dressing SWM can be considered as a coherent superposition

of the signals from one SWM process and one triple nested EWM process, in other words, the four-dressing SWM is actual the interference between the polarizations $\rho_{10}^{\prime(5)}$ and $\rho_{10}^{(7)}$. The relative SWM signal intensity is given by $I_S \propto |\rho_S''|^2$.

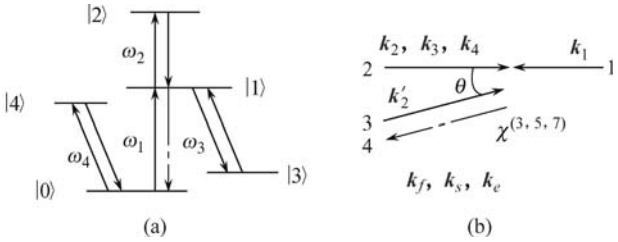

Fig. 4.13. (a) The energy-level diagram of a five-level system for EWM. (b) phase-conjugation geometry.

Therefore, the four-dressing SWM is a quadruply nested dressing scheme which can induce quadruple AT splitting. To clearly analyze the spectra of the four-dressing SWM, we plot the figures by adding dressing field into pure SWM expression step by step.

The four-dressing EWM process coexists with multi-dressed FWM and SWM processes in the five-level system. When all five laser beams are turned on simultaneously, as shown in Fig. 4.13 (b), the EWM signal generating, which is denoted as the EWM perturbation the chain E1, and the pure EWM expression is

$$\rho_{E1} = \rho_{10}^{(7)} = -\mathrm{i}G_C \mathrm{e}^{\mathrm{i}\boldsymbol{k}_e \cdot \boldsymbol{r}} / d_{10}^4 d_{20} d_{30} d_{14}. \tag{4.29}$$

where $G_C = G_B G_3 G_3^*$. With strong dressing fields E_4, E_2, and $E_3, \rho_{10}^{(1)}$ and $\rho_{10}^{(3)}$ in the chain E1 can be modified as $\rho_{G2\pm G4\pm}^{(1)}$ and $\rho_{G3\pm G4\pm}^{(3)}$, respectively, where $\rho_{G2\pm G4\pm}^{(1)}$ can be extended into the sub-chain of the nested scheme (D7) $\rho_{10}^{(1)} \xrightarrow{\omega_2} \rho_{20} \xrightarrow{\omega_4} \rho_{24} \xrightarrow{-\omega_4} \rho_{20} \xrightarrow{-\omega_2} \rho_{10}^{(1)}$. As a result, the four-dressing EWM the chain can be written as (E2) $\rho_{00}^{(0)} \xrightarrow{\omega_1} \rho_{G2\pm G4\pm}^{(1)} \xrightarrow{-\omega_4} \rho_{14}^{(2)} \xrightarrow{\omega_4} \rho_{G3\pm G4\pm}^{(3)} \xrightarrow{\omega_2} \rho_{20}^{(4)} \xrightarrow{-\omega_2} \rho_{10}^{(5)} \xrightarrow{-\omega_3} \rho_{30}^{(6)} \xrightarrow{\omega_3} \rho_{10}^{(7)}$. According to the sub-chains D3, D7, and E2, we can easily obtain the four-dressing EWM expression

$$\rho_{E1}' = \rho_{10}^{(7)} = \frac{-\mathrm{i}\exp(\mathrm{i}\boldsymbol{k}_e \cdot \boldsymbol{r}) G_C}{d_{10} d_{20} d_{30} d_{41}} \frac{1}{d_{10} + \dfrac{|G_2|^2}{d_{20} + |G_4|^2 / d_{24}}} \times \frac{1}{d_{10} + \dfrac{|G_3|^2}{d_{30} + |G_4|^2 / d_{34}}}. \tag{4.30}$$

Two multiplying terms of Eq. (4.30) both contain nested dressing schemes (E_2 and E_4, E_3, and E_4). It means, the dressing effect occurs in two different

transitions process and therefore they are independent with each other and to each dressing part, there are a nested dressing terms: inner dressing field G_2 or G_3 act on the state of EWM transitions while outer dressing filed G_4, act on the states of their transition, respectively. In all, the understanding of these two basic dual-dressing scheme will enable us easily analyze this complicated expression. The relative EWM signal intensity is given by $I_E \propto |\rho_{E3}|^2$.

The EIT displayed in the probe field absorption spectrum is a single-photon transition process which is dressed by the fields G_2, E_3, and E_4. Under the weak probe field approximation, the density matrix for probe filed absorption ρ_{10} is

$$\rho_{10} = \frac{\mathrm{i}G_1}{d_{10} + \dfrac{|G_2|^2}{d_{20} + |G_4|^2/d_{24}} + \dfrac{|G_3|^2}{d_{30} + |G_4|^2/d_{34}}}. \tag{4.31}$$

Equation (4.31) gives the four-dressing EIT case, which shows the sequential combination of two nested schemes (E_2 and E_4, E_3, and E_4). Two sequentially dressing field act on the state $|1\rangle$ together and then they are both but respectively dressed by field G_4. Three dressing fields (E_2, E_3, and E_4) can induce two triple EIT splitting. By changing the offsets and intensities of the dressing fields, we can obtain the different multi-EIT spectra.

When five laser beams are turned on, the five-dressing FWM, four-dressing SWM, four-dressing EWM, and four-dressing EIT as discussed above can exist simultaneously in the five-level system. Such FWM, SWM, and EWM signal beams are in the same direction for the reason of equivalent phase-matching conditions ($\boldsymbol{k}_\mathrm{f}, \boldsymbol{k}_\mathrm{s}$, and $\boldsymbol{k}_\mathrm{e}$). By controlling the offsets and intensities of dressing fields, the coexisting MWMs fall into different EIT windows which can be clearly separated and distinguished.

4.4.2 Numerical Results

Coexisting FWM and SWM processes have been observed in the Cd(S, Se) semiconductor doped glasses [23]. The advantages of solids include high density of atoms, compactness, and absence of atomic diffusion, except relatively broad optical linewidths and fast decoherence rate. However, there is a narrow linewidth in an atomic vapor. In addition, FWM and SWM processes can coexist in the inverted-Y atomic sub-system [$|0\rangle = |5S_{1/2}\rangle(F = 2), |1\rangle = |5P_{3/2}\rangle, |2\rangle = |5D_{3/2}\rangle, |3\rangle = |5S_{1/2}\rangle$, as shown in Fig. 4.13 (a)], there exists a ladder-type EIT window with a linewidth of 50 MHz in transmission Doppler broadening profile (about 500 MHz) [37]. In this paper, we add an additional beam E_4 (connecting transition $|4\rangle = |5P_{1/2}\rangle$ ($F = 3$) to $|0\rangle = |5S_{1/2}\rangle$) into such inverted-Y system, as shown in Fig. 4.13 (a), where the transverse relaxation rate Γ_{ij} between states $|i\rangle$ and $|j\rangle$ is given by $\Gamma_{ij} = (\Gamma_i + \Gamma_j)/2(\Gamma_0 = \gamma_{30} = 0.1$ MHz, $\Gamma_1 = \gamma_{10} + \gamma_{13} = 5.9$ MHz,

$\Gamma_2 = \gamma_{21} + \gamma_{24} = 1.77$ MHz, $\Gamma_3 = \gamma_{30} = 0.1$ MHz and $\Gamma_4 = \gamma_{40} + \gamma_{43} = 5.4$ MHz, where γ_{ij} describes decay rates of coherences between $|i\rangle$ and $|j\rangle$. In Fig. 4.13 (b), nonlinear susceptibility $\chi^{(3)}$ for FWM signal, $\chi^{(5)}$ for SWM signal and $\chi^{(7)}$ for EWM signal in this five-level system interact with up to five laser fields, and we assume that the intensity of probe field G_1 is small while G_2, G_2', G_3, and G_4 can be arbitrary magnitudes.

We have simply discussed multi-dressing schemes and the interaction of dressing fields in the coexisting multi-dressed MWM by their calculated expressions. In this section, we will investigate the normalized MWM spectra based on the above analytic expressions.

For simplicity, Fig. 4.14 presents the suppression of the SWM signal intensity. In Fig. 4.14, the parallel-cascade ρ''_{F1} DDFWM signal intensity without dressing field ($G_3 = G_4 = 0$) is normalized to 1. Hence, the solid curve above or below "1" means enhancement or suppression of the DDFWM signal intensity, respectively. Though the suppression of the DDFWM signal intensity is collectively induced by two coupling fields, the effect of field G_3 is independent of that of field G_4. On the exact resonance condition, the splitting of level is induced by the strong coupling field G_3, which results in the off-resonance of FWM. Furthermore, the DDFWM signal intensity is reduced within the whole range of Δ_4 (with a shifted constant background). When satisfying resonance ($\Delta_4 = 0$), signal intensity is suppressed again by the coupling field G_4. We can apprehend this further in Fig. 4.14.

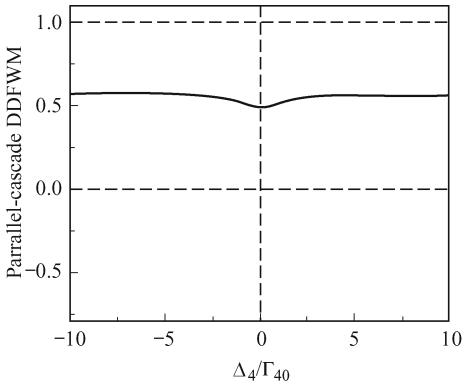

Fig. 4.14. $|\rho''_{F1}|^2$ (solid) and $|\mathrm{Im}\ (\rho''_{F1})|^2$(dash), $|\mathrm{Im}\ (\rho_{S1})|^2$ (dot) versus Δ_4/Γ_{10} when $\Delta_1/\Gamma_{10} = \Delta_2/\Gamma_{10} = \Delta_3/\Gamma_{10} = 0, G_3/\Gamma_{10} = 0.5$, $G_4/\Gamma_{10} = 0.5$. The FWM signal intensity with no coupling field is normalized to 1.

Then the spectra of five-dressing FWM ($|\rho'''_{F1}|^2$) are investigated by plotting and analyzing its two portions ($|\rho_{A1}|^2$ and $|\rho_{A2}|^2$), respectively. The characteristics of spectra of the AT splitting, suppression and enhancement of the FWM signal are generally equivalent to the superposition of the two portions. This method is just a proof of concept theory, and will help us well understand the effects of each dressing terms and their interactions.

At first, let us consider the spectrum of $|\rho_{A2}|^2$ versus Δ_1, as Fig. 4.15 (a–d) shows, in which primary, secondary and triple AT splitting corresponding to the dressed states in Fig. 4.15 (e1–e3) are presented, respectively. We approach the final spectrum by adding the dressing fields one by one. The first step, as Fig. 4.15 (a) shows, the inner dressing field E_4 dressed and splits single-photon resonant peak of the pure FWM into two peaks located at $\Delta_1 = \pm\Delta_{G4}/2 \approx \pm G_4 = \pm 100$ MHz, where Δ_{G4} is the separation between two AT splitting peaks. It is the primary AT splitting corresponding to, in the dressed-states picture, primary dressed states $|G_4\pm\rangle$ [Fig. 4.15 (e1)] generated by E_4 dressing the ground level $|0\rangle$, which corresponds to the left and right peaks in Fig. 4.15 (a), respectively. The second step, by setting a proper offset, the outer dressing field E_2 can exactly hit on one of the primary dressed state, for example $\Delta_2 = 100$ MHz, and create the secondary dressed states $|G_4 + \pm\rangle$ [Fig. 4.15 (e2)]. Reflecting on the spectra, the left peak in Fig. 4.15 (a) splits into two peaks, and then three peaks locate at $\Delta_1 = -\Delta_{G4}/2 \mp \Delta_{G2}/2 = -140$ MHz and -60 MHz, and $\Delta_1 = \Delta_{G4}/2 = 100$ MHz (where$\Delta_{G2}$is the separation induced by E_2) will appear in Fig. 4.15 (b). It is the so-called secondary splitting. The third step, the other outer dressing field E_3 is tuned close to $\Delta_3 = -140$ MHz and then the triply dressed states $|G_4 + +\pm\rangle$ are generated around the secondarily dressed states $|G_4 + +\rangle$ [Fig. 4.15 (e3)]. And in the spectra, the left peak of the secondary peaks will be split into two peaks, as Fig. 4.15 (c) shows. Finally, four peaks which illustrate the triple dressing effect appears in Fig. 4.15 (c), which is located at $\Delta_1 = -\Delta_{G4}/2 - \Delta_{G2}/2 \mp \Delta_{G3}/2 = -160$ MHz and -120 MHz, $\Delta_1 = -\Delta_{G4}/2 + \Delta_{G2}/2 = -60$ MHz and $\Delta_1 = \Delta_{G4}/2 = 100$ MHz, respectively.

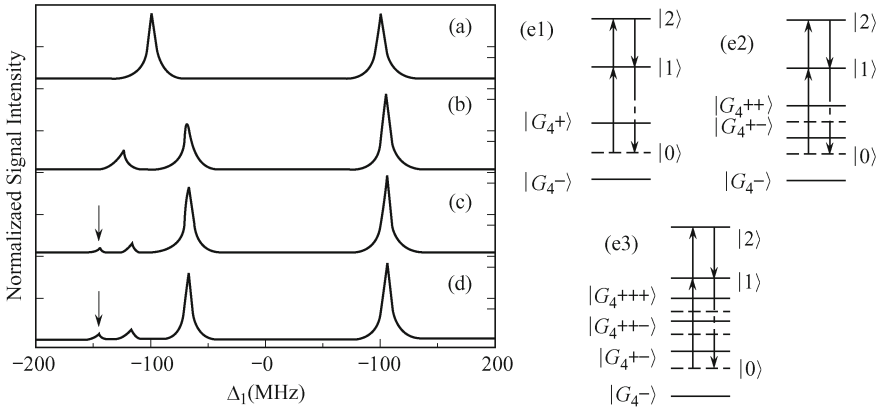

Fig. 4.15. $|\rho_{A2}|^2$ in $|\rho'''_{F1}|^2$ spectra versus Δ_1 for $G_4 = 100$ MHz and $\Delta_4 = 0$ MHz, when (a) $G_2 = G_3 = 0$ MHz, (b) $G_2 = 40$ MHz, $\Delta_2 = 100$ MHz, $G_3 = 0$ MHz, (c) $G_2 = 40$ MHz, $\Delta_2 = 100$ MHz, $G_3 = 20$ MHz and $\Delta_3 = -140$ MHz, (d) $G_3 = 40$ MHz, $\Delta_3 = -100$ MHz, $G_2 = 20$ MHz, $\Delta_2 = 140$ MHz. The maximum of the intensity is normalized to be 1. (e1–e3) the dressed-state pictures.

Similarly, the dressed state $|G_4-\rangle$ can also be secondary dressed by outer

dressing field E_3 (by setting $\Delta_3 \approx -100$ MHz) and the secondary dressed states $|G_4 - \pm\rangle$ is created. Furthermore, the other outer dressing field E_2 ($\Delta_2 = 140$ MHz) creates the triple AT splitting, as shown in Fig. 4.15 (d). The triple AT splitting spectra in Fig. 4.15 (c) and Fig. 4.15 (d) are identical, which prove that the outer dressing fields E_2 and E_3 are interchangeable for the reason of their equivalent status in expression. Three dressing term ($|\rho_{A2}|^2$) can obtain the secondary or triple AT splitting by changing the offsets of the dressing fields (E_2 and E_3) and the results show that the AT splitting of sequential dressing scheme is similar to one of the nested dressing scheme.

On the other hand, the spectra of expression $|\rho_{A2}|^2$ in $|\rho'''_{F1}|^2$ can also present two secondary-dressed AT splitting. As Fig. 4.16 (a) shows, two peaks induced by the inner dressing field E_4 corresponding to $|G_4\pm\rangle$ splits are split again by two outer dressing fields E_2 and E_3 ($\Delta_2 = \Delta_3 = G_4 = 50$ MHz) into two pairs secondary dressed AT splitting peaks [secondary splits $|G_4 + \pm\rangle$ and $|G_4 - \pm\rangle$ as is shown in Fig. 4.16 (d)]. In addition, Fig. 4.16(b) shows two peaks induced by $|\rho_{A1}|^2$ in $|\rho'''_{F1}|^2$.

So, we can see that the five-dressing FWM ($|\rho'''_{F1}|^2$) spectra [Fig. 4.16 (c)] is the superposition of the spectra of Fig. 4.16 (a) and Fig. 4.16 (b). $|\rho'''_{F1}|^2$ is proportional to the multiplication of $|\rho_{A1}|^2$ and $|\rho_{A2}|^2$, and so its spectra of AT splitting caused by five dressing field is the superposition of these two portions ($|\rho_{A1}|^2$ and $|\rho_{A2}|^2$).

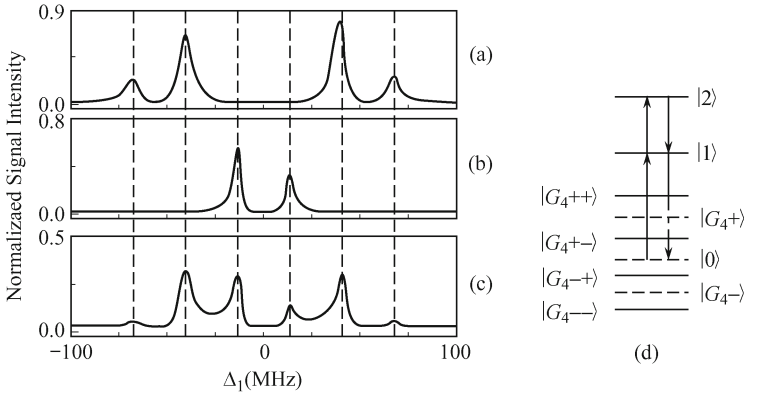

Fig. 4.16. The five-dressing FWM signal intensity versus Δ_1 (a) for $|\rho_{A2}|^2$ in $|\rho'''_{F1}|^2$, (b) $|\rho_{A1}|^2$ in $|\rho'''_{F1}|^2$, (c) for Five-dressing FWM with $G_2 = G_3 = 20$ MHz, $G_4 = 50$ MHz, $\Delta_2 = \Delta_3 = 50$ MHz, $\Delta_4 = 0$. (d) the dressed-state pictures.

Next let us investigate the spectra of the suppression and enhancement of the five-dressing FWM signal. Firstly $|\rho_{A2}|^2$ intensity versus Δ_4 is discussed. Here, the dressed FWM signal intensity is normalized by rating pure FWM which is no dressing fields. The intensity above or below "1" means enhancement or suppression of the FWM signal, respectively. We employ the same

method as above to clear understand the detailed process of the five-dressing FWM. Firstly, the inner dressing field E_4 drives the transition from $|4\rangle$ to $|0\rangle$ and creates the dressed states $|G_4\pm\rangle$, which leads to single-photon transition $|0\rangle \rightarrow |1\rangle$ off-resonance [Fig. 4.17 (b1)]. So, at exact single-photon resonance $\Delta_1 = 0$, the FWM signal intensity is greatly suppressed when scanning the dressing field E_4 across the resonance ($\Delta_4 = 0$), as Fig. 4.17 (a1) shows, one suppressed dip at the line center. Secondly, the outer dressing field E_2 is added and under the condition of $\Delta_1+\Delta_2-\Delta_4 = 0$, the single suppressed dip is split into two small suppressed dips, i.e., $G_2 = 50$ MHz, as Fig. 4.17 (a2) shows. Further calculation give that it has $\Delta_{G2} \approx 2G_2$, under the condition of $G_2 >> \Gamma_{10}$. It means that the outer dressing field E_2 dresses the state $|4\rangle$ to create two new state $|G_2\pm\rangle$ [Fig. 4.17 (b2)], then the inner dressing field E_4 suppresses the resonant FWM signal directly from $|G_2\pm\rangle$. Thirdly, when the other outer dressing field E_3 is tuned close to $\Delta_3 = \Delta_1 - \Delta_{G2}/2$, e.g., $\Delta_3 = -50$ MHz, the left suppressed dip splits into two suppressed dips [Fig. 4.17 (a3)] due to the secondary dressed state $|G_2 + \pm\rangle$ created by G_3. Therefore, a plot reflected the outer dressing fields E_2 and E_3 comprehensive dressing effect are given in Fig. 4.17 (b3). However, it is not the unique manner. Figure 4.17 (a4) shows another: two outer dressing fields E_2 and E_3 ($\Delta_2 = \Delta_3 = 0$ MHz) separate synchronously the suppressed dip in Fig. 4.17 (a1) into two suppressed dips at $\Delta_4 = \Delta_1 \pm \Delta_{G2,G3}/2 = \pm 70$ MHz. Under the condition of $\sqrt{G_2^2 + G_3^2} >> \Gamma_{10}$, it has $\Delta_{G2,G3} \approx 2\sqrt{G_2^2 + G_3^2}$, where

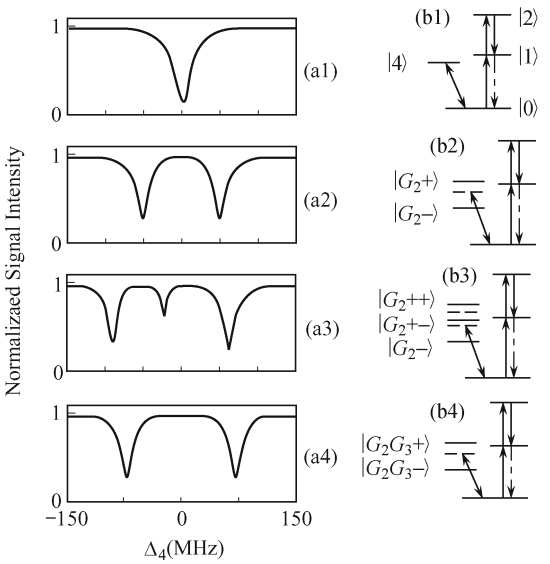

Fig. 4.17. $|\rho_{A2}|^2$ spectra versus Δ_4 for $\Delta_1 = 0$, $G_4 = 5$ MHz, (a1) G_2=G_3= 0; (a2) $G_2 = 50$ MHz, $\Delta_2 = 0$, $G_3 = 0$; (a3) $G_2 = 50$ MHz, $\Delta_2 = 0$,$\Delta_3 = 50$ MHz and $G_3 = 50$ MHz, (a4) $\Delta_2 = \Delta_3 = 0$, $G_2 = G_3 = 50$ MHz. (b1 – b4) the corresponding dressed-state pictures.

$\Delta_{G2,G3}$ is the separation between the dressed states $|G_2G_3\pm\rangle$ induced by two dressing fields together [Fig. 4.17 (b4)]. Hence, the inner dressing field (E_4) suppresses FWM directly, while the outer dressing fields (E_2 and E_3) affect on the dressed states and influence FWM indirectly.

Next, let us discuss $|\rho_{A2}|^2$ versus Δ_2 with $G_3 = 0$. Here the FWM signal intensity is also normalized for observing its suppression and enhancement. As Fig. 4.18 (a) shows, a suppressed dip of which the height increases as G_2 increasing appears. In fact, it induced by the outer dressing field E_2 which can largely weaken the suppression effect of the inner dressing field E_4 on FWM signal, as is shown in Fig. 4.18 (b). Furthermore, we plot $|\rho_{A2}|^2$ versus Δ_2 and Δ_3 in Fig. 4.18 (c) and the results show that suppression of the sequential dressing scheme is like the one of parallel dressing scheme [36]. Specially, two independent suppressed peaks exist at $\Delta_2 = \Delta_3 = 0$, which means that these

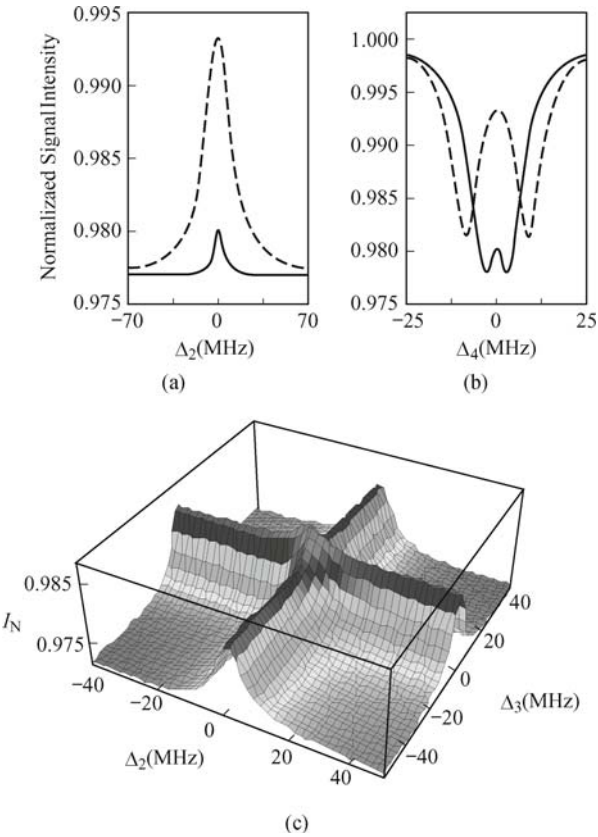

Fig. 4.18. $|\rho_{A2}|^2$ spectra (a) versus Δ_2 for $\Delta_4 = 0$ and (b) versus Δ_4 for $\Delta_2 = 0$ with $G_2 = 2$ MHz (solid curve), $G_2 = 8$ MHz (dashed curve), $G_3 = 0$, $G_4 = 0.5$ MHz, and $\Delta_1 = \Delta_3 = 0$; (c) $|\rho_{A2}|^2$ spectrum versus Δ_2 and Δ_3 for $\Delta_1 = \Delta_4 = 0$, $G_2 = G_3 = 2$ MHz, and $G_4 = 0.5$ MHz. The signal intensity with no dressing fields is normalized to be 1. Adopted from Ref. [41].

two outer dressing fields (E_2 and E_3) are indeed interchangeable.

Next we investigate the spectra of the suppression and enhancement of the five-dressing FWM signal ($|\rho'''_{F1}|^2$) based on the analysis about $|\rho_{A2}|^2$ (e.g., Fig. 4.17). Figure. 4.19 shows the spectra of the suppression and enhancement of the five-dressing FWM signal ($|\rho'''_{F1}|^2$) versus Δ_4 and Δ_3. Under the resonance condition ($\Delta_1 = 0$), three dressing fields only can suppress the FWM signal in Fig. 4.19 (a). Figures 4.20 (a), (b) is the cross sections of Fig. 4.19 (a) versus Δ_4 and Δ_3, respectively. For Fig. 4.20 (a), when the outer dressing field is off-resonance ($\Delta_3 = 200$ MHz), one small enhanced suppression dip at $\Delta_4 = 200$ MHz via the "$\omega_3 + \omega_4$" two-photon resonance [see the inset plot in Fig. 4.20 (a)] and two big suppressed dips induced by the dressing fields E_4 and E_2 of the nested scheme in $|\rho_{A2}|^2$ appears simultaneously. Specially, when $\Delta_3 = 50$ MHz, Fig. 4.20 (b) shows three suppressed dips which are caused by the same inducement as in Fig. 4.16 (b3). Finally, when $\Delta_3 = 0$, $|\rho_{A1}|^2$ in $|\rho'''_{F1}|^2$ dominates in the FWM signal and the outer dressing field E_4 in $|\rho_{A1}|^2$ creates a suppressed peak at $\Delta_4 = 0$ [Fig. 4.20 (c)]. Figure 4.20 (d) shows the five-dressing FWM spectra versus Δ_3. Two suppressed dips are induced by the dressing fields E_3 and E_4 in terms of nested scheme [see the left insert plot of Figure 4.20 (d)] in which shows the $|\rho_{A1}|^2$ in $|\rho'''_{F1}|^2$ as $\Delta_4 = 0$. When $\Delta_4 = 200$ MHz, the dressing field E_3 creates one suppressed dip near $\Delta_3 = 0$ and the dressing field E_4 creates a small enhanced suppression dip via the "$\omega_3 + \omega_4$" two-photon resonance at $\Delta_3 = 200$ MHz [the right inset plot in Fig. 4.20 (d)].

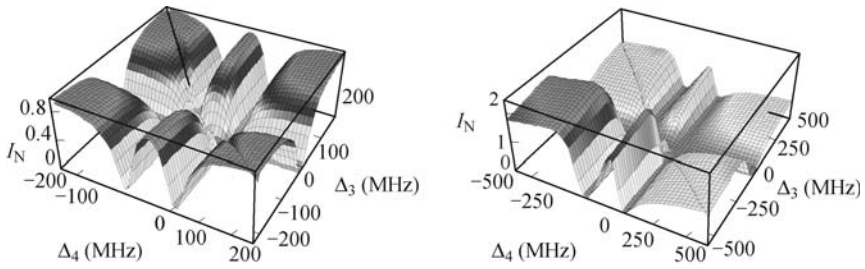

Fig. 4.19. The five-dressing FWM signal intensity versus the dressing field detunings Δ_4 and Δ_3 for (a) $\Delta_1 = \Delta_2 = 0, G_2 = 50$ MHz and $G_3 = G_4 = 10$ MHz, (b) $\Delta_1 = 2$ MHz, $\Delta_2 = 0$, $G_2 = 100$ MHz, and $G_3 = G_4 = 20$ MHz. The FWM signal intensity with no dressing fields is normalized to be 1.

Under the off-resonant condition ($\Delta_1 \neq 0$), three dressing fields can either suppress or enhance the FWM, as is shown in Fig. 4.19 (b). The enhancement effect is specially dramatic in the area of $\Delta_4 < 0$ and $\Delta_3 < 0$ because three dressing fields can reinforce their suppression and enhancement effect each other with the proper offsets.

Previous works [36] certify that the AT splitting of sequential dressing scheme is like the nested dressing scheme, while suppression and enhancement

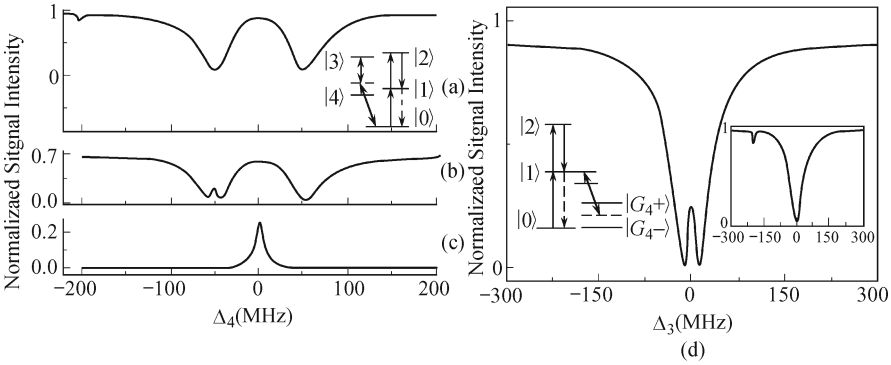

Fig. 4.20. The five-dressing FWM signal intensity versus Δ_4 for (a) $\Delta_3 = 200$ MHz. The inserted plot: the corresponding dressed-state picture; (b) $\Delta_3 = 50$ MHz; (c) $\Delta_3 = 0$. (d) The five-dressing FWM signal intensity versus Δ_3 for $\Delta_4 = 0$, the right insert plot $\Delta_4 = 200$ MHz.The left insert plot is the corresponding dressed-state picture. The FWM signal intensity with no dressing fields is normalized to be 1. The other parameters are $\Delta_1 = \Delta_2 = 0$, $G_2 = 50$ MHz, $G_3 = G_4 = 10$ MHz.

spectra of the sequential dressing scheme is like the one of parallel dressing scheme.

Therefore, in the AT splitting spectra of five-dressing FWM, three dressing fields (E_2, E_3 and E_4) entangle tightly with each other. It generally is equivalent to the superposition of the two portions ($|\rho_{A1}|^2$ and $|\rho_{A2}|^2$). For the suppression and enhancement in the nested dressing scheme, the inner dressing field suppresses FWM directly, while the outer dressing fields create the dressed states to influence FWM indirectly. Moreover, the suppression and enhancement spectra of the sequential dressing scheme are like the one of parallel dressing scheme.

The spectra of the quadruple nested dressed SWM signal are investigated in this section. Also, we plot the spectra of the AT splitting by adding dressing field into pure SWM expression one by one. At this stage this method is just a proof of concept theory.

Figure 4.21 presents the SWM signal intensity versus Δ_1 and the dressed-states picture for quadruple dressing. Firstly, as Fig. 4.21 (b) shows, the inner dressing field E_3 splits the energy level $|1\rangle$ into two primarily dressed states $|G_3\pm\rangle$ corresponding to two peaks from left to right in Fig. 4.21 (a1). Then, the outer dressing field E_4 (when $\Delta_4 = 200$ MHz,) splits state $|G_3-\rangle$ level into secondarily-dressed levels $|G_3 - \pm\rangle$ corresponding to two right peaks from left to right in Fig. 4.21 (a2). After that, the outer dressing fields E_3 splits secondary dressing state $|G_3 - +\rangle$ into triple dressed levels $|G_3-+\pm\rangle$ corresponding to the second and the third peaks from left to right in Fig. 4.21 (a3). At last, as the outer dressing field E_2 is tuning close to one of the triply dressed state $|G_3 - +-\rangle$ ($\Delta_2 = -90$ MHz), it dress to generate the separated quadruple dressed states $|G_3 - + - \pm\rangle$ correspond to the third

and fourth peaks in Fig. 4.21 (a4). Hence, the quadruple AT splitting spectra of the SWM signal is obtained, where three dressing fields (E_2, E_3, and E_4) interact tightly.

Next, we investigate the normalized SWM spectra versus the dressing field's offset Δ_4. Under the resonant condition $\Delta_1 = \Delta_3 = 0$, as Fig. 4.21 (c1) shows, a suppressed peak created by E_4 appears at the line center. The outer dressing field E_3, however, splits such suppressed peak into a pair of suppressed peaks, as is shown in Fig. 4.21 (c2). Under the condition $G_3 >> \Gamma_{30}, \Gamma_{43}$, we can obtain $\Delta_{G3} = 2G_3 = 100$ MHz, where Δ_{G3} is the separation induced by E_3. Finally, as is shown in Fig. 4.21 (c3), when the outer dressing field E_2 is tuned close to $\Delta_2 = \Delta_{G3}/2$, the right suppressed peak generated by E_3 split again into two new small suppressed peaks.

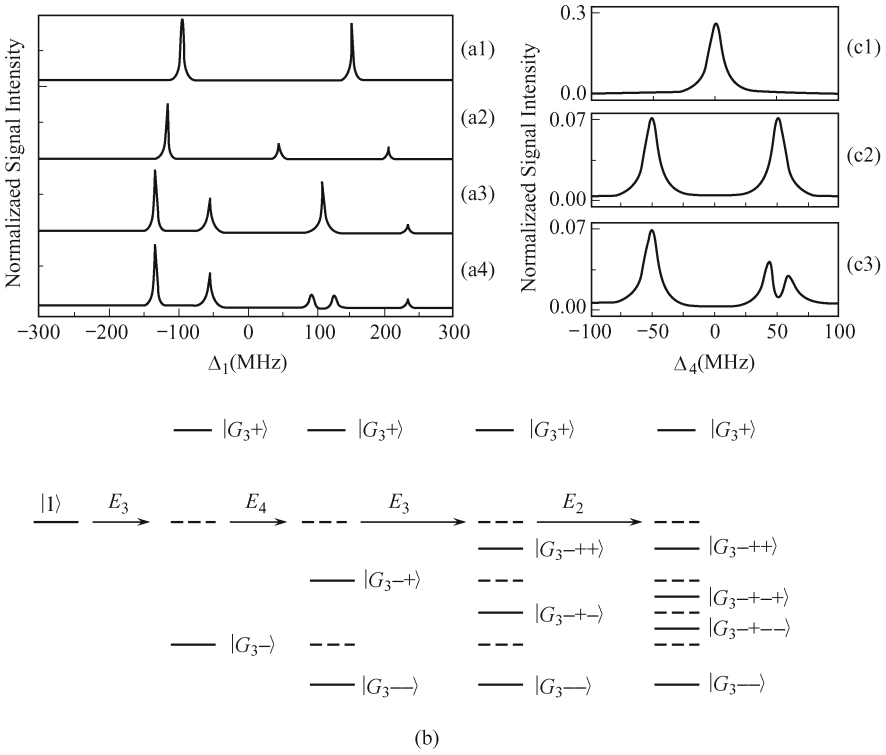

(b)

Fig. 4.21. The four-dressing SWM signal intensity versus Δ_1 for (a1) $G_3 = 120$ MHz, $G_4 = 0$, $\Delta_3 = 60$ MHz. (a2) $G_4 = 100$ MHz, $\Delta_4 = 20$ MHz, we assume $G_3 = 0$ under the outer dressing field E_4. (a3) $G_3 = 120$ MHz, $G_2 = 0$, (a4) $G_2 = 30$ MHz, $\Delta_2 = -90$ MHz. (b) The dressed states picture. The four-dressing SWM signal intensity versus the outer dressing field detuning Δ_4 for (c1) $G_3 = G_4 = 50$ MHz, $\Delta_1 = \Delta_3 = 0$, we assume $G_3 = 0$ below the outer dressing field E_4. (c2) $G_3 = G_4 = 50$ MHz, $\Delta_1 = \Delta_3 = 0, G_2 = 0$, (c3) $G_2 = 10$ MHz, $\Delta_2 = 50$ MHz. The SWM signal intensity with no dressing fields is normalized to be 1.

In this section, we focus on the spectra of AT splitting, suppression, and

enhancement of the four-dressing EWM signal.

To clearly understand the AT splitting spectra of the EWM signal, we consider the spectra of two dressing terms separately, as the method applied in analyzing FWM spectra. Figure 4.22 (a), (b) shows the spectra of the second and third multiplying terms of Eq. (4.30), respectively. Figure 4.22 (c) which is the superposition of the two portions (E_2, E_4 nested dressing term and E_3 and E_4 nested dressing term) show the spectra of AT splitting of the EWM signal. So, as to the spectra of the parallel dressing scheme, it can be viewed as the superposition of the two portions.

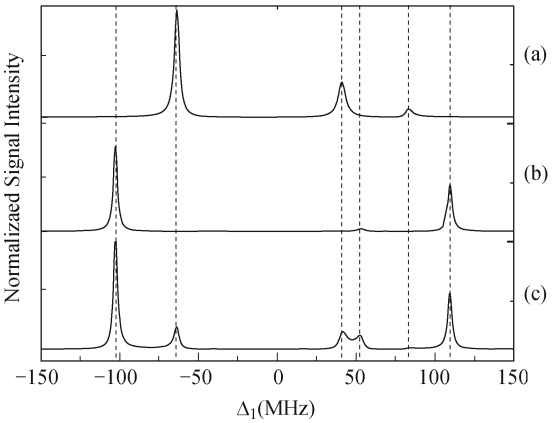

Fig. 4.22. The four-dressing EWM signal intensity versus Δ_1 for (a) the spectra of the second multiplying term of Eq. (4.30), (b) the spectra of the third multiplying term of Eq. (4.30), (c) Four-dressing EWM signal spectra. When $G_2 = 60$ MHz, $G_3 = 100$ MHz, $G_4 = 30$ MHz, $\Delta_2 = \Delta_3 = 0$, $\Delta_4 = 60$ MHz.

In addition, Fig. 4.23 (a) shows the symmetrical full-suppression spectrum of the resonant ($\Delta_1 = 0$) EWM versus Δ_2 and Δ_3. Two suppressed dips in the Δ_2 side are induced by the inner dressing field E_2 and the outer dressing field E_4, while dips in the Δ_3 side are induced by the inner dressing field E_3 and the outer dressing field E_4. Under the off-resonant condition ($\Delta_1 \neq 0$), any dressing fields can either suppress or enhance the EWM signal intensity. More interesting, when the dressing fields are strong enough and $|\Delta_1| >> 0$, a significant full-enhancement with an amplitude of about 100 can be obtained, as is shown in Fig. 4.23 (b). The reason is that the parallel combination nested dressing scheme multiply the enhanced effect. Further calculation based on the dressed-state theory gives the resonant enhanced peaks location which is at $\Delta_2 = -\Delta_1 + \Delta_{G2}/2 + \Delta_4 \pm \Delta_{G4}/2 \approx \pm 50$ MHz and $\Delta_3 = \Delta_1 - \Delta_{G3}/2 - \Delta_4 \pm \Delta_{G4}/2 \approx \pm 50$ MHz, respectively. It means that these dressing fields can enhance the EWM signal constructively with proper offsets. Therefore, whether the AT splitting, or the suppression and enhancement of the EWM signal are generally equivalent to the superposition of the two portions (E_2, E_4 nested dressing term and E_3 and E_4 nested dressing term). Moreover, as to the nest dressed structure, the inner dressing

fields (E_2 and E_3) suppress the EWM signal, while the outer dressing field (E_4) affects the EWM signal indirectly.

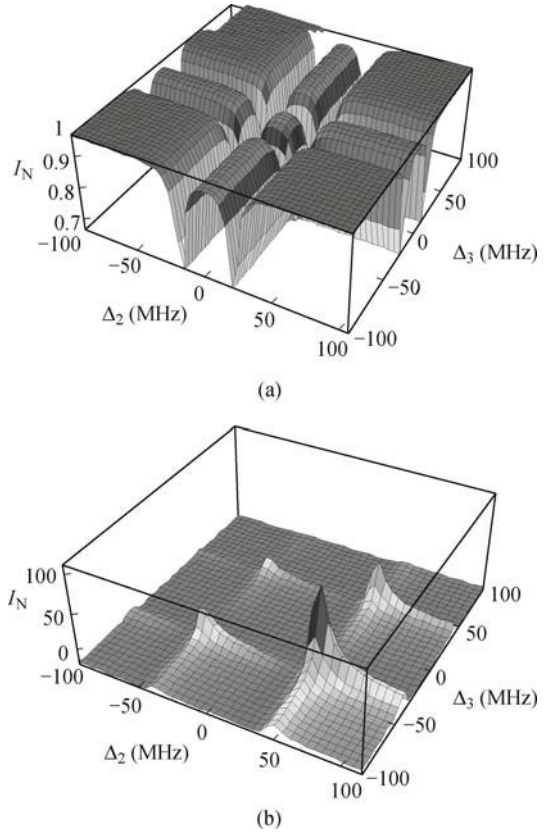

Fig. 4.23. The four-dressing EMW suppression and enhancement (a) $G_2 = G_3 = 2$ MHz, $G_4 = 20$ MHz, $\Delta_1 = \Delta_4 = 0$. (b) $G_2 = G_3 = 20$ MHz, $G_4 = 40$ MHz, $\Delta_1 = 15$ MHz. The EWM signal intensity with no dressing fields is normalized to be 1.

The four-dressing EIT windows induced by interacting dark states are used to transmit the coexisting FWM, SWM, and EWM signals. It is valuable to examine the coherence term ρ_{10} [Eq. (4.31)] in terms of its real and imaginary parts as a function of Δ_1 because the imaginary (real) part of ρ_{10} versus Δ_1 represents the probe absorption (dispersion) spectrum.

Also, we plot the spectra of EIT by adding dressing fields one by one. Firstly, Fig. 4.24 (a1) shows the spectra of the primary EIT splitting, which is induced by the dressing field E_2. Secondly, Fig. 4.24 (a2) presents the spectra of the secondary EIT splitting, which is induced by the dressing field E_3. Thirdly, Figs. 4.24 (a3) and 4.24 (a4) show the spectra of two triple EIT splitting, the former is induced by dressing field E_4 under E_2, and the latter is induced by dressing field E_4 under E_3. When all the dressing fields are

acted, we can obtain the probe absorption spectra as shown in Fig. 4.24 (a5) and corresponding dressed states picture is shown in Fig. 4.24 (b). Figure 4.24 (a5) shows two triple EIT splitting and totally gives four EIT windows.

As to the dispersion curve, as Fig. 4.24 (c1) – (c5) shows, the spectra of EIT dispersion [Re (ρ_{10})] with the same parameters in Fig. 4.24 (a1) – (a5). Figure 4.24 (c1) shows the typical EIT dispersion curve in the $|0\rangle - |1\rangle - |2\rangle$ subsystem and Fig. 4.24 (c2) represents the EIT dispersion in the four-level system with the inverted-Y configuration [42]. It displays a secondary EIT splitting. Figure 4.24 (c3) and 24 (c4), which show the dispersion spectra of triple EIT splitting, the most prominent change appears due to three EIT conditions. We can see that the absorption spectrum exhibits four absorptive peaks in Fig. 4.24 (a3) and (a4), while the corresponding dispersion profile exhibits three steep pure slopes, which should be useful for supporting slow light pulses with different frequencies. Figure 4.24 (c5) presents the dispersion spectra of two triple EIT splitting and exhibits four steep pure slopes.

Next, we discuss the EIT absorption and dispersion curves by changing the offsets of dressing fields. Firstly, as is shown in Fig. 4.25(a), as setting $\Delta_4 = 150$ MHz; the secondarily dressed absorptive peak [the right peak in Fig. 4.24 (a2)] is separated into two triple dressed peaks [the third and the forth peaks in Fig. 4.25 (a) from left to right] by one dressing field E_4, while the other dressing field E_4 [under G_3 in Eq. (4.30)] induces the three-photons absorption peak appearing at $\Delta_1 = \Delta_3 + \Delta_4 = 250$ MHz [Fig.

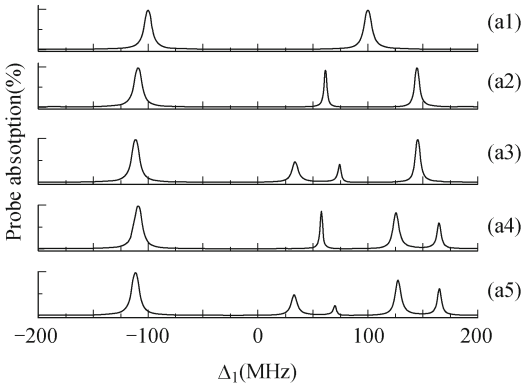

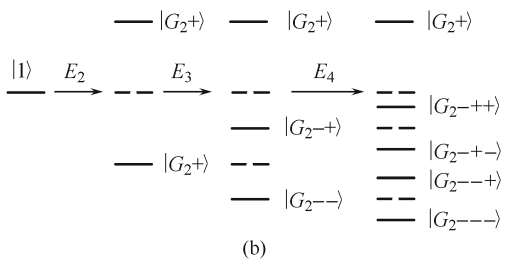

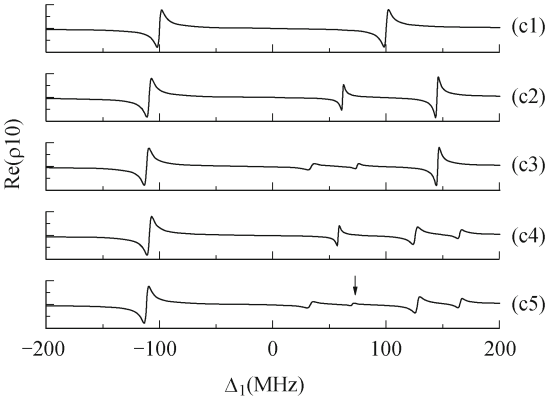

Fig. 4.24. Im(ρ_{10}) as a function of Δ_1 (a1) $G_2 = 100$ MHz and $\Delta_2 = 0$ MHz, when $G_3 = 0$ MHz, $G_4 = 0$ MHz, (a2) $G_3 = 50$ MHz, $\Delta_3 = 100$ MHz, when $G_4 = 0$; (a3) $G_4 = 30$ MHz (G_4 under G_2) and $\Delta_4 = 50$ MHz, when the other $G_4 = 0$; (a4) $G_4 = 30$ MHz (G_4 under G_3), $\Delta_4 = 50$ MHz, when $G_4 = 0$ under G_2; (a5) $G_4 = 30$ MHz, $\Delta_4 = 0$ MHz. (b) the dressed-state picture for EIT system. Re (ρ_{10}) as a function of Δ_1 show in (c1)-(c5) with all other conditions same as in Figs. 4.17(a1)-(a5), respectively.

4.24 (a)]. Secondary, when $\Delta_4 = \Delta_{G2}/2 = -100$ MHz, the left absorptive peak in Fig. 4.25(a) is separated into two peaks in Fig. 4.25 (b), while the dressing field E_4 [under G_3 in Eq. (4.30)] generate a very small three-photon absorption peak at $\Delta_1 = \Delta_3 + \Delta_4 = 0$ [Fig. 4.25 (b)]. Finally, as Fig. 4.25 (c) shows, when $\Delta_4 = -200$ MHz, the left absorption peak in

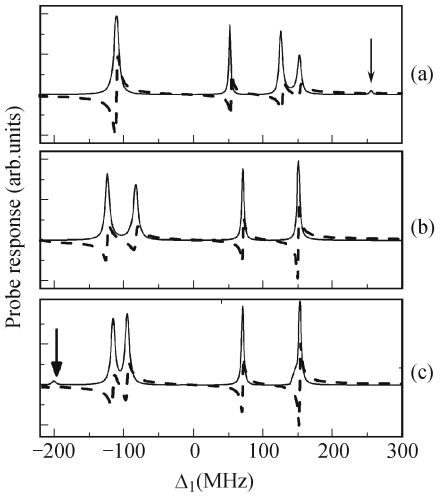

Fig. 4.25. Im(ρ_{10}) as a function of the probe frequency detuning (a) $\Delta_4 = 150$ MHz, (b) $\Delta_4 = -100$ MHz, and (c) $\Delta_4 = -200$ MHz, Other parameters are $G_2 = 100$ MHz, $G_3 = 50$ MHz, $G_4 = 50$ MHz, $\Delta_2 = 0$ and $\Delta_3 = 100$ MHz. The dashed lines are dispersion profiles.

Fig. 4.25 (a) splits into two peaks by the dressing field E_4 [under G_3 in Eq. (4.30)], and the three-photons absorption peak is generated by the dressing field E_4 [under G_2 in Eq. (4.30)] at $\Delta_1 = -\Delta_2 + \Delta_4 = -200$ MHz. The dashed curves in Fig. 4.25 also show the quadruple dressed dispersion corresponding to the solid absorption. So, the different multi-EIT phenomenon is obtained by changing the offsets of the dressing fields and moreover, the locations can be controled as well as shape/height of EIT profile of Im (ρ_{10}) and Re (ρ_{10}) in other ways in this four-dressing EIT system.

4.4.3 Discussion

We investigate the multi-dressed FWM, SWM, and EWM in the paper, which can coexist in different EIT windows. In the five-level system we investigated, when the five laser beams ($E_1, E_2', E_2, E_3$and E_4) are on, there exist three different EIT windows, i.e., $|0\rangle \rightarrow |1\rangle \rightarrow |2\rangle$ (ladder-type) with two counter-propagation beams E_2 (and E_2') and $E_1, |0\rangle \rightarrow |1\rangle \rightarrow |3\rangle$ (Λ-type) with two counter propagation beams E_3 and E_1, and $|0\rangle \rightarrow |1\rangle \rightarrow |4\rangle$ (V-type) with two counter propagation beams E_4 and E_1. Moreover, there also exists one multi-dressed FWM ($\boldsymbol{k}_\mathrm{f} = \boldsymbol{k}_1 + \boldsymbol{k}_2 - \boldsymbol{k}_2'$), two multi-dressed SWM ($\boldsymbol{k}_\mathrm{s} = \boldsymbol{k}_1 + \boldsymbol{k}_2 - \boldsymbol{k}_2' + \boldsymbol{k}_4 - \boldsymbol{k}_4$ and $\boldsymbol{k}_{\mathrm{s}1} = \boldsymbol{k}_1 + \boldsymbol{k}_2 - \boldsymbol{k}_2' + \boldsymbol{k}_3 - \boldsymbol{k}_3$) and one multi-dressed EWM ($\boldsymbol{k}_\mathrm{e} = \boldsymbol{k}_1 + \boldsymbol{k}_2 - \boldsymbol{k}_2' + \boldsymbol{k}_3 - \boldsymbol{k}_3 + \boldsymbol{k}_4 - \boldsymbol{k}_4$) in the five-level system. They are in the same direction determined by the phase-matching conditions, as shown in Fig. 4.22 (b), which enable us to investigate the coexisting, intermixing and temporal and spatial interference between FWM and SWM, or even to EWM. We accomplish this by controlling the offsets and intensities of dressing fields for the aim of MWM coexisting in different EIT windows, which could be individually controlled and the generated MWM signals can be clearly separated and distinguished or pulled together (by frequency offsets) to observe interferences and competitions between them. The relative strengths of the FWM, SWM, and EWM can be adjusted freely by controlling the intensities of the dressed fields (via dressed states). Therefore, the SWM or EWM signal can be enhanced to the same order as the FWM signal [16, 37]. To investigate the efficient energy transfer between FWM ($\boldsymbol{k}_\mathrm{f}' = \boldsymbol{k}_1 + \boldsymbol{k}_2 - \boldsymbol{k}_2'$) and SWM ($\boldsymbol{k}_\mathrm{s}' = \boldsymbol{k}_1 + \boldsymbol{k}_2 - \boldsymbol{k}_2' + \boldsymbol{k}_3 - \boldsymbol{k}_3'$), or EWM ($\boldsymbol{k}_\mathrm{e}' = \boldsymbol{k}_1 + \boldsymbol{k}_2 - \boldsymbol{k}_2' + \boldsymbol{k}_3 - \boldsymbol{k}_3' + \boldsymbol{k}_4 - \boldsymbol{k}_4'$), we can set the different spatial beam geometry, and then the MWM signal propagate different directions due to the phase-matching condition [47].

4.5 Polarization Interference of Multi-Wave Mixing in a Confined Five-level System

High-resolution spectroscopy of atoms confined in an ultra-thin cell is promis-

ing for investigation of the complex spectra of atoms and molecules [48]. Considerable attention is given to the utilization of miniaturized atomic cells in practical metrological standards. An anisotropy, which refers to atoms flying parallel to the windows interact with light during a much longer time than those flying perpendicular to the windows, is responsible for the observation of sub-Doppler features in the spectrum [49]. Recently, the long-range dipole attraction between atomic systems and metallic or dielectric bodies has become a subject of renewed interest because of its fundamental importance in the field of cavity Quantum Electrodynamics (QED) [50]. Nanometer cell has been used to observe the enhancement of the coherent transient atomic response due to Dicke-narrowing features, and to study long-range atom-wall interaction, which is dominated by the universal van der Waals (vdW) attraction between a fluctuating atom dipole and its image. This attractive potential, whose strength grows with the atomic excitation, induces a spectral red-shift [51].

Recently, electromagnetically induced transparency (EIT) has led dark resonances in free space [21, 52], micrometric cell [53], and even in ultra-thin cell [54]. The interaction between double-dark states and splitting of a dark state (the secondarily dressed states) was studied theoretically [42], subsequently, the triple-peak absorption spectrum was observed in the four-level atomic system [39]. After that, three kinds of doubly dressed four-wave mixing (DDFWM) (in nested-, parallel-, and sequential-cascade schemes) were reported in a five-level atomic system [55]. Comparing with previous works, we represented the DDFWM in the five-level confined atomic system in this section [Fig. 4.26 (b)], which exists the competition between Dicke-narrowing and polarization interference [56] in micrometer cell.

In previously studied close-cycled (ladder-, N-, double-Λ, and folded-type) systems, the four-wave mixing (FWM), six-wave mixing (SWM), and eight-wave mixing (EWM) processes cannot coexist in a given configuration, and different order nonlinearities can only be observed individually [26 – 28, 34]. In our recent studies, we demonstrated that the third-order and fifth-order nonlinear processes can coexist in the open (such as V-, Y- and inverted Y-type) atomic systems [37], and the coexisting FWM, SWM, and EWM processes were studied theoretically under certain conditions in the five-level atomic system [36, 46, 55]. The FWM, SWM, and EWM processes have been proven to be able to coexist in the five-level confined atomic system in this section.

The purpose of this section is to theoretically analyze the main spectroscopic feature of MWM in ultra-thin, micrometer and long cells, with an emphasis on line shape, intensity, AT splitting, suppression and enhancement of the MWM signal. We also demonstrated that several features are different and also have the advantage of the previously reported MWM processes mentioned in this section. First, DDFWM, singly dressed SWM (DSWM), and EWM are coexisting in the five-level confined atomic system, which is a good system for studying the interplay between nonlinear optical processes

at different orders. Second, the degree of destructive interference can be modified by the wave vector, dressing field and cell length. Third, there exists the destructive interference in ultra-thin, micrometer and long cells. The oscillation behavior of MWM signal intensities and linewidths results from the destructive interference in thin cell. With a larger destructive interference, the MWM signal shows the narrow spectra and weak intensity in thin cell. On the other hand, the intensity and linewidth of the MWM signal are increasing as decreasing of the destructive interference in long cell. Fourth, we study the interaction between two dressing fields in nested-cascade DDFWM. The inner dressing field cannot only suppress the destructive polarization interference but also induce resonance enhancement, and decrease the contribution of "thin cell terms". On the other hand, the outer dressing field enhances destructive interference, resulted in FWM signal intensity decreases. Specifically, when inner dressing field is a strong field, the FWM signal intensity can be hugely enhanced in Doppler broadened system due to the polarization interference.

The MWM processes in multi-level confined atomic systems can help us to understand the underlying cavity Quantum Electrodynamics (QED) and to effectively optimize the generated multi-channel nonlinear optical signals. Moreover, the MWM narrow spectra in thin cell can be used for high precision measurements and metrological standards.

4.5.1 Basic Theory

In the basic system [see Fig 4.26 (b)] of three energy levels ($|0\rangle, |1\rangle$ and $|2\rangle$) and three laser fields (E_2 or E_2' and E_1), a FWM signal at frequency ω_1 will be generated. Adding another energy level (either $|3\rangle$ or $|4\rangle$) and another laser field (E_3 for level $|3\rangle$ and E_4 for level $|4\rangle$), the original energy level ($|1\rangle$ or $|0\rangle$) will be dressed to produce two dressed states. Such four-level system with a dressing field will modify the original FWM process (call singly dressed FWM) and generate SWM signals. If two energy level $|3\rangle$ and $|4\rangle$) are both added in two additional fields, then the original FWM system is called to be doubly dressed, which generate not only SWM signal, but also EWM. One can consider such system first as four-level system ($|0\rangle, |1\rangle, |2\rangle$, and $|3\rangle$) which generates SWM, and then by adding another level ($|4\rangle$), this four-level atomic system is dressed again to give a singly dressed SWM signal, which will have contributions for EWM under certain conditions.

In a five-level atomic system as shown in Fig. 4.26 (b), states $|i-1\rangle$ to $|i\rangle (i = 1, 2, 3, 4)$ are coupled by laser fields E_i and $E_i'[\omega_i, \boldsymbol{k}_i(\boldsymbol{k}_i')$ with a Rabi frequency $G_i(G_i')]$. The Rabi frequencies are defined as $G_i = E_i\mu_{ij}/\hbar$ and $G_i' = E_i'\mu_{ij}/\hbar$ respectively, where μ_{ij} is the transition dipole moment between level i and level j. Fields E_i and E_i' with the same frequency and different time delays (E_i' is delayed by time τ) propagate along beams 2 and

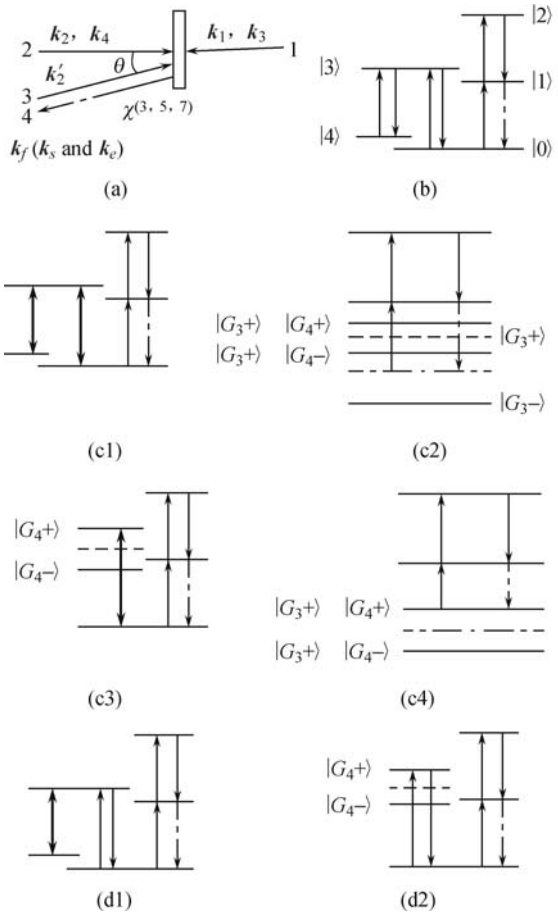

Fig. 4.26. (a) phase-conjugation geometry. (b) Energy-level diagram of five-level confined atomic system. (c1) Energy-level diagram for nested-cascade DDFWM and (c2 – c4) the dressed-state pictures. (d1) Energy-level diagram for dressed DSWM and (d2) Dressed-state picture.

3 with a small angle [Fig. 4.26 (a)], while a weak probe field E_p (beam 1) propagates along the opposite direction of the beam 2.

The nonlinear polarizations, which are responsible for multi-wave mixing signals, are proportional to the off-diagonal density matrix elements $\rho_{10}^{(n)}$. We still assume that G_1 is weak, whereas the laser fields G_2, G_2', G_3, and G_4 become arbitrary magnitudes. Thus, $\rho_{10}^{(n)}$ needs to be calculated to the lowest-order in G_1, but to all orders in other fields under various conditions.

Let us consider a five-level confined atomic system with five laser beams as shown in Fig. 4.26 (b). Three energy levels ($|0\rangle - |1\rangle - |2\rangle$) constitute a ladder type system when the pump beams E_3 and E_4 are blocked. Simultaneously the probe beam (E_1), together with one of the pump beams (E_2 or E_2') is

shown as an electromagnetically induced transparency (EIT) window, since the probe beam E_1 and the pump beam E_2 are in the two-photon Doppler-free (first order) configuration (counter-propagating) [17]. When both beams E_2 and E_2' are tuned on, an efficient FWM process can be generated to produce a conjugate signal at frequency ω_1. The generated FWM signal propagates in the $\boldsymbol{k}_{\mathrm{f}} = \boldsymbol{k}_1 + \boldsymbol{k}_2 - \boldsymbol{k}_2'$ direction due to the phase-matching condition, via the perturbation the chain (F1) ($\rho_{00}^{(0)} \xrightarrow{\omega_1} \rho_{10}^{(1)} \xrightarrow{\omega_2} \rho_{20}^{(2)} \xrightarrow{-\omega_2} \rho_{10}^{(3)}$).

When $E_4(\omega_4, \boldsymbol{k}_4, G_4)$ and $E_3(\omega_3, \boldsymbol{k}_3, G_3)$ are tuned on, the pumping beams E_3 will link the transition $|3\rangle$ to $|0\rangle$, and another pumping beams E_4 will link the transition $|3\rangle$ to $|4\rangle$ [Fig. 4.26 (b1)] via a segment (sub-chain) of the EWM perturbation chain (E1) $\rho_{00}^{(0)} \xrightarrow{\omega_1} \rho_{10}^{(1)} \xrightarrow{\omega_2} \rho_{20}^{(2)} \xrightarrow{-\omega_3} \rho_{23}^{(3)} \xrightarrow{\omega_4} \rho_{24}^{(4)} \xrightarrow{-\omega_4} \rho_{23}^{(5)} \xrightarrow{\omega_3} \rho_{20}^{(6)} \xrightarrow{-\omega_2} \rho_{10}^{(7)}$. In detail, the sub-chain (DF1) $\rho_{23}^{(3)} \xrightarrow{\omega_4} \rho_{24}^{(4)} \xrightarrow{-\omega_4} \rho_{23}^{(5)}$ (related to the dressing field E_4) is nested between the sub-chains "$\rho_{20}^{(2)} \xrightarrow{-\omega_3} \rho_{23}^{(3)}$" and "$\rho_{23}^{(5)} \xrightarrow{\omega_3} \rho_{20}^{(6)}$" due to the dressing field E_3. By virtue of the perturbation chain, we can modify the FWM chain to give the DDFWM chain (F2) $\rho_{00}^{(0)} \xrightarrow{\omega_1} \rho_{10}^{(1)} \xrightarrow{\omega_2} \rho_{2(G4\pm G3\pm)}^{(2)} \xrightarrow{-\omega_2} \rho_{10}^{(3)}$. Here the subscript "0" of $\rho_{20}^{(2)}$ in FWM the chain is replaced by "$G_4 \pm G_3\pm$" in DDFWM the chain, which indicates that the two dressing fields dress the level $|0\rangle$ and influence the identical coherence between states $|0\rangle$ and $|2\rangle$.

Firstly, $\rho_{10}^{(1)}$ can be expressed as (here we only consider the connected matrix elements in the chain (F2) and neglect other matrix elements):

$$L\{\rho_{10}^{(1)}\} = \frac{\mathrm{i}G_1}{s(s+\Lambda_{10})}, \tag{4.32}$$

where L is the Laplace transform operator defined by $L\{f(t)\}=\int_0^\infty f(t)\mathrm{e}^{-st}\mathrm{d}t$, Doppler shifted detuning is defined as $\Lambda_{10} = \Gamma_{10} + \mathrm{i}(\Delta_1 - \boldsymbol{k}_1 v)$.

Secondly, from the sub-chain DF1, using Laplace transformation, we obtain the coupling equations,

$$(s+\Lambda_{20})L\{\rho_{2(G_4\pm G_3\pm)}^{(2)}\} = \mathrm{i}G_2 L\{\rho_{10}^{(1)}\} - \mathrm{i}G_3 L\{\rho_{23}\}, \tag{4.33a}$$

$$(s+\Lambda_{23})L\{\rho_{23}\} = -\mathrm{i}G_3^* L\{\rho_{2(G_4\pm G_3\pm)}^{(2)}\} - \mathrm{i}G_4^* L\{\rho_{24}\}, \tag{4.33b}$$

$$(s+\Lambda_{24})L\{\rho_{24}\} = -\mathrm{i}G_4 L\{\rho_{23}\}, \tag{4.33c}$$

where $\Lambda_{20} = \Gamma_{20} + \mathrm{i}[\Delta_1 + \Delta_2 - k_1(1-\xi_2)v], \Lambda_{23} = \Gamma_{23} + \mathrm{i}[\Delta_1 + \Delta_2 - \Delta_3 - k_1(1-\xi_2-\xi_3)v], \Lambda_{24} = \Gamma_{24} + \mathrm{i}[\Delta_1 + \Delta_2 - \Delta_3 + \Delta_4 - k_1(1-\xi_2-\xi_3-\xi_4)v], \xi_2 = k_2/k_1, \xi_3 = k_3/k_1, \xi_4 = k_4/k_1$.

Then we have,

$$L\{\rho_{20}^{(2)}\}=L\{\rho_{2(G_4\pm G_3\pm)}^{(2)}\}=\frac{\mathrm{i}G_2}{(S+\Lambda_{20})+\dfrac{G_3G_3^*}{(S+\Lambda_{23})+G_4^*G_4/(S+\Lambda_{24})}}L\{\rho_{10}^{(1)}\}. \tag{4.34a}$$

Thirdly, using the same method, we can also obtain $\rho_{10}^{(3)}$

$$L\{\rho_{10}^{(3)}\}=iG_2'L\{\rho_{20}^{(2)}\}/(S+\Lambda_{10}). \tag{4.34b}$$

Finally, using Eqs. (4.32), (4.33a) and (4.33b), we obtain:

$$L\{\rho_{10}^{(3)}\}=\frac{-\mathrm{i}G_A\exp(\mathrm{i}\boldsymbol{k}_\mathrm{f}\cdot\boldsymbol{r})[(S+\Lambda_{23})(S+\Lambda_{24})+G_4^2]}{S(S+\Lambda_{10})^2\{(S+\Lambda_{20})[(S+\Lambda_{23})(S+\Lambda_{24})+G_4^2]+G_3^2(S+\Lambda_{24})\}}, \tag{4.35}$$

where $G_A=G_1G_2(G_2')^*$.

Since the item "Λ_{20}" representing the "$\omega_1+\omega_2$" two-photon process of $\rho_{10}^{(3)}$ is modified directly by the term $|G_3|^2$, then such modified result is affected by the term $|G_4|^2$, Equation (4.35) shows that the two dressing fields are entangled with each other for such nested-cascade scheme. The inner dressing field E_3 controls FWM directly, while the outer dressing field E_4 affects FWM indirectly [46].

In a weak-field limit $|G_3|^2 << \Gamma_{20}\Gamma_{23}$ and $|G_4|^2 << \Gamma_{23}\Gamma_{24}$, $L\{\rho_{10}^{(3)}\}$ can be expanded to the lowest order, which gives

$$\begin{aligned}L\{\rho_{10}^{(3)}\}&=-\mathrm{i}G_A/A_1+\mathrm{i}G_B/A_2-\mathrm{i}G_C/A_3\\&=L\{\rho_{10}^{(3)}\}+L\{\rho_{10}^{(5)}\}+L\{\rho_{10}^{(7)}\}.\end{aligned} \tag{4.36}$$

where $A_1=S(S+\Lambda_{10})^2(S+\Lambda_{20}), A_2=A_1(S+\Lambda_{20})(S+\Lambda_{23}), A_3=A_2(S+\Lambda_{23})(S+\Lambda_{24}), G_B=G_A|G_3|^2$ and $G_C=G_B|G_4|^2$.

This expansion shows that the doubly-dressed FWM process can be converted into a coherent superposition from FWM, SWM and EWM. Where $L\{\rho_{10}^{(3)}\}=-\mathrm{i}G_A/A_1, L\{\rho_{10}^{(5)}\}=\mathrm{i}G_B/A_2$ and $L\{\rho_{10}^{(7)}\}=-\mathrm{i}G_c/A_3$. These expressions represent processes for FWM, SWM and EWM respectively.

After the normalization of Eq. (4.35), we have

$$L\{\rho_{10}^{(3)}\}=\frac{\mathrm{i}[(S+\Lambda_{23})(S+\Lambda_{24})+G_4^2]}{S(S+\Lambda_{10})^2\{(S+\Lambda_{20})[(S+\Lambda_{23})(S+\Lambda_{24})+G_4^2]+G_3^2(S+\Lambda_{24})\}}. \tag{4.37}$$

The inverse-Laplace transformed solution of Eq. (4.37) can be expressed as

$$\rho_{10}^{(3)}(t)=A+\sum_{i=1}^{4}D_i\,|v|/\lambda_i+\sum_{i=1}^{4}D_i\exp(-\lambda_i t), \tag{4.38}$$

where D_i and λ_j are two tedious expressions, and

$$A=\frac{\mathrm{i}(\Lambda_{23}\Lambda_{24}+G_4^2)}{\Lambda_{10}^2[\Lambda_{20}(\Lambda_{23}\Lambda_{24}+G_4^2)+G_3^2\Lambda_{24}]}. \tag{4.39}$$

Take the atomic thermal motion into account, which is assumed to obey the Maxwell distribution $W(v)=(u\sqrt{\pi})^{-1}\exp(-v^2/u^2)$, where $u=\sqrt{2KT/m}$ and m is the mass of an atom, K is Boltzmann's constant, and T the absolute temperature. Then the nonlinear polarization in Eq. (4.38) is given by

$$P(z)=N\mu_{10}\int_0^L \mathrm{d}z\int_{-\infty}^{\infty}\exp[-(v/u)^2[\Theta(v)\rho_{10}^{(3+)}+\Theta(-v)\rho_{10}^{(3-)}]\mathrm{d}v, \quad (4.40)$$

where L is the cell length, $\Theta(v)$ and $\Theta(-v)$ are Heaviside functions, $N$is the density of atoms in the vapor, $\rho_{10}^{(3+)}$ and $\rho_{10}^{(3-)}$ are density matrix elements for $v>0$ and $v<0$, respectively. As usual in ultra-thin cell, initial conditions for the system differ for arriving ($v<0$) and departing ($v>0$) atoms. One has indeed $\rho_{00}(L)=1,\rho_{ij}(L)=0$ for $v<0$; and $\rho_{00}(0)=1$, $\rho_{ij}(0)=0(i,j=0,1,2,3,4)$ for $v>0$ [51]. Atoms, after inelastic collisions with the walls, lose their optical excitation and all memory about the previous state. Then it is justified to assume that atoms get de-excited at a collision with the wall, and are in the ground states at the instant that they leave the wall after a collision. Thus, we use $t=z/v$ for $v>0$ and $t=(z-L)/v$ for $v<0$, equation (4.40) change the integrate orders of v and z, one gets

$$P(z)=N\mu_{10}\int_{-\infty}^{\infty}\exp[-(v/u)^2]B_F(v)\mathrm{d}v, \quad (4.41)$$

where $B_F(v)=AL+D_i\left|v\right|/\lambda_i+D_i\left|v\right|\exp(L\lambda_i/\left|v\right|)/\lambda_i$. We assume

$$S_{F1}=\int_{-\infty}^{\infty}\exp[-(v/u)^2]AL\mathrm{d}v,$$

$$S_{F2}=\int_{-\infty}^{\infty}\exp[-(v/u)^2](D_i\left|v\right|/\lambda_i)\mathrm{d}v,$$

$$S_{F3}=\int_{-\infty}^{\infty}\exp[-(v/u)^2](D_i\left|v\right|\exp(L\lambda_i/\left|v\right|)/\lambda_i)\mathrm{d}v,$$

$$S_F=S_{F1}+S_{F2}+S_{F3}.$$

When cell length is short enough, the first term ("Doppler broadened terms") of $B_F(v)$ provides the usual steady-state Doppler broadened spectra expected in a confined cell. It can be seen that the second term of $B_F(v)$ originates from the buildup of the atomic response to excitation fields. It illustrates that the integration of all possible interactions inside the medium, while the third term of $B_F(v)$ reflects the finiteness of the interaction time L/v, which is limited by the cell length. Both latter terms in $B_F(v)$ are defined as the thin cell terms, When L is long enough, the S_{F2} and S_{F3} can be neglected (i.e., $S\approx S_{F1}$). Only the polarization interference needs to be considered in this case.

The FWM signal intensity is given by

$$I \propto |S|^2 = \left| \int_{-\infty}^{+\infty} \exp[-(v/u)^2] B_F(v) \mathrm{d}\nu \right|^2 .$$

From above equation, we can see that there exists polarization interference, the destructive or constructive interference can cause significant modification of line shape and intensity of FWM signal. To investigate it, instead of $\langle |S_F|^2 \rangle$, we can sum up the signal intensity of each atom motion, i.e., $\int_{-\infty}^{+\infty} \mathrm{d}\nu \exp[-(v/u)^2] \langle |B_F(v)|^2 \rangle$ without inter-atomic polarization interference.

When L is long enough, we will get the nonlinear polarization

$$P \propto \int_{-\infty}^{\infty} \mathrm{d}v W(v) F_F(v),$$

where $F_F(v) = \dfrac{\mathrm{i}(\Lambda_{23}\Lambda_{24} + G_4^2)}{\Lambda_{10}^2[\Lambda_{20}(\Lambda_{23}\Lambda_{24} + G_4^2) + G_3^2\Lambda_{24}]}$.

Specifically, we can see that the expression $F_F(v)$ is equal to Eq. (4.39) in the confined cell, this means that the "Doppler broadened term" A in thin cell is expected to be the same as the long cell term $F_F(v)$. So when L is long enough, FWM signal spectra in the long cell equals to the case of the Doppler broadened cases in free space.

For the homogeneous broadened cases, we will get the following equation [46]

$$\rho_{10}^{(3)} = \frac{-\mathrm{i}G_A \exp(\mathrm{i}\boldsymbol{k}_\mathrm{f} \cdot \boldsymbol{r})}{d_{10}^2 \left(d_{20} + \dfrac{|G_3|^2}{d_{23} + |G_4|^2/d_{24}} \right)}, \tag{4.42}$$

where $d_{10} = \Gamma_{10} + \mathrm{i}\Delta_1$, $d_{20} = \Gamma_{20} + \mathrm{i}(\Delta_1 + \Delta_2)$, $d_{13} = \Gamma_{13} + \mathrm{i}(\Delta_1 - \Delta_3)$, $d_{23} = \Gamma_{23} + \mathrm{i}(\Delta_1 + \Delta_2 - \Delta_3)$, $d_{24} = \Gamma_{24} + \mathrm{i}(\Delta_1 + \Delta_2 - \Delta_3 + \Delta_4)$.

We have deduced the DDFWM expression in ultra-thin and long cells. As the cell length is increasing, the contribution of the Doppler broadened terms in $B_F(v)$ increases, and the effect of the thin cell terms in $B_F(v)$ decreases. Since the cell length is long enough, the thin cell terms in $B_F(v)$ can be neglected, and only the Doppler-broadened terms in $B_F(v)$ are considered.

Next, let us consider coexisting DSWM and EWM in five-level confined atomic system.

When the field E_3' and E_4' are tuned on, there coexist the singly dressed SWM and EWM processes, satisfying the phase-matching directions $\boldsymbol{k}_\mathrm{s} = \boldsymbol{k}_1 + \boldsymbol{k}_2 - \boldsymbol{k}_2' + \boldsymbol{k}_3 - \boldsymbol{k}_3$ and $\boldsymbol{k}_\mathrm{e} = \boldsymbol{k}_1 + \boldsymbol{k}_2 - \boldsymbol{k}_2' + \boldsymbol{k}_3 - \boldsymbol{k}_3 + \boldsymbol{k}_4 - \boldsymbol{k}_4$, respectively.

The SWM process is generated by interaction with one photon each from E_1, E_2, E_2' and two photons from E_3, which is dressed by field E_4 [Fig. 4.26 (c1)]. Similarly, EWM process can also exist at the same time with one photon each from E_1, E_2, E_2', two photons from the same field E_3 and two photons from the same field E_4 as shown in Fig. 4.26 (b).

The sub-process for the dressing field E_4 (DS1), "$\rho_{30}^{(1)} \xrightarrow{-\omega_4} \rho_{40}^{(2)} \xrightarrow{\omega_4} \rho_{30}^{(3)}$" exists in the EWM the chain (E2) $\rho_{00}^{(0)} \xrightarrow{\omega_3} \rho_{30}^{(1)} \xrightarrow{-\omega_4} \rho_{40}^{(2)} \xrightarrow{\omega_4} \rho_{30}^{(3)} \xrightarrow{-\omega_3} \rho_{00}^{(4)} \xrightarrow{\omega_1} \rho_{10}^{(5)} \xrightarrow{\omega_2} \rho_{20}^{(6)} \xrightarrow{-\omega_2} \rho_{10}^{(7)}$. It means that the field E_4 dresses the state $|3\rangle$ and affects the atomic coherences $\rho_{30}^{(1)}$ between $|0\rangle$ and $|3\rangle$. So we have $\rho_{G_4\pm0}^{(1)}$ in the dressed SWM the chain (S1) $\rho_{00}^{(0)} \xrightarrow{\omega_3} \rho_{G_4\pm0}^{(1)} \xrightarrow{-\omega_3} \rho_{00}^{(2)} \xrightarrow{\omega_1} \rho_{10}^{(3)} \xrightarrow{\omega_2} \rho_{20}^{(4)} \xrightarrow{-\omega_2} \rho_{10}^{(5)}$.

The high-order atomic coherence plays a significant role in the enhancement of multi-wave mixing processes. From the sub-chain DS1, we can have coupling equations $(S+\Lambda_{30})L\{\rho_{G_4\pm0}^{(1)}\} = \mathrm{i}G_3L\{\rho_{00}^{(0)}\} + \mathrm{i}G_4L\{\rho_{40}\}, (S+\Lambda_{40})L\{\rho_{40}\} = \mathrm{i}G_4^*L\{\rho_{G_4\pm0}^{(1)}\}$, where $\Lambda_{30} = \Gamma_{30} + \mathrm{i}[\Delta_3 - k_1\xi_3 v], \Lambda_{40} = \Gamma_{40} + \mathrm{i}[\Delta_3 - \Delta_4 - k_1(\xi_3+\xi_4)v]$. We can obtain

$$L\{\rho_{30}^{(1)}\} = \mathrm{i}G_3\frac{\Lambda_{40}}{S(\Lambda_{30}\Lambda_{40} + |G_4|^2)}$$

from the coupling equation for E_4 interaction terms. $L\{\rho_{00}^{(2)}\} = \mathrm{i}G_3L\{\rho_{30}^{(1)}\}/(S+\Gamma_{00}), L\{\rho_{10}^{(3)}\} = \mathrm{i}G_1\rho_{00}^{(2)}/(S+\Lambda_{10}), L\{\rho_{20}^{(4)}\} = \mathrm{i}G_2L\{\rho_{10}^{(3)}\}/(S+\Lambda_{20})$, and $L\{\rho_{10}^{(5)}\} = \mathrm{i}G_2'^*L\{\rho_{20}^{(4)}\}/(S+\Lambda_{10})$ are also obtained from the chain S_1. Thus, we have

$$L\{\rho_{10}^{(5)}\} = \frac{\mathrm{i}G_B\exp[\mathrm{i}k_S r](S+\Lambda_{40})}{S(S+\Gamma_{00})(S+\Lambda_{10})^2(S+\Lambda_{20})[(S+\Lambda_{30})(S+\Lambda_{40}) + |G_4|^2]}.$$

Assuming $|G_4|^2 << \Gamma_{30}\Gamma_{40}$, then through power expansion, we obtain $L\{\rho_{10}^{(5)}\} = \frac{\mathrm{i}G_B\exp[\mathrm{i}(k_1+k_2-k'_2)\boldsymbol{r}]}{S(S+\Gamma_{00})(S+\Lambda_{10})^2(S+\Lambda_{20})(S+\Lambda_{30})}\left[1-\frac{|G_4|^2}{(S+\Lambda_{30})(S+\Lambda_{40})}\right] = L\{\rho_{\mathrm{s}}^{(5)}\} + L\{\rho_{\mathrm{e}}^{(7)}\}$. The dressed SWM process approximately converts to a coherent superposition from SWM $L\{\rho_{\mathrm{s}}^{(5)}\}$ and EWM $L\{\rho_{\mathrm{e}}^{(7)}\}$. Illuminate that $L\{\rho_{\mathrm{s}}^{(5)}\}$ include both fifth- and seventh-order nonlinear optical responses. Finally, similar to DDFWM, we can get the nonlinear polarization:

$$P = N\mu_{10}\int_{-\infty}^{\infty} W(v)B_S(v)\mathrm{d}v,$$

where

$$B_S(v) = A_SL + D_i\,|v|/\lambda_i + D_i\,|v|\exp(L\lambda_i/\,|v|)/\lambda_i,$$

$$A_S = \frac{\mathrm{i}\Lambda_{40}}{\Gamma_{00}\Lambda_{10}^2\Lambda_{20}(\Lambda_{30}\Lambda_{40}) + |G_4|^2)}.$$

The SWM signal intensity is given by $I \propto |S_S|^2 = |S_{S1} + S_{S2}|^2$, where $S_{S1} = \int_{-\infty}^{\infty}\exp[-(v/u)^2]A_SL\mathrm{d}v$, $S_{S2} = \int_{-\infty}^{\infty}\exp[-(v/u)^2](D_i\,|v|/\lambda_i + D_i\,|v|\exp(L\lambda_i/\,|v|)\mathrm{d}v$.

Similarly, when L is long enough, we can obtain the SWM signal intensity $I \propto \int_{-\infty}^{\infty} \exp[-(v/u)^2] F_S \mathrm{d}v$, where $F_S(v) = A_S$ and $I \propto |\rho_{10}^{(5)}|^2$ for the homogeneous broadened cases, where $\rho_{10}^{(5)} = \dfrac{-\mathrm{i}G_B d_{40}}{\Gamma_{00} d_{10}^2 d_{20}(d_{30}d_{40}) + |G_4|^2}$, and $d_{30} = \Gamma_{30} + \mathrm{i}\Delta_3$, $d_{40} = \Gamma_{40} + \mathrm{i}(\Delta_3 - \Delta_4)$.

When all five laser beams are all tuned on simultaneously, the EWM signal will be generated $\boldsymbol{k}_\mathrm{e} = \boldsymbol{k}_1 + \boldsymbol{k}_2 - \boldsymbol{k}_2' + \boldsymbol{k}_3 - \boldsymbol{k}_3 + \boldsymbol{k}_4 - \boldsymbol{k}_4$, via the EWM perturbation the chain $\rho_{00}^{(0)} \xrightarrow{\omega_1} \rho_{10}^{(1)} \xrightarrow{\omega_2} \rho_{20}^{(2)} \xrightarrow{-\omega_2} \rho_{10}^{(3)} \xrightarrow{-\omega_3} \rho_{13}^{(4)} \xrightarrow{\omega_4} \rho_{14}^{(5)} \xrightarrow{-\omega_4} \rho_{13}^{(6)} \xrightarrow{\omega_3} \rho_{10}^{(7)}$. We can obtain the seventh-order nonlinear processes in the homogeneous broadened cases and micrometer cell, $\rho_{E2}^{(7)} = -\mathrm{i}G_C/d_{10}^3 d_{20} d_{13}^2 d_{14}$, $B_E(v) = AL + \sum_{i=1}^{7} D_i |v| / \lambda_i + \sum_{i=1}^{7} D_i F(L)/\lambda_i + \sum_{i=1}^{4} D_i L F(L)/\lambda_i + CF(L)L^2/(2|v|^2\Lambda_{10})$, respectively, where $\Lambda_{13} = \Gamma_{13} + \mathrm{i}[\Delta_1 - \Delta_3 - k_1(1-\xi_3)v], d_{13} = \Gamma_{13} + \mathrm{i}(\Delta_1 - \Delta_3), \Lambda_{14} = \Gamma_{14} + \mathrm{i}[\Delta_1 - \Delta_3 + \Delta_4 - k_1(1-\xi_3-\xi_4)v]$ and $d_{14} = \Gamma_{14} + \mathrm{i}(\Delta_1 - \Delta_3 + \Delta_4)$.

On the other hand, when cell length L is long enough, time-domain correspondence of EWM is given by

$$
\begin{aligned}
P_T = {} & \frac{1}{\sqrt{\pi}u} S(r) \mathrm{e}^{-\mathrm{i}\omega_1 t} \int_{-\infty}^{+\infty} \mathrm{d}v \mathrm{e}^{-(v/u)^2} \times \\
& \int_0^\infty t_7 \int_0^\infty t_6 \int_0^\infty t_5 \int_0^\infty t_4 \int_0^\infty t_3 \int_0^\infty t_2 \int_0^\infty t_1 \times \\
& \mathrm{e}^{-\Lambda_{10}(t_1+t_3+t_7)} \mathrm{e}^{-\Lambda_{20} t_2} \mathrm{e}^{-\Lambda_{13}(t_4+t_6)} \mathrm{e}^{-\Lambda_{14} t_5} \\
= {} & \frac{1}{\sqrt{\pi}u} S(r) \mathrm{e}^{-\mathrm{i}\omega_1 t} \int_{-\infty}^{+\infty} \mathrm{d}v \mathrm{e}^{-(v/u)^2} \times \\
& \int_0^\infty t_7 \int_0^\infty t_6 \int_0^\infty t_5 \int_0^\infty t_4 \int_0^\infty t_3 \int_0^\infty t_2 \int_0^\infty t_1 \mathrm{e}^{-d_{10}(t_1+t_3+t_7)} \times \\
& \mathrm{e}^{-d_{20} t_2} \mathrm{e}^{-d_{13}(t_4+t_6)} \mathrm{e}^{-d_{14} t_5} \times \\
& \mathrm{e}^{\mathrm{i}\boldsymbol{k}_1 v[(t_1+t_3+t_7)+(1-\xi_2)t_2+(1-\xi_3)(t_4+t_6)+(1-\xi_3-\xi_4)t_5]}.
\end{aligned}
$$

We assume

$$
L = \exp\{\mathrm{i}\boldsymbol{k}_1 v[(t_1+t_3+t_7)+(1-\xi_2)t_2+(1-\xi_3)(t_4+t_6)+(1-\xi_3-\xi_4)t_5]\}. \quad (4.43)
$$

Since L involves integration over the velocity distribution function, it reflects the degree of coherence between polarizations of atoms which have different velocities. When $L = 1$, there is no the destructive interference, a Doppler-free EWM spectrum can be obtained. By contrast, $L << 1$, there exists the destructive interference, so, EWM spectra are broadened.

This five-level atomic system with co-existing FWM, SWM and EWM consists of four conventional EIT subsystems, i.e. $|0\rangle - |1\rangle - |2\rangle$ (ladder-type)

with two counter-propagation beams E_2 (or E_2') and E_1, $|0\rangle-|1\rangle-|3\rangle$ (Λ-type) with two propagation beams E_3 (or E_3') and E_1, and $|0\rangle-|1\rangle-|4\rangle$ (V-type) with two propagation beams E_4 (or E_4') and E_1. More explicitly, the ladder-type and Λ-type EIT configurations all satisfy the two-photon Doppler-free condition in Fig 4.26 (b). We have investigated the coexisting FWM, SWM and EWM in the five-level system. With the phase-conjugation geometry shown in Fig. 4.26 (a) for pump and probe laser beams, the coexisting FWM ($\boldsymbol{k}_{\rm f}$), SWM ($\boldsymbol{k}_{\rm s}$) and EWM ($\boldsymbol{k}_{\rm e}$) beams have not only the same frequency (ω_1) but also propagate in the same direction ($\boldsymbol{k}_{\rm f}||\boldsymbol{k}_{\rm s}||\boldsymbol{k}_{\rm e}$).

As we know, the real part $B_S'(v)$ shows a dispersive line shape, which leads to $\int_{-\infty}^{\infty} {\rm d}v \exp^{-(v/u)^2} B_S'(v) = 0$ [56], therefore, only the imaginary part of MWM contributes to the signal. So, we only investigate the imaginary part of MWM. There exists the destructive polarization interference in ultra-thin cell, which can modify the intensities and linewidths (with Dicke narrowing features) via the multi-photon terms of MWM.

(i) When $G_4 = 0$, the imaginary part $B_S(v)$ of SWM can be expressed by Euler transformation (the real part does not contribute to the signal):

$$A_S L + B[1 - \cos(2\pi L/\lambda)] + C[1 - \cos(2\xi_3 \pi L/\lambda)], \tag{4.44}$$

where B and C are coefficients of single-photon and two-photon terms respectively. When $L = \lambda/2$, the SWM signal results from the "thin cell term" (including single-photon and two-photon terms), and the Doppler broadened terms can be neglected. While $L = \lambda$, "thin-cell terms" are non-zero due to the two-photon term (contrary to the probe absorption in two-level system [51]), which contributes to the SWM signal with the "Doppler broadened terms". We demonstrate that there exists the polarization interference in thin cell, which also have a strong impact on the line shape and intensity of SWM signal. With a larger destructive interference, the SWM signal shows narrow spectra (on the contrary the case of long cell).

(ii) For EWM signal, the imaginary part of $B_E(v)$ can be written as by Euler transformation:

$$AL+B[1-\cos(2\pi n)]+C[1-\cos(2k_1(1-\xi_3)n\pi)]+D[1-\cos(2k_1(1-\xi_3-\xi_4)\pi n)], \tag{4.45}$$

where $n = L/\lambda$. Single-photon, two-photon and three-photon terms are all defined as "thin cell terms". Compared with Eq. (4.44), Eq. (4.45) adds a three-photon term, which leads to the periodic behaviors of EWM signal intensity and the line shape is changed drastically. When $L = 1.5\lambda$, the EWM signal intensity shows a maximal value and it is minimum as $L = 3\lambda$. Similarly, the linewidth of EWM spectrum has also been modified.

(iii) So, high-order nonlinear process adds more multi-photon terms, which could change the oscillation behavior of MWM signal intensity and line shape, and leads to the shift of the maximum value of MWM signal intensity.

4.5.2 MWM in Long Cells

We have discussed coexisting FWM, SWM and EWM in ultra-thin, micrometer, and long vapor cells, and the interaction of dressing fields in the five-level atomic system. In this section, we investigate that the wave vector (laser frequency and direction) [56, 57] and dressing field can control the degree of polarization interference in long cell, which can significantly modify the intensity and linewidth of MWM signal.

The polarization interference (destructive or constructive) is the key issue for the line shape and intensity of SWM signal. And the polarization interference can be controlled by the wave vector. In Fig. 4.27 (a), linewidths of SWM signal become much broader when $\xi_3 > 0$. Correspondingly, the SWM signal intensity also decreases drastically due to increasing of the destructive interference [56, 57]. To investigate polarization interference how to affect SWM signal spectrum, instead of $\left|\int_{-\infty}^{\infty} \mathrm{d}v e^{-(v/u)^2} F_S(v)\right|^2$, we sum up SWM signal intensities of individual atoms (i.e., $\int_{-\infty}^{\infty} \mathrm{d}v e^{-(v/u)^2} |F_S(v)|^2$). It has found that in Fig. 4.27 (a) that the linewidth of SWM signal is narrow and basically independent of the value ξ_3 when polarization interference is neglected. Figures 4.27 (b) and 4.27 (c) present the real part $F_S'(v)$ (dashed curves), imaginary part $F_S''(v)$ (solid curves), and absolute value $|F_S(v)|$ (dotted curves) of $F_S(v)$ for $\xi_3 = 0.2$ and $\xi_3 = 0.6$, respectively. Obviously, the real part shows a dispersive line shape, with $\int_{-\infty}^{\infty} \mathrm{d}v e^{-(v/u)^2} F_S'(v) = 0$. So, only the imaginary parts $F_S''(v)$ contribute to the SWM signal. Since $F_S''(v)$ changes the sign on wings of both $v < 0$ and $v > 0$ sides, the destructive interference occurs between atoms, thereby suppressing the total polarization P. So, the increase and decrease of destructive interferences lead to the increase and decrease of linewidths of SWM spectra, respectively (on the contrary the SWM signal intensity).

Similarly, Fig. 4.28 (a), (b) presents the EWM signal intensity versus Δ_4. The EWM signal shows a narrow spectra due to no polarization interference as shown in Fig. 4.28 (a). In addition, from Eq. (4.43), the condition for $L = 1$ is $(t_1 + t_3 + t_7) + (1 - \xi_2)t_2 + (1 - \xi_3)(t_4 + t_6) + (1 - \xi_3 - \xi_4)t_5 = 0$.

Since all values of t_i ($i = 1$ to 7) are positive, the above equation can be satisfied only if $1 - \xi_3 > 0$. For example, when $\xi_3 = 0.8$, there is no the destructive interference [the inset plot in Fig. 4.28 (b)], the EWM signal shows a narrow spectrum [Fig. 4.28 (b)]. On the other hand, when $\xi_3 = 1.2$, the EWM signal spectrum is broadened as shown in Fig. 4.28 (a).

Next, we consider how the weak dressing field affects the line shape of SWM signal spectrum. When the dressing field is very weak, a narrow dip of SWM signal appears first at the centre of the profile due to reduction of destructive interference, as shown by dotted curve in Fig. 4.29. The line

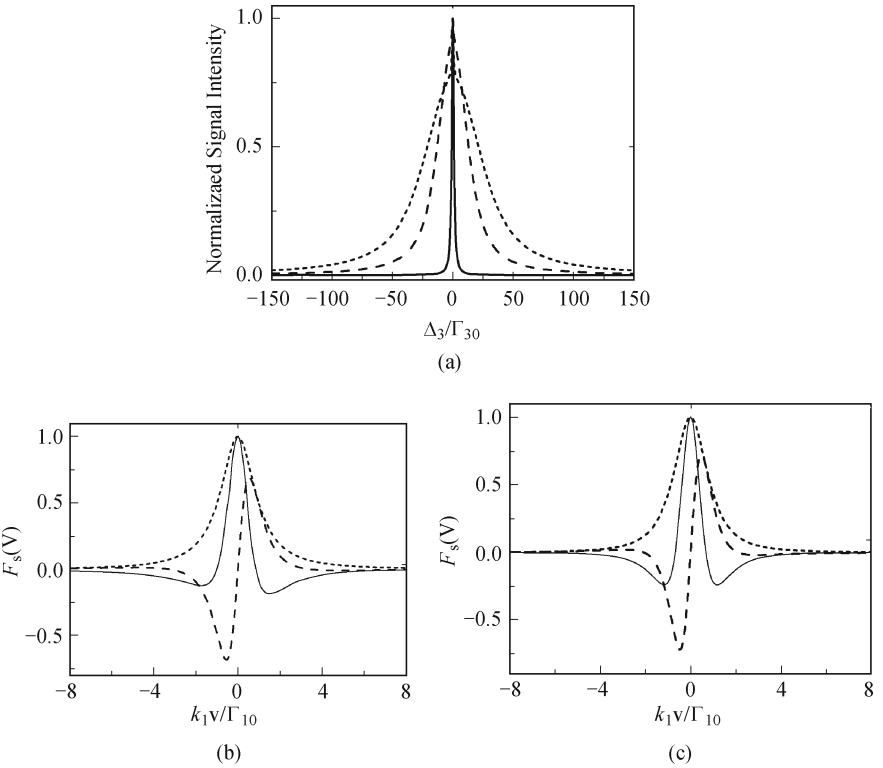

Fig. 4.27. (a) SWM spectra for $\Delta_1/\Gamma_{20} = 0$. $\Gamma_{10}/k_1u = \Gamma_{20}/k_1u = \Gamma_{30}/k_1u = 0.02, \xi_2$=1, and value of ξ_3=0 (solid curve), 0.2 (dashed curve) and 0.6 (dotted curve). The corresponding SWM signal intensity $\rho_{10}I$, relative to the one for $\Delta_3/\Gamma_{30} = 0, I_0 = 1, I_{0.2} = 7.6 \times 10^{-2}, I_{0.4} = 2.4 \times 10^{-2}$. (b) The real part $F'_S(v)$ (dashed curves), the imaginary part $F''_S(v)$ (solid curves), and the absolute value $|F_S(v)|$ (dotted curves) for (b) $\xi_3 = 0.2$, and (c) $\xi_3 = 0.6(m = 2)$.

shape of the spectrum then converts to a single line of homogeneous linewidth with the completely suppressed broad background when $G_3/\Gamma_{30} = 0.2$ (solid curve). If we further increase the dressing field intensity, the SWM signal spectra will exhibit a Dopller-free AT splitting, which will be discussed in the next section.

The dressing field can control the degree of the destructive interference. As G_4/Γ_{40} increases, the linewidth of SWM becomes narrower, and exhibits Doppler-free AT splitting due to reduction of the destructive interference. The distance between two splitting peaks can be approximated as $\Delta_{G_4} \approx 2G_4$ under the condition of $|G_4|^2 >> \Gamma_{30}\Gamma_{40}$. However, the linewidth of SWM spectra is much larger than the homogeneous linewidth without the dressing field [solid curve in Fig. 4.30 (a)].

Figure 4.30 (b) presents the DDFWM spectrum versus Δ_2. The inner dressing field E_3 in DDFWM first suppresses the destructive interference, and then creates dressed states $|G_3+\rangle$ and $|G_3-\rangle$ from the state $|0\rangle$ [dotted

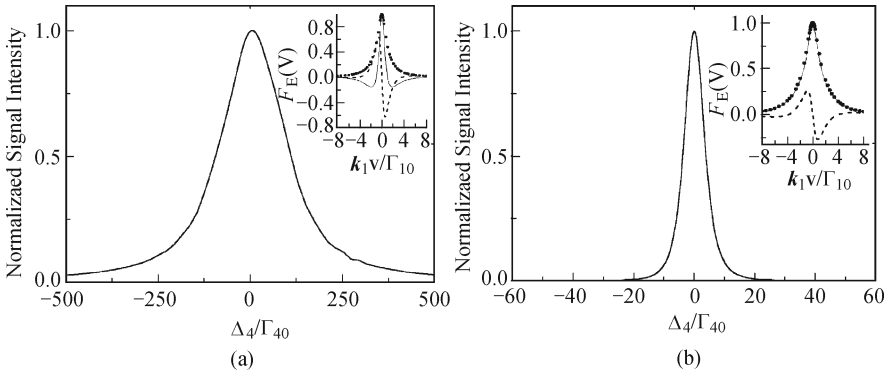

Fig. 4.28. The EWM signal intensity versus Δ_4/Γ_{14} for (a) ξ_3 =1.2, (b) ξ_3 =0.8. The insert plot: (a) ξ_3 =1.2, (b) ξ_3 =0.8, Real part $F'_E(v)$ (solid curves), imaginary part $F''_E(v)$ (dashed curves), and absolute value$|F_E(v)|$ (dotted curves). Other parameters are Δ_1/k_1u =10 and $\Delta_3/k_1u = 10, \Delta_2/k_1u = 0, \Gamma_{10}/k_1u = \Gamma_{20}/k_1u = \Gamma_{13}/k_1u = \Gamma_{14}/k_1u = 0.02, \xi_2 = 1, \xi_4 = 1.2$.

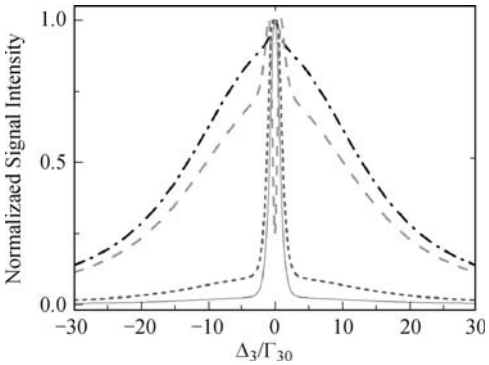

Fig. 4.29. The SWM signal intensity spectra for $G_4/\Gamma_{40} = 0$ (dot-dashed curve), $G_4/\Gamma_{40} = 0.05$ (dashed curve), $G_4/\Gamma_{40} = 0.15$ (dotted curve), $G_4/\Gamma_{40} = 0.2$ (solid curve). When $\Delta_1 = \Delta_2 = \Delta_3 = \Delta_4 = 0$ and $\Gamma_{10}/k_1u = \Gamma_{20}/k_1u = \Gamma_{30}/k_1u = \Gamma_{40}/k_1u = 0.02, \xi_3 = 0.2, \xi_4 = 0.8$.

curve in Fig. 4.30 (b)] (the separation between two peaks located at $\Delta_2 = \pm\Delta_{G3}/2 \approx \pm G_3$, here Δ_{G3} is the separation induced by the dressing field E_3). When the outer dressing field E_4 dresses the primarily dressed state $|G_4+\rangle$ ($\Delta_4 = -G_3$) and creates the secondarily dressed states $|G_3+\rangle|G_4\pm\rangle$ [Fig. 4.26 (c2)], three peaks will locate at $\Delta_2 = -\Delta_{G3}/2 \mp \Delta_{G4}/2$ and $\Delta_2 = \Delta_{G3}/2$, respectively.

(1) We next investigate the polarization interference, which affects intensity and line shape the SWM signal. The SWM signal intensity with no dressing field is normalized to be "1" and the intensity above or below "1" baseline means enhancement or suppression of the SWM signal. At the exact resonance ($\Delta_3 = 0$), it is found that the SWM signal intensity is sup-

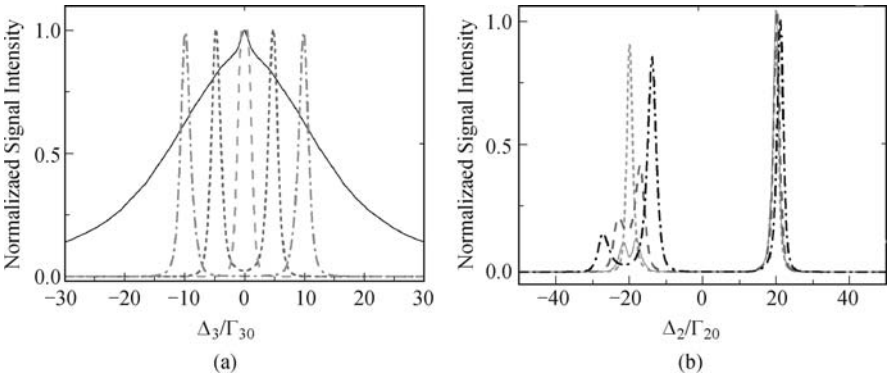

Fig. 4.30. (a) The SWM signal intensity versus Δ_3/Γ_{30} for $G_4/\Gamma_{40} = 0$ (solid curve), $G_4/\Gamma_{40} = 1$ (dashed curve), $G_4/\Gamma_{40} = 5$ (dotted curve) and G_4/Γ_{40}=10 (dot-dashed curve). when $\xi_3 = 0.2, \xi_4 = 0.8$, and $\Gamma_{10}/k_1u = \Gamma_{20}/k_1u = \Gamma_{30}/k_1u = \Gamma_{40}/k_1u = 0.02$. (b) The DDFWM signal intensity versus Δ_2/Γ_{20} for $G_3/\Gamma_{23} = 1$ (dotted curve), $G_3/\Gamma_{23} = 5$ (dashed curve), $G_3/\Gamma_{23} = 10$ (solid curve), when $G_3/\Gamma_{23} = 25$, $\Delta_4/\Gamma_{24} = G_3/\Gamma_{23}$, $\Delta_1/\Gamma_{10} = \Delta_2/\Gamma_{20} = \Delta_3/\Gamma_{23} = 0$ and $\xi_2 = 0.8, \xi_3 = 1.2, \xi_4 = 1.2$. Other parameters are $\Gamma_{10}/k_1u = \Gamma_{20}/k_1u = \Gamma_{23}/k_1u = \Gamma_{24}/k_1u = \Gamma_{30}/k_1u = \Gamma_{40}/k_1u = 0.02$.

pressed when the frequency of the dressing field is scanned across the resonance ($\Delta_4 = 0$) in the homogeneously broadened cases, as shown by the solid curve in Fig. 4.31 (a). From the dressed model viewpoint [Fig. 4.26 (d2)], the suppression of SWM signal is due to the splitting induced by the dressing field, leading to offset of the single-photon ($|0\rangle$ to $|3\rangle$ resonance. When the polarization interference is considered, Fig. 4.31 (b) shows the sharp contrast with that of the homogeneously broadened cases. To study the anomalous behavior, we neglect the polarization interference [dashed curve in Fig. 4.31 (a)], which are consistent with those of the homogeneously broadened cases, proving that the anomalous behavior is due to the polarization interference. This can be understood that the dressing field can suppress the polarization of atoms with $v = 0$ [the inset plot in Fig. 4.31 (b)], leading to a reduction of the degree of the destructive interference. As a result, the SWM signal intensity is enhanced.

Similarly, Fig. 4.32 (a) presents the FWM signal intensity in the homogeneously broadened cases, here the FWM signal intensity with no dressing fields ($G_3 = G_4 = 0$) is normalized to "1". At the exact resonance ($\Delta_2 = 0$), the solid curve in Fig. 4.31 (a) shows that there is suppressed dip at the line center of the profile. Under the suppression condition $\Delta_1 + \Delta_2 - \Delta_3 + \Delta_4 = 0$, such suppressed dip is separated into two small suppressed dips by the outer dressing field E_4. As G_4 is increased, this dip becomes shallow and then splits into two dips. Under the condition $G_4 >> \Gamma_{23}$, we have $\Delta_{G4} \approx 2G_4$. This means that the outer dressing field E_4 dresses the state $|3\rangle$ to create the secondary dressed states $|G_4\pm\rangle$ [Fig. 4.26 (c3)], then the inner dressing field E_3 suppresses the resonant FWM signal directly from $|G_4\pm\rangle$, and induces two

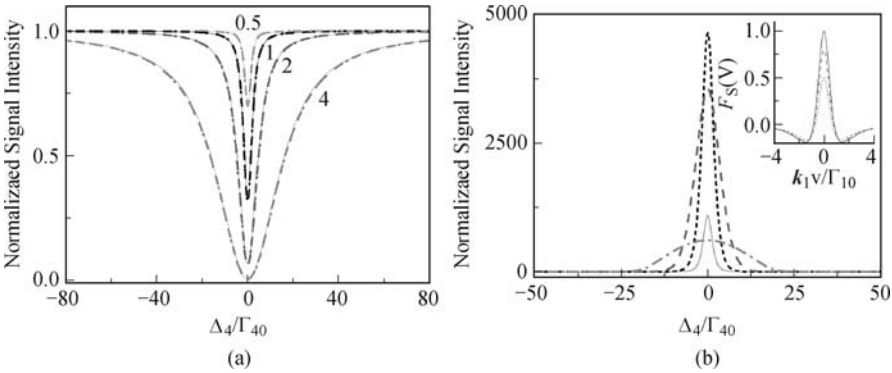

Fig. 4.31. The SWM signal intensity versus Δ_4/Γ_{40} for (a) the homogeneously broadened cases (solid curve) (G_4/Γ_{40} is given near the curves) and when polarization interference is neglected (dashed curves), when G_4/Γ_{40}=0.5 (solid curve), G_4/Γ_{40}=1 (dotted curve), G_4/Γ_{40}=2 (dashed curve), G_4/Γ_{40}= 4 (dot-dashed curve), and Δ_3=0. (b) Doppler broaden cases in long cell. The inset plot show $F'_S(v)$ for G_4/Γ_{40}=0 (solid curve), G_4/Γ_{40}=0.5(dashed curve), G_4/Γ_{40} =1 (dotted curve) when Δ_3=0. The SWM signal intensity with no dressing field is normalized to be 1. Other parameters are $\Delta_1 = \Delta_2$=0, $\xi_3 = 0.2, \xi_2 = 1, \xi_4 = 0.8$ and $\Gamma_{10}/k_1u = \Gamma_{20}/k_1u = \Gamma_{30}/k_1u = \Gamma_{40}/k_1u$ =0.02.

suppressed dips [Fig. 4.32 (a)]. For the Doppler broadened cases, the inner dressing field E_3 suppresses the polarization interference, and enhances the FWM signal intensity [the solid curve in Fig. 4.32 (b)], on the other hand, the outer dressing field E_4 increases the destructive interference [the inset plot in Fig. 4.32 (b)], and results in decreasing of the FWM signal intensity [Fig. 4.32 (b)].

(2) Let us consider the Δ_4 dependence of the SWM spectra for strong dressing fields and large offset. In this case, the SWM signal is enhanced in the homogeneously broadened cases [the solid curves in Fig. 4.33 (a)], which is mainly due to the single-photon ($|0\rangle \rightarrow |G_4+\rangle$) resonance [Fig 4.26 (d2)]. In general, the constructive and destructive interferences between the $|0\rangle \rightarrow |G_4+\rangle$ and $|0\rangle \rightarrow |G_4-\rangle$ SWM channels result in the enhancement of SWM signal. However, such enhancement mainly originates from the dispersion of dressed SWM in the weak dressing field limit [17]. The resonant condition is given by $\Delta_4/\Gamma_{40} = [(G_4/\Gamma_{40})^2 - (\Delta_3/\Gamma_{40})^2]/(\Delta_3/\Gamma_{40})$. Figure 4.33 (b) presents the result in Doppler broadened cases in long cell, and the solid curve in Fig. 4.33 (a) shows the corresponding results when the polarization interference is neglected. We can see that the polarization interference significantly increases the resonant enhancement, so the SWM signal is hugely enhanced, comparing Fig. 4.33 (a) and Fig. 4.33 (b). The significant enhancement of SWM signal in the former is due to the fact that the strong dressing field can not only induce resonance enhancement but also suppress the destructive polarization interference.

Figure 4.34 (a) presents the DDFWM signal intensity versus Δ_3 for the

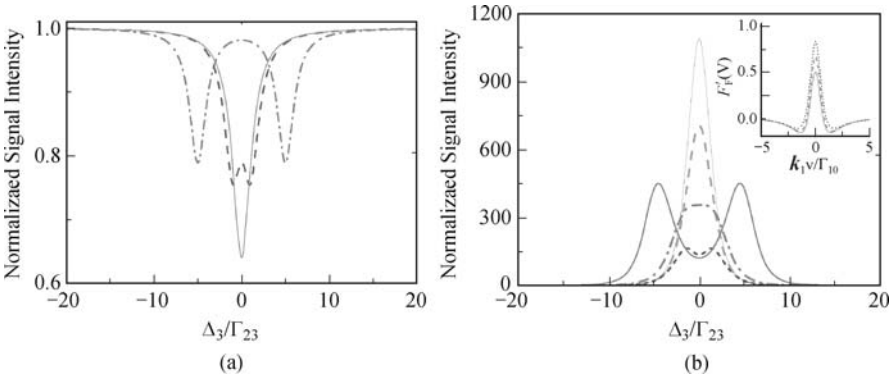

Fig. 4.32. The DDFWM signal intensity versus Δ_3 (a) the homogeneously broadened cases for $G_4/\Gamma_{24} = 0$ (solid curve), $G_4/\Gamma_{24} = 1$ (dashed curve) and $G_4/\Gamma_{24} = 5$ (dotted curve). (b) the Doppler broadened cases in long cell for $G_4/\Gamma_{24} = 0$ (thin solid curve), $G_4/\Gamma_{24} = 0.5$ (dashed curve), G_4/Γ_{24}=1 (dot-dashed curve), $G_4/\Gamma_{24} = 2.5$ (dotted curve), $G_4/\Gamma_{24} = 5$ (solid curve). When $G_3/\Gamma_{23} = 0.5$, $\Delta_1 = \Delta_2 = \Delta_4 = 0$. The insert plot presents $F'_F(v)$ for $G_4/\Gamma_{24} = 0$ (solid curve), $G_4/\Gamma_{24} = 0.5$ (dashed curve), $G_4/\Gamma_{24} = 1$ (dotted curve) when $G_3/\Gamma_{23} = 1$, $\Delta_3 = \Delta_4 = 0$. Other parameters are $\Gamma_{10}/k_1u = \Gamma_{20}/k_1u = \Gamma_{23}/k_1u = \Gamma_{24}/k_1u = 0.02$, $\xi_2 = 0.8$, $\xi_3 = 1.2$, $\xi_4 = 1.2$. The FWM signal intensity with no dressing fields is normalized to be 1.

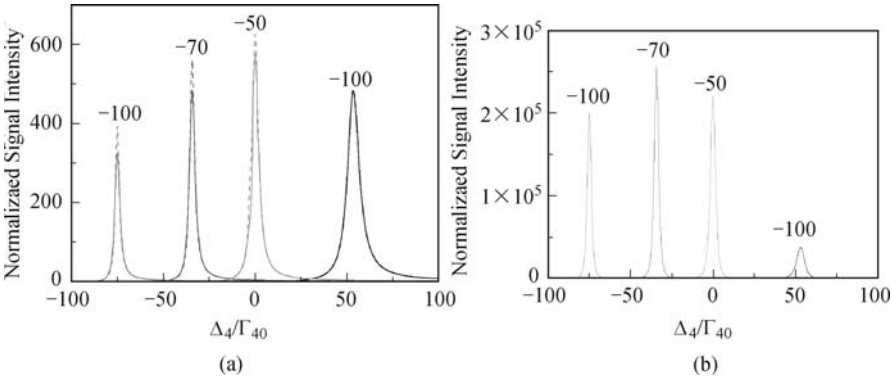

Fig. 4.33. The DSWM signal intensity versus Δ_4/Γ_{40} for (a) homogeneous broadened cases (solid curve), and when the polarization interference is neglected (dashed curve). (b) the Doppler broadened cases in long cell. When $G_4/\Gamma_{40} = 50$, $\xi_3 = 0.2$, $\xi_4 = 1.2$ and $\Gamma_{10}/k_1u = \Gamma_{30}/k_1u = \Gamma_{40}/k_1u = 0.02$, $\Delta_1/\Gamma_{10} = 0$ and the values of Δ_3/Γ_{30} are shown above the peaks. The SWM signal intensity with no dressing field is normalized to be 1.

homogeneously broadened cases. As G_4 is quite large, the outer dressing field E_4 dresses the level $|3\rangle$ and creates the primarily dressed states $|G_4\pm\rangle$ [Fig. 4.26 (c3)]. The inner dressing field E_3, driving the transitions from $|G_4\pm\rangle$ to the ground level $|0\rangle$, creates the secondarily states $|G_3\rangle|G_4\pm\rangle$ from the level $|0\rangle$ [Fig. 4.26 (c4)] to cause the two-photon ($|G_4+\rangle \rightarrow |1\rangle \rightarrow |2\rangle$) reso-

nant, which can cause resonant excitations corresponding to the two enhanced peaks [Fig. 4.33 (a)] if $\omega_1+\omega_2-\omega_3+\omega_4 \approx \Omega_1+\Omega_2-(\Omega_3-\Delta_{G3}/2)+(\Omega_4 \pm \Delta_{G4}/2)$ (i.e. $\Delta_3 \approx \Delta_1+\Delta_2-\Delta_{G3}/2+\Delta_4 \pm \Delta_{G4}/2$. Specially, when the polarization interference is considered, we find that the most profound effect of polarization interference significantly increases the resonant enhancement. For example, when $\Delta_3/\Gamma_{30}=-70$, the FWM signal is enhanced by a factor of 180000 in the Doppler-broadened system [Fig. 4.34 (b)], instead of 350 in the homogeneously broadened cases.

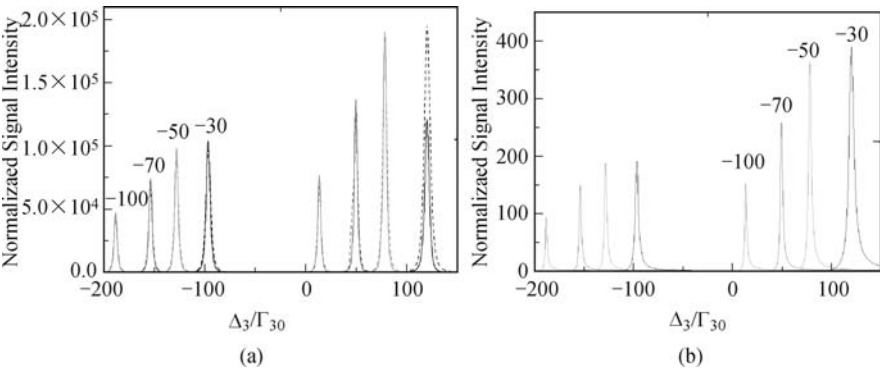

Fig. 4.34. The DDFWM signal intensity versus detuning Δ_3 for (a) the Doppler broadened cases in long cell when $\xi_2=0.8$ (solid curve) and $\xi_2=1.2$ (dashed curve). (b) the homogeneous broadened cases. When $G_3/\Gamma_{23}=50$, $G_4/\Gamma_{24}=100$, $\Delta_1/\Gamma_{10}=\Delta_3/\Gamma_{23}=\Delta_4/\Gamma_{24}=0$, and $\Gamma_{10}/k_1u=\Gamma_{20}/k_1u=\Gamma_{23}/k_1u=\Gamma_{24}/k_1u=0.02$, $\xi_3=1.2$, $\xi_4=1.2$. The values of Δ_2/Γ_{20} are shown above the peaks. Here, the FWM signal intensity with no dressing fields is normalized to be 1.

We have discussed the narrow spectra, AT splitting, suppression and enhancement of MWM in long cell. The MWM signal intensities change drastically due to the polarization interference. And the dressing field can suppress the degree of destructive interference, and result in the enhancement of the MWM signal intensities. In the next Section, we will investigate the degree of polarization interference can be controlled by the cell length. And MWM spectra are modified by the destructive interference in ultra-thin and micrometer cells.

4.5.3 MWM in Ultra-thin and Micrometer Cells

The SWM signal intensity spectra versus $n(L/\lambda)$ is shown in Fig. 4.35 (a). First, we can see that SWM signal intensity varies with λ period, the value of $|S_S|^2$ equals approximately to the value of $|S_{S2}|^2$ when cell length L is short (i.e., $L \leqslant 20\lambda$, corresponding to ultra-thin cell), correspondingly, the "Doppler-broadened term" of $B_S(v)$ can be neglected. When the cell length is increasing, we can see that the oscillation behavior gradually disappears

(corresponding to micrometer cell), and the SWM signal intensity is increasing. When the cell length is long enough, the thin cell terms can be absolutely neglected, $|S_S|^2$ can be approximated to $|S_{S1}|^2$ [the inset plot in Fig. 4.35 (a)].

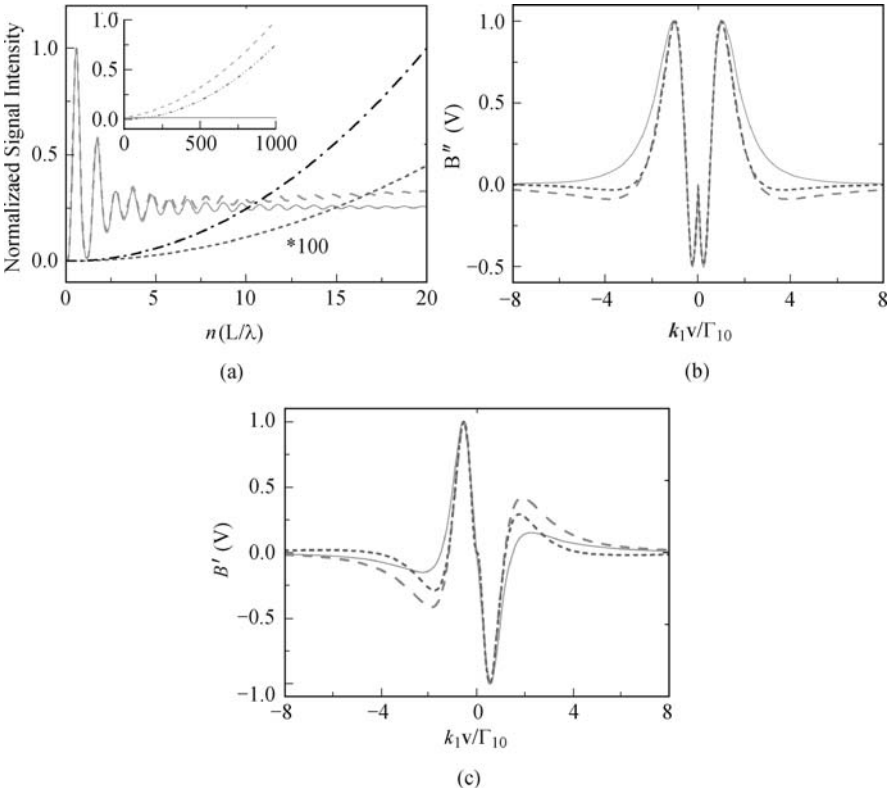

Fig. 4.35. (a) The SWM signal intensity spectra versus $n(L/\lambda)$, $|S_S|^2$ (dashed curve), $|S_{S1}|^2$ (dotted curve), $|S_{S2}|^2$ (solid curve), when polarization interference is neglected (dot-dashed). (b), (c) The imaginary and the real parts when the "Doppler broadened term" is neglected, respectively. $L/\lambda = 0.5$ (solid curves), $L/\lambda = 1$ (dashed curves), $L/\lambda = 1.5$ (dotted curves). Other parameters are $\Delta_1/\Gamma_{10} = \Delta_2/\Gamma_{20} = \Delta_3/\Gamma_{30} = 0$, $\Gamma_{10}/k_1u = \Gamma_{20}/k_1u = \Gamma_{30}/k_1u = 0.02$, $\xi_3 = 0.6$, $G_4/\Gamma_{43} = 0$.

To investigate the oscillation behavior of the SWM signal intensity, we can calculate the imaginary part $B''_S(v)$, real part $B'_S(v)$ of $B_S(v)$, respectively. From Fig. 4.35 (a), since the contribution of "Doppler-broadened term" could be neglected, compared to "thin-cell term", only the latter one is considered in ultra-thin cell. Figure 4.35 (b, c) present the imaginary part $B''_S(v)$ and real part $B'_S(v)$ of $B_S(v)$, respectively. The real part $B'_S(v)$ shows a dispersive line shape, which leads to $\int_{-\infty}^{\infty} \mathrm{d}v W(v) B'_S(v) = 0$; therefore, only

the imaginary part $B''_S(v)$ contributes to the SWM signal. In Fig. 4.35 (b), we can see that there exists the destructive interference in ultra-thin cell. When $L = \lambda/2$, destructive interference is minimum, so the SWM signal intensity shows a maximum value, with periodic revivals at $(2n + 1)\lambda/2$. When $L = \lambda$, destructive interference is maximum, so the SWM signal intensity is minimum. If the polarization interference is neglected (instead of $\int_{-\infty}^{\infty} \mathrm{d}v \exp^{-(v/u)^2} |B_S(v)|^2$), the oscillation behavior of SWM signal intensity vanishes [dot-dashed curve in Fig. 4.35 (a)]. So the oscillation behavior of SWM signal intensity results from the destructive interference.

From Eq. (4.44), the Dicke-narrowing features are determined by both the single-photon and two-photon terms. The single-photon term contributes mainly to the SWM signal intensity, which shows oscillation behavior with a λ period [Fig. 4.35 (a)]. Specifically, when $L = \lambda$, both two-photon and "Doppler broadened term" contribute to the SWM signal.

Similarly, we can obtain the oscillation behavior of the EWM signal intensity (Fig. 4.36). From Eq. (4.45), the single-photon, two-photon, and three-photon terms are all defined as "thin cell terms", which influence the oscillation behavior in common. When $L = 1.5\lambda$, the EWM signal intensity shows a maximum value, with periodic revivals at $(6n + 3)\lambda/2$. While for $L = 3\lambda$, it becomes minimum in ultra-thin cell, as shown in Fig. 4.36. When the cell length L is increasing, the "Doppler-broadened terms" in Eq. (4.45) cannot be neglected. The EWM signal intensity is determined by both the "Doppler broadened terms" and "thin cell terms". And when the cell length is long enough, the EWM signal intensity is determined absolutely by the "Doppler broadened term", as shown in the inserted plot of Fig. 4.36.

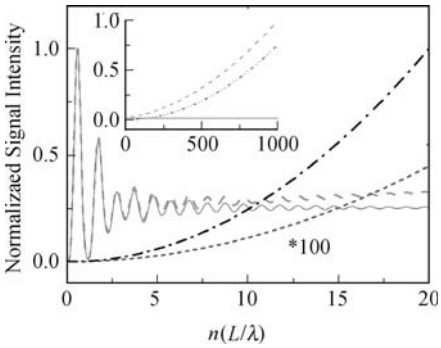

Fig. 4.36. The EWM signal intensity versus L/λ, when $\Delta_4/\Gamma_{14} = 0$. Other parameters are Δ_1/k_1u =10 and $\Delta_3/k_1u = 10, \Delta_2/k_1u = 0, \Gamma_{10}/k_1u = \Gamma_{20}/k_1u = \Gamma_{13}/k_1u = \Gamma_{14}/k_1u = 0.02, \xi_2 = 1, \xi_4 = 1.2$.

We have analyzed the linewidth of the MWM signal spectra in long cell, which are changed due to the destructive interference. In this section, let us compare the line shape of the MWM signal spectra dependence on cell length in ultra-thin and micrometer cells. From Fig. 4.37, we can see that the

minimum values of SWM spectra linewidth are acquired at the cell length $L/\lambda = 1$ and 2. While for $L/\lambda = 0.5$ and 1.5, the linewidth is broadened. In ultra-thin cell, destructive interference is minimum when $L/\lambda = 0.5$ [Fig. 4.35 (c)], the SWM signal linewidth is maximum. But the destructive interference is maximum for $L/\lambda = 1$, so the SWM signal linewidth is minimum. The destructive interference is decreasing at $L/\lambda = 1.5$ while the linewidth is increasing.

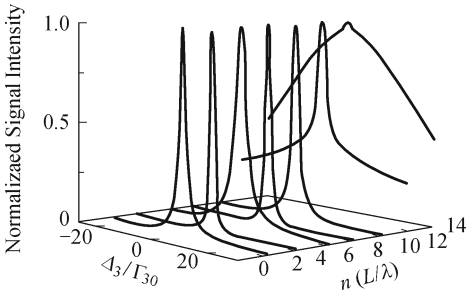

Fig. 4.37. The SWM spectra for $L/\lambda = 0.5$, 1, 1.5, 2, 10, 100, 1000 from 0 to 14, respectively. Other parameters are $\Delta_1/\Gamma_{10} = 0, \Gamma_{10}/k_1u = \Gamma_{20}/k_1u = \Gamma_{30}/k_1u = 0.02, \xi_3 = 0.6$.

When $L/\lambda > 20$, corresponding to micrometer cell, the destructive interference becomes bigger as the cell length is increasing. So, the linewidth of the SWM signal as the cell length is keeping increasing. When L is long enough, the "thin cell terms" can be neglected, only "Doppler- broadened term" is considered, so the SWM spectrum is broadened hugely due to the destructive interference, i.e., $L/\lambda = 1000$ (Fig. 4.37). So, with a larger destructive interference, the SWM signal shows a narrow spectrum, on the contrary the case of long cell.

Similarly, Fig. 4.38 presents the line shape of the EWM signal intensity in ultra-thin, micrometer and long cells. When the cell length L is long enough, only the Doppler-broadened terms in expression $B_E(v)$ are considered, so, the linewidth of EWM spectra is broadened due to the destructive interference in long cell [Figs 4.38 (a) and (b)]. And when $L/\lambda = 10$ and 100, EWM signal spectra show Lorentzian line shape, as shown in Figs. 4.38 (c) and (d), respectively. When $L/\lambda = 1$, corresponding to the ultra-thin cell, the linewidth of EWM spectra is narrow due to Dicke-narrowing features [Fig. 4.38 (e)].

In addition, Figure 4.39 presents the intensity and line shape of the SWM signal in ultra-thin and micrometer cells. As discussed in the previous section, the degree of destructive interference can be controlled by applying a weak dressing field. From Fig. 4.39 (a), when $G_3/\Gamma_{30} = 0.2$, the SWM signal intensity $|S_S|^2$ is approximated to $|S_{S1}|^2$ in ultra-thin cell; the "thin cell terms" can be neglected. More specifically, when the dressing field is increasing, the linewidth of the SWM spectra becomes narrower [Fig. 4.39 (b)], and then

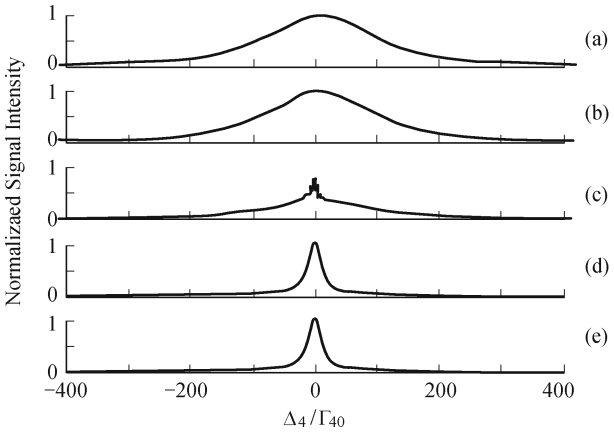

Fig. 4.38. The EWM signal intensity versus Δ_4/Γ_{14} for (a) the Doppler broadened cases in long cell, (b) $L/\lambda = 1000$, (c) $L/\lambda = 100$, (d) $L/\lambda = 100$, (e) $L/\lambda = 10$, (f) $L/\lambda = 1$, when $\xi_3 = 1.2$, $\Delta_1/k_1u = 10$ and $\Delta_3/k_1u = 10$, $\Delta_2/k_1u = 0$, $\Gamma_{10}/k_1u = \Gamma_{20}/k_1u = \Gamma_{13}/k_1u = \Gamma_{14}/k_1u = 0.02$, $\xi_2 = 1$, $\xi_4 = 1.2$.

converts to a single line of homogeneous linewidth in micrometer cell when $G_3/\Gamma_{30} = 0.2$ [the solid curve in Fig. 4.39 (b)]. So, the weak dressing field cannot only control the degree of destructive interference in long cell, but also that in micrometer cell. On the other hand, when $L/\lambda = 0.5$, the weak dressing field cannot change the linewidth of the SWM signal spectra [the inserted plot in Fig. 4.32 (b)] without the destructive interference [Fig. 4.32 (c)].

Next, we investigate the AT splitting of the DSWM signal in ultra-thin and micrometer cells. Due to the polarization interference discussed in previous section, the linewidth of the SWM signal spectrum is much larger than that of the homogeneously broadened cases [solid curve in Fig. 4.40 (a)]. The dressing field can control the degree of destructive interference, so, the linewidth first becomes narrower, and then exhibits Doppler-free AT splitting as the dressing field intensity increases,. And when L/λ =0.5, the SWM spectrum shows Doppler-free AT splitting due to no destructive interference [Fig. 4.40 (b)]. The dressing field can suppress the destructive interference in micrometer cell, and the SWM signal show a Doppler-free AT splitting spectra.

We next investigate suppression and enhancement of the SWM signal intensity in ultra-thin and micrometer cells. At the exact resonance ($\Delta_3 = 0$), it is found that the SWM signal intensity is suppressed [Fig. 4.41 (f)] when the frequency of the dressing field is scanned across the resonance ($\Delta_4 = 0$) in the homogeneously broadened cases in previous section. When $L/\lambda = 0.5$, Fig. 4.41 (e) show the suppressed line shape due to no polarization interference, which is similar to that of the homogeneously broadened cases. On the other hand, we have discussed that the SWM signal intensity is enhanced hugely due to the polarization interference in long cell, and when the cell length is in-

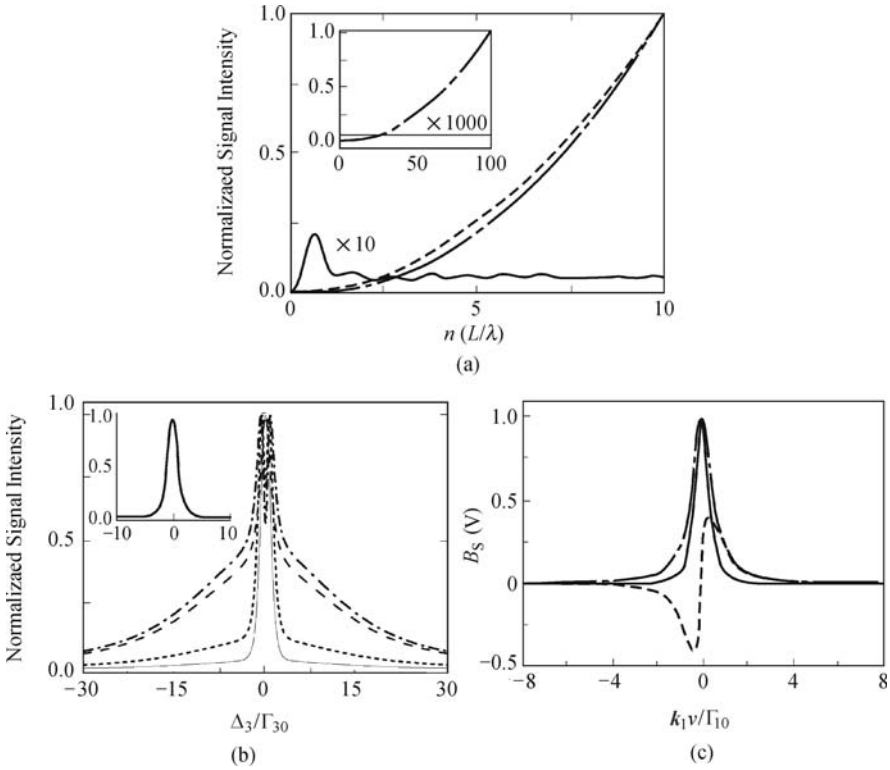

Fig. 4.39. (a) The SWM signal intensity versus $n(L/\lambda)$ for $|S_S|^2$ (dashed curve), $|S_{S1}|^2$ (dotted curve), $|S_{S2}|^2$ (solid curve), when $G_4/\Gamma_{40} = 0.1$. (b) the SWM signal intensity spectra versus Δ_3 for $L/\lambda = 100$, when $G_4/\Gamma_{40} = 0$ (dot-dashed curve), $G_4/\Gamma_{40} = 0.05$ (dashed curve), $G_4/\Gamma_{40} = 0.15$ (dotted curve), $G_4/\Gamma_{40} = 0.2$ (solid curve). The insert plot shows SWM spectra versus Δ_3 for $L/\lambda = 0.5$, when $G_4/\Gamma_{40} = 0$ (solid curve) and G_4/Γ_{40} =0.1 (dotted curve) in ultra-thin cell. (c) The real part $F'_S(v)$ (dashed curves), the imaginary part $F''_S(v)$ (solid curves), and the absolute value $|F_S(v)|$ (dotted curves) in ultra-thin cell, when $L/\lambda = 0.5$. Other parameters are $\Delta_1/\Gamma_{10} = \Delta_2/\Gamma_{20} = \Delta_3/\Gamma_{30} = \Delta_4/\Gamma_{40} = 0$ and $\Gamma_{10}/k_1u = \Gamma_{20}/k_1u = \Gamma_{30}/k_1u = \Gamma_{40}/k_1u = 0.02, \xi_3 = 0.2, \xi_4 = 0.8$.

creasing, the contribution of the thin cell terms in expression $B_S(v)$ becomes weaker, so, the SWM signal intensity is enhanced due to the destructive interference in long cell. So, Figure 4.41 (d) – (b) shows the SWM signal intensity changed from suppression, to semi-suppression and semi-enhancement, and to enhancement, as the cell length keeps increasing.

Similarly, when there is no outer dressing field E_4, the FWM spectra show an enhanced peak due to the polarization interference in long cell, and a suppressed dip in ultra-thin cell. When the outer dressing field E_4 is considered, such enhanced peak or suppressed dip can be separated into two enhanced peaks [Fig. 4.42 (a)] or two suppressed dips [Fig. 4.42 (d)], respectively. When the cell length is increasing, the FWM spectra changes from suppression, to

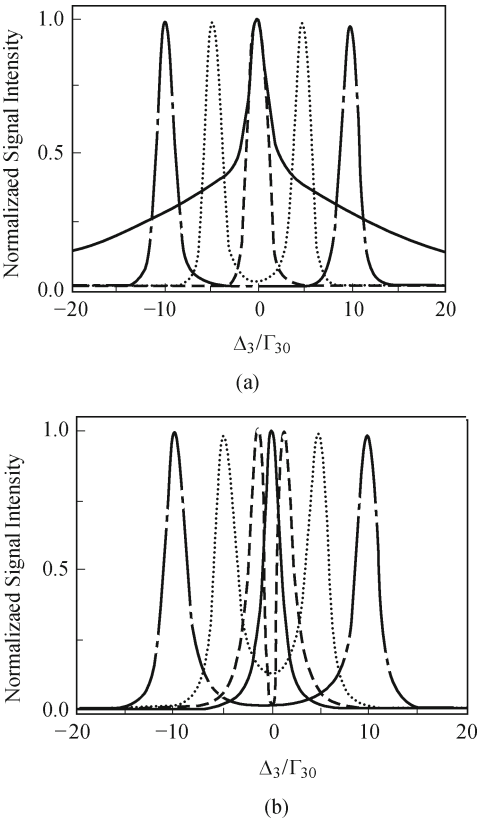

Fig. 4.40. The SWM signal intensity versus Δ_3/Γ_{30} for the dressing field $G_4/\Gamma_{40} = 0$ (solid curve), $G_4/\Gamma_{40} = 1$ (dashed curve), $G_4/\Gamma_{40} = 5$ (dotted curve) and $G_4/\Gamma_{40} = 10$ (dot- dashed curve). (a) $L/\lambda = 100$, (b) $L/\lambda = 1$. Other parameters are $\xi_3 = 0.2, \xi_4 = 0.8$, and $\Gamma_{10}/k_1u = \Gamma_{20}/k_1u = \Gamma_{30}/k_1u = \Gamma_{40}/k_1u = 0.02$.

half-suppression and half-enhancement, and to enhancement.

We discuss the controllable polarization interference in the five-level confined atomic system, the induced polarization is sensitive to the atomic velocity, and interference exists between nonlinear polarizations of atoms with different velocity motions. This interference can have strong impact on the FWM or SWM and EWM spectra. We can sum up the signal intensity of each atom motion [12]. For the former case, there exists polarization interference of atoms with different velocities, while the polarization interference is neglected for the latter case. It is found in Fig. 4.43 that the SWM spectrum is superposition between the case of cold atom sample and the polarization interference neglected in long cell. This indicates that the linewidth of the SWM spectra are due to the polarization interference. We consider interference between the kinds of different velocities in thin cell. The dotted and dot-dashed curves in Fig. 4.43 show that interference between two different

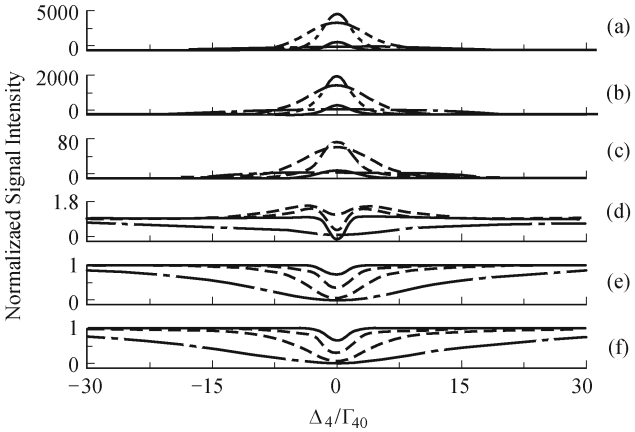

Fig. 4.41. The SWM signal intensity versus Δ_4/Γ_{40} for $G_4/\Gamma_{40} = 0.5$ (solid curve), $G_4/\Gamma_{40} = 1$ (dotted curve), $G_4/\Gamma_{40} = 2$ (dashed curve), $G_4/\Gamma_{40} = 4$ (dot-dashed curve). (a) $L/\lambda = 1000$, (b) $L/\lambda = 100$, (c) L/λ=10, (d) $L/\lambda = 1.5$, (e) $L/\lambda = 0.5$, (f) homogeneous broadened cases. Other parameters are $\Delta_1 = \Delta_2 = \Delta_3$=0, $\xi_3 = 0.2$, $\xi_4 = 0.8$, $\Gamma_{10}/k_1u = \Gamma_{20}/k_1u = \Gamma_{30}/k_1u = \Gamma_{40}/k_1u = 0.02$. The SWM signal intensity with no dressing field is normalized to be 1.

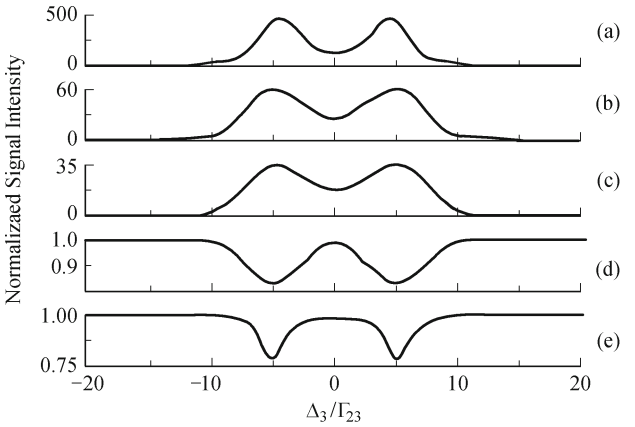

Fig. 4.42. The DDFWM signal intensity versus Δ_3/Γ_{23} for (a) long cell, (b) $L/\lambda = 100$, (c) $L/\lambda = 50$, (d) $L/\lambda = 0.5$, (e) homogeneous broadened cases, when $G_3/\Gamma_{23} = 0.5$, $G_4/\Gamma_{24} = 5$, $\Delta_1/\Gamma_{10} = \Delta_2/\Gamma_{20} = \Delta_3/\Gamma_{23} = \Delta_4/\Gamma_{24}$=0 and $\Gamma_{10}/k_1u = \Gamma_{20}/k_1u = \Gamma_{23}/k_1u = \Gamma_{24}/k_1u = 0.02$, $\xi_2 = 0.8$, $\xi_3 = 1.2$, $\xi_4 = 1.2$. The FWM signal intensity with no dressing fields is normalized to be 1.

velocities is tiny. Specially, when $L/\lambda = 1$, the linewidth of MWM spectrum is narrower due to the enhancement of the coherent transient atomic response [25] than the homogeneous linewidth, as shown by the dashed curve in Fig. 43, this narrow spectral can be used for high precision measurements and metrological standards.

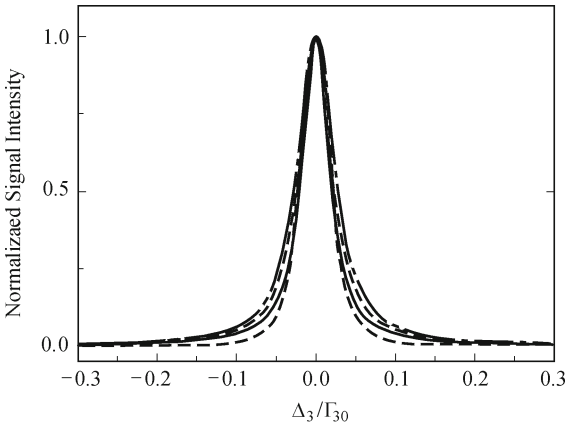

Fig. 4.43. The SWM spectra for Δ_3/Γ_{30}, L/λ=1 (dashed curve), cold atom sample and the polarization interference is neglected in long cell (solid curves), polarization interference is neglected in ultra-thin cell (dotted curve), and polarization interference is neglected between two kinds of different velocity in thin ultra-cell. Other parameters are $\Delta_1/\Gamma_{10} = \Delta_2/\Gamma_{20} = \Delta_3/\Gamma_{30} = 0$, $\Gamma_{10}/k_1u = \Gamma_{20}/k_1u = \Gamma_{30}/k_1u$= 0.02, $\xi_3 = 0.6$, $G_4/\Gamma_{43} = 0$.

4.5.4 Discussion

We have investigated the coexisting FWM, SWM, and EWM in the ultra-thin, micrometer and long cell. Finally, let us compare the line shape of the SWM spectra in several kinds of cases (the homogeneously broadened cases, ultra-thin cell, micrometer cell, long cell and when the polarization interference is neglected in long cell). We can see in Fig. 4.44, that the minimum values of linewidth of the SWM spectrum is achieved at the point of cell length $L/\lambda = 1$ (short dashed curve), and the following case is the homogeneously broadened cases and the neglected polarization interference in long cell (solid curve), and then cell length $L = 0.5\lambda$ (dashed curve). When $L = 100\lambda$, the SWM spectra shows Lorentzian line shape (dotted curve). When L is long enough, the SWM spectrum changes Gaussian line shape (dot-dashed curve). In ultra-thin cell, comparing with the "thin cell terms", the "Doppler-broadened term" is neglected. The linewidth of SWM signal spectra decreases as the destructive interference increasing. When the cell length is increasing, the contribution of the thin cell terms in $B_S(v)$ becomes weaker, and the linewidth of the SWM signal spectra is monotonously increasing. Specifically, when the cell length is long enough, the linewidth of the SWM signal spectra is broadened due to the destructive interference in long cell. In addition, when $B_S(v) = 1$, the linewidth of SWM spectrum is narrower than the homogeneous linewidth, as shown by the dashed curve in Fig. 4.44, such narrow spectrum can be used for high precision measurements and metrological standards.

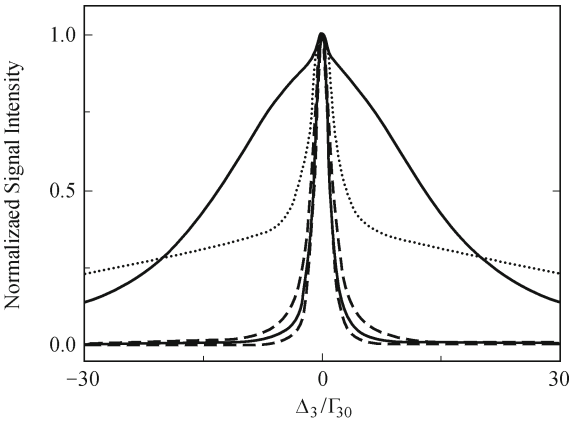

Fig. 4.44. The SWM spectra for Δ_3/Γ_{30}, long cell (dot-dashed curve), $L/\lambda = 100$ (dotted curve), $L/\lambda = 0.5$ (dashed curve), homogeneous broadened cases (solid curve), $L/\lambda = 1$ (short dashed curve), when polarization interference is neglected, the thin solid curves is superposition with the solid curve.

In conclusion, we presented two types of doubly-dressing schemes (i.e., parallel and nested configurations) which can generate co-existing FWM, SWM, and EWM processes in an open five-level system. QI between two FWM, or one FWM and one SWM channels, leads to signal suppression and enhancement. We obtain triple AT splitting in the spectra of FWM signal, quadruple AT splitting in the SWM signal, and two triply splitting in EIT. The spectra of AT splitting, suppression and enhancement of FWM and EWM signals are the superposition of two groups of the different AT splitting peaks. By controlling intensities and frequency offsets of laser fields, these higher-order nonlinear wave-mixing processes can be enhanced and suppressed to obtain desired magnitude of nonlinearities. We also investigate coexisting MWM processes in ultra-thin, micrometer and long cells. The degree of destructive interference can be controlled by the wave vector, dressing field and cell length. Understanding the higher-order multi-channel nonlinear optical processes can help in optimizing these higher-order nonlinear optical processes, which have potential applications in achieving better nonlinear optical materials and opt-electronic devices.

References

[1] Chen C, Yin Y, Elliott D S. Interference between optical-transitions. Phys Rev Lett, 1990 64: 507 – 510.

[2] Dupont E, Corkum P B, Liu H C, et al. Phase-controlled currents in semiconductors. Phys Rev Lett, 1995, 74: 3596 – 3599.

[3] Zhu L, Kleiman V, Li X N, et al. Coherent laser control of the product

distribution obtained in the photoexcitation of hi. Science, 1995, 270: 77 – 80.

[4] Ohmori K, Sato Y, Nikitin E E, et al. High-precision molecular wave-packet interferometry with HgAr dimers. Phys Rev Lett, 2003, 91: 243003.

[5] Gunawardena M , Elliott D S. Atomic homodyne detection of weak atomic transitions. Phys Rev Lett, 2007, 98: 043001.

[6] Yamazaki R, Elliott D S. Observation of the phase lag in the asymmetric photoelectron angular distributions of atomic barium. Phys Rev Lett, 2007, 98: 053001.

[7] Rabitz H, de Vivie-Riedle R, Motzkus M, et al. Chemistry-Whither the future of controlling quantum phenomena. Science, 2000, 288: 824 – 828.

[8] Rice S A, Zhan M. Optical Control of Molecular Dynamics. New York: Wiley, 2000.

[9] Du S W, Wen J M, Rubin M, et al. Four-wave Mixing and biphoton generation in a two-level system. Phys Rev Lett, 2007, 98: 053601.

[10] Zhang Y P , Xiao M. Enhancement of six-wave mixing by atomic coherence in a four-level inverted Y system. Appl Phys Lett, 2007, 90:111104.

[11] Zhang Y P, Brown A W, Xiao M. Opening four-wave mixing and six-wave mixing channels via dual electromagnetically induced transparency windows. Phys Rev Lett, 2007, 99: 123603.

[12] Michinel H, Paz-Alonso M J, Perez-Garcia V M. Turning light into a liquid via atomic coherence. Phys Rev Lett, 2006, 96: 023903.

[13] Udem T, Holzwarth R, Hänsch T W. Optical frequency metrology. Nature, 2002, 416: 233 – 237.

[14] Wen J M, Du S G, Zhang Y P, et al. Nonclassical light generation via a four-level inverted-Y system. Phys Rev A, 2008, 77: 033816.

[15] Hang C, Li Y, Ma L and Huang G X. Three-way entanglement and three-qubit phase gate based on a coherent six-level atomic system. Phys Rev A, 2006, 74: 012319.

[16] Zhang Y P, Khadka U, Anderson B, et al. Temporal and spatial interference between four-wave mixing and six-wave mixing channels. Phys Rev Lett, 2009, 102: 013601.

[17] Gea-Banacloche J, Li Y, Jin S, et al. Electromagnetically Induced Transparency in ladder-type inhomogeneously broadened media: Theory and experiment. Phys Rev A, 1995, 51: 576 – 584.

[18] Boyd R W. Nonlinear Optics. New York: Academic Press, 1992.

[19] Anderson B, Zhang Y P, Khadka U, et al. Spatial interference between four- and six-wave mixing signals. Opt Lett, 2008, 33: 2029 – 2031.

[20] Wang H, Goorskey D, Xiao M. Enhanced Kerr nonlinearity via atomic coherence in a three-level atomic system. Phys Rev Lett, 2001, 87: 073601.

[21] Harris S E. Electromagnetically induced transparency. Phys Today, 1997, 50: 36-42; Xiao M, Li Y, Jin S, et al. Measurement of dispersive properties of electromagnetically induced transparency in rubidium atoms. Phys Rev Lett, 1995, 74: 666 – 669.

[22] Koch M, Feldmann J, Plessen G V, et al. Quantum beats versus polarization Interference-an experimental distinction. Phys Rev Lett, 1992, 69: 3631 – 3634.

[23] DeBeer D, Usadi E, Hartmann S R. Attosecond beats in sodium vapor. Phys Rev Lett, 1998, 60: 1262-1266; Ma H, de Araujo C B. Interference between 3rd-oder and 5th-order polarizations in semiconductor-doped glasses. Phys Rev Lett, 1993 71: 3649 – 3652.

[24] Zhang Y P, de Araujo C B, Eyler E E. Higher-order correlation on polarization beats in Markovian stochastic fields. Phys Rev A, 2001, 63: 043802; Zhang Y P, Gan C L, Song J P, et al. Coherent laser control in attosecond sum-frequency polarization beats using twin noisy driving fields. Phys Rev A, 2005, 71: 023802; Zhang Y P, Gan C L, Li L, et al. Rayleigh-enhanced attosecond sum-frequency polarization beats via twin color-locking noisy lights. Phys Rev A, 2005, 72: 013812.

[25] Fu P M, Mi X, Yu Z H, et al. Ultrafast modulation spectroscopy in a cascade 3-level system. Phys Rev A, 1995, 52: 4867-4870; Sun J, Zuo Z C, Mi X, et al. Two-photon resonant four-wave mixing in a dressed atomic system. Phys Rev A, 2004, 70: 053820; Zhang Y P, Gan C L, Xiao M. Modified two-photon absorption and dispersion of ultrafast third-order polarization beats via twin noisy driving fields. Phys Rev A, 2006, 73: 053801.

[26] Hemmer P R, Katz D P, Donoghue J, et al. Efficient low-intensity optical-phase conjugation based on coherent population trapping in sodium. Opt Lett, 1995, 20: 982-984; Li Y, Xiao M. Enhancement of nondegenerate four-wave mixing based on electromagnetically induced transparency in rubidium atoms. Opt Lett, 1996, 21: 1064-1066; Lu B, Burkett W H, Xiao M. Nondegenerate four-wave mixing in a double-Lambda system under the influence of coherent population trapping. Opt Lett, 1998, 23: 804 – 806.

[27] Kang H, Hernandez G, Zhu Y F. Slow-light six-wave mixing at low light intensities. Phys Rev Lett, 2004, 93: 073601; Zuo Z C, Sun J, Liu X, et al. Generalized n-photon resonant 2n-wave mixing in an (n+1)-level system with phase-conjugate geometry. Phys Rev Lett, 2006, 97: 193904.

[28] Braje D A, Balic V, Goda S, et al. Frequency mixing using electromagnetically induced transparency in cold atoms. Phys Rev Lett, 2004, 93: 183601; Kang H, Hernandez G, Zhang J P, et al. Phase-controlled light switching at low light levels. Phys Rev A, 2006, 73: 011802(R).

[29] Ulness D J, Kirkwood J C, Albrecht A C. Competitive events in fifth order time resolved coherent Raman scattering: Direct versus sequential processes. J Chem Phys,1998, 108: 3897-3902; Ulness D J. On the role of classical field time correlations in noisy light spectroscopy: Color locking and a spectral filter analogy. J Phys Chem A, 2003, 107: 8111-8123; Kirkwood J C, Albrecht A C, Ulness D J. Fifth-order nonlinear Raman processes in molecular liquids using quasi-cw noisy light. I Theory J Chem Phys, 1999, 111: 253 – 271.

[30] Garrett W R, Moore M A, Hart R C, et al. Suppression effects in stimulated hyper-raman emissions and parametric 4-wave-mixing in sodium vapor. Phys Rev A, 1992, 45: 6687 – 6709.

[31] Qi J, Lazarov G, Wang X, et al. Autler-Townes splitting in molecular lithium: Prospects for all-optical alignment of nonpolar molecules. Phys Rev Lett, 1999, 83: 288-291; Qi J, Spano F C, Kirova T, et al. Measurement of transition dipole moments in lithium dimers using electromagnetically induced transparency. Phys Rev Lett, 2002, 88: 173003.

[32] Deng L, Kozuma M, Hagley E W, et al. Opening optical four-wave mixing channels with giant enhancement using ultraslow pump waves. Phys Rev Lett, 2002, 88: 143902.

[33] Fleischhauer M, Imamoglu A, Marangos J P. Electromagnetically induced transparency: optics in coherent media. Rev Mod Phys, 2005, 77: 633 – 673.

[34] Zibrov A S, Matsko A B, Kocharovskaya O, et al. Transporting and time reversing light via atomic coherence. Phys Rev Lett, 2002, 88: 103601; Rostovtsev Y V, Sariyanni Z E, Scully M O. Electromagnetically induced coherent backscattering. Phys Rev Lett, 2006, 97: 113001.

[35] Balic V, Braje D A, Kolchin P, et al. Generation of paired photons with controllable waveforms. Phys Rev Lett, 2005, 94: 183601; Kolchin P, Du S W, Belthangady C, et al. Generation of narrow-bandwidth paired photons: Use of a single driving laser. Phys Rev Lett, 2006, 97: 113602.

[36] Zhang Y P, Anderson B, Xiao M, Coexistence of four-wave, six-wave and eight-wave mixing processes in multi-dressed atomic systems. J Phys B 41 (2008) 045502.

[37] Zhang Y P, Brown A W, Xiao M. Observation of interference between four-wave mixing and six-wave mixing. Opt Lett, 2007, 32: 1120-1122; Zhang Y P, Xiao M. Generalized dressed and doubly-dressed multiwave mixing. Opt Express, 2007, 15: 7182 – 7189.

[38] Wu Y, Saldana J, Zhu Y F. Large enhancement of four-wave mixing by suppression of photon absorption from electromagnetically induced transparency. Phys Rev A, 2003, 67: 013811.

[39] Gea-Banacloche J, Li Y, Jin S, et al. Electromagnetically induced transparency in ladder-type inhomogeneously broadened media - theory and experiment Phys Rev A, 1995, 51: 576 – 584.

[40] Yan M, Rickey E G, Zhu Y F. Observation of doubly dressed states in cold atoms. Phys Rev A, 2001, 64: 013412.

[41] Wilson E A, Manson N B, Wei C. Perturbing an electromagnetically induced transparency in a Lambda system using a low-frequency driving field. II Four-level system. Phys Rev A 72 (2005) 063814.

[42] Li C B, Zhang Y P, Nie Z Q. Controlled Multi-wave mixing via interacting dark states in a five-level system. Opt Commun, 2010, 283: 2918 – 2928.

[43] Drampyan R, Pustelny S, Gawlik W. Electromagnetically induced transparency versus nonlinear Faraday effect: Coherent control of light-beam polarization. Phys Rev A 80, (2009) 033815; Joshi A, Xiao M. Phase gate with a four-level inverted-Y system. Phys Rev A 72 (2005) 062319; Joshi A, Xiao M. Generalized dark-state polaritons for photon memory in multilevel atomic media. Phys Rev A 71 (2005) 041801.

[44] Han Y, Liu Y, Zhang C, et al. Interacting dark states with enhanced nonlinearity in an ideal four-level tripod atomic system. Phys Rev A 77 (2008) 023824; Rebic S, Vitali D, Ottaviani C, et al. Polarization phase gate with a tripod atomic system. Phys Rev A 70 (2004) 032317.

[45] Yang L J, Zhang L S, Li X L, et al. Autler-Townes effect in a strongly driven electromagnetically induced transparency resonance. Phys Rev A 72 (2005) 053801; Wasik G, Gawlik W, Zachorowski J, et al. Competition of dark states: Optical resonances with anomalous magnetic field dependence. Phys Rev A 64 (2001) 051802.

[46] Chalupczak W, Gawlik W, Zachorowski J. 4-wave-mixing in strongly driven 2-level systems. Phys Rev A 49 (1994) 4895 – 4901.

[47] Nie Z Q, Zheng H B, Li P Z, et al. Interacting multiwave mixing in a five-level atomic system. Phys Rev A 77 (2008) 063829.

[48] Zhang Y P, Anderson B, Xiao M. Efficient energy transfer between four-wave-mixing and six-wave-mixing processes via atomic coherence. Phys Rev A, 77, 061801(R) (2008).

[49] Romer R H, Dicke R H. New technique for high-resolution microwave spectroscopy. Phys Rev 99, 532-536 (1955); Firstenberg O, Shuker M, Davidson N, et al. Elimination of the Diffraction of Arbitrary Images Imprinted on Slow Light. Phys Rev Lett 102, 043601 (2009); Ai B, Glassner D S, Knize R J. Enhancement of degenerate 4-wave-mixing by atom-wall collisions in atomic vapors. Phys Rev A 50, 3345-3348 (1994).

[50] Briaudeau S, Bloch D, Ducloy M. Sub-Doppler spectroscopy in a thin film of resonant vapor. Phys Rev A 59, 3723 – 3735 (1999).

[51] Haroche S. Fundamental Systems in Quantum Optics, edited by J. Dalibard, J-M. Raimond, J. Zinn-Justin (North-Holland, 1990).

[52] Dutier G, Saltiel S, Bloch D, et al. Revisiting optical spectroscopy in a thin vapor cell: mixing of reflection and transmission as a Fabry-Perot microcavity effect. J Opt Soc Am B 20, 793-800 (2003); Andreeva C, Cartaleva S, Petrov L, et al. Saturation effects in the sub-Doppler spectroscopy of cesium vapor confined in an extremely thin cell. Phys Rev A 76, 013837 (2007).

[53] Li Y Q, Jin S Z, Xiao M. Observation of an electromagnetically induced change of absorption in multilevel rubidium atoms. Phys Rev A 51, 1754 – 1757 (1995).

[54] Petrosyan D, Malakyan Y P. Electromagnetically induced transparency in a thin vapor film. Phys Rev A 61, 053820 (2000); Failache H, Lenci L, Lezama A, et al. Theoretical study of dark resonances in micrometric thin cells. Phys Rev A 76, 053826 (2007).

[55] Sarkisyan D, Varzhapetyan T, Sarkisyan A, et al. Spectroscopy in an extremely thin vapor cell: Comparing the cell-length dependence in fluorescence and in absorption techniques. Phys Rev A 69, 065802 (2004); Sargsyan A, Sarkisyan D, Papoyan A. Dark-line atomic resonances in a submicron-thin Rb vapor layer. Phys Rev A 73, 033803 (2006); Firstenberg O, Shuker M, Pugatch R, et al. Theory of thermal motion in electromagnetically induced transparency: Effects of diffusion, Doppler broadening, and Dicke and Ramsey narrowing. Phys Rev A 77, 043830 (2008).

[56] Wu Y, Deng L. Ultraslow optical solitons in a cold four-state medium. Phys Rev Lett 93, 143904 (2004).

[57] Zhang Y P, Brown A W, Gan C L, et al. Intermixing between four-wave mixing and six-wave mixing in a four-level atomic system. Phys J B. 40, 3319 – 3329 (2007); Zuo Z C, Sun J, Liu X, et al. Two-photon resonant four-wave mixing in a dressed atomic system: Polarization interference in a Doppler-broadened system. Phys Rev A 75, 023805 (2007).

5 Enhancement and Suppression in Four-Wave Mixing Processes

Interplays between four-wave mixing (FWM) processes in multi-dressed multi-level atomic systems are quite interesting. The generated FWM signal can be selectively enhanced and suppressed via an EIT window. The evolution of dressed effects can be from pure enhancement into pure suppression in the degenerate-FWM processes. On the other hand, since the atomic transitions are very sensitive to the polarization states of the pump and probe beams in multi-Zeeman sub-level atomic systems, the enhancement and suppression of FWM signals are also dependent on the polarization states of the laser beams on real atomic systems (with Zeeman sub-levels). The FWM processes in a multi-Zeeman level atomic system can be enhanced and suppressed by changing the polarization of the pump and probe beams. Different polarization states of the pump and probe beams will act on different transition pathways among the multi-Zeeman levels with different transition strengths, which affect the FWM efficiencies. Understanding the efficiencies of nonlinear wave-mixing processes via laser intensities, frequency detunings, and polarization states in multi-level atomic systems can be very useful in controlling them for various applications, such as coherent quantum control, nonlinear optical spectroscopy, precision measurements, and quantum information processing.

5.1 Interplay Among Multi-dressed Four-Wave Mixing Processes

Under the electromagnetically induced transparency (EIT) condition [1, 2], not only the third-order nonlinear susceptibilities can be resonantly enhanced, but the generated FWM signals can also be allowed to transmit through the resonant atomic medium with little absorption. Enhanced FWM processes due to atomic coherence have been experimentally demonstrated in several multi-level atomic systems [3 – 5]. Interesting effects, such as entangled images in the probe and signal beams in the FWM process [6], phase-controlled light switching at low light level [7], quantum destructive interference in inelastic two-wave mixing [8], and generation of correlated photon pairs [9, 10], have

been experimentally investigated in various coherently-prepared multi-level atomic systems.

Recently, destructive and constructive interferences in a two-level atomic system [9] and competition via atomic coherence in a four-level atomic system [11] with two co-existing FWM processes were studied. In the presence of additional coupling laser fields, more multi-FWM processes are generated, which can be selectively suppressed or enhanced via quantum interference. Also, the Autler-Townes (AT) splitting in triple resonance spectroscopy was reported previously by fluorescence detection [12, 13]. Due to the parametric nature of the FWM process, the generated signal is a coherent radiation.

In this section, experiment of the interplays between different FWM processes in the multi-dressed two-level and V-type three-level atomic systems will be described, as shown in Fig. 5.1 (a), (b). Interesting results, such as mutual suppressing of the two FWM signals, AT splitting of the FWM signal, as well as "inner-dressed" FWM and "outer-dressed" FWM processes, are experimentally investigated. Moreover, a simple method to determine the effective dipole moments of the transitions is shown.

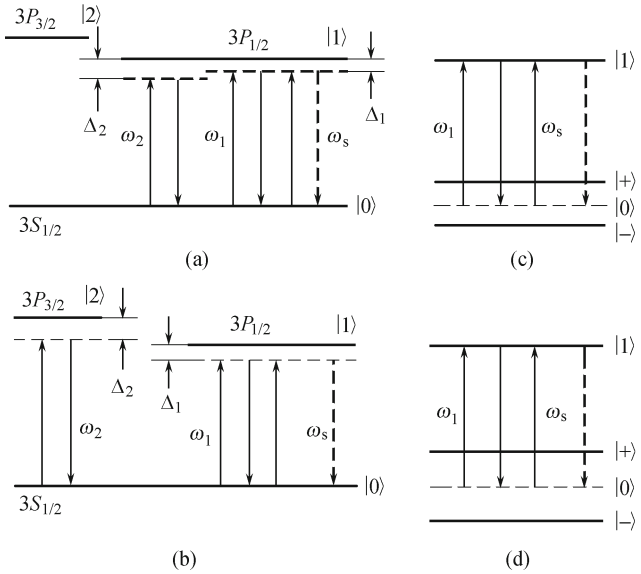

Fig. 5.1. Relevant energy-level schemes in Na atom. (a) "Inner-dressing" case; (b) "Outer-dressing" case; (c) and (d) are the FWM processes in the dressed-state picture.

The two relevant experimental systems are shown in Fig. 5.1 (a), (b). and the pulse laser beams are aligned spatially as shown in Fig. 5.2. Three laser beams come from the same near-transform-limited dye laser (10 Hz rate, 5 ns pulse-width and 0.04 cm^{-1} linewidth) with the same frequency detuning Δ_1. Three energy levels from Na atoms (in heat pipe oven) are involved in the experimental schemes. In Fig. 5.1 (a), energy levels $|0\rangle$ $(3S_{1/2})$

and $|1\rangle$ $(3P_{1/2})$ form the two-level atomic system. Coupling laser beams $\boldsymbol{k}_1$ and $\boldsymbol{k}_1'$ (connecting the transition between $|0\rangle$ to $|1\rangle$) propagate in the opposite direction of the weak probe field $\boldsymbol{k}_3$ (also connecting the transition beween $|0\rangle$ to $|1\rangle$), as shown in Fig. 5.2. The frequency components $\boldsymbol{k}_1$ and $\boldsymbol{k}_1'(\omega_1)$ in beam 1 and beam 2 induce a population grating between states $|0\rangle$ to $|1\rangle$, which is probed by beam 3 with the same frequency ω_1. This is an degenerated-FWM (DFWM) process [Fig. 5.1 (a)] satisfying the phase-matching condition of $\boldsymbol{k}_{s1} = \boldsymbol{k}_3 + \boldsymbol{k}_1 - \boldsymbol{k}_1'$. The signal is detected by a photomultiplier tube (PMT) and a fast gated integrator (gate width of 50 ns). Next, we apply two additional coupling fields $\boldsymbol{k}_2$ and $\boldsymbol{k}_2'$ (one each added onto beam 1 and beam 2, respectively, as shown in Fig. 5.2) with the same frequency detuning Δ_2, which are from another similar dye laser with frequency set at ω_1 to dress the energy levels $|0\rangle$ and $|1\rangle$. We define such energy-level dressing as "inner-dressing". In the presence of the $\boldsymbol{k}_2$ and $\boldsymbol{k}_2'$ frequency components, other three FWM signals are generated with same frequency to have $\boldsymbol{k}_{s2} = \boldsymbol{k}_3 + \boldsymbol{k}_2 - \boldsymbol{k}_2'$, $\boldsymbol{k}_{s2} = \boldsymbol{k}_3 + \boldsymbol{k}_2 - \boldsymbol{k}_2'$, and $\boldsymbol{k}_{s4} = \boldsymbol{k}_3 + \boldsymbol{k}_1 - \boldsymbol{k}_2'$. Therefore, the total signal has contributions from four FWM processes when the five light beams are all turned on, but $\boldsymbol{k}_{\rm s1}$ and $\boldsymbol{k}_{\rm s2}$ are the dominant ones as shown in the inset of Fig. 5.2 (detected by CCD). When the coupling field frequencies of $\boldsymbol{k}_2$ and $\boldsymbol{k}_2'$ are tuned to the $|0\rangle - |2\rangle$ transition (at ω_2), which only dress the energy level $|0\rangle$ for the probe transition of $|0\rangle - |1\rangle$ (and therefore named "outer-dressing"), it forms a V-type three-level system [Fig. 5.1 (b)]. When $\boldsymbol{k}_1, \boldsymbol{k}_1', \boldsymbol{k}_2, \boldsymbol{k}_2'$ and $\boldsymbol{k}_3$ are all turned on simultaneously, a non-DFWM (ND-FWM) process $\boldsymbol{k}_{s2}' = \boldsymbol{k}_3 + \boldsymbol{k}_2 - \boldsymbol{k}_2'$ is generated together with the DFWM $\boldsymbol{k}_{\rm s1}$. These generated FWM signals have the same frequency $\omega_s (= \omega_1)$ and propagate in the same direction.

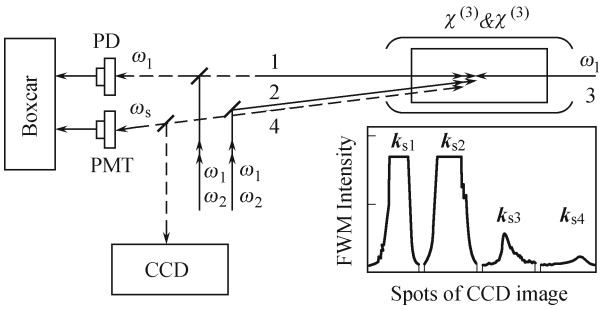

Fig. 5.2. Experimental setup. Inset : measured relative strengths of various FWM signals in the two energy-level systems.

The propagation equation of FWM signals in the oven with Doppler effect is

$$I = I_F - I_A = CN_F^2\mu^2 \int_{v=-\infty}^{v=+\infty} (\mathrm{e}^{-(v/u)^2}|\rho^{(3)}(v)|^2/u\sqrt{\pi})\mathrm{d}v - I_0(1-\mathrm{e}^{-\alpha L})$$

$$= CN_F^2\mu^2 \int_{v=-\infty}^{v=+\infty} \{e^{-(v/u)^2}(|\rho^{(3)}(v)|^2 - K\mathrm{Im}[F(v)])/u\sqrt{\pi}\}\mathrm{d}v, \quad (5.1)$$

where I_F is the total intensity of generated FWM signals; $\rho^{(3)}$ is the density-matrix element of the total FWM signal including pure-FWM $\rho_{10}^{(3)}$ and multi-dressed FWM signals; I_A is the absorption of the FWM signals in the medium. α is the absorption coefficient; $K = I_0 L\boldsymbol{k}_1/CN_F\hbar\varepsilon_0$ and $F = \hbar\varepsilon_0\chi/N_\alpha\mu_1^2$. N_F is the effective atom number and C is a constant; μ is the dipole moment. v is the velocity of the atom due to Doppler effect and u is the most probable velocity. In the presence of I_A, the theory can well explain the interaction and propagation behaviors of FWM signals.

In the experiment, the coupling fields $\boldsymbol{k}_1$ and $\boldsymbol{k}_1'$ (diameter 0.8 mm and power 3 μW) and the probe field $\boldsymbol{k}_3$ (diameter 0.8 mm and power 5 μW) are scanned from 589.3 nm to 589.9 nm ($|0\rangle$ to $|1\rangle$ transition) to generate the DFWM signal $\boldsymbol{k}_{s1}$. The coupling fields $\boldsymbol{k}_2$ and $\boldsymbol{k}_2'$ (diameter 1.1 mm and power 90 μW) are tuned to the line center (589.0 nm) of the $|0\rangle$ to $|2\rangle$ transition, which generate the NDFWM signal $\boldsymbol{k}_{s2}'$ at frequency ω_1 by using one photon each from fields $\boldsymbol{k}_3, \boldsymbol{k}_2$ and $\boldsymbol{k}_2'$. There exist interplay and mutual suppressing between these two FWM signals ($\boldsymbol{k}_{s1}$ and $\boldsymbol{k}_{s2}'$) when five light beams are all on. As can be seen from Fig. 5.3 (a), in the presence of the stronger coupling field $\boldsymbol{k}_2$ or $\boldsymbol{k}_2'$, the DFWM signal $\boldsymbol{k}_{s1}$ (using one photon each from fields $\boldsymbol{k}_3, \boldsymbol{k}_1$ and $\boldsymbol{k}_1'$) is suppressed dramatically [the pentacle and pentagon points in Fig. 5.3 (a)]. Figure 5.3 (b) shows the single-dressing effect of the NDFWM signal $\boldsymbol{k}_{s2}'$ by field $\boldsymbol{k}_1$ or $\boldsymbol{k}_1'$, which is too weak (with Rabi frequencies $G_1 = G_1' = 0.33\ \mathrm{cm}^{-1}$) to affect the NDFWM signal $\boldsymbol{k}_{s2}'$ [the triangle and hexagon points in Fig. 5.3 (b)]. When five laser beams are all on, the individual DFWM signal

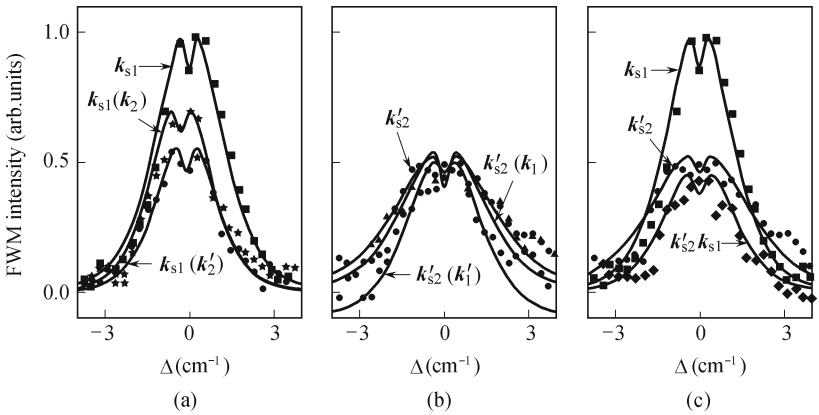

Fig. 5.3. (a) Pure-FWM signal $\boldsymbol{k}_{s1}$ and singly-dressed $\boldsymbol{k}_{s1}$ with $G_2 = G_2' = 1.80\ \mathrm{cm}^{-1}$; (b) Pure-FWM signal $\boldsymbol{k}_{s2}$ and singly-dressed $\boldsymbol{k}_{s2}$ with $G_1 = G_1' = 0.33\ \mathrm{cm}^{-1}$; (c) Pure-FWM signals $\boldsymbol{k}_{s1}, \boldsymbol{k}_{s2}$ and the mutual-dressed signals when all five light beams are on. The scattered points are the experimental results and the solid lines are theoretical results. Adopted from Ref. [13].

$\boldsymbol{k}_{s1}$ [the top curve in Fig. 5.3(c)] and the NDFWM signal [the middle curve in Fig. 5.3(c)] are both significantly suppressed [the lower curve in Fig. 5.3(c)].

One way to explain these effects is by using the dressed-state picture. Both of these mutual dressing processes exist at the same time in the experiment and the two generated FWM signals co-propagate in the same direction, so the total detected FWM signal is proportional to the mod square of $\rho^{(3)}$, where $\rho^{(3)} = \rho_{s1}^{(3)} + \rho_{s2}^{(3)}$. The dressed FWM signals can be written as $\rho_{s1}^{(3)} = -\mathrm{i}\alpha d_2 \mathrm{e}^{\mathrm{i}k_f \cdot r}/d_l^2(\Gamma_{00}d_2 + |G_2 + G_2'|^2)$ and similar result for $\rho_{s2}^{(3)}$, where $G_i = -\mu_i E_i/\hbar$ $(i = 1, 2, 3)$ is the Rabi frequency; Γ_{10}, Γ_{20}, and Γ_{00} are the transverse relaxation rates of the respective energy levels; Δ_i $(i = 1, 2)$ is the frequency detuning; $\alpha = 2G_3G'_1G_1, d_1 = \mathrm{i}\Delta_1 + \Gamma_{10}\sqrt{1 + (4|G_1|^2 + 2|G_3|^2)/\Gamma_{10}^2}$, and $d_2 = \mathrm{i}\Delta_2 + \Gamma_{20}\sqrt{1 + 4|G_2|^2/\Gamma_{20}^2}$ (power broadening is considered). Detail calculations of $\rho_{s1}^{(3)}$ and $\rho_{s2}^{(3)}$ indicate that several interesting physical processes exist in this composite system to show the interplay between these two FWM processes. When the two generated FWM signals overlap in frequency, constructive or destructive interference can result due to the sign change either in $\rho_{s1}^{(3)}$ or $\rho_{s2}^{(3)}$ under certain frequency detuning conditions. However, in the current system the competition between the two coexisting FWM channels is dominated by the contributions from the mutual dressing effect, which can be an order of magnitude lager than the interference effect. After calculating $\rho^{(3)}$ under our experimental conditions and substituting it into Eq. (5.1), excellent agreements are obtained between the theoretical calculations and the experimental data [Fig. 5.3 (c)].

By inserting a tunable attenuation-plate in the path of the coupling beam $\boldsymbol{k}_2'$, we measured the intensities of the generated DFWM signal in $\boldsymbol{k}_{s1}$ under different powers of the dress field $\boldsymbol{k}_2'(\boldsymbol{k}_2$ blocked), as shown in Fig. 5.4 (a). It is clear that the DFWM ($\boldsymbol{k}_{s1}$) intensity is further suppressed as the power of the dress field ($\boldsymbol{k}_2'$) increases [Fig. 5.4 (a)]. At high dress field ($\boldsymbol{k}_2'$) power, the DFWM signal $\boldsymbol{k}_{s1}$ splits within the EIT window with $\Delta_2 = 1.44\ \mathrm{cm}^{-1}$, which is the AT splitting of about $0.9\ \mathrm{cm}^{-1}$, as shown in Fig. 5.4 (b) (circle points). The FWM signal intensity is suppressed when the frequency of the coupling field is scanned across the resonance [see the solid lines in Fig. 5.3 (a), (b)]. Moreover, at the larger power of field $\boldsymbol{k}_2$ or $\boldsymbol{k}_2'(\Delta_2 \neq 0)$, the AT splitting of the DFWM ($\boldsymbol{k}_{s1}$) signal that can be used for measuring the dipole moment12 is observed during scanning the detuning Δ_1 [the solid line of Fig. 5.4 (b)].

Next, let us consider the correlation between the atomic coherence and the conversion efficiency of the NDFWM process $\boldsymbol{k}_{s2}'$ with both $\boldsymbol{k}_1$ and $\boldsymbol{k}_1'$ blocked. Figure 5.4 (c) shows the NDFWM signal $\boldsymbol{k}_{s2}'$ versus the power of the coupling field $\boldsymbol{k}_2'$. As one can see that the perturbation chains of the NDFWM signal $\boldsymbol{k}_{s2}'(\rho_{00}^{(0)} \xrightarrow{-\omega_2} \rho_{02}^{(1)} \xrightarrow{\omega_1} \rho_{12}^{(2)} \xrightarrow{\omega_2} \rho_{10}^{(3)}$ and $\rho_{00}^{(0)} \xrightarrow{\omega_1} \rho_{10}^{(1)} \xrightarrow{-\omega_2} \rho_{12}^{(2)} \xrightarrow{\omega_2} \rho_{10}^{(3)})$ correlate to the two-photon atomic coherence. As one can see in Fig.

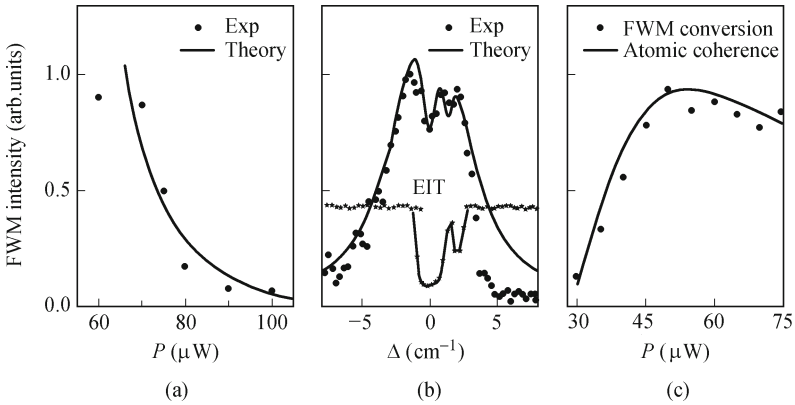

Fig. 5.4. (a) The power dependence of the singly-dressed ($\boldsymbol{k}_2'$) DFWM ($\boldsymbol{k}_{s1}$) signal intensity with $\Delta_2 = 1.44\ \mathrm{cm}^{-1}$; (b) AT-splitting of the DFWM ($\boldsymbol{k}_{s1}$) signal intensity with EIT. $I(\tau, \Delta)$ with $G_2' = 1.89\ \mathrm{cm}^{-1}\Delta_2 = 1.44\ \mathrm{cm}^{-1}$; (c) Relation between the calculated atomic coherence (solid curve) and the measured conversion efficiency of the NDFWM signal (data points) under the power change of field $\boldsymbol{k}_2'$ with $\Delta_2 = 1.44\ \mathrm{cm}^{-1}$.

5.4 (c), there exists a maximum for the calculated atomic coherence (solid curve), which corresponds well to the maximum of the conversion efficiency for the NDFWM signal (dot points). Such comparison indicates that the atomic coherences play a significant role in the enhancements of the FWM processes.

Now, we concentrate on the relation between the "inner-dressing" and "outer-dressing" cases for the DFWM signal $\boldsymbol{k}_{s1}$. First, the dress fields $\boldsymbol{k}_2$ and $\boldsymbol{k}_2'$ (90 μW) are tuned to $|0\rangle - |1\rangle$ transition ("inner-dressing" case). The singly-dressed ($\boldsymbol{k}_2'$) DFWM $\boldsymbol{k}_{s1}$ is obtained (the data points in Fig. 5.5 (a), with $\boldsymbol{k}_2$ blocked). Then, the dress fields $\boldsymbol{k}_2$ and $\boldsymbol{k}_2'$ are tuned to $|0\rangle - |2\rangle$ transition ("outer-dressing" case) with the same experimental conditions and the experiment is repeated [the data points in Fig. 5.5 (b)]. We find that the suppression in the "inner-dressing" case is smaller than in the "outer-dressing" case.

We can analyze this in the dressed-state picture. The perturbed DFWM process can be described by $\rho_{00}^{(0)} \xrightarrow{\omega_1} \rho_{10}^{(1)} \xrightarrow{-\omega_1} \rho_{00}^{(2)} \xrightarrow{\omega_1} \rho_{1\pm}^{(3)}$ (i.e., the ground level $|0\rangle$ is split into $|+\rangle$ and $|-\rangle$). The energy-level splitting of the "inner-dressing" case is smaller than the "outer-dressing" case [see Figs. 5.1 (c) and 5.1 (d)]. From Eq. (5.1), the suppression or enhancement of the DFWM signal is induced by the factor $|G_2'|^2$ in the denominator. In the experimental system, only the effective dipole moment μ can affect the magnitude of the Rabi frequency, which causes the difference in dressing strength. There are twelve degenerate transitions with different Clebseh-Gordan coefficients in $|0\rangle - |1\rangle$ due to Zeeman levels and eighteen in $|0\rangle - |2\rangle$. Since we cannot distinguish then in our experiment, we can only determine the effective (or

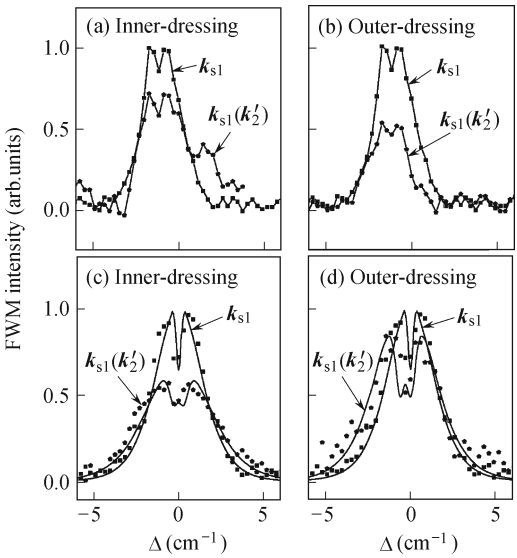

Fig. 5.5. (a) and (b) Comparisons of the "inner-dressed" and the "outer-dressed" DFWM signals ($\boldsymbol{k}_{s1}$) at 589.6 nm ($|0\rangle - |1\rangle$ transition). The curves are fits to the experimental data; (c) and (d) Comparisons of the "inner-dressed" and the "outer-dressed" DFWM signals ($\boldsymbol{k}_{s1}$) at 589.0 nm ($|0\rangle - |2\rangle$ transition). The points are the experimental data and the solid lines are the theoretical results. (a) and (d) $G_2' = 1.27$ cm^{-1} with $\Delta_2 = 1.44$ cm^{-1}; (b) and (c) $G_2' = 1.80$ cm^{-1}.

macroscopic) dipole moments for these transitions.

In order to verify this idea, the coupling fields $\boldsymbol{k}_1, \boldsymbol{k}_1'$ and the probe field $\boldsymbol{k}_3$ (for generating the DFWM signal $\boldsymbol{k}_{s1}$) are tuned from $|0\rangle - |1\rangle$ to $|0\rangle - |2\rangle$ transition. So, the roles of the "inner-dressing" and "outer-dressing" are exchanged. We repeated the experiment and obtained the results as shown in Fig. 5.5 (c), (d). In this case, the suppression effect for the "inner-dressing" case should be larger than for the "outer-dressing" case. Comparing the results in Fig. 5.5 (c), (d), the observations agree well with the theoretical prediction.

In order to obtain agreements with the experimental spectra in Figs. 5.5 (c) and 5.5 (d), the Rabi frequency of the dress field (G_2') is adjusted until the peak-to-peak value matches the experimental data. From such fitting to the experimental data, the relative μ values can be determined experimentally from the fitted Rabi frequencies. From the above experiment, the dipole moments are determined to be: $\mu_{20} = 2.99(24) \times 10^{-29} C \cdot \mathrm{m}$ (for the $|0\rangle - |2\rangle$ transition) and $\mu_{10} = 2.11(24) \times 10^{-29} C \cdot \mathrm{m}$ (for the $|0\rangle - |1\rangle$ transition), which agree well with their real values [14]. Such, this method can be used to measure the unknown effective dipole moments of atoms and molecules. Compared to the method used in Ref. [12], the FWM process is a coherence phenomenon, and the generated signal is a coherent radiation and therefore can be detected easily. More importantly, under the same experimental condi-

tions in different energy level systems, the dressing effects strongly depend on the dipole moments of the transitions, which provides an easy and qualitative way to determine the effective dipole moments of different transitions.

5.2 Observation of Enhancement and Suppression of Four-Wave Mixing Processes

In this section, the experimental studies of enhancement and suppression between two FWM processes in a multi-dressed ladder-type three-level atomic system are described, as shown in Fig. 5.6 (a). The experimental data clearly show the evolutions of the enhancement and suppression, from pure enhancement to partial enhancement/suppression, and then to pure suppression at resonance, which are in good agreement with theoretically calculated results. There also exist interesting interplays between these two FWM processes due to induced atomic coherence in this system. In addition, the power dependences of enhancement and suppression are experimentally studied.

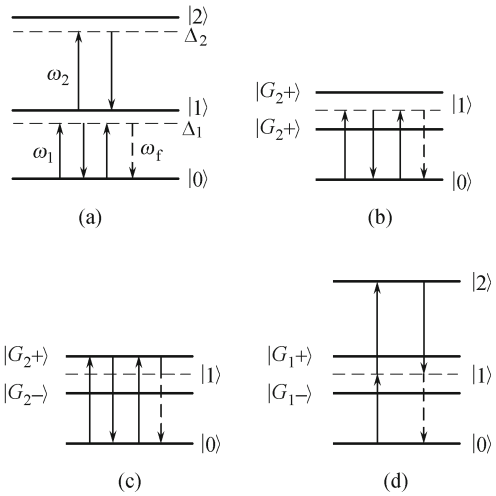

Fig. 5.6. (a) The diagram of relevant Na energy levels. (b) and (c) The dressed-state pictures of the suppression and enhancement of FWM E_1 for the two-level system, respectively. (d) The dressed-state picture of the suppression of FWM E_{f2} for the ladder system.

The experiment is carried out involving three energy levels [Fig. 5.6 (a)]. The pulse laser beams are aligned spatially, as shown in Fig. 5.7. For the transition between $|0\rangle(3S_{1/2})$ to $|1\rangle(3P_{1/2})$, the coupling laser beam $E_1(\omega_1, \boldsymbol{k}_1,$ and $G_1)$ together with $E'(\omega_1, \boldsymbol{k}'_1, G'_1)$ having a small angle (0.3°) propagates in the opposite direction of the weak probe field $E_3(\omega_1, \boldsymbol{k}_3, G_3)$. These three laser beams are with the same frequency detuning $\Delta_1 = \omega_{10} - \omega_1$, where ω_{10}

is the transition frequency between $|0\rangle$ and $|1\rangle$. The frequency components of E_1 and $E_1'(\omega_1)$ in beam 1 and beam 2 induce a population grating between states $|0\rangle$ to $|1\rangle$, which is probed by beam 3 (E_3) with the same frequency ω_1. This interaction generates a degenerate-FWM (DFWM) signal E_{f1} [Fig. 5.6 (a)] satisfying the phase-matching condition of $\boldsymbol{k}_{f1} = \boldsymbol{k}_3 + \boldsymbol{k}_1 - \boldsymbol{k}_1'$. Then, two additional coupling fields $E_2(\omega_2, \boldsymbol{k}_2, G_2)$ and $E_2'(\omega_2, \boldsymbol{k}', G_2')$ are applied as scanning fields connecting the transition between $|1\rangle$ and a third level $|2\rangle$ ($4D_{3/2,5/2}$) with the same frequency detuning $\Delta_2 (= \omega_{21} - \omega_2)$. The laser field E_2 is added onto beam 1 and E'_2 propagates in another plane (xz) perpendicular to the yz plane with a small angle from E_1, as shown in the inset of Fig. 5.7. E_2 and E_2' are from another similar dye laser with its frequency set at ω_2 to dress the energy level $|1\rangle$ [Fig. 5.6 (b)]. The interaction between E_2, E_2', and E_3 generates a non-DFWM (NDFWM) signal E_{f2} satisfying $\boldsymbol{k}_{f2} = \boldsymbol{k}_3 + \boldsymbol{k}_2 - \boldsymbol{k}'$ (for the subsystem $|0\rangle \rightarrow |1\rangle \rightarrow |2\rangle$).

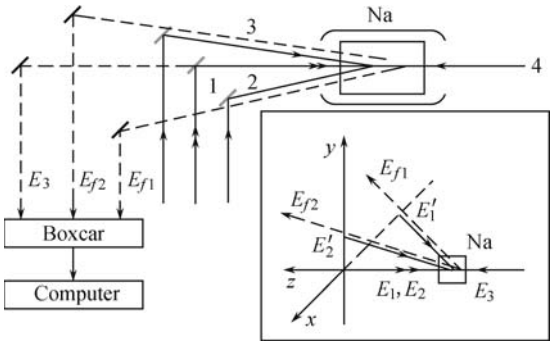

Fig. 5.7. The scheme of the experiment. Inset gives the spatial alignments of the incident beams.

If when E_1, E_1', E_2, E_2', and E_3 are all turned on simultaneously, the DFWM process E_{f1} and NDFWM process E_{f2} are generated simultaneously and there exist interplays between these two FWM signals [13, 15]. In addition, both of these two generated FWM signals are in the same EIT window formed by the ladder system ($|0\rangle \rightarrow |1\rangle \rightarrow |2\rangle$) in the two-photon Doppler-free configuration [2, 5]. These generated FWM signals have the same frequency $\omega_f (= \omega_1)$ and propagate in two directions (i.e., strictly counter-propagating E_1' and approximately counter-propagating E_2', respectively) detected by a photomultiplier tube and a fast gated integrator (gate width of 200 ns), respectively.

In order to better understand the experimental results, we calculate the two interacting FWM processes. First, we consider the DFWM process E_{f1} dressed (or perturbed) by the coupling laser beams E_2, E_2' [Fig. 5.6 (c)]. There are two transition paths for generating FWM, which are described by the dressed perturbation chains [15 – 22]:

$$\rho_{00}^{(0)} \xrightarrow{(E_1)^*} \rho_{\pm 0}^{(1)} \xrightarrow{(E_1')^*} \rho_{00}^{(2)} \xrightarrow{E_3} \rho_{\pm 0}^{(3)}, \tag{5.2}$$

$$\rho_{00}^{(0)} \xrightarrow{(E_1')^*} (\rho_{\pm 0}^{(1)})^* \xrightarrow{E_1} \rho_{00}^{(2)} \xrightarrow{E_3} \rho_{\pm 0}^{(3)}, \tag{5.3}$$

$$\rho_{00}^{(0)} \xrightarrow{E_1} \rho_{\pm 0}^{(1)} \xrightarrow{(E_1')^*} \rho_{\pm\pm}^{(2)} \xrightarrow{E_3} \rho_{\pm 0}^{(3)}, \tag{5.4}$$

$$\rho_{00}^{(0)} \xrightarrow{(E_1')^*} (\rho_{\pm 0}^{(1)})^* \xrightarrow{E_1} \rho_{\pm\pm}^{(2)} \xrightarrow{E_3} \rho_{\pm 0}^{(3)}. \tag{5.5}$$

The solved expressions of the corresponding FWM processes are: $\rho_a^{(3)} = -G_A/(\Gamma_{00}C_1^2), \rho_a^{(3)} = -G_A/(\Gamma_{00}C_1^2), \rho_b^{(3)} = -G_A/(\Gamma_{00}C_1C_1^*), \rho_c^{(3)} = -G_A/(C_1^2C_2)$, and $\rho_d^{(3)} = -G_A/(C_1C_1^*C_2)$, where $G_A = G_1^*G_1G_3, C_1 = d_1 + A_1, C_2 = \Gamma_{11} + A_2 + A_2^*, A_1 = |G_2|^2/d_2, A_2 = |G_2|^2/(\mathrm{i}\Delta_2 + \Gamma_{21})d_1 = \mathrm{i}\Delta_1 + \Gamma_{10}, d_2 = \mathrm{i}(\Delta_2 + \Delta_1) + \Gamma_{20}$. $G_i = -\mu_i E_i/\hbar (i = 1, 2, 3)$ is the Rabi frequency; Γ_{10}, Γ_{20} and Γ_{00} are the transverse relaxation rates. The total contribution is from the sum of the four chains:

$$\rho_{DFWM}^{(3)} = \rho_a^{(3)} + \rho_b^{(3)} + \rho_c^{(3)} + \rho_d^{(3)}. \tag{5.6}$$

Similarly, for the ladder-type three-level system [Fig. 5.6 (d)], the dressed perturbation chain is: (e) $\rho_{00} \xrightarrow{E_3} \rho_{\pm 0} \xrightarrow{E_2} \rho_{20} \xrightarrow{(E_2')^*} \rho_{\pm 0}$. The third-order nonlinear process of the NDFWM E_{f2} can be described by

$$\rho_{NDFWM}^{(3)} = -G_2^*G_2G_3/[d_2(d_1 + B_3)^2], \tag{5.7}$$

where $B_3 = |G_1|^2/\Gamma_{11}$. From Eqs. (5.6) and (5.7), one can see that the two FWM processes are closely connected by dressed effects. By adjusting the frequency detuning Δ_1 and scanning the dressed field detuning Δ_2, many interesting phenomena can be obtained.

We first set Δ_1 at one point and scan Δ_2. Evolution from suppression to enhancement is observed as shown in Fig. 5.8. The probe field is changed from high to low frequency side. As frequency detuning goes from $\Delta_1 < 0$ to zero, the DFWM signal E_{f1} is enhanced gradually to the maximum value [right side of Fig. 5.8 (a)], which is an enhanced process. Then, it undergoes a partial enhancement/suppression [Fig. 5.8 (b)], until the FWM signal is purely suppressed at the resonant point [Fig. 5.9 (b) and the upper curves of Fig. 5.9 (a)]. When Δ_1 changes to be positive, it shows a symmetric process [i.e., a partial suppression/enhancement in Fig. 5.8 (c), and a pure enhanced process in the left side of Fig. 5.8 (a)]. In fact, we observed the evolution figures of theoretical plots of suppression and enhancement showing in inset of Fig. 5.8 (a), (d), (e). The probe field is changed from high frequency to low frequency. As detuning parameter $\Delta_1 < 0$ trends to zero, DFWM signal is enhanced gradually to the maximum [inset of Fig. 5.8 (a)] and then experience a half enhancement and half suppression, until purely suppressed at resonant point [Fig. 5.8 (d)]. Then we have the detuning parameter $\Delta_1 > 0$ which is a symmetric process to above [Fig. 5.8 (e)].

One can explain these observed effects by using the dressed-state picture. Let us first consider the case of large G_2 (e.g., 15.7 GHz). The dressing field

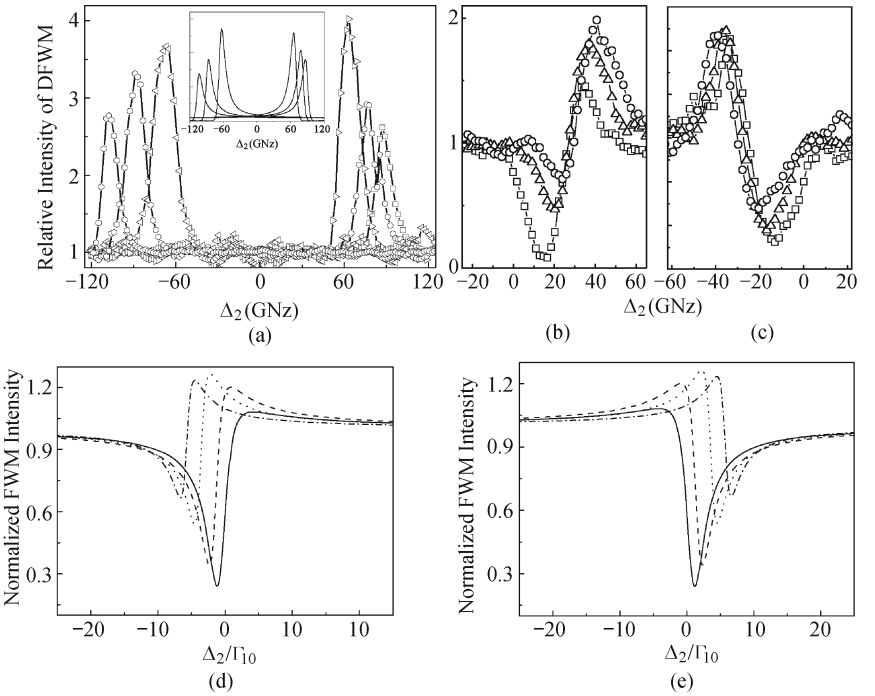

Fig. 5.8. The evolution of the dressed effects for different Δ_1 values: (a) $\Delta_1 = -101$ GHz (squares), -84.3 GHz (circles), -67 GHz (triangles), 71.3 GHz (reverse triangles), 88.6 GHz (pentagons), 105 GHz (hexagons) from right to left. Inset: theoretical plots corresponding to the experimental parameters. (b) $\Delta_1 = -30.3$ GHz (squares), -21.6 GHz (triangles) and -13 GHz (circles) with (d) theoretical plots. (c) $\Delta_1 = 29.3$ GHz (squares), 38 GHz (triangles) and 42.2 GHz (circles) with (e) theoretical plots.

couples the transition $|2\rangle$ to $|1\rangle$ and creates the dressed states $|G_2\pm\rangle$ [Fig. 5.5 (c)]. Therefore, the DFWM signal $E_{\rm f1}$ for a large one-photon detuning is extremely small when $G_2 = 0$, the strong dressing field can cause resonant excitation for one of the dressed states if the condition $\omega_1+\omega_2 = \omega_{10}+(\omega_{21}\pm\Delta_{G2})$ (i.e., $\Delta_1+\Delta_2\pm\Delta_{G2} = 0$) is satisfied [16], where Δ_{G2} is the splitting level relative to the original position of the state $|1\rangle$ by the dressing field E_2 or E_2', so that $\Delta_2 = (G_2^2-\Delta_1^2)/\Delta_1$. For example, the DFWM signal $E_{\rm f1}$ is strongly enhanced in the presence of dressing field when $\Delta_1 = -67$ GHz [Fig. 5.8 (a)], which is mainly due to the one-photon ($|0\rangle \rightarrow |G_2+\rangle$) resonance. Thus, initially, Δ_1 for $E_{\rm f1}$ is very large, so the dressed effect only gives the enhancement. As Δ_1 goes towards zero, the suppression effect gets into play gradually due to the dressed states $|G_2\pm\rangle$ [Fig. 5.5 (b)]. In this case, when the frequency changes from high to low values it results in a suppression for the DFWM signal first and then an enhancement. From the data, we can deduce the condition for the suppressed-dip to be $\omega_1+\omega_2 = \omega_{10}+\omega_{21}$, (i.e. $\Delta_1+\Delta_2 = 0$). At the $\Delta_1 = 0$ point (resonant case), only suppression

effect exists [Fig. 5.5 (b)]. For the $\Delta_1 > 0$ part, it has a symmetric evolution between the enhancement and suppression effects, as shown in Fig. 5.8 (c).

Next, an appropriate Δ_1 value is chosen at the position of either enhanced or suppressed DFWM process E_{f1} (i.e., the peak or dip in Fig. 5.8). The dressing field E_2 is applied to create the dressed state $|G_2\pm\rangle$. First, we set $E_{1,3}$ at a large detuning ($\Delta_1 = -55.8$ GHz), which leads to the one-photon ($|0\rangle \rightarrow |G_2+\rangle$) resonance [Fig. 5.6 (c)] resulting in an enhanced DFWM E_{f1} signal. Under this condition, we measure the power dependence of the enhanced DFWM process by scanning Δ_2 [Fig. 5.9 (a)]. The enhancement effect gets bigger and bigger as the dressing field power increases, until it saturates at certain point, as shown in the inset of Fig. 5.9 (a). Figure 5.9 (b) shows that there is a suppressed dip at the line center, which indicates that at exact one-photon resonance ($\Delta_1 = 0$), the DFWM signal intensity is greatly suppressed when scanning the dressing field E_2 across its resonance ($\Delta_2 = 0$). As expected, the DFWM signal intensity decreases gradually as the coupling intensity increases due to the dressed effect [the inset plot in Fig. 5.9 (b)], which is well described by the theoretical curve (solid line).

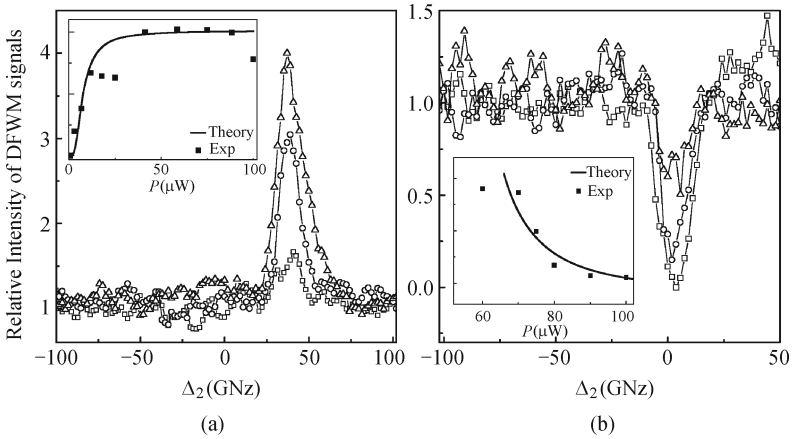

Fig. 5.9. (a) Measured enhanced DFWM signal spectra for different coupling field (E_2) intensities, 17.4 μW (squares), 34.2 μW (circles) and 64.3 μW (triangles). Inset: the experimental data and theoretical curve of the power dependence of the enhanced FWM signal, $E_{p1}\Delta_1 = -55.8$ GHz. (b) Measured suppressed DFWM signal spectra for different coupling field (E_2) intensities, 81.8 μW (squares), 72.7 μW (circles) and 54.6 μW (triangles). Inset: the experimental data and theoretical curve of the power dependence of the suppressed FWM signal, $E_{p1}\Delta_1 = 0$ GHz.

Finally, we concentrate on the interactions between these two FWM processes. Figure 5.10 (a) shows mutual suppression, where the upper curves are the DFWM signal E_{f1}, while the lower curves are the NDFWM signal E_{f2}. Figure 5.10 (b1) depicts the relevant DFWM signal E_{f1} and Fig. 5.10 (b2) plots the NDFWM signal E_{f2}. As shown in Fig. 5.10 (a), different suppressed FWM signals can be seen by blocking different laser beams. The square points

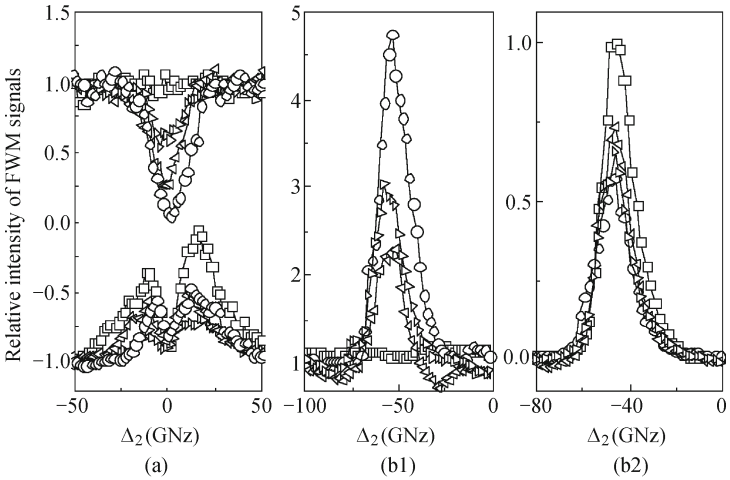

Fig. 5.10. Mutual suppression between the DFWM signal E_{f1} and the NDFWM signal E_{f2}. (a) Upper curves: pure-DFWM signal (squares), singly-dressed DFWM signal (triangles), doubly-dressed DFWM (circles). Lower curves: pure-NDFWM signal (squares), singly-dressed NDFWM signal (triangles), and doubly-dressed NDFWM signal (circles), $\Delta_1 = 0$ GHz. (b) Interplays between (b1) DFWM (E_{f1}) and (b2) NDFWM (E_{f2}) processes. The conditions are the same as in (a), $\Delta_1 = -45.5$ GHz. Adopted from Ref. [15].

are pure DFWM signal case. When the additional laser beam E_2 or E_2' is turned on, suppressed DFWM signals are obtained (triangle points in upper curves). Using the same procedure, we obtain the suppressed NDFWM signals (triangle points in lower curves) comparing to the pure NDFWM signal [square points in lower group]. When all five laser beams are turned on, the two FWM processes couple to each other with mutual suppressions, as shown by the circle points both in upper and lower groups of curves in Fig. 5.10 (a). Then, we set Δ_1 at a point with enhanced DFWM and obtain a group of curves showing interplays between these two FWM processes, where the DFWM signal E_{f1} is enhanced while the NDFWM signal E_{f2} is suppressed by scanning Δ_2. Similarly, comparing to the pure DFWM signal E_{f1} [square points in Fig. 5.10 (b1)], the dressed DFWM signal E_{f1} is enhanced by blocking different laser beams [triangle points and circle points in Fig. 5.10 (b1)]. Other than the DFWM process, the NDFWM process [square points in Fig. 5.10 (b2)] is suppressed by the coupling fields E_1, E_1' [triangle points and circle points in Fig. 5.10 (b2)]. One can explain these observed phenomena by using dressed-state picture [see Figs. 5.6 (c) and 5.5 (d)]. For DFWM signal E_{f1}, the one-photon ($|0\rangle \rightarrow |G_2+\rangle$) resonant condition is satisfied in enhancing E_{f1} in Fig. 5.6 (c). At the same time, for the NDFWM signal E_{f2} in Fig. 5.6 (d), the state $|1\rangle$ is dressed by the coupling fields E_1 and E_1', and separated into the dressed states $|G_1\pm\rangle$, which always suppress E_{p1} due to destructive interference.

5.3 Controlling Enhancement and Suppression of Four-Wave Mixing via Polarized Light

Polarizations of the involved laser beams can play important roles in electromagnetically induced transparency (EIT) [23] and four-wave mixing (FWM) processes [24, 25] when multi-Zeeman energy levels are involved in the atomic systems [26, 27]. Several previous experimental and theoretical studies have shown that EIT and FWM processes can be effectively controlled by selecting different transitions among Zeeman sublevels via the polarization states of the laser beams [23, 25, 26]. Also, additional dressing laser beams can modify FWM efficiencies in multi-level atomic systems. In our previous experiments, we have shown the enhancement and suppression of FWM by controlling the dressing laser beams in the multi-level atomic systems [15].

In this section, we describe an experimental demonstration that the degenerate FWM (DFWM) caused by two strong pumping beams and a weak probe beam in a two-level Zeeman-degenerate atomic system can be modified by the polarization states of the two pumping beams, and by an additional dressing beam interacting with an adjacent atomic transition, as shown in Fig. 5.11 (a). The DFWM process is enhanced or suppressed due to the combined polarization and dressing effects. The polarizations of the pumping beams select the transitions among different Zeeman levels, which usually have different transition strengths [25], and the dressing beam determines the effective frequency detunings of the probe beam from the multi-Zeeman levels. The experimental observations clearly show the evolution of the DFWM enhancement and suppression versus pump field polarizations.

5.3.1 Theoretical Model and Analysis

Three energy levels are shown in Fig. 5.11 (a). The pulse laser beams are spatially aligned as shown in Fig. 5.11 (b). The pumping laser beams $E_1(\omega_1, \boldsymbol{k}_1,$ and Rabi frequency $G_{g,M})$ and $E_1'(\omega_1, \boldsymbol{k}_1', G_{g,M}')$ (having a small angle of 0.3°) are tuned to the transition $|0\rangle(3S_{1/2})$ to $|1\rangle(3P_{3/2})$, and E_1 propagates in the opposite direction of the weak probe field $E_3(\omega_1, \boldsymbol{k}_3, G_{g,M})$, where M denotes the magnetic quantum number of the lower state in transition. This interaction generates a DFWM signal E_f [Fig. 5.11 (a)] satisfying the phase-matching condition [11]: $\boldsymbol{k}_f = \boldsymbol{k}_3 + \boldsymbol{k}_1 - \boldsymbol{k}_1'$.

Then, an additional dressing field $E_2(\omega_2, \boldsymbol{k}_2, G_{d,M})$ is applied to the transition between $|1\rangle$ and the third level $|2\rangle(4D_{3/2,5/2})$ with a frequency detuning $\Delta_2 (= \omega_{21} - \omega_2)$. E_2 is from another similar dye laser. Two quarter-wave plates (QWP) are used for changing the polarizations of the pumping fields $\boldsymbol{k}_1, \boldsymbol{k}_1'$. The generated DFWM signal is split into two equal components by a 50% beam splitter before detection, one is detected directly (denoted as I_T) and

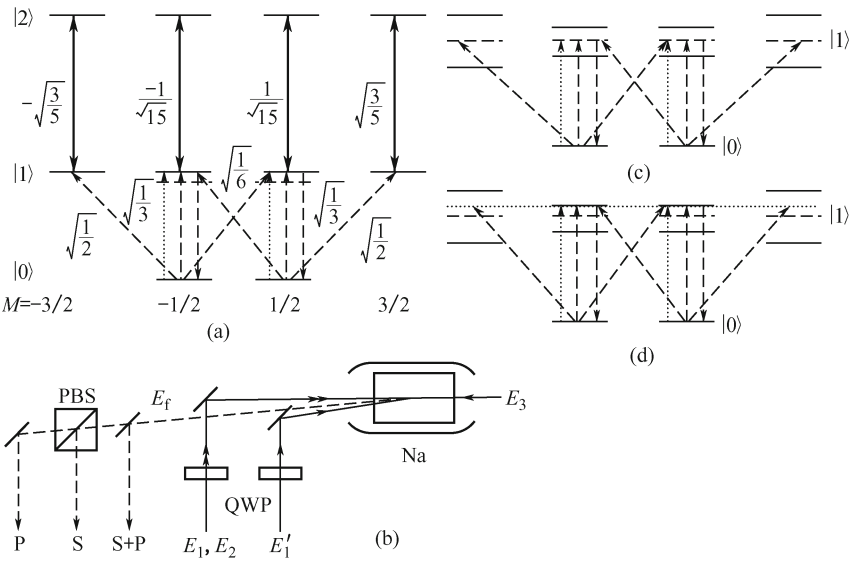

Fig. 5.11. (a) Zeeman structure of the three-level ladder-type atomic system in the experiment and various transition pathways in it. Solid line: dressing field G_d; Short-dashed lines: when the pumping fields are linearly-polarized, G_g, G_g', long-dashed lines: when the pumping fields are circularly- polarized; dotted line: the probe field G_p. (b) The schematic diagram of the experiment. (c) and (d) Schematic diagrams for suppression and enhancement of the DFWM in the dressed-state picture.

the other is further decomposed into P and S polarized components by a polarized beam splitter (PBS), which are denoted as I_P and I_S, respectively.

Figure 5.11(c) depicts the dressed-state picture with split $3P_{3/2}$ Zeeman sublevels, which corresponds to the DFWM suppression case when fields $\boldsymbol{k}_3, \boldsymbol{k}_1, \boldsymbol{k}_1'$ are on resonance with transition $|0\rangle \rightarrow |1\rangle$. Figure 5.11 (d) shows the enhancement case when these fields are tuned to near the dressed energy level. For most cases in this work, only one QWP is used to modify the polarization state of $\boldsymbol{k}_1$, so it can be decomposed into linearly- and circularly-polarized components while all other fields are kept as linearly polarized [Fig. 5.11 (a)]. In fact, we assume P polarization direction as the quantization axis and the component perpendicular to it (S polarization) is decomposed into balanced left- and right-circularly-polarized parts, while the component parallel to it (P polarization) keeps linearly polarized. Then the generated FWM signals will also contain linearly and circularly polarized components denoted as I_L and I_C, and they associate the detected intensities in the P and S polarizations with the equations, namely the detected intensities of I_P, I_S and total intensity I_T in the real experiment can be written as: $I_P = I_L \cos^2\alpha + I_C/2, I_S = I_L \sin^2\alpha + I_C/2$ and $I_T = I_S + I_P = I_L + I_C$, where α is the angle between the P-polarization and the direction of the linearly-polarized signal. The transition pathways in the FWM generation

can be described as following [3]:

$$
|\mathbf{0}_{-1/2}\rangle \begin{cases} \xrightarrow{G_g^0\left(\sqrt{1/3}\right)} |\mathbf{1}_{-1/2}\rangle \begin{cases} \xrightarrow{\left(G'^0_g\right)^*\left(\sqrt{1/3}\right)} |\mathbf{0}_{-1/2}\rangle \xrightarrow{G_p^0\left(\sqrt{1/3}\right)} |\mathbf{1}_{-1/2}\rangle \xrightarrow{\left(G_f^0\right)^*\left(\sqrt{1/3}\right)} |\mathbf{0}_{-1/2}\rangle : \chi_{xxxx} \\ \xrightarrow{\left(G'^-_g\right)^*\left(\sqrt{1/6}\right)} |\mathbf{0}_{1/2}\rangle \xrightarrow{G_p^0\left(\sqrt{1/3}\right)} |\mathbf{1}_{1/2}\rangle \xrightarrow{\left(G_f^+\right)^*\left(\sqrt{1/6}\right)} |\mathbf{0}_{-1/2}\rangle : \chi_{yxyx} \end{cases} \\ \xrightarrow{G_g^-\left(\sqrt{1/2}\right)} |\mathbf{1}_{-3/2}\rangle \xrightarrow{\left(G'^-_g\right)^*\left(\sqrt{1/2}\right)} |\mathbf{0}_{-1/2}\rangle \xrightarrow{G_p^0\left(\sqrt{1/3}\right)} |\mathbf{1}_{-1/2}\rangle \xrightarrow{\left(G_f^0\right)^*\left(\sqrt{1/3}\right)} |\mathbf{0}_{-1/2}\rangle : \chi_{xyyx} \\ \xrightarrow{G_g^+\left(\sqrt{1/6}\right)} |\mathbf{1}_{1/2}\rangle \begin{cases} \xrightarrow{\left(G'^+_g\right)^*\left(\sqrt{1/6}\right)} |\mathbf{0}_{-1/2}\rangle \xrightarrow{G_p^0\left(\sqrt{1/3}\right)} |\mathbf{1}_{-1/2}\rangle \xrightarrow{\left(G_f^0\right)^*\left(\sqrt{1/3}\right)} |\mathbf{0}_{-1/2}\rangle : \chi_{xyyx} \\ \xrightarrow{\left(G'^0_g\right)^*\left(\sqrt{1/3}\right)} |\mathbf{0}_{1/2}\rangle \xrightarrow{G_p^0\left(\sqrt{1/3}\right)} |\mathbf{1}_{1/2}\rangle \xrightarrow{\left(G_f^+\right)^*\left(\sqrt{1/6}\right)} |\mathbf{0}_{-1/2}\rangle : \chi_{yyxx} \end{cases} \end{cases}
\tag{5.8}
$$

$$
|\mathbf{0}_{1/2}\rangle \begin{cases} \xrightarrow{G_g^-\left(\sqrt{1/6}\right)} |\mathbf{1}_{-1/2}\rangle \begin{cases} \xrightarrow{\left(G'^0_g\right)^*\left(\sqrt{1/3}\right)} |\mathbf{0}_{-1/2}\rangle \xrightarrow{G_p^0\left(\sqrt{1/3}\right)} |\mathbf{1}_{-1/2}\rangle \xrightarrow{\left(G_f^-\right)^*\left(\sqrt{1/6}\right)} |\mathbf{1}_{1/2}\rangle : \chi_{yyxx} \\ \xrightarrow{\left(G'^-_g\right)^*\left(\sqrt{1/6}\right)} |\mathbf{0}_{1/2}\rangle \xrightarrow{G_p^0\left(\sqrt{1/3}\right)} |\mathbf{1}_{-1/2}\rangle \xrightarrow{\left(G_f^0\right)^*\left(\sqrt{1/3}\right)} |\mathbf{1}_{-1/2}\rangle : \chi_{xyyx} \end{cases} \\ \xrightarrow{G_g^+\left(\sqrt{1/2}\right)} |\mathbf{1}_{3/2}\rangle \xrightarrow{\left(G'^+_g\right)^*\left(\sqrt{1/2}\right)} |\mathbf{0}_{1/2}\rangle \xrightarrow{G_p^0\left(\sqrt{1/3}\right)} |\mathbf{1}_{-1/2}\rangle \xrightarrow{\left(G_f^0\right)^*\left(\sqrt{1/3}\right)} |\mathbf{1}_{1/2}\rangle : \chi_{xyyx} \\ \xrightarrow{G_g^0\left(\sqrt{1/3}\right)} |1_{1/2}\rangle \begin{cases} \xrightarrow{\left(G'^0_g\right)^*\left(\sqrt{1/3}\right)} |\mathbf{0}_{1/2}\rangle \xrightarrow{G_p^0\left(\sqrt{1/6}\right)} |\mathbf{1}_{-1/2}\rangle \xrightarrow{\left(G_f^0\right)^*\left(\sqrt{1/6}\right)} |\mathbf{1}_{1/2}\rangle : \chi_{xxxx} \\ \xrightarrow{\left(G'^-_g\right)^*\left(\sqrt{1/6}\right)} |\mathbf{0}_{-1/2}\rangle \xrightarrow{G_p^0\left(\sqrt{1/3}\right)} |\mathbf{1}_{-1/2}\rangle \xrightarrow{\left(G_f^-\right)^*\left(\sqrt{1/6}\right)} |\mathbf{1}_{1/2}\rangle : \chi_{yxyx} \end{cases} \end{cases}
\tag{5.9}
$$

We take the transition passage $|0_{-1/2}\rangle \xrightarrow{G_g^0} |1_{-1/2}\rangle \xrightarrow{\left(G'^-_g\right)^*} |0_{1/2}\rangle \xrightarrow{G_p^0} |1_{1/2}\rangle \xrightarrow{\left(G_f^+\right)^*} |0_{-1/2}\rangle$ for an example to explain the transition process. The first step, is that a ground state particle $|0_{-1/2}\rangle$ absorbs a coupling photon G_g^0 and transits to the dressed state $|1_{-1/2}\rangle$, expressed as $|0_{-1/2}\rangle \xrightarrow{G_g^0} |1_{-1/2}\rangle$. In the second step, the particle emits a coupling photon $(G'^-_g)^*$ and transits to the dressed state $|0_{1/2}\rangle$, expressed as $|1_{-1/2}\rangle \xrightarrow{\left(G_g^-\right)^*} |0_{1/2}\rangle$ in the transition passage. Thirdly, the particle absorbs a probe photon G_p^0 and transits to the dressed state $|1_{1/2}\rangle$, expressed as $|0_{1/2}\rangle \xrightarrow{G_p^0} |1_{1/2}\rangle$ in the transition passage. The fourth step is, the particle stimulated transits back to state $|0_{-1/2}\rangle$ and emits a pumping photon $(G_f^+)^*$, expressed as $|1_{1/2}\rangle \xrightarrow{\left(G_f^+\right)^*} |0_{-1/2}\rangle$.

Since the CG coefficients may be different for different transitions between Zeeman sublevels, the Rabi frequencies are different even with the same laser field [25]. For example, considering CG coefficients values [28, 29], we can obtain $|G^{\pm}_{g,\pm 3/2}|^2/|G^{\pm}_{g,\pm 1/2}|^2 = 3$, which indicates that the circularly-polarized DFWM signal is mainly dressed by $G^0_{d,\pm 3/2}$, not by $G^0_{d,\pm 1/2}$. And also from

CG coefficients, we can obtain that $|G^0_{d,\pm 3/2}|^2 = 9|G^0_{d,\pm 1/2}|^2$, which indicates that the dressing effects in the circularly-polarized subsystems are far greater than in the linearly-polarized subsystems.

Based on the discussion above, we can get the expressions for I_L and I_C. As Fig. 5.11 (a) shows, there are two linearly polarized subsystems ($|0_M\rangle \xrightarrow{G^0_{g,M},(G^0_{g,M})^*,G^0_{p,M}} |1_M\rangle$ $(M = \pm 1/2)$) which can generate linearly polarized DFWM, and is dressed by the linearly-polarized dressing transition with $|G^0_{d,\pm 1/2}|^2$. By simply substituting the corresponding dressing terms into Eq. (5.11) of Ref. [21], we can obtain an expression of density-matrix element which induces the FWM signal of linearly polarized component. To simplify the expression, the symmetry of CG coefficients is considered, namely $|G^0_{p(g,d)_M}| = |G^0_{p(g,d)_{-M}}|$ and $|G^+_{p(c,d)_M}| = |G^-_{p(c,d)_{-M}}|$. Moreover, if $G^{0\pm}_{p(c,d)_M} >> \Gamma_{0(1,2),0(1,2)}$, we can have the conditions of $\Gamma_{0(1,2),0(1,2)} \approx \Gamma_{0_M(1_M,2_M),0_M(1_M,2_M)}$. Consequently, the simplified expression is given by: $\rho^{(3)}_L = -2\mathrm{i}\left|G^0_{gM}\right|^2 G^0_{pM}(A_1+2A_2)[1/(A_7+A_3)^2+1/(\Delta_1^2+\Gamma_{10}^2+|G_{dM}|^4/A_4+2A_5\,|G_{dM}|^2/A_6)]$, where $A_1 = 1/\Gamma_{00} + 1/\Gamma_{11}, A_2 = \Gamma_{21}|G_{dM}|^2/(\Delta_2^2+\Gamma_{21}^2)$, $A_3 = |G_{dM}|^2/[\mathrm{i}(\Delta_1+\Delta_2)+\Gamma_{21}], A_4 = (\Delta_1+\Delta_2)^2+\Gamma_{21}^2, A_5 = -\Delta_1\Delta_2 - \Delta_1^2+\Gamma_{10}\Gamma_{20}, A_6 = (\Delta_1+\Delta_2)^2+\Gamma_{20}^2$, and $A_7 = \mathrm{i}\Delta_1+\Gamma_{10}$.

On the other hand, the circularly-polarized subsystems are more complicated [21,25]. In addition, besides being dressed by $\left|G^0_{d,\pm 1/2}\right|^2$, they are also dressed by $\left|G^0_{d,\pm 3/2}\right|^2$. Also, by inserting the dressing terms into Eq. (5.13) of Ref. [21] and under the same simplified conditions, we can obtain the expression of the density-matrix element which induces the FWM signal of the circularly-polarized component as

$$\rho^{(3)}_C = -2B_1/[\Gamma_{00}(A_7+B_2)^2] - \sum_{M=\pm 1/2} 2B_3/[\Gamma_{00}(A_7+\left|G^0_{d_M}\right|^2/A_8)(A_7+|G^0_{d_{M+1}}|^2/A_8)],$$

where $A_8 = \mathrm{i}(\Delta_1+\Delta_2)+\Gamma_{20}, B_1 = \mathrm{i}G^0_{p_{-1/2}}G^+_{g_{-1/2}}(G^0_{g_{-1/2}})^*, B_2 = |G^0_{d_{-1/2}}|^2/A_8$, and $B_3 = \mathrm{i}G^0_{p_M}(G^0_{g_M})^*G^+_{g_M}$. Therefore, the intensities of the FWM in the P and S polarization directions are: $I_L \propto |\rho^{(3)}_L|^2$ and $I_C \propto |\rho^{(3)}_C|^2$, respectively.

5.3.2 Experimental Results

The suppression and enhancement of DFWM processes happen as the probe field is set at different frequency detuning conditions. In Fig. 5.11 (a), the pumping fields E_1 and E_1' (with diameter of 0.8 mm and power of 3 μW) and the probe field E_3 (with a diameter of 0.8 mm and power of 5 μW) are tuned

to the line center (589.0 nm) of the lower $|0\rangle$ to $|1\rangle$ transition, which generate the DFWM signal E_f at frequency ω_1 by using one photon each from fields E_1, E_1' and E_3. When $\Delta_1 = 0$ [Fig. 5.11 (c)], the DFWM signal is suppressed by the dressing field. For clearly understanding the influences of the incident beams to suppression and enhancement of FWM processes, we investigate the signals in P and S polarizations separately while the total intensity is the sum of intensities of these two polarizations components, as shown in Fig. 5.12 (a1) – (a3), (b1) – (b3). The background represents the signal strength of the pure DFWM with no dressing field while the dips represent that the signal was suppressed at different polarizations of the pumping beam. The dressing field E_2 (with a diameter of 1.1 mm and power of 100 μW) scans from 568.5 nm to 569.1 nm (a crossing the upper $|1\rangle$ to $|2\rangle$ transition) to dress the DFWM process. When Δ_1 gets large enough [as in Fig. 5.11 (d)], the DFWM signal is enhanced by the dressing field, as shown in Fig. 5.13 (a1) – (a3), (d1) – (d3). When Δ_1 is set at a proper position which is not too far from the resonant position, both suppression (dips lower than background) and enhancement (peaks higher than background) can occur at the same time, as shown in Fig. 5.13 (a1) – (a3). The linewidths of the measured suppressed dips and enhanced peaks of FWM spectra are about 20 GHz.

Let us first consider the experimental results of the DFWM suppression. Figure 5.12 (a1) – (a3) presents the DFWM spectra (with scanned dressing field Δ_2) from $\theta = 0$ to $\theta = 90°$ per 5°, which is the polarization angle of the pumping field E_1 The dips below the background represent the suppressed DFWM by the dressing field. Figure 5.12 (b1) – (b3) present the θ-dependence curves of the background, the minimum of the suppressed dips, and depth of the suppressed dips (background minus minimum) in Fig. 5.12 (a1) – (a3), respectively. The dressing effect is clearly revealed by Fig. 5.12 (b3) which shows that the suppression depths in P and S polarizations are both ascending as the QWP is rotated from 0 to 45°. This can be explained by changing the DFWM subsystems from linearly-polarized ones to circularly-polarized ones, and then calculating the intensities I_P, I_S and I_T. In fact, as Fig. 5.12 (a1) – (a3) shows, DFWM signals are mainly generated in the linearly-polarized subsystems which are dressed by $G^0_{d,\pm 1/2}$ when k_1 is linearly polarized ($\theta = 0$). As QWP is rotated, the linearly-polarized transitions gradually transform into circularly-polarized ones which then involve the dressing transitions $G^0_{d,\pm 3/2}$ partly instead of $G^0_{d,\pm 1/2}$. Consequently, the dressing effect gets larger and the suppression dips become deeper as QWP is rotated form 0 to 45°. Furthermore, the suppression condition ($\Delta_1 + \Delta_2 = 0$) for DFWM in all the subsystems is uniform because it contains no term relating to the Zeeman structure, which results in the similar dependence curves for S and P polarizations, as well as the total intensity, as shown in Fig. 5.12 (a1) – (a3).

Figure 5.12 (b1) presents the polarization dependence of the background as well as the pure DFWM. The shapes of the curves for the P & S polarizations and the total intensity basically follow the well-expected classical

polarization spectroscopy [17, 18]. Figure 5.12 (b2) shows the polarization dependence of the dressed DFWM signal peak values, which include the pure DFWM and the suppression dips.

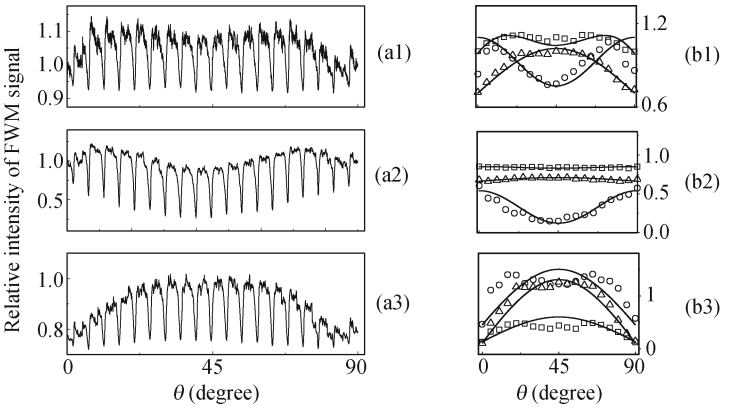

Fig. 5.12. The polarization dependence of the suppressed DFWM signals. (a1)–(a3) variations of I_T, I_P and I_S (by scanning Δ_2) versus rotation angle θ (0°–90° per 5°), respectively. (b1)–(b3) Dependence curves of the background, minimums of the dips, and suppression depths for I_T (squares), I_P (circles) and I_S (triangles) and, respectively. The solid curves in (b1)–(b3) are the corresponding theory results. $\Delta_1 = 0$. Adopted from Ref. [28].

For DFWM enhancement when $\boldsymbol{k}_3, \boldsymbol{k}_1, \boldsymbol{k}_1'$ are far detuned [Fig. 5.11 (d)], as shown in Figs. 5.13 and 5.14, the polarization dependence of the enhanced peak heights (maximum minus background) for the S polarization is different [Fig. 5.13 (b3) triangle points]: it descends as QWP is rotated from 0 to 45°. Comparing expressions of I_L and I_C above, we can see that at far detuning condition for $\boldsymbol{k}_3, \boldsymbol{k}_1, \boldsymbol{k}_1'$, the polarization variation of $\boldsymbol{k}_1$ enlarges α. It means that S polarized components projecting from linearly polarized FWM are increasing while P polarization components are decreasing gradually as rotating QWP. Consequently, the dressing efficiency of the S polarization is relatively reduced as compared with the condition when $\boldsymbol{k}_1$ is linearly polarized. On the other side, the P polarization component is relatively enhanced.

As discussed above, the dressing field Rabi frequencies for different Zeeman sublevels may be different (e.g., $|G^0_{d,\pm 3/2}|^2 = 9|G^0_{d,\pm 1/2}|^2$), which will induce different splitting distances for different sublevels. The exact expression of the split sublevel positions are $\delta_M = (\Delta_2 \pm \sqrt{\Delta_2^2 + 4\,|G_{dM}|^2})/2$. The enhanced peaks appear when the splitting sublevels are on resonance with the generating fields G_g, G_g' and the probe field G_p. This then satisfies the enhancement condition $\Delta_1 + \delta_M = 0$ [16]. Combining it with $\delta_M = (\Delta_2 \pm \sqrt{\Delta_2^2 + 4\,|G_{dM}|^2})/2$, we can obtain the positions of the enhanced peaks in the plotted figure: $O_M = (\Delta_1^2 - |G^0_{d,M}|^2)/\Delta_1$. There should be two distinct enhanced peaks $O_{\pm 3/2}$ and $O_{\pm 1/2}$, which are covered in the

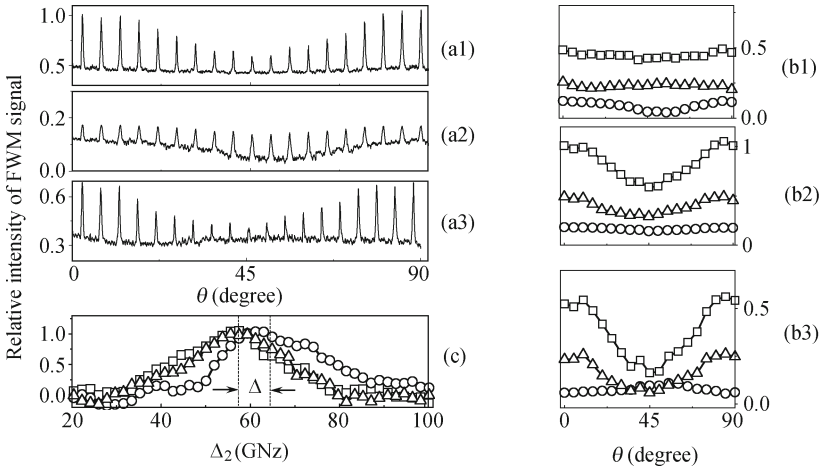

Fig. 5.13. The polarization dependence of the DFWM enhancement versus θ. (a1) – (a3) and (b1) – (b3) DFWM enhancement with conditions parallel to Fig. 5.12 except at $\Delta_1 = -67$ GHz. (c) I_P with scanning Δ_2 for $\theta = 0$ (squares), 45° (circles) and 90° (triangles), when $\Delta_1 = 67$ GHz.

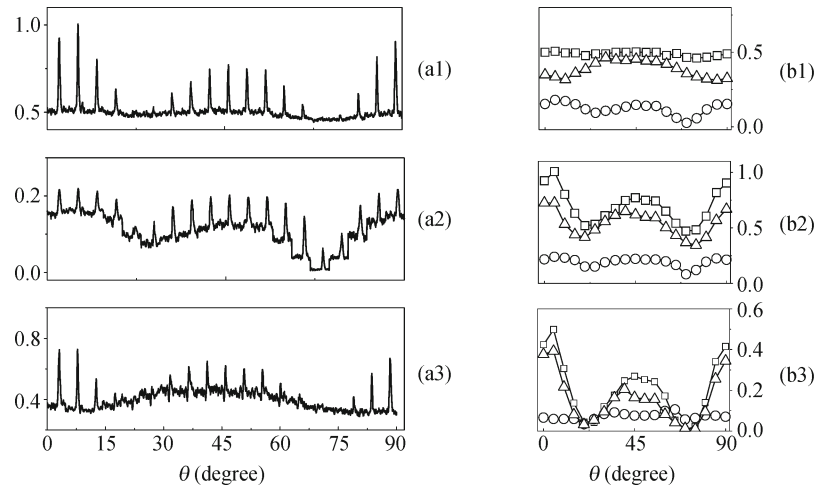

Fig. 5.14. The polarization dependence of the DFWM enhancement versus θ. (a1) – (a3) and (b1) – (b3) are for I_T, I_P and I_S polarization dependences, respectively, when both polarizations of the $\boldsymbol{k}_1$ and $\boldsymbol{k}_1'$ beams are rotated simultaneously, with $\Delta_1 = -67$ GHz.

wide power-broadened profile. However, when $\boldsymbol{k}_1$ is linearly ($\theta = 0$) and circularly ($\theta = 45°$) polarized, the enhanced peaks are primarily created by $M = \pm 1/2$ and $M = \pm 3/2$ which are at $O_{\pm 1/2}$ and $O_{\pm 3/2}$, respectively, as shown in Fig. 5.13 (c). By using O_M expression and the CG coefficients, we can calculate the shift distance between the enhanced peaks as $\Delta = O_{3/2} - O_{1/2} = (|G^0_{d,3/2}|^2 - |G^0_{d,1/2}|^2)/\Delta_1 \approx 8.8$ GHz. The measured shift

distance between the enhanced peaks in Fig. 5.13 (c) is about 7.5 GHz.

When two QWPs are used to change the polarizations of the $\boldsymbol{k}_1$ and $\boldsymbol{k}_1'$ beams simultaneously, as shown in Fig. 5.14 (a1 – a3) and Fig. 5.14 (b1 – b3). The variation period is reduced to half of the case with changing k_1 only. Also, the enhancement peak gets close to 0 at about $\theta = 22.5°$.

Finally, the frequency detuning of $\boldsymbol{k}_3, \boldsymbol{k}_1, \boldsymbol{k}_1'$ is set at an intermediate position (about 30 GHz, smaller than the value in the enhancement case), half enhancement and half suppression appear when the frequency of the dressing field is scanned [11], which is also modified by the polarization variation of $\boldsymbol{k}_1$, as shown in Fig. 5.15. The variation rules also follow the ones discussed above: the background obeys traditional laws [17, 18], the dependences of the suppression and enhancement curves on the polarization are similar to the results in suppression (Fig. 5.12) and enhancement (Figs. 5.13 and 5.14) parts, respectively.

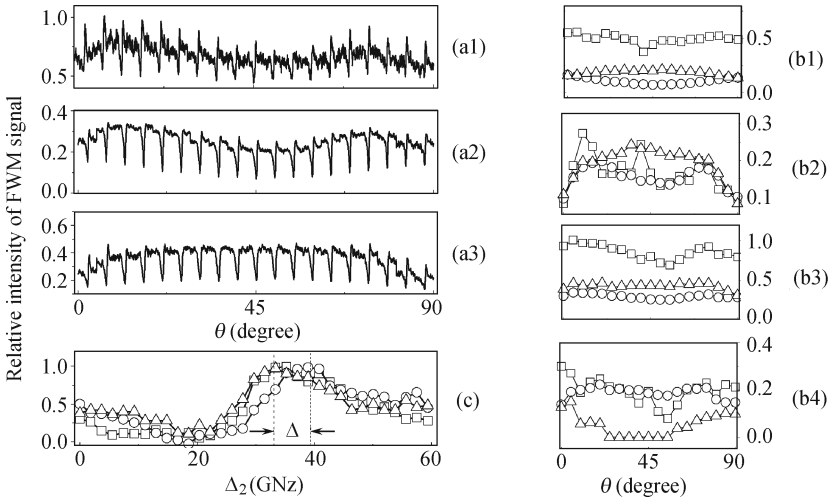

Fig. 5.15. Polarization dependence of DFWM versus the rotation angle θ. (a1) – (a3) Half enhancement and half suppression with the condition parallel to Fig. 5.12 (a1 – a3) except $\Delta_1 = -30$ GHz. (b1) and (b2) dependences of the minimum and maximum of each part on θ, (b3) depths of the suppressed dips and (b4) heights of the enhanced peak for I_T (squares), I_P (circles) and I_S (triangles), respectively. (c) I_P as scanning Δ_2 for 0° (squares), 45° (circles) and 90° (triangles).

5.4 Enhancing and Suppressing Four-Wave Mixing in Electroma-Genetically Induce Transparency Window

The electromagnetically induce transparency (EIT) [1, 23] can reduce linear absorption of a probe beam with strong "coupling beams" resonant with

the up-level transition. The generated four-wave-mixing (FWM) and six-wave-mixing in four-level atomic system can coexist in two ladder-type EIT windows. [22] Recently, the competition between two coexisting FWMs via atomic coherence is studied, and the FWM can be selectively suppressed. [11] On the other hand, when EIT and FWM processes are modulated by the different polarization of the strong coupling fields, it has been demonstrated that selective transitions among polarization dark states of degenerate Zeeman sublevels can be obtain.

In this section, we show the enhancement and suppression of the FWM signal are demonstrated in EIT window for different probe beam detuning and polarizations in the Y-type ^{85}Rb atomic system. The generated FWM signal can be selectively enhanced and suppressed via an EIT window.

The laser beams are aligned spatially as shown in Fig. 5.16 (a). A weak probe beam $E_1(\omega_1, \boldsymbol{k}_1$ and frequency detuning $\Delta_1)$ is modulated by a quarter wave plate (QWP) and propagates through the atomic medium, and two pump beams $E_2(\omega_2, \boldsymbol{k}_2$ and $\Delta_2)$ and $E_2'(\omega_2, \boldsymbol{k}_2'$ and $\Delta_2)$ propagate in the opposite direction with small angle (0.3°) between them to generate one FWM signal beam E_F with phase matching condition $\boldsymbol{k}_F = \boldsymbol{k}_1 + \boldsymbol{k}_2 - \boldsymbol{k}_2'$. At the same time, the strong dressing laser beam $E_3(\omega_3, \boldsymbol{k}_3$ and $\Delta_3)$ propagates in the same direction as beam E_2 to influence on this FWM signal. Here we define detuning $\Delta_i = \omega_i - \Omega_i$. For a simple four-level Y-type atomic system, as shown in Fig. Fig. 5.16 (b), E_2 and E_2' drive the upper transition $|1\rangle$ to $|2\rangle$ and E_3 drives the transition $|1\rangle$ to $|3\rangle$. The laser E_1 probes the lower transition $|0\rangle$ to $|1\rangle$.

In a ^{85}Rb vapor cell, the energy levels $5S_{1/2}(F = 3), 5P_{3/2}(F = 3), 5D_{3/2}$ and $5D_{5/2}(F = 2, 3, 4)$ form such Y-type system. The four laser beams are aligned spatially as in Fig. 5.16 (a). The probe laser beam E_1 with wavelength of 12821 cm^{-1} is from an external cavity diode laser (ECDL) of Co. Toptica Photonics AG, connecting transition $5S_{1/2} - 5P_{3/2}$. It has a power of 3 mW (corresponding to Rabi frequency $G_1 = 0.0025$ cm^{-1}). The other laser beams E_2, E_2' (wavelength of 12887 cm^{-1}, connecting transition $5P_{3/2} - 5D_{5/2}$) are from the second ECDL split with equal power of 16 mW corresponding to $G_2 = G_2' = 0.0075$ cm^{-1} and E_3 (wavelength of 12884 cm^{-1}, connecting transition $5P_{3/2} - 5D_{3/2}$) are from the third ECDL with power of 108 mW corresponding to $G_3 = 0.0509$ cm^{-1}. The generated FWM signal I_P in the direction $\boldsymbol{k}_F$ emerging from the "P" polarization direction and the transmitted probe beam are detected by an avalanche photodiode detector and a photodiode, respectively. In Fig. 5.17 (a), the up-curve is the probe transmission with EIT windows [12] and the down-curve is the measured FWM signal. The up-curve gives four apparent spectra lines. From the left to right, there are four absorption dips corresponding to hyperfine-level transitions from ^{87}Rb $|5S_{1/2}, F = 2\rangle$ *to* $|5P_{3/2}, F' = 1, 2, 3\rangle$, ^{87}Rb $|5S_{1/2}, F = 3\rangle$ to $|5P_{3/2}, F = 2, 3, 4\rangle$,^{85} Rb $|5S_{1/2}, F = 2\rangle$ to $|5P_{3/2}, F' = 1, 2, 3\rangle$, and from ^{87}Rb $|5S_{1/2}, F = 1\rangle$ to $|5P_{3/2}, F' = 0, 1, 2\rangle$, respectively. In the down-curve

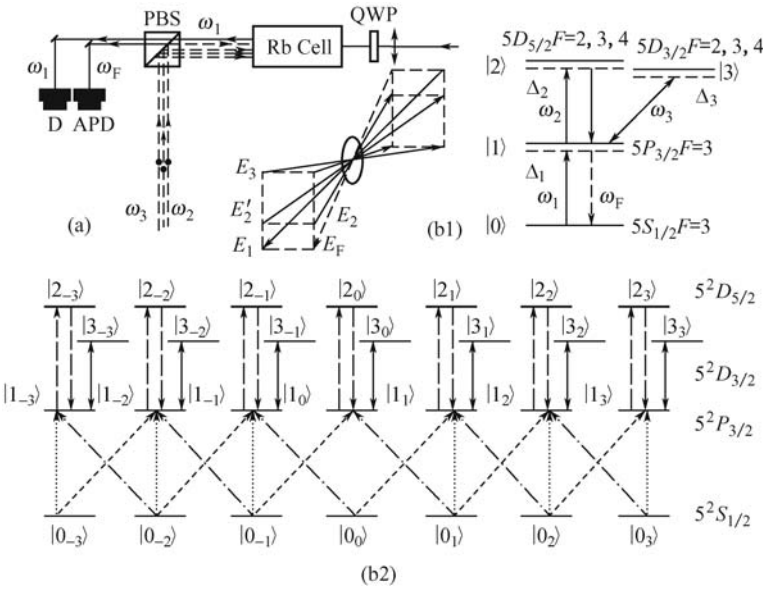

Fig. 5.16. (a) The schematic diagram of the experiment. D denotes the photodiode, APD denotes the avalanche diode detector and PBS denotes the polarized beam splitter. Inset: the spatial alignment of the laser beams. (b1) Relevant ^{85}Rb energy levels and (b2) the corresponding Zeeman sublevels with various transition pathways. Solid line: dressing field E_3; Linearly (dot lines, $q = 0$), left (dash-dot lines, $q = -1$) and right (dash lines, $q = +1$) circularly polarized probe fields; Long-dash lines: the pump fields E_2 and E_2'.

of Fig. 5.17(a), there are two peaks on the absorption dips in the up-curve. The right one of the two peaks is EIT window created by the pump fields E_2 and E_2' in system $|0\rangle - |1\rangle - |2\rangle$, which satisfies the condition $\Delta_1 + \Delta_2 = 0$ and corresponds to double-peak FWM signal. While the left one is created by the dressing field E_3 in system $|0\rangle - |1\rangle - |3\rangle$ and satisfies condition $\Delta_1 + \Delta_3 = 0$. Also, each peak of the pure FWM signal corresponding to the right $|0\rangle - |1\rangle - |2\rangle$ EIT window is split into two peaks due to the dressing effect of E_2 and E_2'.

With the dressing field E_3, the suppression peak satisfies the condition $\Delta_1 + \Delta_3 = 0$ and the enhancement condition is $\Delta_1 + \Delta_3 \pm G_3 = 0$ [15, 16]. Figures 5.17 (b1) – (b3) present evolution of the FWM signal intensity versus the probe field detuning Δ_1 for different Δ_3 values. In Figs. 5.17 (b1) – (b3), the up-curve is the probe transmission with two ladder-type EIT windows, and the down-curve is the measured FWM signal. With E_3 dressing, the perturbation chain is $\rho_{00}^{(0)} \xrightarrow{G_1} \rho_{G_3\pm 0}^{(1)} \xrightarrow{G_2} \rho_{20}^{(2)} \xrightarrow{(G_2')^*} \rho_{G_3\pm 0}^{(3)}$ [11, 22] and the modified third-order nonlinear susceptibility is $\rho_{10}^{(3)} = g/d_2[d_1 + G_3^2/d_3]^2$, where $d_1 = \mathrm{i}\Delta_1 + \Gamma_{10}, d_2 = \mathrm{i}(\Delta_1 + \Delta_2) + \Gamma_{20}, d_3 = \mathrm{i}(\Delta_1 + \Delta_3) + \Gamma_{30}, g = -\mathrm{i}G_1G_2G'^*_2$. In Fig. 5.17 (b1), the left $|0\rangle - |1\rangle - |2\rangle$ (satisfying $\Delta_1 + \Delta_2 = 0$)

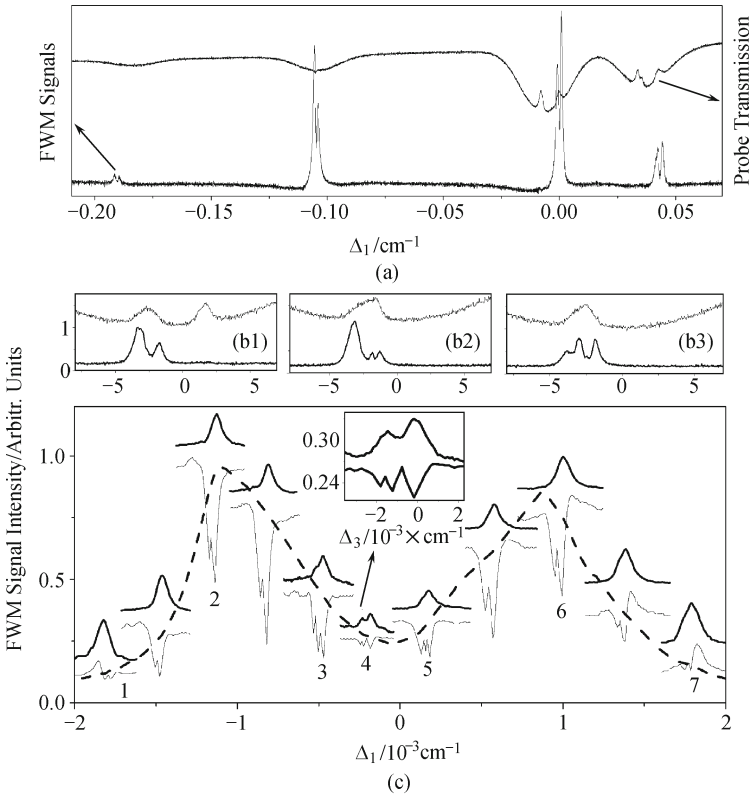

Fig. 5.17. (a) The probe beam transmission with two EIT windows versus the probe detuning Δ_1 and the corresponding measured FWM signals. (b1) – (b3) Measured double-peak FWM signal and the corresponding EIT window induced by the dressing field E_3 versus Δ_1 for $\Delta_2 = 0$, $\Delta_3 = -0.0027$ cm^{-1} (b1), $\Delta_3 = 0$ (b2), $\Delta_3 = 0.0023$ cm^{-1} (b3). (c) The enhanced and suppressed FWM signal (down curves) and the corresponding EIT windows (up curves) versus Δ_3 for different Δ_1 increasing from $\Delta_1 = -0.002$ cm^{-1} to 0.002 cm^{-1} with the step of 0.0004 cm^{-1}. The dash curve is the double-peak FWM signal versus Δ_1. The insert is a zoom onto curve 4.

EIT window created by the pump fields E_2 and E_2' corresponds to the double-peak FWM signal and the right one is $|0\rangle - |1\rangle - |3\rangle$ (satisfying $\Delta_1 + \Delta_3 = 0$) EIT window created by the dressing field E_3. This right EIT window moves to left when the dressing field detuning Δ_3 gets larger. In Fig. 5.17 (b2, b3), we can see that when two EIT windows get close and overlap, due to satisfying the enhancement or suppression condition, the right peak of FWM is suppressed and separated into two-peaks while the left FWM peak is enhanced, then the left peak of FWM is suppressed and separated into two-peaks while the right FWM peak is enhanced.

In Fig. 5.17 (c) we experimentally study the enhancement and suppression of FWM spectra versus the dressing field detuning Δ_3 for different probe

detuning Δ_1. The up-curves in Fig. 5.17 (c) are the probe transmission versus Δ_3. The down-curves are the enhancement and suppression of FWM signals. The constant background (two sides of down-curves) represents the signal intensity of the FWM without dressing field, the dips lower than background (we call them as suppression peaks, e.g., the curves 2–6) and the peaks higher than background (enhancement peaks, e.g., the peaks of curves 1 and 7) represent the FWM signal is suppressed and enhanced, respectively. The dashed curve in Fig. 5.17 (c) is the profile of the double-peak FWM signal versus Δ_1.

Specifically, we can see that all the curves in Fig. 5.17 (c) almost show axial symmetric evolution behavior by $\Delta_1 = 0$. Specifically, in the $\Delta_1 < 0$ region, with Δ_1 increasing, the FWM signals change from all-enhanced to half-suppressed and half-enhanced, and finally all-suppressed around resonant point. By contrast, in the $\Delta_1 > 0$ region, the FWM signals change oppositely. Moreover, we find that the FWM signals show left enhancement and right suppression shapes in half-suppression and half-enhancement region (from $\Delta_1 = -0.00067\ \mathrm{cm}^{-1}$ to $-0.0017\ \mathrm{cm}^{-1}$), but left suppression and right enhancement in $\Delta_1 > 0$ region.

There exist typical structure of two enhancement and two suppression peaks in the FWM spectra versus Δ_3 [e.g., curves 2 and 6 in Fig. 5.17 (c)] which are resulted from the modification of the double-peak FWM signal. Moreover, the dressing field E_3 and the pump field E_2 interact with each other strongly in all-enhancement [19] and all-suppression region, and create triple-peaks of the enhancement (curves 1 and 7) and suppression (curves 3 – 5) spectra. In the insert of Fig. 5.17 (c), two left suppression peaks might be induced by the sequential-cascade double dressing effect [20] of E_3 and E_2 described by the perturbation chain $\rho_{00}^{(0)} \xrightarrow{G_1} \rho_{(G_2 \pm G_3 \pm)0}^{(1)} \xrightarrow{G_2} \rho_{20}^{(2)} \xrightarrow{(G_2')*} \rho_{G_3 \pm 0}^{(3)}$ and the modified third-order nonlinear susceptibility. By solving the following coupled equations: $\partial\rho_{10}/\partial t = -d_1\rho_{10} + \mathrm{i}G_2^*\rho_{20} + \mathrm{i}G_3^*\rho_{30}, \partial\rho_{20}/\partial t = -d_2\rho_{20} + \mathrm{i}G_2\rho_{10}$, and $\partial\rho_{30}/\partial t = -d_3\rho_{30} + \mathrm{i}G_3\rho_{10}$ with weak probe field, we can finally obtain $\rho_{10}^{(3)} = g/[d_2(d_1 + |G_2|^2/d_2 + |G_3|^2/d_3)(d_1 + |G_3|^2/d_3)]$.

Similarly, we can consider the probe transmission versus Δ_3. The height of up-curve represents the transparent degree of probe field E_1 in Fig. 5.17 (c). When the pump field E_2 is blocked, the pure E_3 EIT ($|0\rangle - |1\rangle - |3\rangle$) peak is higher at $\Delta_1 = 0$ than that at large detuning $|\Delta_1|$. However, with E_2 on, since the E_2 field destroys the E_3 EIT condition when $\Delta_1 = -\Delta_3 = -\Delta_2 \approx 0$, we can see the E_3 EIT peak is strongly suppressed at $\Delta_1 = 0$ in Fig. 5.17 (c).

We have shown the enhancement and suppression of the FWM signal in EIT window for different probe beam detuning above. Next we will consider the influence of different probe laser polarization configurations on the enhancement and suppression of the FWM spectra. We use one QWP with a rotation angle θ to change E_1 polarization state to decompose it into linearly-

or circularly-polarized components. Thus the Zeeman sublevels in Fig. 5.16 (b2) need be considered in the FWM process. Figure 5.18 (a), (b) arranges the FWM spectra when scanning the dressing field from $\theta = 0^\circ \sim 90^\circ$ with the variation step of 5° when $\Delta_1 = 0.000\,723\ \mathrm{cm}^{-1}$ and $\Delta_1 = 0.002\,3\ \mathrm{cm}^{-1}$, respectively. The background represents the signal intensity of the FWM with no dressing field while the dips and the peaks represent that the signal was suppressed or enhanced, respectively.

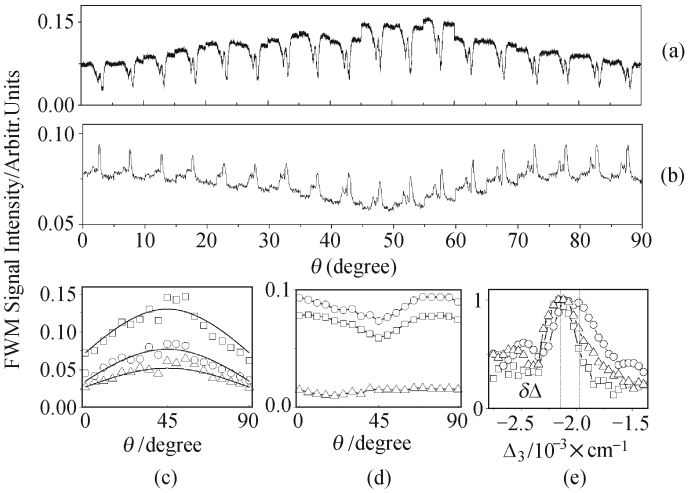

Fig. 5.18. The polarization dependence of (a) the suppression (with $\Delta_1 = 0.00072\ \mathrm{cm}^{-1}$) and (b) the enhancement (with $\Delta_1 = 0.002\,3\ \mathrm{cm}^{-1}$) of FWM signal I_P (by scanning Δ_3) versus rotation angle θ (increases from 0° to 90° with the variation step of 5°) at $\Delta_2 = 0$. Variation of the (c, d) background (square), (c) minimums of the suppression peaks (circle) and suppression depths (triangle), (d) maximums of the peaks (circle) and enhanced height (triangle) of the dependence curves. The solid curves in (c) are the corresponding theory results. (e) Normalized I_P versus Δ_3 for $\theta = 0^\circ$ (square), 45° (circle), and 90° (triangle).

Square points in Fig. 5.18 (c) show the variation of the FWM with no dressing fields [background in Fig. 5.18 (a)] which accord with the classical polarization spectroscopy (sinusoidal law). [17, 18] Triangle points gives the dependence of the max depth of suppression peaks versus θ, which denotes that the dressing strength is increasing as changing E_1 from linearly to circularly polarized state. It is because the polarization variation transforms the energy distribution among various transition paths, for example, linearly polarized transitions to circular ones. Since different FWM transition paths are dressed by different transition dressing fields, the total dressing strength is generally different [Fig. 5.16 (b2)]. The FWM transition paths and their expressions for linearly and circularly polarized sub-systems in Fig. 5.16 (b2) can be written as

$$\rho^{(0)}_{0_M 0_M} \xrightarrow{G^q_{1_{M+q}}} \rho^{(1)}_{1_{M+q} 0_M} \xrightarrow{G_{2_{M+q}}} \rho^{(2)}_{2_{M+q} 0_M} \xrightarrow{(G'_{2_{M+q}})^*} \rho^{(3)}_{1_{M+q} 0_M},$$

$$\rho^{q}_{1_{M+q}0_M} = \sum_{M=-3,-2\ldots3} g_{M+q}/d_{2_{M+q}}(d_{1_{M+q}} + G^2_{3_{M+q}}/d_{3_{M+q}})^2,$$

where $g_{M+q} = -\mathrm{i}G_{2_{M+q}}G^*_{2_{M+q}}G^q_{1_{M+q}}$, $d_{1_{M+q}} = \mathrm{i}\Delta_1 + \Gamma_{1_{M+q}0_M}, d_{2_{M+q}} = \mathrm{i}(\Delta_1 + \Delta_2) + \Gamma_{2_{M+q}0_M}, d_{3_{M+q}} = \mathrm{i}(\Delta_1 + \Delta_3) + \Gamma_{3_{M+q}0_M}$, and $q = 0, \pm 1$. The theoretical curves are fit well with the experimentally measured results [Fig. 5.18 (c)].

Triangle points in Fig. 5.18 (d) give the dependence of the max height of enhancement peaks versus θ, which denotes that the dressing strength is decreasing as change E_1 from linearly to circularly polarized state. We can see that the variation is fairly stable as rotating QWP compared with Fig. 5.18 (c). It discloses that the far detuning condition homogenizes the difference of the transition strengths induced by the CG coefficients [28]. Square points show the variation of the FWM with no dressing fields [background in Fig. 5.18 (b)] which accord with the traditional polarization rules [17, 18]. Moreover, the enhancement peaks are shifting as rotating QWP. The shift distance $\delta\Delta$ between the enhancement peaks is about 5 MHz, as shown in Fig 5.18 (e). It is because that the enhancement conditions are different for different Zeeman sublevels ($\Delta_1 + \Delta_3 \pm G_{3,M} = 0$).

When the frequencies of the probe field set at a proper position ($\Delta_1 = 0.001\ 81\ \mathrm{cm}^{-1}$) which is not too far from the resonant position, both suppression and enhancement appear simultaneously, as shown in Fig. 5.19 (a). The polarization rules for suppression [Fig. 5.19 (b)] and enhancement Fig. 5.19 (c) are both similar to the above results when they appear singly (Fig. 5.18). Also, the positions of the enhanced peaks are shifting with rotating

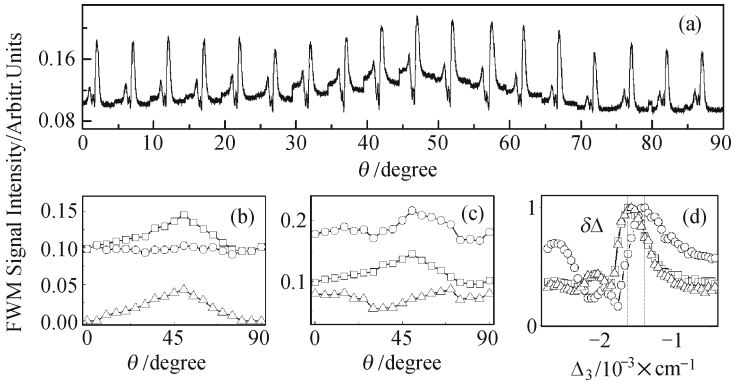

Fig. 5.19. (a) The polarization dependence of the FWM signal I_P (by scanning Δ_3) versus rotation angle θ (increases from 0° to 90° with the variation step of 5°). (b) and (c) Variation of the background (square), (b) minimums of the suppression peaks (circle) and suppressed depth (triangle), (c) maximums of the peaks (circle) and enhanced height (triangle) of the dependence curves. (d) I_P versus Δ_3 for $\theta = 0°$ (square), 45° (circle), and 90° (triangle). The other parameters are $\Delta_1 = 0.0018\ \mathrm{cm}^{-1}, \Delta_2 = 0$. Adopted from Ref. [29].

QWP, as shown in Fig. 5.19 (d). More importantly, we find that in Fig. 5.19 (a) the enhanced triple-peaks transform into two enhancement and two suppression peaks as θ changes from 0° to 45°. It results from the frequency shift $\delta\Delta$ [Fig. 5.19 (d)] due to the different polarization states (i.e., the enhancement condition $\Delta_1 + \Delta_3 \pm (G_3 + \delta\Delta) = 0$).

References

[1] Harris S E. Electromagnetically induced transparency. Phys Today, 1997, 50: 36 – 42.

[2] Gea-Banacloche J, Li Y, Jin S, et al. Electromagnetically induced transparency in ladder-type inhomogeneously broadened media-theory and experiment. Phys Rev A, 1995, 51: 576 – 584.

[3] Zibrov A S, Matsko A B, Kocharovskaya O, et al. Transporting and time reversing light via atomic coherence. Phys Rev Lett, 2002, 88: 103601.

[4] Hemmer P R, Katz D P, Donoghue J, et al. Efficient low-intensity optical-phase conjugation based on coherent population trapping in sodium. Opt Lett, 1995, 20: 982 – 984.

[5] Lu B, Burkett W H, Xiao M. Nondegenerate four-wave mixing in a double-Lambda system under the influence of coherent population trapping. Opt Lett, 1998, 23: 804 – 806.

[6] Boyer V, Marino A M, Pooser R C, et al. Entangled images from four-wave mixing. Science, 2008, 321: 544 – 547.

[7] Kang H, Hernandez G, Zhang J, et al. Phase-controlled light switching at low light levels. Phys Rev A, 2006, 73: 011802(R).

[8] Jiang K J, Deng L, Payne M G. Observation of quantum destructive interference in inelastic two-wave mixing. Phys Rev Lett, 2007, 98: 083604.

[9] Du S W, Wen J M, Rubin M H, et al. Four-wave mixing and biphoton generation in a two-level system. Phys Rev Lett, 2007, 98: 053601.

[10] Balic V, Braje D A, Kolchin P, et al. Generation of paired photons with controllable waveforms. Phys Rev Lett, 2005, 94: 183601.

[11] Zhang Y P, Anderson B, Brown A W, et al. Competition between two four-wave mixing channels via atomic coherence. Appl Phys Lett, 2007, 91: 061113.

[12] Qi J, Lazarov G, Wang X, et al. Autler-Townes splitting in molecular lithium: Prospects for all-optical alignment of nonpolar molecules. Phys Rev Lett, 1999, 83: 288 – 291.

[13] Zheng H B, Zhang Y P, Nie Z Q, et al. Interplay among multidressed four-wave mixing processes. Appl Phys Lett,2008, 93: 241101.

[14] For detail in transition probabilities of D1 and D2 line in Na. http://steck.Us/alkalidata. Accessed 20 July 2010.

[15] Li C B, Zheng H B, Zhang Y P, et al. Observation of enhancement and suppression in four-wave mixing processes. Appl Phys Lett, 2009, 95: 041103; Zuo Z C, Sun J, Liu X, et al. Generalized n-photon resonant 2n-wave mixing in an (n+1)-level system with phase-conjugate geometry. Phys Rev Lett, 2006, 97: 193904.

[16] Tsukiyama K. Parametric four-wave mixing in Kr. J Phys B: At Mol Opt Phys, 1996, 29: L345 – L351.

[17] Chapple P B, Baldwin K G H, Bachor H A. Interference between competing quantum-mechanical pathways for four-wave mixing. J Opt Soc Am B, 1998, 6: 180 – 183.

[18] Garret W R, Zhu Y. Coherent control of multiphoton driven processes: A laser-induced catalyst. J Chem Phys, 1997, 106: 2045 – 2048.

[19] Ma H, Gomes A S L, de Araujo C B. All-optical power-controlled switching in wave mixing: application to semiconductor-doped glasses. Opt Lett, 1993, 18: 414 – 416.

[20] Wang R M, Du Y G, Zhang Y P, et al. Polarization spectroscopy of dressed four-wave mixing in a three-level atomic system. J Opt Soc Am B, 2009, 26: 1710 – 1719.

[21] Du S G, Oh E, Wen J M, et al. Four-wave mixing in three-level systems: Interference and entanglement. Phys Rev A, 2007, 76: 013803.

[22] Zhang Y P, Khadka U, Anderson B, et al. Temporal and spatial interference between four-wave mixing and six-wave mixing channels. Phys Rev Lett, 2009, 102: 013601. Wang B, Han Y X, Xiao J T, et al. Multi-dark-state resonances in cold multi-Zeeman-sublevel atoms. Opt Lett, 2006, 31: 3647 – 3649.

[23] Zheng H B, Zhang Y P, Khadka U, et al. Modulating the multi-wave mixing processes via the polarizable dark states. Opt Express, 2009, 17: 15468 – 15480.

[24] Ling H Y, Li Y Q, Xiao M. Coherent population trapping and electromagnetically induced transparency in multi-Zeeman-sublevel atoms. Phys Rev A, 1996, 53: 1014 – 1026.

[25] Li S J, Wang B, Yang X D, et al. Controlled polarization rotation of an optical field in multi-Zeeman-sublevel atoms. Phys Rev A, 2006, 74: 033821.

[26] For detail in transition probabilities of D1 and D2 line in Rb. http://steck.Us/alkalidata. Accessed 10 July 2010.

[27] Lipsich A, Barreiro S, Akulshin A M, et al. Absorption spectra of driven degenerate two-level atomic systems. Phys Rev A, 2000, 61: 053803.

[28] Li C B, Zhang Y P, Nie Z Q, et al. Controlling enhancement and suppression of four-wave mixing via polarized light. Phys Rev A, 2010, 81: 033801.

[29] Nie Z Q, Zhang Y P, Zhao Y, et al. Enhancing and suppressing four-wave mixing in electromagnetically induce transparency window. J Raman Spectrosc, 2010, 41.

6 Multi-Wave Mixing Processes in Multi-level Atomic System

Since real atomic systems have multiple Zeeman sublevels, one can use polarization states of the coupled laser beams to modulate the strength of the multi-wave mixing processes. By manipulating the dark-state or electromagnetically induced transparency (EIT) windows with the polarization states of the laser beams, the multi-wave mixing (MWM) processes can be modified and controlled. Such studies of controllable intermixing between different-order nonlinear optical processes with phase or polarization states of the laver beams can be very important in high-precision measurements, coherent quantum control, and quantum information processing. In the following, some examples of phase or polarization controlled multi-wave mixing processes in multi-level atomic systems will be described. The degenerate Zeeman sublevels and their dressed-state effects are responsible for these observed phenomena. The relative intensities and polarization characteristics of four-wave mixing (FWM) signals in different laser polarization configurations and different level systems are experimentally investigated and compared. Also the results are theoretically explained by different transition path combinations. In the dressed-FWM processes, the dependence of dressing effect on the incident field's polarization is shown. The FWM signal generated by a linearly-polarized pumping field is suppressed more by the dressing field than the one generated by a circularly-polarized pumping field. However, an opposite effect was observed when the probe field's polarization is changed. The multi-dressing mechanisms are used to explain these effects. In addition, the interference and polarization dependence of the coexisting FWM signals in the same atomic system are discussed. Polarizable dark states are used to describe the multi-level dressed states. The dually-dressed EIT and multi-dressed FWM and SWM processes with Zeeman sublevels are also presented theoretically. Such studies of intermixing between different order nonlinear optical processes with controllable phase delay can have important applications in high-precision measurements, coherence quantum control, and quantum information processing.

6.1 Modulating Multi-Wave Mixing Processes via Polarizable Dark States

The generated MWM signals in multi-level systems can transmit through resonant atomic medium with little absorption under the EIT conditions [1, 2]. Enhanced MWM processes due to laser-induced atomic coherence have been experimentally demonstrated in several multi-level atomic systems [3 – 5]. Interesting effects, such as quantum destructive interference in inelastic two-wave mixing [6], phase-controlled light switching at the low light level [7], entangled images in the probe and signal beams in the FWM process [8], and generation of correlated photon pairs [9, 10], have been experimentally studied in various coherently-prepared multi-level atomic systems. When a strong light field interacts with an atomic transition, the light-atom system can be considered as coupled harmonic oscillators with split normal modes, called dressed states. When more than one light field interacts with the same or connected atomic transitions, multi-dressed states can be formed [11]. Recently, interplay among multi-dressed FWM processes [12], competition via atomic coherence in a four-level atomic system with two co-existing FWM processes [13] and destructive/constructive interferences in a two-level atomic system [9] were studied. In recent years, many schemes have been developed to enhance higher-order nonlinear wave-mixing processes. More importantly, with induced atomic coherence and interference, the higher-order processes can become comparable or even greater in amplitude than the lower order wave-mixing processes [14].

In this section, combined theoretical and experimental studies on the polarization dependence of MWM processes and EIT profile are presented, using rubidium atoms as the nonlinear medium. The results obtained for the intensities of the MWM signals as a function of the polarization of the incident laser beams are shown. The relations between the high-order (e.g., third- and fifth-order) nonlinear susceptibilities and the polarizations of the incident beams are shown. To explain the observed EIT profiles and different rules for MWM signal peaks with different incident beam polarizations, the degenerate Zeeman sublevels and their dressed effects are taken into account. The changes in the spectrum of the MWM processes can be attributed to the modulation in the probe field variation. Theoretically, calculation that takes into account all the 16 relevant Zeeman sublevels in the reversed-Y (RY) system and in good agreements with experimentally measured data is also presented.

The relevant experimental energy-level diagram is shown in Fig. 6.1. Four energy levels from the ^{87}Rb atoms are involved in the experimental schemes used in this work. The laser beams are spatially aligned as shown in Fig. 6.2. In Fig. 6.1, energy levels $E\,|0\rangle$ $(5S_{1/2}, F = 2)$, $|1\rangle$ $(5P_{3/2}, F' = 2)$, $|2\rangle$ $(5D_{3/2}, F'' = 1)$ and $|3\rangle$ $(5S_{1/2}, F = 1)$ form the RY-type four-level atomic system. Strong coupling laser beam E_2 (ω_2, $\boldsymbol{k}_2$, and Rabi frequency G_2) together with

E_2' (ω_2, $\boldsymbol{k}_2'$, and Rabi frequency G_2') with small angle (0.5°) and the same frequency detuning Δ_2 ($= \omega_{21} - \omega_2$), connecting the transition between $|1\rangle$ to $|2\rangle$, propagate in the opposite direction of the weak probe beam E_1 (ω_1, $\boldsymbol{k}_1$, and Rabi frequency G_1), which has the frequency detuning Δ_1 ($= \omega_{10} - \omega_1$) and connects the transition between $|0\rangle$ to $|1\rangle$, as shown in the inset of Fig. 6.2. Two additional coupling beams E_3 (ω_3, $\boldsymbol{k}_3$, and Rabi frequency G_3) and E_3 (ω_3, $\boldsymbol{k}_3'$, and Rabi frequency G_3'), with the same frequency detuning Δ_3 ($= \omega_{13} - \omega_3$) connecting the transition between $|3\rangle$ to $|1\rangle$, also propagate in the opposite direction of the weak probe beam E_1 (Fig. 6.2) with small angles. When all five laser beams (E_1, E_2, E_2', E_3, and E_3') are turned on simultaneously, only one ladder-type EIT subsystem will form due to the two-photon Doppler-free configuration [1] and an EIT window opens, whose position in the frequency domain depends on the frequency detuning of the ω_2 laser beams. Meanwhile, there will be co-existing MWM processes that generate signal beams at frequency ω_M ($\omega_M = \omega_1$) in such a multi-level system. First, without the coupling beams E_3 and E_3', one pure FWM E_F process will be generated in the ladder system ($|0\rangle - |1\rangle - |2\rangle$) satisfying the phase-matching condition of $\boldsymbol{k}_{\rm F} = \boldsymbol{k}_1 + \boldsymbol{k}_2 - \boldsymbol{k}_2'$. The signal emerging from the "P" polarization direction is detected by an avalanche photodiode detector (APD). Second, when all beams (except with E_2' blocked) are turned on, the strong coupling beam E_2 will dress the energy level $|1\rangle$ to create the dressed states $|+\rangle$ and $|-\rangle$. In such a case, there exist a dressed FWM process $\boldsymbol{k}_{\rm F}' = \boldsymbol{k}_1 + \boldsymbol{k}_3 - \boldsymbol{k}_3'$ and a coexisting SWM process, in which two photons from E_2 and one photon each from E_1, E_3, and E_3' participate in the SWM process to generate E_S with the phase-matching condition of $\boldsymbol{k}_{\rm S} = \boldsymbol{k}_1 + \boldsymbol{k}_2 - \boldsymbol{k}_2 + \boldsymbol{k}_3 - \boldsymbol{k}_3'$.

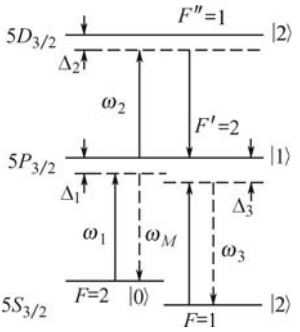

Fig. 6.1. The energy level diagram of relevant ^{87}Rb energy levels.

Although only four energy levels are explicitly shown in Fig. 6.1, there are Zeeman sublevels for each of these energy levels. There are multiple quantum paths for each step of the nonlinear optical processes. The probability amplitudes for these paths depend on the Clebsch-Gordan coefficients, which are intimately related to the polarizations of the input laser beams. Therefore, one can easily manipulate the contributions of the interference terms to

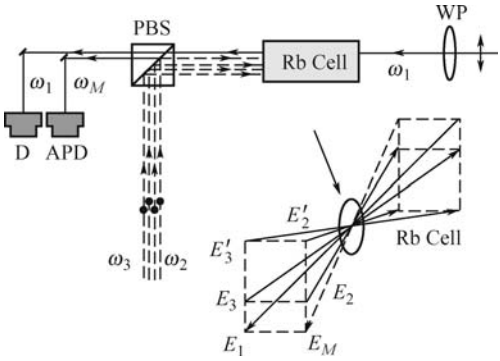

Fig. 6.2. The schematic diagram of the experiment. D denotes the photodiode and APD denotes the avalanche diode detector; PBS denotes the polarized beam splitter and WP denotes the wave plate. Inset: the spatial alignment of the laser beams.

MWM signals by controlling the polarizations of the input laser beams.

To quantitatively investigate the polarization dependence of MWM signals, a theoretical model is developed to treat the polarization-dependent nonlinear processes. The observed MWM signal intensities in the experiments are proportional to the square of the polarizations induced in Rb vapor at frequency ω_M. First, for the FWM signal E_F (by blocking laser beams E_3 and E_3'), the nonlinear atomic polarization $P^{(3)}(\omega_1)$ along the $i(i = x, y)$ direction, from first-order perturbation theory, is given by [15]

$$P_i^{(3)}(\omega_1) = \varepsilon_0 \sum_{jkl} \chi_{ijkl}^{(3)} E_{1j}(\omega_1) E_{2k}^*(\omega_2) E_{2l}(\omega_2), \tag{6.1}$$

where the third-order susceptibility contains the microscopic information about the atomic system. The susceptibility of the nonlinear tensor $\chi_{ijkl}^{(3)}(\omega_F; \omega_1, -\omega_2, \omega_2)$ is also related to the polarization components of the incident and generated fields. For an isotropic medium, as in the rubidium vapor, only four elements are not zero, and they are related to each other by $\chi_{xxxx} = \chi_{xxyy} + \chi_{yxxy} + \chi_{yxyx}$. According to the experimental arrangement, it is assumed that the coupling beams E_2, E_2', E_3, and E_3' have fixed polarization along the y-axis (S polarization), while the probe beam E_1 can have polarization in any direction in the XY plane. In this case, the polarization of the generated FWM signal beam E_F will have two components, i.e., P and S polarizations,

$$\begin{aligned} P_x^{(3)}(\omega_1) &= \varepsilon_0 \chi_x |E_2|^2 |E_1|, \\ P_y^{(3)}(\omega_1) &= \varepsilon_0 \chi_y |E_2|^2 |E_1|, \end{aligned} \tag{6.2}$$

where χ_x and χ_y are the effective susceptibilities. If there is a half-wave plate placed on the path of the probe beam E_1, then

$$\begin{aligned} \chi_x^{(3)} &= \chi_{xyyx} \cos 2\theta, \\ \chi_y^{(3)} &= \chi_{yyyy} \sin 2\theta. \end{aligned} \tag{6.3}$$

For a quarter-wave plate in the probe beam,

$$\chi_x^{(3)} = \chi_{xxxx}\sqrt{\sin^4\phi + \cos^4\phi},$$
$$\chi_y^{(3)} = \chi_{yxxy}\sqrt{2\left|\sin\phi\cos\phi\right|^2}. \tag{6.4}$$

Here θ and ϕ are the rotated angles of the half-wave plate and quarter-wave plate, respectively, relative to the X-axis.

Similarly, for the generated SWM signal E_S (when blocking the coupling laser beam E_2'), the fifth-order nonlinear polarization $P^{(5)}(\omega_1)$ along the $i(i = x, y)$ direction is then given by

$$P_i^{(5)}(\omega_1) = \varepsilon_0 \sum_{jklmn} \chi_{ijklmn}^{(5)} E_{1j}(\omega_1) E_{2k}^*(\omega_2) E_{2l}(\omega_2) E_{3m}^*(\omega_3) E_{3n}(\omega_3), \tag{6.5}$$

where $\chi_{ijklmn}^{(5)}$ is the fifth-order nonlinear susceptibility. For an isotropic medium, as in the Rb vapor, there are sixteen nonzero components and only fifteen of them are independent because they are related to each other by

$$\begin{aligned}\chi_{xxxxxx} = {} & \chi_{yyxxxx} + \chi_{yxyxxx} + \chi_{yxxyxx} + \chi_{yxxxyx} + \chi_{yxxxxy} + \\ & \chi_{xyyxxx} + \chi_{xyxyxx} + \chi_{xyxxyx} + \chi_{xyxxxy} + \chi_{xxyyxx} + \\ & \chi_{xxyyxx} + \chi_{xxyxyx} + \chi_{xxyxxy} + \chi_{xxxyxy} + \chi_{xxxxyy}.\end{aligned} \tag{6.6}$$

Under the same condition as mentioned above for the FWM case, the generated SWM polarization will have two components, parallel and perpendicular to the beam's polarization,

$$P_x^{(5)}(\omega_1) = \varepsilon_0 \chi_x |E_2|^2 |E_3|^2 |E_1|,$$
$$P_y^{(5)}(\omega_1) = \varepsilon_0 \chi_y |E_2|^2 |E_3|^2 |E_1|. \tag{6.7}$$

According to the experimental arrangement, it is assumed that the probe field can have linear polarization in any direction in the XY plane determined by the wave-plate, while the other coupling fields have fixed polarization along the same Y-axis (S polarization). In this case, the polarization of the generated SWM signal beam will have two components, i.e., parallel and perpendicular to the coupling beams' polarization. For a half-wave plate placed in front of the probe beam, the polarizations of the SWM signal beam become

$$\chi_x = \chi_{xyyyyx}\cos 2\theta,$$
$$\chi_y = \chi_{yyyyyy}\sin 2\theta. \tag{6.8}$$

In addition, for a quarter-wave plate, these fifth-order nonlinear susceptibility components are

$$\chi_x = \chi_{xyyyyx}\sqrt{\sin^4\phi + \cos^4\phi},$$
$$\chi_y = \chi_{yyyyyy}\sqrt{2\left|\sin\phi\cos\phi\right|^2}. \tag{6.9}$$

In the experimental (Fig. 6.2), a half-wave plate is used to horizontally polarize the probe beam (P polarization). Then the beam passes through a half-wave plate (or a quarter-wave plate) that is rotated by an angle θ (or ϕ) before going into the ^{87}Rb atomic vapor cell. By blocking different incident beams, the probe beam and the generated FWM signal (or SWM signal) [13] both pass through a polarized beam splitter (PBS) before being detected. The detector D receives the P polarization component of the transmitted probe beam, $E_1(\omega_1)$, whereas the APD receives the horizontally polarized component of the generated MWM signal $E_M(\omega_M)$.

The experiment is done with hot ^{87}Rb atoms by three external cavity diode lasers (ECDL) and linewidths of less than or equal to 1 MHz. Each output power is as follow: 0.7 mW of probe field E_1; 65 mW of coupling beams E_2, E_2', and 15 mW of coupling laser beams E_3, E_3'. The cell whose length is 5 cm is heated up to 60℃ and the density is 2.5×10^{11} cm^{-3}.

Figure 6.3 shows the EIT spectra (lower curves) and the SWM spectra (upper curves) of the ^{87}Rb atoms, by blocking laser beam E_2', for probe field with different polarizations rotated by a half-wave plate. The coupling beams are linearly polarized in the S polarizations direction and the probe beam is linearly polarized in the P polarization direction initially (defined as $\theta = 0°$).

As shown in Fig. 6.3, various polarized configurations of the coupling and probe beams, by rotating the half-wave plate, result in the quite different spectra. The absorption curve of the probe beam changes from EIT to a dispersion-like curve, and then back to EIT again while the polarization of the input probe beam changes one period. Meanwhile, the rules of the two SWM signal peaks change quite differently. These observed experimental results reveal that the degenerate Zeeman sublevels [16, 17] and the dressed-state effects play crucial roles in the EIT and SWM spectra.

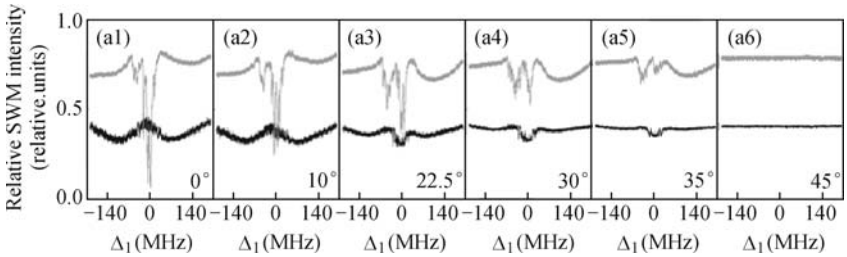

Fig. 6.3. The polarization dependence of the transmitted probe and SWM signal beams versus the rotating angle of the half-wave plate. (a1 – a6) EIT (lower curves) and SWM (upper curves) spectra versus the rotating angle. The experimental parameters are $G_1 = 2\pi \times 5$ MHz, $G_2 = G_2' = 2\pi \times 80$ MHz, $G_3 = G_3' = 2\pi \times 35$ MHz, and $\Delta_2 = \Delta_3 = 0$. Adopted from Ref. [17].

To understand the above experimental results, the theoretical calculation of the probe absorption spectrum considers all the 16 relevant Zeeman sublevels [18] in the RY system. The calculations are limited to the cases that the coupling fields are linearly polarized, and the magnetic field is absent.

Three examples of the excitations of the coupling and the probe beams are illustrated in Fig. 6.4. Figure 6.4 (a) shows the case with the probe beam polarization to be orthogonal to the coupling beams and Fig. 6.4 (c) corresponds to the case with parallel polarization. Figure 6.4 (b) gives the results with probe input polarization in between those two cases. For simplicity, the cascade three-level system is considered (by blocking coupling fields E_3 and E_3'), which forms an EIT configuration. For the case as given in Fig. 6.4 (a), the density-matrix ρ considering all the Zeeman levels is solved with the following equations:

$$\dot{\rho} = (1/\mathrm{i}\hbar)[H_{atom} + H_{coupling} + H_{probe}, \rho] + \{\mathrm{d}\rho/\mathrm{d}t\}, \tag{6.10}$$

$$H_{atom} = \hbar\omega_{10} \sum_{i=6}^{10} |i\rangle\langle i| + \hbar\omega_{21} \sum_{i=11}^{13} |i\rangle\langle i|, \tag{6.11}$$

$$\begin{aligned} H_{coupling} = &- \exp[\mathrm{i}\omega_c t][(\hbar\Omega_{c1}/2)(|7\rangle\langle 11| + |9\rangle\langle 13|) + \\ &(\hbar\Omega_{c2}/2)|8\rangle\langle 12|] + c.c., \end{aligned} \tag{6.12}$$

$$\begin{aligned} H_{probe} = &- \exp[\mathrm{i}\omega_p t][(\hbar\Omega_{p1}/2)(|1\rangle\langle 7| + |5\rangle\langle 9|) + \\ &(\hbar\Omega_{p2}/2)(|2\rangle\langle 8| + |4\rangle\langle 8|) + \\ &(\hbar\Omega_{p3}/2)(|3\rangle\langle 9| + |3\rangle\langle 7| + \\ &(\hbar\Omega_{p4}/2)(|2\rangle\langle 6| + |4\rangle\langle 10|)] + c.c., \end{aligned} \tag{6.13}$$

$$\begin{aligned} \{\mathrm{d}\rho/\mathrm{d}t\} = &-\Gamma_1 \sum_{i=11}^{13} \rho_{ii}|i\rangle\langle i| - \Gamma_2 \sum_{i=6}^{10} \rho_{ii}|i\rangle\langle i| + \\ &\sum_{i=1}^{10} \left(\sum_{j=11}^{13} \Gamma_{ji}\rho_{jj} \right) |i\rangle\langle i| + \sum_{i=1}^{5} \left(\sum_{j=6}^{10} \Gamma_{ji}\rho_{jj} \right) |i\rangle\langle i| - \\ &\frac{1}{2} \left[\Gamma_1 \sum_{i=11}^{13} \sum_{j=1}^{10} \rho_{ij}|i\rangle\langle j| + \Gamma_2 \sum_{i=6}^{10} \sum_{j=1}^{5} \rho_{ij}|i\rangle\langle j| + c.c. \right] - \\ &\left[\Gamma' \sum_{i=11}^{13} \sum_{j=6}^{10} \rho_{ij}|i\rangle\langle j| + \Gamma'' \sum_{i=6}^{10} \sum_{j=1}^{5} \rho_{ij}|i\rangle\langle j| + \right. \\ &\left. \Gamma''' \sum_{i=11}^{13} \sum_{j=1}^{5} \rho_{ij}|i\rangle\langle j| + c.c. \right], \end{aligned} \tag{6.14}$$

where ω_{10} is the $F = 2 \rightarrow F' = 2$ transition frequency and ω_{21} is the $F' = 2 \rightarrow F'' = 1$ transition frequency. ω_c is the frequency of the coupling field, and ω_p is frequency of the probe laser. Ω_N is the Rabi frequency for the transition indicated by its subscripts. The expression of $\{\mathrm{d}\rho/\mathrm{d}t\}$ describes all the relaxation processes in the system. Γ_1 and Γ_2 are the spontaneous decay

rates of the $5D_{3/2}$, $F'' = 1$ and $5P_{3/2}$, $F' = 2$ excited states, respectively. Γ_{ji} is the spontaneous emission rate from an excited state $|j\rangle$ to a ground state $|i\rangle$. Γ', Γ'' and Γ''' are the decoherence rates for the relaxation processes other than the spontaneous decay. To obtain linear susceptibility, the density-matrix Eq. (6.11) under the steady-state condition need to be solved. Under the weak probe field approximation [1], the expressions of the first-order matrix elements can be easily calculated.

For the right-hand-circularly (RHC) polarized sub-ladder systems:

$$\begin{cases} \rho_{1,7}^{+} = \dfrac{\mathrm{i}\Omega_{p1}^{+}}{\mathrm{i}\Delta_{p1} + \Gamma_{1,7} + \dfrac{|\Omega_{c1}|^2}{\mathrm{i}(\Delta_{p1} + \Delta_{c1}) + \Gamma_{11,1}}} \rho_{1,7}^{(0)}, \\ \rho_{2,8}^{+} = \dfrac{\mathrm{i}\Omega_{p2}^{+}}{\mathrm{i}\Delta_{p2} + \Gamma_{2,8} + \dfrac{|\Omega_{c2}|^2}{\mathrm{i}(\Delta_{p2} + \Delta_{c2}) + \Gamma_{12,2}}} \rho_{2,8}^{(0)}, \\ \rho_{3,9}^{+} = \dfrac{\mathrm{i}\Omega_{p3}^{+}}{\mathrm{i}\Delta_{p3} + \Gamma_{3,9} + \dfrac{|\Omega_{c1}|^2}{\mathrm{i}(\Delta_{p3} + \Delta_{c1}) + \Gamma_{13,3}}} \rho_{3,9}^{(0)}, \\ \rho_{4,10}^{+} = \dfrac{\mathrm{i}\Omega_{p4}^{+}}{\mathrm{i}\Delta_{p4} + \Gamma_{4,10}} \rho_{4,10}^{(0)}. \end{cases} \tag{6.15}$$

For the left-hand-circularly (LHC) polarized sub-ladder systems:

$$\begin{cases} \rho_{2,6}^{-} = \dfrac{\mathrm{i}\Omega_{p4}^{-}}{\mathrm{i}\Delta_{p4} + \Gamma_{2,6}} \rho_{2,6}^{(0)}, \\ \rho_{3,7}^{-} = \dfrac{\mathrm{i}\Omega_{p3}^{-}}{\mathrm{i}\Delta_{p3} + \Gamma_{3,7} + \dfrac{|\Omega_{c1}|^2}{\mathrm{i}(\Delta_{p3} + \Delta_{c1}) + \Gamma_{11,3}}} \rho_{3,7}^{(0)}, \\ \rho_{4,8}^{-} = \dfrac{\mathrm{i}\Omega_{p2}^{-}}{\mathrm{i}\Delta_{p2} + \Gamma_{4,8} + \dfrac{|\Omega_{c2}|^2}{\mathrm{i}(\Delta_{p2} + \Delta_{c2}) + \Gamma_{12,4}}} \rho_{4,8}^{(0)}, \\ \rho_{5,9}^{-} = \dfrac{\mathrm{i}\Omega_{p1}^{-}}{\mathrm{i}\Delta_{p1} + \Gamma_{5,9} + \dfrac{|\Omega_{c1}|^2}{\mathrm{i}(\Delta_{p1} + \Delta_{c1}) + \Gamma_{13,5}}} \rho_{5,9}^{(0)}, \end{cases} \tag{6.16}$$

where frequency detuning parameters Δ_{ij} are the differences between the laser frequency and the corresponding atomic transition frequency. For the level configuration shown in Fig. 6.4 (c), the probe Hamiltonian is changed to

$$\begin{aligned} H_{probe} = &- \exp[\mathrm{i}\omega_p t][(\hbar\Omega'_{p1}/2)(|1\rangle\langle 6| + |5\rangle\langle 10|) + \\ &(\hbar\Omega'_{p2}/2)(|2\rangle\langle 7| + |4\rangle\langle 9|) + c.c., \end{aligned} \tag{6.17}$$

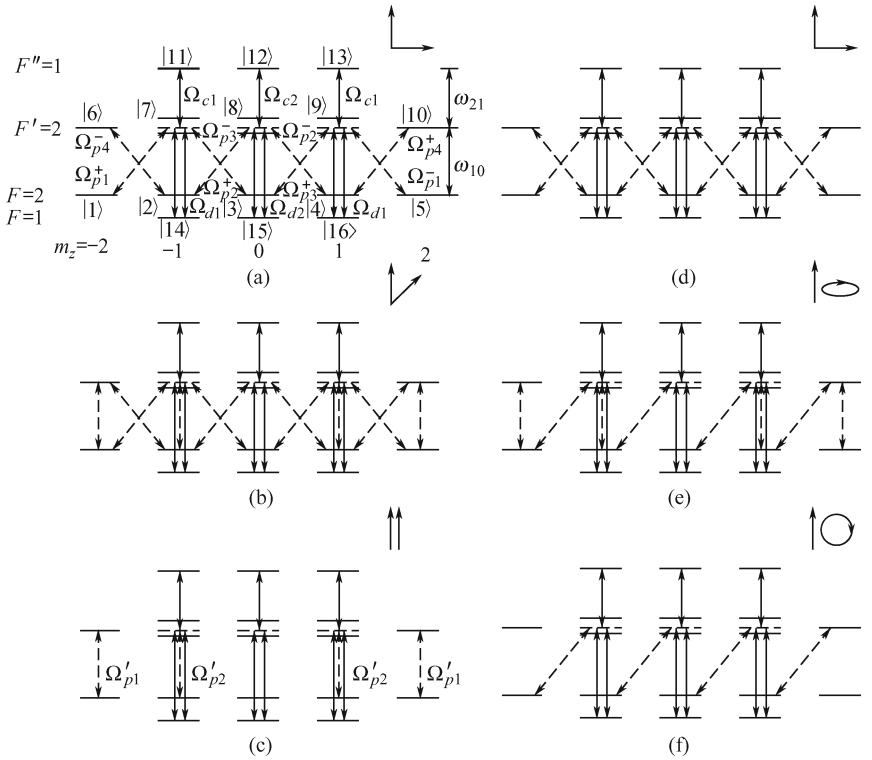

Fig. 6.4. The excitations of the coupling and probe fields among the Zeeman levels in the RY system. (a), (b), and (c) correspond to the case with a half-wave plate in the probe beam; (d) (e), and (f) correspond to a quarter-wave plate.

and the remaining calculations are similar. The expressions of the matrix elements for the linearly polarized sub-ladder systems can be obtained as

$$\begin{cases} \rho_{1,6}^{0} = \dfrac{\mathrm{i}\Omega'_{p1}}{\mathrm{i}\Delta'_{p1} + \Gamma_{1,6}} \rho_{1,6}^{(0)}, \\ \rho_{5,10}^{0} = \dfrac{\mathrm{i}\Omega'_{p1}}{\mathrm{i}\Delta'_{p1} + \Gamma_{5,10}} \rho_{5,10}^{(0)}, \\ \rho_{2,7}^{0} = \dfrac{\mathrm{i}\Omega'_{p2}}{\mathrm{i}\Delta'_{p2} + \Gamma_{2,7} + \dfrac{|\Omega_{c1}|^2}{\mathrm{i}(\Delta'_{p2} + \Delta_{c1}) + \Gamma_{11,2}}} \rho_{2,7}^{(0)}, \\ \rho_{4,9}^{0} = \dfrac{\mathrm{i}\Omega'_{p2}}{\mathrm{i}\Delta'_{p2} + \Gamma_{4,9} + \dfrac{|\Omega_{c1}|^2}{\mathrm{i}(\Delta'_{p2} + \Delta_{c1}) + \Gamma_{13,4}}} \rho_{4,9}^{(0)}. \end{cases} \tag{6.18}$$

The case in Fig. 6.4 (b) is an integration of the results from Fig. 6.4 (a, c). All the theoretical results of the different polarization configurations are obtained in the same way.

When all the Zeeman sublevels in the RY system are taken into account, the unexpected profiles of the EIT spectra and different changing rules of the two SWM signal peaks can then be easily explained. For instance, initially, the polarizations of the probe beam and coupling beams are perpendicular [Fig. 6.4 (a)]. There exist three RHC and three LHC EIT subsystems with one RHC and one LHC probe transitions without the interference of the coupling fields. The observed transmission spectrum is the combination of the Lorentzian absorption profile and the EIT profile for the probe beam. However, in the Fig. 6.4 (a), the intensity of the Lorentzian absorption profile is much smaller than that of the EIT profile, which is the result of different dipole momentums between the Zeeman sublevels [19]. In the case of Fig. 6.4 (b), as the half-wave plate rotating, there are two linearly polarized EIT subsystems with the RHC and LHC EIT subsystems decreasing. Also, there are two additional linear probe transitions. The intensity of the Lorentzian absorption profile is comparable to that of the EIT subspectrums. Therefore, a narrower Lorentzian shape peak can be seen clearly on top of the broader EIT profile as shown in Fig. 6.3 (a3). Due to the detuning of the coupling field, the curve appears to be dispersion-like. When all the laser beams have the same polarization [Fig. 6.4 (c)], there are only two linearly-polarized EIT subsystems and two linear probe transitions. Because of the different dipole momentums among different Zeeman sublevels, the Lorentzian absorption profile is much larger than that of the EIT profile, so the probe transmission has an absorption-type shape with subnatural linewidth [20]. This effect doesn't present in Fig. 6.3 due to our current experimental configuration, i.e., the signal is detected only in the P polarization.

In addition, if the coupling fields E_3 and E_3' are open, there are doubly-dressed effects for the EIT curve. The analytical solutions will be changed as following.

For the RHC-polarized sub-RY systems:

$$\rho_{1,7}^{+}=\frac{\mathrm{i}\Omega_{p1}^{+}}{\mathrm{i}\Delta_{p1}+\Gamma_{1,7}+\dfrac{\left|\Omega_{c1}\right|^{2}}{\mathrm{i}(\Delta_{p1}+\Delta_{c1})+\Gamma_{11,1}}+\dfrac{\left|\Omega_{d1}\right|^{2}}{\mathrm{i}(\Delta_{p1}-\Delta_{d1})+\Gamma_{14,1}}}\rho_{1,7}^{(0)}, \tag{6.19}$$

$$\rho_{2,8}^{+}=\frac{\mathrm{i}\Omega_{p2}^{+}}{\mathrm{i}\Delta_{p2}+\Gamma_{2,8}+\dfrac{\left|\Omega_{c2}\right|^{2}}{\mathrm{i}(\Delta_{p2}+\Delta_{c2})+\Gamma_{12,2}}+\dfrac{\left|\Omega_{d2}\right|^{2}}{\mathrm{i}(\Delta_{p2}-\Delta_{d2})+\Gamma_{15,2}}}\rho_{2,8}^{(0)}, \tag{6.20}$$

$$\rho_{3,9}^{+}=\frac{\mathrm{i}\Omega_{p3}^{+}}{\mathrm{i}\Delta_{p3}+\Gamma_{3,9}+\dfrac{\left|\Omega_{c1}\right|^{2}}{\mathrm{i}(\Delta_{p3}+\Delta_{c1})+\Gamma_{13,3}}+\dfrac{\left|\Omega_{d1}\right|^{2}}{\mathrm{i}(\Delta_{p3}-\Delta_{d1})+\Gamma_{16,3}}}\rho_{3,9}^{(0)}. \tag{6.21}$$

For the LHC-polarized sub-RY systems:

$$\rho_{3,7}^{-}=\frac{\mathrm{i}\Omega_{p3}^{-}}{\mathrm{i}\Delta_{p3}+\Gamma_{3,7}+\dfrac{|\Omega_{c1}|^{2}}{\mathrm{i}(\Delta_{p3}+\Delta_{c1})+\Gamma_{11,3}}+\dfrac{|\Omega_{d1}|^{2}}{\mathrm{i}(\Delta_{p3}-\Delta_{d1})+\Gamma_{14,3}}}\rho_{3,7}^{(0)}, \tag{6.22}$$

$$\rho_{4,8}^{-}=\frac{\mathrm{i}\Omega_{p2}^{-}}{\mathrm{i}\Delta_{p2}+\Gamma_{4,8}+\dfrac{|\Omega_{c2}|^{2}}{\mathrm{i}(\Delta_{p2}+\Delta_{c2})+\Gamma_{12,4}}+\dfrac{|\Omega_{d2}|^{2}}{\mathrm{i}(\Delta_{p2}-\Delta_{d2})+\Gamma_{15,4}}}\rho_{4,8}^{(0)}, \tag{6.23}$$

$$\rho_{5,9}^{-}=\frac{\mathrm{i}\Omega_{p1}^{-}}{\mathrm{i}\Delta_{p1}+\Gamma_{5,9}+\dfrac{|\Omega_{c1}|^{2}}{\mathrm{i}(\Delta_{p1}+\Delta_{c1})+\Gamma_{13,5}}+\dfrac{|\Omega_{d1}|^{2}}{\mathrm{i}(\Delta_{p1}-\Delta_{d1})+\Gamma_{16,5}}}\rho_{5,9}^{(0)}. \tag{6.24}$$

For the linearly-polarized sub-RY systems:

$$\rho_{2,7}^{0}=\frac{\mathrm{i}\Omega_{p2}'}{\mathrm{i}\Delta_{p2}'+\Gamma_{2,7}+\dfrac{|\Omega_{c1}|^{2}}{\mathrm{i}(\Delta_{p2}'+\Delta_{c1})+\Gamma_{11,2}}+\dfrac{|\Omega_{d1}|^{2}}{\mathrm{i}(\Delta_{p2}'-\Delta_{d1})+\Gamma_{14,2}}}\rho_{2,7}^{(0)}, \tag{6.25}$$

$$\rho_{4,9}^{0}=\frac{\mathrm{i}\Omega_{p2}'}{\mathrm{i}\Delta_{p2}'+\Gamma_{4,9}+\dfrac{|\Omega_{c1}|^{2}}{\mathrm{i}(\Delta_{p2}'+\Delta_{c1})+\Gamma_{13,4}}+\dfrac{|\Omega_{d1}|^{2}}{\mathrm{i}(\Delta_{p2}'-\Delta_{d1})+\Gamma_{16,4}}}\rho_{4,9}^{(0)}. \tag{6.26}$$

These expressions indicate that the additional coupling fields will modulate the EIT profiles. Different frequency detuning configurations of the three stronger coupling fields will affect the EIT spectral shape. By controlling the frequency detuning of the coupling fields, either EIT or electromagnetic induced absorption (EIA) spectrum will appear.

In order to quantitatively compare with the observed changes of the SWM signal peaks as probe polarization changes, the calculation of the area of the spectrum under the peak [see Fig. 6.5 (b1)] and the height of each peak [see Fig. 6.5 (b2)] is chosen. As a comparison, the area curve of the EIT [Fig. 6.5 (a1)] and the absorption height of each peak are also presented. From Figs. 6.5, the changes of the SWM spectrum, as well as for the EIT peaks, are well described by the function $\cos^2 2\theta$, as calculated above. It is interesting to see the polarization dependence of the SWM emission signal following the polarization of the probe field. The theoretical curves (the solid lines) are in good agreement with the experimental data. The different change

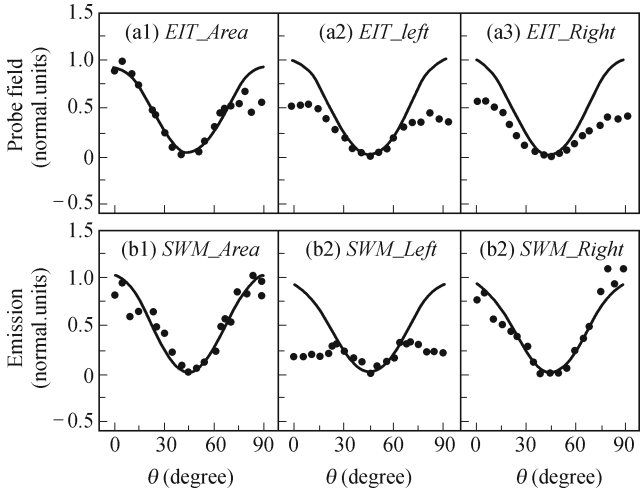

Fig. 6.5. (a) Measured (dots) and calculated (solid curves) areas and heights of the two transmitted EIT peaks. (b) Measured (dots) and calculated (solid curves) areas and heights of the SWM signal peaks.

rules of the two SWM signal peaks can be attributed to the modulation of the modified EIT spectral profile. The dotted lines of Fig. 6.5 (a2, a3) represent the absorption peak heights of the probe field at different polarization states. The dotted lines of Fig. 6.6 (a1, a2) depict the EIT depths which show different coupling processes of the total EIT effect via the different polarization dark states. As we can be seen from the figures, the rule of change in the positive part of the EIT dispersion-like curve [Fig 6.6 (a1)] is dominated by the polarization property. However, in the negative part [Fig. 6.6 (a2)], it gradually changes from EIT to absorption in a half period. After the absorption is larger than the EIT dip, the increase of absorption is faster than the polarized attenuation, and then the roles of them are switched. Figure 6.5 (b2, b3) illustrate the measured dependence of the relative SWM signal intensity on the rotation angle θ (half-wave plate) when the diode laser (probe) is tuned to the $5S_{1/2}$, $F = 2 \rightarrow 5P_{3/2}$, $F' = 2$ one-photon transition. Besides its direct dependence on the polarization of the probe beam, the SWM signal spectrum is also modulated by the EIT effect since it transmits through the medium in the EIT window. Figures 6.6 (b1) and 6.9 (b2) show the corresponding differences of the experiment data and theoretically calculated curves, which represent different coupling paths of the total SWM processes via different polarization configurations. The left peak is always in the positive part of the dispersion-like EIT curve which gets dramatically modulated effect due to EIT. This means that the fifth-order susceptibility $\chi^{(5)}_{ijklmn}$ must be taken into account due to dressed effect, which affects the evolution of the peak together with the polarization dependence of $\cos^2 2\theta$. The right peak is in the negative region of the dispersion-like EIT shape, where it is dominated by the

polarization property due to the increase in absorption. It can be concluded that the evolution of the SWM spectrum is modulated by the modified EIT spectrum.

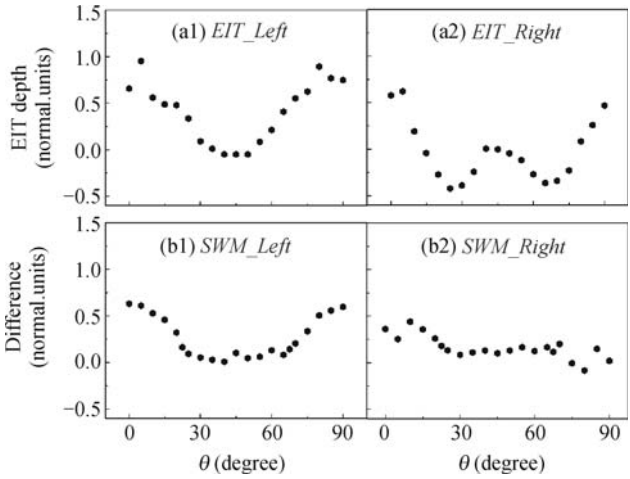

Fig. 6.6. (a) Peak depths for the two EIT transmission peaks. (b) Differences between the theoretical results and experimental data.

Next, the experimentally measured and theoretically calculated probe transmission and FWM spectra are presented by rotating the quarter-wave plate (in front of the input probe beam) whose period is 180° as can be seen in Fig. 6.7. Here, the MWM process is the FWM by blocking laser beams E_3 and E_3' while other beams are turned on. The theoretical results can be obtained from the same procedure as above by eliminating the absent items, that is, LHC subsystems in the RY system. The EIT spectrum also shows the same profile, including the dispersion-like curve. However, the positive peak changes from a single peak into two peaks. Although the way of polarization with a quarter-wave plate is different from with a half-wave plate, its rules of evolution can be explained by the same method as for the half-wave plate. Schemes (d), (e), and (f) in Fig. 6.4 show the ways of coupling in different polarization configurations. Differ from using a half-wave plate whose period is 90°, the right-hand elliptically polarized beam is present during $0° \sim 45°$ and $45° \sim 90°$ [Fig. 6.4 (e)], and a pure RHC-polarized beam at 45° [Fig. 6.4 (f)]. However, within $0° \sim 45°$, the RHC component increases gradually while the linear component decreases. In the region of $45° \sim 90°$ the opposite process is true. Taking the case of $0° \sim 45°$ as an example, we can take the right-hand elliptically-polarized beam being composed of a vertical, linearly-polarized beam and a RHC-polarized beam. Therefore, in our experiment, the original symmetric EIT configurations [Fig. 6.4 (d)] are replaced by two linear EIT and three RHC EIT subsystems [Fig. 6.4 (e)] that are asymmetric due to the difference in the dipole moments among different Zeeman sub-

levels. The destruction of this symmetry results in different polarizable dark states leading to the modified EIT spectrum. It is different from the case with half-wave plate, which does not destroy the symmetry in the EIT spectral shape. The situation in the rest of the period ($45° \sim 90°$) can be discussed in the same way. So, the spectrum by rotating a quarter-wave plate is different from the case of using a half-wave plate.

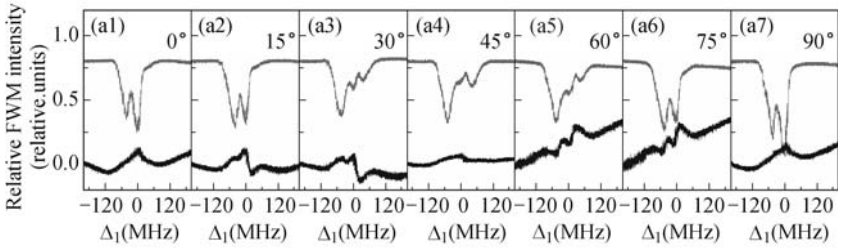

Fig. 6.7. Polarization dependence of the transmitted probe and FWM signal beams versus the rotation angle of the quarter-wave plate. (a1) – (a7) The EIT (lower curves) and FWM (upper curves) spectra versus the rotation angle. The experimental parameters are $G_1 = 2\pi \times 5$ MHz, $G_2 = G_2' = 2\pi \times 80$ MHz, and $\Delta_2 = 0$.

The FWM spectra is modulated by the EIT spectra as shown in Fig. 6.7. As the quarter-wave plate rotates, the FWM spectrum changes from a two-peak structure to a three-peak one. The rule of evolution for each peak includes not only the polarized property, but also effects of dark-state modulation due to the asymmetric coupling structure in EIT spectrum. Similar to the analysis used for the half-wave plate, the rule of evolution in the height of each absorption peak in the EIT profile follows the polarization effect of the probe beam. Although each peak [Fig. 6.8 (a1 – a3)] is significantly modulated, the general trend in its evolution is not destroyed. Moreover, in studying the detail dark-state coupling configuration for each peak, the peak depths of the EIT curves have been investigated [Fig. 6.9 (a1 – a3)]. All of them undergo the combined interactions of the selectively-polarized probe beam and the polarized dark-state modulation. The two peaks in the positive part of the dispersion-like curve can be attributed to the asymmetric EIT configuration, RHC polarization and vertical linearly-polarized EIT subsystems. Due to the increase in absorption [Fig. 6.4 (e)], the right peak in the probe transmission spectrum changes from EIT to EIA [Fig. 6.9 (a3)]. Therefore, based on the above analysis of the EIT spectrum, the rule of change in FWM spectrum can be understood easily. The left FWM peak [Figs. 6.8 (b1)], corresponding to the left EIT peak [Fig. 6.9 (a1)] dominated by the polarized dark-state component, is dramatically modulated and the contribution from polarization change of the probe beam is suppressed. As mentioned above, there could be combined contributions from the third-order nonlinear susceptibility $\chi^{(3)}_{ijkl}(\omega_F; \omega_1, -\omega_2, \omega_2)$ and the polarization effect of the probe field in the form of $\sqrt{\sin^4\phi + \cos^4\phi}$. Although it is affected by

the polarized dark-state modulation, the trend of change for the middle peak [Fig. 6.9 (a2)] follows the polarization change of the probe beam. As a result, the polarization property of the middle FWM peak survives [Fig. 6.8 (b2)]. The right FWM peak is modulated and its height increases gradually due to the increased absorption of the right peak in the probe transmission spectrum. Meanwhile, the middle FWM peak decreases gradually. These two peaks have a competitive relationship, which can explain their opposite phase evolutions [Fig. 6.8 (b3)].

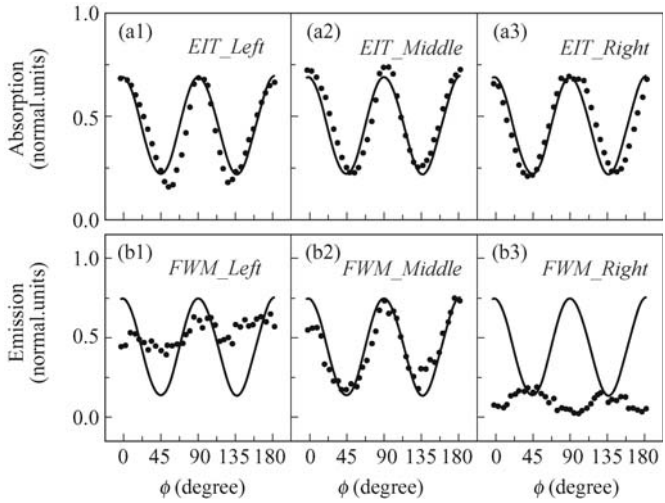

Fig. 6.8. (a) Measured (dots) and calculated (solid curves) heights of the transmitted EIT peaks. (b) Measured (dots) and calculated (solid curves) heights of the FWM signal peaks.

On the other hand, by considering the quantum interference effects, it can be considered that the FWM process and absorption process of probe field affected by the interference among sub-dark states. Three dark states are identified, or noncoupled states for three subsystems of the RY-type system, that are decoupled from the state $|1\rangle$: $|D1\rangle = (\Omega_2 |0\rangle - \Omega_1 |2\rangle)/\sqrt{|\Omega_1|^2 + |\Omega_2|^2} \simeq |0\rangle - \Omega_1 |2\rangle /\Omega_2$, where $\Omega_2 >> \Omega_1$ is used; $|D2\rangle = (\Omega_3 |0\rangle - \Omega_1 |3\rangle)/\sqrt{|\Omega_3|^2 + |\Omega_1|^2} \simeq |0\rangle - \Omega_1 |3\rangle /\Omega_3$, where $\Omega_3 >> \Omega_1$ is used; $|D3\rangle = (\Omega_3 |2\rangle - \Omega_2 |3\rangle)/\sqrt{|\Omega_2|^2 + |\Omega_3|^2} = \cos\theta |2\rangle - \sin\theta |3\rangle$, where $\cos\theta = \Omega_3/\sqrt{|\Omega_2|^2 + |\Omega_3|^2}$, $\sin\theta = \Omega_2/\sqrt{|\Omega_2|^2 + |\Omega_3|^2}$. The total dark state is then given by: $|D\rangle = |D1\rangle + |D2\rangle + |D3\rangle = 2|0\rangle + (\cos\theta - \Omega_1/\Omega_2)|2\rangle - (\Omega_1/\Omega_3 + \sin\theta)|3\rangle$.

The population of the atoms in dark state $|\langle D \mid \psi\rangle|^2$ would like to be found out when the three dark states interfere with each other, where $|\psi\rangle = c_0|0\rangle + c_1|1\rangle + c_2|2\rangle + c_3|3\rangle$ is the wave function of the system in the bare-state basis. Therefore, by considering the interference between dark states

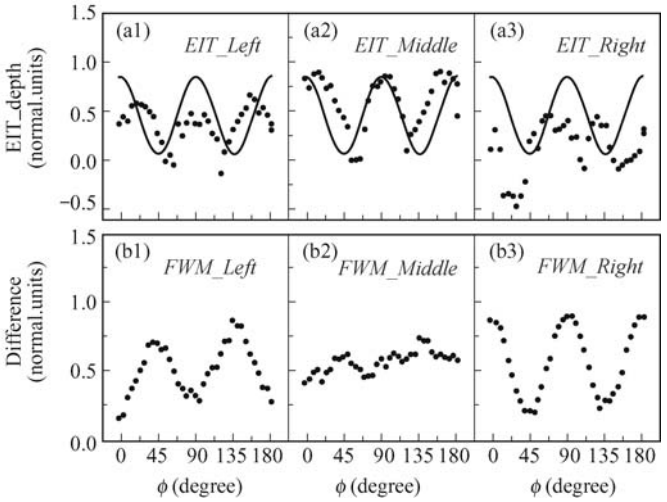

Fig. 6.9. (a) Peak depths for the EIT transmission peaks. (b) Differences between the theoretical results and experimental data.

from subsystems, the intensity of the FWM signal is obtained as following: $I = \left| N' \mu \rho_{10}^{(3)} \right|^2$, where $N' = N \left(1 - |\langle D \mid \psi \rangle|^2 \right)$, and N is the particle number density, namely, it is believed that the particles in the dark state do not interact with outer fields and so do not participate the FWM process. Similarly, for absorption of probe field we have linear $\chi' = N' \mu \rho_{10}^{(1)} / \varepsilon_0 E_1$ and the transmission intensity of probe field is $T' = \exp\left[2\pi \mathrm{Im}[\chi'] z / \lambda\right]$.

6.2 Polarization Spectroscopy of Dressed Four-Wave Mixing in a Three-level Atomic System

The parametric FWM is a useful process for generating coherent radiations from the vacuum ultraviolet to infrared wavelengths. The polarization characteristics of two-photon resonant FWM processes have been investigated in several types of metal vapors gases. Tsukiyama [17] described polarization properties of the near-infrared FWM signal produced in Kr vapor; Museur et al. [18] studied the polarization dependence of the vacuum ultra-violet light generated by a four-wave sum-frequency generation process in Hg; and Ishii et al [15] investigated polarization characteristics of FWM in NO gas. Besides of producing coherent emissions, parametric FWM processes can also be used to study interference effects. Previous studies have used FWM processes to observe interference effects between different atomic polarizations [21 – 25]. Studies of interference effects in multilevel atomic systems have become an active field of research in recent years, which made it possible to coherently

control the optical properties of atomic media [26, 27]. In parametric FWM processes, there are multiple quantum paths for each step of the nonlinear processes, and the probability amplitudes for these different transition paths are intimately related to the polarizations of the input laser fields. Therefore, it is possible to coherently control the nonlinear processes by manipulating the polarization states of incident laser beams.

In this section, both theoretical and experimental studies are given on the polarization dependence of FWM signals generated in Na atomic vapor. Both two-level and three-level systems in Na atoms are used in these studies. The classical, as well as quantum, theoretical models have been developed to explain the dependence of FWM signals on the polarization states of the incident laser beams. By comparing the FWM spectra for different laser polarization configurations, different contributions from third-order nonlinear susceptibility elements under different conditions can be identified. Furthermore, the different contributions by the difference from combinations of transition paths for three incident beam polarization schemes are explained. Moreover, the polarization characteristics of the singly-dressed and doubly-dressed FWM processes in either a two-level or a three-level atomic system in Na vapor are shown. In the three-level atomic system, the FWM signal generated by a linearly-polarized pumping field is greatly suppressed by the dressing field while the one generated by a circularly-polarized pumping field is only slightly influenced by the dressing field. Also, different change rules are observed when the polarization of the probe field is changed. Different dressing effects of two dressing schemes are used to explain this phenomenon. The dressing effects, as well as the interference between the two coexisting FWM signals, have been discussed in different laser polarization configurations. Investigations of the interactions between different FWM processes and their polarization properties can help us to understand the underlying physical mechanisms and to optimize effectively the generated nonlinear optical signals. Controlling nonlinear optical processes can have many potential applications, such as in all-optical switches [28] and quantum-information processing [29, 30].

The experiments are carried out in Na vapor (in a heat pipe oven), which is heated up to a temperature of about 235℃. Three energy levels from Na atoms are involved in the experimental schemes. As shown in Fig. 6.10, energy levels $|0\rangle$ $(3S_{1/2})$ and $|1\rangle$ $(3P_{3/2})$ form the two-level atomic system. Two laser beams E_d (ω_p, $\boldsymbol{k}_d$, and Rabi frequency G_d) and E'_d (ω_p, $\boldsymbol{k}'_d$, and Rabi frequency G'_d), connecting the transition between $|0\rangle$ and $|1\rangle$, propagate in the opposite direction of the weak probe beam E_p (ω_p, $\boldsymbol{k}_p$, and Rabi frequency G_p), which also connects the transition between $|0\rangle$ and $|1\rangle$. The three laser beams come from the same dye laser DL1 (wavelength of 589.0 nm, 10 Hz repetition rate, 5 ns pulse width, and 0.04 cm^{-1} linewidth) with the frequency detuning Δ_1, pumped by the second harmonic beam of a Nd:YAG laser. These three laser fields generate a degenerate-FWM (DFWM) process satisfying the phase-matching condition of $\boldsymbol{k}_{s1} = \boldsymbol{k}_p + \boldsymbol{k}_d - \boldsymbol{k}'_d$. The energy levels

$|0\rangle\,(3S_{1/2}) - |1\rangle\,(3P_{3/2}) - |2\rangle\,(4D_{3/2})$ form the cascade three-level atomic system. Two additional coupling laser beams E_c (ω_c, $\boldsymbol{k}_c$, and Rabi frequency G_c) and E_c' (ω_c, $\boldsymbol{k}_c'$, and Rabi frequency G_c'), connecting the transition between $|1\rangle$ to $|2\rangle$ are from another dye laser DL2 (which has the same characteristics as the DL1) with a frequency detuning Δ_2. E_c, E_c' and E_p fields interact with each other and generate a nondegenerate FWM (NDFWM) signal, satisfying the phase-matching condition of $\boldsymbol{k}_{s2} = \boldsymbol{k}_p + \boldsymbol{k}_c - \boldsymbol{k}_c'$. The generated DFWM and NDFWM signals propagate along slightly different directions due to their different spatial phase-matching conditions. Two photomultiplier tube (PMT) detectors are used to receive the horizontally-polarized component (P polarization) and the vertically-polarized component (S polarization) for one of the signal beams, or horizontally-polarized components of both signal beams, respectively. A half-wave plate (HWP) and a quarter-wave plate (QWP) are selectively used (in different experiments, respectively) to control the polarization states of the incident fields. The generated FWM signals may pass through another HWP and a polarization beam splitter (PBS) before being detected by the two PMTs.

6.2.1 Various Nonlinear Susceptibilities for Different Polarization Schemes

The polarization dependence of FWM signals can be explained using either classical or quantum mechanical description [31]. Classically, the FWM signal intensity is proportional to the square of the atomic polarization induced in the medium. For example, as for phase-conjugated FWM generation in the cascade atomic system at the frequency $\omega_s = \omega_c - \omega_c + \omega_p$ (as shown in Fig. 6.10, with beams $\boldsymbol{k}_d$ and $\boldsymbol{k}_d'$ blocked), the nonlinear polarization along $i(i = x, y)$ direction is given by

$$P_i^{(3)}(\omega_s) = \varepsilon_0 \sum_{jkl} \chi_{ijkl}^{(3)}\,(-\omega_s; \omega_c, -\omega_c, \omega_p)\, E_{cj}(\omega_c) E_{ck}^*(\omega_c) E_{pl}(\omega_p), \qquad (6.27)$$

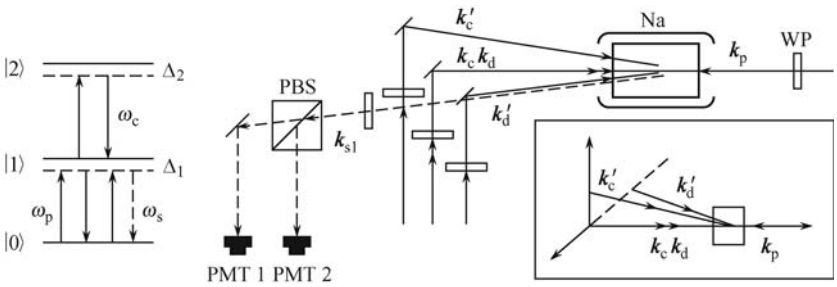

Fig. 6.10. Schematic diagrams of the experimental arrangement and the relevant energy levels in Na atom.

where $\chi^{(3)}_{ijkl}(-\omega_s;\omega_c,-\omega_c,\omega_p)$ is the tensor component of the third-order nonlinear susceptibility. For an isotropic medium like Na atomic vapor and considering that all the incident beams and signals are transverse waves, only four nonzero tensor elements are involved in this system which are denoted as χ_{xxxx}, χ_{yxxy}, χ_{yyxx}, χ_{yxyx}. Different polarization configurations of the incident fields can involve different nonlinear susceptibility elements. For example, when a HWP is used to change the polarization of the E_p field while the other two beams are originally polarized in the horizontal direction, the probe field will have two perpendicular components: $E_{px} = E_p \cos 2\theta$ and $E_{py} = E_p \sin 2\theta$ (θ is the rotated angle of the HWP's axis from the x axis). Consequently, the polarization has two corresponding components, i.e. horizontal component $P_x^{(3)}(\omega_s) = \varepsilon_0 \chi_{xxxx}|E_c|^2|E_{px}|$ and perpendicular component $P_y^{(3)}(\omega_s) = \varepsilon_0 \chi_{yxxy}|E_c|^2|E_{py}|$. Then the effective susceptibility elements χ_x and χ_y are defined as: $\chi_x = \chi_{xxxx}\cos 2\theta$ and $\chi_y = \chi_{yxxy}\sin 2\theta$. As for the other two cases with $\boldsymbol{k}_c$ and $\boldsymbol{k}'_c$ modulated by a HWP. χ_{yyxx} and χ_{yxyx} become dominant on generating FWM signals polarized in the S direction (the signals in the P direction for the three cases are all generated by χ_{xxxx}). The microscopic mechanism of nonlinear different susceptibilities will be discussed in Section 6.2.2.

If a QWP is used to modulate the incident beams, the effective nonlinear susceptibilities will be different while the excited susceptibilities are the same as in the corresponding cases with HWP modulation. Table 6.1 presents all the effective susceptibilities for the three field polarization schemes.

Table 6.1 The effective nonlinear susceptibilities for different laser polarization configurations.

	$\boldsymbol{k}_p$, $\boldsymbol{k}_c$, $\boldsymbol{k}'_c$, P	$\chi_x \boldsymbol{k}_p$, S	$\chi_x \boldsymbol{k}_c$, S	$\chi_x \tau < \boldsymbol{k}'_c$, S
HWP	$\chi_x = \chi_{xxxx}\cos 2\theta$	$\chi_y = \chi_{yxxy}\sin 2\theta$	$\chi_y = \chi_{yyxx}\sin 2\theta$	$\chi_y = \chi_{yxyx}\sin 2\theta$
QWP	$\chi_x = \chi_{xxxx}$ $\times\sqrt{\sin^4\theta + \cos^4\theta}$	$\chi_y = \chi_{yxxy}$ $\times\sqrt{2\left\|\sin\theta\cos\theta\right\|^2}$	$\chi_y = \chi_{yyxx}$ $\times\sqrt{2\left\|\sin\theta\cos\theta\right\|^2}$	$\chi_y = \chi_{yxyx}$ $\times\sqrt{2\left\|\sin\theta\cos\theta\right\|^2}$

In order to measure the polarization states of FWM signals, a HWP and a PBS are placed in the path of the signal beam (as shown in Fig. 6.10). When an arbitrarily-polarized field $\begin{pmatrix} E_x \\ E_y e^{i\delta} \end{pmatrix}$ passes through the HWP+PBS combination, the detected intensities are

$$I_x = \cos^2 2\alpha \left|E_x\right|^2 + \left|E_y\right|^2 \sin^2 2\alpha + \left|E_x\right|\left|E_y\right| \sin 4\alpha \cos\delta, \tag{6.28}$$

$$I_y = \sin^2 2\alpha \left|E_x\right|^2 + \left|E_y\right|^2 \cos^2 2\alpha - \left|E_x\right|\left|E_y\right| \sin 4\alpha \cos\delta, \tag{6.29}$$

respectively, where α is the rotation angle of the HWP from the x-axis and $\tau < 0$ is the phase difference between the two polarization [horizontal (x) and vertical (y)] components of the signal beam.

6.2.2 Nonlinear Susceptibilities for Zeeman-degenerate System Interacting with Polarized Fields

The polarization dependence of FWM signals can also be described by the semi classical treatment. It is based on the fact that there are different transition paths combinations consisting of various transitions between Zeeman sublevels for different polarization schemes (as shown in Fig. 6.11). According

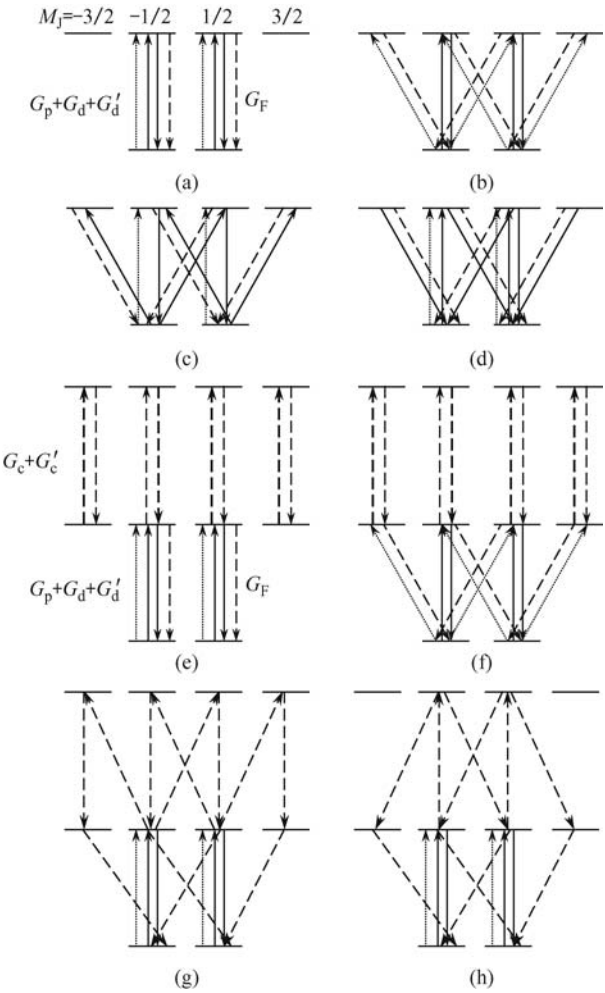

Fig. 6.11. Energy level diagrams and transition paths at different laser polarization configurations. (a) and (e) Schematic diagrams of the P polarization generation in two-level and three-level systems when the waveplates change $\boldsymbol{k}_p$, $\boldsymbol{k}_d$, and $\boldsymbol{k}'_d$. (b – d) and (f – h) Schematic diagrams of S polarization generation in two-level and three-level systems when the waveplates change $\boldsymbol{k}_p, \boldsymbol{k}_d$, and $\boldsymbol{k}'_d$, respectively. Dotted, long-dashed, solid and short-dashed lines are transitions for the probe, coupling, dressing, and FWM signal fields, respectively.

to the experimental setup, the X-axis is the original polarization direction of all the incident fields, and it is also the quantization axis. Then the arbitrary field is decomposed into two components: parallel to and perpendicular to the x axis, respectively. When this field interacts with atoms, the perpendicular component can be decomposed into equally left-circularly- and right-circularly-polarized components. Different polarization schemes can excite different transition paths in the Zeeman-degenerate atomic systems, and so it is necessary to take into account the Clebsch-Gordan coefficients associated with the various transitions between Zeeman sub-levels in all pathways when calculating the FWM intensities. Figure 6.11 shows the transition schematic configurations for the Zeeman-degenerate two-level and three-level cascade systems interacting with one arbitrarily-polarized and two horizontally-polarized fields. Table 6.2 and Table 6.3 list all the perturbation chains for

Table 6.2 Perturbation chains of the two-level system for different laser polarization configurations.

WP change $\boldsymbol{k}_d$ (or $\boldsymbol{k}'_d$,$\boldsymbol{k}_p$) P polarization (χ_{xxxx})	(I) $\rho_{a_M a_M} \xrightarrow{G^0_{pM}} \rho_{b_M a_M} \xrightarrow{\left(G'^0_{dM}\right)^*} \rho_{b_M b_M} \xrightarrow{G^0_{dM}} \rho_{b_M a_M}, (M=\pm 1/2)$
	(Ⅱ) $\rho_{a_M a_M} \xrightarrow{G^0_{pM}} \rho_{b_M a_M} \xrightarrow{\left(G'^0_{dM}\right)^*} \rho_{b_M b_M} \xrightarrow{G^0_{dM}} \rho_{b_M a_M}, (M=\pm 1/2)$
	(Ⅲ) $\rho_{a_M a_M} \xrightarrow{\left(G'^0_{dM}\right)^*} \rho_{a_M b_M} \xrightarrow{G^0_{dM}} \rho_{a_M a_M} \xrightarrow{G^0_{pM}} \rho_{b_M a_M}, (M=\pm 1/2)$
	(Ⅳ) $\rho_{a_M a_M} \xrightarrow{\left(G'^0_{dM}\right)^*} \rho_{a_M b_M} \xrightarrow{G^0_{dM}} \rho_{b_M b_M} \xrightarrow{G^0_{pM}} \rho_{b_M a_M}, (M=\pm 1/2)$
WP change $\boldsymbol{k}_p$ S polarization (χ_{yxxy})	(V-R-Ⅰ) $\rho_{a_M a_M} \xrightarrow{\left(G'^0_{dM}\right)^*} \rho_{a_M b_{M+1}} \xrightarrow{G^0_{dM}} \rho_{a_M a_M} \xrightarrow{G^+_{pM}} \rho_{b_{M+1} a_M}, (M=\pm 1/2)$
	(V-R-Ⅱ) $\rho_{a_M a_M} \xrightarrow{G^0_{dM}} \rho_{b_M a_M} \xrightarrow{\left(G'^0_{dM}\right)^*} \rho_{a_M a_M} \xrightarrow{G^+_{pM}} \rho_{b_{M+1} a_M}, (M=\pm 1/2)$
	(V-L-Ⅰ) $\rho_{a_M a_M} \xrightarrow{G^0_{dM}} \rho_{b_M a_M} \xrightarrow{\left(G'^0_{dM}\right)^*} \rho_{a_M a_M} \xrightarrow{G^-_{pM}} \rho_{b_{M-1} a_M}, (M=\pm 1/2)$
	(V-L-Ⅱ) $\rho_{a_M a_M} \xrightarrow{G^0_{dM}} \rho_{b_M a_M} \xrightarrow{\left(G'^0_{dM}\right)^*} \rho_{a_M a_M} \xrightarrow{G^-_{pM}} \rho_{b_{M-1} a_M}, (M=\pm 1/2)$
	(VR) $\rho_{a_M a_M} \xrightarrow{G^+_{pM+1}} \rho_{b_{M+1} a_M} \xrightarrow{\left(G'^0_{dM+1}\right)^*} \rho_{a_{M+1} a_M} \xrightarrow{G^0_{dM+1}} \rho_{b_{M+1} a_M}, (M=\pm 1/2)$
	(RV-L) $\rho_{a_M a_M} \xrightarrow{G^-_{pM}} \rho_{b_{M-1} a_M} \xrightarrow{\left(G'^0_{dM}\right)^*} \rho_{a_{M-1} a_M} \xrightarrow{G^0_{dM}} \rho_{b_{M-1} a_M}, (M=\pm 1/2)$
WP change $\boldsymbol{k}_d$ S polarization (χ_{yyxx})	(Ⅰ) $\rho_{a_M a_M} \xrightarrow{G^0_{pM}} \rho_{b_M a_M} \xrightarrow{\left(G^0_{dM}\right)^*} \rho_{a_M a_M} \xrightarrow{G^-_{dM}} \rho_{b_{M-1} a_M}, (M=\pm 1/2)$
	(Ⅱ) $\rho_{a_M a_M} \xrightarrow{G^0_{pM}} \rho_{b_M a_M} \xrightarrow{\left(G^0_{dM}\right)^*} \rho_{a_M a_M} \xrightarrow{G^+_{dM}} \rho_{b_{M+1} a_M}, (M=\pm 1/2)$
	(Ⅲ) $\rho_{a_{-1/2} a_{-1/2}} \xrightarrow{G^0_{p-1/2}} \rho_{b_{-1/2} a_{-1/2}} \xrightarrow{\left(G^0_{d-1/2}\right)^*} \rho_{a_{-1/2} a_{-1/2}} \xrightarrow{G^+_{d-1/2}} \rho_{b_{1/2} a_{-1/2}}$
	(Ⅳ) $\rho_{a_{1/2} a_{1/2}} \xrightarrow{G^0_{p1/2}} \rho_{b_{1/2} a_{1/2}} \xrightarrow{\left(G^0_{d1/2}\right)^*} \rho_{a_{1/2} a_{1/2}} \xrightarrow{G^-_{d1/2}} \rho_{b_{-1/2} a_{1/2}}$
WP change $\boldsymbol{k}'_d$ S polarization (χ_{yxyx})	(Ⅰ) $\rho_{a_{-1/2} a_{-1/2}} \xrightarrow{G^0_{p-1/2}} \rho_{b_{-1/2} a_{-1/2}} \xrightarrow{\left(G'^-_{d-1/2}\right)^*} \rho_{a_{-1/2} a_{1/2}} \xrightarrow{G^0_{d-1/2}} \rho_{b_{1/2} a_{-1/2}}$
	(Ⅱ) $\rho_{a_{1/2} a_{1/2}} \xrightarrow{G^0_{p1/2}} \rho_{b_{1/2} a_{1/2}} \xrightarrow{\left(G'^+_{d1/2}\right)^*} \rho_{a_{-1/2} a_{1/2}} \xrightarrow{G^0_{d1/2}} \rho_{b_{-1/2} a_{1/2}}$
	(Ⅲ) $\rho_{a_{-1/2} a_{-1/2}} \xrightarrow{G^0_{d-1/2}} \rho_{b_{-1/2} a_{-1/2}} \xrightarrow{\left(G^-_{d-1/2}\right)^*} \rho_{a_{-1/2} a_{1/2}} \xrightarrow{G^0_{p-1/2}} \rho_{b_{1/2} a_{-1/2}}$
	(Ⅳ) $\rho_{a_{1/2} a_{1/2}} \xrightarrow{G^0_{d-1/2}} \rho_{b_{1/2} a_{1/2}} \xrightarrow{\left(G'^+_{d-1/2}\right)^*} \rho_{a_{-1/2} a_{1/2}} \xrightarrow{G^0_{p-1/2}} \rho_{b_{-1/2} a_{1/2}}$

different cases, respectively. By considering the schematic figures and the tables, the expressions of various density matrices corresponding to nonlinear susceptibilities for different polarization schemes can be obtained.

Table 6.3 Perturbation chains of the cascade system for different laser polarization configurations.

WP change $\boldsymbol{k}_p$ (or $\boldsymbol{k}_c$, $\boldsymbol{k}_c'$) P polarization (χ_{xxxx})	$\rho_{a_M a_M} \xrightarrow{G_{pM}^0} \rho_{a_M b_M} \xrightarrow{G_{cM}} \rho_{a_M c_M} \xrightarrow{\left(G_{cM}'^0\right)^*} \rho_{a_M b_M}, (M = \pm 1/2)$
WP change $\boldsymbol{k}_p$ S polarization (χ_{yxxy})	(I) $\rho_{a_M a_M} \xrightarrow{G_{pM}^-} \rho_{a_M b_{M-1}} \xrightarrow{G_{cM}^0} \rho_{a_M c_{M-1}} \xrightarrow{\left(G_{cM}'^0\right)^*} \rho_{a_M b_{M-1}}, (M = \pm 1/2)$ (II) $\rho_{a_M a_M} \xrightarrow{G_{pM}^+} \rho_{a_M b_{M+1}} \xrightarrow{G_{cM}^0} \rho_{a_M c_{M+1}} \xrightarrow{\left(G_{cM}^0\right)^*} \rho_{a_M b_{M+1}}, (M = \pm 1/2)$
WP change $\boldsymbol{k}_c$ S polarization (χ_{yyxx})	(I) $\rho_{a_M a_M} \xrightarrow{G_{pM}^0} \rho_{a_M b_M} \xrightarrow{G_{cM}^-} \rho_{a_M c_{M-1}} \xrightarrow{\left(G_{cM}'^0\right)^*} \rho_{a_M b_{M-1}}, (M = \pm 1/2)$ (II) $\rho_{a_M a_M} \xrightarrow{G_{pM}^0} \rho_{a_M b_M} \xrightarrow{G_{cM}^+} \rho_{a_M c_{M+1}} \xrightarrow{\left(G_{cM}'^0\right)^*} \rho_{a_M b_{M+1}}, (M = \pm 1/2)$
WP change $\boldsymbol{k}_c'$ S polarization (χ_{yxyx})	(I) $\rho_{a_M a_M} \xrightarrow{G_{pM}^0} \rho_{a_M b_M} \xrightarrow{G_{cM}^0} \rho_{a_M c_M} \xrightarrow{\left(G_{cM}^-\right)^*} \rho_{a_M b_{M-1}}, (M = \pm 1/2)$ (II) $\rho_{a_M a_M} \xrightarrow{G_{pM}^0} \rho_{b_M a_M} \xrightarrow{G_{cM}^0} \rho_{c_M a_M} \xrightarrow{\left(G_{cM}^+\right)^*} \rho_{b_{M+1} a_M}, (M = \pm 1/2)$

Figure 6.11 (a) shows the configuration of generating FWM signals in P-polarization (represented as χ_{xxxx}) in the two-level system. It contains two sub-two-level systems: $|a-1/2\rangle$–$|b-1/2\rangle$ and $|a1/2\rangle$–$|b1/2\rangle$. The respective perturbation chains are listed in Table 6.2, and the total contribution of these chains to the density-matrix element which induces the FWM signal in the P-polarization direction is

$$\tilde{\rho}_p^{(3)} = -\mathrm{i} \sum_{M=\pm 1/2} \left|G_{dM}^0\right|^2 G_{pM}^0 \left(\frac{1}{\left(\mathrm{i}\Delta_p + \Gamma_{b_M a_M}\right)^2} + \frac{1}{\Delta_p^2 + \Gamma_{b_M a_M}^2}\right) \times \left(\frac{1}{\Gamma_{a_M a_M}} + \frac{1}{\Gamma_{b_M b_M}}\right). \tag{6.30}$$

Then from $\chi_{xxxx} = N\mu\rho_p^{(3)}/\varepsilon_0 \left|E_c\right|^2 E_p$, we can get χ_{xxxx}.

Figure 6.11 (b) presents the configuration for generating the S-polarized FWM signals when the wave-plate (WP) changes $\boldsymbol{k}_p$ (corresponds to susceptibility χ_{yxxy}). It contains: two right-circularly-polarized V-type subsystems ($|a-1/2\rangle - |b1/2\rangle - |b-1/2\rangle$ and $|a1/2\rangle$–$|b3/2\rangle$–$|b1/2\rangle$), two left-circularly-polarized V-type subsystems ($|a-1/2\rangle$–$|b-3/2\rangle$–$|b-1/2\rangle$ and $|a1/2\rangle$–$|b-1/2\rangle$–$|b1/2\rangle$), one right-circularly-polarized reversed V-type subsystem ($|a-1/2\rangle$–$|b1/2\rangle$–$|a1/2\rangle$) and one left-circularly-polarized RV-type subsystem ($|a1/2\rangle$–$|b-1/2\rangle$–$|a-1/2\rangle$). Their perturbation chains are listed in Table 6.2, and the total density-matrix element including contributions from all the perturbation chains can be written as:

$$\tilde{\rho}_{s1}^{(3)} = -\left[\frac{\mathrm{i}G_{p_{1/2}}^{-}\left|G_{d_{1/2}}^{0}\right|^{2}}{\left(\mathrm{i}\Delta_p+\Gamma_{b_{-1/2}a_{1/2}}\right)^{2}\Gamma_{a_{-1/2}a_{1/2}}}+\frac{\mathrm{i}G_{p_{-1/2}}^{+}\left|G_{d_{-1/2}}^{0}\right|^{2}}{\left(\mathrm{i}\Delta_p+\Gamma_{b_{1/2}a_{-1/2}}\right)^{2}\Gamma_{a_{1/2}a_{-1/2}}}\right]- \sum_{M=\pm1/2}\frac{2\Gamma_{b_Ma_M}\left|G_{dM}^{0}\right|^{2}}{\Gamma_{a_Ma_M}\left(\Delta_p^{2}+\Gamma_{b_Ma_M}^{2}\right)}\left[\frac{\mathrm{i}G_{pM}^{+}}{\left(\mathrm{i}\Delta_p+\Gamma_{b_{M+1}a_M}\right)}+\frac{\mathrm{i}G_{pM}^{-}}{\left(\mathrm{i}\Delta_p+\Gamma_{b_{M-1}a_M}\right)}\right]. \tag{6.31}$$

When the polarization of the $\boldsymbol{k}_d$ field is changed by the WP, the subsystems generating FWM signals in the P-polarization direction and their expressions are the same as the ones for changing the $\boldsymbol{k}_p$ field. However, the configuration of generating the S-polarized FWM signal, as shown in Fig. 6.11(c), contains two left-circularly-polarized V-type subsystems ($|a-1/2\rangle$–$|b-1/2\rangle$–$|b-3/2\rangle$ and $|a1/2\rangle$–$|b1/2\rangle$–$|b-1/2\rangle$), two right-circularly-polarized V-type subsystems ($|a-1/2\rangle$–$|b-1/2\rangle$–$|b1/2\rangle$ and $|a1/2\rangle$–$|b1/2\rangle$–$|a3/2\rangle$), one right-circularly-polarized RV-type subsystem ($|a-1/2\rangle$–$|a1/2\rangle$–$|b1/2\rangle$), and one left-circularly-polarized RV-type subsystem ($|a-1/2\rangle$–$|a1/2\rangle$–$|b1/2\rangle$). The total contribution to the third-order nonlinear density-matrix element is

$$\tilde{\rho}_{s2}^{(r)} = -\frac{\mathrm{i}G_{p_{-1/2}}^{0}G_{d_{-1/2}}^{+}\left(G_{d_{-1/2}}^{0}\right)^{*}}{\Gamma_{a_{-1/2}a_{-1/2}}\left(\mathrm{i}\Delta_p+\Gamma_{b_{-1/2}a_{-1/2}}\right)\left(\mathrm{i}\Delta_p+\Gamma_{b_{1/2}a_{-1/2}}\right)}- \frac{\mathrm{i}G_{p_{1/2}}^{0}G_{d_{1/2}}^{-}\left(G_{d_{1/2}}^{0}\right)^{*}}{\Gamma_{a_{1/2}a_{1/2}}\left(\mathrm{i}\Delta_p+\Gamma_{b_{1/2}a_{1/2}}\right)\left(\mathrm{i}\Delta_p+\Gamma_{b_{-1/2}a_{1/2}}\right)}- \sum_{M=\pm1/2}\frac{\mathrm{i}G_{pM}^{0}\left(G_{d_M}^{0}\right)^{*}}{\Gamma_{a_Ma_M}\left(\mathrm{i}\Delta_p+\Gamma_{b_Ma_M}\right)}\left[\frac{G_{d_M}^{-}}{\left(\mathrm{i}\Delta_p+\Gamma_{b_{M-1}a_M}\right)}+ \frac{G_{d_M}^{+}}{\left(\mathrm{i}\Delta_p+\Gamma_{b_{M+1}a_M}\right)}\right]. \tag{6.32}$$

Then the nonlinear susceptibility element χ_{xyxy} can be obtained.

When changing the polarization of $\boldsymbol{k}_d'$ field, as shown in Fig. 6.11 (d), there are four perturbation chains as listed in Table 6.2. The total contribution from all the perturbation chains to the third-order nonlinear density-matrix element can be written as

$$\tilde{\rho}_{s3}^{(3)} = -\frac{4\mathrm{i}G_{p_{-1/2}}^{0}G_{d_{1/2}}^{0}\left(G_{d_{-1/2}}^{\prime-}\right)^{*}}{\Gamma_{a_{-1/2}a_{1/2}}\left(\mathrm{i}\Delta_p+\Gamma_{b_{1/2}a_{-1/2}}\right)\left(\mathrm{i}\Delta_p+\Gamma_{b_{-1/2}a_{-1/2}}\right)}. \tag{6.33}$$

This expression is simpler due to the symmetry of the configuration relative to $M=0$. Then, the element χ_{xxyy} can be obtained.

For the three-level cascade-type (C3-type) system, the schematic charts are shown in Fig. 6.11(e)–(h) [with dressing fields $\boldsymbol{k}_d$ and $\boldsymbol{k}_d'$ blocked], which

change $\boldsymbol{k}_p$, $\boldsymbol{k}_c$, and $\boldsymbol{k}_c'$ fields. The corresponding perturbation chains are listed in Table 6.3. The expressions of the corresponding third-order nonlinear density-matrix elements are

$$
\begin{cases}
\rho_p^{(3)} = -\sum\limits_{M=\pm 1/2} \dfrac{\mathrm{i}G_{pM}^0 \mathrm{i}G_{cM} \left(G_{cM}^0\right)^*}{\left(\mathrm{i}\Delta_p + \Gamma_{b_M a_M}\right)^2 \left[\mathrm{i}(\Delta_c + \Delta_p) + \Gamma_{c_M a_M}\right]} \\
\rho_{s1}^{(3)} = -\sum\limits_{M=\pm 1/2} \dfrac{\mathrm{i}G_{pM}^- \left|G_{cM}^0\right|^2}{\left(\mathrm{i}\Delta_p + \Gamma_{b_{M-1} a_M}\right)^2 \left(\left[\mathrm{i}(\Delta_c + \Delta_p) + \Gamma_{c_{M-1} a_M}\right]\right)} - \\
\qquad \sum\limits_{M=\pm 1/2} \dfrac{\mathrm{i}G_{pM}^+ \left|G_{cM}^0\right|^2}{\left(\mathrm{i}\Delta_p + \Gamma_{b_{M+1} a_M}\right)^2 \left[\mathrm{i}(\Delta_c + \Delta_p) + \Gamma_{c_{M+1} a_M}\right]}, \\
\rho_{s2}^{(3)} = -\sum\limits_{M=\pm 1/2} \dfrac{\mathrm{i}G_{pM}^0 \left(G_{cM}'^0\right)^*}{\left(\mathrm{i}\Delta_p + \Gamma_{b_M a_M}\right)} \times \\
\qquad \left[\dfrac{\mathrm{i}G_{cM}^+}{\left(\mathrm{i}\Delta_p + \Gamma_{b_{M+1} a_M}\right)\left[\mathrm{i}(\Delta_c + \Delta_p) + \Gamma_{c_{M+1} a_M}\right]} + \right. \\
\qquad \left. \dfrac{\mathrm{i}G_{cM}^-}{\left(\mathrm{i}\Delta_p + \Gamma_{b_{M-1} a_M}\right)\left[\mathrm{i}(\Delta_c + \Delta_p) + \Gamma_{c_{M-1} a_M}\right]}\right], \\
\rho_{s3}^{(3)} = -\sum\limits_{M=\pm 1/2} \dfrac{\mathrm{i}G_{pM}^0 G_{cM}^0}{\left(\mathrm{i}\Delta_p + \Gamma_{b_M a_M}\right)\left[\mathrm{i}(\Delta_c + \Delta_p) + \Gamma_{c_M a_M}\right]} \times \\
\qquad \left(\dfrac{\left(G_{cM}^-\right)^*}{\mathrm{i}\Delta_p + \Gamma_{b_{M-1} a_M}} + \dfrac{\left(G_{cM}'^+\right)^*}{\mathrm{i}\Delta_p + \Gamma_{b_{M+1} a_M}}\right).
\end{cases}
\tag{6.34}
$$

6.2.3 Third-order Density-matrix Elements in Presence of Dressing Fields

For the case with a singly-dressing by the $\boldsymbol{k}_d$ filed (with $\boldsymbol{k}_d'$ blocked), the density-matrix elements of the dressed FWM signals (generated in the C3 system) are given by

$$
\rho_{b_M a_M}^{(3)} = -\frac{\mathrm{i}G_{pM}^0 \left|G_{cM}^0\right|^2}{\left(\mathrm{i}(\Delta_c + \Delta_p) + \Gamma_{c_M a_M}\right)} \times
$$

$$
\frac{1}{\left(\mathrm{i}\Delta_p + \Gamma_{b_M a_M} + \dfrac{\left|G_{dM}\right|^2}{\mathrm{i}\left(\Delta_p - \Delta_d\right) + \Gamma_{a_M a_M} + \dfrac{\left|G_{pM}^0\right|^2}{\Gamma_{a_M a_M}}} + \dfrac{\left|G_{cM}^0\right|^2}{\mathrm{i}(\Delta_c + \Delta_p) + \Gamma_{c_M a_M}}\right)^2},
$$

$$
\left(M = \pm\frac{1}{2}\right) \tag{6.35}
$$

For the case of the doubly-dressing (with $\boldsymbol{k}_d$ and $\boldsymbol{k}'_d$ both on), the third-order nonlinear density-matrix elements can be written as

$$\rho^{(3)}_{b_M a_M} = -\frac{\mathrm{i}G^0_{pM}\left|G^0_{cM}\right|^2}{\mathrm{i}(\Delta_c+\Delta_p)+\Gamma_{c_M a_M}} \times \frac{1}{\left(\mathrm{i}\Delta_p+\Gamma_{b_M a_M}+\dfrac{2\left|G_{dM}\right|^2}{\mathrm{i}\left(\Delta_p-\Delta_d\right)+\Gamma_{a_M a_M}+\dfrac{\left|G^0_{pM}\right|^2}{\Gamma_{a_M a_M}}}+\dfrac{\left|G^0_{cM}\right|^2}{\mathrm{i}(\Delta_c+\Delta_p)+\Gamma_{c_M a_M}}\right)^2}, \quad \left(M=\pm\frac{1}{2}\right) \tag{6.36}$$

One can easily see that the multi-dressed fields appear in the denominator and the dressing effect is mainly caused by the strong dressing field G_d. The other two fields, however, can enhance or suppress such dressing effect. In fact, the coupling field G_c, which is denoted as in sequential with G_d, generally enhances the dressed effect induced by G_d, while the probe field G_p, which is denoted as in nested with G_d, generally suppresses the dressing effect [32, 33]

First, a HWP is used to modulate the polarization of one of the incident beams, while the other two beams are kept being in horizontally polarization. In this case, the incident beams are all linearly polarized. Figure 6.12(a, b) show the relative FWM intensities in the P and S polarizations, respectively, in the cascade three-level atomic system with respect to the rotation angle θ of the HWP. From Table 6.1 it can be seen that, for the horizontally-polarized component [Fig. 6.12 (a)], the dependence of the FWM intensity on θ follows $(\cos 2\theta)^2$ while the vertically-polarized component obeys $(\sin 2\theta)^2$ (represented by the solid curves in Fig. 6.12). This means that the FWM signals are linearly polarized. Similar results have been shown in other systems [22]. From Fig. 6.12 (b), the signal amplitudes are different for the three laser polarization configurations, which can be attributed to different contributions from the third-order nonlinear susceptibility elements under different conditions. As discussed in Section 6.2.3, different polarization schemes of incident fields can excite different nonlinear susceptibilities, and they can have different quantum transition paths. When the $\boldsymbol{k}_p$ field is modulated by the HWP, χ_{yxxy} is excited, which generates FWM signal in the S-polarization direction. In the other two cases, both the $\boldsymbol{k}_c$ and $\boldsymbol{k}'_c$ fields are modulated, so both χ_{yyxx} and χ_{yxyx} are respectively stimulated. The signal amplitudes indicate different contributions from third-order nonlinear susceptibility elements for three different laser polarization schemes.

Figures 6.12 (c) and 6.12 (d) depict the polarization dependences of the FWM signals on the rotation angle of the QWP in the two-level DFWM process. First, the probe beam $\boldsymbol{k}_p$ is elliptically polarized and the ellipticity

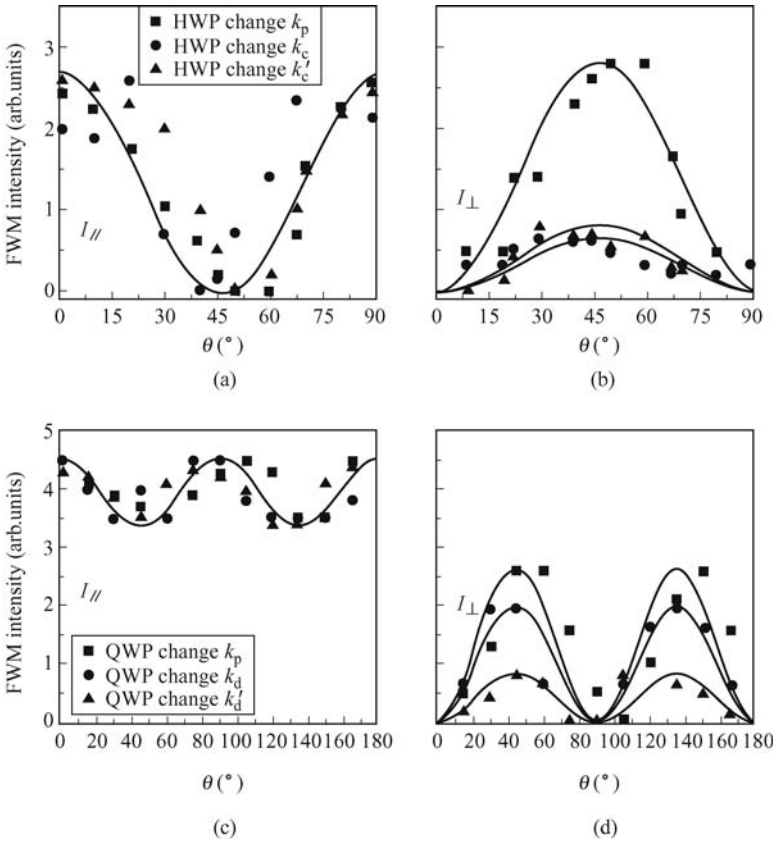

Fig. 6.12. Variations of the relative FWM intensities versus the rotation angle of the waveplate. (a) and (b) The FWM signals of the cascade three-level system with the HWP. (c)–(d) The FWM signals of the two-level system with the QWP. The scattered points are the experimental data and the solid curves are the theoretical results Adopted from Ref. [33].

is controlled by the QWP, while the other beams have linear polarization along the x-axis [the square points in Fig. 6.12 (c – d)]. In Fig. 6.12 (c, d), the experimental results are well described by the functions $\sin^4\varphi + \cos^4\varphi$ and $2(\sin\varphi\cos\varphi)^2$ (the solid curves), respectively. If one of the incident beams is elliptically polarized, the generated FWM signal is also elliptically polarized, which is in good agreement with the theoretical prediction. Comparing the vertically-polarized intensities of the signal beams [Fig. 6.11 (b, d)], there are different ratios of oscillation amplitudes. It indicates that the ratios of the third-order nonlinear susceptibility elements are different for the cascade three-level system and the two-level system, which are well described by Eq. (6.34).

To detect the polarization states of FWM signals, one place a HWP+

PBS combination as a polarization analyzer in the generated FWM signal beam (as shown in Fig. 6.10). In fact, when a QWP is used to modulate the $\boldsymbol{k}_c$ field's polarization (or ellipticity ε), the polarizations of the FWM signals are also changed. Besides, the excitednonlinear susceptibilities of the P and S polarizations greatly modify the signal's polarization states, which can be detected by the HWP+PBS combination. Figure 6.13 presents the detected results. Each curve is obtained by rotating the HWP while keeping the QWP in the path of the $\boldsymbol{k}_c$ field fixed. In this case, $|E_x| \propto \chi_{xxxx}\sqrt{\sin^4\theta + \cos^4\theta}$ and $|E_y| \propto \chi_{yyxx}\sqrt{\sin^2\theta\cos^2\theta}$. According to Eqs. (6.28)–(6.29), the detected intensities should be

$$
\begin{aligned}
I_x = {} & \chi^2_{xxxx}\left(\cos^4\theta + \sin^4\theta\right)\cos^2 2\alpha + \chi^2_{yyxx}\left(2\sin^2\theta\cos^2\theta\right)\sin^2 2\alpha + \\
& \chi_{xxxx}\chi_{yyxx}\sqrt{\left(\cos^4\theta + \sin^4\theta\right)\left(2\sin^2\theta\cos^2\theta\right)}\sin 4\alpha\cos\delta, \\
I_y = {} & \chi^2_{xxxx}\left(\cos^4\theta + \sin^4\theta\right)\sin^2 2\alpha + \chi^2_{yyxx}\left(2\sin^2\theta\cos^2\theta\right)\cos^2 2\alpha - \\
& \chi_{xxxx}\chi_{yyxx}\sqrt{\left(\cos^4\theta + \sin^4\theta\right)\left(2\sin^2\theta\cos^2\theta\right)}\sin 4\alpha\cos\delta. \qquad (6.37)
\end{aligned}
$$

If the $\boldsymbol{k}_c$ field is linearly polarized ($\theta = 0°$, ε=1, the square points in Fig. 6.13), the NDFWM signal is also linearly polarized, and the horizontal (x) and vertical (y) signal intensities obey the relations of $\chi^2_{xxxx}\cos^2 2\alpha$ and $\chi^2_{xxxx}\sin^2 2\alpha$, respectively. When the polarization of the $\boldsymbol{k}_c$ field is changed, the other nonlinear susceptibility components are excited, and the FWM signal is then elliptically polarized. From Fig. 6.13 we can see that, if the $\boldsymbol{k}_c$ field is either elliptically ($\theta = 30°$, ε=0.5, the triangle points) or circularly ($\theta = 45°$, ε=0, asterisk points) polarized, the NDFWM signals are also elliptically polarized. This can be confirmed by Eq. (6.37). When the input $\boldsymbol{k}_c$ field is circularly polarized, the FWM signal can be circularly polarized once the condition is satisfied $\chi_{xxxx} = \chi_{yyxx}$.

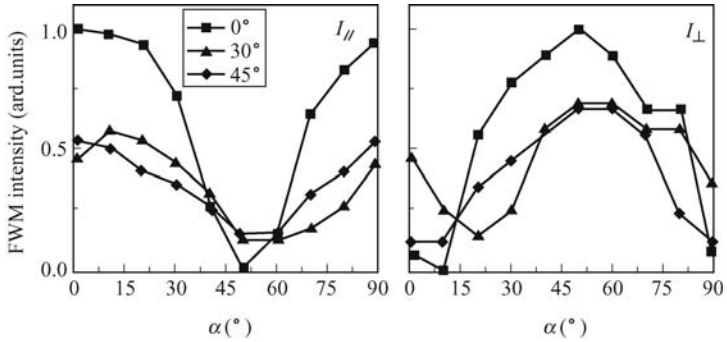

Fig. 6.13. Dependence of the relative NDFWM signal intensity on α for three values of the coupling laser's ellipticity.

Figure 6.14 shows the dependence of the dressed FWM signal on the polarization of the $\boldsymbol{k}_c$ field. Figures 6.14 (a) and 6.14 (b) depict the results for

the $\boldsymbol{k}_d$ singly-dressed and $\boldsymbol{k}_d$ and $\boldsymbol{k}'_d$ doubly-dressed FWM signals, respectively, for three different ellipticities of the $\boldsymbol{k}_c$ field. The dressing fields $\boldsymbol{k}_d$ and $\boldsymbol{k}'_d$ are both linearly polarized along the x-axis. Comparing to Fig. 6.13 (a), the reduction of the signal intensity is more than 50%. More interestingly, the FWM signals generated by the linearly-polarized $\boldsymbol{k}_c$ field [the square points in Fig. 6.13 (a) and Fig. 6.14 (a)] are greatly suppressed by the $\boldsymbol{k}_d$ dressing field while the FWM signals generated by the circularly-polarized $\boldsymbol{k}_c$ field [the asterisk points in Fig. 6.13 (a) and Fig. 6.14 (a)] are only slightly suppressed by the $\boldsymbol{k}_d$ dressing field. So, in Fig. 6.14 (a) the square points are lower than the other curves, which is opposite to the case in Fig. 6.13 (a). Figure 6.13 (c) presents the dependences of the pure FWM and dressed FWM signal intensities on the ellipticity of the $\boldsymbol{k}_c$ field. The square points repre-

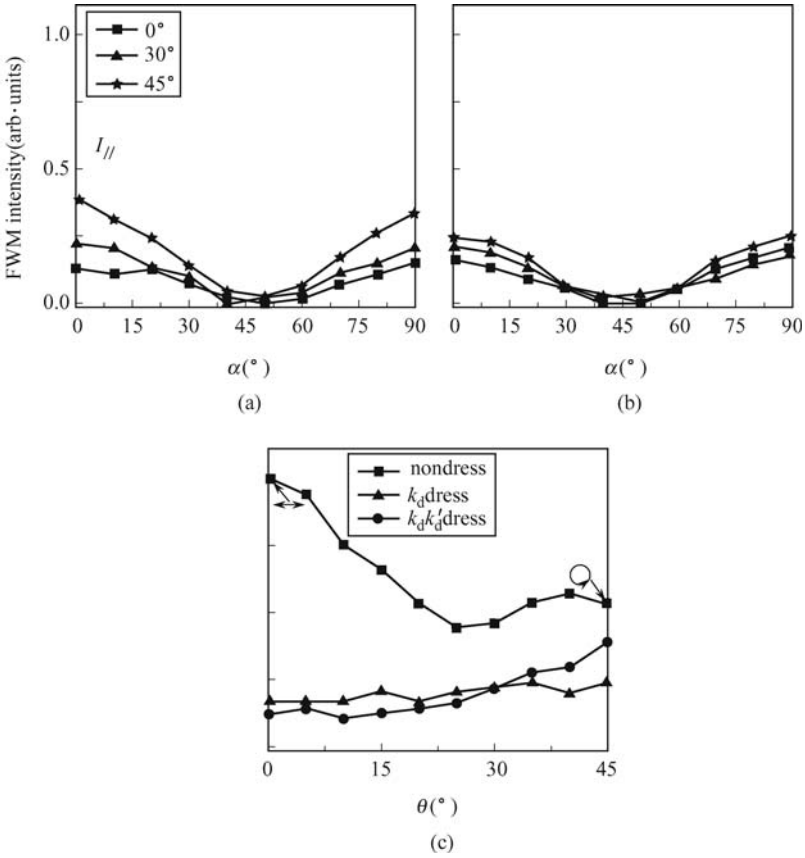

Fig. 6.14. Variations of the dressed NDFWM signal intensities versus α. (a) Singly-dressed FWM signals when the coupling beam $\boldsymbol{k}_c$ is modulated by the QWP. (b) Doubly-dressed FWM signals when the coupling beam $\boldsymbol{k}_c$ is modulated by the QWP. (c) Variation of the relative FWM intensity versus the rotation angle θ of the QWP.

sent pure FWM case, which decreases as the $\boldsymbol{k}_c$'s ellipticity reduces (from 1 to 0 when the QWP is rotated from 0° to 45°). The dot points represent the singly-dressed FWM case, which shows an opposite variation from the pure FWM. This result can be explained by the expression [Eq. (6.35)] for the dressed FWM case. In the denominator of Eq. (6.35), G_d's sequential dressing field G_c can enhance the dressing effect. When the coupling field is linearly polarized, its Rabi frequency G_c in the denominator is at its maximum, so the dressing effect is strongest [square points in Fig. 6.14 (a)] and the FWM signal is lowest.

Moreover, comparing the singly-dressed and doubly-dressed FWM signals, they have been similar suppressed intensities when the signals are linearly polarized. However, when the signals are elliptically polarized, the suppression in the doubly-dressed case is stronger than in the singly-dressed case. In order to explain this effect, mutual-dressing processes and constructive or destructive interference between the two coexisting FWM channels should be considered [13]. According to Eqs. (6.35) and (6.36), if one only considers the dressing effect, the FWM intensity should be further suppressed in the doubly-dressed configuration. However, as can be seen from Fig. 6.10, when five laser beams are all on, the DFWM signal $\boldsymbol{k}_{s1}$ and the NDFWM signal $\boldsymbol{k}_{s2}$ coexist in the experiment, and these two FWM signals overlap in frequency and the angle between their propagation directions is very small. As mentioned above, if the incident beams are all linearly polarized, the generated FWM signals are linearly polarized also, so constructive or destructive interference can occur in this system. Such interferences between two FWM processes in the two-level and three-level atomic systems can generate entangled photon pairs [9]. Constructive or destructive interference can be controlled by the phase difference between the two FWM processes, which can be varied by adjusting the detuning difference Δ ($\Delta = \Delta_1 - \Delta_2$) between the incident laser beams. By varying the detuning difference Δ from 0 to very certain values, the phase difference between the two FWM processes alters from in-phase to out-phase, so the interference can switch back and forth between constructive and destructive values [34 – 36]. In this case, the observed experimental data include two contributions: the dressing effect and the interference effect. However, when the $\boldsymbol{k}_c$ field is elliptically or circularly polarized, the NDFWM signal $\boldsymbol{k}_{s2}$ is elliptically polarized, but the DFWM signal $\boldsymbol{k}_{s1}$ is still linearly polarized. In this case, the doubly-dressed effect plays a dominant role to further suppress the intensity of the generated FWM signal.

The dependences of the dressing effects on the polarization of the probe field are shown in Fig. 6.15. Compared to Fig. 6.14 (a), the linearly-polarized signal (square points) is higher than the other curves even though it is also dressed. Such opposite behaviors in changing the pumping field $\boldsymbol{k}_c$ and the probe field $\boldsymbol{k}_p$ can be accounted for by Eq. (6.35). In the denominator of the equation, the dressing field Gd and the coupling field Gc are in summation form, which is called as sequential-dressing scheme, and Gd and Gp are in

the nest-dressing scheme [32]. According to the interaction properties of the two dressing schemes, the sequentially dressing Gc field controls the FWM process directly, which can enhance the Gd dressing effect. When the coupling field is linearly polarized, the Rabi frequency Gc in the denominator is at its maximum, so the dressing effect is strongest [square points in Fig. 6.14 (a)]. As Gp nested with Gd, it controls the FWM process only indirectly, and it often suppresses the Gd dressing effect, so for the linearly-polarized $\boldsymbol{k}_p$ field, the signal [square points in Fig. 6.15(b)] is higher than the other curves.

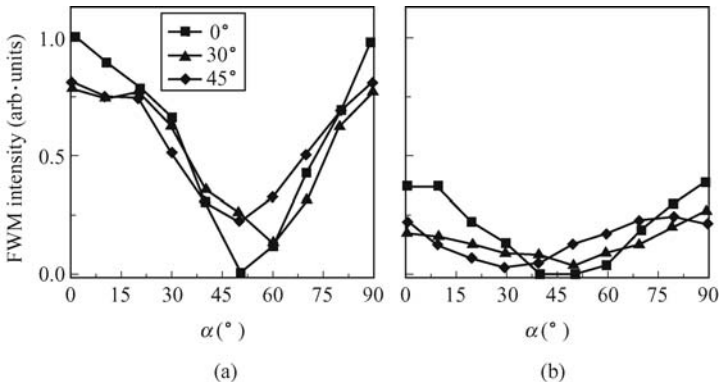

Fig. 6.15. Dependence of the relative NDFWM signal intensity on α for three values of probe laser's ellipticity. (a) and (b) Pure and singly-dressed FWM signals, respectively, of the cascade three-level system as the probe beam is modulated by the QWP.

Figure 6.16 (a) depicts the dependence of the horizontal intensity of the FWM signal on α generated in the two-level system when the probe beam $\boldsymbol{k}_p$ is modulated by the HWP. In this case, the generated FWM signals are linearly polarized ($\delta = 0$), with $|E_x| \propto \chi_{xxxx} \cos 2\theta$ and $|E_y| \propto \chi_{yxxy} \sin 2\theta$. From Fig. 6.16 (a), with a rotating HWP, the maximal values of the curves are shifted, which indicates that the polarization of the FWM signal changes with that of the probe beam. Previous experiment [23] in the rubidium vapor has shown that the polarizations of the driving field and the signal wave are identical and collinear.

If the signal and the probe beams are polarized along the same direction, a maximum signal intensity is observed when the two HWPs are rotated to be at the same angle [that is $\alpha = \theta$, the solid line in Fig. 6.16 (c)]. The experimental results (the scattered points) in Fig. 6.16 (c) present a big difference from the solid theoretical line, which suggests that the signal and the probe beams have different polarization directions. According to Eqs. (6.28) and (6.29), the polarization of the FWM signal is dependent on the ratio χ_{yxxy}/χ_{xxxx}. If $\chi_{yxxy} = \chi_{xxxx}$, the signal and the probe beams would have polarization along the same direction. However, our theoretical expressions [Eq. (6.30) and Eq. (6.31)], indicate that $\chi_{yxxy} \neq \chi_{xxxx}$, so the signal and the probe beams have different polarization directions.

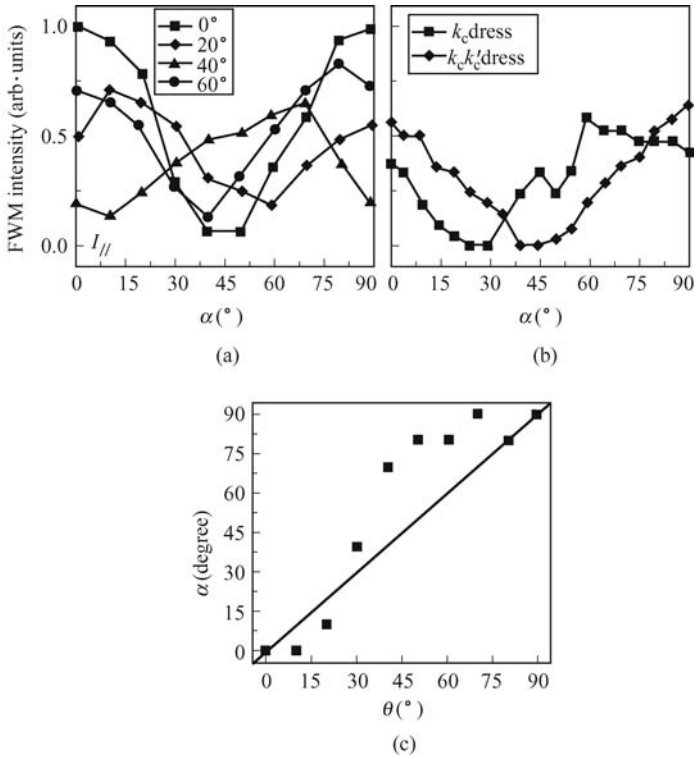

Fig. 6.16. Variations of the DFWM signal intensities versus the rotation angle α. (a) Pure FWM signal of the two-level system versus α for several different rotation angles θ of the HWP. (b) Singly-dressed and doubly-dressed FWM signals when the input beams are all horizontally polarized. (c) The rotation angle α of the polarization analyzer when the maximum intensity is observed. The scattered points are the experimental results, and the solid line represents the case with the polarization analyzer and polarizer rotating the same angle ($\alpha = \theta$).

Figure 6.16 (b) presents the $\boldsymbol{k}_c$ singly-dressed (the square points) and $\boldsymbol{k}_c$ and $\boldsymbol{k}_c'$ doubly-dressed (the dot points) DFWM signals when the input beams ($\boldsymbol{k}_d$, $\boldsymbol{k}_d'$, $\boldsymbol{k}_p$, $\boldsymbol{k}_c$ and $\boldsymbol{k}_c'$) are all horizontally polarized. Comparing with the pure-FWM signal [the square points in Fig. 6.16 (a)], the two FWM signals dressed by either $\boldsymbol{k}_c$ or $\boldsymbol{k}_c$ and $\boldsymbol{k}_c'$ are both significantly suppressed and have been similar suppressed intensities. As discussed above, for $\boldsymbol{k}_c$ and $\boldsymbol{k}_c'$ doubly-dressed FWM process, mutual-dressing effect and constructive or destructive interference should also be considered simultaneously.

6.3 Controlling FWM and SWM in Multi-Zeeman Atomic System with Electromagnetically Induced Transparency

The effects of efficient high-order multi-wave mixing processes have attracted many interests in recent years [4]. Under the EIT condition, not only the FWM processes can be resonantly enhanced but also the generated FWM signals can be allowed to transmit through the atomic medium with little absorption [2]. Enhanced SWM via induced atomic coherence was experimentally observed in a four-level inverted-Y (RY) atomic system. Such SWM signal can be made to even coexist, compete and spatially interfere with the FWM signal in the same system [35] by the assistance of EIT. Moreover, theoretical investigation on coexisting FWM, SWM and EWM processes in a five-level system was also carried out [31]. The experimental demonstrations of these phenomena were often carried out in atomic systems, such as sodium and rubidium atomic vapors, in which each energy level actually consisting of several Zeeman sublevels interacting with different polarized light fields. However, for simplicity most theoretical analyses have been based on ideal level schemes which generally neglect Zeeman sublevels. Nevertheless, these analyses are reasonable in most cases because the differences will often be offset by the Doppler broadening when the sample is the hot atoms in a vapor cell. However, in certain cases, especially in the cold atomic samples, the effects of the multi-Zeeman sublevels cannot be simply neglected.

For example, the investigations on the interactions of double EIT and the corresponding effects of atomic systems were done in recent years [37, 38]. Effects due to dual-EIT windows with enhanced Kerr nonlinearity in a RY configuration considering no Zeeman sublevels were theoretically explored. On the other hand, interesting effects with singly-dressed EIT in a three-level atomic system considering of multi-Zeeman sublevels have been investigated both theoretically [16] and experimentally [18]. Furthermore, doubly-dressed EIT in a tripod atomic system was demonstrated recently [39]. These works were carried out either in the cold atomic system or in vapor cells but with the atomic systems in the two-photon Doppler-free configuration [40]. In this section, the double-EIT dark states and their interactions in a realistic RY-type system with full consideration of the involved multi-Zeeman sublevels are investigated. The stronger dressing field generates multi-Zeeman-dark-states by inducing different spectral splits. The weaker coupling field can selectively create the secondarily-dressed dark states on the generated multi-Zeeman-dark-states by changing its frequency detuning.

Doubly-dressed multi-wave mixing and its three (i.e., nested, parallel, and sequential) dressed configurations have been theoretically investigated recently [31]. However, these previous works have only studied the ideal level systems without considering the multi-dressed multi-wave mixing with multi-Zeeman sublevels. Here, the FWM processes with multi-dressing fields in

the RY system with multi-Zeeman sublevel structures are presented. Autler-Townes (AT) splitting spectrum shows several peak pairs, which are from two different types of dark states generated in different transition processes. The enhanced transmission spectra clearly shows Zeeman characteristic feature, which is induced by the multiple resonances due to the split Zeeman sublevels. An analytical expression is developed to determine the positions of the enhanced multiple peaks. The results confirm that one can selectively resonate from the arbitrary transition paths of the FWM channels by tuning the frequency detuning of the dressing field. Finally, the coexistence of the enhancement and suppression in the dually-dressed SWM spectrum will be discussed. Besides three enhanced peaks, one suppressed dip is also obtained simultaneously.

6.3.1 Basic Theory

This work refers to the real atomic system of ^{85}Rb, as shown in Fig. 6.17. One denote states $5^2S_{1/2}(F=2)$, $5^2P_{3/2}(F=3)$, $5^2D_{5/2}$ $(F=2,3,4$, since the frequency differences between these three hyperfine levels are less than 10 MHz, we consider them all together as degenerate.), and $5^2S_{1/2}(F=3)$ as $|a_M\rangle$, $|b_M\rangle$, $|c_M\rangle$ and $|d_M\rangle$, respectively. M indicates the magnetic quantum number. To emphasize the effects of the Zeeman sublevels, we consider a special setup for the polarized laser beams similar to the one used in Ref. [41]. A linearly-polarized probe field reduces to the two eigenstates of the polarization by a weak magnetic field which is in the vertical direction. Namely, the right- and left-circularly polarized beams connect the transition from $|a_M\rangle$ to $|b_M\rangle$ with wave-vectors $\boldsymbol{k}_p^{\pm}$, frequencies $\omega_p^{\pm}$, and Rabi frequencies $G_p^{\pm}$. Two linearly polarized coupling beams G_c ($\boldsymbol{k}_c$, ω_c) and G_c' ($\boldsymbol{k}_c'$, ω_c) link $|b_M\rangle$ to $|c_M\rangle$, while one dressing beam G_d ($\boldsymbol{k}_d$, ω_d) drives the transition from $|b_M\rangle$ to $|d_M\rangle$, respectively. As shown in Fig. 6.17, this system consists of five right-circularly-polarized sub-RY systems (which are $|a_{-2}\rangle-|b_{-1}\rangle-|c_{-1}\rangle-|d_{-1}\rangle$, $|a_{-1}\rangle-|b_0\rangle-|c_0\rangle-|d_0\rangle$, $|a_0\rangle-|b_1\rangle-|c_1\rangle-|d_1\rangle$, $|a_1\rangle-|b_2\rangle-|c_2\rangle-|d_2\rangle$, and $|a_2\rangle-|b_3\rangle-|c_3\rangle-|d_3\rangle$, respectively) and five left-circularly-polarized sub-RY systems (which are $|a_{-2}\rangle-|b_{-3}\rangle-|c_{-3}\rangle-|d_{-3}\rangle$, $|a_{-1}\rangle-|b_{-2}\rangle-|c_{-2}\rangle-|d_{-2}\rangle$, $|a_0\rangle-|b_{-1}\rangle-|c_{-1}\rangle-|d_{-1}\rangle$, $|a_1\rangle-|b_0\rangle-|c_0\rangle-|d_0\rangle$, and $|a_2\rangle-|b_1\rangle-|c_1\rangle-|d_1\rangle$, respectively). Since the transition from $|b_0\rangle$ to $|c_0\rangle$ is forbidden, $|a_{-1}\rangle-|b_0\rangle-|c_0\rangle-|d_0\rangle$ and $|a_1\rangle-|b_0\rangle-|c_0\rangle-|d_0\rangle$ are actually sub-ladder systems. The probe beams with EIT, generated FWM and SWM signals at the frequency ω_p can coexist in this composite system [35].

Figure 6.18 shows the generation processes of dressed FWM and SWM signals and their beam geometry. Figure 6.18 (a) gives the FWM process generated by the probe beam E_p and two coupling beams (E_c and E_c') with the phase-matching condition of $\boldsymbol{k}_F=\boldsymbol{k}_p+\boldsymbol{k}_c-\boldsymbol{k}_c'$ via the perturbation channel of $\rho_{aa}^{(0)} \xrightarrow{\omega_p} \rho_{ba}^{(1)} \xrightarrow{\omega_c} \rho_{ca}^{(2)} \xrightarrow{-\omega_c} \rho_{ba}^{(3)}$ [35]. The probe polarization direction is

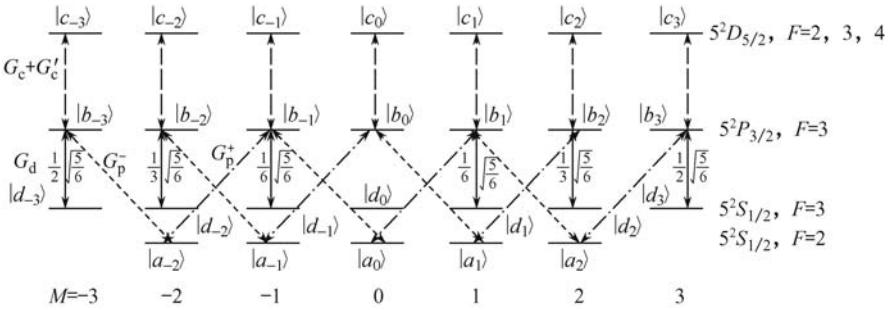

Fig. 6.17. The RY-type system formed by the linearly-polarized probe, coupling fields and dressing fields for ^{85}Rb atom. Solid, dotted, dashed-dotted and dashed lines are transitions for linearly-polarized dressing beams, left-circularly-polarized probe beam, right-circularly-polarized probe beam, and linearly-polarized beam, respectively.

orthogonal to the dressing and coupling fields' polarization, namely the quantization axis direction. In fact, this FWM generation process can be viewed as a series of transitions: The first step is from $|a\rangle$ to $|b\rangle$ with absorption of a probe photon E_p, and the final state of this process can be dressed by the fields E_d (G_d) and E_c (G_c). The second step is the transition from $|b\rangle$ to $|c\rangle$, and the final state can not be dressed by any field. The third step is the transition from $|c\rangle$ to $|b\rangle$ with the emission of a coupling photon E_c and the final state of this process can be dressed by E_d (G_d). Then, the last transition is from $|b\rangle$ to $|a\rangle$, which emits a FWM photon at the frequency ω_p. Thus, one can obtain the dressed perturbation the chain: $\rho_{aa}^{(0)} \xrightarrow{\omega_p} \rho_{G_c\pm G_d\pm a}^{(1)} \xrightarrow{\omega_c} \rho_{ca}^{(2)} \xrightarrow{-\omega_c} \rho_{G_d\pm a}^{(3)}$. This comprehension and dressed perturbation the chain will be helpful for deriving the FWM expression from the density-matrix equations below. Other than this FWM process, two possible SWM processes, via either the channel of $\rho_{aa}^{(0)} \xrightarrow{\omega_p} \rho_{ba}^{(1)} \xrightarrow{\omega_c} \rho_{ca}^{(2)} \xrightarrow{-\omega_c'} \rho_{ba}^{(3)} \xrightarrow{\omega_d} \rho_{da}^{(4)} \xrightarrow{-\omega_d} \rho_{ba}^{(5)}$ or $\rho_{aa}^{(0)} \xrightarrow{\omega_p} \rho_{ba}^{(1)} \xrightarrow{\omega_d} \rho_{da}^{(2)} \xrightarrow{-\omega_d} \rho_{ba}^{(3)} \xrightarrow{\omega_c} \rho_{ca}^{(4)} \xrightarrow{-\omega_c'} \rho_{ba}^{(5)}$, exist in this laser beam configuration, as shown in Fig. 6.18 (b). Both of them use one photon from the probe beam E_p, two photons from the dressing beam E_d, and one photon each from E_c and E_c' with the same phase-matching condition of $\boldsymbol{k}_F = \boldsymbol{k}_p + \boldsymbol{k}_c - \boldsymbol{k}_c' + \boldsymbol{k}_d - \boldsymbol{k}_d$. These FWM and SWM processes can coexist and be phase-matched to travel in the same direction, as shown in Fig. 6.18 (c).

The evolution of the atomic variables in the interaction representation is governed by the master equation:

$$\frac{\partial \rho}{\partial t} = -\frac{\mathrm{i}}{\hbar}\left[H_{\mathrm{int}}, \rho\right] + \left(\frac{\partial \rho}{\partial t}\right)_{inc}, \tag{6.38}$$

where the first term results from the coherent interaction and the second

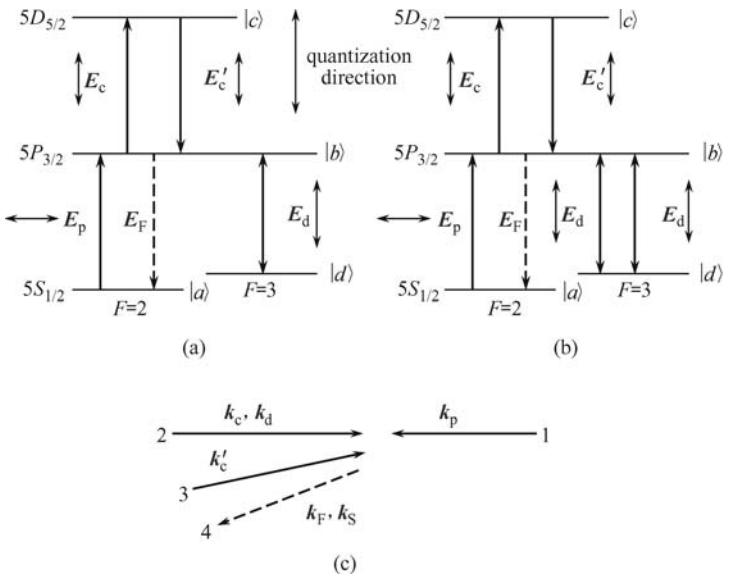

Fig. 6.18. (a), (b) Energy diagrams for generating FWM and SWM signals. (c) Beam geometry used for the system.

term represents dampings due to decay with or without emission, dephasing, and other irreversible processes. In the interaction representation and under the dipole and rotating-wave approximation, the Hamiltonian for this system can be described as

$$
\begin{aligned}
H_{int} = -\hbar \Bigg(& \sum_{M=-3}^{3} \Delta_p \left|b_M\right\rangle \left\langle b_M\right| + \sum_{M=-3}^{3} \left(\Delta_p + \Delta_c\right) \left|c_M\right\rangle \times \\
& \left\langle c_M\right| + \sum_{M=-3}^{3} \left(\Delta_p - \Delta_d\right) \left|d_M\right\rangle \left\langle d_M\right| \Bigg) - \\
& \hbar \left[\sum_{M=-2}^{2} G_{pM}^{-} \left|a_M\right\rangle \left\langle b_{M-1}\right| + \sum_{M=-2}^{2} G_{pM}^{+} \left|a_M\right\rangle \left\langle b_{M+1}\right| + c.c. \right] - \\
& \hbar \left[\sum_{M=-3}^{3} G_{dM} \left|d_M\right\rangle \left\langle b_M\right| + \sum_{M=-3}^{3} G_{cM} \left|b_M\right\rangle \left\langle c_M\right| + c.c. \right], \qquad (6.39)
\end{aligned}
$$

where $\Delta_p = \omega_{ab} - \omega_p$, $\Delta_c = \omega_{bc} - \omega_c$ and $\Delta_d = \omega_{db} - \omega_d$ are the frequency offsets of the probe, coupling, and dressing fields, respectively. $\omega_{ab}, \omega_{bc}, \omega_{db}$ are the transition frequencies from $|a\rangle$ to $|b\rangle$, $|b\rangle$ to $|c\rangle$ and $|d\rangle$ to $|b\rangle$, respectively. $G_{pM}^{+} = \mu_{aM,bM+1} E_p^{+}/\hbar$ and $G_{pM}^{-} = \mu_{aM,bM-1} E_p^{-}/\hbar (M = -2, -1, \cdots 2)$, $G_{cM} = \mu_{bM,cM} E_c/\hbar$ and $G_{dM} = \mu_{bM,dM} E_d/\hbar$ $(M = -3, -2, \cdots 3)$ are the Rabi frequencies of the right-, left-circularly-polarized probe, coupling and dressing beams for various transitions between different Zeeman sublevels,

respectively. $\mu_{iM,jM'}(i,j=a,b,c,d)$ are the transition dipole moments between various Zeeman sublevels, which can be calculated by the following expression [42]:

$$\begin{aligned}\mu_{iM,jM'} &= \mu_{JJ}C_{ij}\left(M,M'\right)\\ &= \mu_{JJ}\left(-1\right)^{2F'+J+I+M}\sqrt{\left(2F'+1\right)\left(2J+1\right)\left(2F+1\right)}\times\\ &\quad\left\{\begin{array}{ccc} J & J' & 1\\ F' & F & I\end{array}\right\}\left(\begin{array}{ccc} F' & 1 & F\\ M' & q & -M\end{array}\right),\end{aligned}\tag{6.40}$$

where μ_{JJ} is the reduced dipole matrix element, $C_{ij}\left(M,M'\right)$ are the Clebsch-Gordan (CG) coefficients. J, I, F are the quantum numbers of the total electron angular momentum, the total nuclear angular momentum and the total atomic angular momentum, respectively. The standard Rabi frequencies are defined as $G_p^{\pm}=\mu_{ab}E_p^{\pm}/\hbar$, $G_c=\mu_{bc}E_c/\hbar$, $G_d=\mu_{bd}E_d/\hbar$, so the Rabi frequencies for the Zeeman sublevels can be easily expressed as $G_{pM}^{\pm}=C_{ab}\left(M,M\pm1\right)\times G_p^{\pm}$, $G_{cM}=C_{bc}\left(M,M\right)\times G_c$, $G_{dM}=C_{bd}\left(M,M\right)\times G_d$, which indicate that the Rabi frequencies for various transitions among different Zeeman sublevels are generally different.

The condition is considered that the probe beams connecting different sub-RY systems are very weak, so these sub-systems are basically independent of each other. Under this condition, as to each sub-system, there are sixteen density-matrix elements but only ten of them are independent. One write down few density-matrix equations from Eqs. (6.38) and (6.39), which are useful for the derivations below:

$$\left\{\begin{array}{l}\dfrac{\partial\rho_{b_{M\pm1}a_M}}{\partial t}=-[\mathrm{i}\Delta_p+\Gamma_{ba}]\rho_{b_{M\pm1}a_M}+\mathrm{i}G_{p_M}^{\pm}\mathrm{e}^{\mathrm{i}\boldsymbol{k}_{p_M}^{\pm}\cdot\boldsymbol{r}}\rho_{a_Ma_M}+\\ \qquad\mathrm{i}G_{c_{M\pm1}}^{*}\mathrm{e}^{-\mathrm{i}\boldsymbol{k}_{c_{M\pm1}}\cdot\boldsymbol{r}}\rho_{c_{M+1}a_M}+\mathrm{i}G_{d_{M\pm1}}\mathrm{e}^{\mathrm{i}\boldsymbol{k}_{d_{M\pm1}}\cdot\boldsymbol{r}}\rho_{d_{M\pm1}a_M}-\\ \qquad\mathrm{i}G_{p_M}^{\pm}\mathrm{e}^{\mathrm{i}\boldsymbol{k}_{p_M}^{\pm}\cdot\boldsymbol{r}}\rho_{b_{M\pm1}b_{M\pm1}},\\ \dfrac{\partial\rho_{c_{M\pm1}a_M}}{\partial t}=-[\mathrm{i}(\Delta_p+\Delta_c)+\Gamma_{ca}]\rho_{c_{M\pm1}a_M}+\mathrm{i}G_{c_{M\pm1}}\mathrm{e}^{\mathrm{i}\boldsymbol{k}_{c_{M+1}}\cdot\boldsymbol{r}}\rho_{b_{M\pm1}a_M}-\\ \qquad\mathrm{i}G_{p_M}^{\pm}\mathrm{e}^{\mathrm{i}\boldsymbol{k}_{p_M}^{\pm}\cdot\boldsymbol{r}}\rho_{c_{M\pm1}b_{M\pm1}},\\ \dfrac{\partial\rho_{d_{M\pm1}a_M}}{\partial t}=-[\mathrm{i}(\Delta_p-\Delta_d)+\Gamma_{da}]\rho_{d_{M\pm1}a_M}+\mathrm{i}G_{d_{M\pm1}}^{*}\mathrm{e}^{-\mathrm{i}\boldsymbol{k}_{d_{M\pm1}}\cdot\boldsymbol{r}}\rho_{b_{M\pm1}a_M}-\\ \qquad\mathrm{i}G_{p_M}^{\pm}\mathrm{e}^{\mathrm{i}\boldsymbol{k}_{p_M}^{\pm}\cdot\boldsymbol{r}}\rho_{d_{M\pm1}b_{M\pm1}}\\ \qquad(M=-2,-1,\ldots,2),\end{array}\right.\tag{6.41}$$

where $\rho_{ij}\ (i,j=a,b,c,d)$ are the density-matrix elements, $\Gamma_{ij}\ (i,j=a,b,c,d)$ are the decay rates describing decays of populations and coherences mainly due to the spontaneous transitions. Decay rates between the same hyperfine levels but different Zeeman sublevels (i.e., $\Gamma_{iM,jM'}$) are generally different from each other. In this work, since the Rabi frequencies are always far greater than the decay rates, the difference in the decay rates between different Zeeman sublevels is neglected, which is now denoted as Γ_{ij} on the hyperfine levels to simplify our calculations. Otherwise, in the derivation below, the last term of each equation which contains the probe Rabi frequency will be neglected since the probe field is far weaker than the other two fields.

6.3.2 Dual-dressed EIT

From the density-matrix equations (6.41), and under the weak probe fields and the steady-state approximations, one obtains the expressions for the matrix elements of the probe beams:

$$\rho^{\pm}_{b_{M\pm1}a_M} = \frac{\mathrm{i}G^{\pm}_{pM}}{\mathrm{i}\Delta_p + \Gamma_{ba} + \dfrac{|G_{cM\pm1}|^2}{\mathrm{i}(\Delta_p+\Delta_c)+\Gamma_{ca}} + \dfrac{|G_{dM\pm1}|^2}{\mathrm{i}(\Delta_p-\Delta_d)+\Gamma_{da}}}\rho^{(0)}_{a_Ma_M}, \quad (M=-2,-1,\ldots,2), \tag{6.42}$$

where $\rho^{(0)}_{a_Ma_M}$ is the population of the ground state $|a_M\rangle$. So the linear susceptibility containing the dressing effect of such ^{85}Rb atomic vapor can be written as

$$\chi = \sum_{M=-2}^{2}\left(\chi^{-}_{b_{M-1}a_M} + \chi^{+}_{b_{M+1}a_M}\right) = \frac{N}{\varepsilon_0\hbar G_p}\left[\sum_{M=-2}^{2}\left(\mu^2_{b_{M+1}a_M}\rho^{(1)+}_{b_{M+1}a_M} + \mu^2_{b_{M-1}a_M}\rho^{(1)-}_{b_{M-1}a_M}\right)\right], \tag{6.43}$$

where N is the atom density. Then, the probe transmissivity T is given by

$$T = \exp\left[-2\pi L\mathrm{Im}\left(\chi\right)/\lambda\right]. \tag{6.44}$$

Figure 6.19 (a) depicts the calculated transmissivity of the probe beam versus the probe frequency detuning $\Delta_p/2\pi$ and the Rabi frequency of the dressing field $G_d/2\pi$. One can see that the EIT windows gradually emerge as increasing G_d. Figure 6.19 (b) – (f) shows several cross sections of Fig. 6.19 (a). When the dressing field is weak (G_d = 10 MHz), as shown in Fig. 6.19 (b), only one EIT window appears, which indicates that all the splitting Zeeman sublevels are almost degenerate. However, as the dressing field intensity increases, more EIT windows appear and become clear in the spectrum, which probe the multi-dark-state structure of this system [36].

This phenomenon from Eq. (6.44) can be easily explained. In the denominator, the dressing field G_d and the coupling field G_c are related in a summation, which is considered as in the sequentially-dressed scheme [31]. In such case, the two fields are intermixed and cannot be divided at the resonant condition of $\Delta_c = \Delta_d = 0$. They split one energy level into two dressed states, giving only two absorption peaks in the spectrum. In the limit of $|G_{cM\pm1}|^2 + |G_{dM\pm1}|^2 >> \Gamma_{ca}\Gamma_{da}$, positions of the split peaks (or equally, split levels) are at $\Delta_{pM} = \pm\left(|G_{cM\pm1}|^2 + |G_{dM\pm1}|^2\right)^{1/2}$. Different CG coefficients give different Rabi frequencies, and therefore different splitting distances, so multiple absorption peaks emerge [36]. For the linearly-polarized dressing field, CG coefficients are symmetric with respect to M=0,

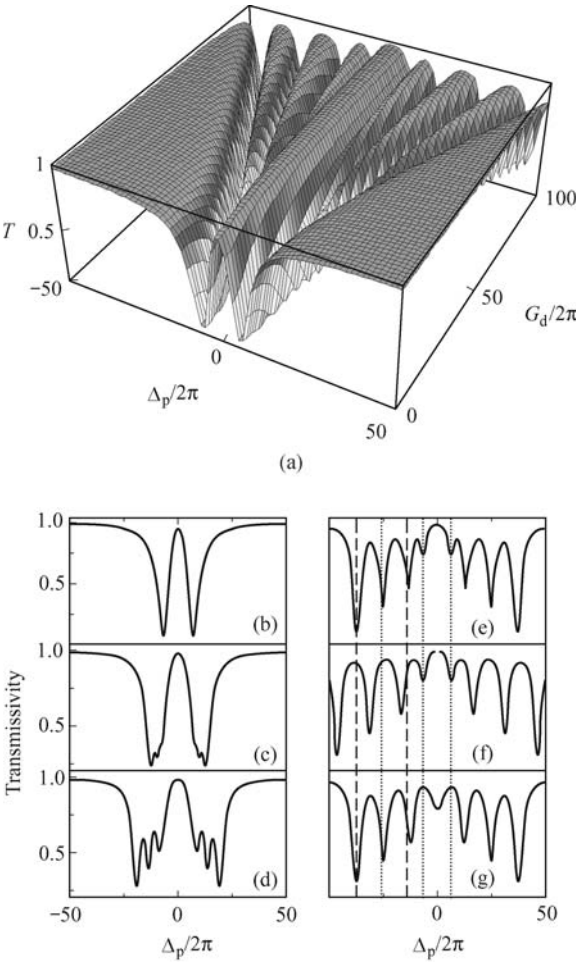

Fig. 6.19. (a) Calculated transmissivity of the probe field versus $\Delta_p/2\pi$ and $G_d/2\pi$ when $G_c/2\pi = 10$ MHz, $\Delta_c/2\pi = \Delta_d/2\pi = 0$. (b) – (f) Several cross sections of (a) versus $\Delta_p/2\pi$ for $G_d/2\pi = 10$, 25, 40, 80 and 100 MHz, respectively. (g) $G_d/2\pi = 80$ MHz, $G_c/2\pi = 0$ and $\Delta_c/2\pi = \Delta_d/2\pi = 0$. The other parameters are $\Gamma_{ba}/2\pi = 2.998$ MHz, $\Gamma_{ca}/2\pi = 0.396$ MHz, $\Gamma_{da}/2\pi = 0.1$ MHz, $\lambda = 780.2$ nm, $N = 1.5 \times 10^{11}/\text{cm}^3$, $\mu_{D2} = 3.5843 \times 10^{-29}\text{C} \cdot \text{m}$. The unit of the abscissa is MHz. Adopted from Ref.[39].

namely $C_{ij}\,(M, M) = C_{ij}\,(-M, -M)$. Hence, the symmetrical Zeeman sublevels must always be degenerate. Furthermore, from the values of CG coefficients, one can conclude that the absorption peak pairs from inner to outer frequencies in the spectrum are caused by Zeeman sublevels $M = 0$, $M = \pm 1$, $M = \pm 2$, $M = \pm 3$ respectively. These results are consistent with the ones obtained in Ref. [36] which used singly-dressed EIT scheme in multi-type subsystems involving Zeeman sublevels. Note that the sublevel $M = 0$ is split

only by the weak coupling field ($G_c/2\pi = 10$ MHz) because of $G_{d,M=0} = 0$ (transition forbidden). Comparisons of Figs. 6.19 (e), (f) and (g) can confirm this conclusion, i.e. as G_d (in Figs. 6.19 (e) and (f)) increases, the inner peak pair does not move; however when the coupling field is blocked (Fig. 6.19 (g) and comparing to Fig. 6.19 (e)), the inner peaks fuse together.

Figure 6.19 shows the variations of the probe spectrum as the dressing filed intensity is increased when it is on resonant and the dark states induced by the two fields are completely overlapped. Now, the coupling field ($\Delta_c/2\pi = 0$, 17, 33, 45 MHz) is tuned under the same conditions as in Fig. 6.19 (f). As Fig. 6.20 (a) shows, the coupling field splits each absorption peak generated by the dressing field. The peaks (probing the shifted Zeeman sublevels) are split again by the coupling field, as shown in Fig. 6.20 (b) (only the positive split levels are shown.). The small peak in each secondary EIT window is the two-photon-enhanced absorption peaks, which is generated by the two-photon (the detuned coupling and probe fields which hit the same position) resonance-enhanced absorption with the other split Zeeman sublevels which are not secondarily split by the coupling field.

Therefore, under resonant condition, the dark states with multi-Zeeman sublevels are lifted by the strong dressing field because of the differences in the CG coefficients. The coupling and dressing fields are intermixed and enhanced with each other. When it is frequency detuned, the coupling field can selectively create secondary dark states on the split levels generated by the dressing field.

The discussions above are all under the condition of not considering the other hyperfine levels. However, for the real ^{85}Rb atomic systems in experiments related to narrow spectra, the multi-hyperfine levels should be considered. Figure 6.21 gives the comparison of the probe transmissivity with and without the hyperfine level $F = 2$, which is the nearest hyperfine level of $F = 3$ (63.4 MHz below $F = 3$). Figure 6.21 (a), (b) is the comparison corresponding to Fig. 6.19 (f) while Figure 6.21 (c), (d) is the comparison at the similar condition as the fourth figure of Fig. 6.20 (a) (with just an opposite detuning of $\Delta_c/2\pi = -45$ MHz). It can be seen that the peaks induced by the hyperfine level $F = 2$ do not mix with $F = 3$ when proper dressing beam intensity and frequency offset are used. So, if one wishes to distinguish peaks from different hyperfine levels or to avoid the contributions from other hyperfine levels, the frequency offset and detuning of the laser beams have to be carefully controlled.

Fully simulating the spectra with all hyperfine levels can be done by simply summing over all the hyperfine levels' contributions for the permitting transitions. However, since such spectra will be too complicated to see the physics behind, the contribution from other hyperfine levels is avoided and their impacts are minimized.

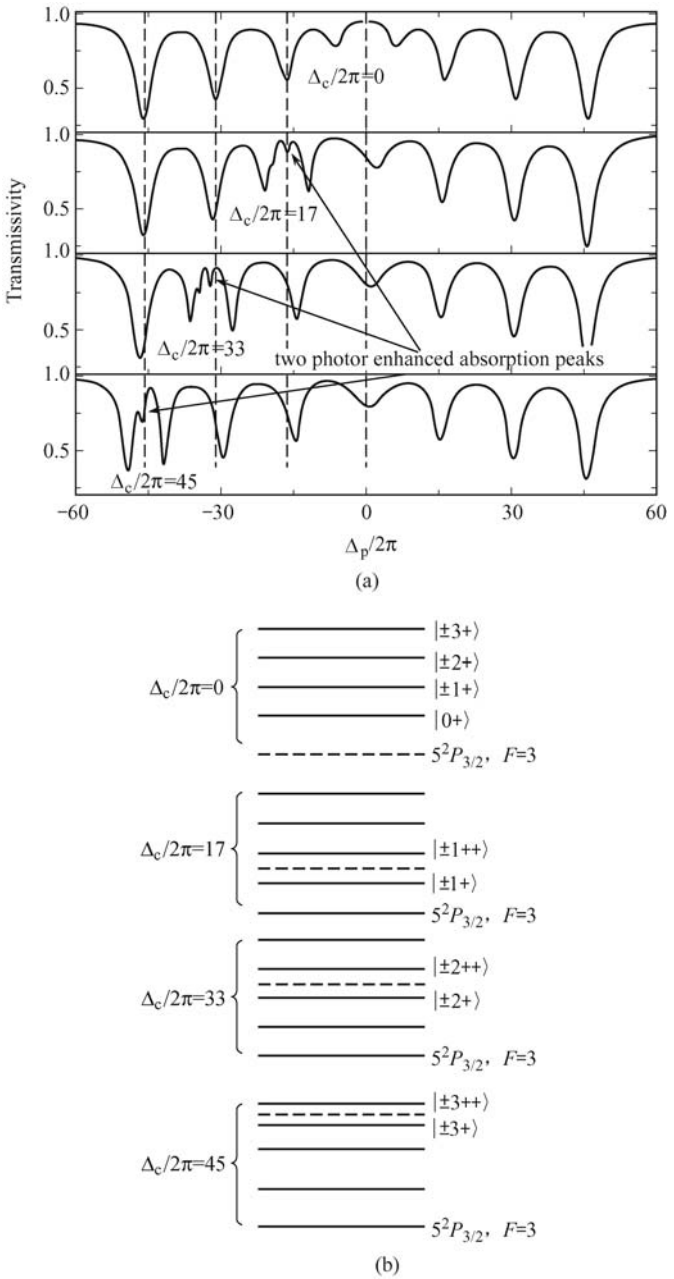

Fig. 6.20. (a) Calculated transmissivity of the probe beam versus $\Delta_p/2\pi$ for $\Delta_c/2\pi = 0, 17, 33, 45$ MHz, respectively when $G_d/2\pi = 100$ MHz, $G_c/2\pi = 10$ MHz and $\Delta_d/2\pi = 0$. (b) Diagram of positive levels (including secondary-splitting) of $5^2P_{3/2}$, $F = 3$ corresponding to (a). Other parameters are the same as in Fig. 6.19. The unit of the abscissa is MHz.

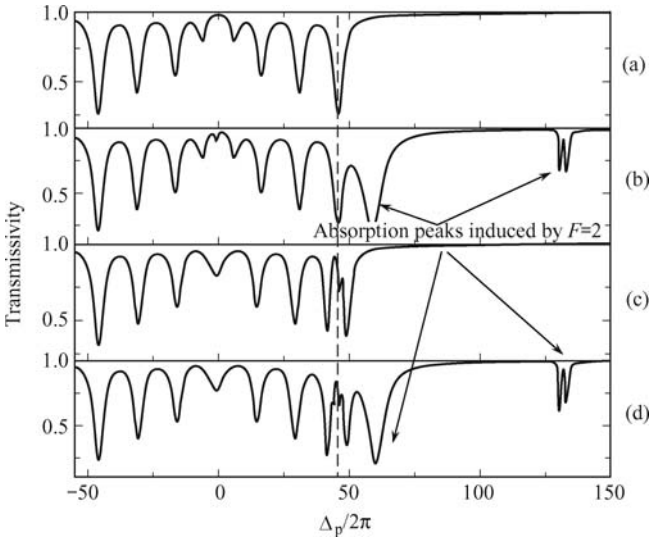

Fig. 6.21. (a), (b) Comparison of the cases of whether to consider the hyperfine level $F = 2$ or not at the same condition of Fig. 6.19 (f). (c), (d) Comparison of the cases of whether to consider the hyperfine level $F = 2$ or not at the similar condition (with just an opposite detuning of $\Delta_c/2\pi = -45$ MHz) of the fourth figure of Fig. 6.20 (a). The unit of the abscissa is MHz.

6.3.3 Four-Wave Mixing

By using the dressed perturbation the chain $\rho_{aa}^{(0)} \xrightarrow{\omega_p} \rho_{G_c \pm G_d \pm a}^{(1)} \xrightarrow{\omega_c} \rho_{ca}^{(2)} \xrightarrow{-\omega_c} \rho_{G_d \pm a}^{(3)}$, One can obtain the expressions for FWM from the density-matrix equations under similar approximations as for EIT:

$$\rho_{b_{M\pm1}a_M,Fa}^{(3)\pm} = -\frac{\mathrm{i}G_{pM}^{\pm}\left|G_{cM\pm1}\right|^2}{\mathrm{i}\Delta_p + \Gamma_{ba} + \dfrac{\left|G_{cM\pm1}\right|^2}{\mathrm{i}(\Delta_p + \Delta_c) + \Gamma_{ca}} + \dfrac{\left|G_{dM\pm1}\right|^2}{\mathrm{i}(\Delta_p - \Delta_d) + \Gamma_{da}}} \times \frac{1}{\mathrm{i}\Delta_p + \Gamma_{ba} + \dfrac{\left|G_{dM\pm1}\right|^2}{\mathrm{i}(\Delta_p - \Delta_d) + \Gamma_{da}}} \frac{1}{\mathrm{i}(\Delta_p + \Delta_c) + \Gamma_{ca}}$$
$$(M = -2, -1, \ldots, 2). \tag{6.45}$$

The signal intensity is proportional to $|N\mu_1\rho|^2$, so the relative FWM signal intensity is given by

$$I_F \propto \left| \sum_{M=-2}^{2} \left(\mu_{b_{M+1}a_M} \rho_{b_{M+1}a_M}^{(3)+} + \mu_{b_{M-1}a_M} \rho_{b_{M-1}a_M}^{(3)-} \right) \right|^2 . \tag{6.46}$$

In order to clearly understand the simulation results, let us analyze the

complex expressions as given by Eq. (6.45). For each expression, there are three production terms. In the denominator of the first term, the Rabi frequencies of the two fields ($G_{cM\pm1}$ and $G_{dM\pm1}$) are in sequential-dressing scheme like the expressions for EIT. $G_{dM\pm1}$ in the denominator of the second term multiply the sequential term, which can be denoted as a parallel-dressing scheme [31]. Therefore, the expression of FWM is a combination of a sequentially-dressed scheme and a singly-dressed scheme. As to the parallel scheme, which is different from the entanglement of two sequential fields, its two multiplying parts do not necessarily interact with each other. So, the two parallel terms may give two independent groups of peaks. Peaks in one group induced by the sequentially-dressed term are located at $\Delta_{pM} = \pm(|G_{cM\pm1}|^2 + |G_{dM\pm1}|^2)^{1/2}$, and the peaks from the other group induced by the singly-dressed term are at $\Delta_{pM} = \pm G_{dM\pm1}$.

Figure 6.22 is the calculated relative intensity of FWM signal for different Rabi frequencies of the dressing and coupling fields. Seven irregular peak pairs (which are denoted as 1, 2, $\cdots$,7 from lower to higher offset, respectively.) are obtained (the single peak in the centre is generated by the two-photon term of the expression which is not our focus of discussion here). However, from comparing the three curves in Fig. 6.22, the complex peak structures can be well understood. For curves (a) and (b), as G_c is changed but not G_d, peaks (pairs) 2, 3, 5, 7 shift, while peaks 1, 4, 6 are stable. So, peaks 2, 3, 5, 7 are generated by the sequential-dressing term (G_c and G_d) which probes the group of multi-Zeeman dark states generated in the first transition of the FWM process. Peaks 1, 4 and 6, however, are split by the singly-dressed parallel G_d, which probes the other group of dark states

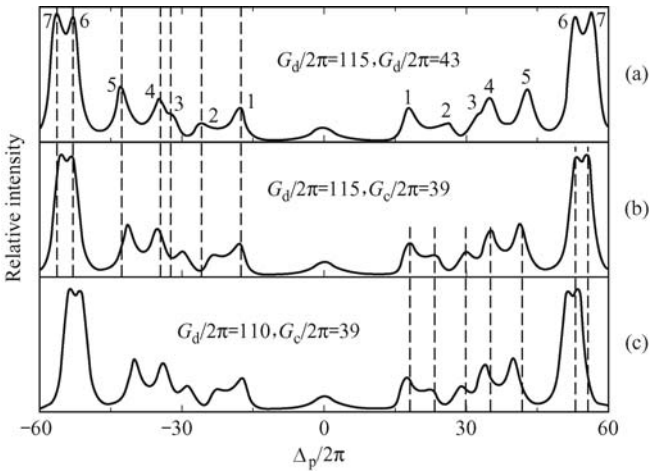

Fig. 6.22. Intensity of the FWM signal versus $\Delta_p/2\pi$ for (a) $G_c/2\pi = 43$ MHz, $G_d/2\pi = 115$ MHz; (b) $G_c/2\pi = 39$ MHz, $G_d/2\pi = 115$ MHz; (c) $G_c/2\pi = 39$ MHz, $G_d/2\pi = 110$ MHz.The parameters are $\Delta_c/2\pi = \Delta_d/2\pi = 0$, $G_p/2\pi = 2$ MHz, and the others are the same as in Fig. 6.19. The unit of the abscissa is MHz.

generated in the third transition of the FWM process. For curves (b) and (c), as G_d is changed but not G_c, the peak 2 is stable while the other peaks move. Similar to EIT, peak 2 must be split only by G_c, since $G_d = 0$ for Zeeman sublevel $M = 0$. Looking at the values of CG coefficients, which peaks of the two groups are induced by which Zeeman sublevels can be decided. By using the expressions of the peak positions, the positions of the peaks for curve (b) can be calculated as: $\Delta_{peak1} = \pm G_{d,\pm1}/2\pi = \pm 17.5$ MHz, $\Delta_{peak2} = \pm G_{c,0}/2\pi = \pm 24.3$ MHz, $\Delta_{peak3} = \pm(|G_{c,\pm1}|^2 + |G_{d,\pm1}|^2)^{1/2}/2\pi = \pm 29.6$ MHz, $\Delta_{peak4} = \pm|G_{d,\pm2}|/2\pi = \pm 35$ MHz, $\Delta_{peak5} = \pm(|G_{c,\pm2}|^2 + |G_{d,\pm2}|^2)^{1/2}/2\pi = \pm 41.6$ MHz, $\Delta_{peak6} = \pm G_{d,\pm3}/2\pi = \pm 52.5$ MHz, and $\Delta_{peak7} = \pm(|G_{c,\pm3}|^2 + |G_{d,\pm3}|^2)^{1/2}/2\pi = \pm 56.2$ MHz. The numerically calculated maxima in curve (b) are at ± 17.9496, ± 23.2243, ± 29.837, ± 35.1064, ± 41.3738, ± 53.2318, and ± 55.4742 MHz, respectively, which agree very well with the analytically calculated results, confirming that the expressions are reasonable. Properly intensity of the dressing and coupling fields were controlled for avoiding bringing hyperfine levels $F = 2$ and $F = 1$ in our discussion.

As discussed above, the sequentially-dressed scheme induces one group of multi-Zeeman dark states and the parallel singly-dressed field induces the other group which does not interact with the first group. The basic reason for such phenomenon is that the parallel dressing scheme represents two transition processes in FWM. The two groups of multi-Zeeman dark states generated in different processes are distinguishable because the weaker coupling field enhances the dressed effect of the dressing field in the first transition process.

For better understanding the enhancement and suppression effects of the signals, Eq. (6.47) is divided by the original FWM expression which has no dressing fields (i.e. let G_c and G_d in the denominator of Eq. (6.47) equal to 0). In such case, when the signal intensity is below one, it means suppression of FWM, while above one means enhancement of FWM signal intensity. The expression for normalized FWM signal with dressing fields reduces to

$$\rho^{\pm}_{b_{M\pm1}a_M} = \frac{\mathrm{i}G^{\pm}_{pM}}{\mathrm{i}\Delta_p + \Gamma_{ba} + \dfrac{|G_{cM\pm1}|^2}{\mathrm{i}(\Delta_p + \Delta_c) + \Gamma_{ca}} + \dfrac{|G_{dM\pm1}|^2}{\mathrm{i}(\Delta_p - \Delta_d) + \Gamma_{da}}} \rho^{(0)}_{a_M a_M}. \quad (M = -2, -1, \ldots, 2). \tag{6.47}$$

The normalized FWM signal intensity is given by

$$\tilde{I}_F \propto \left| \sum_{M=-2}^{2} \left(\mu_{b_{M+1}a_M} \tilde{\rho}^{(3)+}_{b_{M+1}a_M} + \mu_{b_{M-1}a_M} \tilde{\rho}^{(3)-}_{b_{M-1}a_M} \right) \right|^2. \tag{6.48}$$

Figure 6.23 (a) depicts the intensity of the dressed FWM signal versus $\Delta_c/2\pi$ and $\Delta_d/2\pi$ with $\Delta_p/2\pi = -60$ MHz (To avoid the hyperfine level $F = 2$, one choose $\Delta_p/2\pi < 0$, Since for the probe field, the hyperfine level

$F = 4$ over $F = 3$ is forbidden transition level (transition $5S_{1/2}$, $F = 2 \longrightarrow 5P_{3/2}$, $F = 4$ is forbidden), it can not involve other hyperfine levels other than the $F = 3$ while the intensity is not strong enough. The field strengths are $G_d/2\pi = 100$ MHz, $G_c/2\pi = 15$ MHz, $G_p/2\pi = 3$ MHz and the other parameters are the same as in Fig. 6.19. A cross section of Fig. 6.23 (a) versus $\Delta_d/2\pi$ when $\Delta_c/2\pi = 0$, as shown in Fig. 6.23 (b), shows three enhanced peaks, which is different from the case with only one enhanced peak in each curve in Ref. [31]. Surely, the multi-Zeeman splitting sublevels induced by the dressing fields are responsible for this phenomenon. As for the first transition process, the enhancement condition is $\Delta_p - \Delta_{pM} = 0$, where Δ_{pM} is the frequency shift of the given Zeeman sublevel (M). This represents the new resonant condition between the probe field and the splitting levels in the dressed-state picture. As shown in Fig. 6.23 (c) (the coupling beam is omitted because of its less contribution in this case), the probe detuning is fixed at $\Delta_p/2\pi = -60$ MHz, the split Zeeman sublevels move as the dressing field is scanned. Only three positive splitting levels can get through the resonant position ($\Delta_p/2\pi = -60$ MHz). If any of them are set at this position [dashed line in Fig. 6.23 (c)], it will satisfy the enhancement condition and greatly enhance the FWM signal. So the three negative splitting levels generate three enhanced FWM peaks when the dressing field is scanned [as shown in Fig. 6.23 (c) (I–III)]. The huge values in the y-axis are caused by the parallel-dressing scheme since the two simultaneously enhanced terms are multiplied.

Now let us derive the analytical expressions for the enhancement positions. By using Eq. (6.47) and under the approximations of G_d, Δ_d, $\Delta_p >> G_c > \Gamma_{ba}$, the locations of the splitting levels relative to the original position of the state $|b\rangle$ can be obtained as

$$\Delta_{pM} = \frac{1}{2}\left(\Delta_d \pm \sqrt{\Delta_d^2 + 4\left|G_{dM}\right|^2}\right). \tag{6.49}$$

Combining this with the enhancement condition of $\Delta_p - \Delta_{pM} = 0$, the detuning values for the dressing field, when the FWM is enhanced, can be determined to be

$$\Delta_{dM} = \left(\Delta_p^2 - \left|G_{dM}\right|^2\right)/\Delta_p. \tag{6.50}$$

According to Fig. 6.23 (b), the three enhanced peaks are located at $\Delta_d/2\pi = -25.278, -44.568$, and -56.142 MHz. The calculated positions for the three maxima are $-24.968, -44.392$, and -56.083 MHz, respectively, which show very good agreements.

Figure 6.23 (d) presents several cross sections of Fig. 6.23 (a) versus $\Delta_c/2\pi$. for $\Delta_d/2\pi = -25, -45, -56$ MHz. These three curves all give the same dip at $\Delta_c/2\pi = 60$ MHz on the enhancement background. This means that the coupling field greatly suppresses the FWM signals which have been enhanced by the dressing field, as shown in Fig. 6.23 (b). In fact, this obeys the suppression condition: $\Delta_p + \Delta_c = 0$, at which the coupling and probe

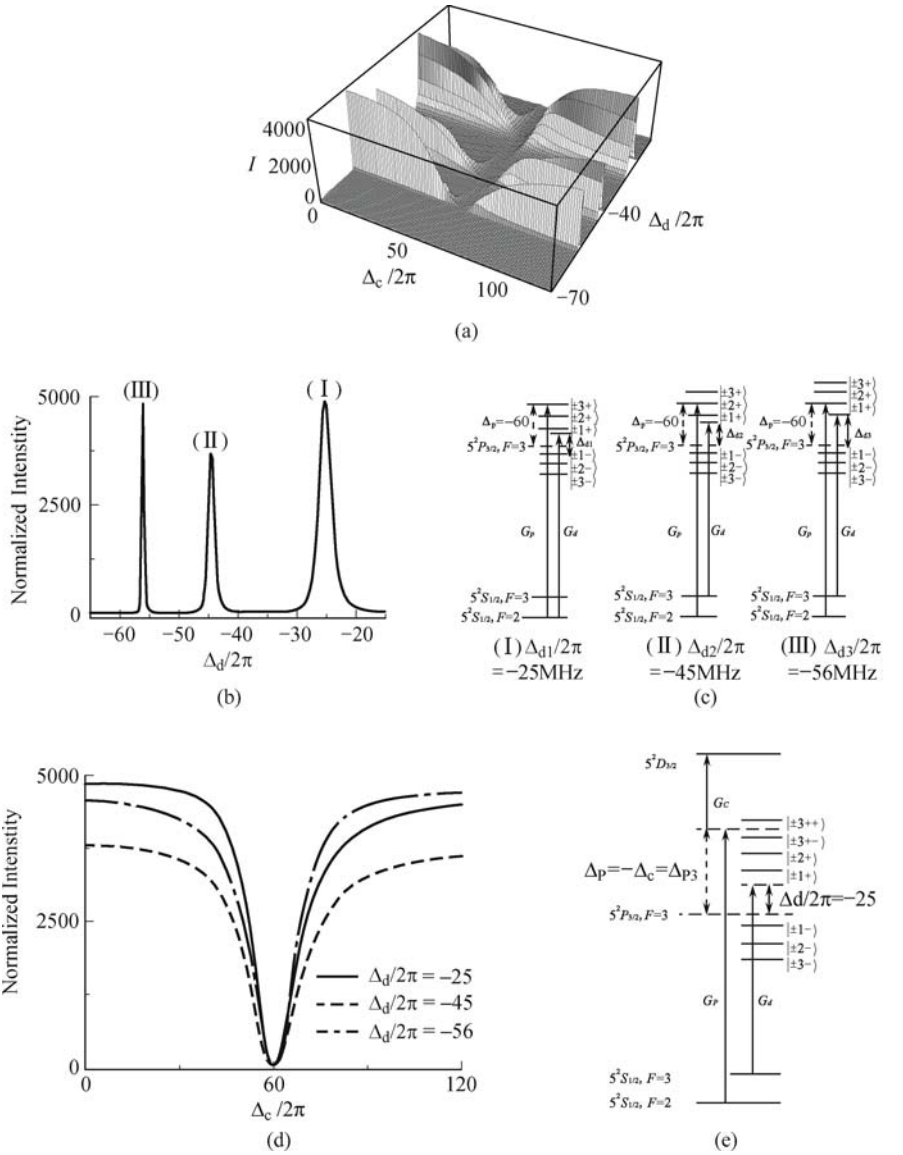

Fig. 6.23. (a) Intensity of FWM signal versus $\Delta_p/2\pi$ and $\Delta_d/2\pi$ with $\Delta_p/2\pi = -60$ MHz. The parameters are $G_d/2\pi = 100$ MHz, $G_c/2\pi = 15$ MHz and $G_p/2\pi = 3$ MHz, the other parameters are the same as in Fig. 6.19 (b) Cross section of (a) versus $\Delta_d/2\pi$ for $\Delta_c/2\pi = 0$. (c) Schematic dressed-state diagram for the enhancement corresponding to (b). (d) Cross sections of (a) versus $\Delta_c/2\pi$ for $\Delta_d/2\pi = -25$ MHz (solid line), -45 MHz (dash-dotted line), -56 MHz (dash-dotted line), respectively. (e) Schematic dressed-state diagram for the suppression of FWM signal, corresponding to (d) (the solid line with $\Delta_d/2\pi = -25$ MHz). The unit of the abscissa is MHz.

fields hit the same position in frequency. So the probability for the probe photon transition at $\Delta_p = -\Delta_c$ has been greatly reduced because of the dressing effect of the coupling field, even when the enhancement condition is also satisfied. Figure 6.23 (e) shows the diagram for the split levels when $\Delta_c/2\pi = 60$ MHz and $\Delta_d/2\pi = -25$ MHz. The split sublevels $|\pm 3+\rangle$ are further split into $|\pm 3++\rangle$ and $|\pm 3+-\rangle$, respectively, by the coupling field, similar to the secondary dressing in EIT case, so the FWM signal is suppressed.

Therefore, the spectrum of the FWM signal versus the dressing field detuning can also reveal the Zeeman structure in the atomic system. These are triple single-photon resonance ($\Delta_p = 0$) enhancements of FWM processes in split Zeeman sublevels. The analytical expressions for the positions of the dressing field fixed show that one can selectively enhance each FWM path consisting of different split Zeeman sublevels. At the same time, secondary dressing effects, induced by the coupling field like in the EIT case, also exist in the FWM spectrum and can greatly suppress the FWM signal.

6.3.4 Six-Wave Mixing

Using similar derivation procedure as for FWM processes in the last section, by means of the density-matrix equations and two SWM perturbation chains and under similar approximation, the expressions for dressed SWM processes can be obtained as [31]

$$\rho^{(5)\pm}_{b_{M\pm1}a_M} = \frac{\mathrm{i}G^{\pm}_{pM}\left|G_{cM\pm1}\right|^2\left|G_{dM\pm1}\right|^2}{\mathrm{i}\Delta_p+\Gamma_{ba}+\dfrac{\left|G_{cM\pm1}\right|^2}{\mathrm{i}(\Delta_p+\Delta_c)+\Gamma_{ca}}}\times \frac{1}{\mathrm{i}\Delta_p+\Gamma_{ba}+\dfrac{\left|G_{dM\pm1}\right|^2}{\mathrm{i}(\Delta_p-\Delta_d)+\Gamma_{da}}}\frac{1}{\mathrm{i}(\Delta_p-\Delta_d)+\Gamma_{da}}\times \frac{1}{\mathrm{i}\Delta_p+\Gamma_{ba}}\frac{1}{\mathrm{i}(\Delta_p+\Delta_c)+\Gamma_{ca}} \quad (M=-2,-1,\cdots,2). \tag{6.51}$$

The normalized expressions for the dressed SWM signals (by dividing the original SWM expression without the dressing fields) with multi-Zeeman sublevels are

$$\tilde{\rho}^{(5)\pm}_{b_{M\pm1}a_M} = \frac{\left(\mathrm{i}\Delta_p+\Gamma_{ba}\right)^2}{\mathrm{i}\Delta_p+\Gamma_{ba}+\dfrac{\left|G_{cM\pm1}\right|^2}{\mathrm{i}(\Delta_p+\Delta_c)+\Gamma_{ca}}}\frac{1}{\mathrm{i}\Delta_p+\Gamma_{ba}+\dfrac{\left|G_{dM\pm1}\right|^2}{\mathrm{i}(\Delta_p-\Delta_d)+\Gamma_{da}}} \quad (M=-2,-1,\cdots,2). \tag{6.52}$$

Since the signal intensity I is proportional to $|N\mu_1\rho|^2$, the relative SWM

signal intensities (normalized) are given by

$$\tilde{I}_S = \left| \sum_{M=-2}^{2} \left(\mu_{b_{M+1}a_M} \tilde{\rho}^{(5)+}_{b_{M+1}a_M} + \mu_{b_{M-1}a_M} \tilde{\rho}^{(5)-}_{b_{M-1}a_M} \right) \right|^2 . \tag{6.53}$$

Since the basic analyses and major results of AT splitting in the SWM case are similar to the case of FWM, as discussed in the last section, it is no need to repeat the discussions here.

Figure 6.24(a) is the normalized SWM intensity according to Eq. (6.52) versus $\Delta_d/2\pi$. when the probe beam is slightly detuned ($\Delta_p/2\pi = -10$ MHz. Other parameters are $G_d/2\pi = 50$ MHz, $G_c/2\pi = 10$ MHz and $\Delta_c/2\pi = 100$ MHz. Similar to the FWM enhancement spectrum, three enhanced peaks (from left to right) are induced by the single-photon resonances of the probe beam with the dressed states $|\pm 3+\rangle$, $|\pm 2+\rangle$, and $|\pm 1+\rangle$, respectively. The curves of Figure 6.24 (b) are respective singly-induced by $|\pm 3+\rangle$ (dashed line), $|\pm 2+\rangle$ (dotted line) and $|\pm 1+\rangle$ (solid line) under the same condition as in Fig. 6.24 (a), which show different enhanced peaks (different positions).

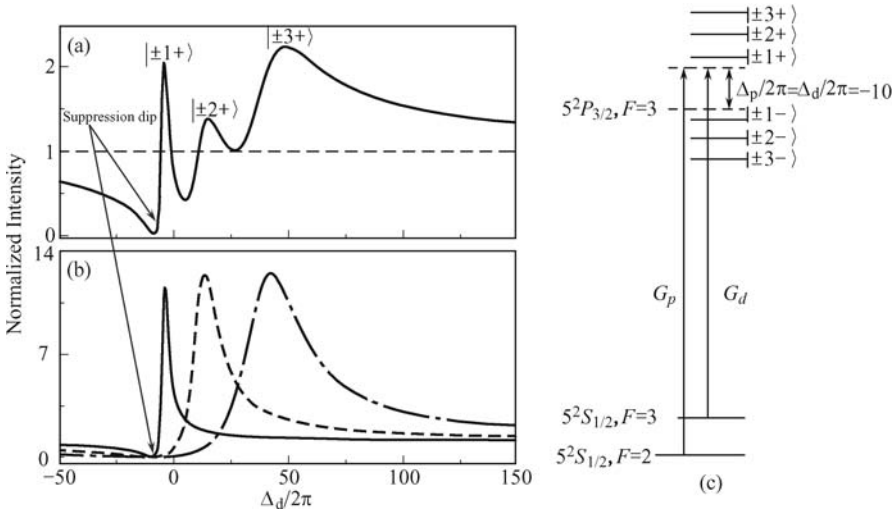

Fig. 6.24. (a) Intensity of SWM signal versus $\Delta_d/2\pi$ with $\Delta_p/2\pi = -10$ MHz. The parameters are $G_d/2\pi = 50$ MHz, $G_c/2\pi = 10$ MHz and $G_p/2\pi = 3$ MHz, $\Delta_c/2\pi = 100$ MHz, the other parameters are the same as in Fig. 6.19 (b) The curves show structures as singly-induced by $|\pm 3+\rangle$ (dashed line), $|\pm 2+\rangle$ (dotted line) and $|\pm 1+\rangle$ (solid line), respectively, under the same condition as in (a). (c) Schematic dressed-state diagram for the signal enhancement corresponding to (a). The unit of the abscissa is MHz.

Also, one suppression dip exists. Because of the suppression condition of $\Delta_p - \Delta_d = 0$, only one suppression dip can exist at $\Delta_d/2\pi = \Delta_p/2\pi = -10$ MHz for all the split Zeeman sublevels. Figures 6.24 (a) and 6.24 (b) both confirm this conclusion. Figure 6.24 (c) is the schematic dressed-state diagram

to show the condition for suppression. One can see that as the dressing field hits the position of the probe field, it effectively suppresses its transition, and therefore, reduces the SWM process.

Therefore, as the dressing field is scanned in frequency, the SWM signal gets not only multiple enhancement peaks, but also suppression dips when the probe field is slightly detuned. The mechanism for enhancement is similar to the one as in FWM. The suppressed dips, however, represent the dressed effects of the dressing field, which cannot reveal the Zeeman structure in the system.

References

[1] Gea-Banacloche J, Li Y, Jin S, et al. Electromagnetically induced transparency in ladder-type inhomogeneously broadened media: Theory and experiment. Phys Rev A, 1995, 51: 576 – 584.

[2] Harris S E. Electromagnetically induced transparency. Phys Today, 1997, 50:36 – 42.

[3] Zibrov A S, Matsko A B, Kocharovskaya O, et al. Transporting and time reversing light via atomic coherence. Phys Rev Lett, 2002, 88: 103601.

[4] Hemmer P R, Katz D P, Donoghue J, et al. Efficient low-intensity optical phase conjugation based on coherent population trapping in sodium. Opt Lett, 1995, 20: 982 – 984.

[5] Lu B L, Burkett W H and Xiao M. Nondegenerate Four-Wave Mixing in a double-system under the influence of coherent population trapping. Opt Lett, 1998, 23: 804 – 806.

[6] Jiang K J, Deng L and Payne M G. Observation of quantum destructive interference in inelastic Two-wave Mixing. Phys Rev Lett, 2007, 98: 083604.

[7] Kang H, Hernandez G, Zhang J, et al. Phase-contrlled light switching at low light levels. Phys. Rev. A, 2006, 73: 011802(R).

[8] Boyer V, Marino A M, Pooser R C, et al. Entangled images from four-wave mixing. Science, 2008, 321: 544 – 547.

[9] Du S W, Wen J M, Rubin M, et al. Four-wave mixing and biphoton generation in a two-level system. Phys Rev Lett, 2007, 98: 053601.

[10] Danielle V B, Braje A, Kolchin P, et al. Generation of paired photons with controllable waveforms. Phys Rev Lett, 2005, 94: 183601.

[11] Cohen-Tannoudji C, Reynaud S. Dreesed-atom description of resonance fluorescence and absorption spectra of a multi-level atom in an intense laser beam. J Phys B, 1997, 10: 345

[12] Zheng H B, Zhang Y P, Nie Z Q, et al. Interplay among multi-dressed four-wave mixing processes. Appl Phys Lett, 2008, 93: 241101.

[13] Zhang Y, Anderson B, Brown A W, et al. Competition between two Four-wave mixing channels via atomic coherence. Appl Phys Lett, 2007, 91: 061113.

[14] Zhang Y and Xiao M. Generalized dressed and doubly-dressed multi-wave mixing. Opt Express., 2007, 15. 7182 – 7189.

[15] Zhu C J, Senin A A, Lu Z H, et al. Polarization of signal wave radiation generated by parametric four-wave mixing in rubidium vapor: Ultrafast (about 150 fs) and nanosecond time scale excitation. Phys Rev A, 2005, 72: 023811.

[16] Ling H Y, Li Q, Xiao M. Coherent population trapping and electromagnetically induced transparency in multi-Zeeman-sublevel atoms. Phys Rev A, 1996, 53: 1014.

[17] Zheng H B, Zhang Y P, Khadka U, et al. Modulating the multi-wave mixing processes via the polarizable dark states. Optics Express, 2009, 17: 15468 – 15480.

[18] Li S, Wang B, Yang X, et al. Controlled polarization rotation of an optical field in multi-Zeeman-sublevel atoms. Phys Rev A, 2006, 74: 033821.

[19] For detail in transition probabilities of D1 and D2 line in Rb. http://steck.Us/alkalidata. Accessed 21 July 2010.

[20] Chen Y, Lin C, Yu Ite A. Role of degenerate Zeeman levels in electromagnetically induced transparency. Phys Rev A, 2000, 61: 053805.

[21] Museur L, Olivero C, Riedel D, et al. Polarization properties of coherent VUV light at 125 nm generated by sum-frequency four-wave mixing in mercury. Appl Phys B, 2000, 70: 499 – 503.

[22] Ishii J, Ogi Y, Tanaka Y, et al. Observation of the two-photon resonant parametric four-wave mixing in the NO $C^2\Pi$ ($v = 0$) state. Opt Commun, 1996, 132: 316 – 320.

[23] Chapple P B, Baldwin K G H, Bachor H A. Interference between competing quantum-mechanical pathways for four-wave mixing. J Opt Soc Am B, 1998, 6: 180 – 183.

[24] Magno W C, Prandini R B, Nussenzveig P, et al. Four-wave mixing with Rydberg levels in rubidium vapor: Observation of interference fringes. Phys Rev A, 2001, 63: 063406.

[25] Garret W R, Zhu Y. Coherent control of multiphoton driven processes: A laser-induced catalyst. J Chem Phys, 1997, 106: 2045 – 2048.

[26] Wu Y, Saldana J, Zhu Y F. Large enhancement of four-wave mixing by suppression of photon absorption from electromagnetically induced transparency. Phys Rev A, 2003, 67: 013811.

[27] Ma H, Gomes A S L, de Araujo C B. All-optical power-controlled switching in wave mixing: application to semiconductor-doped glasses. Opt Lett, 1993, 18: 414 – 416.

[28] Gisin N, Ribordy G, Tittel W, et al. Quantum cryptography. Rev Mod Phys, 2002, 74: 145 – 195.

[29] Bahder T B, Lopata P A, Fidelity of quantum interferometers. Phys Rev A, 2006, 74: 051801(R).

[30] Vianna S S, Nussenzveig P, Magno W C, et al. Polarization dependence and interference in four-wave mixing with Rydberg levels in rubidium vapor. Phys Rev A, 1998, 58: 3000 – 3003.

[31] Nie Z Q, Zheng H B, Li P Z, et al. Interacting multi-wave mixing in a five-level folding atomic system. Phys Rev A, 2008, 77: 063829.

[32] Wang R M, Du Y G, Zhang Y P, et al. Polarization spectroscopy of dressed four-wave mixing in a three-level atomic system. J Opt Soc Am B, 2009, 26: 1710 – 1719.

[33] Du S G, Oh E, Wen J M, Rubin M H. Four-wave mixing in three-level systems: Interference and entanglement. Phys Rev A, 2007, 76: 013803.

[34] Zhang Y P, Xiao M. Multi-wave mixing processes. Higher Education Press, Springer, Berlin, 2009.

[35] Zhang Y P, Brown A W, Xiao M. Opening four-wave mixing and six-wave mixing channels via dual electromagnetically induced transparency windows. Phys Rev Lett, 2007, 99: 123603.

[36] Zhang Y P, Khadka U, Anderson B, et al. Temporal and spatial interference between four-wave mixing and six-wave mixing channels. Phys Rev Lett, 2009, 102: 013601. Wang B, Han Y X, Xiao J T, et al. Multi-dark-state resonances in cold multi-Zeeman-sublevel atoms. Opt Lett, 2006, 31: 3647 – 3649.

[37] Lukin M D, Yelin S F, Fleischhauer M, et al. Quantum interference effects induced by interacting dark resonances. Phys Rev A, 1999, 60: 3225 – 3228.

[38] Yan M, Rickey E G, Zhu Y F. Observation of doubly dressed states in cold atoms. Phys Rev A, 2001, 64: 013412.

[39] Du Y G, Zhang Y P, Zuo C C, et al. Controlling four-wave mixing and six-wave mixing in a multi-Zeeman-sublevel atomic system with electromagnetically induced transparency. Phys Rev A, 2009, 79: 063839.

[40] Xiao M, Li Y Q, Jin S Z, et al. Measurement of dispersive properties of electromagnetically induced transparency in rubidium atoms. Phys Rev Lett, 1995, 74: 666 – 669.

[41] Wang B, Han Y X, Xiao J T, et al. Preparation and determination of spin-polarized states in multi-Zeeman-sublevel atoms. Phys Rev A, 2007, 75: 051801.

[42] Rubidium 85 D line data. http://steck.us/alkalidata. Accessed 12 July 2010.

7 Controlling Spatial Shift and Spltting of Four-Wave Mixing

When multiple laser beams interact with multi-level atomic systems, interesting spatial effects for the probe beam, such as the pattern formation, spatial displacement, and spatial soliton, can occur, controlled by stronger coupling or pumping laser beams. In this chapter, spatial dispersion properties of the probe and generated four-waving mixing (FWM) beams are presented, which can lead to spatial shift and splitting of these weak laser beams. Such beam displacement and splitting can be controlled by the story coupling/pumping laser beams via enhanced cross-Kerr nonlinearity in the multi-level atomic systems near electromagnetically induced transparency (EIT) resonance. Such enhanced spatial dispersion behaviors follow closely to the traditional linear and nonlinear dispersion properties in a frequency domain for multi-level EIT systems. By controlling the spatial displacements of the weak probe and FWM beams with coupling/pumping beams, spatial optical switching and routing of one beam or multiple optical beams can be achieved. Such controllable spatial beam displacement and splitting effects are illustrated in two- and three-level atomic system.

Additional story dressing beams can also affect the spatial splitting and intensity of the FWM beam. Studies of such a controlled beam shift and spatial splitting can be very useful in understanding image storage, spatial soliton formation and dynamics, and in device applications for spatial signal processing inducing switches and routers.

7.1 Basic Theory

The self-Kerr nonlinear index of refraction for rubidium atoms has been theoretically calculated and experimentally measured by Wang [1]. In this section, we will present a simple theoretical treatment of the dressed cross-Kerr nonlinear index of refraction for a two-level atomic system, a V-type and a ladder-type three-level atomic system.

First we consider a two-level system, as shown in Fig. 7.1(a), where the weak probe field E_1 and the strong coupling fields E_1' come from the same laser and both couple levels $|0\rangle$ and $|1\rangle$. They have the same frequency de-

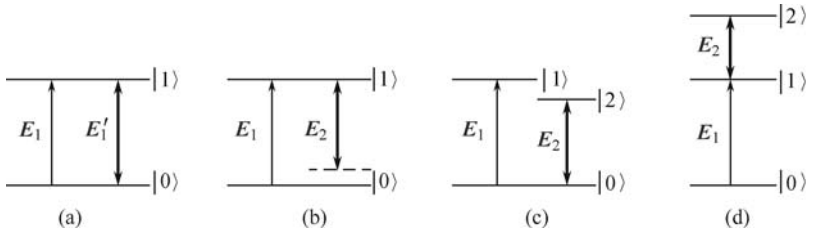

Fig. 7.1. Sketches of the (a) and (b) two-level atomic system, (c) a V-type and (d) a ladder-type three-level atomic systems. E_1 is the weak probe field, E_1' and E_2 are the strong coupling fields.

tuning $\Delta_1 = \Omega_1 - \omega_1$, where Ω_i is the resonant frequency and ω_i is the laser frequency. For this system the following equations are derived for the slowly varying density matrix elements:

$$\begin{cases} \dfrac{\partial \rho_{00}^{(r)}}{\partial t} = -\Gamma_{00}\rho_{00}^{(r)} - \mathrm{i}G_1\rho_{01}^{(r)} + \mathrm{i}G_1^*\rho_{10}^{(r)}, \\ \dfrac{\partial \rho_{11}^{(r)}}{\partial t} = -\Gamma_{11}\rho_{11}^{(r)} - \mathrm{i}G_1^*\rho_{10}^{(r)} + \mathrm{i}G_1\rho_{01}^{(r)}, \\ \dfrac{\partial \rho_{10}^{(r)}}{\partial t} = -[\mathrm{i}\Delta_1 + \Gamma_{10}]\rho_{10}^{(r)} - \mathrm{i}G_1\rho_{11}^{(r)} + \mathrm{i}G_1\rho_{00}^{(r)}, \end{cases} \tag{7.1}$$

where G_i is the Rabi frequency, Γ_{00} and Γ_{11} are the longitudinal relaxation, and Γ_{10} is the transverse relaxation from $|1\rangle$ to $|0\rangle$. A cross-Kerr process of the weak probe field E_1 induced by the strong coupling field E_2 can be simply presented via the four perturbation chains:

$$\begin{cases} \rho_{00}^{(0)} \xrightarrow{E_1'} \rho_{10}^{(1)} \xrightarrow{E_1'^*} \rho_{00}^{(2)} \xrightarrow{E_1} \rho_{10}^{(3)}, \\ \rho_{00}^{(0)} \xrightarrow{E_1'^*} \rho_{01}^{(1)} \xrightarrow{E_1'} \rho_{00}^{(2)} \xrightarrow{E_1} \rho_{10}^{(3)}, \\ \rho_{00}^{(0)} \xrightarrow{E_1'} \rho_{10}^{(1)} \xrightarrow{E_1'^*} \rho_{11}^{(2)} \xrightarrow{E_1} \rho_{10}^{(3)}, \\ \rho_{00}^{(0)} \xrightarrow{E_1'^*} \rho_{01}^{(1)} \xrightarrow{E_1'} \rho_{11}^{(2)} \xrightarrow{E_1} \rho_{10}^{(3)}. \end{cases} \tag{7.2}$$

If we consider the dressing effect of the strong coupling field E_1', both the energy levels $|0\rangle$ and $|1\rangle$ are dressed to create dressed states $|+\rangle$ and $|-\rangle$, respectively. The dressed cross-Kerr nonlinear processes can be described as

$$\begin{cases} \rho_{00}^{(0)} \xrightarrow{E_1'} \rho_{1\pm0\pm}^{(1)} \xrightarrow{E_1'^*} \rho_{0\pm0\pm}^{(2)} \xrightarrow{E_1} \rho_{1\pm0\pm}^{(3)}, \\ \rho_{00}^{(0)} \xrightarrow{E_1'^*} \rho_{0\pm1\pm}^{(1)} \xrightarrow{E_1'} \rho_{0\pm0\pm}^{(2)} \xrightarrow{E_1} \rho_{1\pm0\pm}^{(3)}, \\ \rho_{00}^{(0)} \xrightarrow{E_1'} \rho_{1\pm0\pm}^{(1)} \xrightarrow{E_1'^*} \rho_{1\pm1\pm}^{(2)} \xrightarrow{E_1} \rho_{1\pm0\pm}^{(3)}, \\ \rho_{00}^{(0)} \xrightarrow{E_1'^*} \rho_{0\pm1\pm}^{(1)} \xrightarrow{E_1'} \rho_{1\pm1\pm}^{(2)} \xrightarrow{E_1} \rho_{1\pm0\pm}^{(3)}, \end{cases} \tag{7.3}$$

where $\rho_{1\pm0\pm}$ represents dressing the chain $\rho_{10} \xrightarrow{E_1'^*} \rho_{00} \xrightarrow{E_1'} \rho_{10} \xrightarrow{E_1'^*} \rho_{11} \xrightarrow{E_1'} \rho_{10}$, $\rho_{0\pm1\pm}$ represents dressing the chain $\rho_{01} \xrightarrow{E_1'} \rho_{11} \xrightarrow{E_1'^*} \rho_{01} \xrightarrow{E_1'} \rho_{00} \xrightarrow{E_1'^*} \rho_{01}$, $\rho_{0\pm0\pm}$ represents dressing the chain $\rho_{00} \xrightarrow{E_1'^*} \rho_{01} \xrightarrow{E_1'} \rho_{00} \xrightarrow{E_1'} \rho_{10} \xrightarrow{E_1'^*} \rho_{00}$ and $\rho_{1\pm1\pm}$ represents dressing the chain $\rho_{11} \xrightarrow{E_1'^*} \rho_{01} \xrightarrow{E_1'} \rho_{11} \xrightarrow{E_1'} \rho_{10} \xrightarrow{E_1'^*} \rho_{11}$. Under the condition that the coupling field is much stronger than the probe field and $\rho_{00}^{(0)} \approx 1$, equations can be solve together with the chain to give

$$\rho_{10}^{(3)} = \frac{-\mathrm{i}G_1|G_1'|^2}{F_1}\left(\frac{1}{F_1^*}+\frac{1}{F_1}\right)\left(\frac{1}{F_2}+\frac{1}{F_3}\right), \tag{7.4}$$

where

$$\begin{cases} F_1 = (\Gamma_{10}+\mathrm{i}\Delta_1) + \dfrac{|G_1'|^2}{\Gamma_{00}} + \dfrac{|G_1'|^2}{\Gamma_{11}}, \\ F_2 = \Gamma_{00} + \dfrac{|G_1'|^2}{\Gamma_{10}+\mathrm{i}\Delta_1} + \dfrac{|G_1'|^2}{\Gamma_{01}-\mathrm{i}\Delta_1}, \\ F_3 = \Gamma_{11} + \dfrac{|G_1'|^2}{\Gamma_{10}+\mathrm{i}\Delta_1} + \dfrac{|G_1'|^2}{\Gamma_{01}-\mathrm{i}\Delta_1}. \end{cases} \tag{7.5}$$

Thus we can obtain $\chi^{(3)} \propto \rho_{10}^{(3)}$ and the dressed cross-Kerr nonlinear index of refraction $n_2^X \propto \mathrm{Re}\chi^{(3)}$.

In this two-level system, when the weak probe field E_1 and the strong coupling fields E_2 come from the different lasers but both couple levels $|0\rangle$ and $|1\rangle$, as shown in Fig. 7.1(a). They have the different frequency detunings Δ_1 and $\Delta_2 = \Omega_1 - \omega_2$, respectively. The cross-Kerr process of the weak probe field E_1 induced by the strong coupling field E_2 can be simply presented via the four perturbation chains:

$$\rho_{00}^{(0)} \xrightarrow{E_1} \rho_{10}^{(1)} \xrightarrow{E_2^*} \rho_{00}^{(2)} \xrightarrow{E_2} \rho_{10}^{(3)}. \tag{7.6}$$

If we consider the dressing effect of the strong coupling field E_2, the energy level $|1\rangle$ is dressed to create dressed states $|+\rangle$ and $|-\rangle$. The dressed cross-Kerr nonlinear processes can be described as

$$\rho_{00}^{(0)} \xrightarrow{E_1} \rho_{1\pm0}^{(1)} \xrightarrow{E_2^*} \rho_{00}^{(2)} \xrightarrow{E_2} \rho_{1\pm0}^{(3)}, \tag{7.7}$$

where $\rho_{1\pm0}$ represents the dressing chain $\rho_{10} \xrightarrow{E_2^*} \rho_{00} \xrightarrow{E_2} \rho_{10}$. Under the same condition as before, equations can be solve together with the chain to give

$$\rho_{10}^{(3)} = \frac{-\mathrm{i}G_1|G_2|^2}{\Gamma_{00}\left\{\Gamma_{10}+\mathrm{i}\Delta_1+G_2^2/[\Gamma_{00}+\mathrm{i}(\Delta_1-\Delta_2)]\right\}^2}. \tag{7.8}$$

Similarly, for a V-type three-level system, as shown in Fig. 7.1 (c), the weak probe field E_1 couples levels $|0\rangle$ and $|1\rangle$ with the frequency detuning Δ_1

and the strong coupling fields E_2 couples levels $|0\rangle$ and $|2\rangle$ with the frequency detuning $\Delta_2 = \Omega_2 - \omega_2$. For this system, the following equations are

$$\begin{cases} \dfrac{\partial \rho_{00}^{(r)}}{\partial t} = -\Gamma_{00}\rho_{00}^{(r)} - \mathrm{i}G_2\rho_{02}^{(r)} + \mathrm{i}G_2^*\rho_{20}^{(r)} + \mathrm{i}G_1^*\rho_{10}^{(r)} - \mathrm{i}G_1\rho_{01}^{(r)}, \\ \dfrac{\partial \rho_{10}^{(r)}}{\partial t} = -[\mathrm{i}\Delta_1 + \Gamma_{10}]\rho_{10}^{(r)} - \mathrm{i}G_1\rho_{11}^{(r)} - \mathrm{i}G_2\rho_{12}^{(r)} + \mathrm{i}G_1\rho_{00}^{(r)}, \\ \dfrac{\partial \rho_{20}^{(r)}}{\partial t} = -[\mathrm{i}\Delta_2 + \Gamma_{20}]\rho_{20}^{(r)} - \mathrm{i}G_1\rho_{21}^{(r)} - \mathrm{i}G_2\rho_{22}^{(r)} + \mathrm{i}G_2\rho_{00}^{(r)}. \end{cases} \tag{7.9}$$

Γ_{20} is the transverse relaxation from $|2\rangle$ to $|0\rangle$. A cross-Kerr process of the weak probe field E_1 induced by the strong coupling field E_2 can be simply presented via the four perturbation chains:

$$\begin{cases} \rho_{00}^{(0)} \xrightarrow{E_2} \rho_{20}^{(1)} \xrightarrow{E_2^*} \rho_{00}^{(2)} \xrightarrow{E_1} \rho_{10}^{(3)}, \\ \rho_{00}^{(0)} \xrightarrow{E_2^*} \rho_{02}^{(1)} \xrightarrow{E_2} \rho_{00}^{(2)} \xrightarrow{E_1} \rho_{10}^{(3)}. \end{cases} \tag{7.10}$$

If we consider the dressing effect of the strong coupling field E_2, the energy levels $|0\rangle$ is dressed to create dressed states $|+\rangle$ and $|-\rangle$, respectively. The dressed cross-Kerr nonlinear processes can be described as

$$\begin{cases} \rho_{00}^{(0)} \xrightarrow{E_2} \rho_{20\pm}^{(1)} \xrightarrow{E_2^*} \rho_{0\pm0\pm}^{(2)} \xrightarrow{E_1} \rho_{10\pm}^{(3)}, \\ \rho_{00}^{(0)} \xrightarrow{E_2^*} \rho_{0\pm2}^{(1)} \xrightarrow{E_2} \rho_{0\pm0\pm}^{(2)} \xrightarrow{E_1} \rho_{10\pm}^{(3)}. \end{cases} \tag{7.11}$$

Under the condition that the coupling field is much stronger than the probe field and $\rho_{00}^{(0)} \approx 1$, equations can be solved together with chains to give

$$\rho_{10}^{(3)} = \frac{-\mathrm{i}G_1|G_2|^2}{F_5F_6}\left(\frac{1}{F_4} + \frac{1}{F_4^*}\right). \tag{7.12}$$

where

$$\begin{cases} F_4 = (\Gamma_{20} + \mathrm{i}\Delta_2) + \dfrac{G_2^2}{\Gamma_{22}}, \\ F_5 = \Gamma_{00} + \dfrac{G_2^2}{\Gamma_{20} + \mathrm{i}\Delta_2} + \dfrac{G_2^2}{\Gamma_{02} - \mathrm{i}\Delta_2}, \\ F_6 = (\Gamma_{10} + \mathrm{i}\Delta_1) + \dfrac{G_2^2}{\Gamma_{12} + \mathrm{i}(\Delta_1 - \Delta_2)}. \end{cases} \tag{7.13}$$

At last, for a ladder-type three-level system, as shown in Fig. 7.1 (d), the weak probe field E_1 couples levels $|0\rangle$ and $|1\rangle$ with the frequency detuning Δ_1 and the strong coupling fields E_2 couples levels $|1\rangle$ and $|2\rangle$ with the frequency

detuning Δ_2. For this system, the following equations are

$$\begin{cases} \dfrac{\partial \rho_{00}^{(r)}}{\partial t} = -\Gamma_{00}\rho_{00}^{(r)} + \mathrm{i}G_1^*\rho_{10}^{(r)} - \mathrm{i}G_1\rho_{01}^{(r)}, \\ \dfrac{\partial \rho_{10}^{(r)}}{\partial t} = -[\mathrm{i}\Delta_1 + \Gamma_{10}]\rho_{10}^{(r)} - \mathrm{i}G_1\rho_{11}^{(r)} + \mathrm{i}G_2^*\rho_{20}^{(r)} + \mathrm{i}G_1\rho_{00}^{(r)}, \\ \dfrac{\partial \rho_{20}^{(r)}}{\partial t} = -[\mathrm{i}(\Delta_1 + \Delta_2) + \Gamma_{20}]\rho_{20}^{(r)} - \mathrm{i}G_1\rho_{21}^{(r)} + \mathrm{i}G_2\rho_{10}^{(r)}. \end{cases} \tag{7.14}$$

A cross-Kerr process of the weak probe field E_1 induced by the strong coupling field E_2 can be simply presented via the four perturbation chains:

$$\rho_{00}^{(0)} \xrightarrow{E_1} \rho_{10}^{(2)} \xrightarrow{E_2} \rho_{20}^{(2)} \xrightarrow{E_2^*} \rho_{10}^{(3)}. \tag{7.15}$$

If we consider the dressing effect of the strong coupling field E_2, the energy levels $|1\rangle$ is dressed to create dressed states $|+\rangle$ and $|-\rangle$, respectively. The dressed cross-Kerr nonlinear processes can be described as

$$\rho_{00}^{(0)} \xrightarrow{E_1} \rho_{1\pm0}^{(2)} \xrightarrow{E_2} \rho_{20}^{(2)} \xrightarrow{E_2^*} \rho_{1\pm0}^{(3)}. \tag{7.16}$$

Under the condition that the coupling field is much stronger than the probe field and $\rho_{00}^{(0)} \approx 1$, equations can be solved together with chains to give

$$\rho_{10}^{(3)} = \frac{-\mathrm{i}G_1|G_2|^2}{[\Gamma_{20} + \mathrm{i}(\Delta_1 + \Delta_2)]\{(\Gamma_{10} + \mathrm{i}\Delta_1) + G_2^2/[\Gamma_{20} + \mathrm{i}(\Delta_1 + \Delta_2)]\}^2}. \tag{7.17}$$

7.2 Electromagnetically-induced Spatial Nonlinear Dispersion of Four-Wave Mixing Beams

As two or more laser beams propagate through an atomic medium, the cross-phase modulation (XPM), as well as the modified self-phase modulation (SPM), can significantly affect the propagations and spatial patterns of the traveling laser beams. Laser beam self-focusing [2], deflection [3], beam breaking [4], and pattern formation [5, 6] have been extensively studied with two laser beams propagating in two-level atomic vapors. The previous chapters have shown that the self- and cross-Kerr nonlinearities can significantly enhance and modify the linear and nonlinear optical properties in three-level atomic systems due to laser-induced atomic coherence (or EIT) [7 – 9]. EIT-induced waveguide effect [9], elimination of beam filamentation [10, 11] by atomic coherence, and spatial all-optical switching of laser beams [12] were reported in the past few years. At the same time, FWM processes have been shown to be significantly enhanced in three-level EIT systems [13 – 15].

There are several features in this section that are distinctly different and advantageous over the previously studied spatial shifts of laser beams in

atomic systems. One of the distinct features in multi-level EIT systems is the sharp linear [16], as well as nonlinear [2], dispersions in frequency near the EIT resonance. By arranging the laser beams in certain spatial configurations, such sharp dispersive features in the frequency domain for the probe beam can be converted into spatial beam displacement controlled by the strong coupling laser beam. For a three-level V-type system, as shown in Fig. 7.2 (a), the control (coupling) beam $\boldsymbol{E}_2$ in one transition can spatially deflect the probe beam $\boldsymbol{E}_p$ in another transition when these two laser beams propagate through the atomic medium with a small angle. As the probe frequency is detuned, the spatial deflection shows a dispersion-like change in its displacement, which exactly mimics the dispersion curve as observed for the Kerr-nonlinear index of refraction in the EIT system [2]. Also, when two additional pump laser beams ($\boldsymbol{E}_1$ and $\boldsymbol{E}_1'$) are applied to the probe transition, as shown in Fig. 7.2 (b), to generate a FWM signal $\boldsymbol{E}_{F1}$, this FWM signal beam can also be spatially displaced by the control beam $\boldsymbol{E}_2$. Again, a dispersion-like spatial deflection curve for the FWM signal is seen with respect to the probe frequency detuning. Such electromagnetically-induced spatial dispersion (EISD) can be used for spatial switching and routing, and as an easy way to measure the Kerr-nonlinear indices of refraction for the multi-level atomic media. When the control beam $\boldsymbol{E}_2$ is tuned to the same transition as the probe and pump beams, as shown in Fig. 7.2(c), it becomes an effective two-level system.

The three-level V-type atomic system is shown in Fig. 2 (a). Three energy levels ($|0\rangle(3S_{1/2})$, $|1\rangle(3P_{1/2})$ and $|2\rangle$ $(3P_{3/2})$) from Na atoms (in a heat pipe oven) are involved in the experiments. The pulse laser beams are aligned spatially as shown in Fig. 7.2(d) with the control beam $\boldsymbol{E}_2$ (frequency ω_2, $\boldsymbol{k}_2$) and pumping beams $\boldsymbol{E}_1$ (frequency ω_1, $\boldsymbol{k}_1$) and $\boldsymbol{E}_1'$ (ω_1, $\boldsymbol{k}_1'$) propagating through the atomic medium in the same direction ($\boldsymbol{E}_1$ and $\boldsymbol{E}_2$ are collinear) with a small angle (0.3°) between them in a square-box pattern. The probe beam $\boldsymbol{E}_p$ (ω_1, $\boldsymbol{k}_p$) propagates in the opposite direction with a small angle as shown in Fig. 7.2 (d). The laser beams $\boldsymbol{E}_1$, $\boldsymbol{E}_1'$, and $\boldsymbol{E}_p$ (with Rabi frequencies G_1, G_1' and G_p, respectively, connecting the transition from $|0\rangle$ to $|1\rangle$) are from the same near-transform-limited dye laser with frequency ω_1 (10 Hz repetition rate, 5 ns pulse-width and 0.04 cm^{-1} linewidth), which generate a one-photon resonant FWM process [17]. The generated FWM beam $\boldsymbol{E}_{F1}$ (with Rabi frequency G_{F1}) sampled by a CCD satisfies the phase-matching condition $\boldsymbol{k}_{F1} = \boldsymbol{k}_1 - \boldsymbol{k}_1' + \boldsymbol{k}_p$. The control field $\boldsymbol{E}_2$ (with Rabi frequency G_2) drives the transition from $|0\rangle$ to $|2\rangle$), as shown in Fig. 7.2 (b), which is from another dye laser of the frequency ω_2 with the same characteristics as the first dye laser. When the beams $\boldsymbol{E}_1$, $\boldsymbol{E}_1'$ and $\boldsymbol{E}_p$ are also tuned to the transition $|0\rangle - |2\rangle$, the system becomes an effective two-level one, as shown in Fig. 7.2 (c). When the four laser beams are all on, two one-photon resonant FWM processes, $\boldsymbol{k}_{F1}$ and $\boldsymbol{k}_{F2} = \boldsymbol{k}_2 - \boldsymbol{k}_1' + \boldsymbol{k}_p$, can be generated simultaneously. However, since $\boldsymbol{E}_{F1}$ is always the dominant one [17, 18], we will only consider this FWM process in this work.

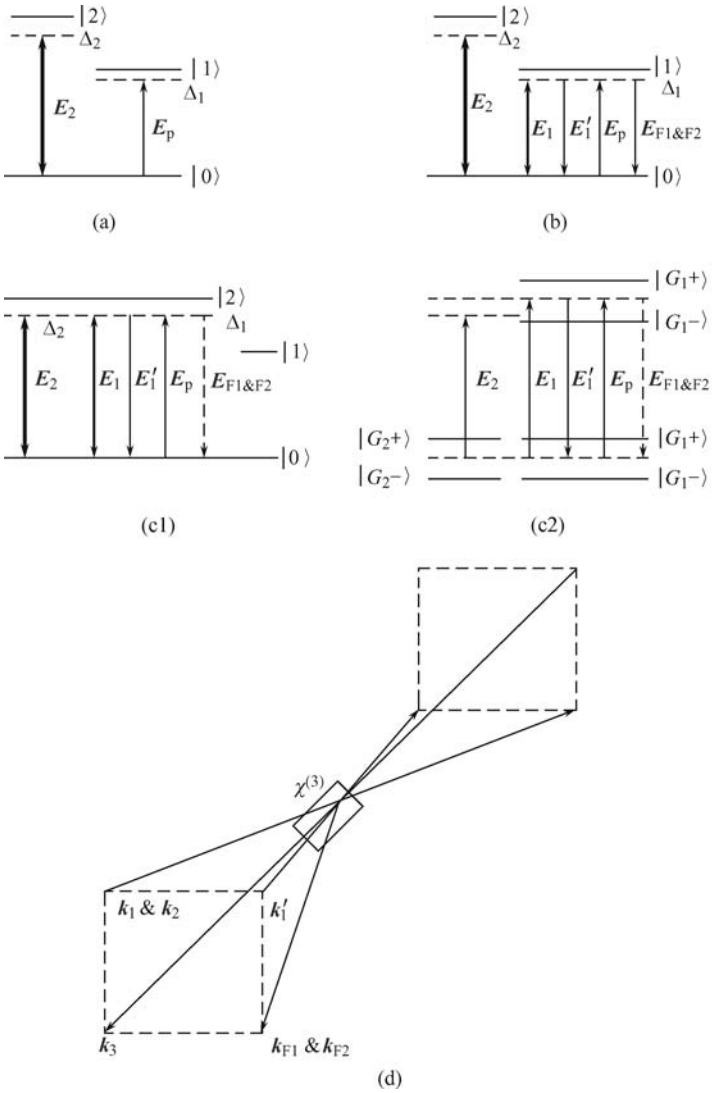

Fig. 7.2. (a) Three-level V-type EIT system. (b) Three-level V-type system with FWM signal $\boldsymbol{E}_{F1}$ generated by the pump beams ($\boldsymbol{E}_1$, $\boldsymbol{E}_1'$) and the probe beam ($\boldsymbol{E}_p$) in the transition of $|0\rangle - |1\rangle$. The FWM process can be modified by the control beam $\boldsymbol{E}_2$. (c1) Two-level system with four laser beams tuned to the same transition. (c2) Dressed-state picture corresponding to the two-level system in (c1). (d) Spatial beam geometry used in the experiments.

Under our experimental conditions, the sodium vapor is an EIT-enhanced Kerr medium for the propagating laser beams. The laser beam $\boldsymbol{E}_2$ (or $\boldsymbol{E}_1$) is approximately 10^2 times stronger than the beam $\boldsymbol{E}_1'$, and 10^4 times stronger than the weak probe beam $\boldsymbol{E}_p$, so $\boldsymbol{E}_1$ and $\boldsymbol{E}_2$ beams can control the weaker

$\boldsymbol{E}_p$ and $\boldsymbol{E}_{F1}$ beams. At the same time, the field $\boldsymbol{E}_1'$ can also slightly affect the displacement of the $\boldsymbol{E}_{F1}$ beam. The mathematical description of the propagation properties of the weak beams $\boldsymbol{E}_p$ and $\boldsymbol{E}_{F1}$ due to self- and cross-Kerr nonlinearities of the control and pump beams can be obtained through numerically solving the following coupled equations:

$$\begin{cases} \dfrac{\partial A_p}{\partial z} - \dfrac{\mathrm{i}\nabla_\perp^2 A_p}{2k_p} = \dfrac{\mathrm{i}k_p}{n_0}(n_2^{S1}\left|A_p\right|^2 + 2n_2^{X1}\left|A_1\right|^2 + 2n_2^{X2}\left|A_2\right|^2)A_p, \\ \dfrac{\partial A_{F1}}{\partial z} - \dfrac{\mathrm{i}\nabla_\perp^2 A_{F1}}{2k_{F1}} = \dfrac{\mathrm{i}k_{F1}}{n_0}\left[n_2^{S2}\left|A_{F1}\right|^2 + 2n_2^{X3}\left|A_1\right|^2 + \right. \\ \qquad\qquad \left. 2n_2^{X4}\left|A_2\right|^2 + 2n_2^{X5}\left|A_1'\right|^2\right]A_{F1}, \end{cases} \tag{7.18}$$

where z is the longitudinal coordinate in the propagation direction, A_1' and $A_{1,2}$ are the slowly varying envelope amplitudes of the fields $\boldsymbol{E}_1'$ and $\boldsymbol{E}_{1,2}$, respectively. $k_p = k_{F1} = \omega_1 n_0/c$ and n_0 is the linear refractive index at ω_1. n_2^{S1} are the self-Kerr nonlinear coefficients of the fields $\boldsymbol{E}_p$ and n_2^{S2} is the self-Kerr nonlinear coefficients of the fields $\boldsymbol{E}_{F1}$. n_2^{X1} is the cross-Kerr nonlinear coefficient of the weak field $\boldsymbol{E}_p$ induced by the strong coupling field $\boldsymbol{E}_1$. n_2^{X2} is the cross-Kerr nonlinear coefficient of the weak field $\boldsymbol{E}_p$ induced by the strong coupling field $\boldsymbol{E}_2$. n_2^{X3} is the cross-Kerr nonlinear coefficient of the weak field $\boldsymbol{E}_{F1}$ induced by the strong coupling field $\boldsymbol{E}_1$. n_2^{X4} is the cross-Kerr nonlinear coefficient of the weak field $\boldsymbol{E}_{F1}$ induced by the strong coupling field $\boldsymbol{E}_2$. n_2^{X5} is the cross-Kerr nonlinear coefficient of the weak field $\boldsymbol{E}_{F1}$ induced by the strong coupling field $\boldsymbol{E}_1'$. The Kerr nonlinear coefficient can be defined as $n_2 = \mathrm{Re}\chi^{(3)}/(\varepsilon_0 c n_0)$, where the third-order nonlinear susceptibility is given by $\chi^{(3)} = D\rho_{10}^{(3)}$ with $D = N\mu_p^2\mu_{i0}^2/(\hbar^3\varepsilon_0 G_p G_i^2)$. μ_p (μ_{i0}) is the dipole matrix element between the states coupled by the probe beam $\boldsymbol{E}_p$ (between $|i\rangle$ and $|0\rangle$). Since high-power pulsed dye lasers are used in the experiment, Doppler effect and the power broadening effect are considered in the calculation using Eq. (7.18). By assuming Gaussian profiles for the input fields, Eqs. (7.18a) and (7.18b) are solved using the split-step method [2].

The first feature in this section that is distinctly different and advantageous over the previously studied spatial shifts of laser beams in atomic systems is that the EISD of both the probe beam and the generated FWM beam can be directly observed and controlled by another strong (control) laser beam. Figure 7.3 shows spatial displacements of the probe field $\boldsymbol{E}_p$ and the FWM beam $\boldsymbol{E}_{F1}$, respectively, versus frequency detuning Δ_1 ($\Delta_1 = \Omega_1 - \omega_1$ for the three-level system or $\Omega_2 - \omega_1$ for the two-level system) with a fixed control beam ($\Delta_2 = \Omega_2 - \omega_2 = 0$). When the pump beams $\boldsymbol{E}_1$ and $\boldsymbol{E}_1'$ are blocked [Fig. 7.2 (a)], it is the simple three-level V-type EIT system. For the fixed control (coupling) beam $\boldsymbol{E}_2$, the measured probe beam displacements show a spatial dispersion-like displacement curve as depicted in Fig. 7.3 (a) (the triangle points). The data points can be fitted well with the calculated cross-Kerr nonlinear coefficient n_2 vs Δ_1. The inset in Fig. 7.3 (a) shows the

images of the measured probe beam spots versus Δ_1 in the two-level system. In the region with $\Delta_1 < 0$, the smaller beam spots are an indication of self-focusing effect for the probe beam due to positive self-Kerr nonlinear index, while the larger beam spots in $\Delta_1 > 0$ region are due to self-defocusing because of the sign change in the self-Kerr nonlinear coefficient. When the probe beam $\boldsymbol{E}_p$ is tuned to the transition between $|0\rangle$ and $|2\rangle$, the system becomes an effective two-level one. Similarly, with the control beam $\boldsymbol{E}_2$ fixed, the spatial displacements (squares) also show the same dispersion-like curve, as shown in Fig. 7.3 (a). Again the solid line is the calculated cross-Kerr nonlinear coefficients as a function of Δ_1, which fits perfectly well with the measured EISD. When the pump beams ($\boldsymbol{E}_1$ and $\boldsymbol{E}_1'$) are on [Fig. 7.2 (b)], an efficient FWM signal $\boldsymbol{E}_{F1}$ is generated by the pump beams together with the probe beam, which propagates in a different direction as shown in Fig. 7.2 (d). With a fixed control beam $\boldsymbol{E}_2$, the generated FWM signal beam $\boldsymbol{E}_{F1}$ (in either the three-level or the two-level system) is deflected differently when the frequency detuning of the probe beam (Δ_1) is scanned, as shown in Fig. 7.3 (b). The dispersion-like curves are narrower than for the cases of the probe beam deflections, but the general behaviors are very similar to the ones as in Fig. 7.3 (a). The spatial deflection curves are well fitted with the calculated cross-Kerr nonlinear indices of refraction for the three-level V-type and two-level systems (solid curves), respectively. The inset in Fig. 7.3 (b) shows the images of the measured FWM beam spots versus Δ_1 in the three-level system. Hence, the second feature that is distinctly different and advantageous over the previously studied spatial shifts of laser beams in atomic systems is that the cross-Kerr nonlinear index of refraction n_2 can be directly measured by such simple EISD technique.

The observed spatial displacements of probe ($\boldsymbol{E}_p$) and FWM ($\boldsymbol{E}_{F1}$) beams are caused by the non-colinear propagations of the laser beams and the enhanced cross-Kerr nonlinear indices of refraction due to the strong laser beams $\boldsymbol{E}_2$ and $\boldsymbol{E}_1$. For simplicity, let us only consider the strong control beam $\boldsymbol{E}_2$. During its propagation through the vapor cell, the wing of the beam $\boldsymbol{E}_2$ interacts with the intensity profile of either $\boldsymbol{E}_p$ or $\boldsymbol{E}_{F1}$, and distorts its phase profile to induce an optical waveguide through XPM. The nonlinear phase shift can be written as $\phi_{NL} = 2k_{F1}n_2 |A_2|^2 z/n_0$ and the additional transverse propagation wave-vector is $\delta k_\perp = \phi'_{NL}$ [2]. In this case, when $n_2 > 0$, the direction of $\delta k_\perp$ is to the beam center of $\boldsymbol{E}_2$, and, therefore, $\boldsymbol{E}_{p,F1}$ is deflected closer to $\boldsymbol{E}_2$; when $n_2 < 0$, the direction of $\delta k_\perp$ is outward from the beam center of $\boldsymbol{E}_2$, thus $\boldsymbol{E}_{p,F1}$ is deflected away from the strong control beam $\boldsymbol{E}_2$. According to the expression for ϕ_{NL}, the amount of spatial shift is proportional to the cross-Kerr nonlinear coefficient, the field intensity and the propagation distance. Hence, the spatial displacements of the probe and FWM beams results from the cross-Kerr nonlinear coefficient induced by the strong control field, therefore, can be controlled by it.

The spatial displacements of the probe and FWM signal beams can be controlled by the intensity of the control beam (G_2), as well as by the atomic

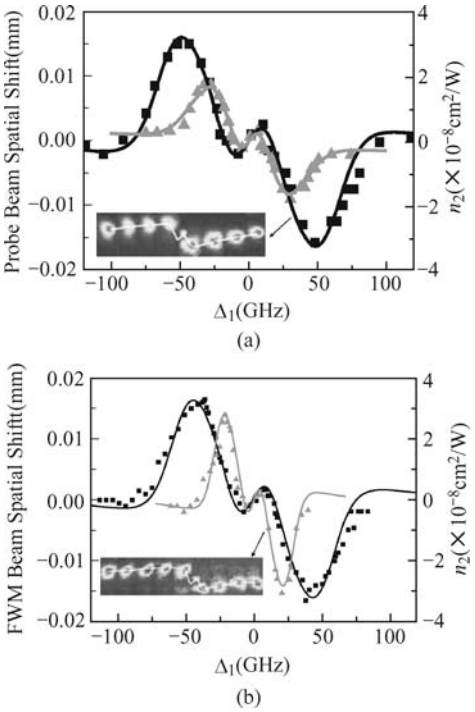

Fig. 7.3. (a) EISD shift of the beam $\boldsymbol{E}_p$ and the fitted cross-Kerr nonlinear coefficient n_2 versus Δ_1 at 200 °C in the two-level system (squares) and the three-level system (triangles), respectively. Inset: EISD spots of $\boldsymbol{E}_p$ versus Δ_1 in the two-level system. (b) EISD shift of the beam $\boldsymbol{E}_{F1}$ and the fitted cross-Kerr nonlinear coefficient versus Δ_1 at 200 °C in the two-level system (squares) and the three-level system (triangles), respectively. Inset: EISD spots of $\boldsymbol{E}_{F1}$ versus Δ_1 in the three-level V-type system. The parameters are $G_p = 0.2$ GHz, $G_1 = G_1' = 1.1$ GHz and Δ. Adopted from Ref. [19].

density N. As the Rabi frequency of the control field increases, not only the spatial displacement gets bigger, but also an additional contribution, independent of the frequency detuning Δ_1, appears, as shown in Fig. 7.4 (a), (c). This constant spatial displacement depends on G_2 and N, and adds a constant shift to the dispersion-like displacement curve, as seen in the two curves with larger G_2 values in Fig. 7.4 (a). Figure 7.4 (a) presents the temperature (atomic density) effects on the spatial displacement with bigger spatial displacements at the higher atomic density. A similar constant shift in the spatial displacement curve also appears at the higher atomic density. The solid curves are the theoretically simulated spatial displacements of the FWM beam based on the coupled equations (7.18). The differences in the maximum spatial displacements for the three-level system [Fig. 7.2 (b)] and effective two-level system [Fig. 7.2 (c)] as functions of the control beam Rabi frequency (G_2) and the atomic density (N) are plotted in Fig. 7.4 (b), (d), respectively.

As one can see that the trends of changes as G_2 and N increase are different for the three-level and two-level systems, which can be better understood in the dressed-state pictures. At low G_2 values, the three-level system has a bigger maximum shift than the two-level one, however, the FWM signal in the two-level system has larger spatial shift when G_2 is increased to certain value [as shown in Fig. 7.4 (b)]. The opposite trend happens as the atomic density increases [Fig. 7.4 (d)]. Hence, the third feature that is distinctly different and advantageous over the previously studied spatial shifts of laser beams in atomic systems is that enhanced cross-Kerr nonlinearity in the spatial domain can be achieved by increasing atomic density (cell temperature) or the power of the strong control beam.

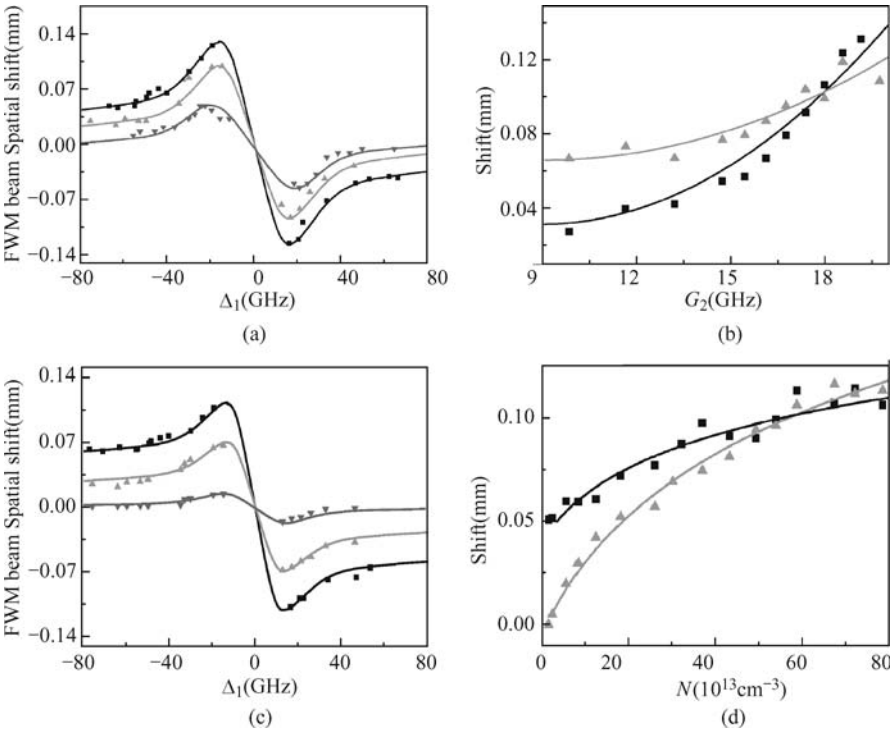

Fig. 7.4. (a) Spatial dispersion curves of $\boldsymbol{E}_{F1}$ in the two-level system versus Δ_1 with $G_2 = 19.1$ (squares), 18.3 (triangles) and 11.7 GHz (reverse triangles) at 260 °C. (b) the maximum spatial displacements of $\boldsymbol{E}_{F1}$ versus G_2 in two-level system (squares) and three-level V-type system (triangles). (c) Spatial dispersion curves of $\boldsymbol{E}_{F1}$ in the two-level system versus Δ_1 with $G_2 = 9.7$ GHz at 330 (squares), 280 (triangles), 230°C (reverse triangles). (d) the maximum spatial displacements of $\boldsymbol{E}_{F1}$ versus atom density N in the two-level system (squares) and three-level V-type system (triangles). The other parameters are $G_p = 0.8$ GHz and $G_1 = G_1' = 3.8$ GHz. The scattered points are the experimental results, and the solid lines are theoretically calculated spatial shifts.

The last feature that is distinctly different and advantageous over the previously studied spatial shifts of laser beams in atomic systems is that the effects of different dressing schemes on spatial deflection of the FWM beam have been carefully considered and compared. Let us consider the spatial displacements of the probe and generated FWM beams with all the control and pump beams on, but with different intensities. Other than the case of having a strong control beam as discussed above (i.e., $G_2 >> G_1, G_1' >> G_p > G_{F1}$), one can also let one of the pump beams (say $\boldsymbol{E}_1$) to be very strong (i.e., $G_1 >> G_2, G_1' >> G_p > G_{F1}$), which is t is the doubly-dressing scheme [18, 19]. Under these different conditions, the strong laser fields dress the energy levels differently, and modify the degree of spatial deflections for the probe [Fig. 7.5 (a)], as well as the FWM beams [Fig. 7.5 (c)], under different conditions.

First, when $\boldsymbol{E}_2$ is the only strong field, it dresses the level $|0\rangle$ to create the dressed states $|G_2\pm\rangle$, as shown in the left side of Fig. 7.2 (c2). Under this condition, we have [18] $\rho_{20}^{(3)} = -\mathrm{i}G_a/[d_1 d_2(d_1 + G_2^2/d_2)]$ for the two-level system and $\rho_{10}^{(3)} = -\mathrm{i}G_a/[d_3 d_4(d_3 + G_2^2/d_4)]$ for the three-level system, where $G_a = G_{p,F1}G_2^2$, $d_1 = \mathrm{i}\Delta_1 + \Gamma_{20}$, $d_2 = \Gamma_2 + \mathrm{i}(\Delta_1 - \Delta_2)$, $d_3 = \mathrm{i}\Delta_1 + \Gamma_{10}$ and $d_4 = \mathrm{i}(\Delta_1 - \Delta_2) + \Gamma_{12}$. Second, the pump field $\boldsymbol{E}_1$ is the only strong field ($G_1 >> G_2, G_1'$). Since $\boldsymbol{E}_1$ and $\boldsymbol{E}_p$ have the same frequency detuning Δ_1, the upper-level ($|2\rangle$ for the two-level system and $|1\rangle$ for the three-level system) and the lower-level (i.e., $u_1(t)$) are always on resonance with and are dressed by $\boldsymbol{E}_1$. In this case, two pairs of dressed states $|G_1\pm\rangle$ are created [right side of Fig. 7.2 (c2)], from which we can write [18] $\rho_{20}^{(3)} = -\mathrm{i}G_b/[d_1\Gamma_2(d_1 + G_1^2/\Gamma_0 + G_1^2/\Gamma_2)]$ and $\rho_{10}^{(3)} = -\mathrm{i}G_b/[d_3 d_4(d_3 + G_1^2/\Gamma_0 + G_1^2/\Gamma_1)]$. These expressions indicate that the strong $\boldsymbol{E}_1$ field induces a larger XPM than the strong $\boldsymbol{E}_2$ can do, so the spatial displacements of $\boldsymbol{E}_p$ and $\boldsymbol{E}_{F1}$, controlled by the stronger $\boldsymbol{E}_1$, is larger than that by the stronger $\boldsymbol{E}_2$ field [as seen for the probe beam $\boldsymbol{E}_p$ in Fig. 7.5 (a) and the FWM beam $\boldsymbol{E}_{F1}$ in Fig. 7.5 (c)]. Third, when both $\boldsymbol{E}_1$ and $\boldsymbol{E}_2$ beams are the strong ones (doubly-dressing case), they share the common level $|0\rangle$ and interact with each other [18]. Under this situation, we have [18] $\rho_{20}^{(3)} = -\mathrm{i}G_a/(d_1 d_2 d_a)$ and $\rho_{10}^{(3)} = -\mathrm{i}G_a/(d_3 d_4 d_b)$ for the cross-Kerr nonlinear coefficients of $\boldsymbol{E}_2$, and $\rho_{20}^{(3)} = -\mathrm{i}G_b/(\Gamma_2 d_1 d_a)$ and $\rho_{10}^{(3)} = -\mathrm{i}G_b/(\Gamma_1 d_1 d_b)$ for the cross-Kerr nonlinear coefficients of $\boldsymbol{E}_1$, where $d_a = d_1 + G_1^2/\Gamma_2 + G_2^2/(d_2 + G_1^2/d_5)$, $d_b = d_3 + G_1^2/\Gamma_1 + G_2^2/(d_4 + G_1^2/d_5)$. $\boldsymbol{E}_1$ (the second G_1 in d_a or d_b, dressing the state$|0\rangle$) suppresses the dressing effect of the "inner" dressing field $\boldsymbol{E}_2$ and contribute to the cross-Kerr nonlinear coefficient indirectly. As a result, the XPM induced by the doubly-dressing fields is weaker than the sum of the effects due to singly-dressing by $\boldsymbol{E}_1$ and $\boldsymbol{E}_2$ alone.

Figure 7.5 (b) depicts the spatial displacements of $\boldsymbol{E}_p$ induced by two dressing fields (strong $\boldsymbol{E}_1$ and $\boldsymbol{E}_2$). The spatial displacement for two-level system (squares) is larger than the one for the three-level system (triangles). That is mainly due to the larger dipole moment μ_{20} (comparing to μ_{10}),

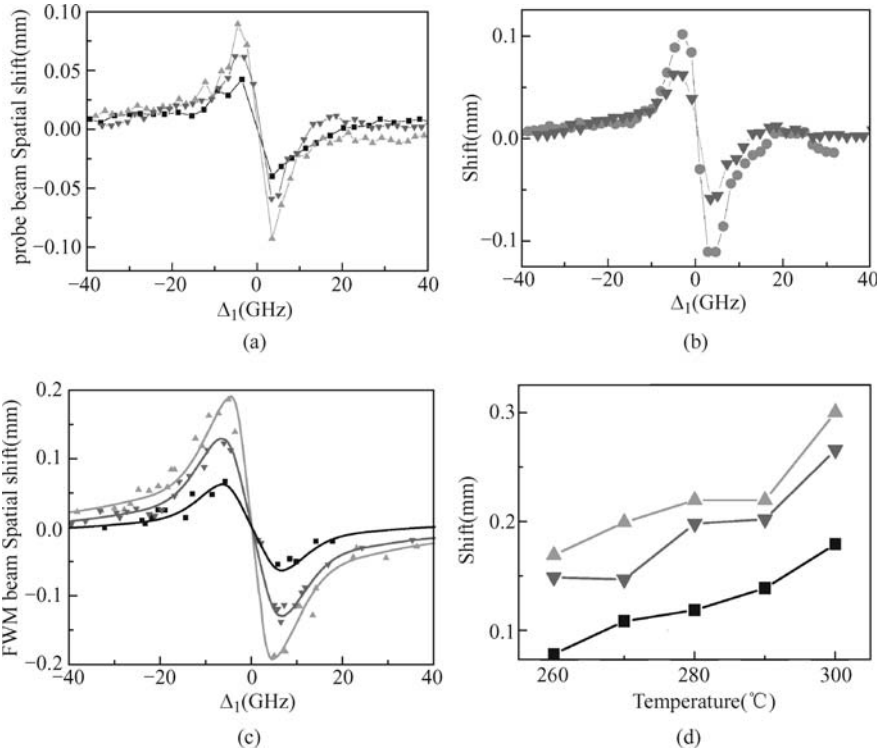

Fig. 7.5. (a) Spatial displacements of $\boldsymbol{E}_p$ versus Δ_1 in the two-level system controlled by $\boldsymbol{E}_2$ (squares), $\boldsymbol{E}_1$ (triangles) and both $\boldsymbol{E}_2$ and $\boldsymbol{E}_1$ (reverse triangles) at 260 °C. (b) spatial dispersion curves of $\boldsymbol{E}_p$ versus Δ_1 in the two-level system (reverse triangles) and V-type system (circles) dressed by both $\boldsymbol{E}_2$ and $\boldsymbol{E}_1$ beams. (c) Spatial dispersion curves of $\boldsymbol{E}_{F1}$ versus Δ_1 dressed by $\boldsymbol{E}_2$ (squares), $\boldsymbol{E}_1$ (triangles) and both $\boldsymbol{E}_2$ and $\boldsymbol{E}_1$ (reverse triangles) at 270 °C. The scattered points are the experimental results, and the solid lines are the theoretically calculated spatial displacements. (d) Temperature dependences of the maximum spatial displacements of $\boldsymbol{E}_{F1}$ dressed by $\boldsymbol{E}_2$ (squares), $\boldsymbol{E}_1$ (triangles) and both $\boldsymbol{E}_2$ and $\boldsymbol{E}_1$ (reverse triangles) in the two-level system. The other parameters are $G_1 = G_2 = 17.6$ GHz and $G_1' = 3.8$ GHz, $G_p = 0.8$ GHz. Adopted from Ref. [19].

which makes n_2 of the two-level system be larger than that of the three-level system [17]. Figure 7.5 (d) shows the temperature dependences of the spatial displacements of $\boldsymbol{E}_{F1}$ in the two-level system with different dressing fields. The spatial displacements are proportional to the temperature, and the spatial displacement with the $\boldsymbol{E}_2$ singly-dressing scheme is the smallest, while that of the doubly-dressing scheme gives a closer but smaller spatial displacement than that with the $\boldsymbol{E}_1$ singly-dressing scheme.

The spatial displacements of the probe and FWM beams are mainly determined and controlled by the large cross-Kerr nonlinear coefficients of the strong laser fields. However, the cross-Kerr effects induced by the relatively

weaker pump beam(s) can also exist. Since each of the pump and probe beams can be spatially displaced by the strong control beam (and by each other), the final spatial displacement of the generated FWM beam can be affected by such secondary displacement effects. In the above discussion and calculations, we have only considered the leading contributions from the strongest fields, which explained the observed spatial displacements quite well. Also, when the fields of $\boldsymbol{E}_p$ and $\boldsymbol{E}_{F1}$ get stronger (with higher probe and more efficient FWM process), incoherently coupled soliton pairs can be formed by these $\boldsymbol{E}_p$ and $\boldsymbol{E}_{F1}$ beams due to the interplays between the diffraction effect and self-Kerr nonlinear effect [4]. Under such conditions, we can obtain the solutions of $A_{p,F1}(x) = A_0\mathrm{sech}(A_0 x)$ for the bright-bright soliton pair in the self-focusing EIT media and $A_{p,F1}(x) = A_0[1 - \mathrm{sech}^2(A_0 x)]^{1/2}$ for the dark-dark soliton pair in self-defocusing EIT media [20]. Here A_0 is the initial envelope amplitude. The enhanced self-Kerr and cross-Kerr nonlinear coefficients due to induced atomic coherence or EISD enable the formations of such spatial soliton pairs with much lower input laser powers, which can be very important for their applications in optical communications.

7.3 Spatial Dispersion Induced by Cross-phase Modulation

In this section, we demonstrate the spatial beam displacement which results from distinct dispersive features in the frequency domain. By arranging the laser beams in a certain spatial configuration, the spatial displacement of the probe beam can be controlled by the strong coupling laser beam.

We put three pulse lasers ($\boldsymbol{E}_1$, $\boldsymbol{E}_2$ and $\boldsymbol{E}_3$) into sodium vapor (in heat pipe oven) which is a Kerr medium. Incident lasers are aligned spatially as shown in Fig. 7.6(a). Beams $\boldsymbol{E}_2$ (frequency ω_2, $\boldsymbol{k}_2$) and $\boldsymbol{E}_3$ (ω_3, $\boldsymbol{k}_3$) propagate in the opposite direction of the probe $\boldsymbol{E}_1$ (frequency ω_1, $\boldsymbol{k}_1$). There is a small angle θ_1 (about 0.3°) between $\boldsymbol{E}_2$ and $\boldsymbol{E}_1$ as well as $\boldsymbol{E}_3$ and $\boldsymbol{E}_1$ in a square-box pattern. Three energy levels ($|0\rangle(3S_{1/2})$, $|1\rangle(3P_{1/2})$ and $|2\rangle$ $(3P_{3/2})$) from Na atoms form three-level V-type atomic system. As shown in Fig. 7.6(b), laser beams $\boldsymbol{E}_2$ (Rabi frequencies G_2) and $\boldsymbol{E}_1$ (G_1) connect transitions from $|0\rangle$ to $|2\rangle$ and from $|0\rangle$ to $|1\rangle$, respectively. The strong control beam $\boldsymbol{E}_2$ can spatially deflect the weak probe beam $\boldsymbol{E}_1$ when these two laser beams propagate through the atomic medium. As the probe frequency is detuned, light bias shows a dispersion-like curve in the section plane of the propagating direction, which exactly mimics the dispersion curve of the Kerr-nonlinear index of refraction in the EIT system [18]. When the beams $\boldsymbol{E}_1$ is also tuned to the same transition as $\boldsymbol{E}_2$, the system becomes an effective two-level one [Fig. 7.6 (c)]. Later, we compare the spatial displacement in these two different atomic systems. Such electromagnetically-induced spatial dispersion (EISD) can be used for spatial switching and routing, and as an easy way to measure

the Kerr-nonlinear indices of refraction for the multi-level atomic media.

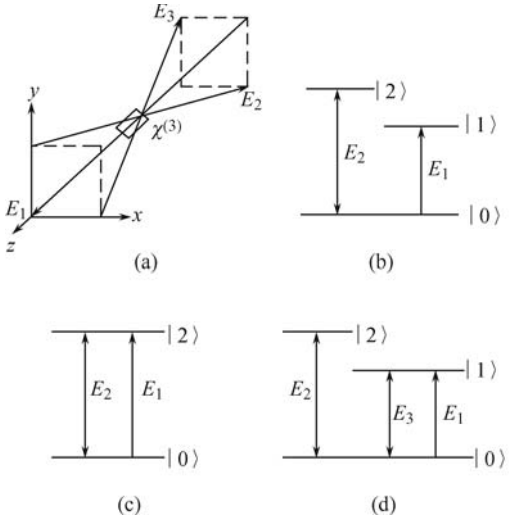

Fig. 7.6. (a) Spatial beam geometry used in the experiments. (b) Three-level V-type EIT system with the strong pump beam $\boldsymbol{E}_2$ in the same transition of $|0\rangle - |2\rangle$ and the probe beam $\boldsymbol{E}_1$ in the transition of $|0\rangle - |1\rangle$. (c) Two-level subsystem with the probe beam $\boldsymbol{E}_1$ and the strong pump beam $\boldsymbol{E}_2$ in the same transition of $|0\rangle - |2\rangle$. (d) Three-level system with two pump beams $\boldsymbol{E}_2$ and $\boldsymbol{E}_3$ as well as the probe beam $\boldsymbol{E}_1$.

In our experiment, the lasers $\boldsymbol{E}_1$ and $\boldsymbol{E}_3$ are from the same near-transform-limited dye laser (10 Hz repetition rate, 5 ns pulse-width and 0.04 cm^{-1} line width), while $\boldsymbol{E}_2$ are from another dye laser with the same characteristics as the first dye laser. The strong pumping beams $\boldsymbol{E}_2$ and $\boldsymbol{E}_3$ are approximately 10^4 times larger than the weak probe beam $\boldsymbol{E}_1$ which is sampled by CCD and a fast gated integrator (gate width of 50 ns). Thus, beams $\boldsymbol{E}_{2,3}$ are strong enough to affect the spatial displacement of beam $\boldsymbol{E}_1$. The spatial displacement of beam $\boldsymbol{E}_1$ that is affected by beams $\boldsymbol{E}_3$ and $\boldsymbol{E}_2$ respectively can be described by coupled equations:

$$\frac{\partial A_1}{\partial z} - \frac{i\partial^2 A_1}{2k_1 \partial x^2} = \frac{ik_1}{n_0}\left(n_2^S \left|A_1\right|^2 + 2n_2^{X1}\left|A_3\right|^2\right) A_1, \tag{7.19}$$

$$\frac{\partial A_1}{\partial z} - \frac{i\partial^2 A_1}{2k_1 \partial y^2} = \frac{ik_1}{n_0}\left(n_2^S \left|A_1\right|^2 + 2n_2^{X2}\left|A_2\right|^2\right) A_1, \tag{7.20}$$

where z is the longitudinal coordinate; n_0 is the linear refractive index at ω_1; n_2^S are the self-Kerr coefficient of $\boldsymbol{E}_1$; n_2^{X1} is the cross-Kerr nonlinear coefficient of the weak field $\boldsymbol{E}_1$ induced by the strong coupling field $\boldsymbol{E}_3$ and n_2^{X2} is the cross-Kerr nonlinear coefficient of the weak field $\boldsymbol{E}_1$ induced by the strong coupling field $\boldsymbol{E}_2$, A_{1-3} are the slowly varying envelope amplitudes of beams $\boldsymbol{E}_{1-3}$, respectively. The Kerr coefficient can be defined as $n_2 =$

$C\mathrm{Re}\chi^{(3)}$, where $C = (\varepsilon_0 c n_0)^{-1}$; the susceptibility is $\chi^{(3)} = D\rho_{10}^{(3)}$, where $D = N\mu_{10}^4/(\hbar^3\varepsilon_0 G_1|G_1|^2)$ for n_2^S, $D = N\mu_{10}^4/(\hbar^3\varepsilon_0 G_1|G_3|^2)$ for n_2^{X1} and $D = N\mu_{10}^2\mu_{20}^2/(\hbar^3\varepsilon_0 G_1|G_2|^2)$ for n_2^{X2}. N is the atomic density in the cell, and μ_{10} (μ_{20}) is the dipole matrix element between $|0\rangle$ and $|1\rangle$ ($|2\rangle$). Assuming that input lasers are Gaussian profiles, Eqs. (7.19) and (7.20) can be solved with the split-step method [2].

The spatial displacement of the weak beam is caused by the non-colinear propagations of the strong laser beams and the enhanced cross-Kerr nonlinear indices of refraction. First, let us only consider the case that the strong control beam $\boldsymbol{E}_2$ affects the weak probe beam $\boldsymbol{E}_1$. During its propagation through the vapor cell, the beam $\boldsymbol{E}_2$ distorts the phase profile of $\boldsymbol{E}_1$ to induce an optical waveguide through cross-phase modulation (XPM). The nonlinear phase shift can be written as $\phi_{NL} = 2k_3 n_2^X |A_2|^2 z/n_0$ and the additional transverse propagation wave-vector is $\delta k_\perp = \phi'_{NL}$ [3]. The change of phase (ϕ_{NL}) in the laser propagating expression is represented as the spatial displacement of the laser beam. According to the expression for ϕ_{NL}, the amount of spatial shift is proportional to the cross-Kerr nonlinear coefficient, the field intensity and the propagation distance.

Figure 7.7 shows the spatial displacement of the probe field $\boldsymbol{E}_1$ versus frequency detuning Δ_1, where $\Delta_1 = \Omega_1 - \omega_1$ in the three-level system and is $\Delta_1 = \Omega_2 - \omega_1$ in the two-level system, with a fixed control beam $\boldsymbol{E}_2$ ($\Delta_2 = \Omega_2 - \omega_2 = 0$). Tuning $\boldsymbol{E}_1$ and $\boldsymbol{E}_2$ respectively to the transition between $|0\rangle$ and $|1\rangle$ and between $|0\rangle$ and $|2\rangle$ as in Fig. 7.6 (b), the probe beam displacement shows an EISD curve (the triangles in Fig. 7.7.) in the three-level V-type EIT system. When the probe beam $\boldsymbol{E}_1$ is tuned on the transition between $|0\rangle$ and $|2\rangle$ as dress beam $\boldsymbol{E}_2$, the spatial displacement (squares) also shows the same dispersion-like curve. Since the dipole moment μ_{20} is larger than the dipole moment μ_{10}, we can deduce that cross-Kerr coefficient n_2 in the two-level system is larger than that in the three-level system [21]. Apparently, the spatial displacement of beam $\boldsymbol{E}_1$ in the two-level system is larger than that in the three-level system. The inset in Fig. 7.7 shows the images of the measured probe beam spots versus Δ_1 in the three-level system.

Figure 7.8 (a) shows the spatial displacement of the probe beam $\boldsymbol{E}_1$ versus Δ_1 in the three-level system. The probe beam moves up ($\Delta_1 < 0$) and down ($\Delta_1 > 0$) with a dispersion-like displacement curve at millimeter order of magnitude. When increasing the Rabi frequency of $\boldsymbol{E}_2$ gradually, i.e. the intensity of $\boldsymbol{E}_2$ increases, the spatial displacement becomes distinct. Here, the scattered points are the experimental results; the solid lines are theoretical shift. They fit each other well. According to the expression of ϕ_{NL}, the spatial displacement of the probe beam $\boldsymbol{E}_3$ can be affected by not only the intensity of the control beam (G_2) but also the atomic density N. Figure 7.8 (b) presents the temperature (atomic density) effects on the spatial displacement. A similar constant shift in the spatial displacement curve also appears at the high atomic density. As we all know, the temperature influences the atomic density N in the vapor cell. Based on the formula of n_2 [18], it is proportional

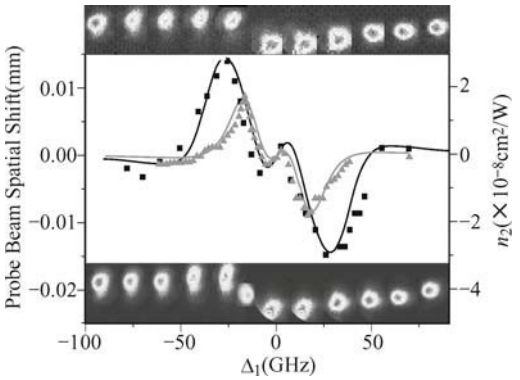

Fig. 7.7. EISD shift of the beam $\boldsymbol{E}_1$ and the fitted cross-Kerr nonlinear coefficient n_2 versus Δ_1 at 230 °C in the two-level system (squares) and the three-level system (triangles), respectively. Upper and lower insets: EISD spots of $\boldsymbol{E}_1$ versus Δ_1 in the three- and two-level system. The parameters are $G_1 = 0.2$ GHz and $G_2 = 9.7$ GHz.

to N. According to theoretical calculation, we can see spatial shift increases along with the thicken atomic density N.

We consider the spatial displacements of the probe with different control beams on. We can let both two pump beams $\boldsymbol{E}_2$ and $\boldsymbol{E}_3$ to be strong (i.e., $G_2, G_3 >> G_1$) to control the probe beam shown in Figs. 7.6 (a) and 7.6 (d), which is the doubly-dressing scheme [12], or control the probe beam with the only one pump beam ($\boldsymbol{E}_2$ or $\boldsymbol{E}_3$), which is the singly-dressing scheme. Under these different conditions, the strong laser fields dress the energy levels differently, and modify the degree of spatial deflections for the probe (Fig. 7.9).

In Fig. 7.9, we can see that the spatial displacement of $\boldsymbol{E}_1$, controlled by $\boldsymbol{E}_3$ is the largest (square) and displacement induced by both the stronger $\boldsymbol{E}_2$ and $\boldsymbol{E}_3$ is larger than that of $\boldsymbol{E}_2$. Actually, when we block $\boldsymbol{E}_3$ and leave the strong field $\boldsymbol{E}_2$ to control $\boldsymbol{E}_1$, $\boldsymbol{E}_2$ dresses the level $|0\rangle$ to create the dressed states $|G_2\pm\rangle$. Under this condition, we have $\rho_{10}^{(3)} = -\mathrm{i}G_a/[(d_1 + G_2^2/d_2)^2 d_2]$ for the three-level system, where $G_a = G_1 G_2^2$, $d_1 = \mathrm{i}\Delta_1 + \Gamma_{10}$, $d_2 = \Gamma_{12} + \mathrm{i}(\Delta_1 - \Delta_2)$. Second, $\boldsymbol{E}_2$ is blocked and the pump field $\boldsymbol{E}_3$ is the only strong field. Since $\boldsymbol{E}_1$ and $\boldsymbol{E}_3$ excite the same transition (from $|0\rangle$ to $|1\rangle$) and have the same frequency detuning Δ_1 (generated from the same laser), the upper-level and the lower-level of $\boldsymbol{E}_1$ induced transition are always dressed by $\boldsymbol{E}_3$. In this case, two pairs of dressed states $|G_3\pm\rangle$ are created, from which we can write $\rho_{10}^{(3)} = -\mathrm{i}G_b/[(d_1 + G_3^2/\Gamma_0 + G_3^2/\Gamma_1)^2 \Gamma_1]$ with $G_b = G_1 G_3^2$. As a result, the corresponding cross-Kerr coefficient n_2 induced by $\boldsymbol{E}_3$ is larger than that of $\boldsymbol{E}_2$. The strong $\boldsymbol{E}_3$ field induces a larger XPM than $\boldsymbol{E}_2$. Third, when both $\boldsymbol{E}_3$ and $\boldsymbol{E}_2$ beams are on (doubly-dressing case), they share the common level $|0\rangle$ and interact with each other [18]. In this situation, we have $\rho_{10}^{(3)} = -\mathrm{i}G_b/\{[d_1 + G_3^2/\Gamma_1 + G_2^2/(d_2 + G_3^2/d_3)]^2 \Gamma_1\}$ for $\boldsymbol{E}_1$, where

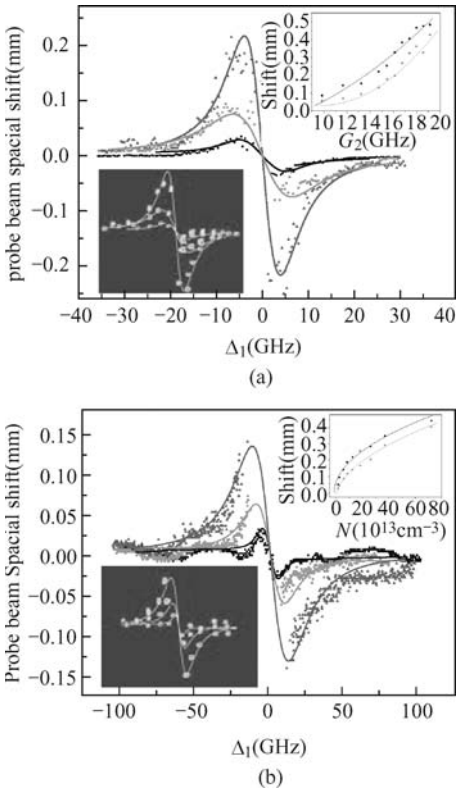

Fig. 7.8. (a) Spatial dispersion curves of $\boldsymbol{E}_1$ in the three-level system versus Δ_1 with $G_2 = 11.7$ GHz (squares), 16.3 GHz (circles), and 19.1 GHz (triangles) at 260 °C. Right inset: the maximum spatial displacements of $\boldsymbol{E}_1$ versus G_2 in the three-level V-type system (circles) and two-level system (squares). Left inset: EISD spots of $\boldsymbol{E}_1$ in the three-level system versus Δ_1 correspondingly. (b) Spatial dispersion curves of $\boldsymbol{E}_1$ in the three-level system versus Δ_1 with $G_2 = 9.7$ GHz at 230 °C (squares), 250 °C (circles), 300 °C (triangles). Right inset: the maximum spatial displacements of $\boldsymbol{E}_1$ versus atom density N in the three-level V-type system (circles) and two-level system (squares). Left inset: EISD spots of $\boldsymbol{E}_1$ in the three-level system versus Δ_1 correspondingly. The other parameters are $G_1 = 0.8$ GHz and $G_2 = 15$ GHz. The scattered points are the experimental results, and the solid lines are theoretically calculated spatial shifts.

$d_3 = \Gamma_{02} - \mathrm{i}\Delta_2$. From these expressions one can see that the dressing field $\boldsymbol{E}_3$ (the first G_3 dressing the upper-level) and the "inner" dressing field $\boldsymbol{E}_2$ (dressing the state $|0\rangle$) contribute to the cross-Kerr coefficient directly, while the "outer" dressing field $\boldsymbol{E}_3$ (the second G_3 dressing the state $|0\rangle$) suppresses the dressing effect of the "inner" dressing field $\boldsymbol{E}_2$ to influence the cross-Kerr nonlinear coefficient indirectly. Thus, the XPM induced by the doubly-dressing fields is weaker than the sum of the effects due to singly-dressing by $\boldsymbol{E}_3$ and $\boldsymbol{E}_2$ alone (Fig. 7.9).

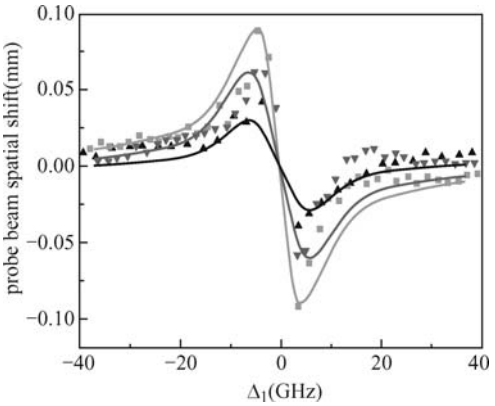

Fig. 7.9. Spatial displacements of $\boldsymbol{E}_1$ versus Δ_1 in the three-level system controlled by $\boldsymbol{E}_2$ (triangles), $\boldsymbol{E}_3$ (squares) and both $\boldsymbol{E}_2$ and $\boldsymbol{E}_3$ (reverse triangles) at 250 °C. The parameters are $G_1 = 0.8$ GHz, $G_2 = G_3 = 13$ GHz, $\Delta_2 = \Delta_3 = 0$. The scattered points are the experimental results and the solid lines are theoretically calculated spatial displacements.

7.4 Experimental Demonstration of Optical Switching and Routing via Four-Wave Mixing Spatial Shift

In order to develop the next generation of all-optical communication and computing, certain optical elements are essential, such as all-optical switches and routers. There have been several new schemes to demonstrate, in principle, such all-optically controlled switching and routing functions [12, 22, 23]. A weak beam was used to turn on/off selectively the spots in the spatial pattern of a stronger laser beam via XPM in a two-level atomic medium [12], showing a spatial switching effect. Also, controlling the linear [22] and nonlinear [23, 24] optical absorptions of one laser beam by another in coherently-prepared atomic media were exploited to show all-optically controlled beam switching. Recently, it was shown that a FWM signal beam can be spatially shifted easily by frequency detunings and intensities of the dressing laser beams following a dispersion-like behavior [19]. Such EISD is greatly enhanced same as for the frequency (linear and nonlinear) dispersions in the EIT systems [7, 16], which can give large and sensitive spatial displacements for FWM and probe beams. Also, if one carefully chooses the parametric regime, the probe and FWM beams can have been focusing effects in a self-defocusing medium due to the strong XPM [1, 3], which compensate the beam diffraction when propagating through the long atomic medium.

In this section, we show that by making use of the EISD effect in a three-level ladder-type atomic system [19], all-optical switching/routing effects can be experimentally demonstrated. The FWM signals are generated by two

coupling beams in the three- or two-level system, with an additional dressing field to shift the spatial location of the generated FWM beams. The intensities of the initial (before shifting) and final (after shifting) spots of FWM signals correspond to the "off" and "on" states of the switch. Different shift directions and spot locations are studied as functions of experimental parameters. Since there are two FWM beams and each beam has more than one final states (spatial locations), it is possible to construct switching arrays in the current system.

7.4.1 Theoretical Model and Experimental Scheme

The relevant experimental system is shown in Fig. 7.10 (a), (b). Three energy levels from sodium atoms (in a heat-pipe oven of length 18 cm) are involved in the experimental schemes. The pulse laser beams are aligned spatially as shown in Fig. 7.10 (c). In Fig. 7.10 (a), energy levels $|0\rangle$ $(3S_{1/2})$, $|1\rangle(3P_{3/2})$ and $|2\rangle$ $(4D_{3/2})$ form a ladder-type three-level atomic system. Coupling field E_2 (wavelength of 568.8 nm, angular frequency ω_2, detuning $\Delta_2 = 0$, wave vector $\boldsymbol{k}_2$, and Rabi frequency $G_2 = 5.1$ GHz) and E_2' (ω_2, $\Delta_2 = 0$, $\boldsymbol{k}_2'$, $G_2' = 15.5$ GHz) connecting the transition between level $|1\rangle$ and level $|2\rangle$, which are from the same near-transform-limited dye laser (10 Hz repetition rate, 5 ns pulse-width and 0.04 cm^{-1} linewidth). The field E_2 in beam 1 propagates in the opposite direction of the weak probe field E_3 (wavelength of 589.0 nm, ω_1, Δ_1, $\boldsymbol{k}_3$, $G_3 = 4.8$ GHz) in beam 4, as shown in Fig. 7.10 (c), connecting the transition between $|0\rangle$ to $|1\rangle$. E_2' in beam 3 propagates in the plane (yz) having a small angle (0.3°) with E_2. With the phase-matching condition, it generates a non-degenerated FWM (NDFWM) process satisfying $\boldsymbol{k}_{F2} = \boldsymbol{k}_3 + \boldsymbol{k}_2 - \boldsymbol{k}_2'$ (called E_{F2} for the subsystem $|0\rangle - |1\rangle - |2\rangle$). Then, additional fields E_1 (ω_1, Δ_1, $\boldsymbol{k}_1$, $G_1 = 5.1$ GHz) and E_1' (ω_1, Δ_1, $\boldsymbol{k}_1'$, G_1') are added, which are from the other dye laser with similar characteristics as the first one, also connecting the transition between $|0\rangle$ to $|1\rangle$. E_1 adds onto beam 1 and E_1' (beam 2) propagates in another plane (xz) which is perpendicular to the yz plane with a small angle relative to E_1, as shown in the inset of Fig. 7.10 (c). When E_1, E_1' and E_3 are turned on simultaneously with blocking E_2, E_2', a DFWM process is generated satisfying the phase-matching condition $\boldsymbol{k}_{F1} = \boldsymbol{k}_1 - \boldsymbol{k}_1' + \boldsymbol{k}_3$ (called E_{F1} for the subsystem $|0\rangle - |1\rangle$) [Fig. 7.10 (b)]. Here we define detuning $\Delta_i = \Omega_i - \omega_i$ with the atomic resonant frequency Ω_i. The average powers of the laser beams E_1, E_1', E_2, E_2' and E_3 are 3, 100, 5, 95, and 0.14 μW, respectively. The laser beams $E_1(E_1')$, $E_2(E_2')$ and E_3 (with diameters of about 0.59, 0.82, and 0.59 mm, respectively) are horizontally polarized.

When E_1, E_1', E_2, E_2', and E_3 are all turned on simultaneously, the NDFWM process E_{F2} and DFWM process E_{F1} are generated simultaneously. These two generated FWM signals have the same frequency $\omega_{F1,2} (= \omega_1)$,

but propagate in two different directions, which are monitored by a charge coupled device (CCD) camera [Fig. 7.10 (c)]. In the experiment, the intensity of laser beams E_1' is about 5 times stronger than the beam E_2', and about 100 times stronger than the beams $E_{1,2,3}$. According to the insert of Fig. 7.10 (c), with cross-Kerr effect, such horizontal alignment of strong dressing field E_1' and E_2' beams induce the horizontal shift of NDFWM $E_{F2}$and DFWM E_{F1}, respectively [19]. The probe E_3beam is influenced by the combined effect of E_1' and E_2' beams but mainly shifted horizontally by E_1' beam. Thus, a pair of E_3 and E_{F2} beams can be switched on and off by E_1' beam, while one E_{F1} beam can be switched on and off by E_2' beam at the same time.

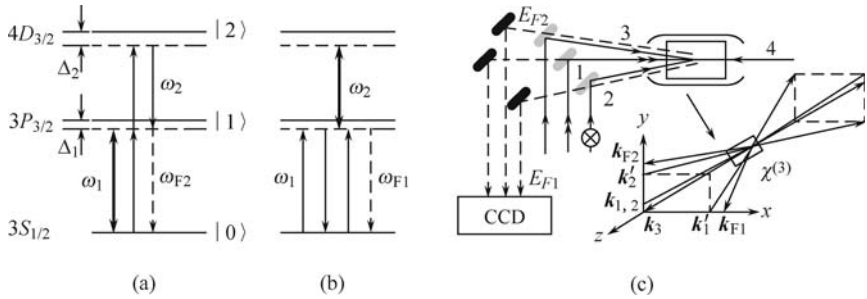

Fig. 7.10. (a), (b) The diagrams of Na energy levels with different coupling schemes. The bold arrows refer to the dressing fields. (c) The experimental scheme and arrangements (Inset: the spatial alignments of the incident beams).

The theoretical description of the spatial properties of the beams $E_{3,F1,F2}$ due to self- and cross-Kerr nonlinearities can be given through numerically solving the following propagation equations:

$$\frac{\partial E_3}{\partial z} - \frac{\mathrm{i}}{2k_3}\frac{\partial^2 E_3}{\partial \xi^2} = \frac{\mathrm{i}k_3}{n_0}(n_2^{S1}\,|E_3|^2 + 2n_2^{X1}\,|E_1'|^2 + 2n_2^{X2}\,|E_2'|^2)E_3, \tag{7.21}$$

$$\frac{\partial E_{F1}}{\partial z} - \frac{\mathrm{i}}{2k_{F1}}\frac{\partial^2 E_{F1}}{\partial \xi^2} = \frac{\mathrm{i}k_{F1}}{n_0}(n_2^{S2}\,|E_{F1}|^2 + 2n_2^{X3}\,|E_1|^2 + 2n_2^{X4}\,|E_2'|^2 + 2n_2^{X5}\,|E_1'|^2)E_{F1}, \tag{7.22}$$

$$\frac{\partial E_{F2}}{\partial z} - \frac{\mathrm{i}}{2k_{F2}}\frac{\partial^2 E_{F2}}{\partial \xi^2} = \frac{\mathrm{i}k_{F2}}{n_0}(n_2^{S3}\,|E_{F2}|^2 + 2n_2^{X6}\,|E_1'|^2 + 2n_2^{X7}\,|E_2|^2 + 2n_2^{X8}\,|E_2'|^2)E_{F2}, \tag{7.23}$$

where $k_3 = k_{F1} = k_{F2} = \omega_1 n_0/c$, z and ξ are the longitudinal and transverse coordinates, respectively, n_0 is the linear refractive index, n_2^{S1-S3} are the self-Kerr coefficients of $E_{3,F1,F2}$, respectively. n_2^{X1} is the cross-Kerr nonlinear

coefficient of the weak field $\boldsymbol{E}_3$ induced by the strong coupling field $\boldsymbol{E}_1'$, n_2^{X2} is the cross-Kerr nonlinear coefficient of the weak field $\boldsymbol{E}_3$ induced by the strong coupling field $\boldsymbol{E}_2'$, n_2^{X3} is the cross-Kerr nonlinear coefficient of the weak field $\boldsymbol{E}_{F1}$ induced by the strong coupling field $\boldsymbol{E}_1$, n_2^{X4} is the cross-Kerr nonlinear coefficient of the weak field $\boldsymbol{E}_{F1}$ induced by the strong coupling field $\boldsymbol{E}_2'$, n_2^{X5} is the cross-Kerr nonlinear coefficient of the weak field $\boldsymbol{E}_{F1}$ induced by the strong coupling field $\boldsymbol{E}_1'$, n_2^{X6} is the cross-Kerr nonlinear coefficient of the weak field $\boldsymbol{E}_{F2}$ induced by the strong coupling field $\boldsymbol{E}_1'$, n_2^{X7} is the cross-Kerr nonlinear coefficient of the weak field $\boldsymbol{E}_{F2}$ induced by the strong coupling field $\boldsymbol{E}_2$, n_2^{X8} is the cross-Kerr nonlinear coefficient of the weak field $\boldsymbol{E}_{F2}$ induced by the strong coupling field $\boldsymbol{E}_2'$. Generally, the Kerr coefficient can be defined by $n_2 = \mathrm{Re}\chi^{(3)}/(\varepsilon_0 c n_0)$, with the nonlinear susceptibility $\chi^{(3)} = D\rho_{10}^{(3)}$, where $D = N\mu_3^2\mu_{ij}^2/\hbar^3\varepsilon_0 G_3 G_j^2$, $\rho_{10}^{(3)}(E_{F1}) = -\mathrm{i}G_{F1}|G_2|^2/\eta$, $\rho_{10}^{(3)}(E_{F2}) = -\mathrm{i}G_{F2}|G_1|^2/\eta$, $\rho_{10}^{(3)}(E_3) = -\mathrm{i}G_3|G_1|^2/\eta$ and $\eta = D_1^2 D_2$. $D_{1,2}$ are the parameters related to the Rabi frequency of the dressing field, the frequency detuning, and the atomic coherence rate. μ_3 (μ_{ij}) is the dipole matrix element between the states coupled by the probe beam E_3 (between $|i\rangle$ and $|j\rangle$). By assuming Gaussian profiles for the input fields, Eqs. (7.21)–(7.23) are solved by the split-step method.

7.4.2 Optical Switching and Routing via Spatial Shift

When four laser beams (E_1', E_2, E_2', and E_3) are on, in the presence of the dressing beam E_1', the spatial shift of E_{F2} beam spot versus probe laser frequency detuning ω_3 is shown in Fig. 7.11 (a). The moving trace of the light spot is dispersion-like as frequency scans [19]. It means E_{F2} beam can have right or left shift. There are two maximal displacements corresponding to the positive maximum nonlinear refraction coefficient and the negative maximum coefficient. Without E_1' beam, the probe field E_3 and E_{F2} are single strong spots, as shown in Fig. 7.12 (a). When the dressing field E_1' is on, the intensities of the probe and E_{F2} beams become weaker [21] and are shifted (one to the right and another to the left of the original position). Since we use one more mirror in the probe beam scheme than that of E_{F2}, they have opposite direction of the shift on CCD screen [Fig. 7.12(a)]. In fact, in the heated pipe both two beams have a right shift, as shown in Fig. 7.12 (b, c). Larger spatial shift occurs with an increasing E_1' intensity, which can be understood from the expression: $\varphi_{NL}(z,\xi) = 2k_{3,F2}n_2 I_1' \exp(-\xi^2)z/n_0$. The nonlinear phase shift φ_{NL} is directly proportional to the dressing intensity I_1'. The component of the wave vector of the ω_3 spot δk_ξ (which we use to measure the shif t effect of the optical switch) is the derivative of φ_{NL}, i.e., $\delta k_\xi = \partial\varphi_{NL}/\partial\xi$, so the beam spots also move more as the dressing laser intensity increases.

Figure 7.11 (b) shows the dressing field dependences of the spatial shifts

based on the numerical calculation and the experimental measurements. Figure 7.11 (c) presents the temperature dependence (atomic density N) of the shift curves for the theoretical and the experimental results, respectively. We see that increasing the atomic density equals to increasing propagation distance z, and the shift of the spot becomes larger.

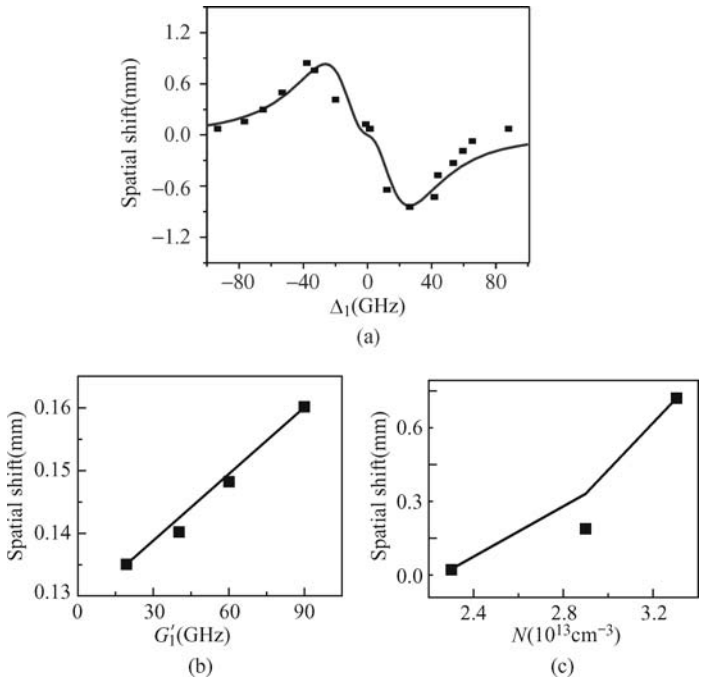

Fig. 7.11. (a) Spatial dispersion curves of E_{F2} in the ladder-type three-level system versus Δ_1 with $G_1' = 52$ GHz at 250°C. (b) The spatial displacement of E_{F2} versus G_1' in the ladder-type three-level system at $\Delta_1 = -18$ GHz and 250°C. (c) The spatial displacement of E_{F2} versus atomic density N with $G_1' = 52$ GHz at $\Delta_1 = -18$ GHz. The solid lines are theoretically calculated spatial shifts, and the scattered points are the experimental results. Adopted from Ref. [24].

So, as shown above the beam spots can have different spatial shifts with different experimental parameters (such as frequency, intensity, and atomic density), which can correspond to different on-off combinations. The switching or routing time is the rising and falling times of the switch-in and switch-out signal. The cross-Kerr refractive index change ($n_2 \propto \mathrm{Re}(\rho_{10}^{(3)})$) limited by the overall spin dephasing time determines the response time of the switch [23, 25, 26]. The estimated switching times of E_{F1} and E_{F2} are about 32 ns and 400 ns, respectively. Here, it should be noted that the overall spin dephasing times of the two-level [Fig. 7.10 (b)] and ladder-type three-level [Fig. 7.10 (a)] atomic systems in sodium are determined by the transverse relaxation rates: $1/(2\pi\Gamma_{10})$ and $1/(2\pi\Gamma_{20})$, where $\Gamma_{10} = 4.85$ MHz and $\Gamma_{20} = 398$

kHz for transitions $|0\rangle - |1\rangle$ and $|0\rangle - |2\rangle$, respectively. However, the switching speed in Fig. 7.12 is limited to a microsecond time scale by the speed of the CCD used to take the image.

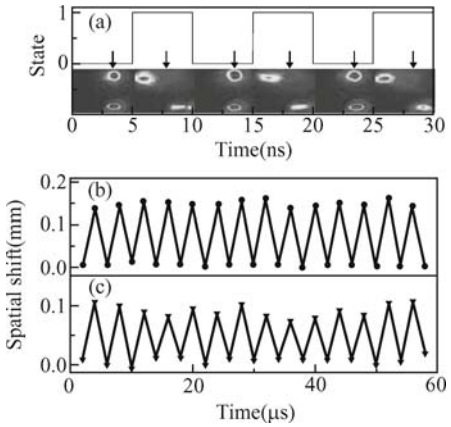

Fig. 7.12. (a) Results of the optical switches and the spot shifts of the probe (lower) and E_{F2} (upper) beams obtained from the CCD at $\Delta_1 = -18$ GHz. The arrows are the initial position in the x direction. The spatial shift of (b) the probe and (c) E_{F2} beams in the ladder-type three-level atomic system with $G_1' = 34$ GHz at $\Delta_1 = -18$ GHz and 250 °C.

Figure 7.12 (a) shows the two states of the probe and E_{F2} beams by switching the strong laser beam E_1' off and on as the laser frequency detuning is tuned to get the maximal spatial displacement. When a spot stays at its initial position, it means that the switch is in the "off" state. When the frequencies of the probe and E_{F2} beams are set at their peak shift positions, the light spots will have their largest shifts, so the switch stands at its "on"-state. Such two states form two ports of the optical switch. The upper spot is the E_{F2} beam, and the lower spot is the probe beam. Initially, two spots are set at same vertical line without the dressing laser beam. As the dressing beam E_1' turns on, the upper spot moves to the left side and the lower spot moves to the right side, both of which leave their initial positions completely. The switching contrast can be defined as $C = (I_{off} - I_{on})/(I_{on} + I_{off})$, where I_{off} is the light intensity at the "off"-state and I_{on} is the light intensity at the "on"-state. The contrast derived from the experiment is about $C = 92\%$. This experiment provides a physical mechanism to realize an all-optical switching/routing by controlling the dressing laser beam.

A chopper is used to control the dressing field, subtracting the laser pulse repetition time of 0.1 s, which is considered as an idle load state. The laser pulse width is 5 ns. The detected switching time is limited by the response time of the CCD, which is about 3 μs, far larger than the laser pulse width. Thus, the switching speed in the current experiment is greatly constrained as shown in Fig. 7.12 (b, c). The on-state just lasts 5 ns, followed by a 3 μs

rising time, and then a 5 ns off-state, followed by a 3 μs falling time, and so on. Since the spatial displacements of the probe and E_{F2} beams are mainly determined and controlled by the large cross-Kerr nonlinear coefficients of the strong laser field E_1', the switching speed should be much faster and limited by the atomic coherence time in nanosecond time scale.

Next, when five laser beams (E_1, E_1', E_2, E_2', and E_3) are all on, there are interplays between the generated $E_{F1,F2}$ signals [21] and we can control the shifts of the probe, E_{F1} and E_{F2} beams, to achieve a triple binary optical switch. The initial locations of the spots are the "off" states and the switches are considered to come to their "on" states when the spots shift away to new locations. The repetition frequency of the chopper is much longer than 5 ns pulse-width of the dressing laser, so the "on"-state lasts several 5ns intervals and then turns to the "off"-state. In Fig. 7.13, at $\Delta_1 = -18$ GHz for the self-focusing side and temperature 250 °C, when E_1' is on, the probe and E_{F2} beams have right shifted due to the E_1' beam via the cross-Kerr nonlinear coefficients. At the same time, the E_{F1} beam is shifted to the left by the dressing field E_2'. When E_1' is off, all the beams come back to their original position ("off"-state). Since the cross-Kerr nonlinear coefficients n_2^{X4} and n_2^{X6} (n_2^{X1}) of the E_{F1} and E_{F2} (probe) beams induced by the dressing fields E_2' and E_1' are all positive, respectively, the spots of E_{F1} and E_{F2} (E_3) beams are shifted to the opposite directions, as shown in Fig. 7.13. According to the nonlinear phase shifts $\varphi_{F1} = 2k_{F1}n_2^{X4}\left|A_2'\right|^2 z_0/n_0$ and $\varphi_{F2} = 2k_{F2}n_2^{X6}\left|A_1'\right|^2 z_0/n_0$ ($\varphi_3 = 2k_3 n_2^{X1}\left|A_1'\right|^2 z_0/n_0$) induced by the dressing fields E_2' and E_1', respectively, we can use two controllable parameters, i.e., the frequency and intensity of the laser, to control the different shifts of the three spots. Such simultaneous optical switching for three beams can perform the functions of choosing different addresses in data transmissions and can be used as the optical routings, the multiplexer or all-optical switching arrays for all-optical

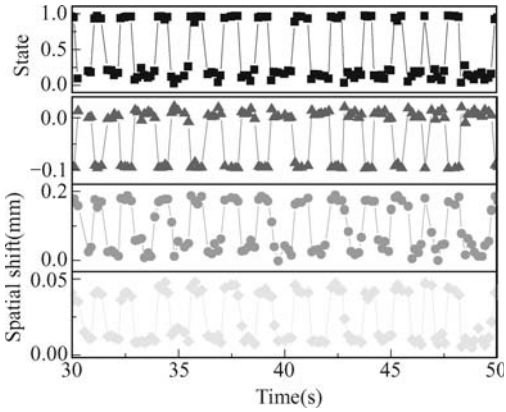

Fig. 7.13. The switching processes of the dressing beam E_1' (square), E_{F1} (triangle), E_{F2} (circle), and the probe beam (diamond) in the ladder-type three-level system with $G_1' = 21$ GHz at $\Delta_1 = -18$ GHz and 250 °C.

networks.

In the above discussion, we have controlled the probe, E_{F1} and E_{F2} by two dressing fields E_2' and E_1', respectively. In that case, E_{F1} and E_{F2} are shifted towards the opposite directions (Fig. 7.13). Actually, such three beams can also be shifted to the same direction when the sign of the cross Kerr-nonlinear coefficient of the E_{F1} signal is opposite to those of the E_{F2} (probe) beams at the proper laser detuning. So, each spot can have left and right locations. Including the initial position, every spot has three possible spatial locations. Totally there are 3×3 controllable spatial positions. It can such achieve a switch array.

7.5 Controlled Spatial Beamsplitter Using Four-Wave Mixing Images

Spatially shifting and splitting one weak laser beam by another stronger beam in Kerr nonlinear optical media were predicted and experimentally demonstrated in early 1990s [2, 4]. These interesting beam coupling effects are governed by the cross-phase modulation (XPM) between the two laser beams in the Kerr nonlinear medium [16]. Also, degenerate and nondegenerate four-wave mixing (FWM) processes in two-level atomic systems have been investigated previously [27 – 29]. Here, we experimentally demonstrate that by arranging the pump and coupling laser beams in a specially-designed spatial configuration (to satisfy phase-matching for the FWM processes), the generated FWM signals from the degenerate and nondegenerate FWM processes can be spatially split easily. Both the spatial separation and the number of the split beams of FWM signals can be well controlled by the additional dressing laser beams via XPM. The enhanced self- and cross-Kerr nonlinearities due to induced atomic coherence in the system [1] are essential in generating the efficient FWM processes, and in the spatial splitting of the FWM signal beams. Full theoretical simulations are carried out and used to provide good matches to the observed phenomena. Studies of the spatial beam shift and splitting can be very useful in understanding the formation and interactions of spatial solitons [30], gap solitons [31, 32], vortex solitons [33], as well as their dynamics [32], in the Kerr nonlinear systems. Also, such spatial beam controls can be very useful for signal processing applications, such as spatial beam splitter [34, 35], routing [19], and switching [12].

Let us consider a two-level atomic system, as shown in Fig. 7.14(a). Five laser beams (with diameters of 0.2 mm) are applied to the atomic system with the spatial configuration given in Fig.1(b). $\boldsymbol{E}_1$ ($\boldsymbol{k}_1$, and the Rabi frequency G_1) and $\boldsymbol{E}_1'$ ($\boldsymbol{k}_1'$, and G_1') are the pump beams propagating in one direction with a small angle (0.3°) between them. $\boldsymbol{E}_3$ ($\boldsymbol{k}_3, G_3$) is the probe beam propagating in the opposite direction with a small angle (0.05°) from beam $\boldsymbol{E}_1$. These three beams ($\boldsymbol{E}_1$, $\boldsymbol{E}_1'$, and $\boldsymbol{E}_3$) have the same frequency ω_1

(from the same laser), and generate an efficient degenerate FWM signal $\boldsymbol{E}_{F1}$ ($\boldsymbol{k}_{F1} = \boldsymbol{k}_1 - \boldsymbol{k}_1' + \boldsymbol{k}_3$) in the direction shown at the lower right corner of Fig. 7.14(b). Another pair of beams, $\boldsymbol{E}_2$ ($\boldsymbol{k}_2$, G_2) and $\boldsymbol{E}_2'$ ($\boldsymbol{k}_2'$, G_2'), are the coupling beams with $\boldsymbol{E}_2$ propagating in the same direction as $\boldsymbol{E}_1$ and $\boldsymbol{E}_2'$ having a small angle (0.3°) from $\boldsymbol{E}_2$. $\boldsymbol{E}_2$ and $\boldsymbol{E}_2'$ have the same frequency ω_2 (from the same laser) and they interact with the probe beam $\boldsymbol{E}_3$ to generate an efficient nondegenerate FWM signal $\boldsymbol{E}_{F2}$ ($\boldsymbol{k}_{F2} = \boldsymbol{k}_2 - \boldsymbol{k}_2' + \boldsymbol{k}_3$) in the direction of the upper left corner in Fig. 7.14 (b) due to the given phase-matching condition.

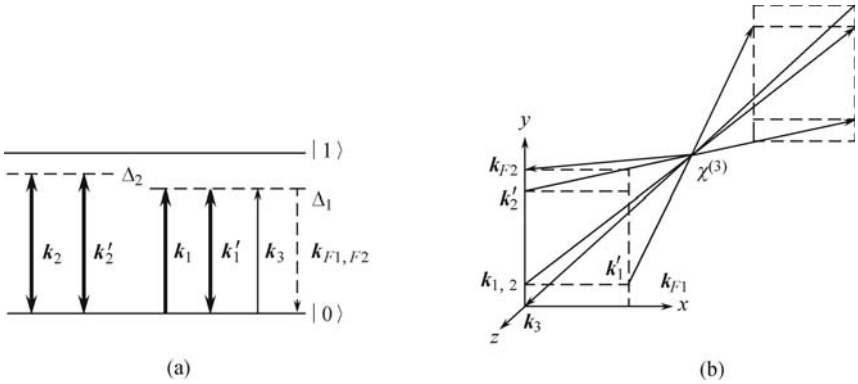

Fig. 7.14. (a) Two FWM processes to generate $\boldsymbol{E}_{F1}$ and $\boldsymbol{E}_{F2}$ in a two-level atomic system. (b) Spatial geometry for the laser beams used in the experiment.

The experiment was done with Na vapor in a 18 cm long heat pipe. The ground state of the two-level system ($|0\rangle$) is the $3S_{1/2}$ energy level and the excited state ($|1\rangle$) is the $3P_{3/2}$ level. Both lasers (with frequencies ω_1 and ω_2, respectively) are near-transform-limited dye lasers with 10 Hz repetition rate, 3.5 ns pulse width, pulse-by-pulse stability of 3%, and energy per pulse of 0.1 mJ. One laser is split to produce beams $\boldsymbol{E}_1$, $\boldsymbol{E}_1'$, and $\boldsymbol{E}_3$ with frequency ω_1, and another laser is used for beams $\boldsymbol{E}_2$ and ω_3. These laser beams are carefully aligned in the spatial configuration as shown in Fig. 7.14 (b). In order to optimize the beam shift and splitting effects, $\boldsymbol{E}_2'$ beam is made to be the strongest, approximately 5 times larger than $\boldsymbol{E}_1'$ beam, 100 times larger than the beam $\boldsymbol{E}_1$, 1000 times larger than the beam $\boldsymbol{E}_2$, and 10^4 times larger than the weak probe beam $\boldsymbol{E}_3$, as well as the two generated FWM signal beams ($\boldsymbol{E}_{F1}$ and $\boldsymbol{E}_{F2}$). These weak beams are recorded by a CCD and a fast gated integrator (gate width of 50 ns).

As shown in the insets of Fig. 7.15 (a), (b) (lower panels), the probe and FWM signal ($\boldsymbol{E}_{F1}$) beams are displaced and split as the frequency of the probe beam (frequency detuning is defined as $\Delta_1 = \Omega_1 - \omega_1$, where Ω_1 is the atomic transition frequency) is scanned through resonance. The displacements of the probe and FWM beams follow the shape of nonlinear dispersion [7, 19]. Here, we concentrate only on the beam splitting effect.

Figure 7.15 (a) gives the splitting distance of the probe beam for different probe frequency detunings. The solid curve is a fit to the cross-Kerr nonlinear index n_2 for the probe beam [1, 7, 16]. The splitting distance of the FWM signal $\boldsymbol{E}_{F1}$ is given in Fig. 7.15 (b) as a function of Δ_1, which is also fitted to n_2, as will be discussed later.

The Kerr nonlinear index is always zero at the exact resonant condition [1]. The temperature dependence of the FWM beam splitting distance is given in Fig. 7.15 (c), which shows a quick increase as temperature rises and then a slow decrease as the temperature further increases. Double-beam profiles are clearly shown in the figure. The intensity dependence of the FWM beam shift as a function of the pump beam ($\boldsymbol{E}_1'$) intensity is depicted in Fig. 7.15 (d), which gives a continued increase as G_1' gets larger. It is interesting to notice that when $\Delta_1 < 0$ the beam splitting occurs in the y (vertical) direction, but becomes in the x (horizontal) direction when $\Delta_1 > 0$ in Fig. 7.15 (a), (b). This phenomenon can be explained by the relative positions between the weak beams and the strong dressing (controlling) beams shown in Fig.

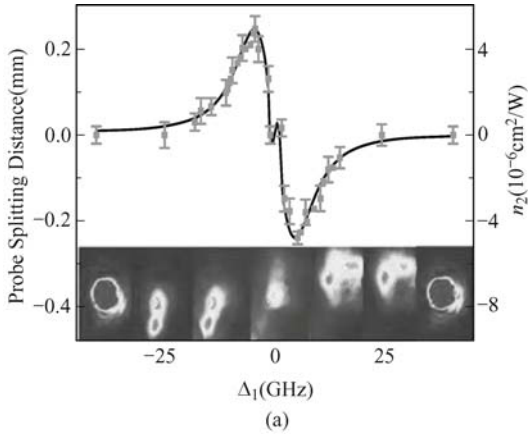

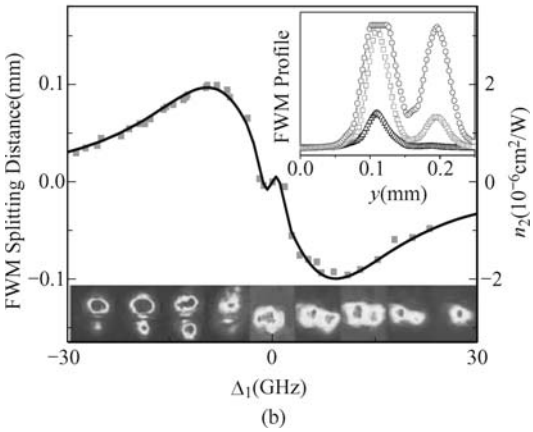

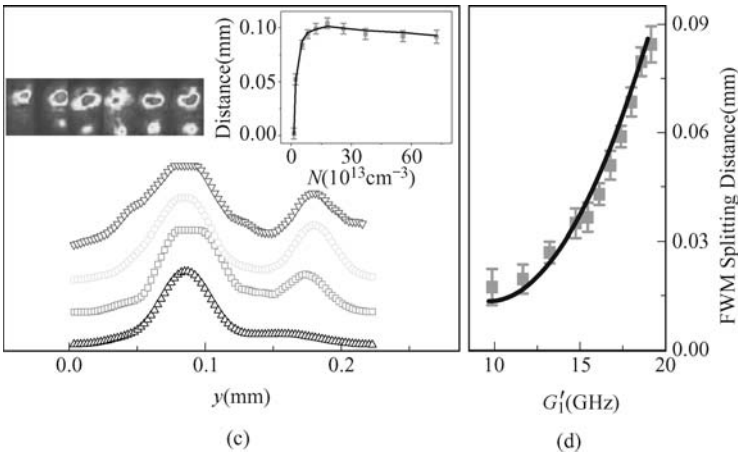

Fig. 7.15. (a) Measured probe beam splitting versus Δ_1 (square) and the fitted n_2 curve (solid) with $G_1' = 20.6$ GHz at 250 °C. Inset: spots of the probe beam versus Δ_1. (b) Measured $\boldsymbol{E}_{F1}$ beam splitting versus $\Delta_1 = -30$ GHz (triangle), $\Delta_1 = -22$ GHz (square), $\Delta_1 = -17$ GHz (circle) in top right corner; and spots of the $\boldsymbol{E}_{F1}$ beam versus Δ_1 in bottom. (c) $\boldsymbol{E}_{F1}$ beam profiles at 230 °C (triangle), 240 °C (square), 260 °C (circle) and 280 °C (reverse triangle), respectively, with $G_1' = 20.6$ GHz at $\Delta_1 = -10$ GHz. Inset: $\boldsymbol{E}_{F1}$ beam splitting versus atomic density N. Spots of $\boldsymbol{E}_{F1}$ beam versus N. (d) $\boldsymbol{E}_{F1}$ beam splitting versus G_1' with $\Delta_1 = -10$ GHz at 265 °C. The other parameters are $\Delta_2 = 0$, $G_2 = 0$, $G_1 = 1.5$ GHz, and $G_2' = 10.8$ GHz. Adopted from Ref. [35].

7.14 (b). For the weak probe beam $\boldsymbol{E}_3$ [Fig. 15 (a)], in the $\Delta_1 < 0$ region, the beam shift in the y direction results from the attraction ($n_2 > 0$) of the strong $\boldsymbol{E}_2'$ beam. This makes it get closer to the $\boldsymbol{E}_2'$ beam, which also splits the probe beam in y direction. In the $\Delta_1 > 0$ region, the probe beam shifts to the down-right direction due to the repulsion ($n_2 < 0$) of the strong $\boldsymbol{E}_2'$ beam (which is slightly misaligned to the left side) and gets closer to the $\boldsymbol{E}_1'$ beam, which can split the probe beam in the x direction. Also, for the weak FWM beam $\boldsymbol{E}_{F1}$ [Fig. 7.15 (b)], in the $\Delta_1 < 0$ region, it shifts above the $\boldsymbol{E}_1'$ beam in the y direction induced by the $\boldsymbol{E}_2'$ beam, and such $\boldsymbol{E}_1'$ beam can split $\boldsymbol{E}_{F1}$ in y direction. While in the $\Delta_1 > 0$ region, the FWM $\boldsymbol{E}_{F1}$ beam shifts in the down-right direction due to the repulsion ($n_2 < 0$) of the $\boldsymbol{E}_2'$ beam and, therefore, splits in the x direction induced by the $\boldsymbol{E}_1'$ beam.

Figure 7.16 depicts the beam profiles of the FWM beam $\boldsymbol{E}_{F2}$ as functions of various parameters. Figure 7.16 (a) presents the FWM beam ($\boldsymbol{E}_{F2}$) profiles for different probe frequency detunings. As one can see that the beam breaks up into two beams at certain value of Δ_1. For $\Delta_1 < 0$, the atomic system is a focusing medium due to self-Kerr nonlinearity. For fixed parameters ($\Delta_1 = -3$ GHz, $\Delta_2 = 0$, $G_3 = 0.1$ GHz, $G_1 = G_1' = 0$), as the temperature of the atomic medium (atomic density N) increases, the FWM beam changes from one into four pieces as shown in Fig. 7.16 (b). Similarly, in the $\Delta_1 > 0$ region, the atomic system is a defocusing medium, and the beam profile

becomes wider. Under the similar experimental parameters (except $\Delta_1 = 3$ GHz), the single FWM beam also breaks up into four as the temperature gets higher [Fig. 7.16 (c)]. The insets in Fig. 7.16 show the spatial beam images.

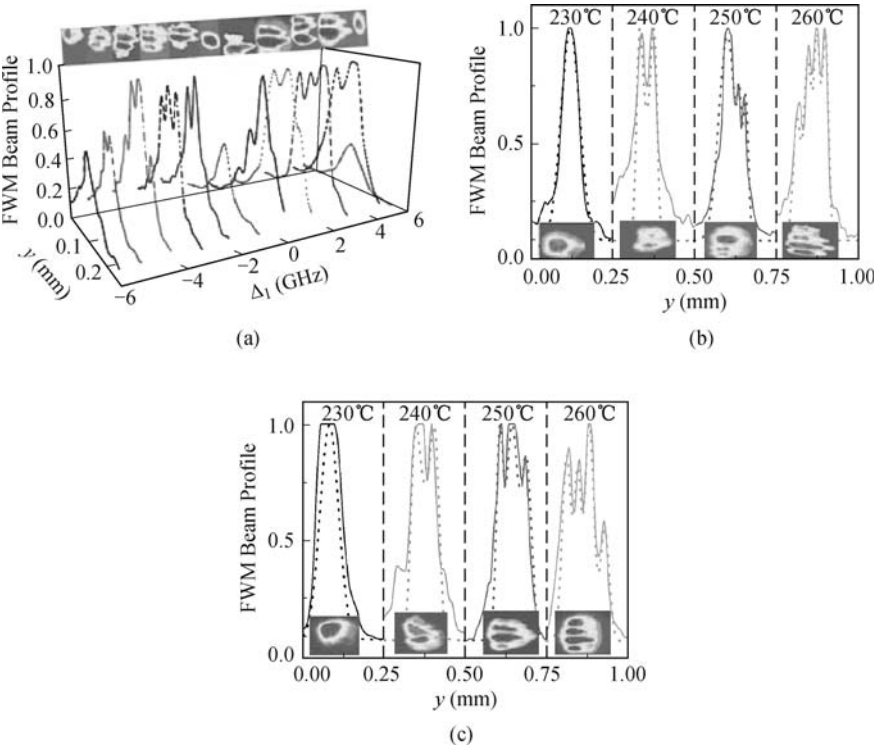

Fig. 7.16. (a) $\boldsymbol{E}_{F2}$ beam profiles versus Δ_1 at 250 °C. $\boldsymbol{E}_{F2}$ beam profiles at (b) $\Delta_1 = -3$ GHz and (c) $\Delta_1 = 3$ GHz at 230 °C, 240 °C, 250 °C and 260 °C. The other parameters are $G_1 = G_1' = 0$, $G_2 = 1.9$ GHz, and $G_2' = 20.8$ GHz. The solid lines are the experimental results, and the dotted lines are the calculated $\boldsymbol{E}_{F2}$ beam profiles.

Figure 7.17 presents the effects due to the doubly-dressing fields. The images in Fig. 7.17 (a) show (i) the FWM $\boldsymbol{E}_{F2}$ beam at different probe detunings; (ii) the FWM $\boldsymbol{E}_{F2}$ beam shifts with $\boldsymbol{E}_1'$ dressing; and (iii) splitting into three or four parts with the $\boldsymbol{E}_2'$ dressing. So, with both the $\boldsymbol{E}_1'$ and $\boldsymbol{E}_2'$ dressing fields on, the FWM $\boldsymbol{E}_{F2}$ beam not only shifts, but also splits, as shown in (iv) of Fig. 7.17 (a). These phenomena are evident in Fig. 7.17 (b), which presents the FWM beam profiles of Fig. 7.17 (a) at $\Delta_1 = 25$ GHz. With stronger $\boldsymbol{E}_2'$ dressing beam, the $\boldsymbol{E}_{F2}$ beam changes from two into five split peaks. The inset of Fig. 7.17 (b) shows that the shift of $\boldsymbol{E}_{F2}$ beam is mainly caused by $\boldsymbol{E}_1'$, since $\boldsymbol{E}_1'$ is at the down-right corner of the $\boldsymbol{E}_{F2}$ beam while $\boldsymbol{E}_2'$ almost overlaps with $\boldsymbol{E}_{F2}$. Thus, $\boldsymbol{E}_{F2}$ is shifted by $\boldsymbol{E}_1'$ and split by $\boldsymbol{E}_2'$.

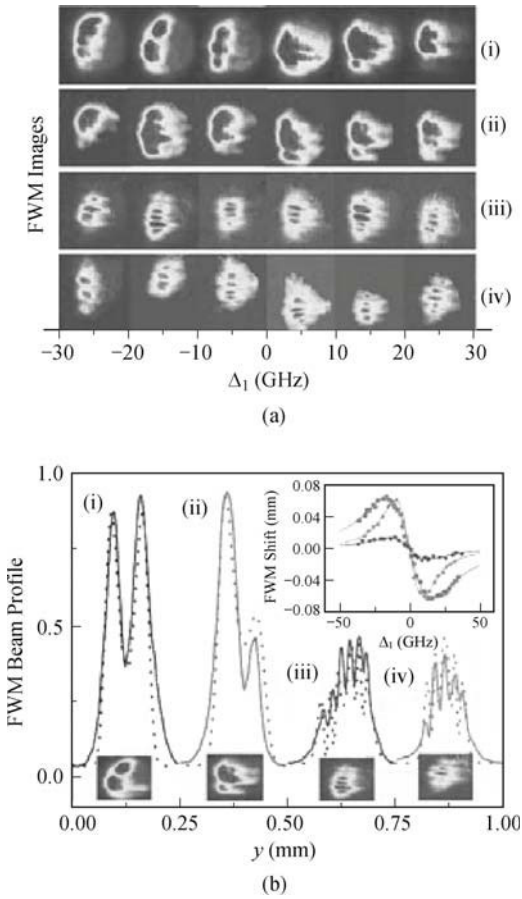

Fig. 7.17. Spots (a) and profiles (b) of the $\boldsymbol{E}_{F2}$ beam versus Δ_1 at 250 °C with $G_1' = 0$ and $G_2' = 1.5$ GHz (i), $G_1' = 20.6$ GHz and $G_2' = 1.5$ GHz (ii), $G_1' = 0$ & $G_2' = 20.6$ GHz (iii), and $G_1' = G_2' = 20.6$ GHz (iv). The solid lines are the experimental results, and the dotted lines are the calculated $\boldsymbol{E}_{F2}$ beam profiles. Inset of (b): spatial shift of the $\boldsymbol{E}_{F2}$ beam versus Δ_1 with $\boldsymbol{E}_1'$ dressing (square), $\boldsymbol{E}_2'$ dressing (reverse triangle), $\boldsymbol{E}_1'$ and $\boldsymbol{E}_2'$ dressing (triangle), respectively. The scattered points are the measured results, and the solid lines are theoretical n_2 curves. The other parameters are $G_1 = G_2 = 1.5$ GHz.

To understand the observed beam splitting and spatial shift of the probe and FWM beams, we need to consider various self-phase modulation (SPM) and XPM processes. The spatial beam breaking is mainly due to the overlap between the weak probe and/or FWM beams and the strong coupling or pump beams [2]. Due to XPM, the nonlinear phase can have more than one minimum when the cross-Kerr index n_2 increases, which generates several intensity minima in the profiles of the FWM beams. The propagation equations for the probe and FWM beams with only the most relevant coupling/pump

beams for beam splitting are

$$\begin{cases} \dfrac{\partial E_3}{\partial z} - \dfrac{\mathrm{i}\nabla_\perp^2 E_3}{2k_3} = \dfrac{\mathrm{i}k_3}{n_1}\left[n_2^{S1}\left|E_3\right|^2 + 2n_2^{X1}\left|E_1'\right|^2 + 2n_2^{X2}\left|E_2'\right|^2\right]E_3, \\ \dfrac{\partial E_{F1}}{\partial z} - \dfrac{\mathrm{i}\nabla_\perp^2 E_{F1}}{2k_{F1}} = \dfrac{\mathrm{i}k_{F1}}{n_1}\left[n_2^{S2}\left|E_{F1}\right|^2 + 2n_2^{X3}\left|E_1'\right|^2\right]E_{F1}, \\ \dfrac{\partial E_{F2}}{\partial z} - \dfrac{\mathrm{i}\nabla_\perp^2 E_{F2}}{2k_{F2}} = \dfrac{\mathrm{i}k_{F2}}{n_1}\left[n_2^{S3}\left|E_{F2}\right|^2 + 2n_2^{X4}\left|E_2'\right|^2\right]E_{F2}. \end{cases} \tag{7.24}$$

Here, z is the longitudinal coordinate; $k_3 = k_{F1} = k_{F2} = \omega_1 n_1/c$; n_1 is the linear refractive index; n_2^{S1-S3} are the self-Kerr coefficients of $\boldsymbol{E}_{3,F1,2}$; n_2^{X1} is the cross-Kerr nonlinear coefficient of the weak field $\boldsymbol{E}_3$ induced by the strong coupling field $\boldsymbol{E}_1'$, n_2^{X2} is the cross-Kerr nonlinear coefficient of the weak field $\boldsymbol{E}_3$ induced by the strong coupling field $\boldsymbol{E}_2'$, n_2^{X3} is the cross-Kerr nonlinear coefficient of the weak field $\boldsymbol{E}_{F1}$ induced by the strong coupling field $\boldsymbol{E}_1'$, and n_2^{X4} is the cross-Kerr nonlinear coefficient of the weak field $\boldsymbol{E}_{F2}$ induced by the strong coupling field $\boldsymbol{E}_2'$. Using Gaussian profiles for the input fields, Eq. (7.24) are solved by using the commonly employed split-step method. Note that the linear and FWM coupling terms ($\rho_{F1}^{(3)} = -\mathrm{i}G_3G_1G_1'^{*}\exp(\mathrm{i}\boldsymbol{k}_{F1}\cdot\boldsymbol{r})F_1^{-1}[(F_1^{*})^{-1} + F_1^{-1}](F_2^{-1} + F_3^{-1})$, $\rho_{F2}^{(3)} = -\mathrm{i}G_3G_2G_2'^{*}\exp(\mathrm{i}\boldsymbol{k}_{F2}\cdot\boldsymbol{r})F_5^{-1}F_6^{-1}[F_4^{-1} + (F_4^{*})^{-1}]$) are neglected [19], where F_i factors are the parameters related to the dressing field, the frequency detuning, and the atomic coherence rate.

The Kerr nonlinear coefficient is negative for a self-defocusing medium and positive for a self-focusing one, which is given by $n_2 \approx \mathrm{Re}\rho_{10}^{(3)}/(\varepsilon_0 c n_0)$. One can solve the coupled density-matrix equations to obtain all $\rho_{10}^{(3)}$, i.e., $\rho_a^{(3)} = -\mathrm{i}G_{F1}G_1'^2/[d_1\Gamma_1(d_1+G_1'^2/\Gamma_0+G_1'^2/\Gamma_1)]$ for n_2^{X3} (induced by the strong $\boldsymbol{E}_1'$ field), $\rho_b^{(3)} = -\mathrm{i}G_{F2}G_2'^2/[d_1d_2(d_1+G_2'^2/d_2)]$ for n_2^{X4} (induced by $\boldsymbol{E}_2'$) and $\rho_c^{(3)} = -\mathrm{i}G_3G_{1,2}'^2/(d_1d_2d_3)$ for $n_2^{X1,2}$ (induced by both $\boldsymbol{E}_1'$ and $\boldsymbol{E}_2'$ fields) with $d_1 = \Gamma_{10} + \mathrm{i}\Delta_1$, $d_2 = \Gamma_1 + \mathrm{i}(\Delta_1 - \Delta_2)$, $d_3 = d_1 + G_1'^2/\Gamma_1 + G_2'^2/(d_2 + G_1'^2/d_4)$, $d_4 = \Gamma_1 - \mathrm{i}\Delta_2$. Here, $G_{F1,F2}$ are the Rabi frequencies of $\boldsymbol{E}_{F1,F2}$ and Δ_1 (Δ_2) is the detuning of the fields $\boldsymbol{E}_{1,3}$ and $\boldsymbol{E}_1'$($\boldsymbol{E}_2$ and $\boldsymbol{E}_2'$). In addition, these three weak beams can be spatially shifted by the other coupling/pump beams that do not have total overlaps with them [19].

The solid curves in Fig. 7.15 (a), (b) are the calculated cross-Kerr nonlinear coefficients, which show good fits to the measured data. So, the measurements of spatial splitting can be used to determine the cross-Kerr nonlinear index. With fixed experimental parameters (such as atomic density, frequency detunings, spot sizes, and atomic decay rates), the measured beam profiles are fitted to the calculated results (from the propagation equations) with adjustable signal amplitudes and constant background, which show excellent agreements, as shown in Figs. 7.16 and 7.17. Such direct comparisons indicate the validity of Eq. (7.24) in describing the spatial splitting of FWM beams by other laser beams. The nonlinear phase for the split beams is given by $\varphi_{NL}(z,\xi) = 2k_{3,F1,2}n_2I_{2,1}\mathrm{e}^{-\xi^2}z/n_0$ and the transverse wave-vector

is $\delta k_\perp = \partial\varphi_{NL}/\partial\xi$. So the amounts of the splitting for the probe and FWM beams are proportional to the dressing beam intensities $I_{2,1}$, the nonlinear dispersion n_2, and the propagation distance z (or equivalently atomic density).

The ability to control spatial position and beam profile of one laser beam (or the FWM signal beam) by another laser beam can be very useful in understanding nonlinear dynamics between multiple laser beams in nonlinear media. In the self-defocused nonlinear medium ($\Delta_1 > 0$), the XPM due to the presence of another laser beam can generate a focusing effect [2, 4], which can be used to generate spatial solitons and other interesting nonlinear effects in the media.

7.6 Spatial Splitting and Intensity Suppression of Four-Wave Mixing in V-type Three-level Atomic System

Recently, we experimentally observe the strong spatial shift and splitting of the probe and generated FWM beams in a two-level system [35 – 37]. The coexisting spatial splitting and intensity suppression of the FWM beam in a V-type three-level system will be discussed in this work.

In this section, by arranging laser beams as illustrated in Fig. 7.18 (a), we demonstrate the spatial splitting of the FWM signal owing to the cross-Kerr effect induced by the control field. Furthermore, the coexisting spatial splitting and intensity suppression of FWM induced by the proper dressing field and control field are also achieved. We also compare the spatial splitting phenomenon in different atomic systems

Three energy levels ($|0\rangle(3S_{1/2})$, $|1\rangle(3P_{1/2})$ and $|2\rangle$ $(3P_{3/2})$) in Na atoms form V-type three-level atomic system, as shown in Fig. 7.18 (b). The laser beams $\boldsymbol{E}_2$ and $\boldsymbol{E}_2'$ (with Rabi frequencies G_2 and G_2' respectively) can be scanned to connect either the transition from $|0\rangle$ to $|1\rangle$ in the V-type three-level or the transition from $|0\rangle$ to $|2\rangle$ in the two-level atomic systems. While the dressing beam $\boldsymbol{E}_1'$ and the probe beam $\boldsymbol{E}_3$ (with G_1' and G_3 respectively) connect the transition from $|0\rangle$ to $|2\rangle$ in both the atomic systems. The generated FWM beam $\boldsymbol{E}_{F2}$ (with Rabi frequency G_{F2}) connect the transition from $|0\rangle$ to $|2\rangle$.

The experiment was carried out with Na vapor in a 18-cm-long heat pipe. The four laser beams come from two dye lasers (10 Hz rate, 5 ns pulse width, and 0.04 cm^{-1} linewidth), the control beam $\boldsymbol{E}_2'$ and beam $\boldsymbol{E}_2$ with the frequency ω_2, the dressing beam $\boldsymbol{E}_1'$ and beam $\boldsymbol{E}_3$ with ω_1. As shown in Fig. 7.18(a), the pulse laser beams (horizontally polarized) with diameters of about 1 mm are aligned spatially with the control beams $\boldsymbol{E}_2$ ($\boldsymbol{k}_2$) and $\boldsymbol{E}_2'$ ($\boldsymbol{k}_2'$) propagating through the atomic medium in the same direction with small angles (0.3°). The probe beam $\boldsymbol{E}_3$ ($\boldsymbol{k}_3$) propagates in the opposite di-

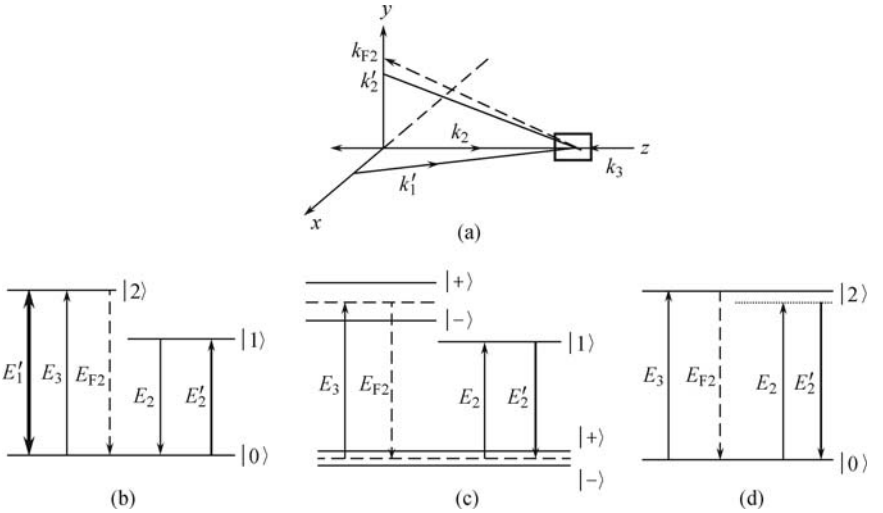

Fig. 7.18. (a) Spatial beam geometry used in the experiments with four laser beams. (b) Energy-level diagram of a V-type three-level and (c) the corresponding dressed-state picture, (d) energy-level diagram of a two-level atomic system.

rection of $\boldsymbol{E}_2$. Satisfying the phase-matching condition $\boldsymbol{k}_{F2} = \boldsymbol{k}_2 - \boldsymbol{k}_2' + \boldsymbol{k}_3$, a generated FWM beam $\boldsymbol{E}_{F2}$ which propagates along the opposite direction of beam $\boldsymbol{E}_2'$ is monitored by a charge coupled device (CCD).

As shown in Fig. 7.18 (a), beams $\boldsymbol{E}_2$, $\boldsymbol{E}_2'$, $\boldsymbol{E}_3$, and $\boldsymbol{E}_{F2}$ are all in the yz plane. The dressing field $\boldsymbol{E}_1'$ propagates in the xz plane, and the intensity is approximately 5 times larger than the control beam $\boldsymbol{E}_2'$, 50 times larger than $\boldsymbol{E}_2$, 100 times larger than P_1 and the probe beam $\boldsymbol{E}_3$. Thus, the dressing beam $\boldsymbol{E}_1'$ can split the resonance levels $|0\rangle$ and $|2\rangle$ into dressed-state $|\pm\rangle$, respectively. Since it does not overlap with the FWM beam $\boldsymbol{E}_{F2}$, it only leads to the suppression of the FWM signal intensity. While $\boldsymbol{E}_2'$ almost overlaps with $\boldsymbol{E}_{F2}$ and the induced cross-Kerr nonlinear effect causes the splitting of the $\boldsymbol{E}_{F2}$ beam spot.

The $\boldsymbol{E}_{F2}$ process is dressed by $\boldsymbol{E}_1'$ in a V-type three-level system, we can easily obtain $\rho_{F2} = -\mathrm{i}G_3G_2'^2/[d_1d_2(d_1 + G_2'^2/d_2)]$ for four-wave mixing (FWM) signal intensity by solving the coupled density-matrix equations under the weak field approximation, here $d_1 = \mathrm{i}\Delta_1 + \Gamma_{10}$, $d_2 = \Gamma_1 + \mathrm{i}(\Delta_1 - \Delta_2)$. On the other hand, for cross-Kerr coefficients of the FWM beam $\boldsymbol{E}_{F2}$, we have $\rho_{10}^{(3)} = \rho_a = -\mathrm{i}G_a/[d_1\Gamma_1(d_1 + G_1'^2/\Gamma_0 + G_1'^2/\Gamma_1)]$, $\rho_{10}^{(3)} = \rho_b = -\mathrm{i}G_b/[d_1d_2(d_1 + G_2'^2/d_2)]$ and $\rho_{10}^{(3)} = \rho_c = -\mathrm{i}G_c/(d_1d_2d_3)$, respectively, where $G_a = G_{F2}G_1'^2$, $G_b = G_{F2}G_2'^2$, $G_c = G_{F2}G_{1,2}'^2$.

The beam splitting can be described by the nonlinear Schrodinger equation

$$\frac{\partial A_{F2}}{\partial z} - \frac{\mathrm{i}\nabla_\perp^2 A_{F2}}{2k_{F2}} = \frac{\mathrm{i}k_{F2}}{n_0}\left[n_2^S\left|A_{F2}\right|^2 + 2n_2^{X1}\left|A_2'\right|^2 + 2n_2^{X2}\left|A_1'\right|^2\right]A_{F2}, \tag{7.25}$$

where z is the longitudinal coordinate, $k_{\mathrm{F}2} = \omega_1 n_0/c$, n_0 is the linear refractive index, n_2^S are the self-Kerr coefficient of $\boldsymbol{E}_{\mathrm{F}2}$, n_2^{X1} is the cross-Kerr nonlinear coefficient of the weak field $\boldsymbol{E}_{\mathrm{F}2}$ induced by the strong coupling field $\boldsymbol{E}_2'$ and n_2^{X2} is the cross-Kerr nonlinear coefficient of the weak field $\boldsymbol{E}_{\mathrm{F}2}$ induced by the strong coupling field $\boldsymbol{E}_1'$. $A_{\mathrm{F}2}$, A_1', and A_2' are the slowly varying envelope amplitudes of beams $\boldsymbol{E}_{F2}$, $\boldsymbol{E}_1'$, and $\boldsymbol{E}_2'$, respectively. Assuming that input lasers are Gaussian profiles, Eq. (7.25) can be numerically solved with the split-step method. For a self-defocusing medium, the Kerr coefficient is negative, while for a self-focusing one it is positive. We can obtain the nonlinear phase shift $\phi_{NL}(z,x) = 2k_{F2}n_2 I\mathrm{e}^{-(w_0'x)^2}z/n_{0(F2)}$, where $n_2 = C\mathrm{Re}\chi^{(3)}$, $C = (\varepsilon_0 c n_0)^{-1}$, the susceptibility $\chi^{(3)} = D\rho_{10}^{(3)}$ and $D = N\mu_{10}^4/(\hbar^3\varepsilon_0 G_{F2}G_i^2)$. N is the atomic density in the sample cell, and μ_{10} is the dipole matrix element between $|0\rangle$ and $|2\rangle$.

The nonlinear phase shift $\phi_{NL}(z,x)$ becomes larger with increasing n_2, and due to $|\boldsymbol{E}_{\mathrm{F}2}|^2 \propto \sin^2\phi_{NL}$ more spatial splitting appears in the $\boldsymbol{E}_{\mathrm{F}2}$ beam profile. Figure 7.19 shows the spatial splitting evolution of $\boldsymbol{E}_{\mathrm{F}2}$ beam versus the frequency detuning $\boldsymbol{E}_{\mathrm{p}1}$. Since $\boldsymbol{E}_2'$ is just below the $\boldsymbol{E}_{\mathrm{F}2}$ beam, the FWM signal beam is vertically split by $\boldsymbol{E}_2'$, as shown in Fig. 7.18 (a). Correspondingly, the peak separation number in the $\boldsymbol{E}_{\mathrm{F}2}$ beam profiles increases from one to three while the nonlinear refractive index $|n_2|$ changes from the minimum to the maximum. There is no peak separation at the resonant frequency where n_2 approximates to zero. Apparently, when $|n_2|$ reaches the largest, we can obtain strong peak separation.

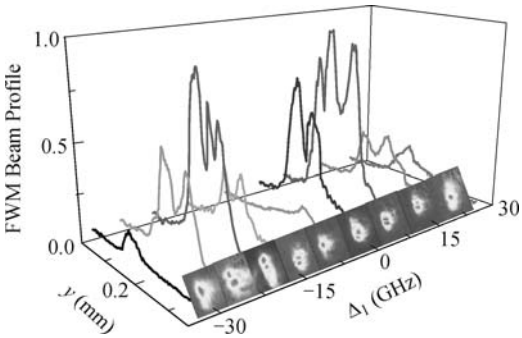

Fig. 7.19. $\boldsymbol{E}_{\mathrm{F}2}$ beam profiles versus Δ_1 at 250 °C in a V-type three-level system. The parameters are $\Delta_2 = 0$, $G_1' = 0$ ($\boldsymbol{E}_1'$is blocked), $G_3 = 0.1$ GHz, $G_2 = 1.9$ GHz, $G_2' = 20.8$ GHz.

Figure 7.20 shows the spatial splitting of the $\boldsymbol{E}_{\mathrm{F}2}$ beam profile when $\boldsymbol{E}_1'$ increases gradually. In fact, according to $\rho_{\mathrm{F}2} = -\mathrm{i}G_3G_2'^2/(d_1d_2d_3)$, we can see that $\boldsymbol{E}_{F2}$ is suppressed when $\boldsymbol{E}_1'$ becomes stronger. The reason is that $\boldsymbol{E}_1'$ breaks the resonance levels $|0\rangle$ and $|2\rangle$ into dressed-state $|\pm\rangle$ respectively, as shown in Fig. 7.18 (c). Moreover, when $\boldsymbol{E}_1'$ is small and $\boldsymbol{E}_{\mathrm{F}2}$ is partly overlaped with the laser beam $\boldsymbol{E}_2'$, the $\boldsymbol{E}_{\mathrm{F}2}$ beam splits into two asymmetric parts (the square, circle, and triangle curves). When $\boldsymbol{E}_1'$ is strong enough, the

$\boldsymbol{E}_{\mathrm{F2}}$ beam has down a shift induced by $\boldsymbol{E}_1'$ and overlap $\boldsymbol{E}_2'$. Thus the splitting of the FWM beam will be more balance, and two splitting parts turn almost the same at $G_1' = 20.6$ GHz (diamond curve).

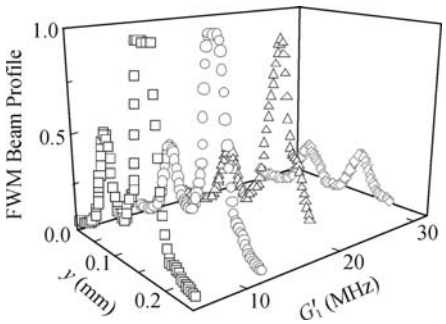

Fig. 7.20. $\boldsymbol{E}_{\mathrm{F2}}$ beam profiles with $G_1' = 6.8$ GHz (square), 13.8GHz (circle), 19.7 GHz (triangle) and 20.6 GHz (diamond) at 265 °C in a V-type three-level system. The other parameters are $\Delta_1 = 17$ GHz, $\Delta_2 = 0$, $G_3 = 0.1$ GHz, $G_2 = 1.5$ GHz, $G_2' = 10$ GHz.

As it is known, the temperature influences the atomic density in the vapor medium which is proportional to the propagation distance z in $\phi_{NL}(z, x) = 2k_{F2}n_2Ie^{-(w_0'x)^2}z/n_{0(F2)}$. With increasing temperature, ϕ_{NL} becomes larger, which indicates more spatial splitting in the FWM beam profile. To examine the temperature effect imposed on the FWM signal, the temperature in the vapor sample is increased gradually. Figure 7.21 shows intensity curves of FWM signals under different temperatures. The peak separation number of the FWM beam profiles increases as temperature rises. There are four separation peaks of the beam profile at 280 °C.

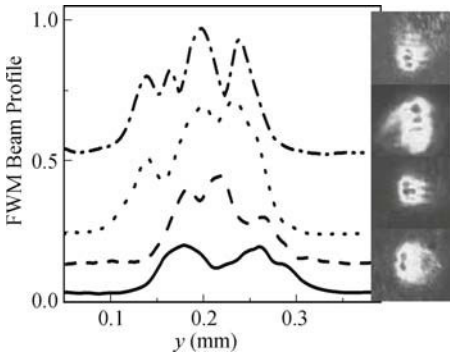

Fig. 7.21. $\boldsymbol{E}_{\mathrm{F2}}$ beam profiles in a V-type three level system at 230 °C (solid curve), 240 °C (dashed curve), 260 °C (doted curve) and 280 °C (dash doted curve). Inset: spots of $\boldsymbol{E}_{\mathrm{F2}}$ beam profile at 280 °C to 230 °C from top to bottom. The other parameters are $\Delta_1 = -10$ GHz, $\Delta_2 = 0$, $G_3 = 0.1$ GHz, $G_2 = 1.5$ GHz, $G_2' = 10$ GHz.

The different Kerr nonlinear index of refraction n_2 leads to the change of ϕ_{NL} in the spatial phase expression which is represented by spatial splitting of the FWM beam. Since the dipole moment μ_{20} of transition $|0\rangle - |2\rangle$is larger than the dipole moment μ_{10} transition $|0\rangle - |1\rangle$ we can deduce that the cross-Kerr coefficient n_2 in a two-level system is larger than that in a V-type three-level system [35 – 37]. We can see that the peak separation number of beam profile in a two-level system (solid curve) is more than that in a V-type three level system (dashed curve) for larger n_2. The inset in Fig. 7.22 shows the spatial splitting of $\boldsymbol{E}_{\mathrm{F2}}$ via n_2 in two different atomic energy-level systems at 230°C, 240°C, 260°C, and 280°C from top to bottom where all the spot-splitting in the two-level system is apparently larger than that in the V-type three-level system.

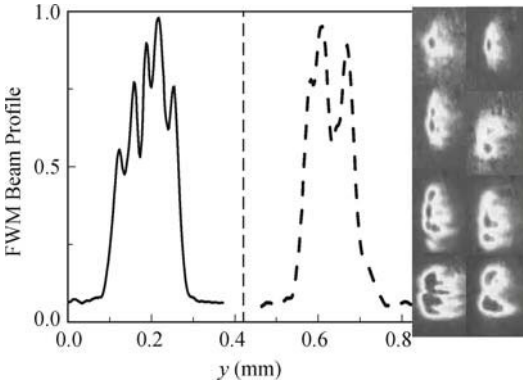

Fig. 7.22. $\boldsymbol{E}_{F2}$ beam profiles in a two-level (solid) and V-type three-level (dash) atomic systems at 260°C. Curves: Intensities of $\boldsymbol{E}_{F2}$ beams versus frequency detuning in a two-level (left) and V-type three-level (right) atomic systems at 230°C, 240°C, 260°C, and 280°C from top to bottom. The other parameters are $\Delta_1 = -10$ GHz, $\Delta_2 = 0$, $G_3 = 0.1$ GHz, $G_2 = 1.5$ GHz, $G_2' = 10$ GHz.

Above sections have shown that EISD shifts for the probe and FWM beams can be induced by the enhanced cross-Kerr nonlinear effects due to induced atomic coherence in mulit level atomic systems, which can be used as the "on" and "off" states of the spatial all-optical switch. At the same time, the opposite-direction shifting has been realized simultaneously for different FWM beams, which could be employed to construct switching/routing arrays. Also, controllable beam splitting for the degenerate and nondegenerate FWM signal beams exist in the two-level and three-level atomic systems. The spatial shift and splitting of beams can be well controlled by the intensities and frequencies of the laser beams, as well as atomic density. Further, these observed splitting can be fitted to the calculated cross-Kerr nonlinear coefficients in the systems, which provide a new and easier way to determine various cross-Kerr nonlinear coefficients in the multi-level atomic systems. The current work opens the doors for further studies on formations of spatial soliton pairs [20], spatially correlated (entangled) laser beams [15], and

storage of images [38] in multi-level coherent atomic systems.

References

[1] Wang H, Goorskey D, Xiao M. Enhanced Kerr nonlinearity via atomic coherence in a three-level atomic system. Phys Rev Lett, 2001, 87: 073601.

[2] Agrawal G P. Induced focusing of optical beams in self-defocusing nonlinear media. Phys Rev Lett, 1990, 64: 2487 – 2490.

[3] Stentz A J, Kauranen M, Maki J J, et al. Induced focusing and spatial wave breaking from cross-phase modulation in a self-defocusing medium. Opt Lett, 1992, 17: 19 – 21

[4] Hickmann J M, Gomes A S L, de Araújo C B. Observation of Spatial Cross-Phase Modulation Effects in a Self-Defocusing Nonlinear Medium. Phys Rev Lett, 1992, 68: 3547 – 3550.

[5] Desyatnikov A S, Sukhorukov A A, Kivshar Y S. Azimuthons: spatially modulated vortex solitons. Phys Rev Lett, 2005, 95: 203904.

[6] Bennink R S, Wong V, Marino A M, et al. Honeycomb pattern formation by laser-beam filamentation in atomic sodium vapor. Phys Rev Lett, 2002, 88: 113901.

[7] Harris S E. Electromagnetically induced transparency. Phys Today, 1997, 50: 36 – 42.

[8] Harris S H, Yamamoto Y. Photon switching by quantum interference. Phys Rev Lett, 1998, 81: 3611 – 3614.

[9] Truscott A G, Friese M E G, Heckenberg N R, et al. Optically written waveguide in an atomic vapor. Phys Rev Lett, 1999, 82: 1438 – 1441.

[10] Jain M, Merriam A J, Xia H, et al. Efficient nonlinear frequency conversion with maximal atomic coherence. Phys Rev Lett, 1996, 77: 4326 – 4329.

[11] Firstenberg O, Shuker M, Davidson N, et al. Elimination of the diffraction of arbitrary images imprinted on slow light. Phys Rev Lett, 2009, 102: 043601.

[12] Dawes A M C, Illing L, Clark S M, et al. All-optical switching in rubidium vapor. Science, 2005, 308: 672 – 674.

[13] Li Y, Xiao M. Enhancement of nondegenerate four-wave mixing based on electromagnetically induced transparency in rubidium atoms. Opt Lett, 1996, 21: 1064 – 1066.

[14] Boyer V, Marino A M, Lett P D. Generation of spatially broadband twin beams for quantum imaging. Phys Rev Lett, 2008, 100: 143601.

[15] Boyer V, Marino A M, Pooser R C, et al. Entangled images from four-wave mixing. Science, 2008, 321: 544 – 547.

[16] Xiao M, Li Y Q, Jin S Z, et al. Measurement of dispersive properties of electromagnetically induced transparency in rubidium atoms. Phys Rev Lett, 1995, 74: 666 – 669.

[17] Zheng H B, Zhang Y P, Nie Z Q, et al. Interplay among multidressed four-wave mixing processes. Appl Phys Lett, 2008, 93: 241101; Zhang Y P, Anderson B, Brown A W, et al. Competition between two four-wave mixing channels via atomic coherence. Appl Phys Lett, 2007, 91: 061113.

[18] Nie Z Q, Zheng H B, Li P Z, et al. Interacting multiwave mixing in a five-level atomic system. Phys Rev A, 2008 77: 063829.

[19] ZhangY P, Nie Z Q, Zheng H B, et al. Electromagnetically induced spatial nonlinear dispersion of four-wave mixing. Phys Rev A, 2009, 80: 013835.

[20] Krolikowski W, Bang O. Solitons in nonlocal nonlinear media: Exact solutions. Phys Rev E, 2001, 63: 016610.

[21] ZhangY P, Khadka U, Anderson B, et al. Temporal and spatial interference between four-wave mixing and six-wave mixing channels. Phys Rev Lett, 2009, 102: 01360.

[22] Brown A M, Xiao M. All-optical switching and routing based on an electromagnetically induced absorption grating. Opt Lett, 2005, 30: 699 – 701.

[23] Yan M, Rickey E G, Zhu Y F. Observation of absorptive photon switching by quantum interference. Phys Rev A, 2001, 64: 041801.

[24] Nie Z Q, Zheng H B, Zhang YP, et al. Experimental demonstration of optical switching and routing via four-wave mixing spatial shift. Opt Express, 2010, 18: 899 – 905.

[25] Ham B S, Hemmer P R. Coherence switching in a four-level system: quantum switching. Phys Rev Lett, 2000, 84: 4080 – 4083.

[26] Zhang J P, Hernandez G, Zhu Y F. Optical switching mediated by quantum interference of Raman transitions. Opt Express, 2008, 16: 19112 – 19117.

[27] Camacho R M, Vudyasetu P K, Howell J C. Four-wave-mixing stopped light in hot atomic rubidium vapour. Nature Photonics, 2009, 3: 103 – 106.

[28] Boyd R W. Nonlinear optics. New York:Academic Press, 1992.

[29] Du S W, Wen J M, Rubin M H, et al. Four-wave mixing and biphoton generation in a two-level system. Phys Rev Lett, 2007, 98: 053601.

[30] Krolikowski W, Saffman M, Luther-Davies B, et al. Anomalous interaction of spatial solitons in photorefractive media. Phys Rev Lett, 1998, 80: 3240 – 3243.

[31] Garanovich I L, Sukhorukov A A, Kivshar Y S, et al. Surface multi-gap vector solitons. Opt Exp, 2006, 14: 4780 – 4785.

[32] Rosberg C R, Neshev D N, Krolikowski W, et al. Observation of surface gap solitons in semi-infinite waveguide arrays. Phys Rev Lett, 2006, 97: 083901.

[33] Swartzlander G A, Law C T. Optical vortex solitons observed in Kerr nonlinear media. Phys Rev Lett, 1992, 69: 2503 – 2506.

[34] Xiao Y H, Klein M, Hohensee M, et al. Slow light beam splitter. Phys Rev Lett, 2008, 101: 043601.

[35] Zhang Y P, Zuo C C, Zheng H B, et al. Controlled spatial beam splitter using four-wave-mixing images. Phys Rev A, 2009, 80: 055804.

[36] Qi Y R, Gao H, Zhang S G. Enhanced spin depolarization and storage time in a Rb vapor. Chin Phys Lett, 2009, 26: 114211.

[37] Lu X S, Chen Q F, Shi B S, et al. Generation of a non-classical correlated photon pair via spontaneous four-wave mixing in a cold atomic ensemble. Chin Phys Lett, 2009, 26: 064204.

[38] Shuker M, Firstenberg O, Pugatch R, et al. Storing images in warm atomic vapor. Phys Rev Lett, 2008, 100: 223601.

8 Spatial Modulation of Four-Wave Mixing Solitons

Since the cross-Kerr and self-Kerr nonlinearities are greatly enhanced in the multi-level electromagnetically-induced transparency (EIT) systems, the spatial diffractions of the probe, as well as the generated four-waving mixing (FWM) beams can be the compensated to form spatial solitons during their propagations. When multiple laser beams are involved, the spatial patterns can be quite complicated depending on their beam overlaps, frequency detunings, atomic density, and relative intensities. Various novel soliton patterns can appear in different parametric regions for the probe and the generated FWM beams, making the multi-level atomic systems good playground to investigate novel types of solitons, such as gap, dipole, and vortex solitons. Due to the easy access of experimental parameters in the multi-level EIT system, the soiton patterns can be easily controlled, so the transition from one type of solion pattern to another can be experimentally observed. Such easy controllability provides a platform for comparisons between theoratical models and experimental observations. Controlling spatial solitons can find important applications in imaging storage, processing, and communication.

8.1 Basic Theory

In the previous section, we have shown the simple theoretical treatment of the cross-Kerr nonlinear index of refraction dressed by one strong coupling field for two- and three-level atomic systems; in this section, the calculation of the self-Kerr and the cross-Kerr nonlinear index of refractions dressed by two different strong coupling fields, the inner dressing field and the outer dressing field, in a two-level atomic system, a V-type and a ladder-type three-level atomic system. On the other hand, exact analytical solutions of bright and dark spatial solitons to one-dimensional the nonlinear propagation equation in Kerr media have been presented.

8.1.1 Calculation of Double Dressed Cross-Kerr Nonlinear Index of Refraction

In the two-level atomic system, V-type and ladder-type three-level atomic systems of Fig. 8.1, there exist two types of strong coupling fields, or dressing fields, to influence the probe field E_1. The first one is the inner dressing field E_1', it comes from the same laser as the probe field E_1. They both couple levels $|0\rangle$ and $|1\rangle$ and have the same frequency detuning $\Delta_1 = \Omega_1 - \omega_1$, where Ω_i is the resonant frequency and ω_i is the laser frequency. The second one is the outer dressing field E_2. It comes from the different laser and has the different detuning Δ_2 from the weak probe field E_1.

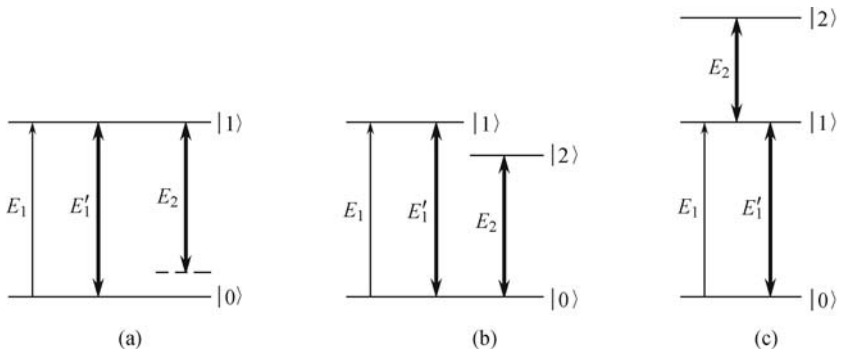

Fig. 8.1. Sketches of the (a) two-level atomic system, (b) a V-type, and (c) a ladder-type three-level atomic systems. E_1 is the weak probe field, E_1' is the strong inner dressing field and E_2 is the strong outer field corresponding to the probe field.

First we consider a two-level system, as shown in Fig. 8.1 (a). The inner dressing field E_1' and the outer dressing field E_2 both couple levels $|0\rangle$ and $|1\rangle$ and the outer dressing field E_2 has the frequency detuing $\Delta_2 = \Omega_1 - \omega_2$. For this system, the following equations are derived for the slowly varying density matrix elements:

$$\begin{cases} \dfrac{\partial \rho_{00}^{(r)}}{\partial t} = -\Gamma_{00}\rho_{00}^{(r)} - iG_1\rho_{01}^{(r)} + iG_1^*\rho_{10}^{(r)}, \\ \dfrac{\partial \rho_{11}^{(r)}}{\partial t} = -\Gamma_{11}\rho_{11}^{(r)} - iG_1^*\rho_{10}^{(r)} + iG_1\rho_{01}^{(r)}, \\ \dfrac{\partial \rho_{10}^{(r)}}{\partial t} = -[i\Delta_1 + \Gamma_{10}]\rho_{10}^{(r)} - iG_1\rho_{11}^{(r)} + iG_1\rho_{00}^{(r)}, \end{cases} \tag{8.1}$$

where G_i is the Rabi frequency, Γ_{ii} is the longitudinal relaxation, and Γ_{ij} is the transverse relaxation from $|i\rangle$ to $|j\rangle$. A self-Kerr process of the probe field E_1 can be simply presented via the four perturbation chains:

$$\begin{cases} \rho_{00}^{(0)} \xrightarrow{E_1} \rho_{10}^{(1)} \xrightarrow{E_1^*} \rho_{00}^{(2)} \xrightarrow{E_1} \rho_{10}^{(3)}, \\ \rho_{00}^{(0)} \xrightarrow{E_1^*} \rho_{01}^{(1)} \xrightarrow{E_1} \rho_{00}^{(2)} \xrightarrow{E_1} \rho_{10}^{(3)}, \\ \rho_{00}^{(0)} \xrightarrow{E_1} \rho_{10}^{(1)} \xrightarrow{E_1^*} \rho_{11}^{(2)} \xrightarrow{E_1} \rho_{10}^{(3)}, \\ \rho_{00}^{(0)} \xrightarrow{E_1^*} \rho_{01}^{(1)} \xrightarrow{E_1} \rho_{11}^{(2)} \xrightarrow{E_1} \rho_{10}^{(3)}. \end{cases} \tag{8.2}$$

Then we consider the dressing effect of the strong inner dressing field E_1' which dresses both the energy levels $|0\rangle$ and $|1\rangle$ to create dressed states $|+\rangle$ and $|-\rangle$, respectively, and the dressing effect of the strong outer dressing field E_2 which only dresses the energy level $|1\rangle$ to create dressed states $|+\rangle$ and $|-\rangle$. The dressed self-Kerr nonlinear processes can be described as

$$\begin{cases} \rho_{00}^{(0)} \xrightarrow{E_1} \rho_{1\pm0\pm}^{(1)} \xrightarrow{E_1^*} \rho_{0\pm0\pm}^{(2)} \xrightarrow{E_1} \rho_{1\pm0\pm}^{(3)}, \\ \rho_{00}^{(0)} \xrightarrow{E_1^*} \rho_{0\pm1\pm}^{(1)} \xrightarrow{E_1} \rho_{0\pm0\pm}^{(2)} \xrightarrow{E_1} \rho_{1\pm0\pm}^{(3)}, \\ \rho_{00}^{(0)} \xrightarrow{E_1} \rho_{1\pm0\pm}^{(1)} \xrightarrow{E_1^*} \rho_{1\pm1\pm}^{(2)} \xrightarrow{E_1} \rho_{1\pm0\pm}^{(3)}, \\ \rho_{00}^{(0)} \xrightarrow{E_1^*} \rho_{0\pm1\pm}^{(1)} \xrightarrow{E_1} \rho_{1\pm1\pm}^{(2)} \xrightarrow{E_1} \rho_{1\pm0\pm}^{(3)}, \end{cases} \tag{8.3}$$

where $\rho_{1\pm0\pm}$ represents the dressing the chain

$$\rho_{10} \xrightarrow{E_1'^*} \rho_{00} \xrightarrow{E_1'} \rho_{10} \xrightarrow{E_2^*} \rho_{00} \xrightarrow{E_2} \rho_{10} \xrightarrow{E_1'^*} \rho_{11} \xrightarrow{E_1'} \rho_{10}, \tag{8.4}$$

$\rho_{0\pm1\pm}$ represents the dressing the chain

$$\rho_{01} \xrightarrow{E_1'} \rho_{11} \xrightarrow{E_1'^*} \rho_{01} \xrightarrow{E_1'} \rho_{00} \xrightarrow{E_1'^*} \rho_{01} \xrightarrow{E_2} \rho_{00} \xrightarrow{E_2^*} \rho_{01}, \tag{8.5}$$

$\rho_{0\pm0\pm}$ represents the dressing the chain

$$\rho_{00} \xrightarrow{E_1'^*} \rho_{01} \xrightarrow{E_1'} \rho_{00} \xrightarrow{E_1'} \rho_{10} \xrightarrow{E_1'^*} \rho_{00},$$

$\rho_{1\pm1\pm}$ represents the dressing the chain

$$\rho_{11} \xrightarrow{E_1'^*} \rho_{01} \xrightarrow{E_1'} \rho_{11} \xrightarrow{E_2^*} \rho_{01} \xrightarrow{E_2} \rho_{11} \xrightarrow{E_1'} \rho_{10} \xrightarrow{E_1'^*} \rho_{11} \xrightarrow{E_2} \rho_{10} \xrightarrow{E_2^*} \rho_{11}. \tag{8.6}$$

Under the condition that the coupling field is much stronger than the probe field and $\rho_{00}^{(0)} \approx 1$, equations can be solved together with chains to give

$$\rho_{10}^{(3)} = \frac{-\mathrm{i}G_1|G_1|^2}{F_1}\left(\frac{1}{F_1^*}+\frac{1}{F_1}\right)\left(\frac{1}{F_2}+\frac{1}{F_3}\right), \tag{8.7}$$

where

$$\begin{cases} F_1 = (\Gamma_{10} + \mathrm{i}\Delta_1) + \dfrac{|G_1'|^2}{\Gamma_{00}} + \dfrac{|G_2|^2}{\Gamma_{00} + \mathrm{i}(\Delta_1 - \Delta_2)} + \dfrac{|G_1'|^2}{\Gamma_{11}}, \\ F_2 = \Gamma_{00} + \dfrac{|G_1'|^2}{\Gamma_{10} + \mathrm{i}\Delta_1} + \dfrac{|G_1'|^2}{\Gamma_{01} - \mathrm{i}\Delta_1}, \\ F_3 = \Gamma_{11} + \dfrac{|G_1'|^2}{\Gamma_{10} + \mathrm{i}\Delta_1} + \dfrac{|G_1'|^2}{\Gamma_{01} - \mathrm{i}\Delta_1} + \dfrac{|G_2|^2}{\Gamma_{10} + \mathrm{i}\Delta_2} + \dfrac{|G_2|^2}{\Gamma_{01} - \mathrm{i}\Delta_2}. \end{cases} \tag{8.8}$$

On the other hand, the cross-Kerr process of the probe field E_1 induced by the strong coupling field E_1' can be simply presented via the four perturbation chains:

$$\begin{cases} \rho_{00}^{(0)} \xrightarrow{E_1'} \rho_{10}^{(1)} \xrightarrow{E_1'^*} \rho_{00}^{(2)} \xrightarrow{E_1} \rho_{10}^{(3)}, \\ \rho_{00}^{(0)} \xrightarrow{E_1'^*} \rho_{01}^{(1)} \xrightarrow{E_1'} \rho_{00}^{(2)} \xrightarrow{E_1} \rho_{10}^{(3)}, \\ \rho_{00}^{(0)} \xrightarrow{E_1'} \rho_{10}^{(1)} \xrightarrow{E_1'^*} \rho_{11}^{(2)} \xrightarrow{E_1} \rho_{10}^{(3)}, \\ \rho_{00}^{(0)} \xrightarrow{E_1'^*} \rho_{01}^{(1)} \xrightarrow{E_1'} \rho_{11}^{(2)} \xrightarrow{E_1} \rho_{10}^{(3)}. \end{cases} \tag{8.9}$$

Then we consider the dressing effect of the strong inner dressing field E_1' and the strong outer dressing field E_2. The dressed cross-Kerr nonlinear processes can be described as

$$\begin{cases} \rho_{00}^{(0)} \xrightarrow{E_1'} \rho_{1\pm0\pm}^{(1)} \xrightarrow{E_1'^*} \rho_{0\pm0\pm}^{(2)} \xrightarrow{E_1} \rho_{1\pm0\pm}^{(3)}, \\ \rho_{00}^{(0)} \xrightarrow{E_1'^*} \rho_{0\pm1\pm}^{(1)} \xrightarrow{E_1'} \rho_{0\pm0\pm}^{(2)} \xrightarrow{E_1} \rho_{1\pm0\pm}^{(3)}, \\ \rho_{00}^{(0)} \xrightarrow{E_1'} \rho_{1\pm0\pm}^{(1)} \xrightarrow{E_1'^*} \rho_{1\pm1\pm}^{(2)} \xrightarrow{E_1} \rho_{1\pm0\pm}^{(3)}, \\ \rho_{00}^{(0)} \xrightarrow{E_1'^*} \rho_{0\pm1\pm}^{(1)} \xrightarrow{E_1'} \rho_{1\pm1\pm}^{(2)} \xrightarrow{E_1} \rho_{1\pm0\pm}^{(3)}. \end{cases} \tag{8.10}$$

Under the condition that the coupling field is much stronger than the probe field and $\rho_{00}^{(0)} \approx 1$, equations can be solved together with chains to give

$$\rho_{10}^{(3)} = \frac{-\mathrm{i}G_1|G_1'|^2}{F_1} \left(\frac{1}{F_1^*} + \frac{1}{F_1}\right) \left(\frac{1}{F_2} + \frac{1}{F_3}\right). \tag{8.11}$$

Third, the cross-Kerr process of the probe field E_1 induced by the strong coupling field E_2 can be simply presented via the four perturbation the chain:

$$\rho_{00}^{(0)} \xrightarrow{E_1} \rho_{10}^{(1)} \xrightarrow{E_2^*} \rho_{00}^{(2)} \xrightarrow{E_2} \rho_{10}^{(3)}. \tag{8.12}$$

The dressed cross-Kerr nonlinear processes can be described as

$$\rho_{00}^{(0)} \xrightarrow{E_1} \rho_{1\pm0\pm}^{(1)} \xrightarrow{E_2^*} \rho_{0\pm0\pm}^{(2)} \xrightarrow{E_2} \rho_{1\pm0\pm}^{(3)}. \tag{8.13}$$

We can obtain

$$\rho_{10}^{(3)} = \frac{-\mathrm{i}G_1|G_2|^2}{F_1^2 F_4}, \tag{8.14}$$

where

$$F_4 = \Gamma_{00} + \mathrm{i}(\Delta_1 - \Delta_2) + \frac{|G_1'|^2}{\Gamma_{10} + \mathrm{i}(2\Delta_1 - \Delta_2)} + \frac{|G_1'|^2}{\Gamma_{01} - \mathrm{i}\Delta_2}. \tag{8.15}$$

Similarly, for a V-type three-level system, as shown in Fig. 8.1 (b), the strong coupling fields E_2 couples levels $|0\rangle$ and $|2\rangle$ with the frequency detuning $\Delta_2 = \Omega_2 - \omega_2$. For this system the following equations are

$$\begin{cases} \dfrac{\partial \rho_{00}^{(r)}}{\partial t} = -\Gamma_{00}\rho_{00}^{(r)} - \mathrm{i}G_2\rho_{02}^{(r)} + \mathrm{i}G_2^*\rho_{20}^{(r)} + \mathrm{i}G_1^*\rho_{10}^{(r)} - \mathrm{i}G_1\rho_{01}^{(r)}, \\ \dfrac{\partial \rho_{11}^{(r)}}{\partial t} = -\Gamma_{11}\rho_{11}^{(r)} - \mathrm{i}G_1^*\rho_{10}^{(r)} - \mathrm{i}G_2\rho_{12}^{(r)} + \mathrm{i}G_1\rho_{01}^{(r)} + \mathrm{i}G_2^*\rho_{21}^{(r)}, \\ \dfrac{\partial \rho_{10}^{(r)}}{\partial t} = -[\mathrm{i}\Delta_1 + \Gamma_{10}]\rho_{10}^{(r)} - \mathrm{i}G_1\rho_{11}^{(r)} - \mathrm{i}G_2\rho_{12}^{(r)} + \mathrm{i}G_1\rho_{00}^{(r)}, \\ \dfrac{\partial \rho_{20}^{(r)}}{\partial t} = -[\mathrm{i}\Delta_2 + \Gamma_{20}]\rho_{20}^{(r)} - \mathrm{i}G_1\rho_{21}^{(r)} - \mathrm{i}G_2\rho_{22}^{(r)} + \mathrm{i}G_2\rho_{00}^{(r)}, \\ \dfrac{\partial \rho_{21}^{(r)}}{\partial t} = -[\mathrm{i}(-\Delta_1 + \Delta_2) + \Gamma_{21}]\rho_{21}^{(r)} - \mathrm{i}G_1^*\rho_{20}^{(r)} + \mathrm{i}G_2\rho_{01}^{(r)}, \\ \dfrac{\partial \rho_{22}^{(r)}}{\partial t} = -\Gamma_{22}\rho_{22}^{(r)} - \mathrm{i}G_2^*\rho_{20}^{(r)} + \mathrm{i}G_2\rho_{02}^{(r)}. \end{cases} \tag{8.16}$$

The self-Kerr process of the probe field E_1 is the same as that in the two-level system. If we consider the dressing effect of the strong coupling field E_2, the energy levels $|0\rangle$ is dressed to create dressed states $|+\rangle$ and $|-\rangle$, respectively. In the dressed self-Kerr nonlinear processes, $\rho_{1\pm0\pm}$ represents the dressing the chain

$$\rho_{10} \xrightarrow{E_1'^*} \rho_{00} \xrightarrow{E_1'} \rho_{10} \xrightarrow{E_1'^*} \rho_{11} \xrightarrow{E_1'} \rho_{10} \xrightarrow{E_2^*} \rho_{12} \xrightarrow{E_2} \rho_{10}, \tag{8.17}$$

$\rho_{0\pm1\pm}$ represents the dressing the chain

$$\rho_{01} \xrightarrow{E_1'} \rho_{11} \xrightarrow{E_1'^*} \rho_{01} \xrightarrow{E_2} \rho_{21} \xrightarrow{E_2^*} \rho_{01} \xrightarrow{E_1'} \rho_{00} \xrightarrow{E_1'^*} \rho_{01}, \tag{8.18}$$

$\rho_{0\pm0\pm}$ represents the dressing the chain

$$\begin{aligned} &\rho_{00} \xrightarrow{E_1'^*} \rho_{01} \xrightarrow{E_1'} \rho_{00} \xrightarrow{E_2^*} \rho_{02} \xrightarrow{E_2} \rho_{00} \xrightarrow{E_1'} \rho_{10} \xrightarrow{E_1'^*} \rho_{00} \\ &\xrightarrow{E_2} \rho_{20} \xrightarrow{E_2^*} \rho_{00}, \end{aligned} \tag{8.19}$$

$\rho_{1\pm1\pm}$ represents the dressing the chain

$$\rho_{11} \xrightarrow{E_1'^*} \rho_{01} \xrightarrow{E_1'} \rho_{11} \xrightarrow{E_1'} \rho_{10} \xrightarrow{E_1'^*} \rho_{11}. \tag{8.20}$$

Under the condition that the coupling field is much stronger than the probe field and $\rho_{00}^{(0)} \approx 1$, equations can be solved together with chains to give

$$\rho_{10}^{(3)} = \frac{-\mathrm{i}G_1|G_1|^2}{F_5}\left(\frac{1}{F_5^*}+\frac{1}{F_5}\right)\left(\frac{1}{F_6}+\frac{1}{F_7}\right), \tag{8.21}$$

where

$$\begin{cases} F_5 = (\Gamma_{10}+\mathrm{i}\Delta_1) + \dfrac{|G_1'|^2}{\Gamma_{00}} + \dfrac{|G_2|^2}{\Gamma_{12}+\mathrm{i}(\Delta_1-\Delta_2)} + \dfrac{|G_1'|^2}{\Gamma_{11}}, \\ F_6 = \Gamma_{00} + \dfrac{|G_1'|^2}{\Gamma_{10}+\mathrm{i}\Delta_1} + \dfrac{|G_1'|^2}{\Gamma_{01}-\mathrm{i}\Delta_1} + \dfrac{|G_2|^2}{\Gamma_{02}-\mathrm{i}\Delta_2} + \dfrac{|G_2|^2}{\Gamma_{12}+\mathrm{i}\Delta_2}, \\ F_7 = \Gamma_{11} + \dfrac{|G_1'|^2}{\Gamma_{10}+\mathrm{i}\Delta_1} + \dfrac{|G_1'|^2}{\Gamma_{01}-\mathrm{i}\Delta_1}. \end{cases} \tag{8.22}$$

On the other hand, the cross-Kerr process of the probe field E_1 induced by the strong coupling field E_1' is the same as that in the two-level system, and the dressed cross-Kerr nonlinear process can be solved to give

$$\rho_{10}^{(3)} = \frac{-\mathrm{i}G_1|G_1'|^2}{F_5}\left(\frac{1}{F_5^*}+\frac{1}{F_5}\right)\left(\frac{1}{F_6}+\frac{1}{F_7}\right). \tag{8.23}$$

A cross-Kerr process of the weak probe field E_1 induced by the strong coupling field E_2 can be simply presented via the two perturbation chains:

$$\begin{cases} \rho_{00}^{(0)} \xrightarrow{E_2} \rho_{20}^{(1)} \xrightarrow{E_2^*} \rho_{00}^{(2)} \xrightarrow{E_1} \rho_{10}^{(3)}, \\ \rho_{00}^{(0)} \xrightarrow{E_2^*} \rho_{02}^{(1)} \xrightarrow{E_2} \rho_{00}^{(2)} \xrightarrow{E_1} \rho_{10}^{(3)}. \end{cases} \tag{8.24}$$

The dressed cross-Kerr nonlinear processes can be described as

$$\begin{cases} \rho_{00}^{(0)} \xrightarrow{E_2} \rho_{20\pm}^{(1)} \xrightarrow{E_2^*} \rho_{0\pm0\pm}^{(2)} \xrightarrow{E_1} \rho_{1\pm0\pm}^{(3)}, \\ \rho_{00}^{(0)} \xrightarrow{E_2^*} \rho_{0\pm2}^{(1)} \xrightarrow{E_2} \rho_{0\pm0\pm}^{(2)} \xrightarrow{E_1} \rho_{1\pm0\pm}^{(3)}, \end{cases} \tag{8.25}$$

where $\rho_{20\pm}$ represents the dressing the chain

$$\rho_{20} \xrightarrow{E_1'^*} \rho_{21} \xrightarrow{E_1'} \rho_{20} \xrightarrow{E_2^*} \rho_{22} \xrightarrow{E_2} \rho_{20}, \tag{8.26}$$

$\rho_{0\pm2}$ represents the dressing the chain

$$\rho_{02} \xrightarrow{E_1'} \rho_{12} \xrightarrow{E_1'^*} \rho_{02} \xrightarrow{E_2} \rho_{22} \xrightarrow{E_2^*} \rho_{02}. \tag{8.27}$$

Under the condition that the coupling field is much stronger than the probe field and $\rho_{00}^{(0)} \approx 1$, equations can be solved together with chains to give

$$\rho_{10}^{(3)} = \frac{-\mathrm{i}G_1|G_2|^2}{F_5 F_6}\left(\frac{1}{F_8} + \frac{1}{F_8^*}\right), \tag{8.28}$$

where

$$F_8 = (\Gamma_{20} + \mathrm{i}\Delta_2) + \frac{G_2^2}{\Gamma_{22}} + \frac{G_1'^2}{\Gamma_{21} + \mathrm{i}(\Delta_2 - \Delta_1)}. \tag{8.29}$$

At last, for a ladder-type three-level system, as shown in Fig. 8.1(c), the strong coupling fields E_2 couples levels $|1\rangle$ and $|2\rangle$ with the frequency detuning Δ_2. For this system, the following equations are

$$\begin{cases} \dfrac{\partial \rho_{00}^{(r)}}{\partial t} = -\Gamma_{00}\rho_{00}^{(r)} - \mathrm{i}G_2\rho_{02}^{(r)} + \mathrm{i}G_2^*\rho_{20}^{(r)} + \mathrm{i}G_1^*\rho_{10}^{(r)} - \mathrm{i}G_1\rho_{01}^{(r)}, \\ \dfrac{\partial \rho_{11}^{(r)}}{\partial t} = -\Gamma_{11}\rho_{11}^{(r)} - \mathrm{i}G_1^*\rho_{10}^{(r)} - \mathrm{i}G_2\rho_{12}^{(r)} + \mathrm{i}G_1\rho_{01}^{(r)} + \mathrm{i}G_2^*\rho_{21}^{(r)}, \\ \dfrac{\partial \rho_{10}^{(r)}}{\partial t} = -[\mathrm{i}\Delta_1 + \Gamma_{10}]\rho_{10}^{(r)} - \mathrm{i}G_1\rho_{11}^{(r)} - \mathrm{i}G_2\rho_{12}^{(r)} + \mathrm{i}G_1\rho_{00}^{(r)}, \\ \dfrac{\partial \rho_{20}^{(r)}}{\partial t} = -[\mathrm{i}\Delta_2 + \Gamma_{20}]\rho_{20}^{(r)} - \mathrm{i}G_1\rho_{21}^{(r)} - \mathrm{i}G_2\rho_{22}^{(r)} + \mathrm{i}G_2\rho_{00}^{(r)}, \\ \dfrac{\partial \rho_{21}^{(r)}}{\partial t} = -[\mathrm{i}\Delta_2 + \Gamma_{21}]\rho_{21}^{(r)} - \mathrm{i}G_1^*\rho_{20}^{(r)} - \mathrm{i}G_2\rho_{22}^{(r)} + \mathrm{i}G_2\rho_{11}^{(r)}, \\ \dfrac{\partial \rho_{22}^{(r)}}{\partial t} = -\Gamma_{22}\rho_{22}^{(r)} - \mathrm{i}G_2^*\rho_{21}^{(r)} + \mathrm{i}G_2\rho_{12}^{(r)}. \end{cases} \tag{8.30}$$

The self-Kerr process of the probe field E_1 is the same as that in the two-level system. If we consider the dressing effect of the strong coupling field E_2, the energy levels $|1\rangle$ is dressed to create dressed states $|+\rangle$ and $|-\rangle$, respectively. In the dressed self-Kerr nonlinear processes, where $\rho_{1\pm0\pm}$ represents the dressing the chain

$$\rho_{10} \xrightarrow{E_1'^*} \rho_{00} \xrightarrow{E_1'} \rho_{10} \xrightarrow{E_2} \rho_{20} \xrightarrow{E_2^*} \rho_{10} \xrightarrow{E_1'^*} \rho_{11} \xrightarrow{E_1'} \rho_{10}, \tag{8.31}$$

$\rho_{0\pm1\pm}$ represents the dressing the chain

$$\rho_{01} \xrightarrow{E_1'} \rho_{11} \xrightarrow{E_1'^*} \rho_{01} \xrightarrow{E_1'} \rho_{00} \xrightarrow{E_1'^*} \rho_{01} \xrightarrow{E_2^*} \rho_{02} \xrightarrow{E_2} \rho_{01}, \tag{8.32}$$

$\rho_{0\pm0\pm}$ represents the dressing the chain

$$\rho_{00} \xrightarrow{E_1'^*} \rho_{01} \xrightarrow{E_1'} \rho_{00} \xrightarrow{E_1'} \rho_{10} \xrightarrow{E_1'^*} \rho_{00}, \tag{8.33}$$

$\rho_{1\pm1\pm}$ represents the dressing the chain

$$\rho_{11} \xrightarrow{E_1'^*} \rho_{01} \xrightarrow{E_1'} \rho_{11} \xrightarrow{E_2} \rho_{21} \xrightarrow{E_2^*} \rho_{10} \xrightarrow{E_1'} \rho_{10} \xrightarrow{E_1'^*} \rho_{11} \xrightarrow{E_2^*} \rho_{12} \xrightarrow{E_2} \rho_{10}. \tag{8.34}$$

Under the condition that the coupling field is much stronger than the probe field and $\rho_{00}^{(0)} \approx 1$, equations can be solved together with chains to give

$$\rho_{10}^{(3)} = \frac{-\mathrm{i}G_1|G_1|^2}{F_9}\left(\frac{1}{F_9^*}+\frac{1}{F_9}\right)\left(\frac{1}{F_{10}}+\frac{1}{F_{11}}\right), \tag{8.35}$$

where

$$\begin{cases} F_9 = (\Gamma_{10}+\mathrm{i}\Delta_1) + \dfrac{|G_1'|^2}{\Gamma_{00}} + \dfrac{|G_2|^2}{\Gamma_{20}+\mathrm{i}(\Delta_1+\Delta_2)} + \dfrac{|G_1'|^2}{\Gamma_{11}}, \\ F_{10} = \Gamma_{00} + \dfrac{|G_1'|^2}{\Gamma_{10}+\mathrm{i}\Delta_1} + \dfrac{|G_1'|^2}{\Gamma_{01}-\mathrm{i}\Delta_1}, \\ F_{11} = \Gamma_{11} + \dfrac{|G_1'|^2}{\Gamma_{10}+\mathrm{i}\Delta_1} + \dfrac{|G_1'|^2}{\Gamma_{01}-\mathrm{i}\Delta_1} + \dfrac{|G_2|^2}{\Gamma_{21}+\mathrm{i}\Delta_2} + \dfrac{|G_2|^2}{\Gamma_{12}-\mathrm{i}\Delta_2}. \end{cases} \tag{8.36}$$

On the other hand, the cross-Kerr process of the probe field E_1 induced by the strong coupling field E_1' is the same as before, and the dressed cross-Kerr nonlinear process can be solved to give

$$\rho_{10}^{(3)} = \frac{-\mathrm{i}G_1|G_1'|^2}{F_9}\left(\frac{1}{F_9^*}+\frac{1}{F_9}\right)\left(\frac{1}{F_{10}}+\frac{1}{F_{11}}\right). \tag{8.37}$$

A cross-Kerr process of the probe field E_1 induced by the strong coupling field E_2 can be simply presented via the perturbation the chain

$$\rho_{00}^{(0)} \xrightarrow{E_1} \rho_{10}^{(2)} \xrightarrow{E_2} \rho_{20}^{(2)} \xrightarrow{E_2^*} \rho_{10}^{(3)}. \tag{8.38}$$

The dressed cross-Kerr nonlinear processes can be described as

$$\rho_{00}^{(0)} \xrightarrow{E_1} \rho_{1\pm0\pm}^{(2)} \xrightarrow{E_2} \rho_{20\pm}^{(2)} \xrightarrow{E_2^*} \rho_{1\pm0\pm}^{(3)}. \tag{8.39}$$

Under the condition that the coupling field is much stronger than the probe field and $\rho_{00}^{(0)} \approx 1$, equations can be solved together with chains to give

$$\rho_{10}^{(3)} = \frac{-\mathrm{i}G_1|G_2|^2}{F_9^2[\Gamma_{20}+\mathrm{i}(\Delta_1+\Delta_2)+G_1'^2/(\Gamma_{21}+\mathrm{i}\Delta_2)]}. \tag{8.40}$$

8.1.2 Calculation of Analytical Solution of One-dimensional Bright and Dark Spatial Solitons

The nonlinear Schrodinger equation is the main equation which describes the evolution of optical fields in a nonlinear medium. We consider the nonlinear Schrodinger equation which governs the evolution for a continuous

wave beam propagating inside a nonlinear optical medium with Kerr nonlinearity. We assume the two copropagating beams propagate along the z-axis and diffract along the two transverse directions x-and y-axis. In the paraxial approximation, we take the equation form

$$\frac{\partial A_1}{\partial z} - \frac{\mathrm{i}}{2k_1}\left(\frac{\partial^2 A_1}{\partial x^2} + \frac{\partial^2 A_1}{\partial y^2}\right) = \frac{\mathrm{i}k_1}{n_1}\left[n_2^S|A_1|^2 + n_2^X A_2\right] A_1, \tag{8.41}$$

where A_1 and A_2 are the slowly varying envelope amplitude of the probe, and the copropagating field, $k_1 = 2\pi n_1/\lambda_1$ and n_1 is the linear refractive index at the wavelength λ_1. The nonlinearity coefficient n_2^S is the self-Kerr coefficient of the probe field and n_2^X is the cross-Kerr coefficient of the probe field induced by the copropagating field. Since it is hand to solve two-dimension equations, we allow the probe beam diffract only along the x direction and introduce the normalized variables

$$\xi = \frac{x}{w_0}, \quad Z = \frac{z}{k_1 w_0^2}, \quad U_1 = \frac{A_1}{I_1^{1/2}}, \quad U_2 = \frac{A_2}{I_1^{1/2}}, \tag{8.42}$$

where w_0 is the spot size, and I_1 is the peak intensity of the probe beam. For simplicity, we consider the cross-Kerr term is constant, i.e., $g = n_2^X|U_2|^2$. Equation 8.42 can be written as

$$\frac{\partial U_1}{\partial Z} - \frac{\mathrm{i}\partial^2 U_1}{2\partial\xi^2} = \frac{\mathrm{i}k_1^2 w_0^2 I_1}{n_1}\left[n_2^S|U_1|^2 + g\right] U_1. \tag{8.43}$$

Let us consider a self-focusing nonlinearity which corresponds to $n_2^S > 0$. We search for the bright soliton solution to Eq. 8.43 with the form

$$U_1 = u\left(\xi\right)\exp\left(\mathrm{i}\Gamma Z\right). \tag{8.44}$$

where the profile $u\left(x\right)$ is real, symmetric, and exponentially localized, Γ is the propagation constant. We substitute Eq. 8.44 into Eq. 8.43 and obtain

$$\mathrm{i}\Gamma u(\xi)\exp(\mathrm{i}\Gamma Z) - \frac{\mathrm{i}\partial^2 u(\xi)}{2\partial\xi^2}\exp(\mathrm{i}\Gamma Z) = \frac{\mathrm{i}k_1^2 w_0^2 I_1}{n_1}[n_2^S u(\xi)^2 + g]u(\xi)\exp(\mathrm{i}\Gamma Z). \tag{8.45}$$

We canceling the common factors $\mathrm{i}\exp(\mathrm{i}\Gamma Z)$ and lead to

$$\Gamma u(\xi) - \frac{\partial^2 u(\xi)}{2\partial\xi^2} = \frac{k_1^2 w_0^2 I_1}{n_1}[n_2^S u(\xi)^2 + g]u(\xi), \tag{8.46}$$

i.e.,

$$\Gamma u(\xi) - \frac{\partial^2 u(\xi)}{2\partial\xi^2} = \left[\frac{k_1^2 w_0^2 I_1 n_2^S}{n_1}u(\xi)^2 + \frac{g k_1^2 w_0^2 I_1}{n_1}\right] u(\xi). \tag{8.47}$$

We take the first term of left hand to right hand,

$$-\frac{\partial^2 u(\xi)}{2\partial\xi^2} = \left[\frac{k_1^2 w_0^2 I_1 n_2^S}{n_1}u(\xi)^2 + \frac{g k_1^2 w_0^2 I_1}{n_1} - \Gamma\right] u(\xi), \tag{8.48}$$

i.e.,

$$\frac{\partial^2 u(\xi)}{\partial \xi^2} = \left[2\left(\Gamma - \frac{gk_1^2 w_0^2 I_1}{n_1}\right) - \frac{2k_1^2 w_0^2 I_1 n_2^S}{n_1} u(\xi)^2\right] u(\xi). \tag{8.49}$$

For simplicity, we let

$$a = 2\left(\Gamma - \frac{gk_1^2 w_0^2 I_1}{n_1}\right), \quad b = \frac{2k_1^2 w_0^2 I_1 n_2^S}{n_1}. \tag{8.50}$$

Thus Eq. 8.49 can be written as

$$u'' = \left(a - bu^2\right) u. \tag{8.51}$$

Both sides of Eq. 8.51 are multiplied by $u'(x)$ and we obtain

$$u''u' = auu' - bu^3 u'. \tag{8.52}$$

Then we integrate both sides of Eq. 8.52 and have

$$\int u' \mathrm{d}u' = \int (au - bu^3) \mathrm{d}u, \tag{8.53}$$

i.e.,

$$\frac{1}{2}(u')^2 = \frac{a}{2}u^2 - \frac{b}{4}u^4 + C. \tag{8.54}$$

For the index solution, we have $C = 0$, i.e.,

$$\frac{1}{2}(u')^2 + \left(\frac{b}{4}u^2 - \frac{a}{2}\right) u^2 = 0. \tag{8.55}$$

The boundary conditions are obvious that at the beam center $\xi = 0$ the peak amplitude is u_0, i.e., $u(\xi)|_{\xi=0} = u_0$ and $\partial_\xi u|_{\xi=0} = 0$. Substitution of these equations into Eq. 8.55 leads to the relation $a = bu_0^2/2$. Hence, Eq. 8.55 can be simplified to

$$\begin{aligned}
&(u')^2 + \frac{b(u^2 - u_0^2)u^2}{2} = 0. \\
&(u')^2 = \frac{b(u_0^2 - u^2)u^2}{2}. \\
&(u')^2 = \pm u \frac{\sqrt{u_0^2 - u^2}}{\sqrt{2/b}}. \\
&\frac{\sqrt{2/b}}{u\sqrt{u_0^2 - u^2}} \mathrm{d}u = \pm \mathrm{d}\xi.
\end{aligned} \tag{8.56}$$

The expression of left hand of Eq. 8.56 is integrated as

$$\int \frac{\mathrm{d}u}{u\sqrt{(u_0^2 - u^2)}} = \int \frac{\mathrm{d}u}{uu_0\sqrt{\left(1 - \frac{u^2}{u_0^2}\right)}} = \frac{1}{u_0^2} \int \frac{\mathrm{d}u}{\frac{u}{u_0}\sqrt{\left(1 - \frac{u^2}{u_0^2}\right)}}. \tag{8.57}$$

Let $u/u_0 = \sin\theta$, thus Eq. 8.57 becomes

$$\frac{1}{u_0^2}\int \frac{u_0\cos\theta \mathrm{d}\theta}{\sin\theta\cos\theta} = \frac{1}{u_0}\int \frac{\mathrm{d}\theta}{\sin\theta} = \frac{1}{u_0}\int \frac{\sin\theta \mathrm{d}\theta}{\sin^2\theta} = -\frac{1}{u_0}\int \frac{\mathrm{d}\cos\theta}{1-\cos^2\theta}.$$

Let $\cos\theta = t$, thus we have

$$\begin{aligned} -\frac{1}{u_0}\int \frac{\mathrm{d}\cos\theta}{1-\cos^2\theta} &= \frac{1}{u_0}\int \frac{\mathrm{d}t}{t^2-1} = \frac{1}{2u_0}\int \left(\frac{1}{t-1}-\frac{1}{t+1}\right)\mathrm{d}t \\ &= \frac{1}{2u_0}\left[\ln|t-1| - \ln|t+1|\right] \\ &= \frac{1}{2u_0}\ln\left|\frac{t-1}{t+1}\right| = \frac{1}{2u_0}\ln\left|\frac{\cos\theta-1}{\cos\theta+1}\right|. \end{aligned} \tag{8.58}$$

Due to $\sin\theta = u/u_0$, we have $\cos\theta = \sqrt{u_0^2-u^2}/u_0$ and Eq. 8.58 becomes

$$\begin{aligned} \frac{1}{2u_0}\ln\left|\frac{u_0-\sqrt{u_0^2-u^2}}{u_0+\sqrt{u_0^2-u^2}}\right| &= \frac{1}{2u_0}\ln\left|\frac{u_0^2-\left(u_0^2-u^2\right)}{\left(u_0+\sqrt{u_0^2-u^2}\right)^2}\right| \\ &= \frac{1}{u_0}\ln\left|\frac{u}{u_0+\sqrt{u_0^2-u^2}}\right| \\ &= -\frac{1}{u_0}\ln\left|\frac{u_0+\sqrt{u_0^2-u^2}}{u}\right|. \end{aligned}$$

Thus, we finally obtain

$$\int \frac{\mathrm{d}u}{u\sqrt{(u_0^2-u^2)}} = -\frac{1}{u_0}\ln\left|\frac{u_0+\sqrt{u_0^2-u^2}}{u}\right|. \tag{8.59}$$

We substitute Eq. 8.59 into Eq. 8.56 and lead to the equations

$$-\frac{\sqrt{2/b}}{u_0}\ln\left|\frac{u_0+\sqrt{u_0^2-u^2}}{u}\right| = \pm\xi,$$

$$\ln\left|\frac{u_0+\sqrt{u_0^2-u^2}}{u}\right| = \pm u_0\left(b/2\right)^{1/2}\xi,$$

$$\frac{u_0+\sqrt{u_0^2-u^2}}{u} = \exp\left(\pm u_0\left(b/2\right)^{1/2}\xi\right),$$

$$\sqrt{u_0^2-u^2} = u\exp\left(u_0\left(b/2\right)^{1/2}\xi\right) - u_0,$$

$$u_0^2-u^2 = u^2\exp\left(u_0^2\left(b/2\right)\xi^2\right) + u_0^2 - 2u_0u\exp\left(u_0\left(b/2\right)^{1/2}\xi\right),$$

$$u^2 + u^2\exp\left(u_0^2\left(b/2\right)\xi^2\right) = 2u_0u\exp\left(u_0\left(b/2\right)^{1/2}\xi\right),$$

$$u + u\exp\left(u_0^2\left(b/2\right)\xi^2\right) = 2u_0\exp\left(u_0\left(b/2\right)^{1/2}\xi\right).$$

Finally, we can obtain the bright soliton solution as

$$u = \frac{2u_0 \exp\left(u_0 (b/2)^{1/2} \xi\right)}{1 + \exp\left(u_0^2 (b/2) \xi^2\right)},$$

$$u = \frac{u_0}{\left[\exp\left(-u_0 (b/2)^{1/2} \xi\right) + \exp\left(u_0 (b/2)^{1/2} \xi\right)\right]/2},$$

i.e.,

$$u = u_0 \text{sech}\left[u_0 (b/2)^{1/2} \xi\right]. \tag{8.60}$$

We substitute Eq. 8.50 into Eq. 8.60 and have the bright soliton solution of Eq. 8.43 as

$$u = u_0 \text{sech}\left[u_0 \left(\frac{k_1^2 w_0^2 I_1 n_2^S}{n_1}\right)^{1/2} \xi\right]. \tag{8.61}$$

8.2 Novel Spatial Gap Solitons of Four-Wave Mixing

As a laser beam propagates in a Kerr-type nonlinear medium, its spatial beam profile can become unchanged when the spatial diffraction is balanced by the self-focusing effect due to the self-phase modulation Kerr nonlinearity, which is generally called spatial optical solitons [1]. Also, optical solitons can form in the nonlinear media due to cross-phase modulation (XPM) in the self-defocusing regime [2, 3], in which the spatial diffraction of the beam is compensated by the strong XPM nonlinearity [4]. In recent years, many new spatial soliton effects, such as discrete solitons [5, 6], gap solitons [7], surface gap solitons [8, 9], and vortex solitons [10], have been investigated (both theoretically and experimentally) in waveguide arrays [9], fiber Bragg gratings [11], Bose-Einstein condensates [12], and photorefractive crystals [5, 6]. In achieving such interesting spatial effects, large refractive index modulations are needed either by fixed periodic structures (such as waveguide arrays and fiber Bragg grating) or reconfigurable optical lattices by laser beams as in the photorefractive crystals [7]. For example, to observe spatial gap solitons in a photorefractive crystal, two strong laser beams are used to write an optical lattice in the crystal with refractive index variation of at least 10^{-4}. When two probe Gaussian laser beams are launched into this optical lattice in the opposite directions, the two counter-propagating waves are Bragg scattered and nonlinearly coupled to generate spatial gap solitons at the output [7].

Spatial solitons were observed in atomic media many years ago [1]. In the following, we can show that by making use of the greatly enhanced Kerr nonlinearity due to atomic coherence in multi-level atomic systems [13], large refractive index modulation can be achieved with pulsed laser beams. Also, due to strongly enhanced four-wave mixing (FWM) processes in such atomic

media [14 – 18], the strong nonlinear couplings between propagating waves can easily generate modulated spatial optical solitons, or gap solitons, in the probe laser beams, as well as in the generated FWM beams. More importantly, the spatial Kerr nonlinear index of the atomic medium, and therefore, the spatial gap soliton patterns, can be easily controlled by the intensities and frequency detunings of the pump (dressing) laser beams [13, 16].

Two relevant experimental systems are shown in Fig. 8.2 (b, c). Three energy levels from Na atoms (in a heat-pipe oven) are involved in the experimental schemes. In Fig. 8.2 (c), energy levels of $|0\rangle$ $(3S_{1/2})$,$|1\rangle(3P_{1/2})$ and $|2\rangle$ $(3P_{3/2})$ form a three-level V-type atomic system. When the energy level $|2\rangle$ is not used, the system reduces into a two-level one [Fig. 8.2(b)]. The laser beams are aligned spatially as shown in Fig. 8.2(a), with two dressing beams

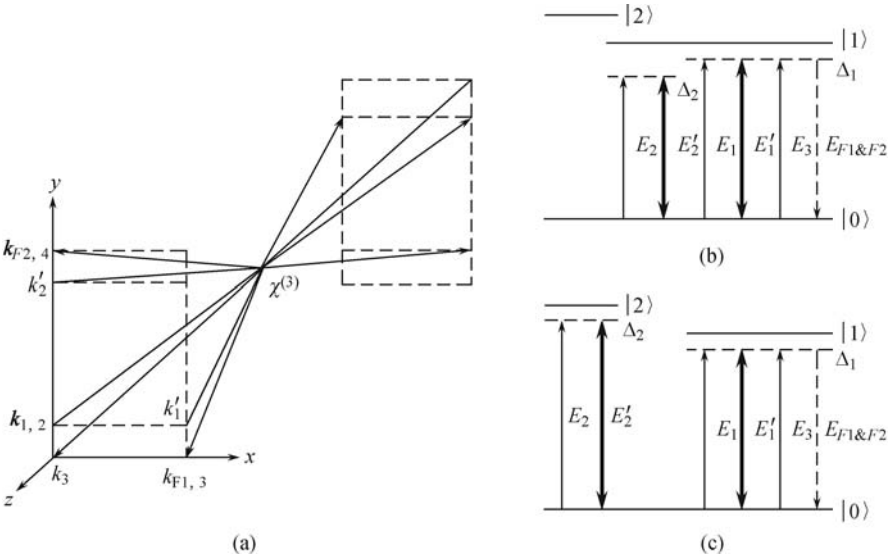

Fig. 8.2. (a) Spatial beam geometry used in the experiments. (b) The FWM processes (to generate $\boldsymbol{E}_{F2}$ or $\boldsymbol{E}_{F1}$ with two beams $\boldsymbol{E}_2$ and $\boldsymbol{E}_2'$ or $\boldsymbol{E}_1$ and $\boldsymbol{E}_1'$, respectively) in a two-level atomic system. (c) The FWM processes (to generate $\boldsymbol{E}_{F2}$ or $\boldsymbol{E}_{F1}$ with two beams $\boldsymbol{E}_2$ and $\boldsymbol{E}_2'$ or $\boldsymbol{E}_1$ and $\boldsymbol{E}_1'$, respectively) in the V-type three-level atomic system.

($\boldsymbol{E}_1'$ and $\boldsymbol{E}_2'$) and two pump beams ($\boldsymbol{E}_1$ and $\boldsymbol{E}_2$) propagating through the atomic medium in the same direction with small angles (0.3°) between them in a square-box pattern. The probe beam ($\boldsymbol{E}_3$) propagates in the opposite direction with a small angle as shown in Fig. 8.2(a). Three laser beams ($\boldsymbol{E}_1$, $\boldsymbol{E}_1'$, and $\boldsymbol{E}_3$, with Rabi frequencies G_1, G_1' and G_3, connecting transition $|0\rangle$ to $|1\rangle$) have the same frequency ω_1 (from the same laser with a 10 Hz repetition rate, 5 ns pulse-width and 0.04 cm^{-1} line-width), and generate an efficient degenerate FWM signal $\boldsymbol{E}_{F1}$ ($\boldsymbol{k}_{F1} = \boldsymbol{k}_1 - \boldsymbol{k}_1' + \boldsymbol{k}_3$) [Fig. 8.2 (b)] in the direction shown at the lower right corner of Fig. 8.2 (a). The beams $\boldsymbol{E}_2$

and $\boldsymbol{E}_2'$ (with Rabi frequencies G_2 and G_2', and connecting transition $|0\rangle$ to $|1\rangle$) are from another near-transform-limited dye laser of frequency ω_2 and form a nondegenerate FWM process to generate $\boldsymbol{E}_{F2}$ ($\boldsymbol{k}_{F2} = \boldsymbol{k}_3 + \boldsymbol{k}_2 - \boldsymbol{k}_2'$) [Fig. 8.2(b)]. When the five laser beams are all on, there also exist other two one-photon resonant nondegenerate FWM processes $\boldsymbol{k}_{F3} = \boldsymbol{k}_3 + \boldsymbol{k}_2 - \boldsymbol{k}_1'$ and $\boldsymbol{k}_{F4} = \boldsymbol{k}_3 + \boldsymbol{k}_1 - \boldsymbol{k}_2'$. However, the coexisting $\boldsymbol{E}_{F1}$ and $\boldsymbol{E}_{F2}$ are the dominant ones [14,16].

When the beams $\boldsymbol{E}_2$ and $\boldsymbol{E}_2'$ are tuned to $|0\rangle - |2\rangle$, the system becomes the three-level V-type one [Fig. 8.2 (c)], which generates a different one-photon resonant nondegenerate FWM process $\boldsymbol{E}_{F2}$ [14].

In the experiments, the sodium vapor is heated to 255℃ (with an atomic density of $3.6 \times 10^{13}\mathrm{cm}^{-3}$ approximately) when the typical gap solitons start to appear. The stronger dressing beams $\boldsymbol{E}_{1,2}'$ are approximately 10 times larger than the pump beams $\boldsymbol{E}_{1,2}$, and 1000 times larger than the weak probe beam $\boldsymbol{E}_3$ and the two generated FWM beams $\boldsymbol{E}_{F1,2}$. So, $\boldsymbol{E}_{1,2}'$ can strongly influence the signal beams $\boldsymbol{E}_{F1,2}$. The mathematical description of the self- and cross-Kerr nonlinearities of the weak beams $\boldsymbol{E}_{F1,2}$ can be obtained by numerically solving the following propagation equations:

$$\frac{\partial u_{F1}}{\partial Z} - \frac{\mathrm{i}\partial^2 u_{F1}}{2\partial \xi^2} = \frac{\mathrm{i}k_{F1}^2 w_0^2 I_1}{n_1}(n_2^{S1}|u_{F1}|^2 + 2n_2^{X1}|u_1'|^2 + 2n_2^{X2}|u_2'|^2)u_{F1}, \tag{8.62a}$$

$$\frac{\partial u_{F2}}{\partial Z} - \frac{\mathrm{i}\partial^2 u_{F2}}{2\partial \xi^2} = \frac{\mathrm{i}k_{F2}^2 w_0^2 I_1}{n_1}(n_2^{S2}|u_{F2}|^2 + 2n_2^{X3}|u_1'|^2 + 2n_2^{X4}|u_2'|^2)u_{F2}, \tag{8.62b}$$

where $Z = z/L_D$ ($L_D = k_1 w_0^2$ has the physical meaning of the Rayleigh range, and w_0 is the spot size of the probe beam); $\xi = x/w_0$ and y/w_0 are the longitudinal and transverse coordinates, respectively; $u_{F1,2} = A_{F1,2}/I_1^{1/2}$ and $u_{1,2}' = A_{1,2}'/I_1^{1/2}$ are the normalized amplitudes of the beams $\boldsymbol{E}_{F1,2}$ and $\boldsymbol{E}_{1,2}', k_{F1} = k_{F2} = \omega_1 n_1/c$, with n_1 being the linear refractive index. $n_2^{S1,2}$ are the self-Kerr indices for the $\boldsymbol{E}_{F1}$ and $\boldsymbol{E}_{F2}$ beams, respectively; n_2^{X1} is the cross-Kerr nonlinear coefficient of the weak field $\boldsymbol{E}_{F1}$ induced by the strong coupling field $\boldsymbol{E}_1', n_2^{X2}$ is the cross-Kerr nonlinear coefficient of the weak field $\boldsymbol{E}_{F1}$ induced by the strong coupling field $\boldsymbol{E}_2', n_2^{X3}$ is the cross-Kerr nonlinear coefficient of the weak field $\boldsymbol{E}_{F2}$ induced by the strong coupling field $\boldsymbol{E}_1'$, and n_2^{X4} is the cross-Kerr nonlinear coefficient of the weak field $\boldsymbol{E}_{F2}$ induced by the strong coupling field $\boldsymbol{E}_2'$; The FWM signal fields $\boldsymbol{E}_{F1}$ (from four perturbation chains) and $\boldsymbol{E}_{F2}$ (from two perturbation chains), dressed by $\boldsymbol{E}_1'$ and $\boldsymbol{E}_2'$, in Fig. 8.2(b) can be obtained by solving the density-matrix equations. Similarly, the cross-Kerr nonlinear coefficients [13, 16] are $n_2^{X1} \propto G_3|G_1'|^2/\eta_1$, $n_2^{X2} \propto G_3|G_2'|^2/\eta_2$, $n_2^{X3} \propto G_3|G_1'|^2/\eta_3$ and $n_2^{X4} \propto G_3|G_2'|^2/\eta_4$ in this two-level atomic system, where η_{1-4} represent the complex formulas with frequency detuning, relaxation rates and Rabi frequency of the dressing

fields.

The interference pattern from the beams $\boldsymbol{E}_1$ and $\boldsymbol{E}_1'$ (or $\boldsymbol{E}_2$ and $\boldsymbol{E}_2'$) induces the spatial grating (or the optical "lattice" with a period Λ) for generating the gap solitons, which are observed in the images captured by a CCD camera. The refractive index varies inside the spatial grating. We need to include both the frequency detuning and intensity dependences of the refractive index in addition to its one-dimensional periodic variation along the ξ axis by using $n(\Delta, I, \xi) = n_1(\Delta) + n_2(\Delta)I + \delta n(\xi)$, where I is the dressing field intensity. $\delta n = n_2 \cos(2\pi\xi/\Lambda)$ accounts for the periodic index variation inside the grating, with the refractive index contrast to be about $n_2(\Delta)I = 2.65 \times 10^{-4}$. The grating period is given by $\Lambda = \lambda/\theta \approx 10$ μm, where $\theta = 0.3°$ is the angle between the beams $\boldsymbol{E}_1$ and $\boldsymbol{E}_1'$ ($\boldsymbol{E}_2$ and $\boldsymbol{E}_2'$).

For simplicity, one can get $u_{F1,2} \approx u_0 \mathrm{sech}[u_0(k_{F1,2}^2 w_0^2 I_1 n_2^{S1,S2}/n_1)^{1/2}\xi]$ $\cos\phi_{NL}$, where the nonlinear phase shift $\phi_{NL}(z,\xi) = 2k_{F1,2}n_2 I e^{-[w_0'(\xi-1)]^2} z/n_1$ and w_0' is the spot size of the dressing beams. n_2 is negative for a self-defocusing medium while positive for a self-focusing medium. We assume Gaussian profiles for the input beams and solve. (Eg. 8.62) by using the commonly employed split-step method.

Figure 8.3 shows the splitting in the self-focusing region ($\Delta_1 < 0$) and forming of gap solitons in the self-defocusing region ($\Delta_1 > 0$) of the FWM signal $\boldsymbol{E}_{F1}$, and the nonlinear refractive index n_2 versus Δ_1. In the self-focusing side, while the nonlinear refractive index n_2 changes from the minimum to the maximum (left to right), $\boldsymbol{E}_{F1}$ beam breaks up from one to three parts, with one large and two small pieces. Thus, the $\boldsymbol{E}_{F1}$ beam in the self-focusing side propagates with discrete diffraction. However, in the self-defocusing side, where the n_2 changes from near zero to large negative value, E_{F1} beam breaks up into many peaks with an approximate fringe space of Λ and forms gap solitons, which is due to the nonlinear coupling between the laser beams in the Kerr nonlinear medium [4]. There only exists one spot at resonance where n_2 is close to zero. The reason is that according to the expression of nonlinear phase shift ϕ_{NL}, when n_2 is zero, $\phi_{NL}(y)$ becomes zero too. With increasing n_2, the oscillation frequency $w(n_2)$ ($\phi_{NL}(y) \approx w(n_2)y^2$), proportional to n_2 along ξ, gets big too. When the XPM-induced focusing [2–4] exactly compensates the diffraction, the beam becomes trapped and forms spatial solitons. Here, we have demonstrated a transition from a self-focusing to a self-defocusing region and from forming discrete to gap solitons solely by adjusting the nonlinear dispersion with frequency detuning [6].

With the temperature in the heat pipe oven increased gradually, the temperature effect on the FWM signal can be investigated. Figure 8.4 (a) presents intensity curves of the FWM signal $\boldsymbol{E}_{F2}$ under different temperatures. The beam profile of the FWM signal is quite irregular at low temperatures ($T = 230$ °C and 240 °C), but becomes more vivid at higher temperatures. The atomic density N is determined by the temperature in the atomic vapor, which is equivalent to the change in the propagation distance z. The

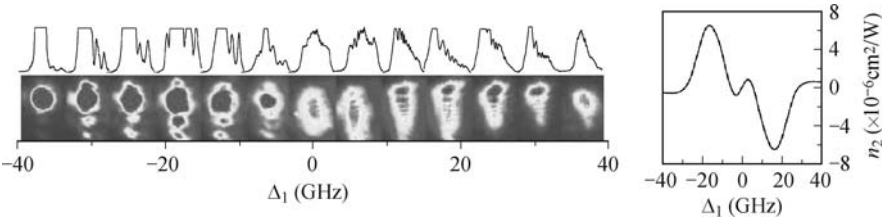

Fig. 8.3. Images (lower) and cross sections in the y-direction (upper) of $\boldsymbol{E}_{F1}$ signal versus Δ_1 in the two-level system with $G_1 = 1.2$ GHz, $G_1' = 15.2$ GHz and $G_3 = 0.5$ GHz at 250 ℃. The corresponding nonlinear dispersion is illustrated in the figure at the right side.

periodic refractive index of the medium is modulated by the term $\cos^2 \phi_{NL}$ in $u_{F1,2}^2$, which is the reason of forming the gap solitons in such system. Now, let us consider the influence of the dressing field on of the FWM signal, as shown in Fig. 8.4 (b). Gap soliton in the $\boldsymbol{E}_{F2}$ beam does not exist when the dressing field power (G_2') is low. When G_2' gets larger, the influence of the dressing field intensity on gap solitons becomes dramatic, and gap solitons obviously appear with $G_2' = 14.5$ GHz and $G_2' = 21.7$ GHz. This is due to the fact that for $\boldsymbol{E}_{F2}$, the gap solitons are induced by the interference patterns formed by $\boldsymbol{E}_2'$ and $\boldsymbol{E}_2$ beams. One can also explain this phenomenon with $\phi_{NL}(x)$, i.e., when the dressing field $\boldsymbol{E}_2'$ becomes stronger, the oscillation frequency $w(I)$ gets larger accordingly. Figure 8.4 (c) shows the difference of the FWM signal $\boldsymbol{E}_{F2}$ between the two-level and the V-type three-level systems. Apparently, the gap solitons in the FWM beam profile are more vivid in the two-level system than in the V-type three-level system. This is because the gap solitons of $\boldsymbol{E}_{F2}$ are caused by the interference between the $\boldsymbol{E}_2'$ and $\boldsymbol{E}_2$ beams, which are the inner dressing fields for the two-level system and have stronger cross-Kerr effect. However, for the V-type three-level system, these fields are the outer dressing fields and have a weaker cross-Kerr effect [16]. The dotted curves in Fig. 8.4 are the simulated results from the propagation equations with practical parameters used in the experiment, which show excellent agreements with the experimentally measured spatial profiles.

To get the steady gap solitons, the focusing effect due to the XPM should exactly compensate the spatial diffraction of the generated FWM signal beam. Figure 8.5 (a, b) show the trapped gap solitons of the $\boldsymbol{E}_{F1}$ and $\boldsymbol{E}_{F2}$ beams in the two-level system, respectively. As one can see that with increasing temperature, the spatial profiles of the $\boldsymbol{E}_{F1}$ and $\boldsymbol{E}_{F2}$ beams change very little (except with a breathing). This indicates that at certain probe frequency detuning and dressing field intensity, steady propagation of gap solitons (i.e., no change with increasing temperature) can be achieved.

Figure 8.6 presents an interesting phenomenon: splitting gap solitons. With $\boldsymbol{E}_2'$ field dressing, the $\boldsymbol{E}_{F2}$ beam forms gap solitons in the x-direction [Fig. 8.6 (i)]. Figure 8.6 (iii) shows the gap solitons in the x-direction and splitting in the y-direction with $\boldsymbol{E}_1'$ and $\boldsymbol{E}_2'$ dressing, respectively. One can

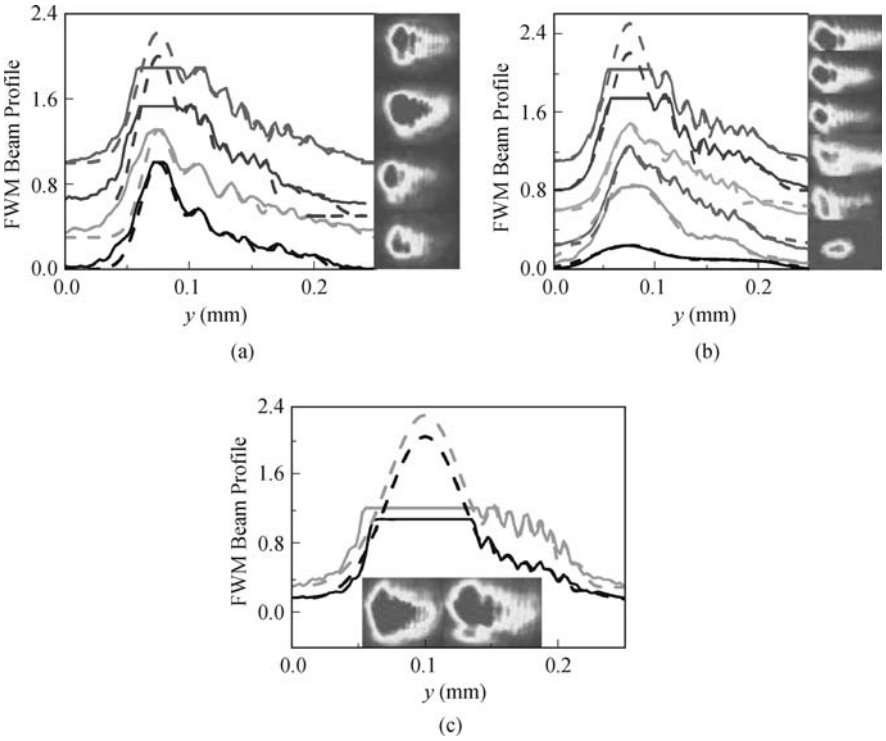

Fig. 8.4. (a) Cross-sections (left) and images (right) of $\boldsymbol{E}_{F2}$ beam in the two-level system versus Δ_1 with T=230, 240, 250 and 260 ℃, respectively (from down to up). (b) Cross-sections (left) and images (right) of $\boldsymbol{E}_{F2}$ beam in the two-level system versus Δ_1 with $G_2' = 0$, 4.8, 9.6, 14.5, 21.7, and 29.7 GHz, respectively (from down to up). (c) $\boldsymbol{E}_{F2}$ profile in two-level system and three-level V-type system. Inset: images of $\boldsymbol{E}_{F2}$ beam in the two-level system (left) and the three-level V-type system (right). The dotted curves are the theoretical results.

understand the formation of the splitting gap solitons [Fig. 8.6 (iii)] in the following. The dressing field $\boldsymbol{E}_2'$ and the signal field $\boldsymbol{E}_{F2}$ overlap partially in the x-direction [Fig. 8.2 (a)], so the influence of the intensity of the dressing field $\boldsymbol{E}_2'$ leads to the formation of gap solitons of $\boldsymbol{E}_{F2}$ in the x-direction. At the same time, the dressing field $\boldsymbol{E}_1'$ and the signal field $\boldsymbol{E}_{F2}$ overlap in the y-direction, which induces a splitting of the $\boldsymbol{E}_{F2}$ beam in the y-direction. Similarly, with the $\boldsymbol{E}_1'$ and $\boldsymbol{E}_2'$ dressings, $\boldsymbol{E}_{F1}$ beam shows the gap solitons in the y-direction and the splitting in the x-direction [Fig. 8.6 (iv)]. The cross sections of the $\boldsymbol{E}_{F1}$ and $\boldsymbol{E}_{F2}$ beam images in the y-direction and x-direction are shown in the right side of Fig. 8.6. Furthermore, interacting FWM gap soliton pairs of $\boldsymbol{E}_{F1}$ and $\boldsymbol{E}_{F2}$ beams can coexist in the same self-defocusing atomic system

Comparing with the gap solitons created in the photorefractive crystals, the gap solitons formed in the atomic medium are with flexible and easy to control parameters, such as atomic density, intensities of the dressing fields,

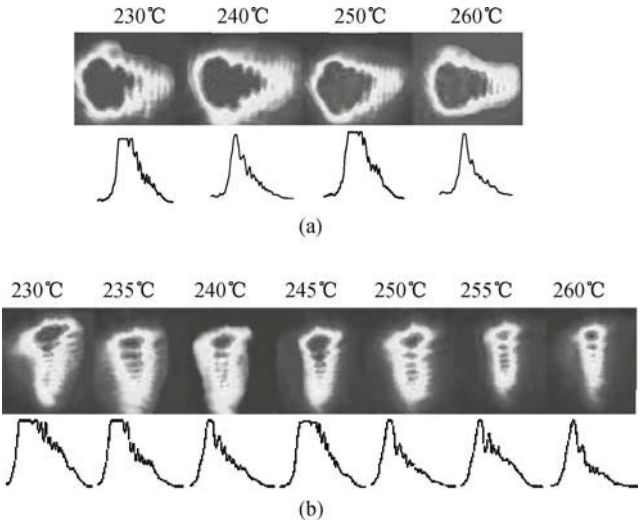

Fig. 8.5. (a) Images of the $\boldsymbol{E}_{F2}$ beam with $\boldsymbol{E}_2'$ dressing field in the two-level system with different temperatures from 230 ℃ to 260 ℃ with $G_2' = 15.2$ GHz and $\Delta_1 = 15.3$ GHz. (b) Images of the $\boldsymbol{E}_{F1}$ beam with $\boldsymbol{E}_1'$ dressing in the two-level system with different temperatures from 230 ℃ to 260 ℃ with $G_1' = 9.6$ GHz and $\Delta_1 = 14.2$ GHz.

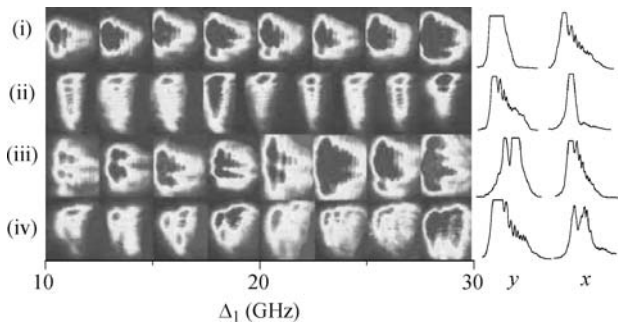

Fig. 8.6. Images of $\boldsymbol{E}_{F2}$ beam (i) with $G_2' = 14.5$ GHz and $\boldsymbol{E}_{F1}$ (ii) with $G_1' = 15.2$ GHz with different Δ_1 values. Images of $\boldsymbol{E}_{F2}$ (iii) and $\boldsymbol{E}_{F1}$ (iv) beams with $G_1' = 15.2$ GHz and $G_2' = 14.5$ GHz with different Δ_1 values in the two-level system. Corresponding cross sections of the $\boldsymbol{E}_{F1}$ and $\boldsymbol{E}_{F2}$ field in the y-direction (left) and x-direction (right) with $\Delta_1 = 14$ GHz, respectively.

and nonlinear dispersion.

8.3 Dipole-mode Spatial Solitons of Four-Wave Mixing

If a phase mask is used to introduce a certain phase delay for half of the soliton beam, the soliton can split into two parts with opposite (π) phases between them, called dipole-mode vector soliton with a Hermite-Gaussian mode structure [19, 20]. In an optically-induced two-dimensional photonic lattice, the dipole-mode solitons can be created with either opposite phases or same phase between the two parts [21]. Vector solitons with one nodeless fundamental component and another dipole-mode component can couple to each other and be trapped jointly in the photonic lattices [19, 22]. The radially symmetric vortex-mode solitons can decay into radially asymmetric dipole-mode solitons that have nonzero angular momentum, which can survive for very long propagation distances [19]. In the past few years, studying formations and properties of such novel spatial solitons has become an active field of research [1, 4, 19 – 29].

Such dipole-mode solitons can also be created in the FWM beams generated inside a multi-level atomic medium with greatly enhanced self-Kerr and cross-Kerr nonlinearities [13]. The key is to create a high enough index contrast (via Kerr nonlinearity $n_2 I$) in the atomic medium by laser-induced index gratings. This can be achieved at high atomic density and large pump laser powers with certain frequency detunings, so the Kerr nonlinear index n_2 is enhanced and at its maximum [16]. Two-component dipole-mode solitons are generated in two coexisting FWM signal beams in two- and three-level atomic systems. Interesting phenomena, such as energy exchange or breathing between soliton components, decays of more complicated vortex solitons into the dipole-mode ones, and suppression/enhancement of such dipole solitons, are also observed under various experimental conditions. The easy controls of the experimental parameters in the multi-level atomic systems make the current system ideal to investigate the formations of multi-component solitons and their nonlinear dynamics [23 – 25].

The laser beams are spatially aligned as shown in Fig. 8.7 (a). Four energy levels of Na atoms (in a heat-pipe oven) are involved in the three experimental configurations as shown in Fig. 8.7 (b – d). In Fig. 8.7 (b), energy levels $|0\rangle$ $(3S_{1/2})$, $|1\rangle(3P_{1/2})$ and $|2\rangle$ $(4D_{3/2})$ form a cascade three-level atomic system. Two fields E_1 and E_1' (with Rabi frequencies G_1 and G_1', and frequency ω_1) connecting transition $|0\rangle$ to $|1\rangle$, with a small angle $\theta_1 \approx 0.3^\circ$ between them, propagate in the opposite direction of a weak probe field E_3 (with Rabi frequency G_3 and frequency ω_1), as shown in Fig. 8.7 (a). The three beams are from the same near-transform-limited dye laser (10 Hz repetition rate, 5 ns pulse-width and 0.04 cm^{-1} linewidth). They generate an efficient one-photon resonant FWM signal E_{F1} satisfying the phase-matching condition of $\boldsymbol{k}_{F1} = \boldsymbol{k}_3 + \boldsymbol{k}_1 - \boldsymbol{k}_1'$, which propagates nearly opposite to the field E_1', and sampled by a CCD camera. Two additional coupling fields E_2 and E_2' (with Rabi frequencies G_2 and G_2', and a small angle $\theta_2 \approx 0.3^\circ$ between them) are applied between the transition $|1\rangle$ and $|2\rangle$, which are from another similar dye

laser with frequency ω_2. They, together with the probe beam E_3, generate a two-photon resonant FWM signal $\boldsymbol{E}_{F2}$ with $\boldsymbol{k}_{F2} = \boldsymbol{k}_3 + \boldsymbol{k}_2 - \boldsymbol{k}_2'$, propagating nearly opposite to the field E_2' [Fig. 8.7 (a)] [15, 16].

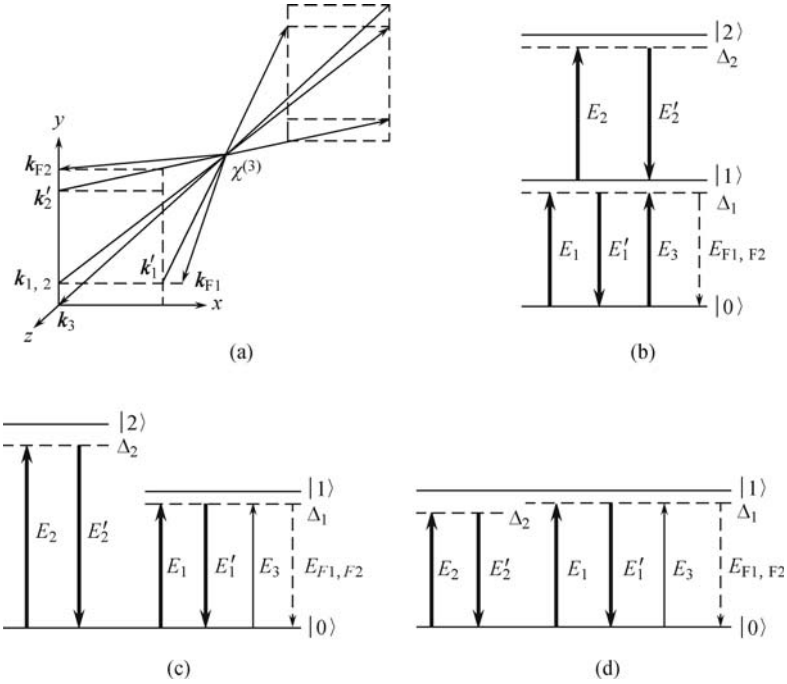

Fig. 8.7. (a) Spatial beam geometry used in the experiment. Two FWM processes E_{F1} and E_{F2} with five beams E_1, E_1', E_2, E_2', and E_3 on, in (b) cascade three-level, (c) V-type three-level, and (d) two-level atomic systems, respectively. E_{F1} and E_{F2} are mainly steered by the horizontally and vertically aligned beams E_1' and E_2'.

When the two fields E_2 and E_2' are tuned to the transition $|3S_{1/2}\rangle - |3P_{3/2}\rangle$, they generate another one-photon resonant nondegenerate FWM signal E_{F2} in the V-type three-level system [Fig. 8.7 (c)]. Also, when they are changed to the transition $|3S_{1/2}\rangle - |3P_{1/2}\rangle$, another one-photon resonant nondegenerate FWM signal E_{F2} is generated in the two-level system [Fig. 8.7 (d)]. Two-component dipole solitons are induced by the balanced interactions between the spatial diffractions and the cross-Kerr nonlinearities of the fields $E_{1,2}$ and $E_{1,2}'$. To generate dipole-mode solitons, the sodium atomic density needs to reach $2.9 \times 10^{13}\text{cm}^{-3}$ ($T = 250\ ^\circ\text{C}$), which can produce a variation in the nonlinear index of $\Delta n = 1.94 \times 10^{-4}$ at high enough laser intensities. The dipole-like patterns of E_{F1} and E_{F2} are created by the horizontally and vertically aligned beams E_1' and E_2' in Fig. 8.7 (a), respectively. One of the advantages of such spatial solitons is that the waveguiding effect is induced by focusing due to cross-Kerr nonlinearity of the FWM beam, not self-focusing with a catastrophic absorption [4].

A radially asymmetric dipole-mode vector soliton includes one nodeless component (probe beam E_3) and two dipole-like components with spatial structures of Hermite-Gaussian (HG_{10} for E_{F1} and HG_{01} for E_{F2}) modes. We mainly study the two coupled FWM beams E_{F1} and E_{F2} (with the same frequency), which have perpendicularly oriented dipole components, propagating along z direction and diffusing along a transverse direction. We assume $E_{F1} = A_{F1}(x)\exp(\mathrm{i}k_{F1}z)$, $E_{F2} = A_{F2}(x)\exp(\mathrm{i}k_{F2}z)$, and $E_{tot} = E_{F1} + E_{F2}$. Such the two coupled FWM fields satisfy the evolution equations in the Kerr medium as

$$\frac{\partial A_{F1}}{\partial z} - \frac{\mathrm{i}}{2k_{F1}}\frac{\partial^2 A_{F1}}{\partial x^2} = \frac{\mathrm{i}k_{F1}}{n_0}(n_2^{S1}|A_{F1}|^2 + 2n_2^{X1}|A_1|^2 + 2n_2^{X2}|A_1'|^2 + 2n_2^{X3}|A_2'|^2)A_{F1} + \eta_1 A_1(A_1')^* A_{F2}, \tag{8.63a}$$

$$\frac{\partial A_{F2}}{\partial z} - \frac{\mathrm{i}}{2k_{F2}}\frac{\partial^2 A_{F2}}{\partial x^2} = \frac{\mathrm{i}k_{F2}}{n_0}(n_2^{S2}|A_{F2}|^2 + 2n_2^{X4}|A_2|^2 + 2n_2^{X5}|A_2'|^2 + 2n_2^{X6}|A_1'|^2)A_{F2} + \eta_2 A_2(A_2')^* A_{F1}. \tag{8.63b}$$

The two-component dipole-mode solitons are natural results from such energy-dependent nonlinear propagation equations. $n_2^{S1,S2}$ are the self-Kerr nonlinear coefficients of E_{F1} and E_{F2}, and n_2^{X1-X6} are the cross-Kerr nonlinear coefficients due to fields $E_{1,2}$ and $E'_{1,2}$, respectively. The Kerr nonlinear coefficients are defined as $n_2 = Re\chi^{(3)}/(\varepsilon_0 c n_0)$. The third-order nonlinear susceptibility $\chi^{(3)} = D\rho_{10}^{(3)}$, where $D = N\mu_{10}^4/(\hbar^3\varepsilon_0 g G_i^2)$ with $g = G_{F1,2}$ (the Rabi frequencies of $E_{F1,2}$). N is the atomic density and μ_{10} is the dipole-matrix element between $|0\rangle$ and $|1\rangle$. For the cross-Kerr nonlinear coefficients of the weak FWM beams $E_{F1,2}$ induced by E_1' dressing, we have

$$\rho_{10}^{(3)} = -\mathrm{i}gG_1'^2[F_1^{-1} + (F_1^*)^{-1}][F_2^{-1} + (F_3^{-1})]F_1^{-1},$$

where $F_1 = d_1 + G_1'^2/[\Gamma_{11} + G_2'^2/d_2] + G_1'^2/\Gamma_{00} + G_2'^2/d_3$, $F_2 = \Gamma_{11} + G_1'^2[d_1^{-1} + (d_1^{-1})^*] + G_2'^2[d_2^{-1} + (d_2^{-1})^*]$, $F_3 = \Gamma_{00} + G_1'^2/(d_1 + G_2'^2 d_3^{-1}) + G_1'^2/[d_1^* + G_2'^2(d_2^*)^{-1}]$, $d_1 = \Gamma_{10} + \mathrm{i}\Delta_1$, $d_2 = \Gamma_{12} - \mathrm{i}\Delta_2$, $d_3 = \Gamma_{20} + \mathrm{i}(\Delta_1 + \Delta_2)$ for the cascade three-level system. Δ_1 and Δ_2 are the frequency detunings between the fields $E_{1,3,F1,2}$ and E_1' (E_2 and E_2'). Similarly, we can obtain other Kerr nonlinear coefficients.

The resulting superposition of the two perpendicular dipole soliton components, E_{F1} and E_{F2}, can be regarded as a generalization from a two-component dipole-mode soliton (E_3, E_F) to a three-component one (E_3, E_{F1}, E_{F2}). However, in the current case, the total intensity of E_{F1} and E_{F2} is approximately constant (two-component FWM dipole soliton $|E_F|^2 = |E_{F1}|^2 + |E_{F2}|^2$, where $E_{F1} = E_F\cos\psi$ and $E_{F2} = E_F\sin\psi$ with ψ being a transformation parameter), and the power of the probe beam is close to that of $E_{F1} + E_{F2}$. The total intensity ($I = |E_3|^2 + |E_{F1}|^2 + |E_{F2}|^2$) of the three components is quasi-stable in propagation after a long enough propagation

distance (or high enough atomic density). The three components of the solution carry topological charges 0, +1, −1, respectively, and the total angular momentum is zero, which makes the solution stable [24].

The in-phase dipole modes of E_{F1} and E_{F2} are created (or split) by the horizontally and vertically aligned beams E_1' and E_2', respectively. Thus, the two-component dipole-mode soliton solutions of E_{F1} and E_{F2} can be written as $E_{F1} \propto u_1 \operatorname{sec h}[u_1(k_{F1}n_2^{S1}/n_0)^{1/2}(r-r_1)]\cos(M\varphi/2)\exp(\mathrm{i}m_1\varphi + \mathrm{i}\phi_1)\exp(\mathrm{i}k_{F1}z)$ and $E_{F2} \propto u_2 \operatorname{sec h}[u_2(k_{F2}n_2^{S2}/n_0)^{1/2}(r-r_2)]\cos(M\varphi/2)\exp(\mathrm{i}m_2\varphi + \mathrm{i}\phi_2)\exp(\mathrm{i}k_{F2}z)$, where $u_{1,2}$ are soliton amplitudes; $r_{1,2}$ are initial peak positions; M is the number of intensity peaks; $m_{1,2}$ are topological charges; and $\phi_{1,2}$ are the nonlinear phase shifts ($\phi_{1,2} = 2k_{1,2}n_2I_{2,1}\mathrm{e}^{-r^2/2}z/n_0$). Such solutions possess the dipole-soliton characteristics with $m_{1,2} = \pm 1$, and two humps form the two poles of the dipole soliton.

The generated E_{F2} beam is dressed by G_1', G_1, or G_1' & G_1 in the cascade three-level system (Fig. 8.8). We present the vertical dipole-mode solitons of E_{F2} with different dressing configurations. The E_{F2} beam splits into two coherent spots (i.e., dipole pattern, as shown in Fig. 8.8) due to the modulated transverse nonlinear phase shift ϕ_2 induced by the vertically-aligned beam E_2'. At low nonlinear dispersion $|n_2|$, E_{F2} beam only experiences the linear diffraction. With maximum $|n_2|$ at $|\Delta_1| = 10$ GHz vertically-oriented dipole soliton is generated due to the balanced interaction between the spatial diffraction and the cross-Kerr nonlinearity. In the self-focusing region of the atomic medium (from $\Delta_1 = -30$ GHz to $\Delta_1 = -10$ GHz), there exists energy exchange between the two parts of the E_{F2} dipole mode. At resonance or large frequency detunings, the dipole-mode soliton of E_{F2} decays into a nodeless fundamental one. In dressing enhancement case [Fig. 8.8(a)], E_{F2} with both G_1' and G_1 dressing is stronger than with G_1' or G_1 dressing separately, or without dressing field. For stronger G_1', the dressing effect of G_1' is larger than that of G_1. In the suppressed case with dressing fields [Fig. 8.8 (b)] [15, 16], E_{F2} with both G_1' and G_1 dressing fields gets weaker than with G_1' or G_1 dressing separately, or without dressing field.

When five laser beams are turned on at the same time in the cascade three-level system, as shown in Fig. 8.9 (a), the probe beam acts as a fundamental nodeless soliton and propagates with a stable shape for different atomic densities (or effective propagation distances [4]). However, the beam shapes of E_{F1} and E_{F2} become quite different at different propagation distances (or atomic densities) showing rich dynamics. The probe, E_{F1} and E_{F2} beams have the same wavelength. E_{F1} beam has the dipole component with the horizontal orientation ($m_1 = -1$) while the $\boldsymbol{E}_{F2}$ beam has the vertical dipole component ($m_2 = +1$), which are induced by the horizontally- and vertically-aligned beams E_1' and E_2', respectively. During propagations of the E_{F1} and E_{F2} beams, energy flows back and forth between the two spots, so the dipole solitons of E_{F1} and E_{F2} survive with strong oscillation and breathing in propagation. The superposition of these modes shows intriguing dynamics, associated with rotation instability in $E_{F1} + E_{F2}$ [24]. The fun-

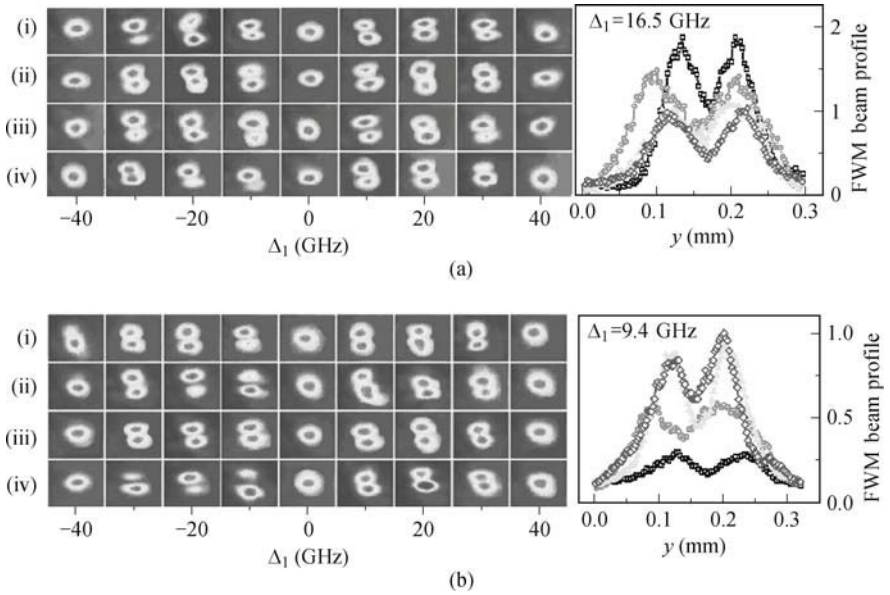

Fig. 8.8. Images (left) and profiles (right) of dipole-soliton component E_{F2} in the cascade three-level system at different frequency detunings in (a) enhanced or (b) suppressed case with $G_1' = 55$ GHz and $G_1 = 45$ GHz [(i) and square], $G_1' = 55$ GHz and $G_1 = 0$ [(ii) and circle], and $G_1' = 0$ and $G_1 = 45$ GHz [(iii) and triangle], and without dressing fields [(iv) and diamond]

damental probe soliton is stable, which has the stronger contribution to the total superposition mode.

Moreover, when the propagation distance increases gradually, one can see energy transfers among the probe, E_{F1} and E_{F2} beams [30]. The energy exchanges between the probe and $E_{F1} + E_{F2}$ components (start at a certain propagation distance), as shown in the right side of Fig. 8.9 (a). The total intensity of the probe, E_{F1} and E_{F2}reaches an equilibrium state (no energy exchange afterward) after a long interaction distance.

For different frequency detunings, the energy of the dipole soliton can be concentrated in one part or another. With Δ_1 changes from –26 GHz to –10 GHz in the self-focusing regime, energy flows from the left spot of E_{F1} (or upper spot of E_{F2}) to the right (or lower) spot. The symmetric behaviors appear in the positive frequency detuning (self-defocusing) side [Fig. 8.9 (b)]. Since the phase ϕ in the current dipole solution has values $0 < \phi < \pi$ (the out-of-phase repelling dipole soliton is more stable than the in-phase attracting one) [21, 22], energy exchange occurs. Because of the bounding effect induced by the cross-phase modulation (XPM) of the strong dressing field, energy will flow between the two parts of the dipole-mode soliton periodically.

Figure 8.9 (c) presents the discrete dipole soliton [26] of E_{F1} beam in the cascade three-level system, which is induced by periodic nonlinear refraction

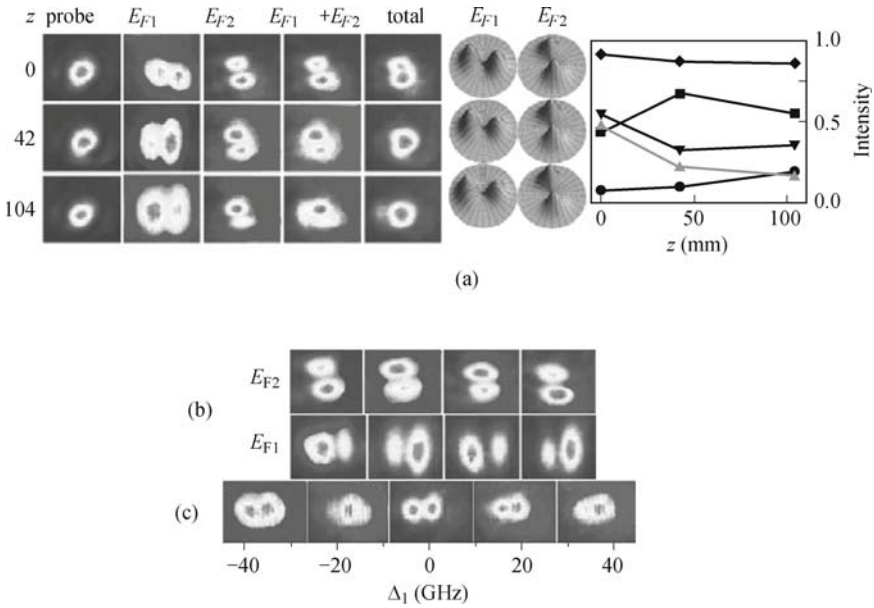

Fig. 8.9. (a) Experimental (left) and numerical (middle) results of three-component dipole solitons of probe, E_{F1} and E_{F2} with $z = 0$, 42, 104 in the cascade three-level system at $\Delta_1 = -15$ GHz, $\Delta_2 = -10$ GHz. Intensity changes (right) of dipole-soliton components during propagation for the probe (square), E_{F1} (circle), E_{F2} (triangle), $E_{F1} + E_{F2}$ (reverse triangle), and total (diamond) fields. (b) Breathing effects of E_{F1} (lower) and E_{F2} (upper) versus Δ_1. (c) Dipole soliton of E_{F1} only dressed by G_2 versus Δ_1 in the cascade three-level system.

due to the interference pattern of the two dressing beams G_1' and G_1. When Δ_1 is close to zero, the periodic modulation of the nonlinear refraction index via the interference pattern will disappear, i.e., the discrete dipole soliton decays into the general dipole soliton at resonance [Fig. 8.9 (c)].

Figure 8.10 (a) shows the evolutions of the three-component solitons (i.e., the nodeless probe, horizontal dipole-mode E_{F1} and vertical dipole-mode E_{F2} beams) versus Δ_1 in the cascade three-level system. The probe beam is a fundamental soliton, which propagates with a stable Gaussian shape for different frequency detunings. The E_{F1} dipole component is horizontally oriented while E_{F2} is the vertically oriented dipole mode. The dipole solutions can appear at different conditions for E_{F1} and E_{F2} beams. Also, a fundamental soliton can become a breathing dipole soliton for E_{F1} beam. E_{F2} beam also shows energy exchange between the dipole parts. Since the probe component is strong and stable, it dominates in the superimposed total images.

Since there exist three [Fig. 8.7 (c)] or five [Fig. 8.7 (d)] waves with the same frequency in the three-level V-type or two-level system in generating FWM E_{F1}, their spatial destructive interference patterns create certain phase

singularities or optical vortices [31, 32]. Figure 8.10(b) depicts evolutions of the two vector-soliton components, i.e. vortex-mode E_{F1} and dipole-mode E_{F2} beams, versus probe detuning in the three-level V-type system. The crescent vortex solitons [27] with the horizontal orientation of E_{F1} are observed at large detunings in both the self-focusing and self-defocusing sides, which decay into the modulated vortex soliton with the peak number $M = 3$ at $\Delta_1 = -41.5$ GHz. In the self-defocusing (positive detuning) side, the E_{F1} beam first becomes dipole-mode soliton, then breaks and forms the modulated vortex soliton with $M = 3$. The dipole soliton of E_{F2} rotates in the self-focusing regime, where energy exchange occurs within the dipole soliton. While in the self-defocusing case E_{F2} dipole soliton does not rotate, but becomes unstable and splits into three spots along the vertical direction, and finally returns to the stable dipole-mode soliton, as the frequency detuning changes from $\Delta_1 = 10.9$ GHz to $\Delta_1 = 67$ GHz.

Figure 8.10 (c) presents the evolutions of the three-component solitons of the dipole-mode probe (induced by the vertically-aligned beams E_1 and E_2), the vortex-mode E_{F1} (created by the interference pattern of the five waves in Fig. 8.7 (d)), and the dipole-mode E_{F2} (induced by the vertically-aligned beam E_2') beams versus probe detuning in the two-level system. The attraction between two in-phase spots in the probe beam leads to the generation of a fundamental nodeless soliton when $|n_2|$ is small. The repulsive interaction with large $|n_2|$ ($\Delta_1 = -47.3$ GHz) results in an increased relative separation between the two parts. Under the self-focusing condition ($\Delta_1 < 0$), the nodeless probe component first undergoes radial breaking into the dipole soliton. While for E_{F1}, the beam rotates, then splits into four spots ($M = 4$) with energy exchanging circularly, and finally fuses into a modulated vortex soliton induced by the interferences of the five waves [31,32]. However, for E_{F2}, the beam has the stable dipole spots where the energy current is bounded by the strong XPM. We also observed crescent vortex soliton ($\Delta_1 = -3.9, -2.1$ GHz) in the E_{F1} beam, and breathing vertical dipole soliton in the E_{F2} beam. Such bound effects are induced by the asymmetric energy flow in the transverse direction.

In conclusion, we have experimentally demonstrated controllable dipole-mode solitons for the generated FWM beams in the three-level cascade, the V-type, and the two-level atomic systems. These composite spatial solitons with perpendicularly-oriented dipole components are steady with the propagation distance variation. Energy exchanges occur between the two parts in the dipole solution. We also discussed the decays into the dipole soliton from the discrete dipole soliton of E_{F1} and vortex soliton, as well as the suppressed and enhanced dipole solitons under different dressing conditions. Theoretically simulated results match well with the experimentally observed phenomena. This study will help us to understand fundamental mechanisms in soliton formation and dynamics. It exploits new ways in controlling the diffraction of optical beams and designing new devices of spatial optical switching, and logic gating for optical communication and all-optical signal processing.

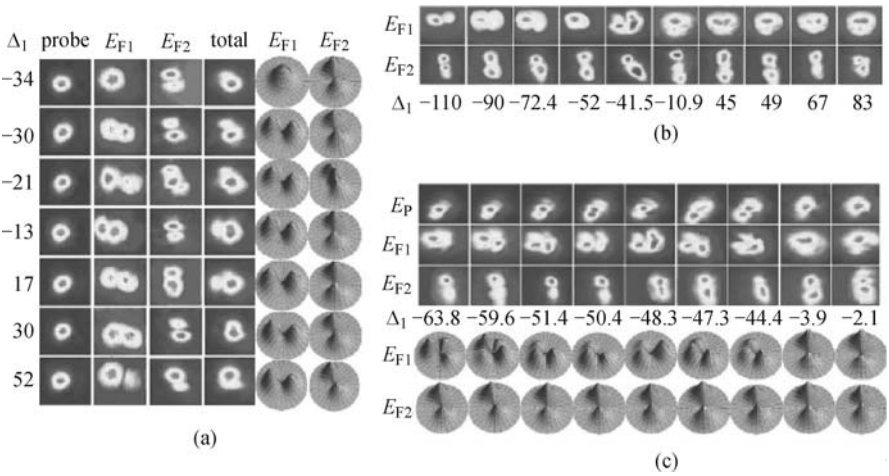

Fig. 8.10. (a) Families of the three-component dipole solitons of probe, E_{F1} and E_{F2} versus Δ_1 in the cascade three-level system. (b) Two perpendicular dipole components of E_{F1} and E_{F2} versus Δ_1 in the V-type three-level system. (c) Families of the three-component dipole-mode solitons of probe, E_{F1} and E_{F2} versus Δ_1 in the two-level system.

8.4 Modulated Vortex Solitons of Four-Wave Mixing

Vortices play important roles in many branches of physics [1]. The first experimental observation of optical vortex soliton was reported in a self-defocusing medium where the field propagates as a soliton, owing to the counterbalanced effects of diffraction and nonlinear refraction at the phase singularity [20]. Such singularity corresponding to vortices can exist in the Bose-Einstein condensates, which links the physics of superfluidity, phase transitions, and singularities in nonlinear optics [33 – 36]. The topological states of a Bose-Einstein condensate can be prepared experimentally [34]. Spatially modulated vortex solitons (azimuthons) have been theoretically considered in self-focusing nonlinear media [10]. Transverse energy flow occurs between the intensity peaks (solitons) associated with the phase structure, which is a staircase-like nonlinear function of the polar angle φ. The necklace-ring solitons can merge into vortex and fundamental solitons in dissipative media [37].

With the self-phase modulation, spatial bright soliton in self-focusing medium or dark soliton in the self-defocusing medium can be created [1]. Focusing effect can also be induced by XPM in a self-defocusing nonlinear medium [2]. In such case, the spatial soliton can form by balancing the spatial diffraction with the XPM-induced focusing [4]. Moreover, when three or more planewaves overlap in the medium, complete destructive interference patterns can give rise to phase singularities or optical vortices [31, 32, 38,

39], which are associated with zeros in the modulated light intensity patterns and can be recognized by specific helical wavefronts.

In this section, we present experimentally demonstration of the formations of modulated vortex solitons in two generated FWM waves in a two-level, as well as a cascade three-level, atomic systems. These vortex solitons are created by the interference patterns by superposing three or more waves, and by the greatly enhanced cross-Kerr nonlinear dispersion due to atomic coherence [13, 40].

Two relevant experimental systems are shown in Figs. 8.11 (a) and 8.11 (b). Three energy levels from Na atoms (the atomic vapor is heated with an atomic density of $5.6 \times 10^{13}\text{cm}^{-3}$ and a refractive index contrast of $\Delta n = n_2 I = 4.85 \times 10^{-4}$ approximately, where n_2 is the cross-Kerr nonlinear coefficient and I is the beam intensity) are involved in the experimental schemes. In Fig. 8.11 (b), energy levels $|0\rangle$ $(3S_{1/2})$, $|1\rangle(3P_{3/2})$ and $|2\rangle$ $(4D_{3/2,5/2})$ form a three-level cascade atomic system. When the energy level $|2\rangle$ is not used, the system reduces into a two-level one [Fig. 8.11 (a)]. The laser beams are aligned spatially as shown in Fig. 8.11 (c), with two dressing beams ($\boldsymbol{E}_1'$ and $\boldsymbol{E}_2'$) and two pump beams ($\boldsymbol{E}_1$ and $\boldsymbol{E}_2$) propagating through the atomic medium in the same direction with small angles (0.3°) between them in a square-box pattern. The probe beams ($\boldsymbol{E}_3$ and $\boldsymbol{E}_3'$) propagate in the opposite direction with a small angle as shown in Fig. 8.11 (c). Three laser beams ($\boldsymbol{E}_1$, $\boldsymbol{E}_1'$, and $\boldsymbol{E}_3$, with Rabi frequencies G_1, G_1', and G_3, connecting transition $|0\rangle$ to $|1\rangle$) have the same frequency ω_1 (from the same dye laser with a 10 Hz repetition rate, 5 ns pulse-width and 0.04 cm^{-1} line-width), and generate an efficient degenerate FWM signal $\boldsymbol{E}_{F1}$ ($\boldsymbol{k}_{F1} = \boldsymbol{k}_1 - \boldsymbol{k}_1' + \boldsymbol{k}_3$) [Fig. 8.11 (a)] in the direction shown at the lower right corner of Fig. 8.11 (c). These beams $\boldsymbol{E}_2$, $\boldsymbol{E}_2'$, and $\boldsymbol{E}_3'$ (with Rabi frequencies G_2, G_2' and G_3', and connecting the same transition $|0\rangle$ to $|1\rangle$ in the two-level system) are from another near-transform-limited dye laser of frequency ω_2, and produce a nondegenerate FWM signal $\boldsymbol{E}_{F2}$ ($\boldsymbol{k}_{F2} = \boldsymbol{k}_2 - \boldsymbol{k}_2' + \boldsymbol{k}_3$) [Fig. 8.11 (a)]. All laser beams are horizontally polarized. The diameters of the laser beams are about 25 μm. When the six laser beams are all on, there also exist other two FWM processes $\boldsymbol{k}_{F3} = \boldsymbol{k}_1 - \boldsymbol{k}_1' + \boldsymbol{k}_3'$ and $\boldsymbol{k}_{F4} = \boldsymbol{k}_2 - \boldsymbol{k}_2' + \boldsymbol{k}_3'$. However, the coexisting $\boldsymbol{E}_{F1}$ and $\boldsymbol{E}_{F2}$ are the dominant ones in the experiment due to phase-matching and chosen beam intensities [15, 40].

When $\boldsymbol{E}_2$ and $\boldsymbol{E}_2'$ are tuned to the $|1\rangle - |2\rangle$ transition, the system becomes a cascade three-level system [Fig. 8.11 (b)], which generates a two-photon resonant nondegenerate FWM process $\boldsymbol{E}_{F2}$ [15, 40].

The mathematical description of the two generated (dominant) FWM beams (including the self- and cross-Kerr nonlinearities) can be obtained by numerically solving the following propagation equations in cylindrical coor-

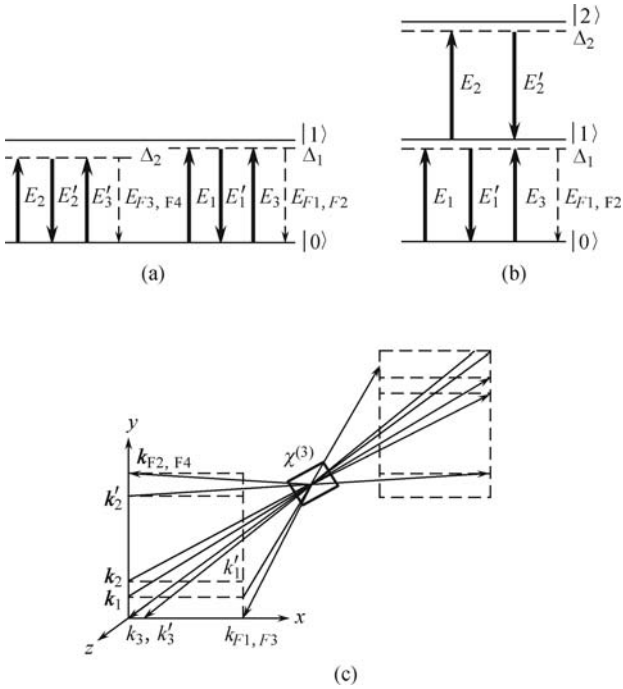

Fig. 8.11. Two FWM processes $\boldsymbol{k}_{F1}$ and $\boldsymbol{k}_{F2}$ with five beams $\boldsymbol{k}_1$, $\boldsymbol{k}_1'$, $\boldsymbol{k}_2$, $\boldsymbol{k}_2'$, $\boldsymbol{k}_3$, and $\boldsymbol{k}_3'$ in (a) two-level and (b) cascade three-level atomic systems, respectively, dressed by two beams $\boldsymbol{k}_1'$ and $\boldsymbol{k}_2'$. (c) Spatial beam geometry used in the experiment.

dinate:

$$\frac{\partial E_{F1}}{\partial z} - \frac{\mathrm{i}}{2k_{F1}}\left(\frac{1}{r}\frac{\partial E_{F1}}{\partial r} + \frac{\partial^2 E_{F1}}{\partial r^2} + \frac{1}{r^2}\frac{\partial^2 E_{F1}}{\partial \varphi^2}\right) = \frac{\mathrm{i}k_{F1}}{n_1}(n_2^{S1}\left|E_{F1}\right|^2 + 2n_2^{F1})E_{F1}, \tag{8.64a}$$

$$\frac{\partial E_{F2}}{\partial z} - \frac{\mathrm{i}}{2k_{F2}}\left(\frac{1}{r}\frac{\partial E_{F2}}{\partial r} + \frac{\partial^2 E_{F2}}{\partial r^2} + \frac{1}{r^2}\frac{\partial^2 E_{F2}}{\partial \varphi^2}\right) = \frac{ik_{F2}}{n_1}(n_2^{S2}\left|E_{F2}\right|^2 + 2n_2^{F2})E_{F2}, \tag{8.64b}$$

where $n_2^{F1} = \sum_{i=1}^{5}\Delta n_2^{Xi} = n_2^{X1}\left|E_3\right|^2 + n_2^{X2}\left|E_1\right|^2 + n_2^{X3}\left|E_2\right|^2 + n_2^{X4}\left|E_1'\right|^2 + n_2^{X5}\left|E_2'\right|^2$ and $n_2^{F2} = \sum_{i=6}^{10}\Delta n_2^{Xi} = n_2^{X6}\left|E_3\right|^2 + n_2^{X7}\left|E_1\right|^2 + n_2^{X8}\left|E_2\right|^2 + n_2^{X9}\left|E_1'\right|^2 + n_2^{X10}\left|E_2'\right|^2$. n_2^{S1-S2} are the self-Kerr nonlinear coefficients of $\boldsymbol{E}_{F1,2}$, respectively. n_2^{X1} is the cross-Kerr nonlinear coefficient of the field $\boldsymbol{E}_{F1}$ induced by the field $\boldsymbol{E}_3$, n_2^{X2} is the cross-Kerr nonlinear coefficient of

the field $\boldsymbol{E}_{F1}$ induced by the field $\boldsymbol{E}_1$, n_2^{X3} is the cross-Kerr nonlinear coefficient of the field $\boldsymbol{E}_{F1}$ induced by the $\boldsymbol{E}_2$, n_2^{X4} is the cross-Kerr nonlinear coefficient of the field $\boldsymbol{E}_{F1}$ induced by the field $\boldsymbol{E}_1'$, n_2^{X5} is the cross-Kerr nonlinear coefficient of the field $\boldsymbol{E}_{F1}$ induced by the field $\boldsymbol{E}_2'$, n_2^{X6} is the cross-Kerr nonlinear coefficient of the field $\boldsymbol{E}_{F2}$ induced by the field $\boldsymbol{E}_3$, n_2^{X7} is the cross-Kerr nonlinear coefficient of the field $\boldsymbol{E}_{F2}$ induced by the field $\boldsymbol{E}_1$, n_2^{X8} is the cross-Kerr nonlinear coefficient of the field $\boldsymbol{E}_{F2}$ induced by the field $\boldsymbol{E}_2$, n_2^{X9} is the cross-Kerr nonlinear coefficient of the field $\boldsymbol{E}_{F2}$ induced by the field $\boldsymbol{E}_1'$, and n_2^{X10} is the cross-Kerr nonlinear coefficient of the field $\boldsymbol{E}_{F2}$ induced by the field $\boldsymbol{E}_2'$. The Kerr nonlinear coefficients are defined as $n_2 = \mathrm{Re}\chi^{(3)}/(\varepsilon_0 c n_1)$. The third-order nonlinear susceptibility is given by $\chi^{(3)} = N_0\mu_{10}^4\rho_{10}^{(3)}/(\hbar^3\varepsilon_0 G_{3,F1,F2}G_i^2)$. N_0 is the atomic density. μ_{ij} is the dipole matrix element between transition $|i\rangle$ to $|j\rangle$. Δ_1 ($\Delta_2 = 0$) is the detuning of the fields $\boldsymbol{E}_{1,\,3}$ and $\boldsymbol{E}_1'$ ($\boldsymbol{E}_2$ and $\boldsymbol{E}_{2,\,3}'$) from the atomic transition. We can obtain these Kerr nonlinear coefficients of the FWM beams $\boldsymbol{E}_{F1,2}$ by calculating the density-matrix element $\rho_{10}^{(3)}$ [13, 40]. In addition, the Doppler effect and power broadening effect are considered in calculating these Kerr nonlinear coefficients.

Solving the propagation equations in the cylindrical coordinate, we demonstrate that the modulated vortex solitons with a screw-type dislocation phase can be characterized by two independent integer numbers [1,10] (i.e., the topological charge m and the number of intensity peak N), and parametrized by the rotating angular velocity (i.e., energy flow velocity) w. We can obtain the stationary transverse solution of the modulated vortex soliton as [10, 37] $E_{F1} \propto E\,\mathrm{sec\,h}[E(k_{F1}n_2^{S1}/n_1)^{1/2}(r-R_0)]\cos(N\varphi/2)\exp(im\varphi+i\phi_{NL})$ with an initial radius R_0. Moreover, we have $w_1 = \phi_{NL}(r,z)/z = 2k_{F1}n_2I_2\mathrm{e}^{-r^2/2}/n_1$, $w_2 = \phi_{NL}(r,z)/n_2 = 2k_{F1}I_2\mathrm{e}^{-r^2/2}z/n_1$ and $w_3 = \phi_{NL}(r,z)/I_2 = 2k_{F1}n_2\mathrm{e}^{-r^2/2}z/n_1$.

The spatial interference patterns are formed by superposing three or more waves ($\boldsymbol{E}_{1,\,2,\,3}$ and $\boldsymbol{E}_{1,\,2,\,3}'$) in the medium, as shown in Fig. 8.11 (c). The destructive interference of two waves with similar intensity can result in spatial patterns with zero intensities, which create phase singularities or optical vortices [32]. When multi-beam interference occurs, spatial polygon patterns (i.e, closed triangle from three beams, quadrangle from four beams, which gives one vortex point [31, 32].) can be formed, with the side lengths being the complex amplitude vectors of the waves. The polygons with more beams will look like a circular shape, and the phase complexity will be enhanced. The complex amplitude vectors can be overlaid at the observation plane and give rise to the total complex amplitude vector (C_X, C_Y) of the interfering planewaves [31, 32]. The local structures of the optical vortices are given by the polarization ellipse relation $C_X^2/(T_X^2+T_Y^2)\sin^2(\beta+\alpha) + C_Y^2/(T_X^2+T_Y^2)\cos^2(\beta+\alpha) = 1$, where $\beta = \arctan(T_X/T_Y)$ and α is the ellipse orientation. The ellipse axes T_X, T_Y are related to the spatial configuration (including the incident beam directions, phase differences between beams, etc.) and beam intensities.

The dressing beams $\boldsymbol{E}'_{1,\,2}$ are approximately 10 times stronger than the beams $\boldsymbol{E}_{1,\,2}$, 10^2 times stronger than the weak probe beams $\boldsymbol{E}_3$ and $\boldsymbol{E}'_3$, and 10^4 times stronger than the two generated FWM beams $\boldsymbol{E}_{F1,\,2}$. The generated weak beam $\boldsymbol{E}_{F1}$ (or $\boldsymbol{E}_{F2}$) partly overlaps with the strong beam $\boldsymbol{E}'_1$ (or $\boldsymbol{E}'_2$), and other stronger beams ($\boldsymbol{E}_{1,\,2,\,3}$, $\boldsymbol{E}'_3$) lie around them [Fig. 8.11 (c)]. As a result, the same frequency waves can interfere to the construct polarization ellipse, create phase singularity [31, 32], and induce local changes of the refractive index. The interference induces a vortex pattern with the superposed $n_2^{F1} = \sum_{i=1}^{5} \Delta n_2^{Xi}$ and $n_2^{F2} = \sum_{i=6}^{10} \Delta n_2^{Xi}$ (the center of such a vortex lies in the minimum of $n_2^{F1,2}$), and the horizontally- and vertically-aligned dressing fields $\boldsymbol{E}'_1$ and $\boldsymbol{E}'_2$ modulate a circular-type splitting, with three or four parts around the ellipse. Note that $\boldsymbol{E}'_1$ (or $\boldsymbol{E}'_2$) is the dominant dressing field of $\boldsymbol{E}_{F1}$ (or $\boldsymbol{E}_{F2}$). Such two contributions induce the vortices and splittings of $\boldsymbol{E}_{F1}$ (or $\boldsymbol{E}_{F2}$), and finally form the modulated vortex solitons in the two- and three-level atomic systems, as shown in Figs. 8.12–8.15 below.

Figure 8.12 (a) presents the effects of spatial dispersion on the FWM signal $\boldsymbol{E}_{F1}$ in the two-level system, which shows the splitting in the self-focusing region ($\Delta_1 < 0$) and formation of vortex solitons in the self-defocusing region ($\Delta_1 > 0$). In the self-focusing side, while the nonlinear refractive index n_2 increases from left to right, $\boldsymbol{E}_{F1}$ beam breaks up from one to three parts via $\phi_{NL}(n_2^{X4})$, with one large and two small pieces. Thus, the $\boldsymbol{E}_{F1}$ beam propagates with discrete diffraction in the self-focusing side. By contrast, in the $\Delta_1 > 0$ region, the strong dressing fields $\boldsymbol{E}'_{1,2}$ separate the $\boldsymbol{E}_{F1}$ beam into three spots along a ring ($N = 3$). Then these spots propagate through the induced spiral phase polarization ellipse. Such screw dislocations create a stationary beam structure with a phase singularity. The interference among the four beams ($\boldsymbol{E}_{1,3}$ and $\boldsymbol{E}'_{1,2}$) induced a modulated vortex pattern with $n_2^{F1} = \sum_{i=1, i\neq 3}^{5} \Delta n_2^{Xi}$. Finally, the $\boldsymbol{E}_{F1}$ beam spot decays into a modulated vortex soliton due to the balanced interaction between the spatial diffraction and the cross-Kerr nonlinearity. There are energy exchanges among three the spots, which rotate around the point of phase singularity. However, when n_2 is very small with large detuning or $\Delta_1 = 0$, the phase singularity disappears and the three spots fuse together into a stable fundamental spot.

Figure 8.12 (b) shows the modulated vortex solitons of $\boldsymbol{E}_{F1}$ for different intensities of the dressing field $\boldsymbol{E}'_2$ in the self-defocusing regime. With increasing $\boldsymbol{E}'_2$ intensity, the spiral phase of $\boldsymbol{E}_{F1}$ changes into jumping phase between two parts, and the modulated vortex soliton of $\boldsymbol{E}_{F1}$ decays into the dipole-mode soliton at the high intensity, which is created by the horizontally aligned beam $\boldsymbol{E}'_1$. Specifically, $\boldsymbol{E}_{F1}$ is circularly modulated by the horizontally-aligned $\boldsymbol{E}'_1$ and vertically-aligned $\boldsymbol{E}'_2$ beams. With $\boldsymbol{E}'_2$ getting stronger, $\boldsymbol{E}_{F1}$ is shifted away from $\boldsymbol{E}'_2$ and then splits into two parts by $\boldsymbol{E}'_1$.

The dominant phase of $\boldsymbol{E}_{F1}$ is changed gradually from a spiral phase evolution to a jumping phase (i.e., from interference among four beams $\boldsymbol{E}_{1,3}$, $\boldsymbol{E}'_{1,2}$ to the dressing of $\boldsymbol{E}'_1$.

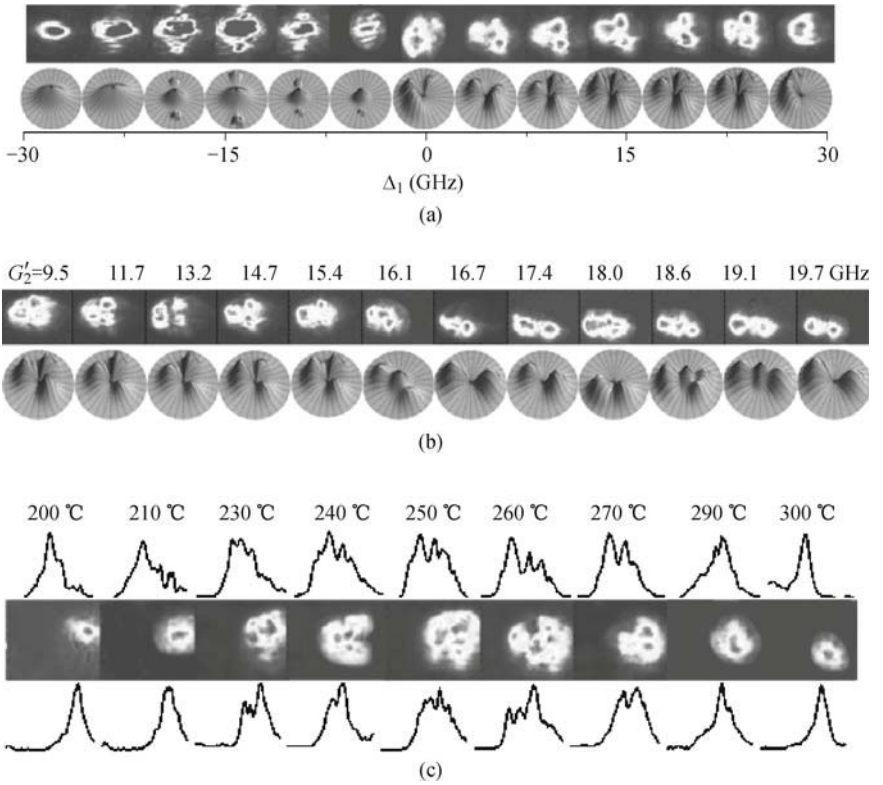

Fig. 8.12. (a) Images of $\boldsymbol{E}_{F1}$ versus Δ_1 with $G'_2 = 14.7$ GHz at 265 ℃. (b) Images of $\boldsymbol{E}_{F1}$ at $\Delta_1 = 8$ GHz with different values of G'_2 at 265 ℃. Upper and lower panels are for experimental and simulated results, respectively. (c) Images of $\boldsymbol{E}_{F1}$ at $\Delta_1 = 8$ GHz with different temperatures from 200 ℃ to 300 ℃. $G'_2 = 9.5$ GHz. Top and bottom rows are the cross sections in y and x directions, respectively. The parameters are $G'_1 = 12.7$ GHz, $G_1 = 1.8$ GHz, and $G_3 = 0.2$ GHz in the two-level system. Adopted from Ref. [36].

Figure 8.12 (c) shows $\boldsymbol{E}_{F1}$ soliton cluster with different temperatures between 200 ℃ and 300 ℃ in the two-level system. $\boldsymbol{E}_{F1}$ beam is a single spot at both low and high temperature sides. The single spot breaks up into several fragments (soliton cluster) as the temperature increases from 200 ℃ to 240 ℃, the nonlinear phase ϕ_{NL} gets larger as the temperature (equivalent to propagation distance z) rises, which leads to several splitting parts with weak absorption. As the temperature gets higher with an increased absorption, the beam intensity decreases. ϕ_{NL} (proportional to both beam intensity and propagation distance z) reaches its optimal value at 250 ℃. Moreover, the

soliton cluster of $\boldsymbol{E}_{F1}$ results from two contributions in the two-level system: (i) the interference among the four waves ($\boldsymbol{E}_{1,3}$, $\boldsymbol{E}'_{1,2}$) with the same frequency induces an interference pattern with $n_2^{F1} = \sum_{i=1,i\neq 3}^{5} \Delta n_2^{Xi}$, and (ii) $\boldsymbol{E}'_{1,2}$ induce a beam splitting via $\phi_{NL}(n_2^{X4})$ and $\phi_{NL}(n_2^{X5})$. As temperature gets even higher, the dressing beams are significantly absorbed by the hot atoms, so their intensities are reduced and the cross Kerr nonlinear effects are gradually weakened too. Under such condition, the spots merge into a single spot due to strong absorption. So the ideal temperature for the modulated vortex soliton is around 265 ℃ for the given experimental conditions (i.e., the modulated vortex soliton can be obtained at a certain propagation distance).

In the cascade three-level system with five laser beams ($\boldsymbol{E}_{1,2,3}$, $\boldsymbol{E}'_{1,2}$) on, the frequencies of $\boldsymbol{E}_2$ and $\boldsymbol{E}'_2$ are different from $\boldsymbol{E}_{1,3}$ and $\boldsymbol{E}'_1$. The interference $\left(n_2^{F2} = \sum_{i=6,i\neq 8}^{9} \Delta n_2^{Xi}\right)$ among three beams $\boldsymbol{E}_1$, $\boldsymbol{E}'_1$, and $\boldsymbol{E}_3$ induces a rotating vortex. Figure 8.13 (a, b) show the rotating vortices of the FWM beams with three spots ($N = 3$) for different frequency detunings. Here, the ellipse orientation α approaches to zero and $T_X/T_Y \approx 1.1$. From $I \propto \cos^2(N\varphi/2)\cos^2(m\varphi + \Omega_2|n_2|)$ with $\Omega_2 = \mathrm{sgn}[n_2]w_2$ ($I_2 = 51$ W/cm^2, $r = 0.25$ mm), $\boldsymbol{E}_{F2}$ circumvolves anticlockwise with $n_2 > 0$ and $\Omega_2 = 1.63 \times 10^3$ W/cm$^2 > 0$ in the self-focusing regime [Fig. 8.13 (a)], while moves clockwise with $n_2 < 0$ and $\Omega_2 = -1.63\times 10^3$ W/cm$^2 < 0$ in the self-defocusing regime [Fig. 8.13 (b)].

Figure 8.13 (c) presents the stationary solitons with $w_2 = 0$ in the cascade three-level system. n_2^{X4} can be a positive value with resonant dressing of $\boldsymbol{E}'_1$. When n_2^{X1} and n_2^{X2} have negative values under the self-defocusing condition, the superposed $n_2^{F1} = \sum_{i=1,i\neq 3}^{4} \Delta n_2^{Xi}$ is close to zero (or $\phi_{NL} \approx 0$). Under this condition, a uniform energy flow exists along the ring, and nonrotating ($w_2 = 0$) spatially-localized multihump structures can be obtained.

Comparing to the three-level system, there exist five nearly degenerate frequency waves ($\boldsymbol{E}_{1,\,2,\,3}$, $\boldsymbol{E}'_{1,\,2}$) in the two-level system. Figure 8.14 (a) shows the rotating vortices of the FWM beam with four spots ($N = 4$) for different frequency detunings in the two-level system. The modulated vortex pattern ($N = 4$) of $\boldsymbol{E}_{F2}$ is induced by the interference of five waves, and the nonresonant dressing field $\boldsymbol{E}'_2$ induces a splitting via $\phi_{NL}(n_2^{X10})$. For $\boldsymbol{E}_{F2}$, $\boldsymbol{E}'_2$ is the nonresonant dressing field, energy flow exists along the ring of spots unequally, inducing a modulated vortex [Fig. 8.14 (a)].

In Fig. 8.14 (b), there exists a stationary, four-spot modulated vortex soliton with $N = 4$ and non-uniform energy distribution for different detunings in the two-level system. The vortex pattern (horizontally-oriented polarization ellipse with $\alpha = 0$ and $T_X/T_Y = 1.5$) is induced by the interference of the

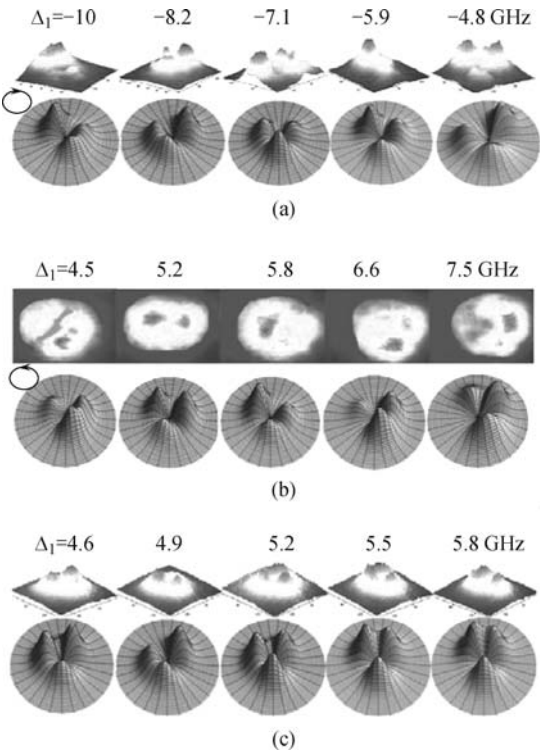

Fig. 8.13. The rotating $\boldsymbol{E}_{F2}$ solitons with (a) $\Omega_2 > 0$ and (b) $\Omega_2 < 0$ versus Δ_1. (c) Stationary nonrotating $\boldsymbol{E}_{F1}$ solitons ($w_2 = 0$) versus Δ_1. Lower images are the simulated results ($N = 3$, $m = 1$). The parameters are $G_2' = 19.7$ GHz, $G_1' = 12.7$ GHz, $G_1 = 1.8$ GHz, $G_2 = 1.1$ GHz, and $G_3 = 0.2$ GHz in the cascade three-level system at 265 ℃.

five beams. With the nonresonant dressing of $\boldsymbol{E}_2'$, all terms in n_2^{F2} have the same negative sign [Fig. 8.14 (a)], but the positive n_2^{X4} in $n_2^{F1} = \sum_{i=1}^{5} \Delta n_2^{Xi}$ has an opposite sign with the other terms $n_2^{X1,2,3,5}$ in n_2^{F1} due to the resonant dressing of $\boldsymbol{E}_1'$, so one can get $n_2^{F1} \approx 0$. Therefore, there exist four spots in the stationary ($\phi_{NL} \approx 0$) modulated vortex soliton of $\boldsymbol{E}_{F1}$ with $N = 4$ and energy is mainly stored in one diagonal pair of spots [Fig. 8.14 (b)], which results from the resonant dressing of $\boldsymbol{E}_1'$.

The radially symmetric vortex solitons ($m = 1$) in a self-defocusing medium are depicted in Fig. 8.15 (a, b), which separately demonstrate vortices and steady crescent FWM vortex solitons under different temperatures (atomic densities). The effective propagation distance z increases with the temperature. According to the solution of Eq. (8.3) $E_{F2} \propto E \operatorname{sec h}[E(k_{F2} n_2^{S2}/n_1)^{1/2}(r - R_0)] \cos(N\varphi/2) \exp(\mathrm{i}m\varphi + \mathrm{i}w_1 z)$, the spots rotate with an angular

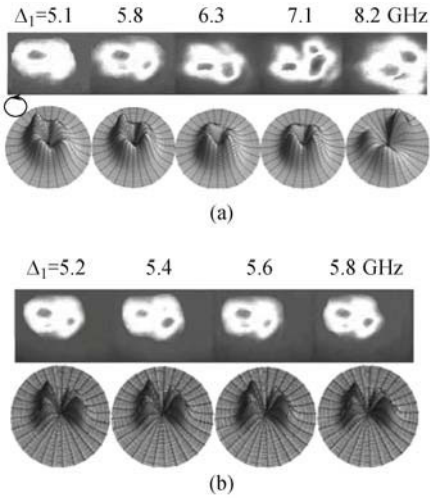

Fig. 8.14. (a) Anticlockwise rotating ($\Omega_2 = -1.53 \times 10^3$ W/cm^2)$\boldsymbol{E}_{F2}$ solitons and (b) stationary nonrotating $\boldsymbol{E}_{F1}$ solitons with four spots versus Δ_1 at 265 ℃ in the two-level system. Lower images are simulated ($N = 4$, $m = 1$) results. The parameters are $G_2' = 15$ GHz, $G_1' = 12.7$ GHz, $G_1 = 1.8$ GHz, $G_2 = 1.1$ GHz, and $G_3 = 0.2$ GHz.

velocity w_1. In the two-level system with $n_2^{F2} = \sum_{i=6, i\neq 7}^{10} \Delta n_2^{Xi}$, the vortex pattern of $\boldsymbol{E}_{F2}$ is induced by the interference of $\boldsymbol{E}_{2,3}$, $\boldsymbol{E}_{1,2}'$ while the dressing fields $\boldsymbol{E}_{1,2}'$ generate the circular splittings. Here, $\boldsymbol{E}_{F2}$ forms a crescent FWM modulated vortex soliton with an anticlockwise rotation [Fig. 8.15 (a)], Moreover, $w_1 z$ changes 300° from 245 ℃ to 275 ℃. When setting $z = 1$ at 245 ℃, we obtain $w_1 = -1.1$ rad/m, which is close to the theoretical value of $w_1 = -1.03$ rad/m. However, in Fig. 8.15 (b) with the resonant dressing $\boldsymbol{E}_1'$ and $n_2^{F1} = \sum_{i=1, i\neq 3}^{5} \Delta n_2^{Xi} \approx 0$, $\boldsymbol{E}_{F1}$ beam becomes a stationary vortex soliton at certain I_1 and z values.

Last, we let all six beams on, and set the $\boldsymbol{E}_{1,\,2,\,3}$ and $\boldsymbol{E}_3'$ beams just 10 times weaker than the dressing beams $\boldsymbol{E}_{1,\,2}'$. Figure 8.15 (c) shows the optical vortices created by the interferences of three, four, five, six waves (and the dressing fields) in the two-level system, respectively. Initially, there are three beams $\boldsymbol{E}_{1,\,3}$, $\boldsymbol{E}_1'$ on, which create the image 3 in Fig. 8.15 (c) As fourth interference beam $\boldsymbol{E}_2'$ is added, the split spots change from two to three [Image 4 in Fig. 8.15 (c)]. Similarly, as beams $\boldsymbol{E}_2$ and $\boldsymbol{E}_3'$ are added gradually, the interference beams increase from four to five (Image 5); and then to six (Image 6), the split spots in the vortex patterns of $\boldsymbol{E}_{F1}$ then change from three to four, and then to six, respectively, along the ring, and the shape of the vortex ellipse tends to become more circular. The final

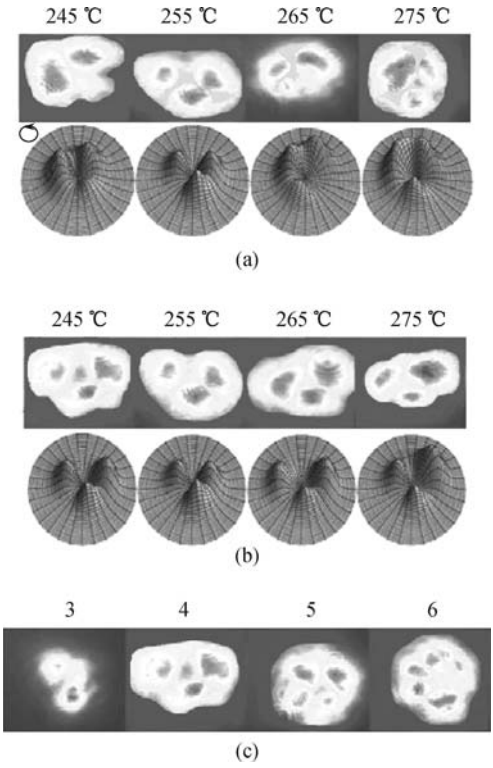

Fig. 8.15. Under different temperatures, (a) the rotating $\boldsymbol{E}_{F2}$ solitons ($w_1 = -1.1$rad/m) with $\boldsymbol{E}_{2,3}$ and $\boldsymbol{E}'_1$ on, and (b) stationary nonrotating $\boldsymbol{E}_{F1}$ solitons ($w_1 = 0$) with $\boldsymbol{E}_{1,3}$ and $\boldsymbol{E}'_{1,2}$ on. Lower images are simulation ($N = 3$, $m = 1$) results. (c) Optical vortices of $\boldsymbol{E}_{F1}$ formed by the interferences of three, four, five, and six waves at 265 ℃, respectively. The parameters are $G'_2 = 19.7$ GHz, $G'_1 = 12.7$ GHz, $G_1 = 1.8$ GHz, $G_2 = 1.1$ GHz, $G_3 = G'_3 = 0.2$ GHz, and $\Delta_1 = 6$ GHz in the two-level system.

superposition nonlinear index is $n_2^{F1} = \sum_{i=1}^{5} \Delta n_2^{Xi} + n_2^{X11} |E'_3|^2$, where n_2^{X11} is the nonlinear index induced by $\boldsymbol{E}'_3$. The FWM modulated vortex solitons are created jointly by the effects of the complex patterns induced by the multiple interference waves [31, 32] and the cross-Kerr nonlinear dispersions induced by the dressing field [4].

In conclusion, we have experimentally demonstrated controllable modulated vortex solitons of the degenerate and nondegenerate FWM beams created by the interference patterns via the superposing three or more waves and the cross-Kerr nonlinear dispersion due to atomic coherence in the two-level and cascade three-level atomic systems. The vortex angular velocity and intensity split peaks of the FWM modulated vortex solitons can be controlled by laser intensities, nonlinear dispersion, as well as atomic density. Our theo-

retical model can explain the observed FWM modulated vortex solitons very well. The current study has opened the door to understand better the formation and dynamics of complex vortex solitons, especially in multi-level atomic media, in which more parameters can be easily controlled. Understanding the formation and control of complex solitons can lead to potential applications in soliton communications and computations.

In this chapter, we have experimentally demonstrated controllable gap solitons, dipole-mode solitons, and modulated vortex solitons of FWM beams. The modulated vortex solitons are created by the interference patterns via the superposing three or more waves and the cross-Kerr nonlinear dispersion due to atomic coherence. Comparing with the gap, dipole-mode, and modulated vortex solitons created in the photorefractive crystals, spatial solitons formed in the atomic medium are with flexible and easy to control parameters, such as atomic density, intensities of the dressing fields, and nonlinear dispersion. These studies will help us to understand fundamental mechanisms in soliton formation and dynamics. It exploits new ways in controlling the diffraction of optical beams and designing new devices of spatial optical switching, and logic gating for optical communication and all-optical signal processing.

References

[1] Kivshar Y S, Agrawal G P. Optical solitons: from fibers to photonic crystals academic. San Diego: Academic, 2003.

[2] Agrawal G P. Induced focusing of optical beams in self-defocusing nonlinear media. Phys Rev Lett, 1990, 64: 2487 – 2490.

[3] Stentz A. J, Kauranen M, Maki J J, et al. Induced focusing and spatial wave breaking from cross-phase modulation in a self-defocusing medium. Opt Lett, 1992, 17: 19 – 21.

[4] Bortman-Arbiv D, Wilson-Gordon A D, Friedmann H. Induced optical spatial solitons. Phys Rev A, 1998, 58: 3403 – 3406.

[5] Chen Z G, Martin H, Eugenieva E D, et al. Formation of discrete solitons in light-induced photonic lattices. Opt Express, 2005, 13: 1816 – 1826.

[6] Zhang P, Liu S, Zhao J, et al. Optically induced transition between discrete and gap solitons in a nonconventionally biased photorefractive crystal. Opt Lett, 2008, 33: 878 – 880.

[7] Neshev D, Sukhorukov A A, Hanna B, et al. Controlled generation and steering of spatial gap solitons. Phys Rev Lett, 2004, 93: 083905.

[8] Kartashov Y V, Vysloukh V A, Torner L. Surface gap solitons. Phys Rev Lett, 2006, 96: 073901.

[9] Rosberg C R, Neshev D N, Krolikowski W, et al. Observation of surface gap solitons in semi-infinite waveguide arrays. Phys Rev Lett, 2006, 97: 083901.

[10] Desyatnikov A S, Sukhorukov A A, Kivshar Y S. Azimuthons: spatially modulated vortex solitons. Phys Rev Lett, 2005, 95: 203904.

[11] Eggleton B J, Slusher R E, de Sterke C M, et al. Bragg grating solitons. Phys Rev Lett, 1996, 76: 1627 – 1630.

[12] Eiermann B, Anker T, Albiez M, et al. Bright bose-einstein gap solitons of atoms with repulsive interaction. Phys Rev Lett, 2004, 92: 230401.

[13] Wang H, Goorskey D, Xiao M. Enhanced Kerr nonlinearity via atomic coherence in a three-level atomic system. Phys Rev Lett, 2001, 87: 073601.

[14] Zheng H B, Zhang Y P, Nie Z Q, et al. Interplay among multidressed four-wave mixing processes. Appl Phys Lett, 2008, 93: 241101.

[15] Zhang Y P., Khadka U, Anderson B, et al. Temporal and spatial interference between four-wave mixing and six-wave mixing channels. Phys Rev Lett, 2009, 102: 013601.

[16] Zhang Y P, Nie Z Q, Zheng H B, et al. Electromagnetically induced spatial nonlinear dispersion of four-wave mixing. Phys Rev A, 2009, 80: 013835.

[17] Vudyasetu P K, Camacho R M, Howell J C. Storage and retrieval of multimode transverse images in hot atomic rubidium vapor. Phys Rev Lett, 2008, 100: 123903.

[18] Boyer V, Marino A M, Pooser R C, et al. Entangled images from four-wave mixing. Science, 2008, 321: 544 – 547.

[19] Krolikowski W, Ostrovskaya E A, Weilnau C, et al. Observation of dipole-mode vector solitons. Phys Rev Lett, 2000, 85: 1424 – 1427.

[20] Swartzlander G A, Law C T. Optical vortex solitons observed in kerr nonlinear media. Phys Rev Lett, 1992, 69: 2503 – 2506.

[21] Yang J K, Makasyuk I, Bezryadina A, et al. Dipole solitons in optically induced two-dimensional photonic lattices. Opt Lett, 2004, 29: 1662 – 1664.

[22] Chen Z G, Bezryadina A, Makasyuk I, et al. Observation of two-dimensional lattice vector solitons. Opt Lett, 2004, 29: 1656 – 1658.

[23] Desyatnikov A S, Kivshar Y S. Necklace-ring vector solitons. Phys Rev Lett, 2001, 87: 033901.

[24] Desyatnikov A S, Kivshar Y S, Motzek K, et al. Multicomponent dipole-mode spatial solitons. Opt Lett, 2002, 27: 634 – 636.

[25] Neshev D, McCarthy G, Krolikowski W, et al. Dipole-mode vector solitons in anisotropic nonlocal self-focusing media. Opt Lett, 2001, 26: 1185 – 1187.

[26] Tang L G, Lou C B, Wang X S, et al. Observation of dipole-like gap solitons in self-defocusing waveguide lattices. Opt Lett, 2007, 32: 3011 – 3013.

[27] He Y J, Malomed B A, Mihalache D, et al. Crescent vortex solitons in strongly nonlocal nonlinear media. Phys Rev A, 2008, 78: 023824.

[28] Becker C, Stellmer S, Soltan-Panahi P, et al. Oscillations and interactions of dark and dark-bright solitons in Bose-Einstein condensates. Nature Phys., 2008, 4: 496 – 501.

[29] Liu X X, Pu H, Xiong B, et al, Formation and transformation of vector solitons in two-species Bose-Einstein condensates with a tunable interaction. Phys Rev A, 2009, 79: 013423.

[30] Zhang Y P, Anderson B, Xiao M. Efficient energy transfer between four-wave-mixing and six-wave-mixing processes via atomic coherence. Phys Rev A, 2008, 77: 061801.

[31] Leach J, Dennis M R, Courtial J, et al. Laser beams: knotted threads of darkness. Nature, 2004, 432: 165.

[32] O'Holleran K, Padgett M J. Topology of optical vortex lines formed by the interference of three, four, and five plane waves. Opt Express, 2006, 14: 3039 – 3044.

[33] Anderson B P, Haljan P C, Regal C A, et al. Watching dark solitons decay into vortex rings in a Bose-Einstein condensate. Phys Rev Lett, 2001, 86: 2926 – 2929.

[34] Williams J E, Holland M J. Preparing topological states of a Bose-Einstein condensate. Nature, 1999, 401: 568 – 572.

[35] Matthews M R, Anderson B P, Haljan P C, et al. Vortices in a Bose-Einstein condensate. Phys Rev Lett, 1999, 83: 2498 – 2501.

[36] Zhang Y P, Nie Z Q, Zhao Y, et al. Modulated vortex soliton of four-wave mixing. Opt Express, 2010, 18: 10963.

[37] He Y J, Malomed Boris A, Wang H Z. Fusion of necklace-ring patterns into vortex and fundamental solitons in dissipative media. Opt Express, 2007, 15: 17502 – 17508.

[38] Soskin M S, Gorshkov V N, Vasnetsov M V. Topological charge and angular momentum of light beams carrying optical vortices. Phys Rev A, 1997, 56: 4064 – 4075.

[39] Jiang W, Chen Q F, Zhang Y S, et al. Computation of topological charges of optical vortices via nondegenerate four-wave mixing. Phys Rev A, 2006, 74: 043811.

[40] Zhang Y P, Zuo C C, Zheng H B, et al. Controlled spatial beam splitter using four-wave-mixing images. Phys Rev A, 2009, 80: 055804.

Index